0830-H-10
312

NAS1.55:3083

NASA Conference Publication 3083

AUG 10 1990

Fire Science Results 1988

Proceedings of a conference held in
Vail, Colorado
July 11–15, 1988

DW

NASA Conference Publication 3083

Fire Science Results 1988

Edited by
David S. McDougal and H. Scott Wagner
NASA Langley Research Center
Hampton, Virginia

Proceedings of a conference sponsored by
the National Aeronautics and Space Administration,
the National Science Foundation, the Office of Naval
Research, the Department of Energy, the Air Force
Geophysics Laboratory, and the National Oceanic and
Atmospheric Administration, and held in
Vail, Colorado
July 11–15, 1988

NASA
National Aeronautics and
Space Administration
Office of Management
Scientific and Technical
Information Division
1990

I

PREFACE

FIRE is the FIRST ISCCP Regional Experiment, a U.S. program formed in 1984 to increase our basic understanding of cirrus and marine stratocumulus cloud systems, to develop realistic parameterizations for these cloud systems, and to validate and improve ISCCP cloud parameters. The Science Meeting held in Vail, Colorado, July 11-15, 1988, highlighted presentations of results based on FIRE research activities focusing on these objectives over the first 4 years of FIRE.

This Conference Publication contains the full text of the extended abstracts of papers presented at the FIRE Science Meeting. The presentations described important elements of the FIRE Intensive Field Observations (IFO), the Extended Time Observations (ETO), and modeling activities. Judging from the research results presented at the meeting, it is apparent that the FIRE science community has made significant progress in the analysis of the data collected at the 1986 Cirrus IFO, the 1987 Marine Stratocumulus IFO, and the ETO.

In order to keep this volume to a manageable size and to encourage authors to complete their papers and submit them to refereed journals, summaries were restricted to a maximum of 5 pages.

The managers of the sponsoring agencies wish to express their thanks and appreciation to the FIRE investigators, not only for their conscientious and skillful efforts in preparation for and displayed at this meeting, but also for their scientific enthusiasm and dedication that they have exhibited during the first 4 years of FIRE.

We are pleased to acknowledge the contributions of the session chairmen: Thomas P. Ackerman, Bruce A. Albrecht, Philip H. Austin, James A. Coakley, Jr., Stephen K. Cox, Andrew J. Heymsfield, Michael D. King, Stephen Nicholls, David A. Randall, Kenneth Sassen, David O'. C. Starr, and Bruce A. Wielicki. It is with grateful appreciation that we recognize the talents and efforts of Doris Stroup, STX, for the excellent logistics in planning, preparing, and conducting this meeting. Lastly, we would like to highlight the efforts of Gianna Karalfa, STX, for her excellent secretarial support in the preparation of this document.

AGENDA

FIRE SCIENCE TEAM MEETING
JULY 11-15, 1988
LION SQUARE LODGE
VAIL, COLORADO

MONDAY - JULY 11, 1988

CIRRUS:

LARGE SCALE ENVIRONMENT AND MODELING	David O'C Starr
LIDAR/RADIATIVE PROPERTIES/MICROPHYSICAL	Andrew J. Heymsfield
RADIATIVE PROPERTIES	Thomas P. Ackerman

TUESDAY - JULY 12, 1988

SATELLITE STUDIES	Bruce A. Wielicki
CASE STUDY OF OCTOBER 27-28, 1986	Kenneth Sassen
CIRRUS POSTER SESSION	Stephen K. Cox

WEDNESDAY - JULY 13, 1988

PANEL DISCUSSION OF CIRRUS "NEXT"	David O'C Starr

MARINE STRATOCUMULUS:

MARINE STRATOCUMULUS LARGE SCALE ENVIRONMENT AND MODELING	David A. Randall

THURSDAY - JULY 14, 1988

SATELLITE STUDIES	James A. Coakley, Jr.
LIDAR/RADIATIVE PROPERTIES/MICROPHYSICAL	Philip H. Austin
RADIATIVE PROPERTIES	Michael D. King
THERMODYNAMIC AND DYNAMIC PROPERTIES	Bruce A. Albrecht
MARINE STRATOCUMULUS POSTER SESSION	David A. Randall

FRIDAY - JULY 15, 1988

CASE STUDIES -MARINE STRATOCUMULUS IFO	Stephen Nicholls
PANEL DISCUSSION OF MARINE STRAT IFO "NEXT"	David A. Randall

TABLE OF CONTENTS

FIRE SCIENCE TEAM MEETING
VAIL, COLORADO
JULY 11-15, 1988

PAGE

CIRRUS

LARGE SCALE ENVIRONMENT AND MODELING - David O'C Starr Monday, July 11, 1988

Synoptic Conditions Producing Cirrus During the FIRE Cirrus IFO 3
Starr, David O'C.; and Donald P. Wylie

Where are Cirrus Clouds and Why are They There? 11
Wylie, Donald

ISCCP Results for the FIRE IFO Regions and Times 17
Rossow, William B.

ISCCP Modeling - First Look Analysis of ISCCP Cloud Observations ***
Schlesinger, Michael

Cloud Information for FIRE from Surface Weather Reports 19
Hahn, Carole J.; Stephen G. Warren, and Julius London

Cirrus Cloud Model Parameterizations: Incorporating Realistic Ice Particle Generation 25
Sassen, K.; G. C. Dodd, and D. O'C. Starr

Evidence for Asymmetric Inertial Instability in the FIRE Satellite Dataset 29
Stevens, Duane E.; and Paul E. Ciesielski

Climate Data System Supports FIRE 35
Olsen, Lola M.; Dominick Iascone, and Mary G. Reph

The Effects of Cloud Radiative Forcing on an Ocean-Covered Planet 39
Randall, David A.

LIDAR/RADIATIVE PROPERTIES/MICROPHYSICAL - Andrew J. Heymsfield Monday, July 11, 1988

A Synopsis of Langley Research Center's Lidar Effort for the 1986 FIRE IFO 47
Alvarez, J. M.; M. P. McCormick, J. D. Moore, W. H. Hunt, B. R. Rouse, L. R. Poole, and B. D. Poole

Optical and Morphological Properties of Cirrus Clouds Determined by the High Spectral Resolution Lidar During FIRE 49
Grund, Christian J.; and Edwin W. Eloranta

Hydrometer Development in Cold Clouds in FIRE 55
Heymsfield, Andrew J.; Nancy C. Knight, and Kenneth Sassen

TABLE OF CONTENTS

PAGE

Lidar and Aircraft Studies of Deep Cirrus Systems from the 1986 FIRE IFO 61
Sassen, K.; A. Heymsfield, and N. Knight

Vertical Velocities within a Cirrus Cloud from Doppler Lidar and Aircraft Measurements During FIRE: Implications for Particle Growth 67
Gultepe, Ismail; and Andrew Heymsfield

RADIATIVE PROPERTIES - Thomas P. Ackerman Monday, July 11, 1988

Radiative Properties of Visible and Subvisible Cirrus: Scattering on Hexagonal Ice Crystals 75
Flatau, Piotr J.; Graeme L. Stephens, and Bruce T. Draine

Cirrus Microphysics and Radiative Transfer: A Case Study 81
Kinne, Stefan A.; Thomas P. Ackerman, and Andrew J. Heymsfield

Subvisual Cirrus Cloud Properties Derived from a FIRE IFO Case Study 85
Sassen, K.; M. K. Griffin, and G. C. Dodd

Multi-spectral Window Radiance Observations of Cirrus from Satellite and Aircraft - November 2, 1986 "Project FIRE" 89
Smith, W. L.; H. E. Revercomb, H. B. Howell, and M. -X. Lin

Cirrus Cloud Statistics: Temperatures and Optical Depths 95
Valero, Francisco P. J.; Thomas P. Ackerman, and Warren J. Y. Gore

The Radiation Budget of a Cirrus Layer Deduced from Simultaneous Aircraft Observations and Model Calculations 99
Ackerman, Thomas P.; Stefan Kinne, Andrew J. Heymsfield, and Francisco P. J. Valero

Lidar and Radiometer Results from the ER-2 for the FIRE Field Experiments 101
Spinhirne, James

Identification of Cirrus over Wausau During the 1986 FIRE IFO from Ground-Based Radiometer Data 105
Robinson, David A.; and Allan Frei

Interpretation of Satellite-Measured Bidirectional Reflectance from Cirrus Cloudy Atmospheres 111
Takano, Y.; K. N. Liou, and P. Minnis

SATELLITE STUDIES - Bruce A. Wielicki Tuesday, July 12, 1988

Comparison of NOAA-9 ERBE Measurements with Cirrus IFO Satellite and Aircraft Measurements 117
Ackerman, Steven A.; Hyosang Chung, Stephen K. Cox, Leroy Herman, William L. Smith, and Donald P. Wylie

TABLE OF CONTENTS

PAGE

ERBE and AVHRR Cirrus Cloud FIRE Study 123
Harrison, E. F.; P. Minnis, B. A. Wielicki, P. W. Heck, S. K. Gupta, D. F. Young, and G. G. Gibson

Cloud Parameters from GOES Visible and Infrared Radiances During the FIRE Cirrus IFO, October 1986 129
Heck, Patrick W.; David F. Young, Patrick Minnis, and Edwin F. Harrison

Cloud Altitude Determinations from Infrared Spectral Radiances 135
Smith, William L.; and Richard Frey

AVHRR and VISSR Satellite Instrument Calibration Results for both Cirrus and Marine Stratocumulus IFO Periods 141
Whitlock, C. H.; W. F. Staylor, J. T. Suttles, G. Smith, R. Levin, R. Frouin, C. Gautier, P. M. Teillet, P. N. Slater, Y. J. Kaufman, B. N. Holben, W. B. Rossow, C. Brest, and S. R. LeCroy

Cirrus Cloud Properties Derived from Coincident GOES and Lidar Data During the 1986 FIRE Cirrus Intensive Field Observations 147
Minnis, Patrick; Jose M. Alvarez, David F. Young, Patrick W. Heck, and Kenneth Sassen

CASE STUDY OF OCTOBER 27-28, 1986 - Kenneth Sassen Tuesday, July 12, 1988

Overview of the 27-28 October FIRE Cirrus IFO Case: Meteorology and Cloud Fields 155
Starr, David O'C.; and Donald P. Wylie

A Four-Lidar View of Cirrus from the FIRE IFO: 27-28 October 1986 157
Sassen, Kenneth.; Christian John Grund, Jose M. Alvarez, and Freeman F. Hall

Radiative Properties of Cirrus Clouds: FIRE IFO Case 10/28/86 159
Hein, Paul F.; William L. Smith, Jr., and Stephen K. Cox

FIRE Cirrus on 10/28/86: Landsat; ER-2; King Air; Theory 163
Wielicki, Bruce A.; John T. Suttles, Andrew J. Heymsfield, Ronald M. Welch, James D. Spinhirne, Lindsay Parker, and Robert F. Arduini

Surface Radiation Observations for October 27-28, 1986 During the Wisconsin FIRE/SRB Experiment 169
Whitlock, C. H.; L. R. Poole, S. R. LeCroy, and D. A. Robinson

CIRRUS POSTER SESSION - Stephen K. Cox Tuesday, July, 12, 1988

The New FIRE Cloud Lidar at Langley Research Center 175
Alvarez, J. M.; M. P. McCormick, M. A. Vaughn, G. Kent, W. H. Hunt, W. H. Fuller, B. R. Rouse, and R. Dubinsky

TABLE OF CONTENTS

PAGE

Interpretation of the Optical and Morphological Properties of Cirrus Clouds from Lidar Measurements 177
Grund, Christian J.; and Edwin W. Eloranta

Temperature Sensitivity of Eppley Broadband Radiometers 183
Smith, Jr., William L.; Stephen K. Cox, and Vince Glover

Both Sides Now 187
Wylie, Donald

Sub-Visual Cirrus Detection and Characterization 191
Schmidt, E.; G. Grams, and E. Patterson

Cloud Atlas for the FIRE Cirrus Intensive Field Observation: October 5 - November 10, 1986 193
Arking, Albert; Jeffrey D. Childs, John Merritt, and Sharen L. Williams

Optical and Morphological Properties of Cirrus Clouds Determined by the High Spectral Resolution Lidar and Volume Imaging Lidar ***
Grund, Christian

Joint HSRL-HIS Lidar-IR Radiometer Experiment: June 13-17, 1988 ***
Grund, Christian

Satellite Measurements Over the Cirrus IFO, October 28, 1986 ***
Harrison, Edward F.; Patrick Minnis, and Paul Heck

Radiative Properties of Cirrus Clouds? FIRE IFO Case 10/28/86 ***
Hein, Paul F.; William L. Smith, Jr., and Stephen K. Cox

Cirrus Microphysics and Radiative Transfer: A Case Study on 10/28/86 ***
Kinne, S.; Thomas P. Ackerman, and A. J. Heymsfield

Climate Data Systems Supports FIRE ***
Olsen, Lola M.

FIRE Extended Time/Limited Area Observations at Palisades, NY ***
Robinson, David; George Kukla, and Allan Frei

FIRE Cirrus on 10/28/86; LANDSAT; ER-2; King Air; Theory ***
Wielicki, Bruce A.; John T. Suttles, Andrew J. Heymsfield, Ronald M. Welch, James D. Spinhirne, Lindsay Parker, and Robert F. Arduini

Evidence for Asymmetric Inertial Instability in the FIRE Satellite Data ***
Stevens, Duane; and Paul Ciesielski

Lidar Measurements of Antarctic Polar Stratospheric Clouds in Support of Ozone Hole Studies ***
Uthe, Edward

TABLE OF CONTENTS

PAGE

Airborne/Lidar/Radiometric Study of Cirrus in Support of DOD Sensor Test Programs ***
Uthe, Edward

Operational Results for Surface Radiation Observations for October 27-28, 1986 During The Wisconsin FIRE/SRB Experiment
Whitlock, C. H.; L. R. Poole, S. R. LeCroy, and D. A. Robinson ***

Cirrus Radiation Parameters 10/28/86 ***
Spinhirne, J.

PANEL DISCUSSION OF CIRRUS "NEXT" - David O'C Starr Wednesday, July 13, 1988

Panel and Audience Discussions ***

MARINE STRATOCUMULUS

LARGE SCALE ENVIRONMENT AND MODELING - David A. Randall Wednesday, July 13, 1988

Extended Time Observations of California Marine Stratocumulus Clouds from GOES for July 1983-1987 201
Minnis, Patrick; Edwin F. Harrison, and David F. Young

The Relationship of Marine Stratus to Synoptic Conditions 207
Wylie, Donald; Barry Hinton, Peter Grimm, and Kevin Kloesel

Analysis of Diurnal Variation of SCu Layer Using 2 Days of CLASS Soundings on San Nicolas Island 213
Betts, Alan K.

Diurnal Variation of Marine Stratocumulus over San Nicholas Island During the FIRE IFO 215
Davies, R.; and M. Blaskovic

Analysis of Tethered Balloon, Ceilometer, and Class Sounding Data Taken on San Nicolas Island During the FIRE Project 221
Schubert, Wayne H.; Paul E. Ciesielski, Thomas A. Guinn, Stephen K. Cox, and Thomas B. McKee

Radiative Control on Tropical Convective Boundary Layer Equilibrium 225
Betts, A. K.; and W. Ridgway

A GCM Parameterisation for the Shortwave Radiative Properties of Water Clouds 227
Slingo, A.

Preliminary Mixed-Layer Model Results for FIRE Marine Stratocumulus IFO Conditions 229
Barlow, R.; and S. Nicholls

Simulations and Observations of Cloudtop Processes 231
Siems, S. T.; C. S. Bretherton, and M. B. Baker

TABLE OF CONTENTS

PAGE

A Cloud Classification Scheme Applied to the Breakup Region of Marine Stratocumulus 237
Khalsa, Siri Jodha S.; and Catherine Gautier

Fractional Cloudiness in Shallow Cumulus Layers 243
Randall, David A.

Studying Marine Stratus with Large Eddy Simulation 249
Moeng, Chin-Hoh

SATELLITE STUDIES - James A. Coakley, Jr. Thursday, July 14, 1988

Cloud Spatial Structure During the FIRE MS IFO 253
Cahalan, Robert F.

Reflectivities of Uniform and Broken Marine Stratiform Clouds 259
Coakley, Jr., James A.

Marine Stratocumulus Cloud Characteristics from Multichannel Satellite Measurements 265
Durkee, Philip A.; and Gary M. Mineart

Structures Observed on the SPOT Radiance Fields During the FIRE Experiment 271
Seze, Genevieve; Leonard Smith, and Michel Desbois

Analysis of Stratocumulus Cloud Fields using LANDSAT Imagery: Size Distributions and Spatial Separations 277
Welch, R. M.; S. K. Sengupta, and D. W. Chen

Cloud Parameters Derived from GOES During the 1987 Marine Stratocumulus FIRE Intensive Field Observation Period 279
Young, David F.; Patrick Minnis, and Edwin F. Harrison

LIDAR/RADIATIVE PROPERTIES/MICROPHYSICAL - Philip H. Austin Thursday, July 14, 1988

Aerosol Measurements in the Stratocumulus Project 287
Hudson, James G.

In Situ Measurements of "Ship Tracks" 291
Radke, Lawrence F.; Jamie H. Lyons, and Peter V. Hobbs

Estimated Accuracy of Ground-Based Liquid Water Measurements During FIRE 295
Snider, J. B.

NRL Tethered Balloon Measurements at San Nicholas Island During FIRE IFO 1987 299
Gerber, Hermann; Stuart Gathman, Jeffrey James, Mike Smith, Ian Consterdine, and Scott Brandeki

TABLE OF CONTENTS

PAGE

RADIATIVE PROPERTIES - Michael D. King Thursday, July 14, 1988

Estimating Integrated Cloud Liquid Water from Extended Time Observations of Solar Irradiance 307
Fairall, C. W.; Raja El-Salem Rabadi, and J. Snider

A Study of Marine Stratocumulus using Lidar and other FIRE Aircraft Observations 313
Jensen, Jorgen B.; and Donald H. Lenschow

Cloud Absorption Properties as Derived from Airborne Measurements of Scattered Radiation within Clouds 319
King, Michael D.; Teruyuki Nakajima, Lawrence F. Radke, and Peter V. Hobbs

Cloud Optical Parameters as Derived from the Multispectral Cloud Radiometer 327
Nakajima, Teruyuki; and Michael D. King

THERMODYNAMIC AND DYNAMIC PROPERTIES - Bruce A. Albrecht Thursday, July 14, 1988

Aircraft Measurements of the Mean and Turbulent Structure of Marine Stratocumulus Clouds During FIRE 335
Albrecht, Bruce A.; Kevin A. Kloesel, Kerry A. Moyer, Jefferey J. Nucciarone, and George Young

Cloud and Boundary Layer Structure Over San Nicolas Island During FIRE 337
Albrecht, Bruce A.; Christopher W. Fairall, William J. Syrett, Wayne H. Schubert, and Jack B. Snider

Thermodynamic Structure of the Stratocumulus-Capped Boundary Layer on 5 July, 1987 339
Austin, Philip H.; Reinout Boers, and Alan K. Betts

Analysis of Tethered Balloon Data from San Nicolas Island on 8 July 1987 341
Cox, Stephen K.; David P. Duda, Thomas A. Guinn, Christopher M. Johnson-Pasqua, Wayne H. Schubert, and Jack B. Snider

Turbulence Measurements using Tethered Balloon Instrumentation During FIRE '87 357
Hignett, Phillip

Horizontal Variability of the Marine Boundary Layer Structure Upwind of San Nicolas Island During FIRE, 1987 359
Jensen, Douglas R.

An Overview of UK C130 Observations from the FIRE Marine Stratocumulus IFO 365
Nicholls, S.; J. Leighton, and R. Barlow

Boundary Layer Roll Circulations During FIRE 367
Shirer, Hampton N.; and Tracy Haack

TABLE OF CONTENTS

PAGE

Winds and Turbulence above San Nicolas Island During FIRE 371
White, Allen B.; William J. Syrett, Christopher W. Fairall, and Dennis W. Thomson

MARINE STRATOCUMULUS POSTER SESSION - David A. Randall Thursday, July 14, 1988

ER-2 Lidar Measurements of Stratocumulus Cloud Top Structure on July 14, 1987 375
Boers, Reinout; and James D. Spinhirne

Dependence of Marine Stratocumulus Reflectivities on Liquid Water Paths 377
Coakley, Jr., J. A.; and J. B. Snider

Near Infra-red Radiances Observed by the UK C130 Multi-channel Radiometer During the Marine Stratocumulus IFO and Preliminary Comparison with Model Calculations 383
Foot, J. S.

Plume Mechanics and Stratocumulus Convection 393
Hanson, Howard P.

FIRE Extended Time/Limited Area Observations at Palisades, New York 397
Robinson, David A.; George Kukla, and Allan Frei

Measurements of the Light-Absorbing Material Inside Cloud Droplets and its Effect on Cloud Albedo 403
Twohy, C. H.; A. D. Clarke, S. G. Warren, L. F. Radke, and R. J. Charlson

Preliminary Results of Radiation Measurements from the Marine Stratus FIRE Experiment 409
Valero, Francisco P. J.; Philip D. Hammer, Thomas P. Ackerman, Warren J. Y. Gore, and Melinda L. Weil

Third Generation Earth Radiation Budget Measurements; ERBE in the Context of Earlier Systems 411
Vonder Harr, Thomas H.

San Nicolas Island Surface Radiation - Meteorology Data 417
Johnson-Pasqua, Christopher M.; and Stephen K. Cox

A Cloud Classification Scheme Applied to FIRE Stratocumulus Data ***
Khalsa, Siri Jodha Singh; and Catherine Gautier

Determination of Cloud Radiative and Microphysical Parameters from Airborne Radiation Measurements ***
King, M. D.; T. Nakajima, J. D. Spinhirne, P. V. Hobbs, and L. F. Radke

Mean and Turbulent Boundary Layer Measurements for a Tethered Balloon ***
Hignett, Phil

Marine Stratocumulus Cloud Characteristics from Multichannel Satellite Measurements ***
Durkee, P. A.; and G. M. Mineart

TABLE OF CONTENTS

PAGE

Initial Analyses of GOES VISSR Data for Marine Stratocumulus IFO and ETO ***
Minnis, Patrick; Edwin F. Harrison, and D. F. Young

Analysis of Tethered Balloon Data from San Nicholas Island on 8 July 1987 ***
Cox, Stephen K.; David P. Duda, Christopher M. Johnson-Pasqua, Wayne H. Schubert, and Jack B. Snider

CASE STUDIES - MARINE STRATOCUMULUS IFO - Stephen Nicholls Friday, July 15, 1988

Comparison and Calibration of NCAR Electra Instruments: July 5 and July 7, 1987 425
Austin, Philip H.; and Reinout Boers

Thermodynamic Structure of the Stratocumulus-Capped Boundary Layer on 7 July 1987 429
Boers, Reinout; Alan K. Betts, and Philip H. Austin

Aircraft/Island/Ship/Satellite Intercomparison: Preliminary Results from July 16, 1987 433
Hanson, Howard P.; Ken Davidson, Herman Gerber, Siri Jodha Singh Khalsa, Kevin A. Kloesel, Ronald Schwiesow, Jack B. Snider, Bruce A. Wielicki, and Donald P. Wylie

A Preliminary Analysis of LANDSAT and UK C130 Data from Mission 197-A, on 16 July 1987 437
Nicholls, S.

PANEL DISCUSSION OF MARINE STRAT IFO "NEXT" - David A. Randall Friday, July 15, 1988

Panel and Audience Discussions ***

FIRE SCIENCE TEAM MEETING
VAIL, COLORADO
JULY 11-15, 1988

CIRRUS

LARGE SCALE ENVIRONMENT AND MODELING - David O'C Starr Monday, July 11, 1988

PAGE

Synoptic Conditions Producing Cirrus During the FIRE Cirrus IFO 3
Starr, David O'C.; and Donald P. Wylie

Where are Cirrus Clouds and Why are They There? 11
Wylie, Donald

ISCCP Results for the FIRE IFO Regions and Times 17
Rossow, William B.

ISCCP Modeling - First Look Analysis of ISCCP Cloud Observations ***
Schlesinger, Michael

Cloud Information for FIRE from Surface Weather Reports 19
Hahn, Carole J.; Stephen G. Warren, and Julius London

Cirrus Cloud Model Parameterizations: Incorporating Realistic Ice Particle Generation 25
Sassen, K.; G. C. Dodd, and D. O'C. Starr

Evidence for Asymmetric Inertial Instability in the FIRE Satellite Dataset 29
Stevens, Duane E.; and Paul E. Ciesielski

Climate Data System Supports FIRE 35
Olsen, Lola M.; Dominick Iascone, and Mary G. Reph

The Effects of Cloud Radiative Forcing on an Ocean-Covered Planet 39
Randall, David A.

ABSTRACT

Synoptic Conditions Producing Cirrus During the FIRE Cirrus IFO

by

David O'C. Starr
NASA Goddard Space Flight Center
Greenbelt, Maryland 20771

and

Donald P. Wylie
Space Science and Engineering Center
University of Wisconsin
Madison, Wisconsin 53706

1. Introduction

Although direct observations of cirrus clouds by the FIRE research aircraft were usually confined to the area of the IFO surface network (~100 km in dimension), these cirrus were generally part of a more extensive ($\geq$500 km) zone of upper level cloudiness. It is these large scale patterns of cirriform cloud and their relationship to the corresponding synoptic environment which are the prime focus of this paper. We present three conceptual models and classify each of the individual cases into one these categories. Although the cases manifest significant differences in intensity and small scale structure, we believe they are best viewed in this unified context. The descriptions given below are mostly qualitative, however, quantitative descriptions of the synoptic control and its relationship to cloud structure for all the IFO cases will be summarized during the presentation. A paper giving more detailed and quantitative information on each of the individual cases will be distributed.

The synoptic situations in which extensive cirriform clouds were observed are classified into three basic types: 1) warm front cases, 2) cold front cases, and 3) closed low aloft cases. A simplified summary of each type of situation is presented in the following sections. Our terminology reflects our reliance on the standard upper air and surface analyses provided by the National Weather Service and our cognizance of classical notions of cyclone structure. However, satellite imagery (primarily from GOES) was indispensable in the development and application of our classification scheme. Our categories do have some precedence in the area of satellite image interpretation. The warm front class is always associated with an upper level short wave. Weldon (1976) uses the term "baroclinic leaf" cirrus to describe situations resembling these cases, although, if there is significant development at the surface and middle levels, he uses the term "comma cloud" to describe the whole multilevel system . Our cold front cases correspond to Weldon's "baroclinic zone" cirrus pattern. However, he applies this term to an even larger class of cases whose unifying feature is their correspondence in scale and location with planetary waves (Rossby-Haurwitz waves) .

The three classes of extensive upper level cloud systems described here are not intended to be exclusive, but rather representative of situations encountered during the Fall 1986 field campaign. One obvious class not included is the "mesoscale anvil" cloud associated with mesoscale convective systems in tropical and extratropical regions. In fact, cumulonimbus, which often produce cirrus by injection of moisture and condensate into upper levels, did not occur within the IFO region during the experiment. However, weak cumulonimbus activity was observed in the upstream flow with some of the closed low aloft cases.

2. WARM FRONT CIRRUS

In the classic view, warm front cirrus are the harbingers of an approaching extratropical cyclone with its attendant deep cloud development and precipitation. The presence of cirrus is typically ascribed to gentle broadscale slope convection (upglide) along an elevated warm front as depicted in Figure 1. This is the picture given in numerous meteorological text books. However, it is our opinion that this may be a misleading interpretation of the actual situation as seen in the following description.

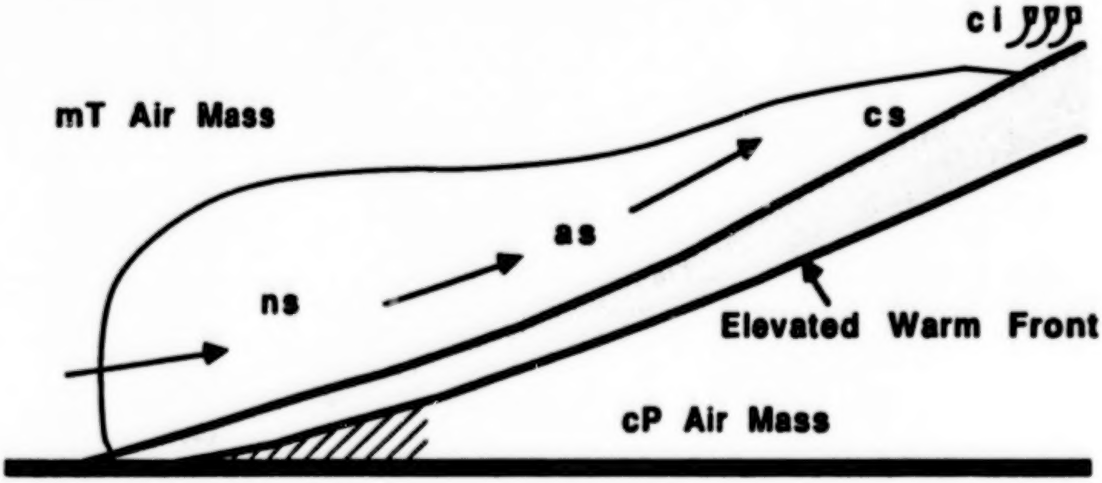

Figure 1: Classic view of clouds along a warm front.

Our view of warm front cirrus is that it is always associated with an upper level short wave as shown schematically in Figure 2a. Its preferred location is capping the short wave ridge with a relatively sharp northern boundary corresponding to the axis of the jet stream and a ragged southern boundary. Streaks or fingers of cirrus generally protrude downstream of the denser ridge-capping region and may reach nearly halfway to the preceding short wave trough. This leading edge of the cloud tends to contain convective cirrus, e.g., uncinus, spissatus and fibratus. Patches of cirrostratus may also be present. A denser cirrostratus overcast is typically found in the ridge-capping region where convective cells are often embedded within the larger cloud mass. Upstream of the ridge axis, patchy cirrostratus are typically found, though cirrostratus overcast is common. The cirrus here usually appear continuous with the ridge-capping cirrostratus. It should be noted that these clouds usually extend upstream of the surface warm front location often to the location of the surface cold front and its associated jet axis. The tops of the highest clouds within this pattern are usually at or not far below the tropopause. In Figure 2a, attention should be given to the correspondence or lack thereof, between the surface features and the corresponding cloud pattern with respect to the classic picture shown in Figure 1.

Ahead of the ridge axis and surface warm front, multilayered development is quite common. Merging of individual upper level cirrostratus layers is often found near the ridge axis where the depth of the entire cloudy layer may reach more than 3 km. A separate lower layer of denser cirrostratus is found in cases when the surface cyclone is of more than minimal intensity. This middle level cloud layer often borders on being an altostratus cloud and typically exhibits moderate convective development originating near cloud base (~6 km). Though dominated by ice

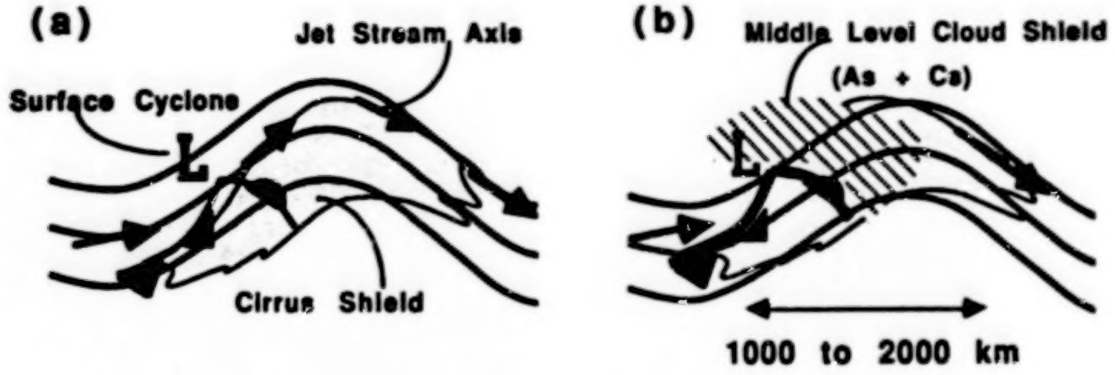

Figure 2: Traveling Short Wave and Warm Front Cirrus Shield:
(a) without middle level clouds ("baroclinic leaf")
(b) with middle level clouds ("comma cloud").

processes, all three phases of water may be found in the vicinity of the cloud base. In weak cyclones, this layer does not develop appreciable vertical extent. However, when the cyclone is of moderate intensity, it may develop vertically through convective processes and actually merge with the high level clouds which grow downward through an ice precipitation process, i.e., a total depth of ~5 km. Development of the lower level cloud layer ceases with the passage of the warm front as illustrated in Figure 2b.

We believe that this dense middle level cloud layer results from upglide along the warm front. It is found in the proper location and the tendency for convective instability to increase as the layer develops ahead of the surface front, is consistent with the classic notions. However, the high level cirrus appears to develop independently. The spatial pattern of this extended cloud area does not fit the classic notion. Although the cirrus uncinus and spissatus comprising the leading edge of this pattern are the first signs of an approaching disturbance, it does not appear that they are initiated or maintained by a frontal upglide process as is implied in the classic picture. Rather, this upper layer more likely results directly from the effects of the thermodynamic and dynamic structure of the upper level flow, e.g., ascent up the sloping isentropic surfaces of the ridge and possibly differential vertical temperature advection associated with the vertical structure of the jet leading to convective instability near the tropopause (i.e., uncinus). The development of the surface cyclone, which forces the development of the middle level cloud layer, is also dynamically coupled (independently) to the upper level disturbance. This picture is consistent with the notions given by Weldon (1976) where the upper level cloud corresponds to his "baroclinic leaf" cirrus (Fig. 2a) and the middle level clouds form part of the "comma" which is seen when there is significant surface development (Fig. 2b). We acknowledge that the cases we considered in developing the above model had weak to moderate development at the surface. This fact supports our contention since the upper level cirrus were observed with little apparent forcing from below. Furthermore, it is likely that this model also applies to situations of strong surface cyclones, though the separation between the upper layers and the middle layers are probably much less distinct in these cases. In this situation, the convective development of the middle level clouds (and also probably the low level clouds rooted in the boundary layer) leads to a physical connection between the layers and an appreciable vertical transport of water to upper levels, which results in an enhancement of the density (ice contents) and extent of the upper level clouds.

Two of the FIRE Cirrus IFO cases most clearly fit the pattern of warm front cirrus presented above: the **27-28 October and 2 November** cases. In each case, a distinct upper level short wave ridge moved from west to east through the IFO region superimposed on a pattern of weak (20 m/s) and generally zonal upper level flow along the US-Canadian border. A surface cyclone with its attendant warm and cold fronts formed in the Montana area and also propagated eastward. Though the surface fronts were well-defined, the cyclone did not intensify appreciably, i.e., no widespread precipitation developed. Upper level cirrus (~9-11 km) were observed below the tropopause in advance of the warm front and also after its passage. The "baroclinic leaf" pattern, which passed directly over the IFO area, was not filled in with a dense cirrostratus overcast. However, the zone where cirrus were present did define a region whose outline was similar to that show in Figure 2a. The high level cirrus were mixture of uncinus, spissatus and patchy cirrostratus. Alto/cirrostratus were intermittently observed between about 4 and 7 km prior to the passage of the warm front at the surface. On the 28th, they were visible in GOES imagery through the high cirrus layer and the trailing edge of this cloud layer clearly paralleled the surface warm front. An underlying layer of very scattered shallow cumulus was also present on each day.

Three other cases also fit the warm front cirrus pattern: the **15, 19 and 30 October** cases. Unlike the previously described cases, the large-scale flow was from the northwest on the 15th. Wisconsin was situated between a ridge over the Canadian Rockies and a trough to the east (axis on a line from eastern Michigan to Louisiana) of a high amplitude long wave pattern. An extensive cirrus shield capped a well-defined short wave ridge that was moving to the southeast. A weak but clearly defined surface cyclone and associated warm front were moving toward Wisconsin from the northwest, i.e., central Canada. No middle level clouds were observed in Wisconsin, though some may have developed to the north in Canada. Stratocumulus were prevalent as cold air behind a recently passed cold front was modified. With respect to the pattern depicted in Figure 2a, the major differences in this case were the orientation of the ridge axis (WSW-ENE) and the breadth of the cirrus shield along the ridge axis relative to its length along the flow, i.e.,greater along the axis than along the flow. It should also be noted that the entire system of relatively dense cirrus moved by mostly to the northeast of the IFO region, i.e., only the ragged southern portion (between the warm and cold fronts of the cyclone that was centered roughly under the ridge axis) of the pattern presented in Figure 2a was actually sampled. Tenuous convective cirrus, often aligned in bands, were observed near the tropopause (~11 km) and extended down to the 9 km level.

On 19 October, a region of cirrus developed rapidly near the Minnesota-North Dakota border. It did not clearly have the shape of the "baroclinic leaf" nor was a short wave ridge clearly evident. However, this may have been a result of distortions imposed by a strong closed low system centered over eastern Nevada. The cloud development was rapid and did seem to correspond with the passage of a weak and poorly defined short wave ridge that emanated from the closed low system - actually, when this feature was superimposed on the relatively stationary exit region ridge feature of the closed low circulation (see Section 4). At the surface, a weak front was advancing from the west. Though analyzed as a cold front extending from a low pressure center in central Canada to a developing cyclone in southeast Utah, it is evident only as a distinct line of changing wind direction at the surface (SE to NW) with little or no temperature or moisture contrast. The cirrus developed rapidly in both areal and vertical extent in advance of this front. Multiple layers, chaotically arranged, were observed from ~11 -7 km. However, two distinct generating levels were evident at ~10 and ~8 km, respectively. The entire system propagated rapidly to the ESE and passed over the IFO area during the evening.

Initially, the 30 October case closely resembled the 27-28 October and 2 November cases, i.e., an extensive zone of cirrus capping an eastward moving short wave ridge. However, the major portion of the cloud shield was west of the IFO region. Only the "protruding fingers" region of the leading edge was actually sampled. These cirrus bands were composed of convective cirrus cells as shown by Sassen at al. (1988). Cloud tops were just below the tropopause (~11.5 km) and each band showed progressively greater vertical development, i.e., base heights lowering from ~10.5 to below 8 km. On the 30th, two low pressure centers moved toward Wisconsin from Montana, each with a cold front trailing to the southwest. During the evening, these systems merged and intensified in northeast North Dakota. A warm front formed and the entire system rapidly swept to the ENE through Wisconsin producing widespread light precipitation at the surface during the night. By morning, the upper level short wave had moved well to the northeast of the IFO region and the capping cloud shield had evolved from the "leaf" shape to the "comma" shape. The trailing cold fronts joined and stretched from the intensifying system in the southwest US to southeast Canada.

3. COLD FRONT CIRRUS

Cold front cirrus were one of the most extensive cirrus cloud patterns observed during FIRE. Though only observed in the IFO region during the two-day period of **31 October and 1 November**, this pattern could be found somewhere in the northern hemispheric region viewed by GOES on most days during the IFO. Typically, a channel of nearly contiguous cirrus extends from a long wave trough axis northeastward to the preceding ridge (Fig. 3), which is also capped by cirrus much as seen for the traveling short waves (described above) though of much greater horizontal extent. The length of this cloud system is more than 3000 km while the width is ~500 km. The northern edge of the cloud mass is quite distinct while the southern edge is diffuse in appearance. The northern edge corresponds to the axis of the polar (or midlatitude) jet stream which overlies a similarly extensive air mass boundary. The large scale cirrus system is most developed when the long wave is of moderate or greater amplitude. Typically, this occurs when the contrast between the underlying air masses is high and the jet stream is correspondingly strong, which has led to the use of the term "baroclinic zone" cirrus for these situations. Viewed from a large scale perspective, the air mass boundary is a cold front since it tends to progressively sink to the southeast as the long wave slowly propagates eastward. Thus, our choice of the terminology "cold front" cirrus. Distinct banded structures are often evident in the upper level clouds where the bands are aligned roughly parallel to the jet axis as described by Conover (1960) who termed these clouds "jet stream" cirrus. Cirrus formation occurs at multiple levels within the system where a strong tendency for development of a convective layer near the tropopause appears prevalent. Traveling short waves with their associated warm front cirrus ("baroclinic leaf") patterns may move rapidly through the large scale baroclinic channel with the respective upper level cloud patterns being superimposed. These traveling disturbances may trigger development at lower levels and evolve to the "comma cloud" pattern associated with a mature extratropical cyclone by the time they near the long wave ridge axis.

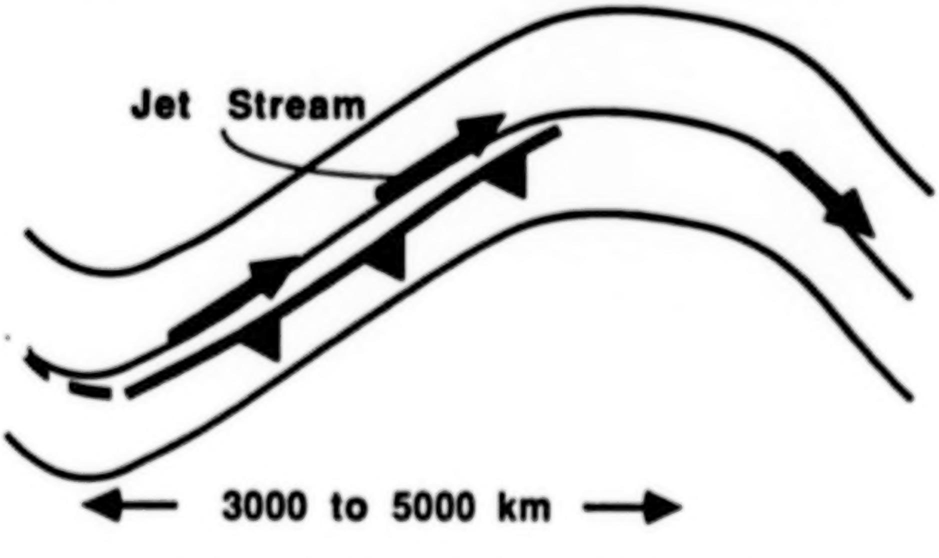

Figure 3: Planetary Wave and Cold Front Cirrus.

On the 31st, the cold front and jet axis were initially to the north of the IFO region. Cirrus, comprising the diffuse southern half of the channel, were observed at the tropopause (~13 km) and at other levels extending down to nearly 7 km. Altostratus were observed between 4 and 7 km with a stratocumulus undercast below. Cloud conditions were broken to patchy at middle and upper levels with banded structure often evident in the high level cirrus. Wind speeds exceeding 50 m/s were encountered in the upper troposphere. The entire system drifted slowly to the east (front moving to the southeast). [Showers along the front restricted aircraft operations on the 1st, however, the surface lidar at Wausau did sample very thin and high cirrus overhanging the distinct northern boundary. On the 2nd, the system had passed to the south and east. However, the ER-2 overflew some of this system early in the day over Illinois.] A remarkable upper level dry zone (parallel and north of the jet axis) - dramatically seen on the GOES water vapor channel imagery - separated this system from the warm front cirrus system which evolved on the 2nd. An important factor in this case which apparently led to appreciable enhancement of cirrus within the large scale baroclinic channel was the disturbance which developed to the east of the intense closed low at the base of the long wave trough in the southwest US. This feature appeared to "pump" moisture into upper levels. In should also be noted that a "baroclinic leaf" rapidly propagated through the channel on the 1st. There was no associated surface cyclone development though showers along the cold front may have been enhanced. The associated short wave was not well-defined in the height pattern, which is often the case when superimposed on such an intense large scale feature.

4. Closed Low Cirrus:

Upper level closed lows generated the most areally extensive cirrus shields observed during the Cirrus IFO. Though lacking the length scale of the linear cold front cirrus systems described above, these systems are equally or more extensive by virtue of their oval shape as depicted schematically in Figure 4. The actual shape assumed by the cirrus cloud shield does appear sensitive to the specific relationship between the closed low flow pattern and the larger scale flow environment, i.e., the whole pattern - clouds and/or flow - may be rotated and/or distorted. Closed lows represent disturbed conditions and tend to be rather stationary for an extended period of time. However, when the pattern does eventually open up, it generally moves rapidly and is quickly absorbed into the larger scale flow. As shown in Figure 4, the cloud mass is located on the eastern (downstream) side of the closed low but may also extend back into the central and southern regions. This was particularly evident when very short waves, evident primarily in the GOES water vapor channel imagery, propagated through the system. High level cirrus (near the tropopause) are typically found capping the stationary exit region ridge and extending downstream from there. These clouds appear to result directly from the upper level structure of the flow much as described for the warm front cirrus. There may not be clouds underlying the northernmost portion of these high cirrus. However, there may be extensive middle level (cirrostratus and altostratus) and low level clouds. East of the center of the closed low circulation aloft, extensive lower level cirrostratus and altostratus cloud decks, low level clouds and precipitation are prevalent over a wide region. In addition to the nimbostratus, there may also be embedded deep convection, i.e., cumulonimbus. Precipitation is generally widespread and of light to moderate intensity.

Often the surface feature associated with the closed low aloft system are not well defined. Typically, there is a relatively stationary surface trough under the axis of the upper level trough feature. In addition, one or more slow moving or stationary fronts may often be found extending to the east under the main mass of vertically developed clouds and precipitation. However, these features are generally indistinct with respect to thermal gradient and wind shear and their analysis often relies more on persistence of previous features than present surface conditions. This is probably a consequence of their stationarity and the cumulative effects of widespread precipitation around the frontal boundary in the absence of any strong frontogenetic forcing from above, i.e., the upper level flow is usually weak. The disturbed region typically exhibits southerly flow over a rather deep layer. North of the stationary weak surface front(s), precipitation is stratiform in character though mesoscale regions of embedded convection may be present. The middle level altostratus and cirrostratus in this region appear to be associated with a frontal upglide process, i.e., the fronts may be better defined aloft than at the surface. To the south, deep convection is more prevalent and apparently injects moisture into middle and upper levels.

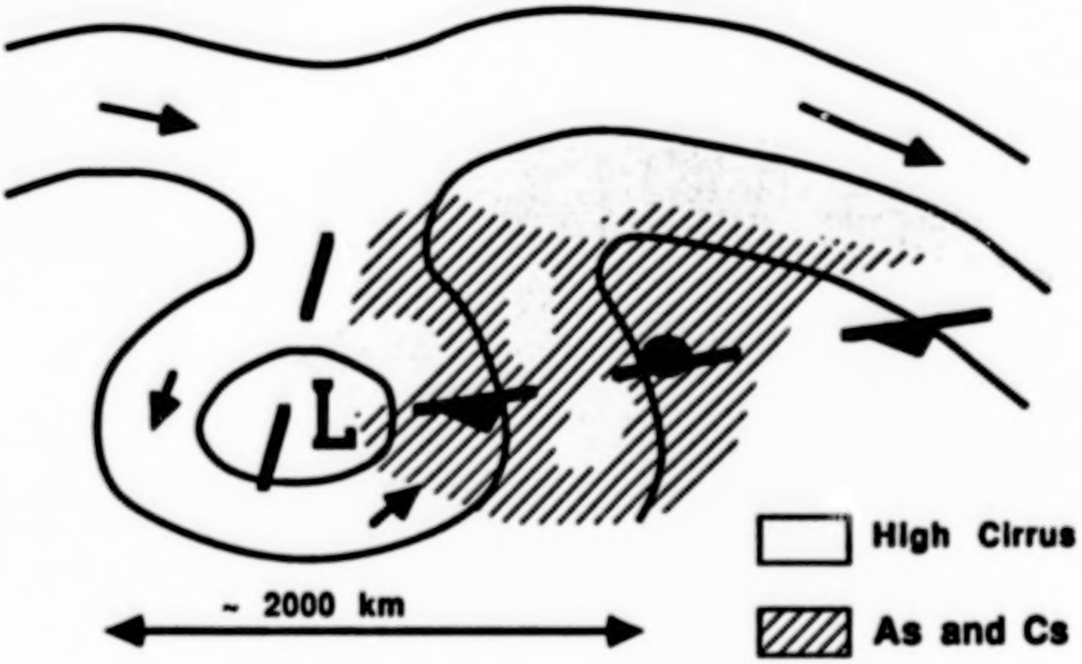

Figure 4: Cloud Pattern for Closed Low Aloft

Two closed low systems were observed during the IFO: the first was the **13 October** case. The second system dominated the synoptic situation over the most of the central US from the Rockies to the Ohio Valley from **21-26 October**. On the 13th, the center of the closed low contours were located in western Iowa. The IFO region was in the center of the disturbed region on the backside of a cyclone centered just north of Lake Huron. A cirrus shield was present to the north with tops generally at about 9 km and bases extending down to about 7 km. As the disturbance drifted toward the northeast, cirrus tops lowered to about 8 km and the layer became more broken. An extensive broken to overcast altostratus deck was present between 3 and 4 km over a low level stratocumulus layer (~1 km). There were scattered showers over the region. This system was short lived as the pattern, which had formed the previous evening, opened up and moved off on the morning of the 14th.

The second system was very extensive and long-lived. Missions were flown on each day except the 23rd when rain precluded aircraft operations. Closed height contours at the level of the jet stream were first observed over Nevada on the 18th. By the 0000 GMT on the 20th, the closed circulation had become largely cutoff from the planetary scale pattern and was centered over Utah. The system drifted slowly to the ENE over northern Colorado into southwest Nebraska over the next 72 hours. Over the next 48 hours, it continued to drift eastward but during this time the pattern opened up and appeared ready to move more rapidly and rejoin the large scale westerly flow to the north. However, during the night of the 24th, the closed circulation was again established and was centered over southwest Iowa and northeast Kansas. The system then slowly drifted eastward toward and into Illinois before the wave pattern finally opened up and moved rapidly off during the night of the 26th.

On the 21st, a long (~1000 km), narrow (~50-100 km) band of high cirrus forming the leading edge of this system was observed by aircraft over central Iowa. We are calling this the "hydrodynamic band" case. This feature was evident in satellite imagery from the 20th to the 22nd and, since our attention was drawn to it, we have observed that it is a common feature of situations like this. We hope to present results of a detailed analysis of this case in the near future. The band was composed of cirrostratus with embedded convection. Cloud top was at about 12 km and the base generally was above 10.5 km. Distinct waves were observed at cloud top (~0.5 km amplitude) in the ER-2 lidar images for one of the overpasses. Distinct thin cirrostratus layers were often found near cloud top.

On the 22nd, a high cirrostratus deck was observed in the vicinity of the exit region ridge. Cirrus were present in a layer from near the tropopause at about 12.5 km (thin layers) down to below 7 km. Generation was apparent at a number of levels with embedded uncinus cells whose tops were variously at ~12 km, 10.5 km and 8.5-10 km. A layer of convective clouds with bases at about 6 km (altostratus/altocumulus/cirrostratus) was below. This middle level cloud deck developed with some convective cells apparently reaching to the 10 km level. It is our feeling that the middle level cloud layer resulted from a frontal upglide process, i.e., southerly flow over an elevated frontal surface sloping up from the south - an east-west stationary front was analyzed through northern Illinois the previous evening but had been dropped from the analysis by the 22nd. However, we believe that the upper level cirrus resulted independently from the upper level flow features. In particular, there is qualitative evidence that differential (in the vertical) horizontal temperature advection maintained the instability reflected in the convective character of the high cirrus in this case (We hope to be able to quantify this). On the 23rd, the situation in Wisconsin became quite disturbed with widespread precipitation which precluded flight operations. On the 24th, a very similar situation (to the 22nd) occurred. However, the cirrus were generally less dense and less convective. Low level clouds generated light showers over the region. Middle level clouds were mostly absent, except for a scattered layer at about 4 km.

On the 25th and 26th, widespread precipitation over the region greatly restricted operations. However, missions were flown to the northern part of the IFO area where conditions were less severe. These cases were characterized by a high level cirrostratus layer between ~10 and 11 km, a secondary patchy layer between ~8.5 and 9.5 km, and a well-developed middle level cloud layer between about 5.5 km and 8 km. By the 26th, the IFO region was under the entrance ridge region of the closed low. This area and the center of the closed low had each become cloud filled as was the entire area to the east.

WHERE ARE CIRRUS CLOUDS AND WHY ARE THEY THERE?

Donald Wylie
Space Science and Engineering Center
University of Wisconsin-Madison

This paper is a summary of the cirrus cloud climatology of Wylie and Menzel (1988) and some ancillary studies of cirrus clouds that have been made using the same data set. The Wylie and Menzel climatology is a unique data set of cloud statistics extracted from the GOES/VAS satellite. With these data we can describe the geographical distributions of clouds, there seasonal changes, some diurnal changes, and also what atmospheric conditions cause the clouds.

The GOES/VAS cloud analysis algorithm separates cloud cover on the satellite imagery into two classes; 1) those clouds that are opaque to terrestrial radiation, and 2) those that are semi-transparent to the upwelling infrared radiation. The technique identifies the semi-transparent clouds using the multi-spectral channels of the GOES VISSR Atmospheric Sounder (VAS). Some of these channels are sensitive to different levels in the atmosphere. Ideally, a low altitude cloud can not be seen by a channel sensitive only to the upper atmosphere while a high altitude cloud will be seen on all channels. The strength of the cloud signature from the cloud free background varies between the channels because each is sensitive to a different level in the troposphere. This method has also been called the "CO_2 Slicing Method" (Menzel et al., 1983) because VAS channels are capable of viewing only "slices" of the troposphere.

The differential sensitivity of the VAS channels allows the radiative transfer equation to be solved for the cloud top height independently from the emissivity of the cloud. This allows a segregation of clouds on the GOES/VAS image into opaque clouds and partially transmissive clouds which are called cirrus by Wylie and Menzel (1988). In reality, cirrus clouds are more correctly defined as ice clouds some of which are thick enough to be opaque to terrestrial radiation. A large number are sufficiently thin to upwelling terrestrial radiation. The thin clouds are very important to studies of the radiative heating of the earth because they allow solar radiation to penetrate through while partially blocking some of the upwelling infrared radiation. In this paper we use the term "cirrus" to mean only the thin and semi-transparent clouds.

Cirrus clouds are more frequent than previously estimated. They are found over the Continental United States and bordering oceans from 25 to 35 % of the time. Opaque clouds were found ~ 45% of the time and no clouds (clear skies) were found ~ 25% of the time.

Opaque cloud cover has large geographical variations while cirrus do not (see Figures 1 and 2). The "Sun Belt" where opaque clouds are infrequent and clear skies are frequently found, are obvious in the geographical summaries (Figures 1 and 2). They are found in southern Texas and Mexico during the winter and over most of the southwestern United States, Texas, New Mexico, Arizona, and California, in the summer.

Cirrus clouds, on the other hand, have very small geographical variances. They were slightly less frequent in the southwest than the rest of the United States. The only area where few cirrus were found was in the Eastern Pacific Ocean. Here a large seasonal change also can be seen because of the northward migration of the Subtropical High in the summer.

The seasonal changes over the area shown in Figures 1 and 2 are summarized in Table 1. The geographical bounds of this study are 25° to 50° north latitude and 60° to 140° west longitude. The probability of finding both opaque and cirrus clouds increases in the winter. In the summer the average probability of opaque clouds is 42% which increases to 46% in the winter. Cirrus clouds increased by a similar amount from a probability of 24% in the summer to 29% in the winter. The probability of clear skies correspondingly decreases from summer to winter, 34% to 25%.

TABLE 1: THE PROBABILITY OF CLOUDS

Season	Cirrus	Opaque	Clear sky
Summer	24%	42%	34%
Winter	29%	46%	25%

To seek answers to the question of "why are the cirrus clouds present?" the GOES/VAS cloud reports were compared to atmospheric dynamic and thermodynamic conditions which are suspected to cause clouds. To cause cirrus clouds, the upper troposphere has to be rising which can lead to saturation.. Moistening of upper layers also can lead to saturation which will cause cirrus generation. This can happen by a number of mechanisms. Cumulonimbus convection obviously is one mechanism which comes to mind because the large cirrus anvil clouds seen on top of the cumulonimbus clouds.

To determine what fraction of the cirrus clouds are related to the cumulonimbus convection, we counted the percentage of cirrus reports near radar echoes using the echoes as indicators of the presence of the cumulonimbus clouds. The radar summary from the National Weather Service was used for locating the radar echoes (Figure 3). The radar summary is a pictorial summary of all echo reports from all weather radars in the United States. Regions where echoes are reported are shaded on these summaries along with numeric information on the maximum heights of the echoes and their speeds and directions of movement.

The echo summary areas were extended to allow for cirrus blow off from the cumulonimbus. The extended boundary (solid line) was drawn from 50 to 300 km outward from the echo summary boundary. The extended boundary was placed 100 to 300 km downwind of the echo boundary. The distance was apportioned using the 300 mb wind speed allowing for advection over three hours. On the cross wind and upwind sides of the echo boundary, the extended boundary was placed ~50 km from the echo boundary to allow for lateral spreading of the cirrus anvil.

The GOES/VAS cirrus analyses at 00:00 GMT and 12:00 GMT were used in this study. The extended echo boundaries for all NWS radar summaries in the time period three hours prior to the GOES/VAS analysis were used to define the extended boundary. This study was performed in two seasons. The month of June 1986 was chosen to represent a summer season and January 1988 to represent a winter season.

The cirrus reports were separated into either being close to the radar echoes (inside the boundary) or away from any echoes (outside of the boundary). The same separation also was made for all cloud reports (cirrus and opaque) of high cloud above 500 mb. The results are given in Table 2.

In the summer approximately one-half of the cirrus and high cloud (both cirrus and opaque cloud) reports were close to or over radar echoes (52 to 57%). The other half were far away from the echoes (48 to 43%). This statistic implies that Cb convection only explains one half of the cirrus in the summer.

In the winter a different picture was found. Only 22% of the cirrus and 24% of the high cloud reports were near the radar echoes. The other 76 to 78% were separated from the echoes. The amount of area covered by radar echoes decreased in the winter while the number of cirrus and opaque cloud reports increased. Thus in winter, most of the cirrus have no relation to Cb clouds.

The cirrus not directly caused by Cb clouds must be created and maintained by other motions in the atmosphere. We are currently examining vorticity and temperature advection for their relationships to cirrus and high clouds. The polar and sub-tropical jet streams also will be examined.

TABLE 2: THE PROBABILITY OF FINDING CLOUD OBSERVATIONS WITH RESPECT TO RADAR ECHOES.

Type of Cloud	Near or Over Echoes	Not Related to Echoes
Cirrus in summer	52%	48%
Cirrus in winter	22%	78%
All clouds <500 mb in summer	57%	43%
All clouds <500 mb in winter	24%	76%
October 86 (FIRE IFO) Cirrus	32%	68%
October 86 (FIRE IFO) All clouds	34%	66%

REFERENCES

Menzel, W. P.,W. L. Smith, and T. R. Stewart, 1983: Improved cloud motion wind vector and altitude assignment using VAS. J. Clim. Appl. Meteor., 22, 377-384.

Wylie, D. P., and W. P. Menzel, 1988: Cloud cover statistics from GOES/VAS, in preparation.

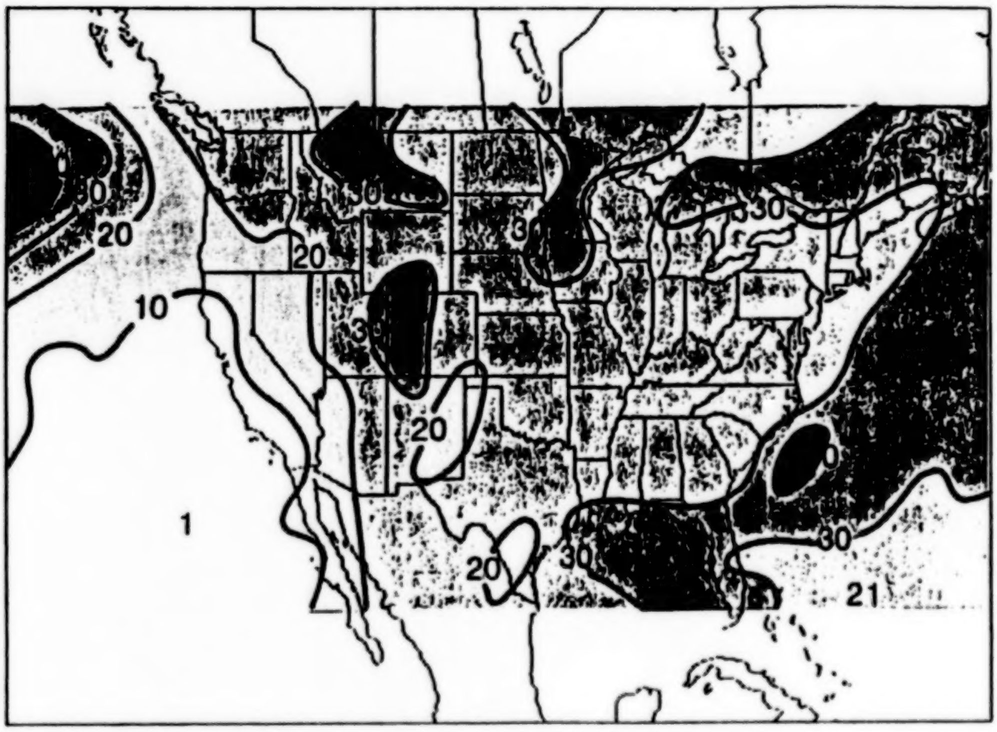
30
20
20
10
30
30
30
20
1
30
30
20
30
21

PROBABILITY OF CIRRUS IN SUMMER

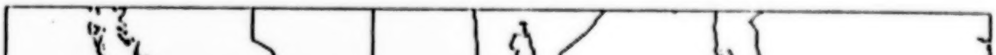
20
20
30
30
30
30
20
20
30
30
14
15

PROBABILITY OF CIRRUS IN WINTER

Figure 1: Probability of finding cirrus clouds in summer (June- August) and winter (December-February). Two winters and summers were averaged together.

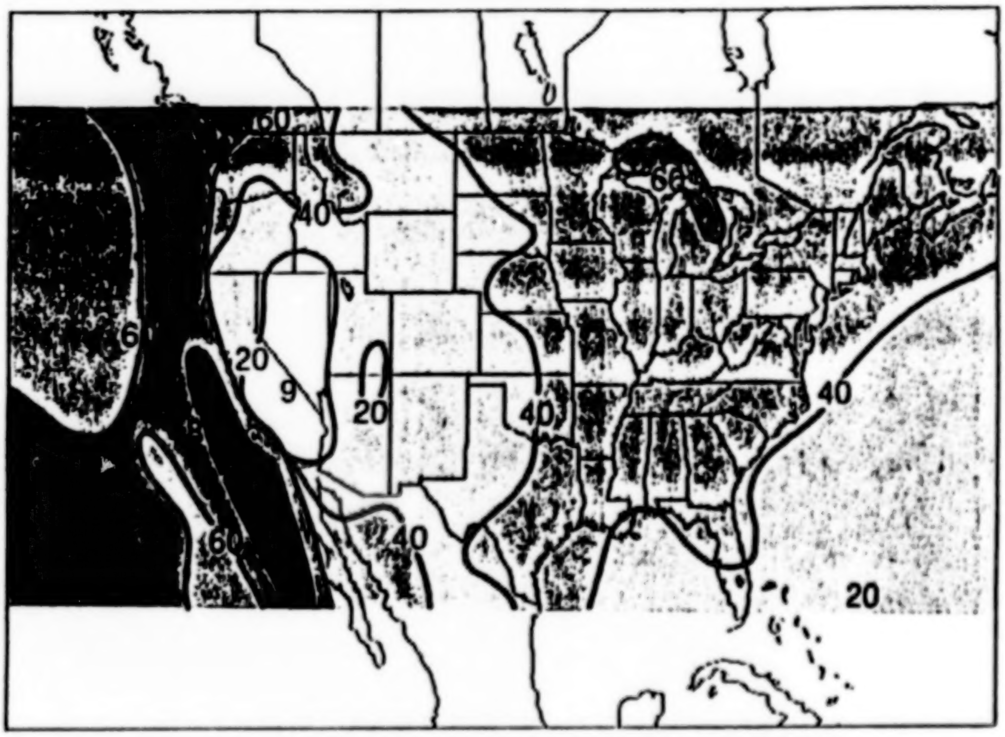
60
60
40
6
20
9
20
40
40
60
40
20

PROBABILITY OF OPAQUE CLOUD IN SUMMER

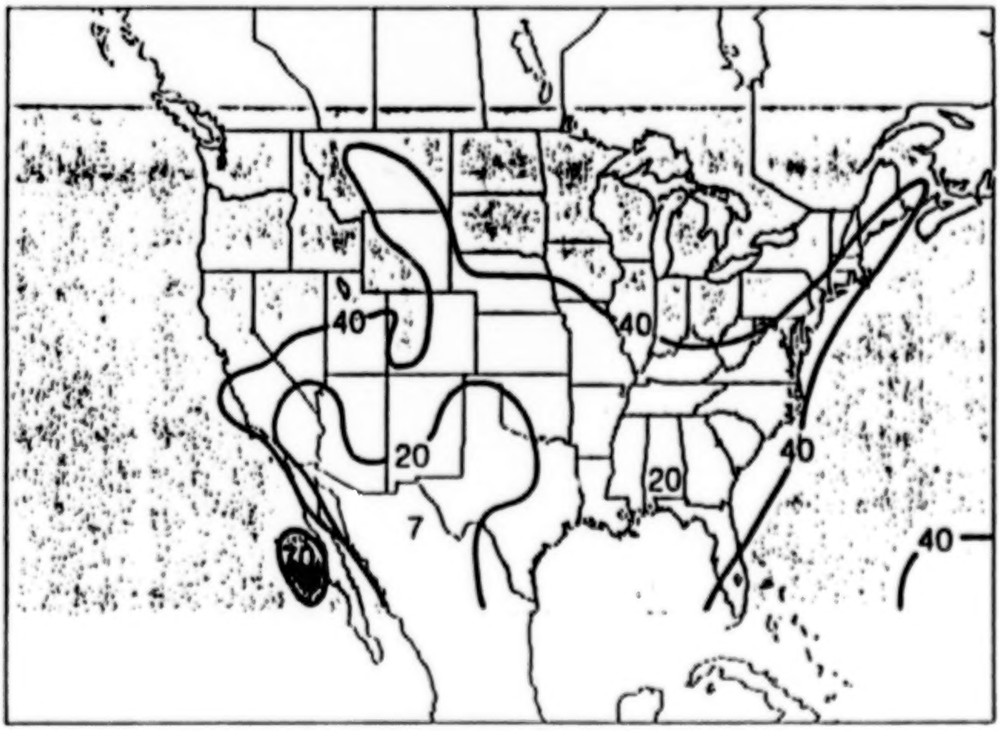
40
40
20
20
40
7
40
70

PROBABILITY OF OPAQUE CLOUD IN WINTER

Figure 2: Probability of finding Opaque clouds in summer and winter.

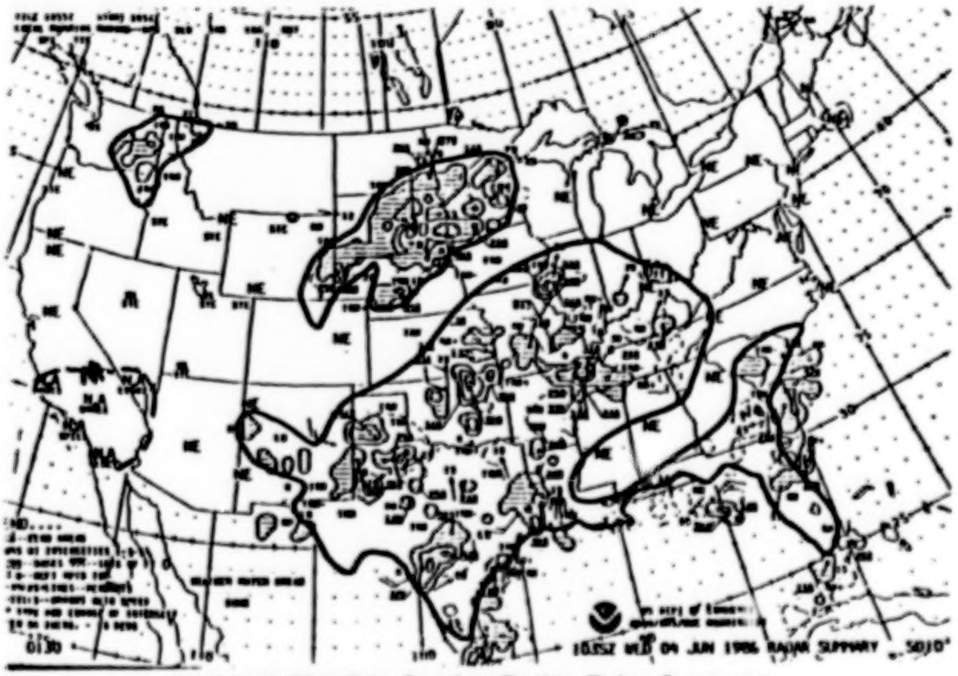

National Weather Service Radar Echo Summary

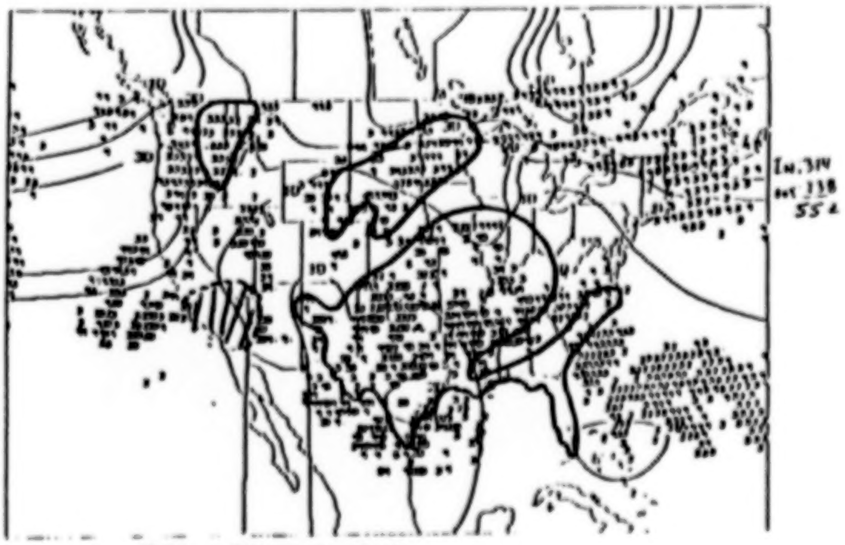

Cirrus Cloud Analysis

Figure 3: An example of a National Weather Service Radar Echo Summary used of defining locations of cumulonimbus clouds. The extended boundary of probable cirrus anvil is defined by the thick line.

FIRE/FSET MEETING ABSTRACT

ISCCP RESULTS FOR THE FIRE IFO REGIONS AND TIMES

William B. Rossow

NASA Goddard Space Flight Center
Institute for Space Studies
2880 Broadway
New York, New York 10025

The ISCCP analysis of cloud conditions during and in the vicinity of the FIRE Cirrus and Marine Stratus IFOs is presented in two forms: (1) the standard climatology product, which is averaged to a nominal 250 km resolution and (2) a pixel-by-pixel version that samples the original data at about 30 km spacing every three hours. These results are based on NOAA-9 and GOES-6 images covering October-November 1986 and July 1987 for the FIRE Extended Area. Comparisons of these results with other FIRE observations will serve to check the accuracy of the clear sky radiances inferred by the ISCCP analysis, which determine the accuracy of the cloud detections. Of more interest is the exploration of the dependence of the inferred cloud properties on the data resolution. Comparison to the higher resolution FIRE observations allows for direct evaluation of the role of small scale variability of cloud properties on the radiation field. This is illustrated by preliminary results obtained for the scales contained in the ISCCP data. The ISCCP analysis also sets the larger scale context of the FIRE data: (1) comparisons of the clouds occurring in the FIRE IFOs with nearby locations and times will be presented and (2) comparisons of the cloud conditions for the same months in other years will be shown.

Abstract for FIRE Science Experiment Team Meeting, Vail, CO, July 1988

CLOUD INFORMATION FOR FIRE FROM SURFACE WEATHER REPORTS

Carole J. Hahn[1], Stephen G. Warren[2], and Julius London[3]

[1] Cooperative Institute for Research in Environmental Sciences, University of Colorado, Boulder, CO 80309

[2] Dept. of Atmospheric Sciences AK-40, University of Washington, Seattle, WA 98195

[3] Dept. of Astrophysical, Planetary and Atmospheric Sciences, University of Colorado, Boulder, CO 80309

We have analyzed surface weather observations of clouds to obtain a global cloud climatology (Warren et al, 1986; 1988). The form of the synoptic weather code limits the types of cloud information which are available from these reports. Comparison of surface weather reports with instrumental observations during the FIRE field experiments can help to clarify the operational definitions which we have had to make in our climatology because of the nature of the synoptic code. The long-term climatology from surface weather observations can also be useful background for planning the location and timing of intensive field experiments.

1. Wisconsin cirrus experiment

As shown in Figure 2 of Warren et al (1985), cirrus occurs alone more often over the continents than over the ocean, and more often in winter than in summer. It was therefore appropriate to plan the field experiment for autumn in Wisconsin, and cases of cirrus-alone were indeed encountered.

Comparison of surface weather observations with the observations from aircraft and lidar may be used to estimate the minimum optical thickness that ground observers can detect. We collected the observations from surface observing stations made during the intensive field program October-November 1986. There are four stations in the area, but only two (Madison and Green Bay) include cloud type information in their weather reports. The observations are listed in Table 1 and summarized in Tables 2 and 3.

Based on the reports in which the presence or absence of cirrus could be ascertained, the frequency of occurrence of cirrus during the field experiment was 42% at Madison and 37% at Green Bay. Table 2 shows that cirrus was reported to be present alone in the weather observations from 22 October, 27-28 October, 31 October, and 1-3 November (after converting from GMT to local time), both at Madison and Green Bay. These are the same days that were chosen for intensive case-studies of cirrus in the field experiment. Three of these four cases were immediately preceded by reports of "clear sky". When the quantitative lidar results become available, we will therefore be able to determine at what optical thickness the cirrus was first detectable by the weather observers, as the cloud thickened from subvisible to visible.

Table 1. Cloud reports for Madison (station number 72641) and Green Bay (72645), 13 October - 3 November 1986. Symbols are defined in Table 4.

YR	MM	DY	HRZ	STA	WW	N	NH	CL	CM	CH
86	10	13	6	72641	**	8	8	8	*	*
86	10	13	6	72645	**	8	8	5	*	*
86	10	13	12	72641	2	8	8	5	*	*
86	10	13	12	72645	**	8	8	5	*	*
86	10	13	18	72641	**	8	8	5	*	*
86	10	13	18	72645	**	8	8	5	*	*
86	10	14	0	72641	61	8	8	5	*	*
86	10	14	0	72645	80	8	8	5	*	*
86	10	14	6	72641	1	8	5	5	5	*
86	10	14	6	72645	25	8	8	5	*	*
86	10	14	12	72641	51	8	6	7	*	*
86	10	14	12	72645	61	8	8	7	*	*
86	10	14	18	72641	71	8	8	5	*	*
86	10	14	18	72645	68	8	8	7	*	*
86	10	15	0	72641	1	7	5	5	0	8
86	10	15	0	72645	2	8	3	5	3	1
86	10	15	6	72641	**	1	1	0	5	0
86	10	15	6	72645	1	2	2	5	0	0
86	10	15	12	72641	**	0	*	*	*	*
86	10	15	12	72645	**	0	*	*	*	*
86	10	15	18	72641	**	1	1	1	0	0
86	10	15	18	72645	**	6	6	5	0	0
86	10	16	0	72641	**	0	*	*	*	*
86	10	16	0	72645	**	8	2	0	7	1
86	10	16	6	72641	**	8	2	0	5	7
86	10	16	6	72645	**	8	5	0	7	7
86	10	16	12	72641	**	9	8	0	5	*
86	10	16	12	72645	21	8	8	5	*	*
86	10	16	18	72641	**	1	1	5	0	0
86	10	16	18	72645	**	8	8	5	*	*
86	10	17	0	72641	**	8	8	6	*	*
86	10	17	0	72645	**	8	8	5	*	*
86	10	17	6	72641	**	8	8	6	*	*
86	10	17	6	72645	**	8	8	5	*	*
86	10	17	12	72641	**	8	5	5	*	*
86	10	17	12	72645	**	8	8	5	*	*
86	10	17	18	72641	**	6	6	5	0	0
86	10	17	18	72645	**	8	8	5	*	*
86	10	18	0	72641	**	2	2	5	0	0
86	10	18	0	72645	**	2	2	5	0	0
86	10	18	6	72641	**	0	*	*	*	*
86	10	18	6	72645	**	0	*	*	*	*
86	10	18	12	72641	**	6	6	5	0	0
86	10	18	12	72645	**	5	5	5	0	0
86	10	18	18	72641	**	4	4	5	0	0
86	10	18	18	72645	**	7	7	5	0	0
86	10	19	0	72641	**	0	*	*	*	*
86	10	19	0	72645	**	0	*	*	*	*
86	10	19	6	72641	**	0	*	*	*	*
86	10	19	6	72645	**	0	*	*	*	*
86	10	19	12	72641	48	0	*	*	*	*
86	10	19	12	72645	11	0	*	*	*	*
86	10	19	18	72641	2	0	*	*	*	*
86	10	19	18	72645	2	0	*	*	*	*
86	10	20	0	72641	**	0	*	*	*	*
86	10	20	0	72645	**	0	*	*	*	*
86	10	20	6	72641	10	0	*	*	*	*
86	10	20	6	72645	44	0	*	*	*	*
86	10	20	12	72641	**	6	3	5	7	0
86	10	20	12	72645	42	3	3	0	3	0
86	10	20	18	72641	**	0	*	*	*	*
86	10	20	18	72645	5	3	2	1	0	1
86	10	21	0	72641	**	3	1	0	5	1
86	10	21	0	72645	5	3	3	4	6	0
86	10	21	6	72641	**	0	*	*	*	*
86	10	21	6	72645	10	0	*	*	*	*
86	10	21	12	72641	11	1	1	5	0	0
86	10	21	12	72645	44	0	*	*	*	*
86	10	21	18	72641	5	0	*	*	*	*
86	10	21	18	72645	42	0	*	*	*	*
86	10	22	0	72641	**	0	*	*	*	*
86	10	22	0	72645	5	5	*	*	*	*
86	10	22	6	72641	**	0	*	*	*	*
86	10	22	6	72645	**	0	*	*	*	*
86	10	22	12	72641	10	6	0	0	0	6
86	10	22	12	72645	**	6	0	0	0	1
86	10	22	18	72645	**	8	6	0	1	7
86	10	23	0	72641	61	8	3	5	5	*
86	10	23	0	72645	5	8	8	0	2	*
86	10	23	6	72641	21	8	8	5	*	*
86	10	23	6	72645	**	8	8	0	2	*
86	10	23	12	72641	10	8	8	5	*	*
86	10	23	12	72645	46	8	8	5	*	*
86	10	23	18	72641	20	8	8	7	*	*
86	10	23	18	72645	**	8	8	6	*	*
86	10	24	0	72641	**	8	8	5	*	*
86	10	24	0	72645	**	8	8	5	*	*
86	10	24	6	72641	10	8	8	6	*	*
86	10	24	6	72645	**	7	6	5	7	0
86	10	24	12	72641	**	8	8	6	*	*
86	10	24	12	72645	**	8	8	5	*	*
86	10	24	18	72641	10	8	8	6	*	*
86	10	24	18	72645	**	8	2	5	0	7
86	10	25	0	72641	**	8	8	6	*	*
86	10	25	0	72645	**	8	8	5	*	*
86	10	25	6	72641	61	8	8	7	*	*
86	10	25	6	72645	**	8	8	5	*	*
86	10	25	12	72641	10	8	5	6	7	*
86	10	25	12	72645	**	6	6	5	0	0
86	10	25	18	72641	2	8	8	5	*	*
86	10	25	18	72645	**	8	8	5	*	*
86	10	26	0	72641	61	8	8	7	*	*
86	10	26	0	72645	**	8	8	5	7	*
86	10	26	6	72641	61	8	8	7	*	*
86	10	76	6	72645	**	8	8	5	*	*
86	10	26	12	72641	61	8	8	7	*	*
86	10	26	12	72645	51	8	8	7	*	*
86	10	26	18	72641	60	8	8	7	*	*
86	10	26	18	72645	51	8	8	7	*	*
86	10	27	0	72641	51	8	8	7	*	*
86	10	27	0	72645	10	8	8	6	*	*
86	10	27	6	72641	10	8	8	6	*	*
86	10	27	6	72645	42	8	8	6	*	*
86	10	27	12	72641	10	1	1	5	0	0
86	10	27	12	72645	10	7	7	5	0	0
86	10	27	18	72641	**	1	1	1	0	0
86	10	27	18	72645	5	2	2	1	0	0
86	10	28	0	72641	**	3	0	0	0	1
86	10	28	0	72645	**	2	0	0	0	1
86	10	28	6	72641	**	0	*	*	*	*
86	10	28	6	72645	**	0	*	*	*	*
86	10	28	12	72641	**	1	0	0	0	1
86	10	28	12	72645	10	0	*	*	*	*
86	10	28	18	72641	**	8	0	0	0	7
86	10	28	18	72645	**	8	0	0	0	7
86	10	29	0	72641	**	8	0	0	0	7
86	10	29	0	72645	**	6	0	0	0	8
86	10	29	6	72641	**	2	0	0	0	8
86	10	29	6	72645	**	4	1	0	7	8
86	10	29	12	72641	**	8	8	5	*	*
86	10	29	12	72645	**	8	8	5	*	*
86	10	29	18	72641	**	8	8	5	*	*
86	10	29	18	72645	**	3	3	5	0	0
86	10	30	0	72641	**	0	*	*	*	*
86	10	30	0	72645	**	0	*	*	*	*
86	10	30	6	72641	**	0	*	*	*	*
86	10	30	6	72645	**	4	4	0	3	0
86	10	30	12	72641	**	0	*	*	*	*
86	10	30	12	72645	**	7	7	5	0	0
86	10	30	18	72641	**	1	1	1	0	1
86	10	30	18	72645	**	7	7	5	0	0
85	10	31	0	72641	**	2	0	0	0	1
86	10	31	0	72645	**	3	3	5	0	0
86	10	31	6	72641	**	8	0	0	0	7
86	10	31	6	72645	**	6	0	0	0	6
86	10	31	12	72641	**	2	0	0	0	8
86	10	31	12	72645	**	7	3	0	7	8
86	10	31	18	72641	**	8	3	5	0	7
86	10	31	18	72645	**	8	3	5	7	7
86	11	1	0	72641	**	8	8	5	*	*
86	11	1	0	72645	**	8	8	5	*	*
86	11	1	6	72641	61	8	8	7	*	*
86	11	1	6	72645	61	8	8	7	*	*
86	11	1	12	72641	2	8	8	6	*	*
86	11	1	12	72645	1	8	8	5	*	*
86	11	1	18	72641	**	8	1	5	5	*
86	11	1	18	72645	**	3	2	1	0	1
86	11	2	0	72641	**	7	5	0	7	7
86	11	2	0	72645	**	8	8	0	1	*
86	11	2	6	72641	**	3	0	0	0	2
86	11	2	6	72645	**	2	0	0	0	7
86	11	2	12	72641	**	2	0	0	0	5
86	11	2	12	72645	**	0	*	*	*	*
86	11	2	18	72641	**	1	0	0	0	2
86	11	2	18	72645	**	0	*	*	*	*
86	11	3	0	72641	**	6	0	0	0	6
86	11	3	0	72645	**	7	0	0	0	8
86	11	3	6	72641	**	8	0	0	2	*
86	11	3	6	72645	**	8	0	0	0	7
86	11	3	12	72641	**	8	0	0	0	7
86	11	3	12	72645	**	8	8	5	*	*
86	11	3	18	72641	**	8	1	0	5	7
86	11	3	18	72645	**	8	6	0	3	2
86	11	4	0	72641	**	8	8	5	*	*
86	11	4	0	72645	**	3	8	5	*	*

Table 2. Analysis of cloud observations for cirrus at Madison and Green Bay, 13 October - 3 November 1986. Symbols are defined in Table 4.

	MADISON				GREEN BAY			
YRMODYHRZ	N	CH	A	CH=0 N/0	N	CH	A	CH=0 N/0
86101306	8	*			8	*		
86101312	8	*			8	*		
86101318	8	*			8	*		
86101400	8	*			8	*		
86101406	8	*			8	*		
86101412	8	*			8	*		
86101418	8	*			8	*		
86101500	7	8			8	1		
86101506	1			Y	2			Y
86101512	0				0			
86101518	1			Y	6			Y
86101600	0				8	1		
86101606	8	7			8	7		
86101612	8	*			8	*		
86101618	1			Y	8	*		
86101700	8	*			8	*		
86101706	8	*			8	*		
86101712	8	*			8	*		
86101718	6			Y	8	*		
86101800	2			Y	2			Y
86101806	0				0			
86101812	6			Y	5			Y
86101818	4			Y	7			Y
86101900	0				0			
86101906	0				0			
86101912	0				0			
86101918	0				0			
86102000	0				0			
86102006	0				0			
86102012	6			Y	3			Y
86102018	0				3	1		
86102100	3	1			3			Y
86102106	0				0			
86102112	1			Y	0			
86102118	0				0			
86102200	0				5	*		
86102206	0				0			
86102212	6	6	A		6	1	A	
86102218	*				8	7		
86102300	8	*			8	*		
86102306	8	*			8	*		
86102312	8	*			8	*		
86102318	8	*			8	*		
86102400	8	*			8	*		
86102406	8	*			7			Y
86102412	8	*			8	*		
86102418	8	*			8	7		
86102500	8	*			8	*		
86102506	8	*			8	*		
86102512	8	*			6			Y
86102518	8	*			8	*		
86102600	8	*			8	*		
86102606	8	*			8	*		
86102612	8	*			8	*		
86102618	8	*			8	*		
86102700	8	*			8	*		
86102706	8	*			8	*		
86102712	1			Y	7			Y
86102718	1			Y	2			Y
86102800	3	1	A		2	1	A	
86102806	0				0			
86102812	1	1	A		0			
86102818	8	7	A		8	7	A	
86102900	8	7	A		6	8	A	
86102906	2	8	A		4	8		
86102912	8	*			8	*		
86102918	8	*			3			Y
86103000	0				0			
86103006	0				4			Y
86103012	0				7			Y
86103018	1	1			7			Y
86103100	2	1	A		3			Y
86103106	8	7	A		6	6	A	
86103112	2	8	A		7	8		
86103118	8	7			8	7		
86110100	8	*			8	*		
86110106	8	*			8	*		
86110112	8	*			8	*		
86110118	8	*			3	1		
86110200	7	7			8	*		
86110206	3	2	A		2	7	A	
86110212	2	5	A		0			
86110218	1	2	A		0			
86110300	6	6	A		7	8	A	
86110306	8	*			8	7	A	
86110312	8	7	A		8	*		
86110318	8	7			8	2		
86110400	8	*			3	*		

Table 3. Summary of cirrus reports for Madison and Green Bay, 13 October-3 November 1986. Symbols are defined in Table 4.

	Number of reports	
	Madison	Green Bay
Total	87	88
N = 0	18	17
CH = *	37	36
Cirrus present	21	19
Cirrus alone	14	8
Cirrus absent, other clouds present	11	16

2. San Nicolas Island stratocumulus experiment

Our proposed contribution to this experiment was in support of the long-term monitoring study by remote-sensing instruments located on San Nicolas Island (SNI), which was begun during the intensive field program but continuing after it. Our proposed work was to evaluate the extent to which the island could influence the cloud patterns directly above, with the possibility that the measurements might not be representative of the surrounding ocean.

We acquired ship observations for the area from the California coast to the open ocean beyond SNI and analyzed them. We also obtained the weather observations from the station at the airport on the island. This station stopped making routine reports in 1986. Unfortunately, the island observations were made only in the Airways Code, whereas the ship reports were made only in the Synoptic Code. This precluded a comparison of the island station with the ships for cloud types, but a comparison of total cloud cover was possible.

This particular analysis turned out not to be useful because the site of the remote-sensing instruments, on the windward (northwest) tip of the island, experiences cloud conditions very similar to the ocean upwind and quite different from the airport (S. Cox, personal communication).

Ship observations show a strong increase in annual average cloud cover from land to ocean. The gradient is largest along the coast but is still evident out to 130°W (as much as 1000 km off shore). SNI is approximately 100 km from the shore and the gradients in this region can be locally quite large. Figure 1 shows an analysis of only a restricted set of these observations: the cloud reports from ships and land stations made during the time of the intensive field study.

Acknowledgement. This research was funded by NASA grant 2206-CL-229.

References

Warren, S.G., C.J. Hahn, J. London, R.M. Chervin and R.L. Jenne, 1986: Global Distribution of Total Cloud Cover and Cloud Type Amounts Over Land. NCAR Technical Note TN-273+STR, 29 pp + 200 maps.

Warren, S.G., C.J. Hahn, J. London, R.M. Chervin and R.L. Jenne, 1988: Global Distribution of Total Cloud Cover and Cloud Type Amounts over the Ocean. NCAR Technical Note in preparation.

Warren, S.G., C.J. Hahn and J. London, 1985: Simultaneous occurrence of different cloud types. J. Clim. Appl. Meteor., 24, 658-667.

Table 4. Symbols used in the tables

A	cirrus present alone	N	total cloud cover code
CH	high cloud type code	NH	low or middle cloud amount code
CL	low cloud type code	STA	station identification code
CM	middle cloud type code	WLON	west longitude
DY	day	WW	present weather code
HRZ	hour GMT	Y	cirrus absent but other clouds present
LAT	latitude	YR	year
MN	month	*	not reported

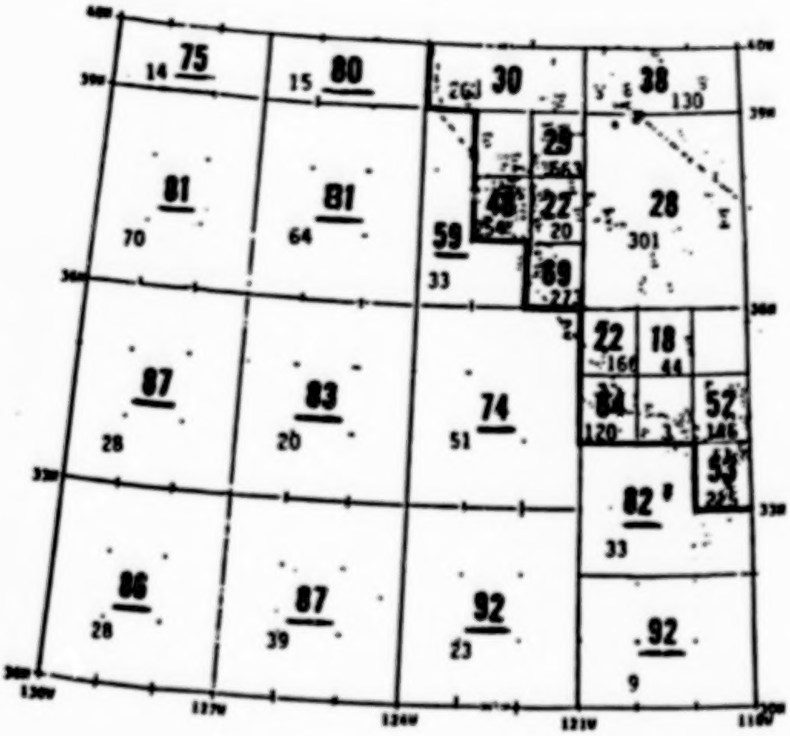
40N
39N
36N
33N
30N
130W
127W
124W
121W
118W
14 75
15 80
263 30
38 130
29 563
48
22 20
69 272
70 81
64 81
59 33
28 301
22 166
18 44
28 87
20 83
51 74
84 120
3
52 186
53 225
82 33
28 86
39 87
23 92
9 92

Figure 1a. Average total cloud cover for FIRE study area, 29 June - 20 July 1987. Bold face numbers in center of boxes are total cloud cover, numbers in smaller type are number of observations. The analysis was done for 1°x1° or 3°x3° grid boxes. The heavy line separates boxes with land-data predominating from boxes with ship data predominating.

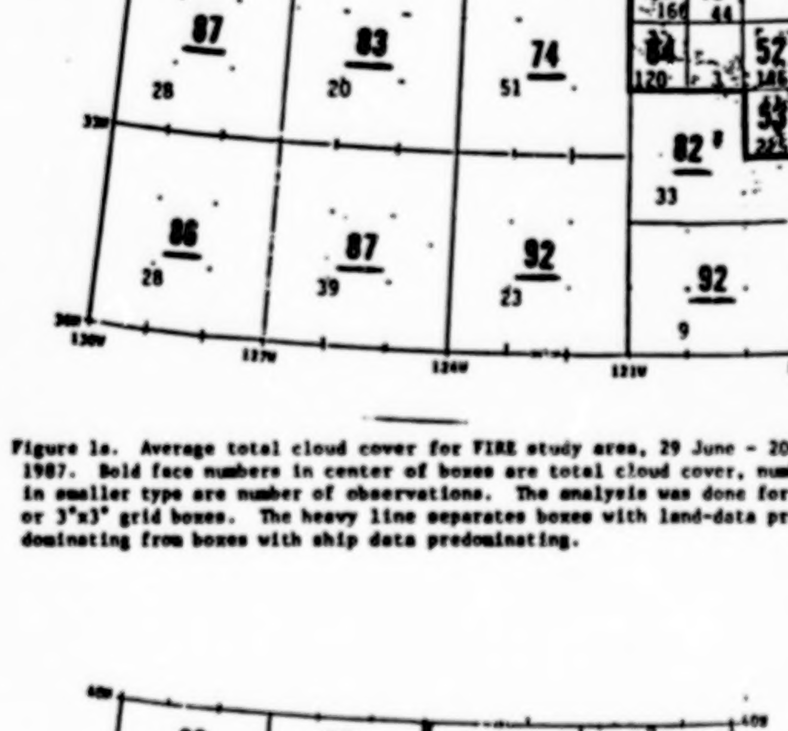
40N
39N
36N
33N
30N
130W
127W
124W
121W
118W
13 30
13 39
218 2
1125 3
1 604
7 127
3 15
63 53
62 49
27 44
21
247 0
0 110
0 23
24 54
16 47
44 33
21 99
0 52
29 201
28 40
28 54
33 62
19 61
9 72

Figure 1b. Average amount of stratocumulus for FIRE study area, 29 June - 20 July 1987.

CIRRUS CLOUD MODEL PARAMETERIZATIONS: INCORPORATING REALISTIC ICE PARTICLE GENERATION

K. Sassen and G.C. Dodd
Department of Meteorology, University of Utah
Salt Lake City, UT 84112

D.O'C. Starr
NASA Goddard Space Flight Center
Greenbelt, MD 20771

Recent cirrus cloud modeling studies (Starr and Cox, 1985; Starr, 1986) have involved the application of a time-dependent, two-dimensional Eulerian model, with generalized cloud microphysical parameterizations drawn from experimental findings. Employed in the model are a grid resolution of 100 m and a time step of 30 s. For computing the ice-versus-vapor phase changes (at 3-min intervals), the ice mass content is linked to the maintenance of a relative humidity with respect to ice (RHI) of 105%; ice growth occurs both with regard to the introduction of new particles and the growth of existing particles. To initiate ice particle formation in regions devoid of ice particles, a RHI of 120% is required. In a simplified cloud model designed to investigate the basic role of various physical processes in the growth and maintenance of cirrus clouds, these parametric relations are justifiable.

In comparison, the one-dimensional cloud microphysical model recently applied to evaluating the nucleation and growth of ice crystals in cirrus clouds (Sassen and Dodd, 1988) explicitly treated populations of haze and cloud droplets, and ice crystals within a 200 m height domain above cloud base, using 0.25-s time steps and specified updraft velocities. The model findings were used to infer a cloud droplet homogeneous freezing rate in compliance with aircraft and ground-based polarization lidar observations. Moreover, implications for ice particle formation outside the limited height domain of the model were suggested by the findings.

Although these two modeling approaches are clearly incompatible, the goal of the present numerical study is to develop a parametric treatment of new ice particle generation, on the basis of detailed microphysical model findings, for incorporation into improved cirrus growth models. For example, we can determine the relation between temperature and the relative humidity required to generate ice crystals from ammonium sulfate haze droplets, whose probability of freezing through the homogeneous nucleation mode are a combined function of time and droplet molality, volume, and temperature. Within cirrus clouds at temperatures colder than about -37°C, homogeneous drop freezing will most likely result from a decrease in molality as the droplet equilibrium size increases in response to increasing relative humidity, which can be caused by either enhanced updraft velocities or a decrease in water vapor competition effects (from ice crystal fallout). Molality dominates the haze droplet freezing process as a consequence of the very strong dependence of the freezing rate on drop temperature, which is modified by the freezing point depression as a function of drop molality. The adjustment of haze droplets to new equilibrium sizes in an accelerating parcel occurs very rapidly.

As an example of this approach, in Fig. 1 we present the results of cloud microphysical simulations showing the rather narrow domain in the temperature/humidity field where new ice crystals can be generated. The three solid curves (a,b,c) represent the conditions under which equilibrium haze droplets of ammonium sulfate (with CCN masses and radii given in the figure caption) have an even chance of freezing homogeneously within typical cirrus growth model time steps--the relation $P_f(0,60) = 0.5$ is the probability that one-half of the equilibrium droplets will freeze within a 60-s time interval. The area beneath the three curves represents a reservoir of stable haze droplets; the curves themselves are both a sink for haze droplets and a source of ice crystals; and the area above the curves becomes, in effect, a forbidden domain of temperature and humidity. The boundary defined by the curves has the same significance as the 100% relative humidity barrier, which is rarely exceeded by more than a few percent in atmospheric clouds, that must be overcome to form clouds at temperatures warmer than about -37°C.

When viewed in this manner, it is clear that much higher ice supersaturations than recent modeling efforts have employed are required to produce ice crystals within the homogeneous nucleation temperature domain. We note, however, that the RHI = 150% value indicated in Fig. 1 for new ice particle generation is similar to that derived from cirrus uncinus studies by Heymsfield (1975) for populations of ammonium sulfate droplets. Ice particle nucleation within cirrus will be modulated by vapor competition effects from existing ice particles such that, as the relative humidity increases, the growth of the haze droplets that freeze first (i.e., the largest droplets) inhibits further nucleations from the remaining reservoir of haze droplets (formed from smaller CCN masses). Hence, depending on the CCN concentrations and size spectra, depletion of the largest haze particles present would, over time, require gradually increasing relative humidities in order to generate new ice crystals, as shown in Fig. 1 by the intersection of an isotherm with curves c through a.

These microphysical simulations point out the need for detailed CCN studies at cirrus altitudes and haze droplet measurements within cirrus clouds, but also suggest that a relatively simple treatment of ice particle generation, which includes cloud chemistry, can be incorporated into cirrus cloud growth models.

Acknowledgments. This study is being supported by Grant ATM-85 13975 from the National Science Foundation.

References

Heymsfield, A., 1975: Cirrus uncinus generating cells and the evolution of cirriform clouds. Part III: Numerical computations of the growth of the ice phase. J. Atmos. Sci., 32, 820-830.
Sassen, K. and G.C. Dodd, 1988: Homogeneous nucleation rate for highly supercooled cirrus cloud droplets. J. Atmos. Sci., 45, 1357-1369.
Starr, D.O'C., 1986: Cirrus clouds: Effects of microphysical composition and radiative processes. Preprints (Vol. 3), Conference on Cloud Physics, Snowmass, CO, Am. Meteor. Soc., J187-J190.
Starr, D.O'C. and S.K. Cox, 1985: Cirrus clouds. Part I: A cirrus cloud model. J. Atmos. Sci., 42, 2663-2681.

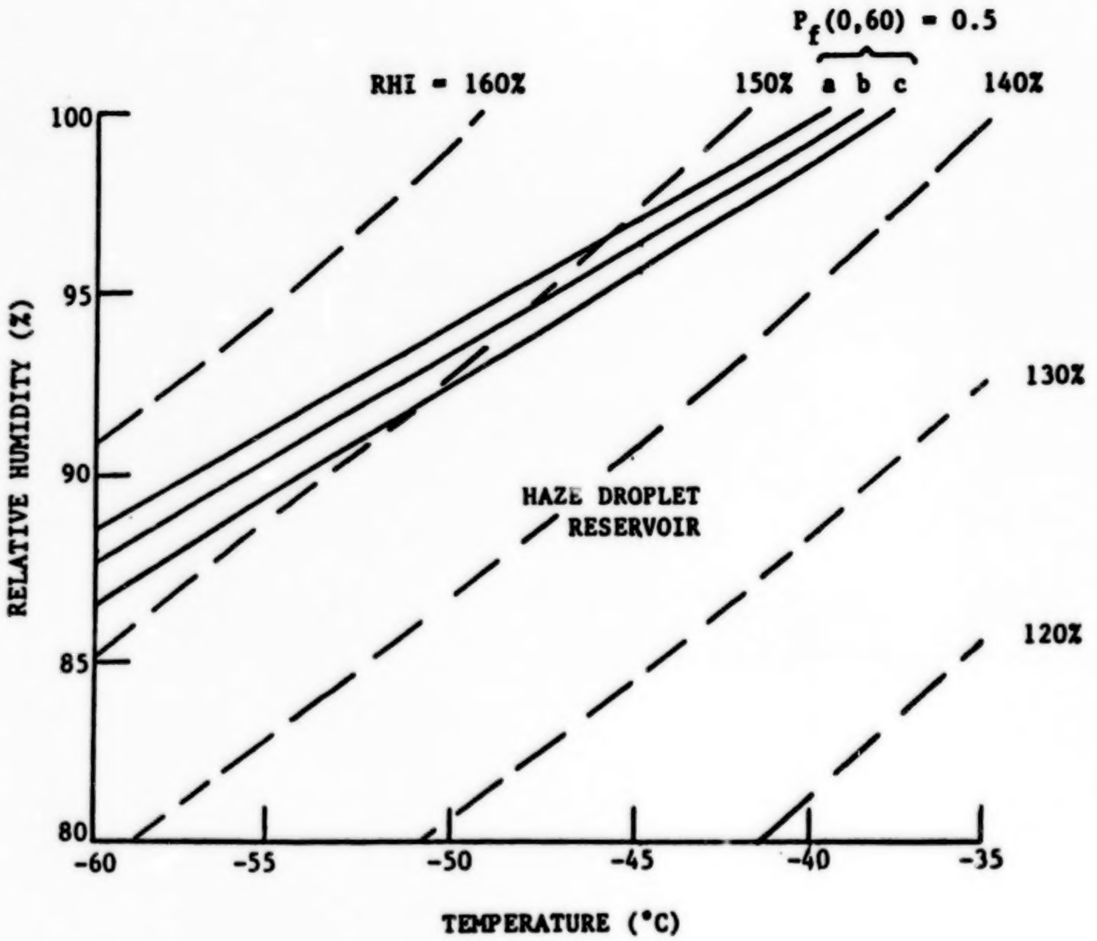

Fig. 1 A schematic representation of the temperature dependency in relative humidity values (with respect to water) needed to nucleate new ice crystals from the homogeneous freezing of haze droplets. The three curves are for ammonium sulfate cloud condensation nuclei (CCN) masses and radii of a) 10^{-14} g and 0.11 µm; b) 10^{-13} g and 0.24 µm; and c) 10^{-12} g and 0.51 µm. The dashed curves give relative humidities with respect to ice (RHI). The homogeneous freezing rate derived by Sassen and Dodd (1988) and a constant pressure of 300 mb have been used in the calculations.

EVIDENCE FOR ASYMMETRIC INERTIAL INSTABILITY IN THE FIRE SATELLITE DATASET

Duane E. Stevens and Paul E. Ciesielski
Department of Atmospheric Science, Colorado State University, Fort Collins, CO 80523

1. Introduction

One of the main goals of the First ISCCP regional experiment (FIRE) as stated in the original research plan – 'is obtaining the basic knowledge to better interpret satellite images of clouds on regional and smaller scales'. In this paper an analysis of a mesoscale circulation phenomenon as observed in hourly FIRE satellite images is presented. Specifically, the phenomenon of interest appeared on satellite images as a group of propagating cloud wavelets located on the edge of a cirrus canopy on the anticylonic side of a strong, upper–level subtropical jet. These wavelets, which were observed between 1300 and 2200 GMT 25 February 1987, are seen most distinctly in the GOES-West infrared satellite picture at 1800 GMT (Fig. 1). *The purpose of this paper is to document that these wavelets were a manifestation of asymmetric inertial instability.* (In this context, asymmetric means that the unstable perturbations exhibit structure in the direction of the basic state flow). During their lifetime, the wavelets were located over the North American synoptic sounding network, so that the meteorological conditions surrounding their occurrence could be examined (Section 2). A particular emphasis of the analysis in Section 2 is on the jet streak in which the wavelets were imbedded. The characteristics of the wavelets are examined in Section 3 using hourly satellite imagery. In Section 4 we examine the hypothesis that inertial instability is the dynamical mechanism responsible for generating the observed cloud wavelets. To further substantiate this contention, the observed characteristics of the wavelets are compared to, and found to be consistent with, a theoretical model of inertial instability by Stevens and Ciesielski (1986; hereafter referred to as SC). Our conclusions are summarized in Section 5.

2. Meteorological conditions

The meteorological conditions associated with the evolution of the cloud wavelets shown in Fig. 1 were investigated over the western two-thirds of the United States using conventional sounding data. Due to the paucity of these observations only the gross features of the upper–level flow field have been captured in our analysis. This problem is compounded even further by missing data which occurred in the vicinity of the jet stream probably due to radiosonde tracking problems.

On February 23, 1987, a vigorous winter storm system began affecting the western United States. By the 24th, the system was nearly occluded with an intense surface low centered over Nevada. The upper level features were dominated by a large, positively tilted trough which extended from Saskatchewan, Canada into a cutoff low centered over Nevada. Over the next few days the system weakened, but began to reorganize and intensify over New Mexico early on the 26th as an upper–level short wave propagating through the trough moved into a position favorable for support of the surface wave.

The upper–level jet stream in which the wavelets were imbedded is of particular interest to this study. Fig. 2 (left–hand panel) shows the wind speed analysis at 250 mb for 1200 GMT 25 February. At this time the jet core had maximum winds of 100 ms^{-1} and was centered around 250 mb; below this level vertical shears of 40 ms^{-1} $(100\ mb)^{-1}$ were present. South of the jet axis, horizontal shears were 10 ms^{-1} $(100\ km)^{-1}$. It is in this region of strong anticyclonic shear that the cloud wavelets were observed. In the 12 hour period following 1200 GMT 25 February the maximum intensity of the jet remained approximately constant (Fig 2, right–hand panel), however the horizontal wind shear on the anticyclonic side of the jet core reduced significantly to 7 ms^{-1} $(100\ km)^{-1}$.

3. Characteristics of the cloud wavelets

The predominant large–scale features in the satellite image of Fig. 1 are the cloudiness associated with the surface low over New Mexico and the broad shield of mainly high and middle–level clouds extending from southwest of Mexico to over the central states. This latter feature, which is often referred to as a 'baroclinic cloud leaf', is associated with a rising, moist airstream within the subtropical jet. Weldon (1979) has noted that the sharp western boundary of the upper tropospheric cloud leaf often coincides closely with a wind speed maximum or with a zone of strong winds.

In the satellite images prior to 1300 GMT, the western edge of the cloud leaf was relatively sharp and unperturbed. At 1300 GMT the cloud leaf over Baja, California showed the first evidence of being perturbed. During the next three hours two distinct wavelets grew over this region and propagated northeastward parallel to the jet core axis until they appear to dissipate around 1700 GMT. Contemporary, with the dissipation of these wavelets a second group began to form near the U.S.–Mexican border. By 1800 GMT three cloud wavelets are observed. These wavelets propagated in a similar fashion to those described above and can be tracked until they dissipated around 2200 GMT; no wavelets could be identified after this time.

By creating a loop of hourly satellite images for the 25th, we were able to track the position of individual wavelets from one hour to the next. Fig. 3 shows the hourly positions of one of these wavelets superimposed with the locations of the jet axis. Fig. 3 also depicts the orientation and size of the wavelet during its life cycle. The general shape of the wavelets was that of an ellipse with its major axis oriented parallel to the jet axis. The life cycle of these wavelets appeared to have a growth stage (~ 1 hour), a mature stage (2–3 hours) and a decay stage (~ 1 hour) in which their identification becomes increasingly difficult. During their mature stage the wavelets varied in size from 200–250 km (along their major axis) and 65–100 km (along their minor axis). In addition, it appears that the wavelets moved parallel to the jet axis, in groups of two or three, and at a distance about 50 km to its anticyclonic side. In their mature stage the average distance between the centers of adjacent wavelets was ~ 400 km. Using this scale as the wavelength (L_x) of the wavelets and noting that their average speed of propagation (c) was ~ 80 ms^{-1}, we arrive at a period (L_x/c) for the wavelets of 1.4 hours. The brightness temperature in the interior of the cloud canopy ranged from -44 to -52 °C. Based on these values and the observed temperatures from soundings taken in the vicinity of these clouds, it appears that the wavelets and cloud leaf were composed of ice particles with cloud tops around 250 mb.

4. Dynamical mechanism for perturbed flow

Although several dynamical mechanisms (gravity waves, barotropic instability and inertial instability) could be hypothesized as the cause for the perturbed flow described above, the following discussion examines the most likely one, that is, *inertial instability*.

In the general case of flow with horizontal and vertical shear, a necessary condition for inertial instability is $fP < 0$ somewhere in the fluid where P is the potential vorticity and f the Coriolis parameter. Figs. 4 (left–hand panel) shows the analysis of potential vorticity for three layers between 200 and 400 mbs at 1200 GMT on the 25th. Due to the large number of missing and bad wind observations in the vicinity of the jet, we elected to use the geostrophic wind in the evaluation of P. Height data, which is used in the computation of geostrophic wind, had much better spatial coverage than winds for the times under consideration. The key feature in the analysis of potential vorticity on the 25th is a region of negative potential vorticity over New Mexico extending southwestward to over Baja, California. The region of negative P is evident in all three layers but is most pronounced above 300 mb where the anticyclonic shear associated with the jet streak was strongest. An alternate view of the potential vorticity analyses is presented in Fig. 5 which shows its relationship to the geostrophic wind in a cross–section through the jet. At the time of this analysis, the core of the jet streak and the associated region of large negative P were located several hundred kilometers upstream of where this cross–section was taken. The 'X' in Fig. 5 shows the observed location of the wavelets at 1800 GMT. From the analyses presented in Figs. 4 and 5, we conclude that *the condition for inertial instability was satisfied in the region and over the time frame that the wavelets existed*. A second area of weak negative potential vorticity is evident over southeastern Texas; however, its existence is questionable due to our lack of confidence in the geostrophic winds over this area.

The only significant change in the potential vorticity analysis at 0000 GMT on the 26th (Fig. 4, right–hand panel) is that the area of negative P directly to the anticylonic side of the jet streak, which on the 26th was positioned over Kansas, no longer existed. This suggests that the mechanism responsible for generating the wavelets also resulted in the elimination of the region of negative P.

Since inertial instability appears to be a reasonable explanation for the appearance of the wavelets, we now compare their characteristics (as discussed in Section 3) with theoretical estimates for asymmetric inertial instability from SC. For a Bickley jet of 75 ms^{-1} and a half–width of 3° at latitude 45° N, SC found that asymmetric perturbations would propagate at ~ 45 ms^{-1} with respect to the ground (or 30 ms^{-1} slower than the maximum wind). The observed wavelets propagated at an average speed of 80 ms^{-1} (or 25 ms^{-1} slower than the maximum wind). Using SC's estimates of growth rate for asymmetric perturbations in the present case results in an unstable e-folding time scale of 5.4 hours; the wavelets life cycle was between 4–5 hours. Finally, SC estimated that the length scale of the asymmetric perturbations in the direction of the jet axis ($L_x/2\pi$) is comparable to the width of the unstable region. For the observed wavelets this length scale is ~ 70 km whereas the width of the region with $P < 0$ varied between 100–200 km in the 250–300 mb layer. Although we have no means of estimating the vertical depth of the perturbed flow from the observed data, SC found that asymmetric modes of instability are preferred over the symmetric one for vertical scales greater than 3 km.

5. Concluding remarks

From the analyses in the previous sections we hypothesise the following scenario of events. At 1200 GMT on the February 25th a strong jet streak imbedded within the subtropical jet current was observed over Baja, California. South of the jet streak was an area of negative potential vorticity associated with the strong anticylonic shear in this region. During the next twelve hours this jet streak moved along the front side of a deep upper-level trough over the western U.S. at an average speed of ~ 25 ms^{-1}. During this period asymmetric inertial instability developed in response to the negative potential vorticity. This instability was manifested in a series of mesoscale cloud wavelets which formed along the western edge of a cirrus canopy. These wavelets, which were observed in satellite images between 1300 GMT and 2200 GMT on the 25th, propagated parallel to the jet core at an average speed of 80 ms^{-1}. These unstable perturbations acted to mix the flow thereby reducing the horizontal shears until the region of negative potential vorticity was eliminated.

This paper has presented the hypothesis that the wave disturbances observed in the satellite pictures of 25 February 1987 were excited by inertial instability. The characteristics of the cloud wavelets tend to support this hypothesis through comparison between observations and the theoretical estimates of SC. Analysis of the potential vorticity fields has been used to provide further evidence of a dynamical source of the instability. The observations represent a positive verification of the theoretical and numerical prediction of asymmetric instability in SC.

One might reasonably question the relationship between these observations and the extensive work of Emanuel and collaborators (e.g., Emanuel, 1979; Emanuel, 1982). In these papers Emanuel treated neutral waves which manifested a balance between the destabilising influence of vertical shear and stabilising Newtonian dissipation. Perturbations with structure along the direction of the parallel jet were not considered. By contrast, the instability treated here results primarily from the horizontal shear. Nevertheless, the *effect* of the instability is similar to that assumed in more recent Emanuel papers, that is, regardless of the particular structural characteristics of the perturbations, inertial instability serves to mix the potential vorticity, thereby causing the modified flow to have non-negative potential vorticity.

Our ability to describe the detailed characteristics of the instability presented in this paper has been limited by the sparseness of direct observations. These deficiencies in the observational data base have left us with many interesting, but unanswered questions. (e.g., What is the vertical scale of the perturbed flow? Are the instabilities characterised by vertical motion?) *The most direct way to answer these and other relevant questions would be with an intensive field observational program such as FIRE Cirrus IFO (Starr, 1987).* An alternate approach, which we are currently pursuing, is to model these instabilities. To our knowledge, explicit calculation of inertial instabilities in a two-dimensionally sheared basic state has not been accomplished.

Finally, it may be noted that initial analyses in numerical models may contain regions of negative potential vorticity and spurious rapid growth of unstable perturbations. One approach, already suggested by Dunkerton (1983) for equatorial shear, is to increase the numerical dissipation in order to eliminate the instability. Perhaps a more representative initialisation procedure would include an inertial adjustment step in which fP was required to be non-negative at every point in the domain.

Acknowledgements

The authors wish to thank Kelly Dean and Dick Johnson for their valuable contributions to this work. This research was supported by the Presidential Young Investigator Award (NSF Grant ATM-8352205) to D. Stevens.

REFERENCES

Emanuel, K. A., 1979: Inertial instability and mesoscale convective systems. Part I: Linear theory of inertial instability in rotating viscous fluids. *J. Atmos. Sci.*, **36**, 2425–2499.

Emanuel, K. A., 1982: Inertial instability and mesoscale convective systems. Part II: Symmetric CISK in a baroclinic flow. *J. Atmos. Sci.*, **39**, 1080–1097.

Starr, D. O'C, 1987: A cirrus-cloud experiment: Intensive field observations planned for FIRE. *Bull. Amer. Meteor. Soc.*, **68**, 119-124.

Stevens, D. E., and P. E. Ciesielski, 1986: Inertial instability of horizontally sheared flow away from the equator. *J. Atmos. Sci.*, **43**, 2845–2856.

Weldon, R. B., 1979: Cloud patterns and upper air wind field. *Part IV, Satellite Training Course Notes.* [Available from Satellite Application Laboratory, NESDIS/NOAA, Washington, D.C., 20233, 80 pp.]

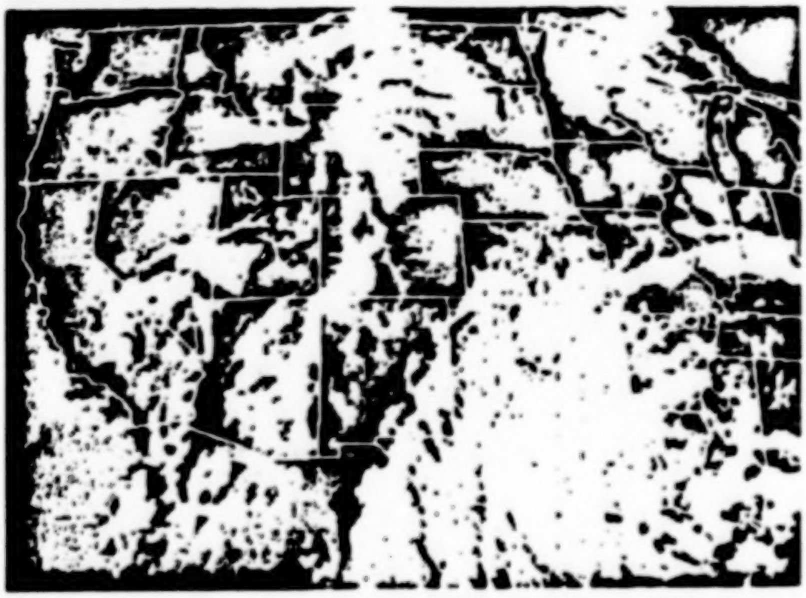

Figure 1. GOES-West infrared satellite image for 1800 GMT, 25 February 1987 showing mesoscale cloud wavelets over New Mexico.

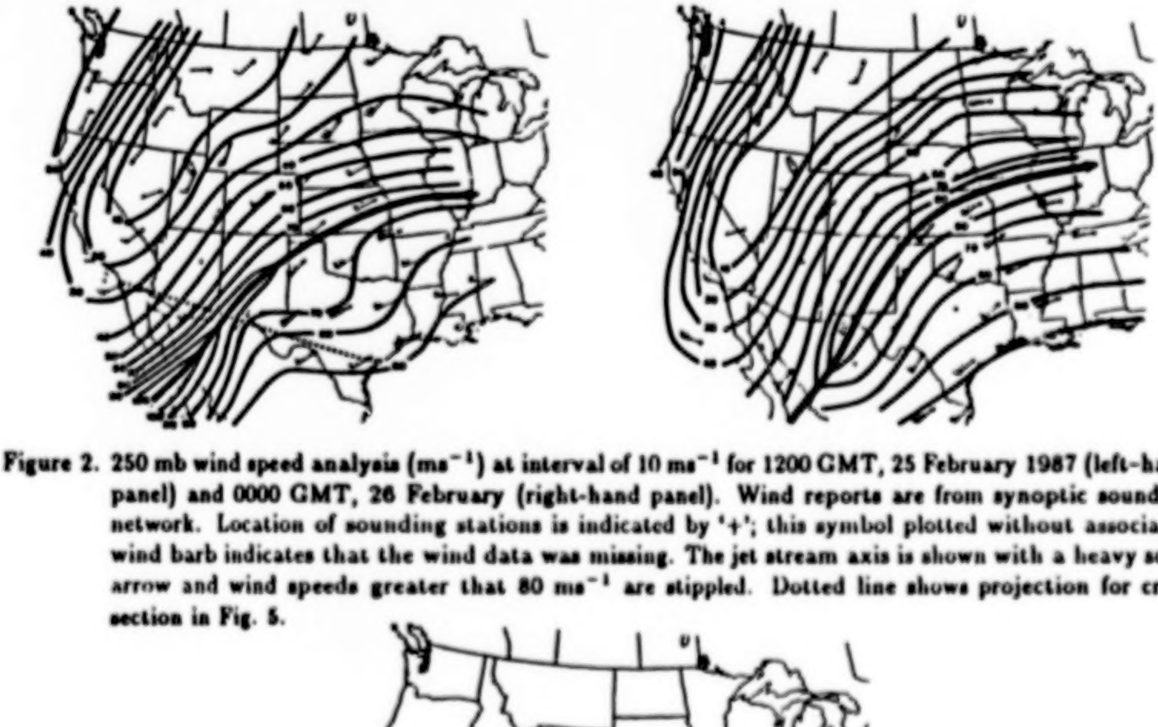

Figure 2. 250 mb wind speed analysis (ms^{-1}) at interval of 10 ms^{-1} for 1200 GMT, 25 February 1987 (left-hand panel) and 0000 GMT, 26 February (right-hand panel). Wind reports are from synoptic sounding network. Location of sounding stations is indicated by '+'; this symbol plotted without associated wind barb indicates that the wind data was missing. The jet stream axis is shown with a heavy solid arrow and wind speeds greater that 80 ms^{-1} are stippled. Dotted line shows projection for cross section in Fig. 5.

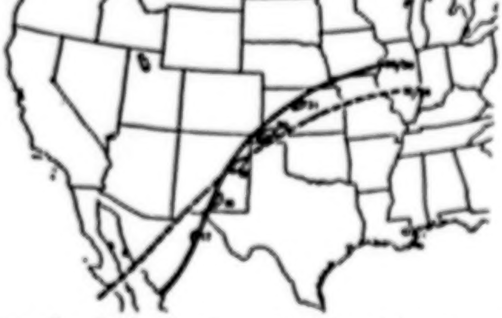

Figure 3. Hourly positions and shape of a single cloud wavelet inferred from satellite images. Numbers plotted by wavelet indicate the time (GMT) at which that position was observed. Also shown here are the positions of the jet stream axis at 1200 GMT, 25 February, 1987 (dashed line) and at 0000 GMT, 26 February, 1987 (solid line).

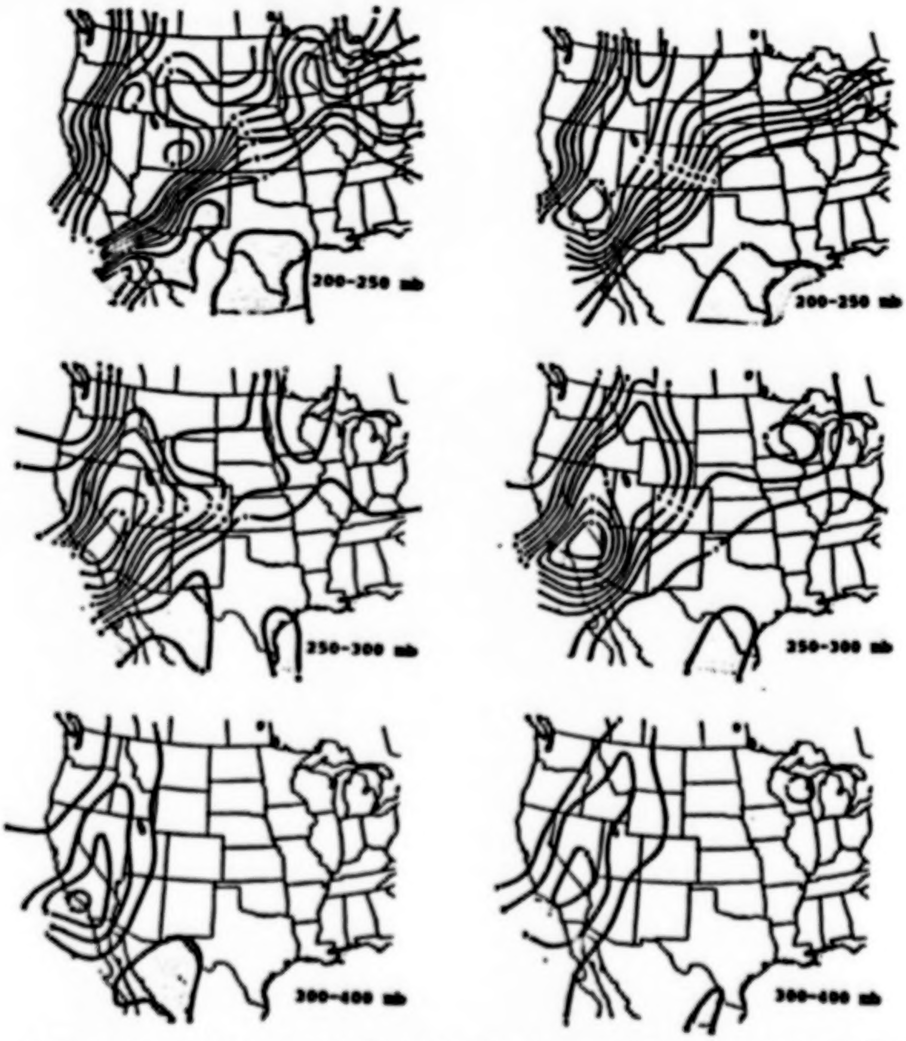

Figure 4. Analysis of potential vorticity ($m^2KKg^{-1}s^{-1}$) at 1200 GMT, 25 February 1987 (left-hand panel) and 0000 GMT, 26 February 1987 (right-hand panel) for the layers 200–250 mb (top), 250–300 mb (middle) and 300–400 mb (bottom). Values in figure have been multiplied by 10^6.

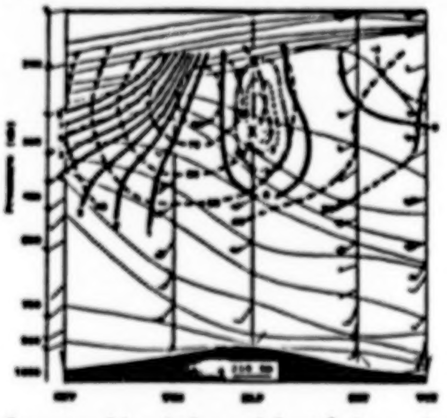

Figure 5. Cross-section analysis of geostrophic wind speed (ms^{-1}, heavy dashed lines) at intervals of 10 ms^{-1} and potential temperature (K, thin solid lines) at intervals of 5 K along dotted line in Fig. 2 for 1200 GMT, 25 February 1987. Plotted wind barbs show observed wind (ms^{-1}) for comparison to geostrophic wind speed. Analysis of potential vorticity ($m^2KKg^{-1}s^{-1}$, heavy solid line for positive values at intervals of 10^6 and dotted lines for negative values at intervals of 10^5). Position of wavelets at 1800 GMT on the 25th are denoted with an 'X'. Rawinsonde soundings are from San Diego, California (MYF), Tucson, Arizona (TUS), El Paso, Texas (ELP), Del Rio, Texas (DRT), Victoria, Texas (VCT).

Climate Data System Supports FIRE

Lola M. Olsen
Dominick Iascone
Mary G. Reph

National Space Science Data Center
NASA Goddard Space Flight Center
Greenbelt, MD 20771

Extended Abstract for Oral and Poster Presentation

The NASA Climate Data System (NCDS) at Goddard Space Flight Center is serving as the FIRE Central Archive, providing a centralized data holding and data cataloging service for the FIRE project. NCDS members are carrying out their responsibilities by holding all reduced observations and data analysis products submitted by individual principal investigators (PIs) in the agreed upon format, by holding all satellite data sets required for FIRE, by providing copies of any of these data sets to FIRE investigators, and by producing and updating a catalog with information about the FIRE holdings.

FIRE researchers were requested to provide their reduced data sets in the Standard Data Format (SDF) to the FIRE Central Archive. This standard format is proving to be of value among FSET members who share their data. An improved Standard Data Format (SDF) document is now available. There are no format changes – only improvements in clarity. The document provides an example from an actual FIRE SDF data set and clearly states the guidelines for formatting data in SDF. Researchers may refer to these instructions to create an SDF tape header or utilize the interactive GOFIRE program which exists on the NCDS "sample" SDF tape. Several data producers have used GOFIRE successfully to produce FIRE tape headers.

NCDS has received sample Standard Data Format (SDF) tapes from a number of investigators. These tapes have been analyzed and comments provided to the producers. These comments primarily consisted of compatibility and efficiency suggestions for the final product. Several investigators have delivered their complete reduced data set in "final" form to the NCDS. An NCDS programmer has completed software to inventory SDF tapes, and these tapes will be inventoried as they are received. By checking the NCDS Inventory Subsystem, FIRE PIs can immediately determine which data sets are available. NCDS will make copies of these tapes available to any FIRE PI on request. In addition, software has been completed to automatically convert the SDF data to the Common Data Format (CDF). In CDF, these data can be previewed, accessed, or browsed using the tools provided by the NCDS DATA MANIPULATION and GRAPHICS Subsystems. The staff at NCDS has been preparing for the arrival of more SDF data sets.

One product which is now available is William J. Syrett's sodar data product from the Marine Stratocumulus Intensive Field Observation. These data were automatically ingested into the NCDS, and the GRAPHICS Subsystem was used to produce the displayed plot. Verification of the NCDS's interpretation of Syrett's SDF data was possible by comparing this plot with a similar one contained in his publication – *Hourly Wind, Potential Temperature and Richardson Number Profiles at San Nicolas Island During Project FIRE*, **FIRE Technical Report No. 2.** Other interpretation checks are done by comparing data to those listed in the producer's test file.

Sample plots from all SDF tapes submitted to the archive will be available to FSET members. NCDS currently restricts access to data products in the FIRE Central Archive to researchers associated with the FIRE project. At a later time – when these data are to be released to the public by the Principal Investigators – NCDS will transition these data to public access and provide its usual data services. This should remove some burden on the producers in meeting their research obligations.

Members of the NCDS staff are continuing to archive FIRE satellite tapes for distribution to FIRE Science Team members. Extensive holdings of AVHRR GAC, LAC, and HRPT; TOVS HIRS, MSU, and SSU; and GOES VISSR data are available to FIRE researchers. Limited LANDSAT scenes are also available. NCDS will provide listings of available products. Investigators can also interactively check NCDS's on-line inventory to obtain the most current listing. This inventory also offers information on other useful data products, such as the ISCCP B-3 satellite data, and FSET members may obtain copies of any of these tapes.

Related cloud products are also available through NCDS. NCDS provides access - both in the form of tape copy and in Common Data Format - for the Nimbus-7 Temperature Humidity Infrared Radiometer (THIR) Cloud Product (THIR CMATRIX). This product is available for April 1979 through March 1985. The same level of access will be available for the ISCCP Cloud Products, ISCCP-C1 and ISCCP-C2. Sample plots from these data sets will be available for scrutiny.

Entries describing the FIRE data sets are being provided for the NCDS on-line catalog. Detailed information for the Extended Time Observations is available in the general FIRE catalog entry. Separate catalog entries are being written for the Cirrus Intensive Field Observation (IFO) and for the Marine Stratocumulus IFO. Updates for these catalog entries are made as changes in information and data are received at NCDS. Short descriptions of each FIRE data set will be installed into the NCDS Summary Catalog. These descriptions are available as one-screen displays in NCDS's catalog format.

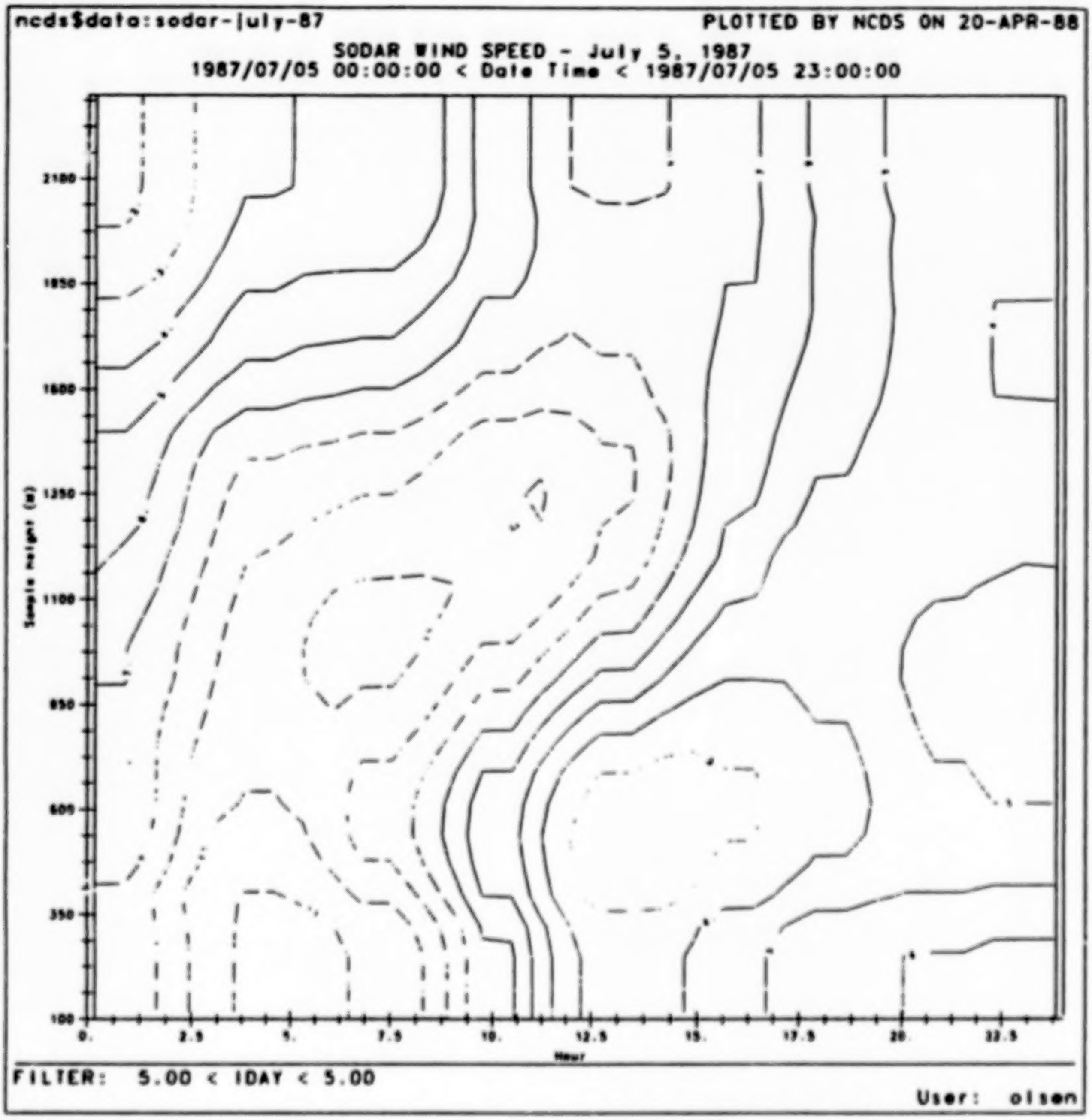

ncds$data:sodar-july-87

PLOTTED BY NCDS ON 20-APR-88

SODAR WIND SPEED - July 5, 1987
1987/07/05 00:00:00 < Date Time < 1987/07/05 23:00:00

FILTER: 5.00 < IDAY < 5.00

User: olsen

THE EFFECTS OF CLOUD RADIATIVE FORCING ON AN OCEAN-COVERED PLANET

David A. Randall
Department of Atmospheric Science
Colorado State University
Fort Collins, Colorado 80523

1. Introduction Cloud radiative forcing (CRF) may be defined as the difference between the radiative flux (at the top of the atmosphere, say) which actually occurs in the presence of clouds, and that which would occur if the clouds were removed but the atmospheric state were otherwise unchanged. The term CRF can also be used to denote warming or cooling tendencies due to cloud-radiation interactions.

The Colorado State University general circulation model (GCM) is being used to simulate the CRF. Like most current climate models, the CSU GCM does not include an interactive ocean. As a result, the simulated surface CRF acts only on the land surface. The model results show, however, that the surface CRF and the atmospheric CRF (hereafter, ACRF) have very different effects on the large-scale circulation.

In order to isolate the effects of the ACRF, we have simulated the general circulation of an ocean-covered earth, which we call "Seaworld." The key simplifications in Seaworld are the fixed boundary temperature with no land points, the lack of mountains, and the zonal uniformity of the boundary conditions.

2. Computational procedure The CSU GCM is derived from the UCLA GCM developed by A. Arakawa and collaborators. The main differences in the CSU model are revised parameterizations of terrestrial and solar radiation, which have been introduced in order to allow more satisfactory simulations of cloud-radiation interactions.

Three types of clouds are generated by the model: convective "anvil" clouds, supersaturation clouds, and boundary layer stratocumulus clouds. Cumulus convection is parameterized following the theory of Arakawa and Schubert (1974). Convective clouds are assumed to have negligible cloud fraction below 400 mb. If convection penetrates above 400 mb, however, an optically thick "anvil" cloud is assumed to horizontally fill the grid column, from 400 mb to the highest level reached by the convection. Supersaturation clouds are assumed to occur when the relative humidity equals or exceeds 100%, are assigned a cloud fraction of 1, and are assumed to vertically fill the GCM layer where they occur. Boundary-layer clouds can be arbitrarily thin; their cloud fraction is 1 when they are more than 12.5 mb deep, and decreases to zero linearly as their pressure thickness decreases from 12.5 mb to zero. The optical properties of the supersaturation and boundary-layer clouds are assumed to vary with cloud pressure-thickness and also with temperature, such that cold clouds are optically thinner than warm clouds of the same pressure-thickness. This crudely represents the "optical depth feedback". The clear-sky radiative fluxes have been saved as diagnostic results before cloud effects are accounted for; they are thus defined for all grid points, not just those that happen to be cloud-free.

The prescribed zonally uniform sea-surface temperatures of Seaworld are based on the simulated zonally averaged (including both land and sea) boundary temperature obtained in a July "Earth" simulation. For simplicity, an albedo appropriate to the oceans has been used everywhere; we have not included any effects of seaice.

The Seaworld simulations were initialized from the June 1 conditions of the Earth simulation, and all boundary conditions were instantaneously changed to those of Seaworld, except that the mountains were gradually flattened out over a period of two simulated days, to avoid extreme sloshing of the model atmosphere. We performed two 90-day "perpetual July" simulations, and analyzed the last 60 days of each. The first run included all of the model's physical parameterizations, while the second omitted the effects of clouds in both the solar and terrestrial radiation parameterizations. Since the boundary temperatures are fixed and identical in the two runs, the clouds can affect the results *only* through the ACRF; the differences between the two runs, therefore, reveal the direct and indirect effects of the ACRF on the large-scale circulation and the parameterized hydrologic processes.

3. Results The ACRF in the cloudy run corresponds very well to the radiative heating perturbation relative to the cloud-free run. Fig 1 shows the integral of the ACRF across the atmosphere in the cloudy run. This represents a warming of up to 70 W m^{-2} in the Northern Hemisphere tropics. Also shown in the figure are the change in the net radiation into the atmosphere (including both the earth's surface and the top of the atmosphere), and the change in the total energy flux into the atmosphere, from both radiation and turbulent sensible and latent heat fluxes. The change in the net radiation between the two runs essentially reflects the existence of ACRF in the cloudy run. The change in the total energy flux is similar to the change in the change in the net radiation, but the tropical peak is higher. The tropical atmosphere adjusts to the ACRF in such a way that *the warming due to the ACRF is amplified, i.e., there is a positive feedback.*

Fig. 2 shows the zonally averaged precipitable water for both runs. Interestingly, the clouds act to drastically increase the moisture content of the atmosphere. The cloudy run has much more precipitable water than the cloud-free run--almost twice as much in the tropics. This increased moisture has qualitatively the same effect on the atmospheric radiation balance as the ACRF: both tend to warm the atmosphere. The atmospheric moisture content of the cloudy Seaworld is much more earth-like than that of the cloud-free Seaworld, although of course it is not clear to what extent we should expect "Seaworld" to look like the earth.

The net effect of the ACRF is to warm the middle troposphere by up to 8 K at the 6 km level. The increased precipitable water content of the cloudy model atmosphere cannot be explained by assuming fixed relative humidity and taking into account the warmer temperatures. The actual reason for the increased moisture content of the cloudy atmosphere involves the large-scale motions, as discussed further below.

Fig. 3 shows the zonally averaged precipitation for both the clear and cloudy runs. There is a double tropical rain band in the cloud-free run, and a single, more intense tropical rain band in the cloudy run. Generally, the precipitation is much more concentrated in the cloudy run, and much more diffuse in the cloud-free run. The cloud-free run produces relatively weak but frequent convection, while the cloudy run produces relatively intense but infrequent convection. The globally averaged precipitation is about 15% greater in the cloudy run, which is a remarkably small change considering the large difference in the moisture content of the atmosphere. Tropical evaporation increases significantly in the cloudy run. The increased evaporation is partly due to the fact that the tropical PBL air is about 2 g kg^{-1} drier in the cloudy run, and partly due to a 3 m s^{-1} increase of the PBL wind speed in the cloudy run. The reason for the stronger winds is discussed further below.

Not surprisingly, the mean meridional circulation differs quite substantially between the two runs. As shown in Fig. 4, both runs produce two Hadley Cells--a weak cell in the Northern Hemisphere, and a strong one in the Southern Hemisphere. With clouds, the main Hadley Cell transports slightly more than 200 x 10^9 kg sec^{-1}, and is centered on the equator, with its rising branch at about 10 ° N. Without clouds, it transports only about 120 x 10^9 kg sec^{-1}, and is centered at about 10 ° south. The mean meridional circulation in the cloudy run is considerably more realistic than that in the cloud-free run.

In association with the stronger Hadley circulation in the cloudy run, the PBL wind speed increases by about 3 m s^{-1} in the tropics. This is partly responsible for the stronger surface evaporation. The increased surface latent heat flux in the cloudy run explains the "amplification" of the atmospheric warming due to the ACRF.

The cloudy run has more deep convective activity, concentrated in a narrow band near 15 ° N, where the intense Hadley Cell has its rising branch. The cloud-free run has two relatively weak convective heating maxima, near 10° S and 25° N. When ACRF is included, radiative cooling at the tops of avils leads to intense penetrative convection from the PBL, and it also promotes moist adjustment in the upper tropical troposphere. This intense convective activity leads to increased tropical precipitation. This drives a stronger Hadley circulation, further increasing the precipitation. The Northern Hemisphere circulation is selectively amplified because the sea surface temperatures are warmer there. The subsidence associated with the Northern Hemisphere Hadley Cell tends to suppress the Southern Hemisphere Hadley Cell and its associated precipitation. When ACRF is present, the system selects a relatively narrow but intense zone of latent heating.

Naturally, the zonal wind is strongly influenced by the changes discussed above. The ACRF increases the intensity of the tropical easterlies, particularly near the surface and the tropopause; and it also enhances the midlatitude westerly jets, shifting the Northern Hemisphere jet equatorward.

The PBL is considerably deeper in the cloudy run particularly near 10 ° N, where the cloudy run has strong low-level rising motion. Increased large-scale convergence favors an increased PBL depth in this region. A deeper PBL is also favored by the warmer troposphere in the cloudy run, which implies a weaker inversion at the PBL top; and by radiative cooling at the tops of PBL stratus clouds, which promotes rapid entrainment.

As a result of the increased PBL depth, the precipitable water content of the PBL is much larger in the cloudy run, even though, as noted above, the PBL specific humidity is actually slightly smaller. Most of the simulated increase in the precipitable water occurs in the troposphere above the PBL, however. Moisture is introduced there by a two-step process. First, it is carried out of the PBL and injected into the troposphere by cumulus detrainment; the cumulus clouds transport moisture upwards even as they rain it out. It is then redistributed vertically, through advection by the rising branch of the Hadley Cell, and also by large-scale precipitation/re-evaporation.

The cloudy run has a strong maximum of cumulus detrainment that coincides precisely with a radiative cooling maximum due to cumulus anvil tops. The intense deep convection in the ITCZ of the cloudy run is promoted by radiative destabilization of the column. It is also favored by the increased strength of the Hadley circulation. The Hadley Cell is invigorated by the greater warming at 10° N, due to both ACRF and cumulus convection.

Of course, in the "cloud-free" run the clouds were radiatively inactive, but we saved their distribution as a diagnostic. The upper tropical troposphere is almost twice as cloudy in the "cloud-free" run as in the cloudy run. This is partly due to an increase in the relative humidity there, associated with cooler temperatures, but it is also due to the increased frequency of cumlus activity, which leads to greater anvil cloudiness.

The ACRF is the only difference between the model formulations used in the two Seaworld runs. The effects of ACRF on Seaworld's climate are dramatic, to say the least. By destabilizing the tropical atmosphere, and at the same time providing a net warming of the column, it favors both an enhanced Hadley circulation and deeper, more intense, but less widespread convection. The intensified convection further invigorates the Hadley circulation, and vice versa. The stronger surface winds associated with the more intense Hadley circulation lead to greater surface evaporation in the tropics, while the rising branch of the Hadley circulation dramatically moistens the free atmosphere. At the same time, the greatly reduced frequency of convection and the increased temperature of the tropical middle troposphere tend to reduce the cloudiness, especially at the upper levels, and so feedback on the ACRF.

The net effects of ACRF on the radiative-convective-dynamical system of Seaworld are to locally intensify deep cumulus convection, to reduce the cumulus incidence, to amplify the mean meridional circulation, and to dramatically increase the moisture content of the atmosphere, at the same time reducing the upper level cloudiness that is primarily responsible for the ACRF. All of this occurs without any major changes in the *globally averaged* precipitation or evaporation rates. These results illustrate a three-way regional interaction among the ACRF, the convection, and the large-scale dynamics. The feedbacks among the three components are strongly positive. At the same time, however, each of the three components feeds back negatively on itself: the ACRF warms the column and so tends to reduce the relative humidity; the convection increases the moist static stability of the column and so tends to shut itself off; and the large-scale circulation depletes its own source of available potential energy. These negative feedbacks determine how the system equilibrates.

8. Summary and concluding remarks Cumulus anvil clouds, whose importance has been emphasized by observationalists in recent years, exert a very powerful influence on deep tropical convection by tending to radiatively destabilize the troposphere. In addition, they radiatively warm the column in which they reside. Their strong influence on the simulated climate argues for a much more refined parameterization in the GCM.

For Seaworld, the ACRF has a powerful influence on such basic climate parameters as the strength of the Hadley circulation, the existence of a single narrow ITCZ, and the precipitable water content of the atmosphere. It seems likely, however, that in the real world the surface CRF feeds back negatively to suppress moist convection and the associated cloudiness, and so tends to counteract the effects of the ACRF. Many current climate models have fixed sea surface temperatures but variable land-surface temperatures. The tropical circulations of such models may experience a positive feedback due to ACRF over the oceans, and a negative or weak feedback due to surface CRF over the land. The overall effects of the CRF on the climate system can only be firmly established through much further analysis, which can benefit greatly from the use of a coupled ocean-atmosphere model.

ACKNOWLEDGEMENTS: I am grateful to Harshvardhan and D. Dazlich for useful discussions. This research has been supported by NASA's Climate Program. Computing resources were provided by the Numerical Aerodynamic Simulation Program at NASA/Ames. References have been made informally, to save space.

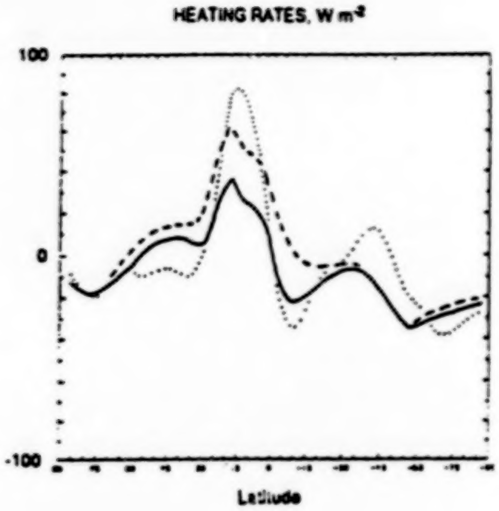

Figure 1 (left): *Differences* between the Seaworld runs with and without clouds. Solid line: The ACRF across the atmosphere. Dashed line: Net radiation into the atmosphere, including both the earth's surface and the top of the atmosphere. Dotted line: Total energy flux into the atmosphere, from both radiation and turbulent sensible and latent heat fluxes.

Figure 2 (right): Zonally averaged precipitable water for the cloudy run (solid line) and the cloud-free run (dashed line).

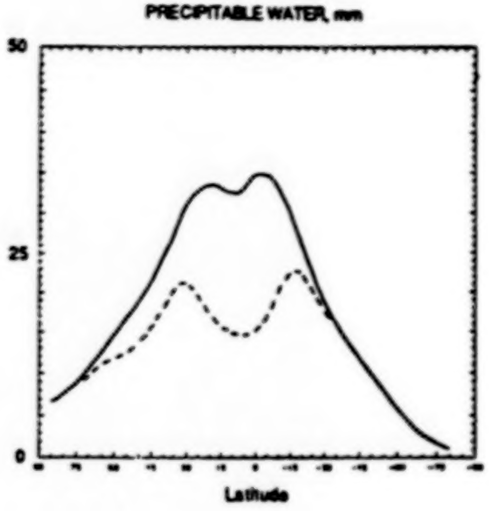

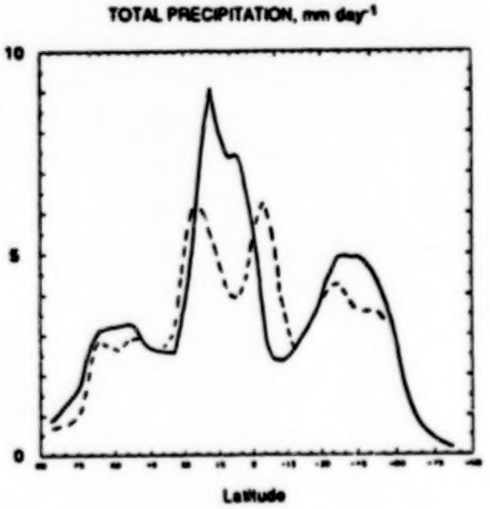

Figure 3: Zonally averaged precipitation for the cloudy run (solid line) and the cloud-free run (dashed line).

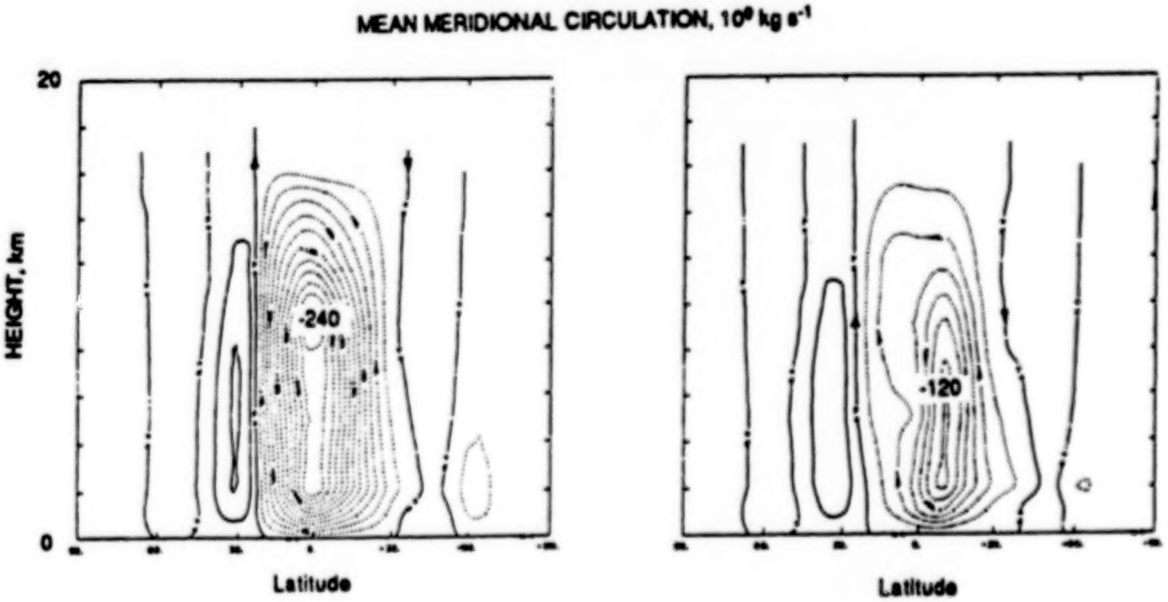

Figure 4: Mean meridional circulations for the cloudy run (left panel) and the cloud-free run (right panel).

FIRE SCIENCE TEAM MEETING
VAIL, COLORADO
JULY 11-15, 1988

CIRRUS

LIDAR/RADIATIVE PROPERTIES/MICROPHYSICAL - Andrew J. Heymsfield   Monday, July 11, 1988

PAGE

A Synopsis of Langley Research Center's Lidar Effort for the 1986 FIRE IFO ... 47
Alvarez, J. M.; M. P. McCormick, J. D. Moore, W. H. Hunt, B. R. Rouse, L. R. Poole, and B. D. Poole

Optical and Morphological Properties of Cirrus Clouds Determined by the High Spectral Resolution Lidar During FIRE ... 49
Grund, Christian J.; and Edwin W. Eloranta

Hydrometer Development in Cold Clouds in FIRE ... 55
Heymsfield, Andrew J.; Nancy C. Knight, and Kenneth Sassen

Lidar and Aircraft Studies of Deep Cirrus Systems from the 1986 FIRE IFO ... 61
Sassen, K.; A. Heymsfield, and N. Knight

Vertical Velocities within a Cirrus Cloud from Doppler Lidar and Aircraft Measurements During FIRE: Implications for Particle Growth ... 67
Gultepe, Ismail; and Andrew Heymsfield

A SYNOPSIS OF LANGLEY RESEARCH CENTER'S LIDAR EFFORT FOR THE 1986 FIRE IFO

by

J. M. Alvarez[1], M. P. McCormick[1], J. D. Moore[2], W. H. Hunt[2], B. R. Rouse[1],
L. R. Poole[1], and B. D. Poole[1]

The lidar data obtained by the Langley 14" Aircraft Lidar in October 1986 in Wisconsin is being reduced in a transparent, simple fashion and will be published in its reduced form in a NASA Reference Publication (RP). This reduced data will also be submitted to the FIRE data archives. Some of this reduced data will be presented at the FIRE FSET Workshop to acquaint the Science Team with the data format to be used in the archive and the upcoming catalog contained in the RP.

A new method was utilized in Wisconsin for obtaining the depolarization ratio of aerosols. This method involves using a half-wave plate to calibrate the lidar under field conditions. The theory behind this technique will be presented at this workshop as well as some of the lidar calibration results. The lidar calibration will be utilized in interpreting some of the dual polarization lidar data obtained during the IFO in Wisconsin. Some of these data will also be discussed at this workshop.

A continuous wave laser lab-type lidar simulator was constructed during the previous year. One of the primary reasons for the construction of the simulator was to attempt dual-polarization lidar-like calibrations under laboratory, rather than field conditions. The data collected by this system was used to experimentally check and thus, inspire confidence in the algorithms being used to interpret the lidar data obtained in the field. A computer program which simulates noisy lidar data was used as part of this effort in order to obtain some feel for the noise in the inversion parameters as a function of noise in the actual measurements. The lidar simulation will be described at this workshop in addition to presenting some of the lab-generated calibration data.

---

[1] NASA Langley Research Center, Atmospheric Sciences Division,
Hampton, VA 23665-5225
[2] Wyle Laboratories, Hampton, VA 23666

Optical and Morphological Properties of Cirrus Clouds Determined by the High Spectral Resolution Lidar During FIRE

Christian J. Grund and Edwin W. Eloranta
University of Wisconsin, Department of Meteorology
1225 W. Dayton St., Madison, WI. 53706

I. Introduction

Cirrus clouds reflect incoming solar radiation and trap outgoing terrestrial radiation; therefore, accurate estimation of the global energy balance depends upon knowledge of the optical and physical properties of these clouds. Scattering and absorption by cirrus clouds affect measurements made by many satellite-borne and ground-based remote sensors. Scattering of ambient light by the cloud, and thermal emissions from the cloud can increase measurement background noise. Multiple scattering processes can adversely affect the divergence of optical beams propagating through these clouds. Determination of the optical thickness and the vertical and horizontal extent of cirrus clouds is necessary to the evaluation of all of these effects. Lidar can be an effective tool for investigating these properties.

During the FIRE cirrus IFO in Oct.-Nov. 1986, the High Spectral Resolution Lidar (HSRL) was operated from a rooftop site (43^{0} 4' 29" N, 89^{0} 24' 26", 347.8 m msl) on the campus of the University of Wisconsin at Madison, Wisconsin. Approximately 124 hours of fall season data were acquired under a variety of cloud optical thickness conditions. Since the IFO, the HSRL data set has been expanded by more than 63.5 hours of additional data acquired during all seasons. This paper will present measurements of the range in optical thickness and backscatter phase function of cirrus clouds, as well as contour maps of extinction corrected backscatter cross sections indicating cloud morphology.

In our talk, we will present color enhanced images of range-time indicator (RTI) displays of a variety of cirrus clouds with ~30 sec time resolution. We will also demonstrate the importance of extinction correction on the interpretation of cloud height and structure from lidar observations of optically thick cirrus.

II. Technique

Because the lidar return signal from any range depends on both the backscatter cross section and the 2-way optical depth to that range, simple lidar systems, which make one measurement at each range, may not separately measure backscatter and extinction. Accurate knowledge of the extinction at one range, and a profile of the range dependence of the backscatter to extinction ratio (backscatter phase function), is essential to the determination of extinction from these lidar systems[1]. The HSRL differs from simple lidar systems in that it separates the particulate backscatter component from the molecular backscatter component of the lidar return.[2] Extinction is directly and unambiguously determined from the separated molecular backscatter return and an atmospheric density profile. This is possible because the atmospheric density determines the molecular backscatter cross section, thereby establishing a known target available at every range. The separation of molecular from particulate backscatter is achieved by observing differences in the spectral distribution of the scattered energy. The rapid thermal motion of the molecules Doppler-broadens the molecular backscatter spectrum. Particulates are more massive than molecules and are thus characterized by slower Brownian drift velocities which produce insignificant broadening of the scattered spectrum. The HSRL observes the return signal in two channels: a spectrally broad channel encompassing the molecular backscatter spectrum, and a spectrally narrow channel centered on the transmitted wavelength. With a system calibration[3], the 2-channel signals may be inverted to provide separate profiles of particulate and molecular scattering. Once the extinction is determined, the separated particulate scattering profile may be directly employed to determine the backscatter phase function.

III. Data Analysis

The particulate backscatter cross sections presented in fig.'s 1 - 4 were produced from inverted, time averaged particulate and molecular scattering profiles acquired during fixed, vertically-pointing HSRL operations. They represent contour maps of the extinction corrected backscatter intensity of the cirrus clouds as they evolve in time and drift over the HSRL with the ambient winds. To reduce statistical noise, and mitigate the effects of aerosol-molecular channel cross talk, the HSRL in-cloud molecular backscatter signal has been obtained according to the following algorithm: 1) regions of small particulate-molecular channel cross talk (i.e. regions characterized by background aerosol and/or pure Rayleigh backscatter) are identified both above and below the cloud, 2) in these cloud-free regions, a least squares fit is produced of the observed molecular signal to the expected profile for a pure molecular scattering atmosphere calculated from a density profile, 3) the clear air observed signals are replaced with the smooth best fit estimates above and below the cloud, 4) the total cloud extinction is determined from the decrease in the best fit molecular signal across the cloud determined in step 3, while accounting for the expected decrease in molecular cross section with altitude, 5) on the assumption of a constant backscatter phase function and constrained by the optical thickness determined in step 4, a Bernoulli[4] solution for the extinction distribution within the cloud is produced from the inverted particulate backscatter profile, 6) the in-cloud molecular backscatter signal is replaced with a smooth estimate calculated from the extinction profile determined in step 5 and the known altitude distribution of of the molecular backscatter cross section. In this way, noise is removed from the molecular scattering profile, while the distribution of extinction is closely maintained.

Temporal averaging has been applied to the backscatter cross section profiles used to produce fig.'s 1 - 4. Noise considerations are such that 8-15 minute time resolution is possible at night, depending upon output power and upon cloud altitude and optical thickness. Daytime temporal resolution is somewhat degraded because of an increase in the background noise due to scattered sun light. Signal averaging times were chosen so as to limit the errors due to statistical fluctuations to ~±15% of the average in-cloud backscatter cross section for each profile. The resolution of the profiles used to produce fig. 1 is ~8 minutes and ~12 minutes for fig. 3. Fig. 2 has a time resolution ~1 hour, and the range resolution has been reduced to 900 meters in order to filter noise from the small particulate signals observed during that time period. Operations on Jan. 29-30, 1988 provided exceptional data, with 10 minute averaging possible during daylight and nighttime observations, even though the measured optical thicknesses occasionally exceeded 2.

The dashed lines presented in these plots represent a best estimate for an optical mid-cloud height. Half the cloud optical thickness is accumulated below this line as determined from the Bernoulli solution to the in-cloud extinction. Because the optical thickness of cirrus clouds may be generated by a highly irregular vertical distribution of extinction, this optical mid-cloud level could be useful in conjunction with (or instead of) cloud top and bottom altitudes in radiative transfer models.

IV. Discussion

On examining fig.'s 1-4 it is evident that cirrus clouds are produced in a variety of forms with large variations in cloud altitude and, thickness. For instance, during the ETO (10/30/87), we observed a ~100 m thick single layer cirrus cloud which persisted at 12.5 km for more than 1 hour. In contrast, fig. 4 (1/29-30/88) shows an 8 hour period of repeated, vertically developed cells, imbedded in an unbroken cirrus cloud layer having a vertical extent which occasionally exceeded 8 km.

Fig. 1 shows a contour plot of the backscatter cross section of an isolated cirrus cloud structure occurring on 10/27/86. Assuming no temporal development, and translation of the cloud with the ambient wind, the horizontal extent of this feature is estimated to be 48 km. The maximum value for the backscatter cross section was observed to be $4.4 \cdot 10^{-6}\ m^{-1} sr^{-1}$. The average optical thickness of this cloud was .03 ±.006, with a bulk backscatter phase function of .028±.005 sr^{-1}.

Occasionally, background veils of optically thin (sub-visible) cirrus have been observed . Fig. 2 is a contour plot of such an event. In the vertical, this 3-5 km thick layer had an average optical thickness of .01±.004. It is important to note that the 19 m/s wind speeds at 10 km altitude imply a 266 km horizontal extent for this veil. One implication of such large scale "thin" cirrus is that remote sensors attempting to view horizontally within such layers could encounter optical thicknesses approaching 1 even though the cloud may not be visually apparent.

Fig. 3 depicts the backscatter cross section map of a cirrus cloud complex with a wind-drift-estimated horizontal extent of ~96 km. The maximum observed backscatter cross section was determined to be $2.4 \cdot 10^{-5}\ m^{-1} sr^{-1}$. Profiles averaged between 5:40 and 7:40 GMT indicated a mean optical thickness of .58±.05 and a bulk backscatter phase function of .047±.007 sr^{-1}.

Fig. 4 shows an 8 hour segment of the backscatter cross section for a warm frontal cirrus system which occurred on 1/29-30/88. The maximum backscatter cross section of $4.3 \cdot 10^{-5}$ $m^{-1}sr^{-1}$ was observed near 1:30 GMT. Twenty minute averaged optical thickness varied between between .081 and 2.27 (see fig. 5), while the backscatter phase function varied from .031 - .057 sr^{-1} (see fig. 6). At the time of this writing, error bars had not been established for this data, but they should be comparable to previously reported values. It is interesting to note the large and systematic variation in backscatter phase function during a period of nearly constant optical thickness occurring between 18:00-20:00 GMT. This implies that a substantial portion of the structural information conveyed in fig. 4 is due to changes in the backscatter phase function and not just modulations of the extinction cross section. Thus, caution must be used in the application of simple lidar backscatter profiles to infer cloud radiative properties, even in a relative sense.

Table 1 summarizes the cirrus cloud optical thickness and bulk backscatter phase function estimates thus far completed. The mid-cloud optical altitude has been taken as representative for the determination of cloud temperature. These measurements represent only the analysed portion of the much larger HSRL cirrus cloud data set acquired since October,1986. They were produced from 15 - 120 minute data averages, and are indicative of the bulk properties across the entire cloud layer. The backscatter phase function dependence on mid-cloud temperature reported by Platt and Dilley[6] has not been observed in the HSRL data set.

V. Summary

Since the fall of 1986, we have observed cirrus clouds with backscatter cross sections ranging from $1 \cdot 10^{-7}$ - $4.2 \cdot 10^{-5}$ $m^{-1}sr^{-1}$, optical thicknesses from .001 - 2.3, and exhibiting backscatter phase functions in the range of .021 - .061 sr^{-1}. Persistent cirrus cloud layers have been observed with vertical thicknesses of ~.1 - 8 km. Coherent structural details ranging from 10's of meters and exceeding 250 km have been recorded. However, significant improvements in HSRL measurement statistics will be necessary to produce optical thickness and backscatter phase function measurements on time scales of less than 10 minutes, to reveal details of internal cloud optical properties, or to produce real time volume scans.

Fortunately, we are in the process of upgrading the system with a more powerful and spectrally stable laser which will decrease our time average requirements by a factor of ~40. This laser should also provide additional reductions in the aerosol-molecular channel cross talk terms, improving detailed analysis of backscatter phase function and extinction within cirrus clouds. It is possible that the HSRL will be operational with this new set of capabilities by the July 1988 meeting date.

This research has been supported under ARO grant DAAG29-84-K-0069 and ONR contract N00014-85-K-0581.

References

1. F. Fernald, B.M. Herman, J.A. Reagan, Determination of aerosol Height Distributions by Lidar, J.Appl.Meteor. 11, 482, (1972).
2. C.J. Grund, Measurement of Cirrus Cloud Optical Properties by High Spectral Resolution Lidar, Ph.D. Thesis, U.Wisconsin-Madison, (1987).
3. C.J. Grund and E.W. Eloranta, Interpretation of the Optical and Morphological Properties of Cirrus Clouds from Lidar Measurements, elsewhere in this volume.
4. J.A.Weinman, The Derivation of Atmospheric Extinction Profiles and Wind Speed Over the Ocean from a Satellite Borne Lidar, Submitted to App.Opt., (1988).
5. Platt, C.M.R. and A.C.Dilley, Determination of Cirrus Particle Single-Scattering Phase Function from Lidar and Solar Radiometric Data, App.Opt. 23, 380, (1984).

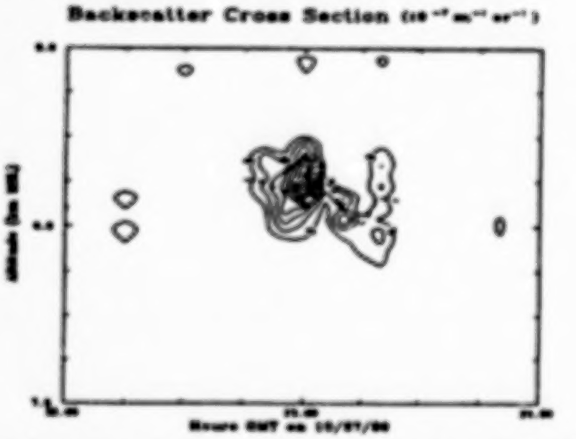

Fig. 1 Contour plot showing the particulate backscatter cross section (10^{-7} $m^{-1}sr^{-1}$) distribution within a cirrus cloud (——). The dashed line indicates the optical mid cloud height (- - -, see text). The average optical thickness of this cloud was .03 with a bulk backscatter phase function of .029 sr^{-1}.

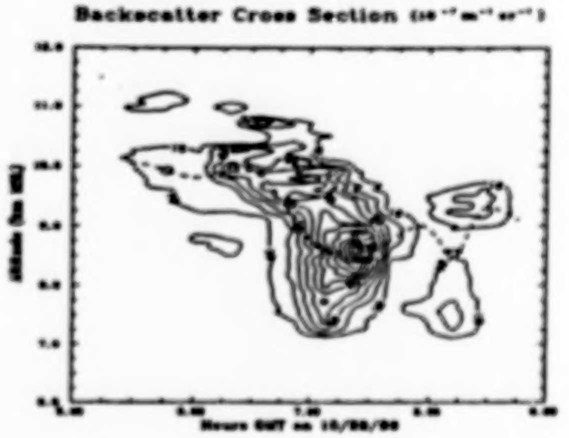

Fig. 3 Backscatter cross section (——) and mid cloud optical height(- - -) of a cirrus cloud complex. Average optical thickness of this system was found to be .58 with a bulk backscatter phase function of .047 sr^{-1}. Contour units are 10^{-7} $m^{-1}sr^{-1}$.

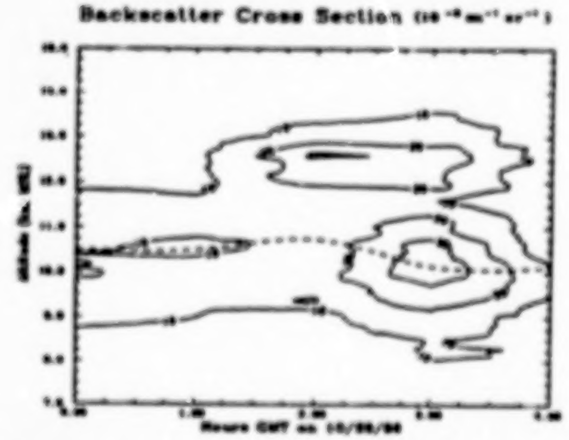

Fig. 2 Background veil of enhanced particulate backscatter may persist at cirrus cloud altitudes even when cirrus are not apparent. The range resolution has been reduced to 900 m to improve the noise statistics of this low backscatter data. Contour units are 10^{-8} $m^{-1}sr^{-1}$.

Table 1 Data Summary

Date	Time GMT	Altitude km	Optical Thickness	$P_{\pi}/4\pi$ sr^{-1}	T C°	Δ Time Minutes
[illegible]	[illegible]	[illegible]	[illegible]	[illegible]	[illegible]	[illegible]
[illegible]	[illegible]	[illegible]	[illegible]	[illegible]	[illegible]	[illegible]
[illegible]	[illegible]	[illegible]	[illegible]	[illegible]	[illegible]	[illegible]
[illegible]	[illegible]	[illegible]	[illegible]	[illegible]	[illegible]	[illegible]
[illegible]	[illegible]	[illegible]	[illegible]	[illegible]	[illegible]	[illegible]
[illegible]	[illegible]	[illegible]	[illegible]	[illegible]	[illegible]	[illegible]
[illegible]	[illegible]	[illegible]	[illegible]	[illegible]	[illegible]	[illegible]
[illegible]	[illegible]	[illegible]	[illegible]	[illegible]	[illegible]	[illegible]
[illegible]	[illegible]	[illegible]	[illegible]	[illegible]	[illegible]	[illegible]
[illegible]	[illegible]	[illegible]	[illegible]	[illegible]	[illegible]	[illegible]
[illegible]	[illegible]	[illegible]	[illegible]	[illegible]	[illegible]	[illegible]
[illegible]	[illegible]	[illegible]	[illegible]	[illegible]	[illegible]	[illegible]
[illegible]	[illegible]	[illegible]	[illegible]	[illegible]	[illegible]	[illegible]
[illegible]	[illegible]	[illegible]	[illegible]	[illegible]	[illegible]	[illegible]
[illegible]	[illegible]	[illegible]	[illegible]	[illegible]	[illegible]	[illegible]
[illegible]	[illegible]	[illegible]	[illegible]	[illegible]	[illegible]	[illegible]
[illegible]	[illegible]	[illegible]	[illegible]	[illegible]	[illegible]	[illegible]
[illegible]	[illegible]	[illegible]	[illegible]	[illegible]	[illegible]	[illegible]
[illegible]	[illegible]	[illegible]	[illegible]	[illegible]	[illegible]	[illegible]
[illegible]	[illegible]	[illegible]	[illegible]	[illegible]	[illegible]	[illegible]
[illegible]	[illegible]	[illegible]	[illegible]	[illegible]	[illegible]	[illegible]
[illegible]	[illegible]	[illegible]	[illegible]	[illegible]	[illegible]	[illegible]
[illegible]	[illegible]	[illegible]	[illegible]	[illegible]	[illegible]	[illegible]
[illegible]	[illegible]	[illegible]	[illegible]	[illegible]	[illegible]	[illegible]
[illegible]	[illegible]	[illegible]	[illegible]	[illegible]	[illegible]	[illegible]
[illegible]	[illegible]	[illegible]	[illegible]	[illegible]	[illegible]	[illegible]
[illegible]	[illegible]	[illegible]	[illegible]	[illegible]	[illegible]	[illegible]
[illegible]	[illegible]	[illegible]	[illegible]	[illegible]	[illegible]	[illegible]
[illegible]	[illegible]	[illegible]	[illegible]	[illegible]	[illegible]	[illegible]
[illegible]	[illegible]	[illegible]	[illegible]	[illegible]	[illegible]	[illegible]
[illegible]	[illegible]	[illegible]	[illegible]	[illegible]	[illegible]	[illegible]
[illegible]	[illegible]	[illegible]	[illegible]	[illegible]	[illegible]	[illegible]
[illegible]	[illegible]	[illegible]	[illegible]	[illegible]	[illegible]	[illegible]
[illegible]	[illegible]	[illegible]	[illegible]	[illegible]	[illegible]	[illegible]
[illegible]	[illegible]	[illegible]	[illegible]	[illegible]	[illegible]	[illegible]
[illegible]	[illegible]	[illegible]	[illegible]	[illegible]	[illegible]	[illegible]
[illegible]	[illegible]	[illegible]	[illegible]	[illegible]	[illegible]	[illegible]
[illegible]	[illegible]	[illegible]	[illegible]	[illegible]	[illegible]	[illegible]
[illegible]	[illegible]	[illegible]	[illegible]	[illegible]	[illegible]	[illegible]
[illegible]	[illegible]	[illegible]	[illegible]	[illegible]	[illegible]	[illegible]
[illegible]	[illegible]	[illegible]	[illegible]	[illegible]	[illegible]	[illegible]
[illegible]	[illegible]	[illegible]	[illegible]	[illegible]	[illegible]	[illegible]

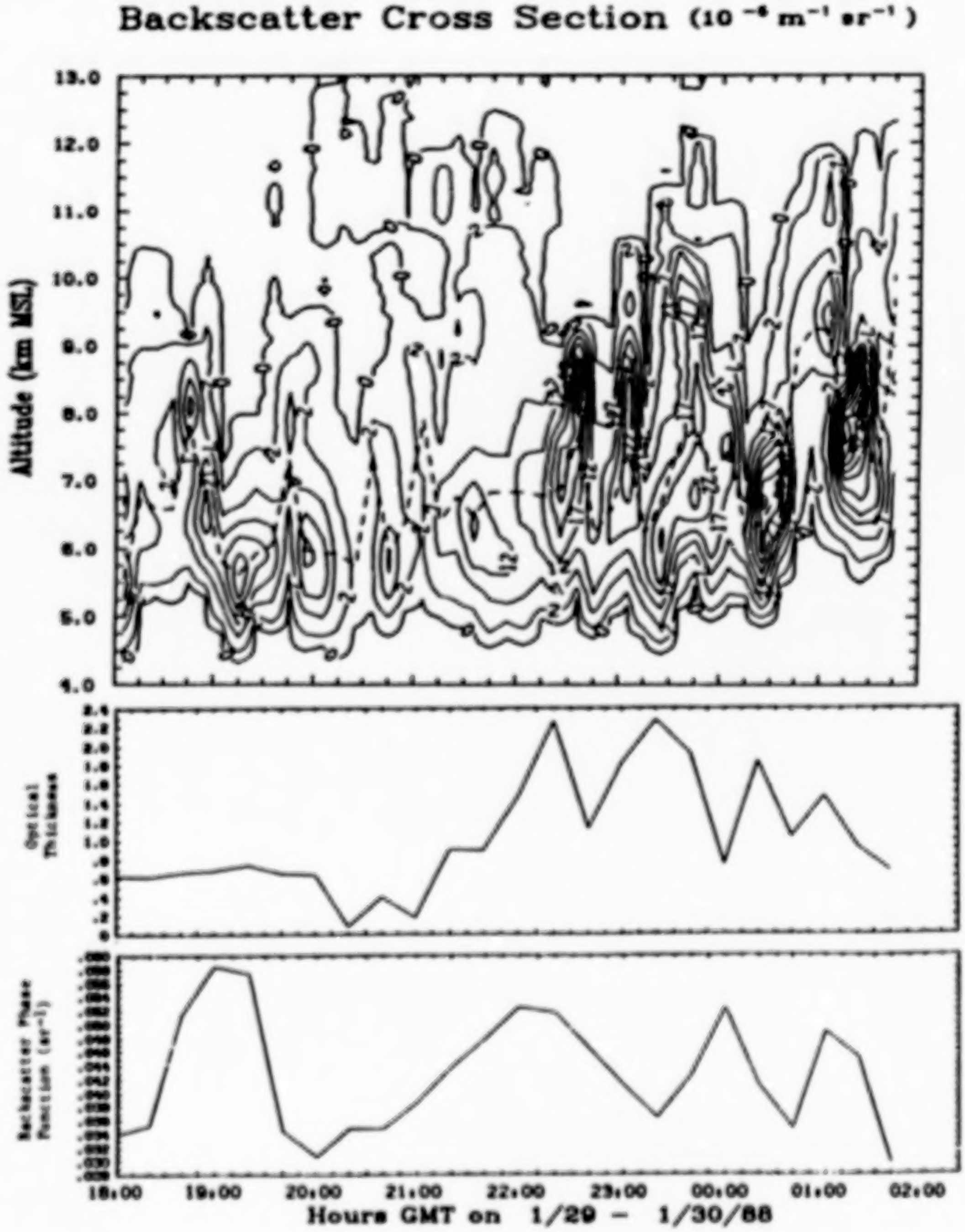

Fig. 4 (top) Backscatter cross section (——) and mid-cloud optical height (· · ·) of a cirrus cloud shield preceding a warm front. Notice the series of repeated cells of enhanced backscatter. Modulations of the mid-cloud height (1-2 km) are closely tied to the cell patterns. Fig. 5 (middle) Optical thickness record for 1/29-30/88 (20 minute independent averages). Fig. 6 (bottom) Backscatter phase function record for 1/29-30/88 (20 minute independent averages). Note the large systematic change in the backscatter phase function during the first 2 hours of the data set. This change occurred even though the average optical thickness remained constant, indicating that much of the structural information conveyed in fig. 4 was not simply produced by modulation of the extinction. Thus, caution must be used in the application of simple lidar backscatter profiles to infer cloud radiative properties, even in a relative sense.

HYDROMETEOR DEVELOPMENT IN COLD CLOUDS IN FIRE

Andrew J. Heymsfield and Nancy C. Knight

National Center for Atmospheric Research*
Boulder, Colorado 80307, USA

Kenneth Sassen

Department of Meteorology, University of Utah
Salt Lake City, Utah 84112

---

* The National Center for Atmospheric Research is sponsored by the National Science Foundation.

1. INTRODUCTION

The role of cirrus clouds, particularly in weather and climate processes, has been increasingly investigated. Numerical models have demonstrated the importance of the solar reflectivity and infrared radiation of cirrus clouds in the earth's radiation budget and climate. These properties depend upon the cloud microphysical characteristics, density, and altitude and hence justify investigation. The results reported herein were obtained from cold clouds (-20 to -46°C) in the mid to upper troposphere during ten flights of the NCAR King Air as part of the First ISCCP Research Experiment (FIRE) in Wisconsin.

2. LIQUID WATER CONTENT MEASUREMENTS

The number of seconds during which liquid water was observed in FIRE clouds between -25 and -35°C, is given in Fig. 1 as a function of amount detected. Data were obtained from a Rosemount Icing Detector (RICE), a Particle Measuring Systems' Forward Scattering Spectrometer Probe (FSSP), and two hot wire probes, the Johnson-Williams (J-W) and the King. Although the J-W and the King hot-wire probes have been the instruments of choice in past investigations of liquid water in cold clouds, they are limited by detection thresholds of 0.02 to 0.05 g m^{-3}, an order of magnitude higher than the RICE or the FSSP. The results given in Fig. 1 are taken from the FSSP data and illustrate the importance of measurements at smaller LWC; most of the liquid water observed at temperatures colder than -20°C was below the detection limits of the hot-wire probes. The data from which Fig. 1 was derived show the largest amounts of liquid water between -30 and -35°C, indicating that in this range, meteorology is more important than temperature.

The operating principles and calibration procedures of all but the RICE have been reported in the formal literature. The RICE collects water droplets and measures corresponding changes in the frequency of a vibrating cylinder. The upper noise limit was determined by examining all output obtained from the instrument at temperatures lower than -40°C where all water is assumed to be frozen. At the true air speed appropriate for the King Air, ~ 100 m s^{-1}, the limit was found to be 3 mV s^{-1}. FSSP spectra of the same temperatures were used to determine ice particle contamination in the data from that instrument, resulting in a conservative threshold of 1.5 cm^{-3} particles per each size bin (3 to 45 μm). Examination of the data taken at warmer temperatures indicated that the RICE and FSSP corrections were valid to -20°C.

As will be illustrated in another paper to be presented here, these measurements of supercooled liquid water were obtained within relatively thin altocumulus cloud layers found in association with cirrus cloud systems. Polarization lidar observations from the Wausau site reveal that the altocumulus frequently became incorporated in deep cirrus ice clouds as precipitating cirrus particles reached the height of the liquid layer. This process was observed to occur during all four of the deep cirrus cloud occurrences studied from Wausau during the FIRE IFO, and appears to have been important to the development of the cirrus at low levels.

3. ICE PARTICLE EVOLUTION

The types of ice crystals in the cold clouds and their size and number were determined from data obtained from two PMS imaging probes, 2D-C and P, and from collecting actual crystals *in situ* on oil-coated slides.

The evolution of ice particles in the cloud layers was examined using patterns in which the aircraft performed Lagrangian spirals, slowly descending through the layers while drifting with the ambient wind. The particle-size spectra derived from the imaging probes during one such Lagrangian spiral are given in Fig. 2a. Inhomogeneities have been removed by averaging each spectrum over the entire spiral. Measurements taken from the aircraft during the flight showed a zone of ice subsaturation between 7.4 and 8.8 km msl and ice supersaturations from 10 to 20% at other altitudes, all below the top of the cloud layer which the aircraft was unable to reach. In broadening with decreasing altitude the spectra shown are typical of those obtained in all of the flights. Again, typically, much of the growth occurs in the larger sizes. Examples of the particles, primarily bullet rosettes, collected during the same descent are also shown in Fig. 2b. Bullet rosettes were predominant in many of the collections and columns or plates in others.

4. ICE PARTICLE AGGREGATION

At all temperatures the imaging probe data from every flight gave evidence of particle aggregation; usually of bullet rosettes joined at their tips, as is illustrated in Fig. 2c and d. Aggregations of plates and columns were also observed, the former joined at edges and the latter end-to-end. At temperatures lower than -25°C the aggregations were almost always of two, equi-dimensional particles with concentrations unvaried with altitude, typically 0.1 to 0.5 ℓ^{-1}. As temperatures warmed above -25°C, the number of aggregates increased as did the number of particles comprising them, their size, and their concentration in the total number of particles.

5. CONCLUSIONS

During the FIRE experiment, the microphysical characteristics of cold clouds have been examined, using the NCAR King Air. The clouds investigated ranged in temperature from -20 to -46°C. Liquid water was detected in these clouds at -35°C and may exist at even colder temperatures. Evaluation of the conditions under which it exists at such low temperatures is continuing.

Aircraft patterns in the form of Lagrangian spirals were used to interpret particle growth processes. Significant broadening of the particle size spectra was observed with minor changes in the spectra at small sizes. Virtually all of the broadening observed was attributable to ice particle aggregation which occurred at all temperatures. The crystals comprising the aggregates were of comparable size, joined either at tips or edges, and were usually two in number at temperatures lower than -25°C, increasing to three or more at warmer temperatures. The data strongly suggest that sintering is the mechanism through which the crystals aggregate.

Aggregation appears to be important in the transfer of water mass from upper to lower levels in clouds. Investigation of the aggregation process is continuing in greater detail.

ACKNOWLEDGEMENTS

The participation of the authors in FIRE was funded in part by NASA project order #L-98100B. University of Utah lidar observations were supported by the National Science Foundation Grant ATM-85 13975, and aircraft support was obtained through the same NSF grant. The authors are grateful for Larry Miloshevich's contribution in the preparation of Fig. 1.

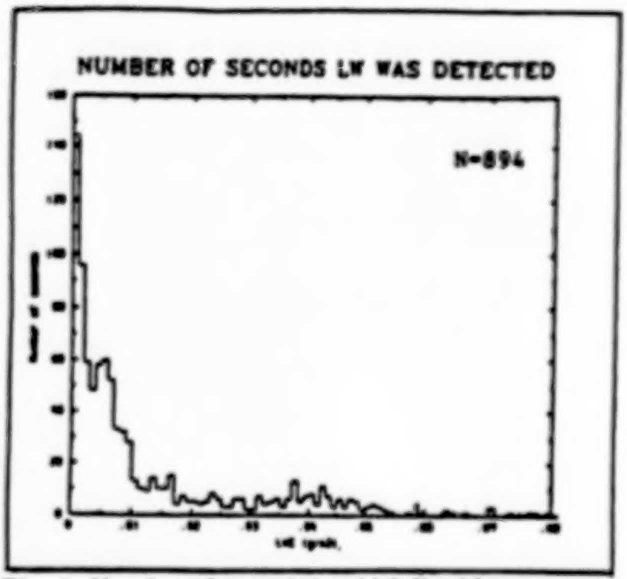

Fig. 1: Number of seconds in which liquid water was detected during FIRE flights as a function of LWC (g m^{-3}) in temperatures between -25 and -35°C. Bin widths are 0.001 g m^{-3}.

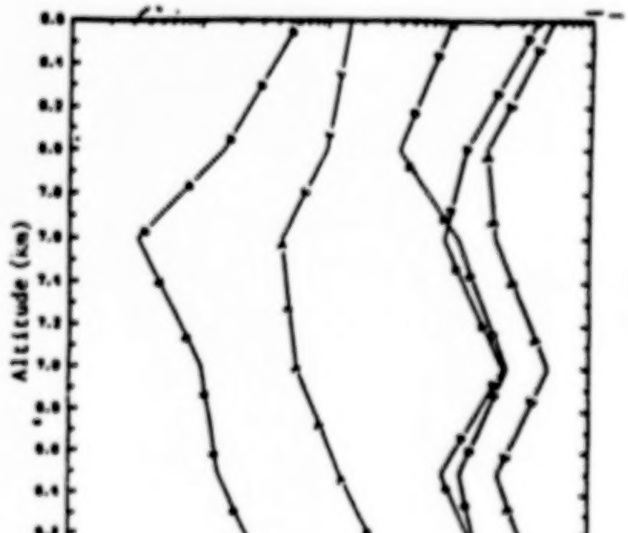

Fig. 2a: LAGRANGIAN SPIRAL, 2 November 1986. Particle concentration (number per liter) as a function of altitude. Size range (microns): a) 75 - 200; b) 200 - 500; c) 500 - 800; d) > 800; e) total.

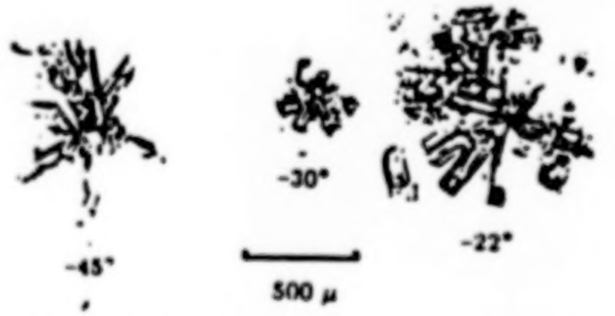

Fig. 2b: Particles collected *in situ* at temperatures given (°C).

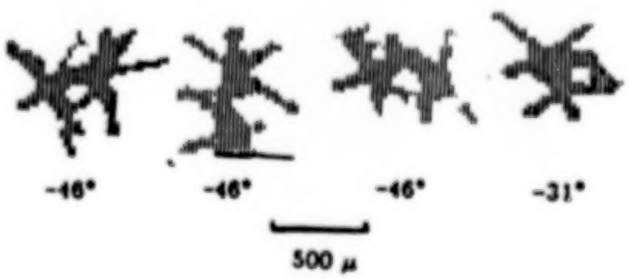

Fig. 2c: 2D-C probe images at temperatures given (°C).

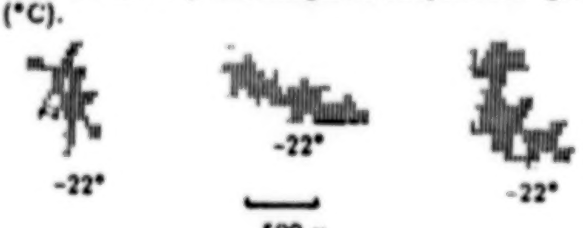

Fig. 2d: 2D-P probe images at temperatures given (°C).

LIDAR AND AIRCRAFT STUDIES OF DEEP CIRRUS SYSTEMS FROM THE 1986 FIRE IFO

K. Sassen

Meteorology Department
University of Utah
Salt Lake City, Utah 84112

A. Heymsfield and N. Knight

National Center for Atmospheric Research*
Boulder, Colorado 80307

Several NCAR King Air flight missions were conducted during the Wisconsin FIRE IFO experiment in support of University of Utah polarization lidar observations of deep cirrus cloud systems at the Wausau ground site. Data collected from four cirrus systems are included in this analysis, including those of 22 and 28 October, and 1 and 2 November. Lidar data were generally obtained at 2-min intervals in the zenith direction over observation periods that ranged from ~4 to 10 h, bracketing the aircraft missions. The data have been processed to yield height-time (HTI) displays of lidar linear depolarization ratio δ and relative range-normalized returned power P. King Air operations consisted of a combination of rapid profiling and Lagrangian spiral descents and stacked race-track patterns (flown approximately along the cirrus level wind direction) in the vicinity of the field site. From the spiral descents are constructed vertical profiles of ice particle (≥75 µm) concentration N_i and ice mass content IWC derived from PMS 2D-probe imagery and, when detected, FSSP cloud droplet concentration N_w and liquid water content LWC. Aircraft flight leg data are presented for vertical velocity W and the same ice and water cloud content parameters. In addition, aerosol particle concentrations (0.1-3.0 µm) obtained with the ASAS probe are examined, and photographs of ice particles collected in situ on oil-coated slides are presented to illustrate ice particle habit.

As an example of a partial dataset from a deep cirrus cloud system, we present for the 1 November 1986 case study, HTI displays of lidar relative (range-normalized) returned laser power and δ values (bottom of Fig. 1, see caption), and aircraft temperature, ice mass content and crystal concentration vertical profiles obtained during two spiral descents through the cloud (Fig. 2). The altitude of the aircraft over the ground site during the mission is shown in the displays as the solid line, and the times that the ice crystal slide samples given in Fig. 3 were obtained are depicted by the circles. The position of the aircraft generally remained within 15 km of the ground site during the period shown in Fig. 1.

---

*The National Center for Atmospheric Research is supported by the National Science Foundation.

The cloud structure on 1 November is similar to that of the three other deep cirrus cloud systems in that altocumulus layers containing supercooled liquid were connected with the cirrus development at low levels. As indicated at the beginning of the data display of Fig. 1, the relatively low $\delta \lesssim 0.15$ values (filled-in) and enhanced returns that occur just above the frontal inversion at 5.3 km (-19°C) reveal the presence of supercooled cloud droplets. Below the altocumulus is a thin virga layer, which often appears to be composed of horizontally oriented plate crystals. Although dense cirrus is initially present above 7.5 km, the region immediately above the altocumulus appears to be cloud free until ~1830, when ice particles precipitating from the cirrus reach cloud base. This precipitation trail contains strong laser returns and the relatively high $\delta \sim 0.5$ values indicative of complex ice crystals or aggregates. Subsequently, a series of additional precipitation trails generated within the upper level cirrus provide a more or less continuous supply of ice particles to the newly established cirrus cloud base, which develops into a strongly scattering layer. Clearly, the cloud generation processes responsible for the thin altocumulus were also responsible for the development of the dense cirrus cloud base layer, once sufficiently strong cirrus particle precipitation occurred to humidify and breach the intervening cloud free layer.

Aircraft microphysical data from the first spiral descent (Fig. 2a) show relatively high particle concentrations within an upper cirrus level generating region above ~8 km (see top of Fig. 1), and variable concentrations below ~7 km. In terms of ice mass content, a gradual increase in IWC is present with decreasing height in the lower cloud region, with the peak occurring at the 5.3 km level formerly occupied by the altocumulus layer. The photomicrographs of Fig. 3 reveal that the strongly scattering cloud base region displaying $\delta \sim 0.5$ values contained complex, hollow column crystals. During the second spiral descent (Fig. 2b), ice crystal concentrations decrease slightly, while IWC values tend to increase. The IWC $\gtrsim 0.01$ g m^{-3} values present between 5.3-7.4 km correspond to a layer of strong laser returns and $\delta \sim 0.5$ values, which produced sufficient optical attenuation to have limited the lidar detection of the upper cirrus cloud region at that time.

The vertical profiles of IWC obtained during both spiral descents suggest that ice particle aggregation was occurring within the deep cirrus. On the basis of the lidar data, ice crystal production appears to have occurred primarily within the generating regions near cloud tops, and also within the occasionally water-saturated cloud base region. Further analyses are underway to obtain more detailed knowledge of the effects of the aggregation process.

Acknowledgments. This research has been supported primarily by Grant ATM-85 13975 from the National Science Foundation and by NASA project order #L-08100B.

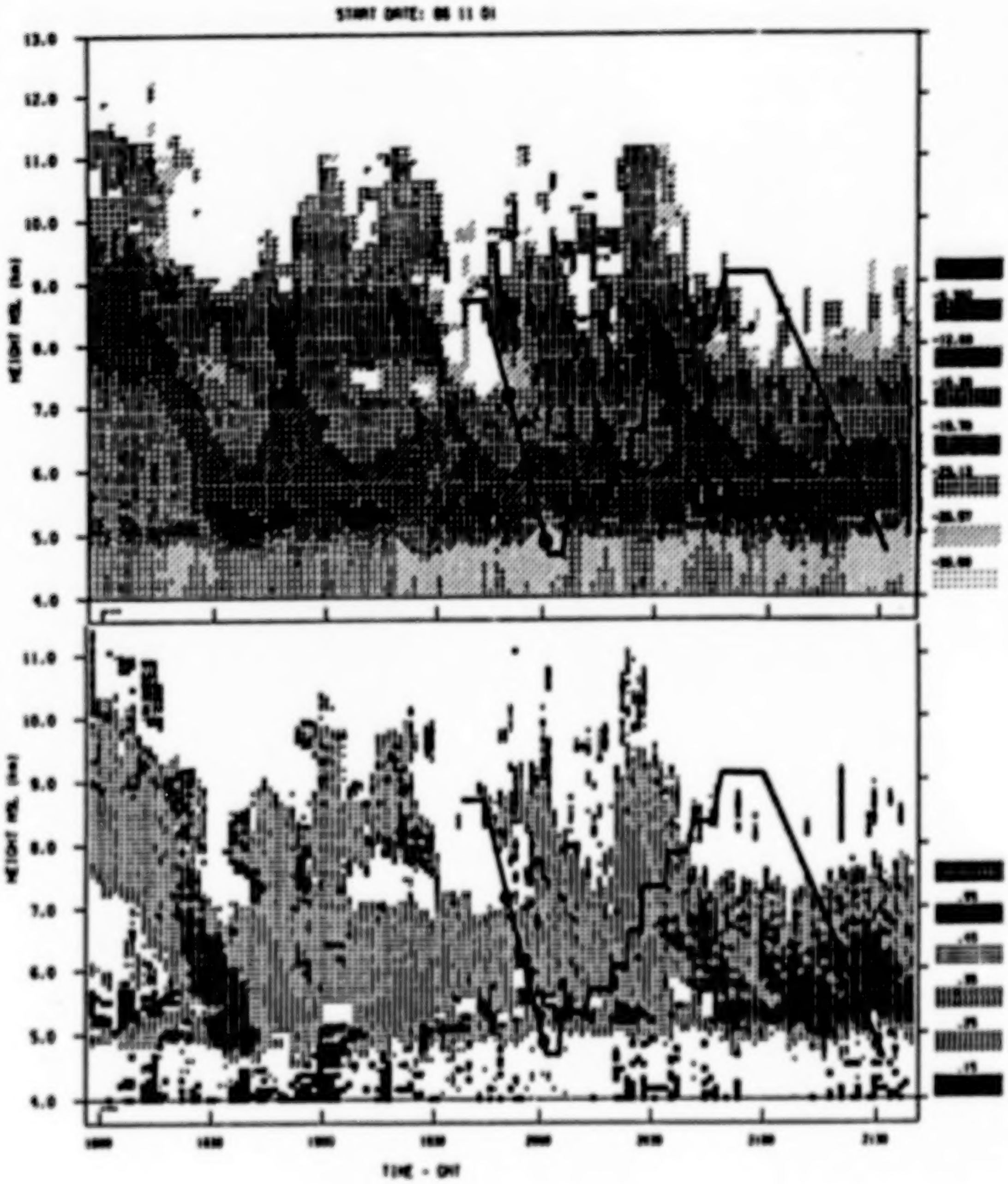

Fig. 1 Height-time displays of lidar relative returned laser power in dB of the maximum range-normalized signal (top, note gray scale at right) and linear depolarization ratio (bottom, with δ value scale at right) for the 1 November 1986 FIRE IFO cirrus cloud system. The approximate position of the King Air aircraft in the vicinity of the Wausau ground site is shown by the lines for the two spirals and stepped ascent ramps, where the circles represent the ice crystal slide samples given in Fig. 3.

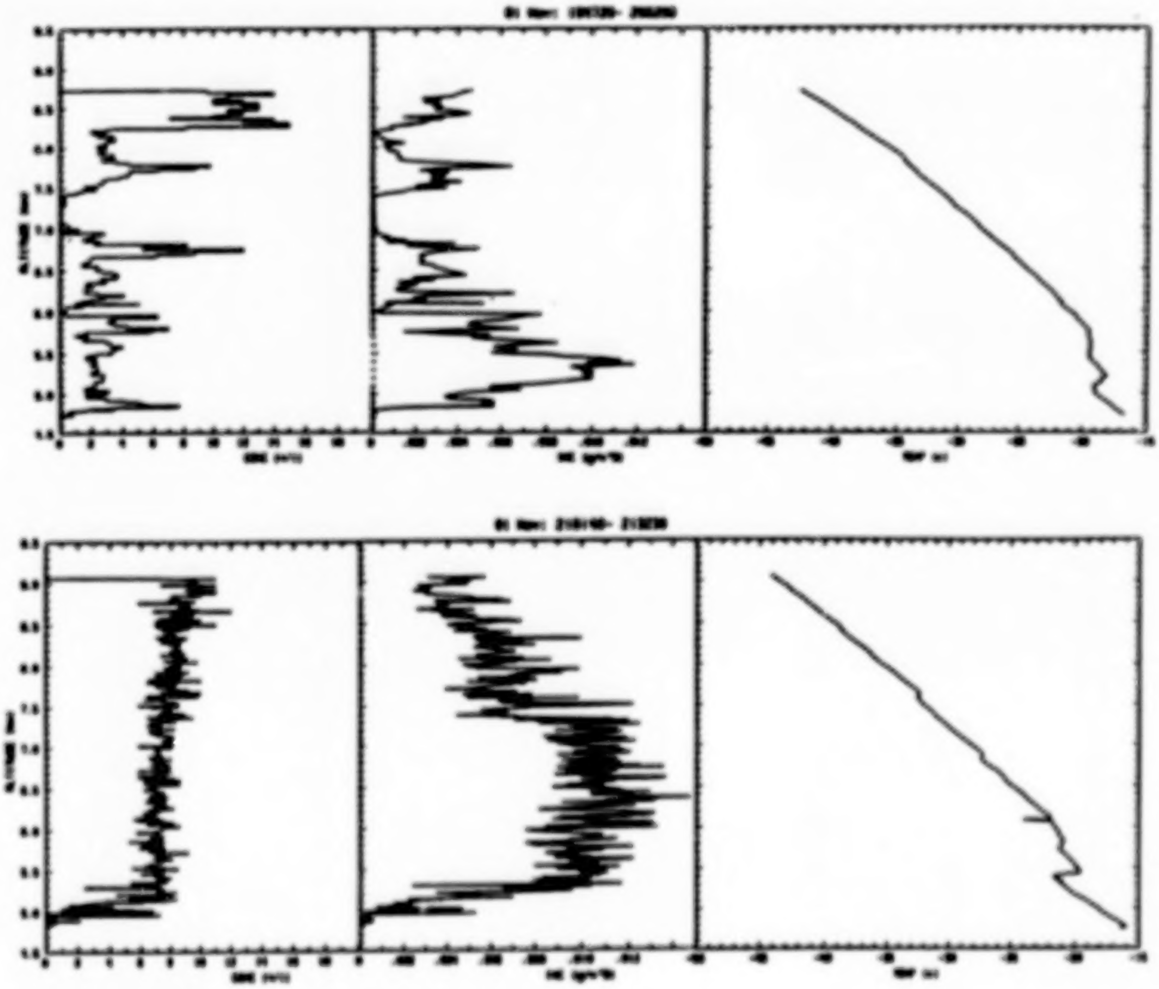

Fig. 2 Aircraft microphysical and temperature profiles obtained during the two spiral descents shown in Fig. 1. Given are the concentrations of ice crystals (per liter) and the ice mass content IWC (g m^{-3}) derived from PMS 2D-probe imagery.

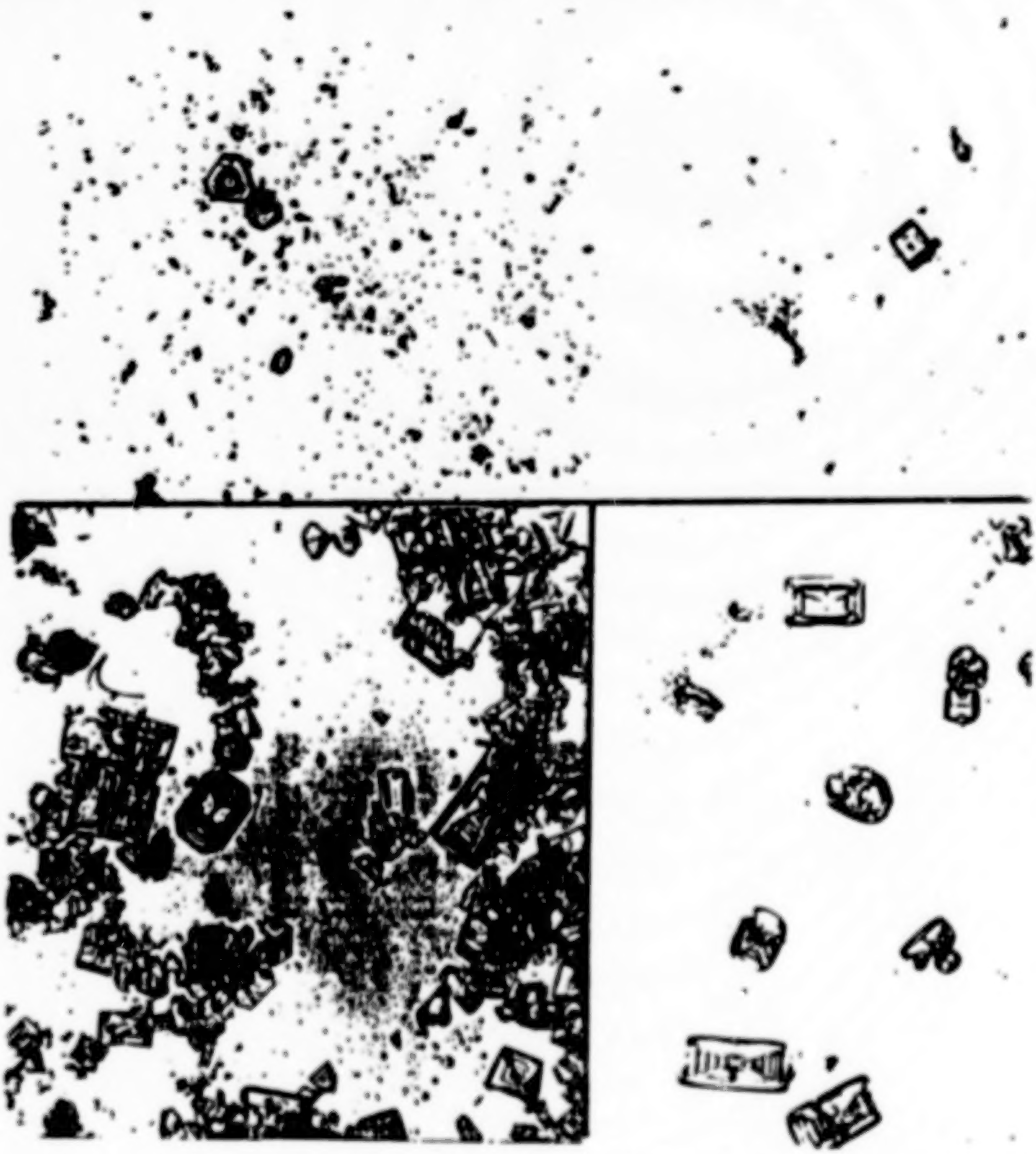

Fig. 3 Photomicrographs of ice crystals collected on three slides during the first aircraft spiral. At top are short column and thick plate crystals from a thin ice cloud at 7.15 km (−29.3°C); at bottom left are hollow columns displaying considerable internal structure from the lower cloud region at 6.15 km (−21.9°C); and at bottom right are hollow columns with rounded edges and a loss of internal structure due to evaporation, from 4.84 km (−17.6°C). The loss of crystalline scattering properties from evaporation typically causes lidar δ values to decrease at cloud base (see Fig. 1).

VERTICAL VELOCITIES WITHIN A CIRRUS CLOUD FROM DOPPLER LIDAR AND AIRCRAFT MEASUREMENTS DURING FIRE: IMPLICATIONS FOR PARTICLE GROWTH

Ismail GULTEPE and Andrew HEYMSFIELD
National Center for Atmospheric Research[1]
P.O. Box 3000
Boulder, Colorado 80307

1. INTRODUCTION

This paper uses a large and comprehensive data set taken by the NOAA CO_2 Doppler lidar, the NCAR King Air, and rawinsondes on 31 October 1986 during the FIRE (First International Regional Experiment) field program which took place in Wisconsin. Vertical velocities are determined from the Doppler lidar data, and are compared with velocities derived from the aircraft microphysical data. The data will be used for discussion of particle growth and dynamical processes operative within the cloud.

2. SYNOPTIC DISCUSSIONS

There was no large scale disturbances over the experimental area on 31 October 1986. The 1800 GMT surface map showed that there was a cold front 600 km to the west of the experimental area. At 1200 GMT, there was a weak upper level trough at the 200 mb level. The jet stream, with maximum wind speeds of about 45 m s^{-1}, was situated north of Wisconsin. Cirrus cloud formation occurred to the south of the jet stream in a warm air zone. There was not a direct relationship between the cirrus cloud location and the jet stream. A sounding from Green Bay at 11 CST (Figure 1) shows a moisture increase at upper levels where later the cirrus cloud formed. The base of the moisture zone is at about 450 mb with an isothermal layer just under the base. The cloud studied extended over an area of 45×20 km.

3. DISCUSSION OF AIRCRAFT AND LIDAR MEASUREMENTS

The NCAR King Air collected data within the cirrus cloud using six horizontal penetrations from 7.6 km (−29.6°C), cloud base, to 9.2 km (−42.6°C), cloud top. The King Air sampling period for each penetration was about 5 minutes, corresponding to 30 km horizontal legs. The time for total sampling through cloud layer was approximately 30 minutes.

The principal equipment used for cloud particle spectra measurements were Particle Measuring System (PMS) 2D-C and 2D-P probes, although only the size spectra from the 2D-C probe were used. The 2D-C probe sized in the range 25 μm to 1400 μm.

The velocity azimuth display (VAD) technique is used to calculate vertical velocities from the Doppler lidar measurements. This technique was first proposed by LHERMITTE

---

[1] The National Center for Atmospheric Research is sponsored by the National Science Foundation

and ATLAS (1961), and later developed by BROWNING and WEXLER (1968). In the VAD scanning mode, the beam is scanned continously in azimuth angles while the zenith angle is held constant. Backscatter power and azimuth angle are digitized in real time and stored on magnetic tape. The radial velocities are measured at intervals of 300 m along the beam.

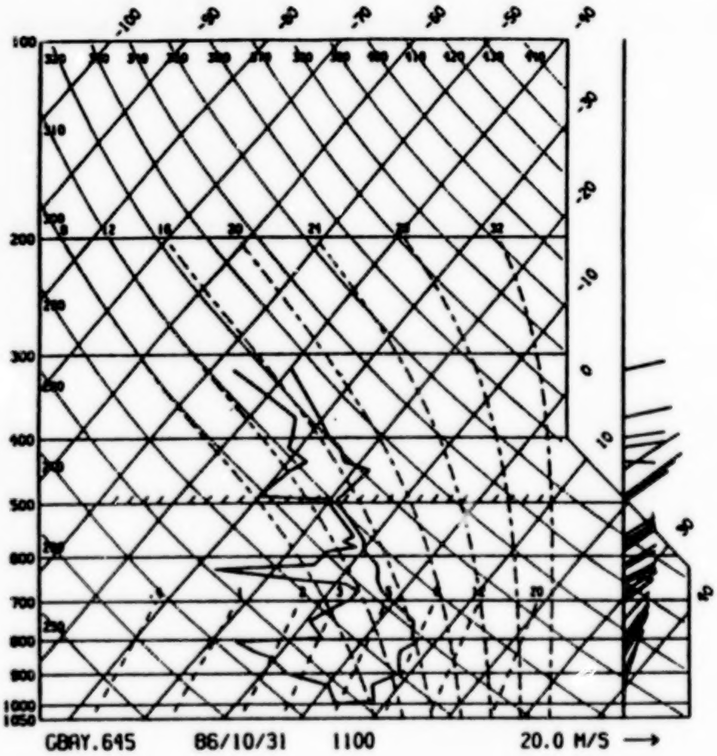

Figure 1: A skew T-log P diagram from Green Bay at 1100 CST on 31 October 1986. The moisture increase is seen approximately between 400 and 300 mb.

4. VERTICAL VELOCITY CALCULATIONS FROM AIRCRAFT MEASUREMENTS

In order to calculate vertical velocities from aircraft measurements, the precipitation rate, ice water content and terminal velocity were calculated from 2D-C probe size spectra measurements. HEYMSFIELD (1977) presented equations for calculations the above parameters. A mean size spectrum was obtained for each sampling pass. Particle habits observed in the 2D-C probe and from direct collections on oil coated slides were predominantly columns and bullet rosettes although some plates were detected (N. Knight, private communication). We then calculated the vertical velocity distribution with altitude.

4.1 STEADY-STATE TECHNIQUE

The basis of this technique is the conservation equation for total vapor, liquid and solid substances in a rising parcel of air (HEYMSFIELD, 1975). The assumption is made that ice supersaturation (S_i) remains constant with time (t) at any given level. Thus, the crystal growth and resulting depletion of vapor are balanced due to the updraft. The vertical air velocity is then derived from

$$U_A = \frac{\phi_2}{\phi_1}\frac{dw_i}{dt} , \tag{1}$$

where U_A is the air velocity, and ϕ_1, ϕ_2 are coefficients (HEYMSFIELD, 1977). $\frac{dw_i}{dt}$, the cumulative growth rate of the particle size spectrum, is not known until the supersaturation with respect to ice (S_i) is obtained (see discussion below).

4.2 FLUX TECHNIQUE

The second technique employed in calculating the vertical air velocity from the size spectra measurements is the flux method (HEYMSFIELD, 1977). In this technique, the vertical velocity was calculated by equating the decrease in moisture between a lower and upper sampling levels to the increase in the precipitation rate between the same levels. The velocity is calculated from

$$U_A = \frac{\Delta R}{\Delta IWC + \frac{RH}{100}\Delta\rho_s} \tag{2}$$

where ΔR is precipitation rate difference between level 1 and 2, ΔIWC is ice water content difference between the two levels, RH is the mean relative humidity, and $\Delta\rho_s$ is the vapor difference between level 2 and 1. Equations (1) and (2) can be solved simultaneously to yield U_A, RH and S_i (HEYMSFIELD, 1977).

5. VERTICAL VELOCITY CALCULATIONS FROM DOPPLER LIDAR MEASUREMENTS

Conically scanning Doppler lidar measurements were used to compute the mean divergence field, the horizontal wind speed, and direction. The VAD technique is based on a least squares technique for obtaining Fourier coefficients. Using the anelastic continuity equation, the vertical velocities are calculated at different altitudes through the cloud layer. Assuming that the particle velocity is equal to the terminal velocity, the zeroth order Fourier coefficient is given as (SRIVASTAVA *et al.*, 1986)

$$a_o = \overline{DIV}\frac{r\cos\alpha}{2} - \overline{V_t}\sin\alpha . \tag{3}$$

$\overline{DIV}$ is mean divergence, r is the horizontal range, $\overline{V_t}$ is mean backscatter-weighted terminal velocity, and α is the elevation angle. The mean horizontal divergence can be calculated from a_o, $\overline{V_t}$, r and α. According to BROWNING and WEXLER (1968), inhomegeneities in the particle fall speed is a primary source of error for the divergence calculation. From concurrent DMSP satellite infrared images, it is reasonable to assume that the cirrus cloud had formed a homogenous structure.

Mean backscatter-weighted terminal velocities ($\overline{V_t}$) are estimated from the particle size spectrum. $\overline{V_t}$ is found from:

$$\overline{V_t} = \frac{\sum_{j=1}^{m}\sum_{i=1}^{n} N_{i,j} D_{eq_{i,j}}^2 V_{t_{i,j}} \Delta D}{\sum_{j=1}^{m}\sum_{i=1}^{n} N_{i,j} D_{eq_{i,j}}^2 \Delta D} \tag{4}$$

where $N_{i,j}$ is number concentration in size class i with habit j. The physical diameter (D), which is used to calculate V_t, is converted to an equivalent diameter (D_{eq}) (HEYMSFIELD, 1972; 1975). Then, using the anelastic continuity equation and assuming vertical air velocities are zero at cloud top and base, the vertical air velocities are calculated. A variational adjustment technique is used to correct the divergence field. Vertical air velocity corrections are made following LIN *et al.* (1986).

6. RESULTS AND CONCLUSIONS

The aircraft vertical velocity and temperature measurements showed that the cirrus cloud formed in considerably stable atmospheric conditions on 31 October 1986. Maximum vertical shear of the horizontal wind was only $1.5 \times 10^{-2}\ s^{-1}$ (at about 8.8 km). The cirrus cloud may be formed because of a weak wave pattern or large scale lifting.

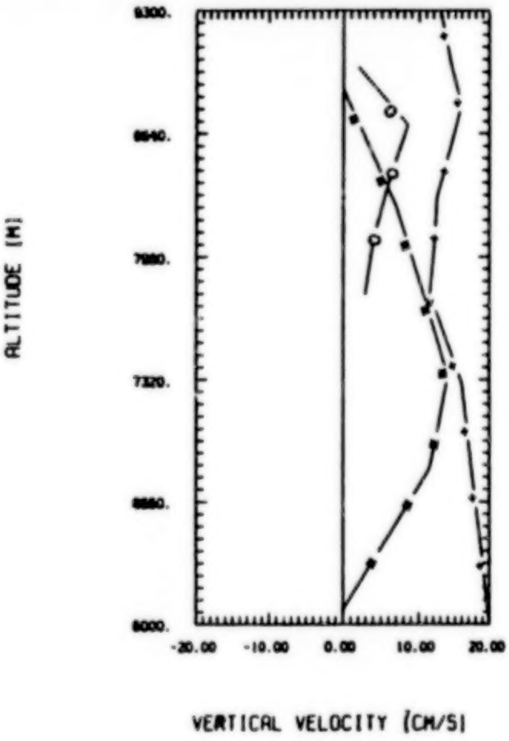

Figure 2: The calculated vertical air velocities from aircraft (o), rawinsonde (+) and lidar (*) measurements on 31 October 1986.

The ice crystal habits were predominantly columns and bullet rosettes at altitudes between 7.6 (−29.6°C) and 9.2 (−42.6°C) km. The total ice crystal concentration changed from 5.5 l^{-1} (7.6 km) to a maximum of 22.5 l^{-1} (8.8 km) where peak vertical velocities are found from the calculations based on aircraft and rawinsonde measurements. The ice water content values of 10^{-3} to 10^{-2} g m^{-3} through the cloud layer are significantly lower than found in convective cirrus, obviously as a result of weaker vertical motions.

The peak velocity from the VAD technique with 60 degree elevation angle was about 34 cm s^{-1} at about 7.4 km but with 30 and 40 degree elevation angles was only about 14 cm s^{-1} at 7.3 km ASL (see Figure 2) while vertical velocities changed from 9 cm s^{-1} at the cloud base to 0 cm s^{-1} at the cloud top. The calculated air velocities from the aircraft in-situ measurements showed a peak (10 cm s^{-1}) at about 8.8 km where the highest calculated ice crystal growth rates (about 0.2×10^{-4} g m^{-3} s^{-1}), ice supersaturation 42% and relative humidity with respect to water of 94% were found. The calculated vertical velocities are similar to that are found by HEYMSFIELD (1975), in thin ice clouds, ranging from 2–10 cm s^{-1} in frontal overrunning systems to 25–50 cm s^{-1} in clouds associated with closed lows aloft, longitudinal rolls and isolated convective cells. Maximum vertical air velocity derived from the triangle technique (BELLAMY, 1949) using three rawinsondes along baselines of approximately 200 km was found of about 15 cm s^{-1} (at 8.8 km) in the cirrus cloud layer (see Figure 2). Differences in derived vertical velocities between the triangle, Doppler lidar, and aircraft techniques can be attributed to scale effects.

REFERENCES

BELLAMY, J.C., : Objective calculations of divergence, vertical velocity and vorticity. *Bull. Amer. Meteor. Soc.*, **30** (1949) 45–49.

BROWNING, K.A., and WEXLER, R.: The determination of kinematic properties of a wind field using Doppler radar. *J. Atmos. Sci.*, **7** (1968) 105–113.

HEYMSFIELD, A.J.: Ice crystal terminal velocities. *J. Atmos. Sci.* **29** (1972) 1348–1357.

HEYMSFIELD, A.J.: Cirrus uncinus generating cells and the evolution of cirriform clouds. Part I: Aircraft measurements of the growth of the ice phase. *J. Atmos. Sci.* **32** (1975) 789–808.

HEYMSFIELD, A.J.: Precipitation development in stratiform ice clouds: A microphysical and dynamical study. *J. Atmos. Sci.* **34** (1977) 367–381.

LHERMITTE, R.M., and D. ATLAS: Precipitation motion by pulse Doppler. *Proc. Ninth Weather Radar Conf.*, Boston, Amer. Meteor. Soc. (1961) 43, 2302–2327.

LIN, *et al.*: Pressure and temperature perturbations within a squall line thunderstorm derived from SESAME Dual-Doppler radar data., *J. Atmos. Sci.*, **43, 21** (1986) 2302–2327.

SRIVASTAVA, R.C., T.J. MATEJKA, and T.J. LORELLO: Doppler radar study of the trailing anvil region associated with a squall line. *J. Atmos. Sci.*, **43** (1986) 356–377.

FIRE SCIENCE TEAM MEETING
VAIL, COLORADO
JULY 11-15, 1988

CIRRUS

RADIATIVE PROPERTIES - Thomas P. Ackerman Monday, July 11, 1988

PAGE

Radiative Properties of Visible and Subvisible Cirrus: Scattering on Hexagonal Ice Crystals 75
Flatau, Piotr J.; Graeme L. Stephens, and Bruce T. Draine

Cirrus Microphysics and Radiative Transfer: A Case Study 81
Kinne, Stefan A.; Thomas P. Ackerman, and Andrew J. Heymsfield

Subvisual Cirrus Cloud Properties Derived from a FIRE IFO Case Study 85
Sassen, K.; M. K. Griffin, and G. C. Dodd

Multi-spectral Window Radiance Observations of Cirrus from Satellite and Aircraft - November 2, 1986 "Project FIRE" 89
Smith, W. L.; H. E. Revercomb, H. B. Howell, and M. -X. Lin

Cirrus Cloud Statistics: Temperatures and Optical Depths 95
Valero, Francisco P. J.; Thomas P. Ackerman, and Warren J. Y. Gore

The Radiation Budget of a Cirrus Layer Deduced from Simultaneous Aircraft Observations and Model Calculations 99
Ackerman, Thomas P.; Stefan Kinne, Andrew J. Heymsfield, and Francisco P. J. Valero

Lidar and Radiometer Results from the ER-2 for the FIRE Field Experiments 101
Spinhirne, James

Identification of Cirrus over Wausau During the 1986 FIRE IFO from Ground-Based Radiometer Data 105
Robinson, David A.; and Allan Frei

Interpretation of Satellite-Measured Bidirectional Reflectance from Cirrus Cloudy Atmospheres 111
Takano, Y.; K. N. Liou, and P. Minnis

RADIATIVE PROPERTIES OF VISIBLE AND SUBVISIBLE CIRRUS: SCATTERING ON HEXAGONAL ICE CRYSTALS

PIOTR J. FLATAU, GRAEME L. STEPHENS
Department of Atmospheric Science, Colorado State University, Fort Collins, CO 80523

BRUCE T. DRAINE
Princeton University Observatory, Peyton Hall, Princeton NJ 08544

(April 1988)

1. Introduction

One of the main objectives of the First International Satellite Cloud Climatology Project (ISCCP) Regional Experiment (FIRE) is to provide a better understanding of the physics of upper level clouds. There are a number of factors that have complicated the study of these clouds leaving our present understanding of upper level clouds in a less than satisfactory state. One factor is simply the distance of the clouds from the surface. It is easier to study a low-level cloud system because of their proximity to the ground. Added to this observational problem is the fact that clouds in the upper troposphere seem to be governed by an intricate balance of not so well understood phenomena. Among the factors that have added to the complexity of the problem is the fact that particles are no longer spherical and both the solid and liquid water phases may coexist. Turbulence develops in the stable layer environment with its fine scales of vertical motion. Horizontal eddies (two dimensional turbulence) may be important for cloud morphology, and a host of interactions between gravity waves, turbulence, radiation, and microphysics all seem possible.

This paper concentrates on just one specific aspect of cirrus physics, namely on characterizing the radiative properties of single, nonspherical ice particles. While focused in this way, this study provides the basis for further more extensive studies of the radiative transfer through upper level clouds. Radiation provides a potential mechanism for strong feedback between the divergence of in-cloud radiative flux and the cloud microphysics and ultimately on the dynamics of the cloud.

We will firstly describe some aspects of ice cloud microphysics that are relevant to the radiation calculations. Next, the Discrete Dipole Approximation (DDA) is introduced and some new results of scattering by irregular crystals are presented. We also adopt the Anomalous Diffraction Theory (ADT) to investigate the scattering properties of even larger crystals. In this way we are able to determine the scattering properties of non spherical particles over a range of particle sizes. The study reported here is still preliminary and at the time of writing this abstract, the results are incomplete. We aim to incorporate the microphysics data collected during FIRE into these calculations and in a companion study plan to use these scattering properties to determine cloud radiative heating rates.

2. Cloud microphysics

Characterizing the shape and size of ice crystals in terms of their environment continues to be a subject of extensive research. For environments typical of cirrus clouds and for even the colder environments of polar stratospheric clouds (PSC's), ice exists in single- and polycrystalline forms. The more commonly perceived large composite crystals, of the order of $500\mu m$, are actually observed more readily at lower temperatures. Crystal sizes of the order of $10\mu m$ and $1\mu m$ are, respectively, more representative of high cirrus in the tropics (Heymsfield, 1986) and PSC's (Rosen *et al.*, 1988). To emphasize this point we present the variation of crystal shape drawn in proportion to their size in Fig. 1 over the temperature range $-20^\circ C$ to $-90^\circ C$. The crystals at cirrus temperatures, say $-40^\circ C$, are hexagonal columns although variations of this type of crystal exist in the form of hexagonal bullets and hollow columns. In this study we will focus only on single solid hexagonal crystals although the foundation to study crystals of more complex shape has been developed.

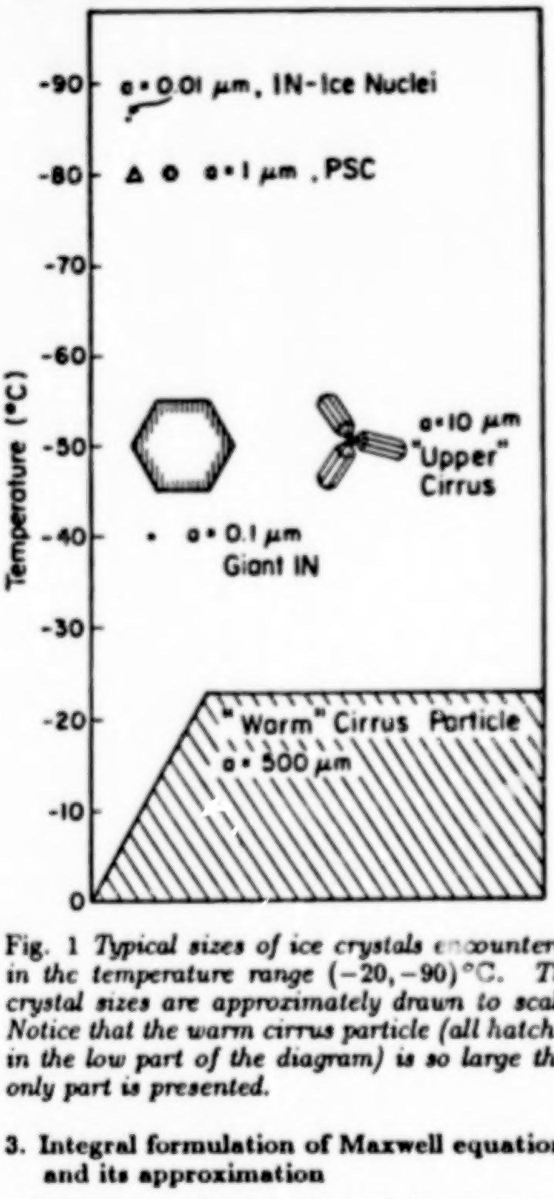

Fig. 1 *Typical sizes of ice crystals encountered in the temperature range* $(-20, -90)\,^{\circ}$C. *The crystal sizes are approximately drawn to scale. Notice that the warm cirrus particle (all hatched in the low part of the diagram) is so large that only part is presented.*

3. Integral formulation of Maxwell equations and its approximation

Only a very brief outline of the scattering methods are described here. We begin with Maxwell equations written in the integral form (Saxon, 1955)

$$\mathbf{E}(\mathbf{x}) = \mathbf{E}_0(\mathbf{x}) + 4\pi k^2 \times \int \mathbf{G}(\mathbf{x},\mathbf{x}') \cdot \frac{\epsilon(\mathbf{x}') - 1}{4\pi} \cdot \mathbf{E}(\mathbf{x}')\, d^3\mathbf{x}' \tag{1}$$

where $\mathbf{E}_0(\mathbf{x})$ is the incident electric field, $\epsilon(\mathbf{x})$ is a dielectric tensor, and Green's function is defined as

$$\mathbf{G}(\mathbf{x},\mathbf{x}') = (\mathbf{1} - \hat{\mathbf{r}}\hat{\mathbf{r}})\frac{e^{ikr}}{4\pi r} + (3\hat{\mathbf{r}}\hat{\mathbf{r}} - \mathbf{1})\left(\frac{1}{k^2r^2} - \frac{i}{kr}\right)\frac{e^{ikr}}{4\pi r} \tag{2}$$

where $\mathbf{r} = \mathbf{x} - \mathbf{x}'$, $r = |\mathbf{x} - \mathbf{x}'|$, and $\hat{\mathbf{r}} = \mathbf{r}/r$. Boldfaced $\mathbf{1}$ is a unit matrix, and $\hat{\mathbf{r}}\hat{\mathbf{r}}$ is a dyadic (or tensor) multiplication of two unit vectors $\hat{\mathbf{r}}$. The incident electric field $\mathbf{E}_0(\mathbf{x})$ is

$$\mathbf{E}_0(\mathbf{x}) = E_0\hat{\mathbf{e}}e^{ik\hat{\mathbf{k}}\cdot\mathbf{x}} \tag{3}$$

where $\hat{\mathbf{e}}$ is a unit vector specifying the wave's polarization, E_0 is the intensity of incident wave, $\hat{\mathbf{k}}$ is a unit vector defining the wave propagation, $k = 2\pi/\lambda$, and λ is wavelength. We now seek a solution of this integral equation to obtain the electric field and all the relevant scattering properties follow from this solution. Unfortunately, the integral (Fredholm) equation (1) is *not* easily solvable although it is amenable to a variety of approximations commonly used in scattering problems. In fact the approximate methods such as the Rayleigh approximation (also known as the Rayleigh-Gans-Debye (RGD), the Rayleigh-Gans-Rocard or the Kirchoff or the first Born approximation), the second and higher Born approximations, Anomalous Diffraction Theory (ADT) also known as High Energy Approximation (HEA) or the equivalent WKB method, the Discrete Dipole Approximation (DDA) and the Extended Boundary Method can all be derived directly from (1) (Saxon, 1955; Flatau and Stephens, 1988b).

4. Discrete Dipole Approximation

A useful and general way to solve (1) is to discretize the integral term thus reducing the integral equation to a linear system of equations. In the DDA approximation one assumes that each volume element may be replaced by a point dipole, whose (tensor) polarizability is related to the volume of the element and the dielectric tensor using the Clausius-Mossotti relations, corrected for the effects of radiative reaction. Each of the dipoles acquires a (time-dependent) polarization in response to the electric field at the position of the dipole, which includes contributions from all of the other dipoles plus the incident wave. This is the approach of the DDA as originally formulated by deVoe (1964) and Purcell and Pennypacker (1973). Consider our hexagonal crystal in this instance divided into

N discrete domains of volume v_j (Fig. 2) centered around point $\mathbf{x}_j$, where $j = 1, \ldots, N$.

The volume of such an elementary domain is

$$v_j = \frac{V}{N} \tag{4}$$

where V is the volume of the particle, and N is the number of domains. Thus we are able to form a set of $3N$ equations from (1) since there are three components of the $\mathbf{E}$ field at each $\mathbf{x}_i$. The resulting equation set can then be represented in the form

$$\mathcal{A}\mathcal{P} = \mathcal{E}_0 \tag{5}$$

where P is the 3N-dimensional vector whose elements are the dipole moments of the N dipoles. For further details of the matrix structure and computational solution procedures the interested reader can consult the recent work of Draine (1988). The electric field everywhere in the three-dimensional space is given in terms of the structure matrix $\mathcal{A}$ which depends only on *particle's shape, refractive index and incident wavelength* but is independent of the direction and polarization of the incident wave $\mathbf{E}_0(\mathbf{x})$. Once $\mathcal{P}$ is determined then single scattering properties of the particle can be derived from the relationships reported by Draine (1988).

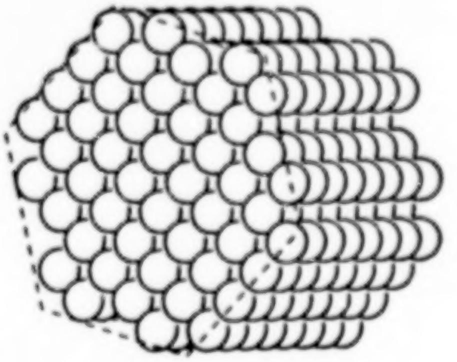

Fig. 2 *Hexagonal discrete dipole arrays with $N = 384$. Higher resolution was actually used, see text for further comments.*

The DDA method has been applied to calculate the scattering properties of small hexagonal ice crystals. Figure 2 presented the discrete dipole array for $N = 384$ dipoles but for the calculations reported in this paper actually used 2208 dipoles. The wavelength of $\lambda = 3.8\mu m$ and the corresponding value for the refractive index of ice $m = 1.38 + i0.0067$ was employed as was $\lambda = 10.8\mu m$ with a corresponding value $m = 1.089 + i0.182$. The wavelengths represent near infrared and infrared regions with small and relatively large absorption, respectively and correspond to central wavelengths of the AVHRR imager. The $10.8\mu m$ wavelength is also a relevant wavelength for application to CO_2 lidar studies.

The scattered intensity is presented in Fig. 3 as a function of scattering angle for two scattering planes, one perpendicular to $\mathbf{E}_0$ and the other parallel to $\mathbf{E}_0$.

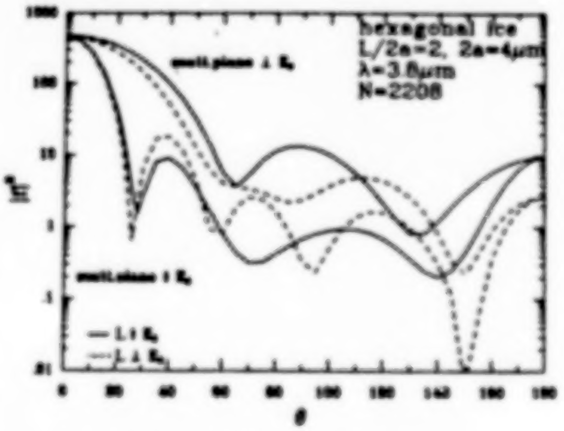

Fig. 3 *Intensities for hexagonal ice for an incident wave perpendicular to the crystal (average) and $\lambda = 3.8\mu m$. Results for two scattering planes are presented. Crystal length $L = 8\mu m$, crystal radius $a = 2\mu m$. $N = 2208$ discrete dipoles were used.*

The incident direction was taken to be normal to the L-axis of the hexagon, the length of the crystal used in the calculations is specified by L, and the aspect ratio is defined as $p = L/2a$ where $2a$ is the width of the crystal. Results are shown for two cases: incident electric field parallel to, and perpendicular to, the L-axis of the hexagon. Because the hexagon is not rotationally symmetric, the scattering problem depends upon the orientation of the hexagon. Two cases have been considered: (1) with the hexagon oriented so that the $\mathbf{k}$ vector is normal to one of the 6 rectangular faces, and (2) with the hexagon rotated by 30 degrees, so that the $\mathbf{k}$ vector is parallel to a line connecting a vertex to the center of the hexagon. (Each of these two cases has reflection symmetry which greatly reduces the amount of computing required to obtain a solution). The scattering intensities shown in Figures 3 and 4 are the averages of the scattering intensities for the above two cases.

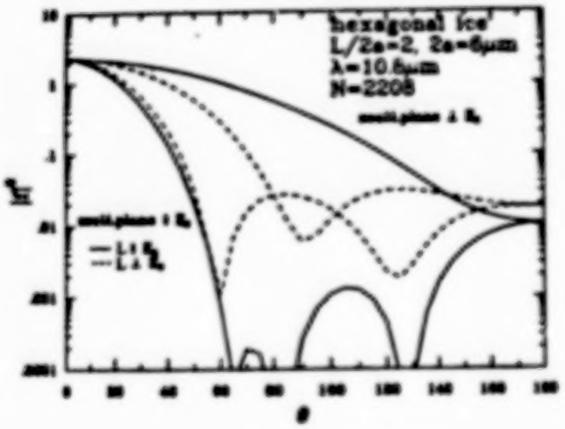

Fig. 4 *Same as Fig. 3 but for $\lambda = 10.8\mu m$. Crystal length $L = 8\mu m$, crystal radius $a = 2\mu m$.*

Figure 5 shows the results of the Mie calculation for a sphere with a volume equal to that of the hexagonal crystal. The intensities $|f|^2_{\parallel}$ and $|f|^2_{\perp}$ are presented here as a function of scattering angle and

$$|f|^2 = k^2 \frac{dC_{sca}}{d\Omega}. \tag{6}$$

(see e.g. Bohren and Huffman, 1983). There are several features worthy of mention in comparing between Figs. 3, 4 and 5. For example the backscatter linear polarization, defined as

$$\delta(\theta = 180) = \frac{|f|^2_{\perp}(\theta = 180) - |f|^2_{\parallel}(\theta = 180)}{|f|^2_{\perp}(\theta = 180) + |f|^2_{\parallel}(\theta = 180)} \tag{7}$$

is non-vanishing in case of hexagonals as compared to a zero depolarization for spheres. This is a well known characteristic of scattering by non-spherical particles but the quantitative relationship between δ and particle shape has never been convincingly established. The first minimum in intensity doesn't correspond to the Mie case, thus indicating that care has to be taken when interpreting results from the forward scattering PMS probes. This again is well established experimentally fact but its theoretical confirmation has to date been scarce. It seems that the extinction can be modelled, as it usually is, using a sphere of equivalent volume or surface, and we plan to perform more detailed calculations for the angularly averaged case.

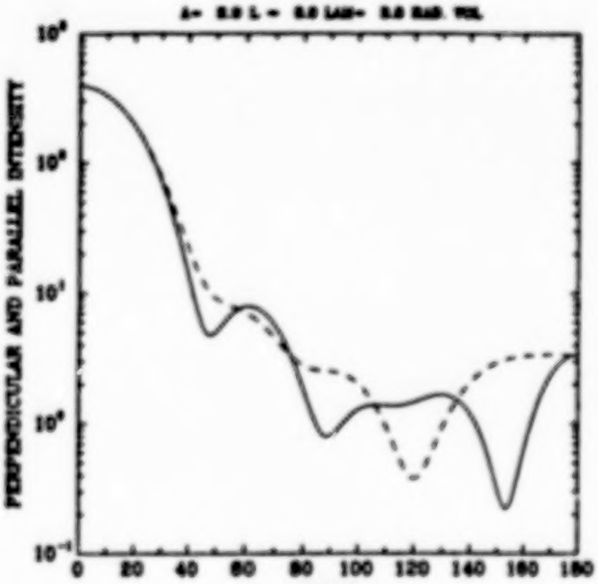

Fig. 5 *Mie results for equivalent volume spheres $r = 3.41\mu m$, and $\lambda = 3.8\mu m$.*

5. Anomalous Diffraction Theory

The anomalous diffraction theory (ADT) belongs to the broad class of approximations (together with the Rayleigh-Gans-Debye or Born expansions for example) in which one *makes some assumption about* the electric field under the integral of (1). This was noticed by Saxon (1955) and derived independently by van de Hulst (1957) on the basis of geometrical optics and diffraction. In the present context one assumes that the electric field inside the particle is given by

$$\mathbf{E}(\mathbf{x}) = E_0\hat{\mathbf{e}} \exp\left[ik\hat{\mathbf{k}} \cdot (\mathbf{b} + \hat{\mathbf{e}}_z z) - \chi(\mathbf{b}, z)\right] \tag{8}$$

where $\chi(\mathbf{b}, z)$ corresponds to the phase change due to the changed refractive index inside the particle. The impact vector $\mathbf{b}$ is perpendicular to the z axis (see Fig. 6). The explicit formulation of $\chi(\mathbf{b}, z)$ and relation of ADT to other theories such as High Energy Approximation and DDA is contained in Flatau and Stephens (1988). The anomalous diffraction theory (ADT) (Stephens, 1984) holds for particles with a refractive index close to unity $(m - 1) \ll 1$ and for a particle with a size to wavelength ratio $x \gg 1$. Since the index of refraction is close to 1, the problem of *total* extinction in the ADT theory reduces to calculations of the interference between the almost straight transmission and the light diffracted according to Huygens' principle.

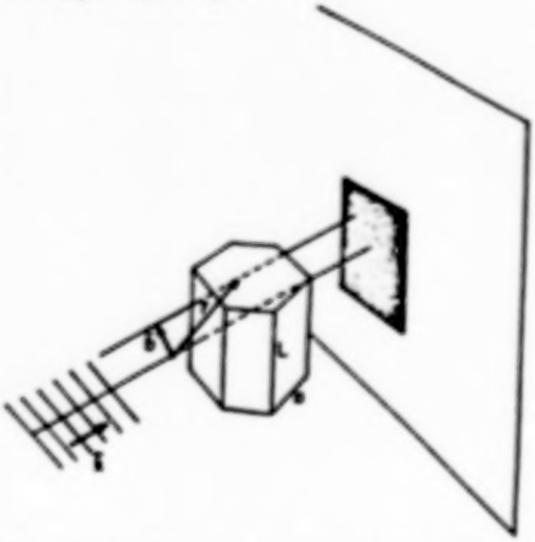

Fig. 6 *Geometry for Anomalous Diffraction Theory calculations.* b *is an impact parameter,* r *the position vector,* k *the direction of plane wave. The shadow area is in the far field and only forward scattering is considered here.*

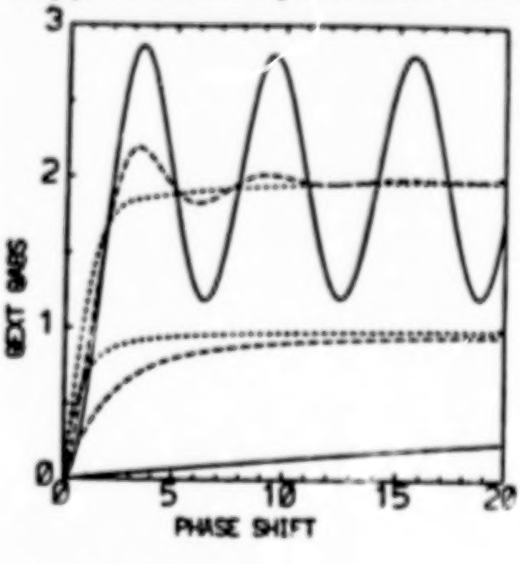

Fig. 7 *Extinction efficiency (converging or oscillating around 2 for large phase shift values) and absorption efficiency for hexagonal ice crystals for 3 different values of complex refractive index as a function of phase shift.*

Thus, in the anomalous diffraction approximation, the forward scattering amplitude $S(0)$ is given by

$$S(\vartheta = 0) = \frac{k^2}{2\pi} \int_A \left(1 - e^{-i\phi^*}\right) dA \qquad (9)$$

where $\phi^* = kd(m-1)$, d is the particle thickness, and m is the complex refraction: $m = n - in'$. The quantity ϕ^* is the complex phase shift of light passing through the particle relative to that passing around it. The kdn' term contributes to absorptive attenuation.

The extinction and absorption coefficients are defined as

$$C_{ext} = \frac{2}{A} Re \int_A \left(1 - e^{-i\phi^*}\right) dA \qquad (10)$$

and

$$C_{abs} = \frac{1}{A} \int_A \left(1 - e^{-2kdn'}\right) dA \qquad (11)$$

and the single scattering albedo is

$$\omega = \frac{C_{ext} - C_{abs}}{C_{ext}}. \qquad (12)$$

Therefore application of the ADT requires the relatively straight forward determination of the path length through the particle and evaluation of integrals for C_{ext} and C_{abs}. Notice that (8) is more general because it provides, in principle, the full phase function. Calculations of C_{ext}, C_{abs}, and ω for hexagonal crystals are presented in Figs. 7 and 8 using this approximation for the geometry depicted in Fig. 6. Full details of the method are planned in a forth coming paper and we also plan to compare these results, including phase functions, with solutions obtained from geometric optics and DDA.

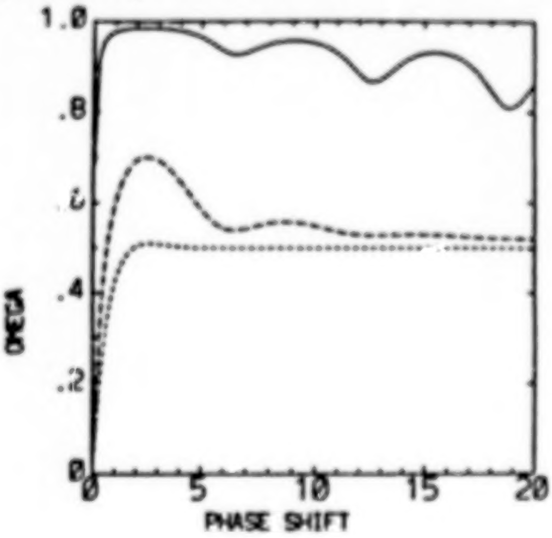

Fig. 8 *Single scattering albedo for hexagonal ice crystal in ADT approximation for 3 different values of complex refractive index.*

6. Summary

This paper reports on new calculations of the scattering of radiation by hexagonal ice crystals. Results are presented for small crystals which are not only the first of their type but also employ methods, to our knowledge, not previously used in atmospheric scattering problems. Scattering properties of large hexagonal crystals were also modelled using more approximate theories. While the results presented in this paper apply only to hexagonal crystals, the methods are general and particles of other geometries will be considered in further studies.

The work reported in this paper is preliminary and we plan to use the microphysic data collected during FIRE into these calculations to obtain the optical properties needed in the radiative transfer simulations of the cloud flux measurements.

Acknowledgments. We wish to thank Dr Warren Wiscombe for providing us with his newest set of Mie codes. The research presented in this paper has been supported in part by the grant from the Air Force AFOSR-88-0143 and in part by the NSF grants AST-8612013 and ATM-8519160.

REFERENCES

Bohren, C. F. and D. R. Huffman, 1983: *Absorption and scattering of light by small particles*, Wiley, New York.

DeVoe, H., 1964: Optical properties of molecular aggregates. I. Classical model of electronic absorption and refraction, *J. Chem. Phys.*, **41**, 393-400, 1964.

Draine, B. T., 1988: The discrete-dipole approximation and its application to interstellar graphite grains, *to be published by Astrophys. J.*

Flatau, P. J., G. L. Stephens, and B. T. Draine, 1988a: *To be submitted to Appl. Opt.*

Flatau, P. J., G. L. Stephens, 1988b: On the approximate theories of light scattering on small particles, *In preparation.*

Heymsfield, A. J., 1986: Ice particles observed in a cirriform cloud at −83°C and implications for Polar Stratospheric Clouds. *J. Atmos. Sci.*, **43**, 851–855.

Purcell, E. M. and C. R. Pennypacker, 1973: Scattering and absorption of light by nonspherical dielectric grains. *Astrophys. J.*, **186**, 705–714.

Rosen, J. M., D. J. Hofmann, and J. W. Harder, 1988: Aerosol measurements in the winter/spring Antarctic stratosphere 2. Impact on polar Stratospheric Cloud theories, *J. Geophys. Res.*, **93**, 677–686.

Saxon, D. S., 1955, *Lectures on Scattering of Light*, University of California, Los Angeles, Dept. of Meteorology, Scientific Report No. 9, 100pp.

Stephens, G. L., 1984, Scattering of plane waves by soft obstacles: anomalous diffraction theory for circular cylinders, *Appl. Opt.*, **23**, 954–959.

van de Hulst, H. C., 1957, *Light scattering by small particles*, Dover, New York.

Cirrus Microphysics and Radiative Transfer: A Case Study

Stefan A. Kinne NASA-Ames MS 245-3, Moffett Field, CA 94035
Thomas P. Ackerman Penn State, Dep of Meteorology, PA 16802
Andrew J. Heymsfield NCAR, P.O.Box 3000, Boulder, CO 80307

During the Cirrus Intensive Field Operation of FIRE, data collected by the NCAR King-Air in the vincinity of Wausau,WI on October 28th were selected to study the influence of Cirrus cloud microphysics on radiative transfer and the role of microphysical approximations in radiative transfer models.

The instrumentation of the King-Air provided, aside from temperature and wind data, up- and downwelling broadband solar and infrared fluxes as well as detailed microphysical data (e.g., particle size distributions and two-dimensional particle images).

The selected case saw the aircraft traverse on seven flight legs of constant altitude from the cloud bottom (6km) to the cloud top (8km), as indicated in Figure 1.

FIRE: FLIGHT TRAJECTORIES (10/28/86)

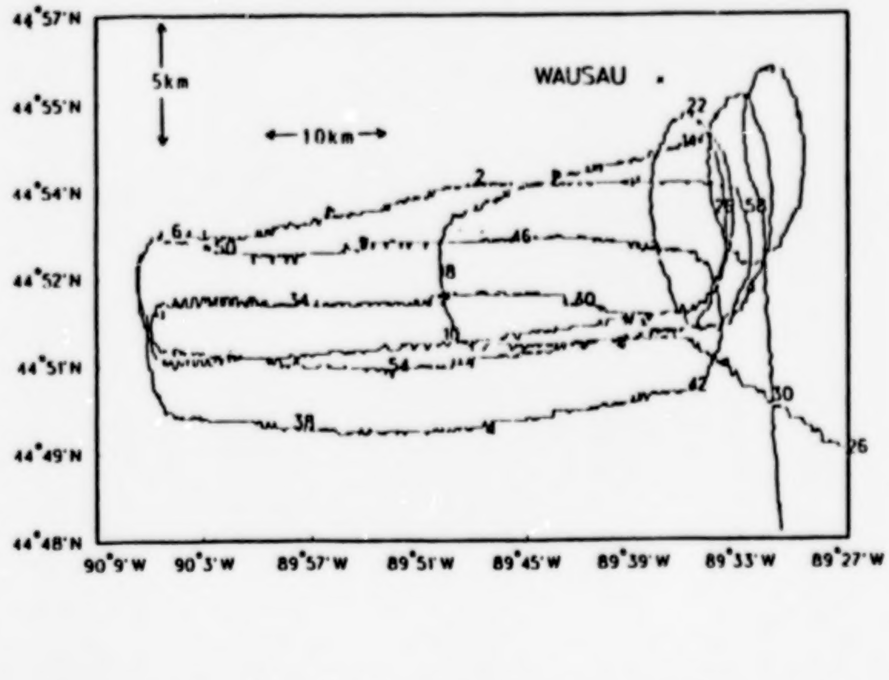
44°57'N
44°55'N
44°54'N
44°52'N
44°51'N
44°49'N
44°48'N
90°9'W
90°3'W
89°57'W
89°51'W
89°45'W
89°39'W
89°33'W
89°27'W
5km
10km
WAUSAU
22
2
14
6
50
46
26
58
8
34
40
10
54
42
30
38
26

Figure 1
Trajectories of the NCAR King-Air aircraft on the 28th of October 1986 between 16.26 and 17.31 GMT. (the digits indicate the minutes of the hour, the arrows indicate the direction)

The aircraft data, supplied every second, are averaged over these legs to represent the properties for that altitude. The resulting vertical profiles, however, suffer from the fact that each leg represents a different cloud column path. Figure 2 shows these legs as they appear to a fixed cloud system at 17 GMT.

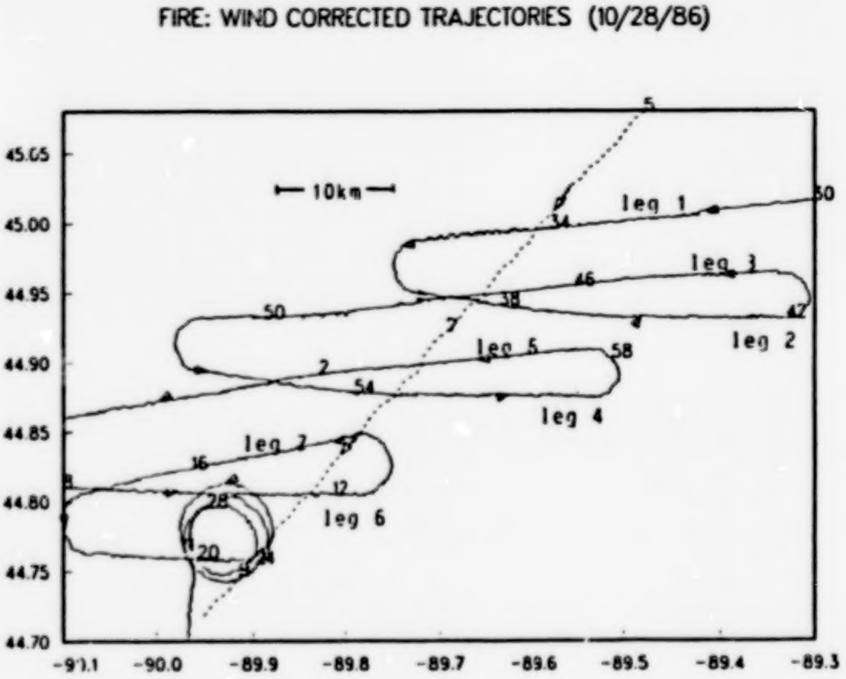

Figure 2

Trajectories of the NCAR King-Air (solid line) and the NASA ER-2 (dashed line) as they relate to a fixed cloud field at 17.00 GMT, for the time interval of Figure 1.

Except for the first leg below the cloud all other flight legs pairwise penetrate almost the identical cloud column path. This helps to correct any irregularities in the vertical profiles of the averaged data and provides information about the vertical structure of an individual cloud cell as well.

Based on the measured microphysical data particle size distributions of equivalent spheres for each cloud level are developed. Accurate radiative transfer (MIE and Matrix-Operator) calculations are performed, incorporating atmospheric and radiative data from the ground (Wausau) and the stratosphere (NASA-ER2). The location of Wausau is indicated in Figure 1, while the corrected flight tracks of the ER-2 aircraft are displayed in Figure 2. The radiative transfer calculations determine solar and infrared fluxes below, in and above the cirrus cloud.

Comparing calculated to the measured up- and downwelling fluxes at the seven cloud levels for both the averaged and the three "crossover" data will help to assess the validity of particle size and shape approximation as they are frequently used to model cirrus-clouds. Once agreement is achieved the model results may be applied to determine, in comparison to a cloudfree case, the influence of this particular cirrus on the radiation budget of the earth atmosphere system.

SUBVISUAL CIRRUS CLOUD PROPERTIES DERIVED FROM A FIRE IFO CASE STUDY

K. Sassen, M.K. Griffin and G.C. Dodd

Meteorology Department
University of Utah
Salt Lake City, UT 84112, U.S.A.

From the central Wisconsin IFO field site at Wausau, the University of Utah Mobile Polarization Lidar and a surface radiation station from the Lamont-Doherty Geological Observatory of Columbia University observed two very tenuous cirrus clouds on 21 October 1986. The clouds were present just below the height of the tropopause (12.78 km MSL), between -60 to -70°C. The first cloud was not detected visually, and is classified as subvisual cirrus. The second, a relatively narrow cloud band that was probably the remnants of an aircraft contrail, can be termed zenith-subvisual since, although it was invisible in the zenith direction, it could be discerned when viewed at lower elevation angles and also due to strong solar forward-scattering and corona effects. The observations provide an opportunity to assess the threshold cloud optical thickness associated with cirrus cloud visibility.

Ruby lidar (0.693 µm) backscattered signals were converted to isotropic volume backscatter coefficients (β, km^{-1} sr^{-1}) by applying the pure-molecular scattering assumption just below cloud base. The backscattering coefficient β_c due to the cloud is then obtained and expressed in relation to the molecular backscattering coefficient β_m in terms of the scattering ratio $R = (\beta_m + \beta_c)/\beta_m$. The linear depolarization ratio $\delta = \beta_\perp/\beta_\parallel$ for the cloud is computed after removing the essentially parallel-polarized scattering contributions from air molecules. The β_c values are also applied to determining the cloud optical thickness τ_c through the use of a backscatter-to-extinction ratio k, and the concentration of cloud particles using the backscattering gain g, and the effective diameter d_e of the particles obtained from the analysis of solar corona photographs. The sizes of the particles generating the corona are related to the angular separations between the centers of the red bands and the sun, as described in Sassen (1979), yielding diameters of ~25 µm. The direct and diffuse components of shortwave radiation fluxes (0.28-2.8 µm), measured by full hemispheric pyranometers, were used to compute the nadir optical thickness of the total atmosphere τ_t. Slight perturbations in the surface fluxes occurred during the cirrus passage, and the resultant variations in total optical thickness were equated with τ_c.

Given in Fig. 1 are lidar data in the form of height-versus-time displays of the scattering ratio R and linear depolarization ratio δ. To aid in the rejection of spurious data dominated by signal noise, 45-m (6 digitized data point) averages are used, a threshold of $R = 2.5$ is employed to define the cloud boundaries, and δ values are computed for $R \geq 5.0$. Both the structure and depolarizing properties of the subvisual (1545-1610) and zenith-subvisual (1625-

1700) cirrus clouds differ significantly. The former cloud displays a layered structure and low δ values, while the latter displays a concentric arrangement of scattering ratio contours and δ values more typical of cirrus. The appearance of the zenith-subvisual cloud is quite similar to that of long-lasting aircraft contrails. The weakly scattering layers that straddle the tropopause and extend into the lower stratosphere also appear to be composed of ice crystals.

The τ_c derived from the lidar and radiometric data are compared in Fig. 2, where the time scale of the radiometric data has been offset by 20 min to account for the advection time associated with cloud movement (at 16 m s^{-1}) between the zenith and solar elevation angles. (Note that local noon occurred at 1645 GMT). The two passive data records reflect the uncertainty in determining a "cloudless" optical thickness from the total atmospheric τ. The range of lidar-derived τ_c data values corresponds to the 0.05-0.10 range of k values considered appropriate for simple cirrus cloud particles. Although the cloud properties could be expected to display spatial and temporal variations, it is clear that both analysis methods yield comparable τ_c values. Given the inferred sizes of the cloud particles, which are relatively large in comparison to visible light wavelengths, differences between the broadband shortwave radiometric and monochromatic lidar data should not be significant.

Inferences about the microphysical composition of the zenith-subvisual cirrus cloud band can be drawn from combined photographic and lidar observations. Although the solar corona analysis reveals that the cloud particles must have been near-spherical and ~25 µm in diameter, the degree of lidar linear depolarization (Fig. 1) is consistent with hexagonal ice crystals, indicating that the thick-plate ice crystal habit (with axial ratios close to unity) was dominant. On the other hand, the subvisual cirrus probed prior to 1610 displayed much lower δ values and no optical phenomena, indicating differences in particle shapes and sizes. Compiled in Table 1 are the derived optical and microphysical quantities in terms of mean and maximum values for the subvisual and zenith-subvisual cirrus observation periods. The surface flux τ_c corresponds to the average of the two curves in Fig. 2, and the lidar data are derived for $k = 0.075$ and $g = 0.01$. The vertical depth of the cloud Δz is defined with respect to $R \geq 2.5$, and N_i and M_i represent the concentrations and ice mass contents of the clouds based on the 25 µm particle diameter estimate. In general, the microphysical properties of the zenith-subvisual cirrus are rather similar to those of an aircraft-sampled subvisual tropical cirrus (Heymsfield, 1986).

With regard to the zenith-subvisual cloud, which is of primary interest, a $\tau_c = 0.03$ value can be assigned as a threshold optical thickness for subvisual-versus-visual cirrus. This value compares favorably with the $\tau_c = 0.06$ reported by Platt et al. (1987) for a cirrus that was visible but very hazy in appearance. With regard to the $\tau_c = 0.03$ threshold value, it would appear that subvisual cirrus could have an impact on radiation transfer that is similar to the effects produced by the stronger episodes of stratospheric aerosol loading from volcanic eruptions or polar stratospheric clouds. Moreover, recent Stratospheric Aerosol and Gas Experiment (SAGE) satellite findings (Woodbury and McCormick, 1986) indicate that a category of optically thin cirrus, displaying extinction values at 1.0 µm between 8×10^{-4} to 8×10^{-3} km^{-1}, is fairly widespread on a global average. This extinction range is comparable to that obtained from the β_c coefficients for our subvisual cirrus, suggesting that subvisual cirrus may represent a relatively significant component in the radiation balance of the earth-atmosphere system.

Acknowledgments. This research has been supported by NASA Grants NAG-1-686 and NAG-1-718, and by NSF Grant ATM-85 13975. The authors would like to thank D. Robinson of Lamont-Doherty Observatory for providing the surface radiation flux data.

References

Heymsfield, A.J., 1986: Ice particles observed in a cirriform cloud at -83°C and implications for polar stratospheric clouds. J. Atmos. Sci., 43, 851-855.

Platt, C.M.R., J.C. Scott and A.C. Dilley, 1987: Remote sounding of high clouds. Part VI: Optical properties of midlatitude and tropical cirrus. J. Atmos. Sci., 44, 729-747.

Sassen, K., 1979: Iridescence in an aircraft contrail. J. Opt. Soc. Am., 68, 1080-1083.

Woodbury, G.E. and M.P. McCormick, 1986: Zonal and geographical distributions of cirrus clouds determined from SAGE data. J. Geophys. Res., 91, 2775-2785.

Table 1. Mean and maximum (45 m-average) optical and microphysical properties for subvisual and zenith-subvisual cirrus derived from ruby lidar (0.694 μm) and surface shortwave (0.28-2.8 μm) flux data.

	Surface Flux	Lidar					Photographic + Lidar		
	τ_c	τ_c	R	β_c (km sr)$^{-1}$	Δz km	δ	d_e μm	N_i ℓ^{-1}	M_i mg m^{-3}
				Subvisual Cirrus					
Mean	0.011	0.007	5.2	5.8×10^{-4}	0.77	0.19	--	---	---
Maximum	0.016	0.009	11.3	1.5×10^{-3}	1.00	----	--	---	---
				Zenith-Subvisual Cirrus					
Mean	0.014	0.015	11.1	1.4×10^{-3}	0.65	0.35	25	25	0.2
Maximum	0.030	0.026	45.1	6.4×10^{-3}	0.95	----	25	110	0.9

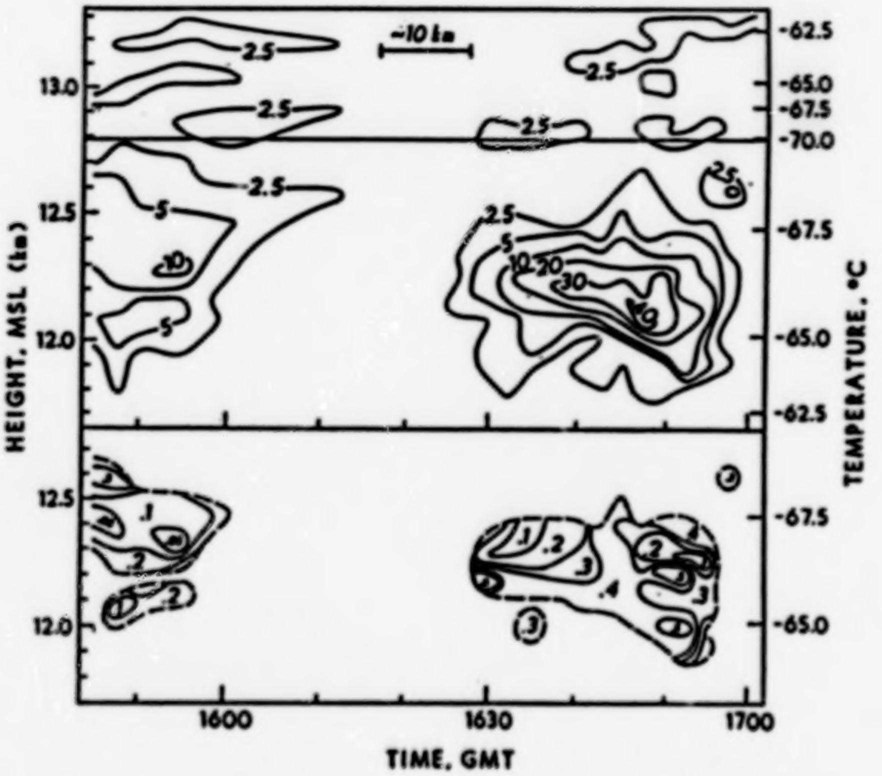

Fig. 1 Height-time displays of lidar scattering ratio R *(top) and linear depolarization ratio δ (bottom) for the subvisual (prior to 1615) and zenith-subvisual cirrus clouds located just below the tropopause (line at 12.78 km).*

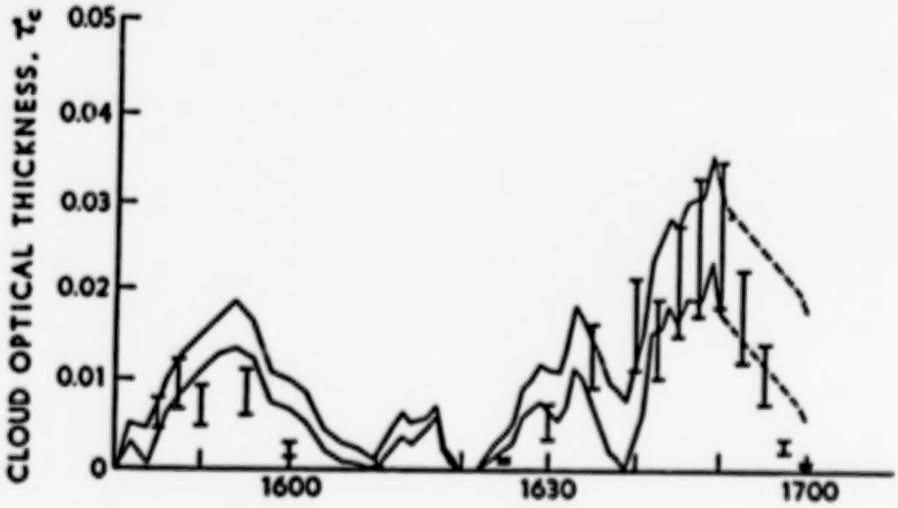

Fig. 2 Comparison of cloud optical thicknesses τ_c derived from lidar (bars for each shot) and surface shortwave radiation flux (continuous lines, for two approaches) during the passage of the cirrus. Dashed line segments correspond to a 9 min gap in the radiation records.

Multi-spectral Window Radiance Observations of Cirrus from Satellite and Aircraft - November 2, 1986 "Project FIRE"

W. L. Smith, H. E. Revercomb, H. B. Howell, and H.-X. Lin[1]

Cooperative Institute for Meteorological Satellite Studies
University of Wisconsin-Madison
Madison, Wisconsin

[1]State Meteorological Administration
National Meteorological Bureau
Beijing, China

Abstract

High resolution infrared radiance spectra achieved from the NASA ER2 airborne HIS experiment are used to analyze the spectral emissivity properties of CIRRUS cloud within the 8-12μm atmospheric "window" region. Observations show that the cirrus emissivity generally decreases with increasing wavenumber (i.e., decreasing wavelength) within this band. A very abrupt decrease in emissivity (increase in brightness temperature) exists between 930 cm^{-1} (10.8μm) and 1000 cm^{-1} (10.0μm), the magnitude of the change being associated with the cirrus optical thickness as observed by lidar. The HIS observations are consistent with theoretical calculations of the spectral absorption coefficient for ice.

The HIS observations imply that cirrus cloud can be detected unambiguously from the difference in brightness temperatures observed within the 8.2μm and 11.0μm window regions of the HIRS sounding radiometer flying on the operational NOAA satellites. This ability is demonstrated using simultaneous 25 km resolution HIRS observations and 1 km resolution AVHRR imagery achieved from the NOAA-9 satellite. Finally, the cirrus cloud location estimates combined with 6.7μm channel moisture imagery portray the boundaries of the ice/vapor phase of the upper troposphere moisture. This phase distinction is crucial for infrared radiative transfer considerations for weather and climate models, since upper tropospheric water vapor has little effect on the earth's outgoing radiation whereas cirrus cloud has a very large attenuating effect.

1. Importance of Cirrus Detection

The detection of cirrus clouds from satellites is important for at least two reasons: (1) the monitoring of long-term changes of cloud cover, since cirrus variability greatly impacts the greenhouse effect, and (2) the elimination of infrared radiances observed by sounding radiometers effected by cloud prior to the temperature profile retrieval process since undetected cirrus cloud contamination leads to a systematic cold bias in the result.

2. Prior Work

Several authors have addressed the optically thin cirrus detection problems (Prabahkara, 1987; Inoue, 1985, Wu, 1987). Smith et al. (1969), Arking (1985), and Wu (1987) point out that thin cirrus cloud can be detected by the difference in brightness temperature observed in the 3.8μm and 11μm window regions because of the different Planck radiant energy dependence upon temperature at these two wavelengths. When viewing through thin cirrus, the measured radiance is a function of both the cold cloud and warm surface temperatures. Because of the higher ordered dependence of radiance upon temperature at 3.8μm, the 11μm brightness temperature will be observed to be lower than the 3.8μm brightness temperature in the presence of thin cirrus. However, this relationship is not unique in that similar differences occur during the daytime due to differential reflected sunlight contributions to the two channels and for broken middle or low clouds due to the differential Planck effect. More recently, Inoue (1985) and Prabahkara (1987) pointed out that the absorption for ice is larger at 12μm than at 11μm so that the "split window" difference (i.e., the difference in brightness temperatures observed in the 11μm and 12μm channels of the Advanced Very High Resolution Radiometer (AVHRR) flying aboard the operational NOAA satellites) can be used to detect thin cirrus cloud. However, this differential relation is not unique either, since water vapor absorption can produce a similar effect.

3. HIS Observations

Most recently, spectral radiometric observations of cirrus clouds were achieved during the First ISCCP Regional Experiment (FIRE) conducted over southcentral Wisconsin during October-November 1986. The observations were conducted with the High resolution Interferometer Sounder (HIS) flying aboard the NASA ER2 aircraft. Here we discuss the cirrus observed over Wisconsin on November 2, 1986. As shown in the Fig. 1 example, the HIS spectral radiances reveal an increase in cirrus cloud absorption and emissivity (decrease in radiating brightness temperature) across the 10-12μm window region with a very sharp increase taking place between 10 and 11μm (i.e., 1000-900 cm^{-1}. HIS observations between 8 and 10μm (not shown) reveal no significant change in cirrus emissivity between 8 and 10μm. The HIS observations are in good agreement with theoretical calculations of ice absorption by Irvine and Pollack (1968) as shown in Fig. 2. (Figures 4 and 5 show satellite images of the cirrus observed from the ER2.)

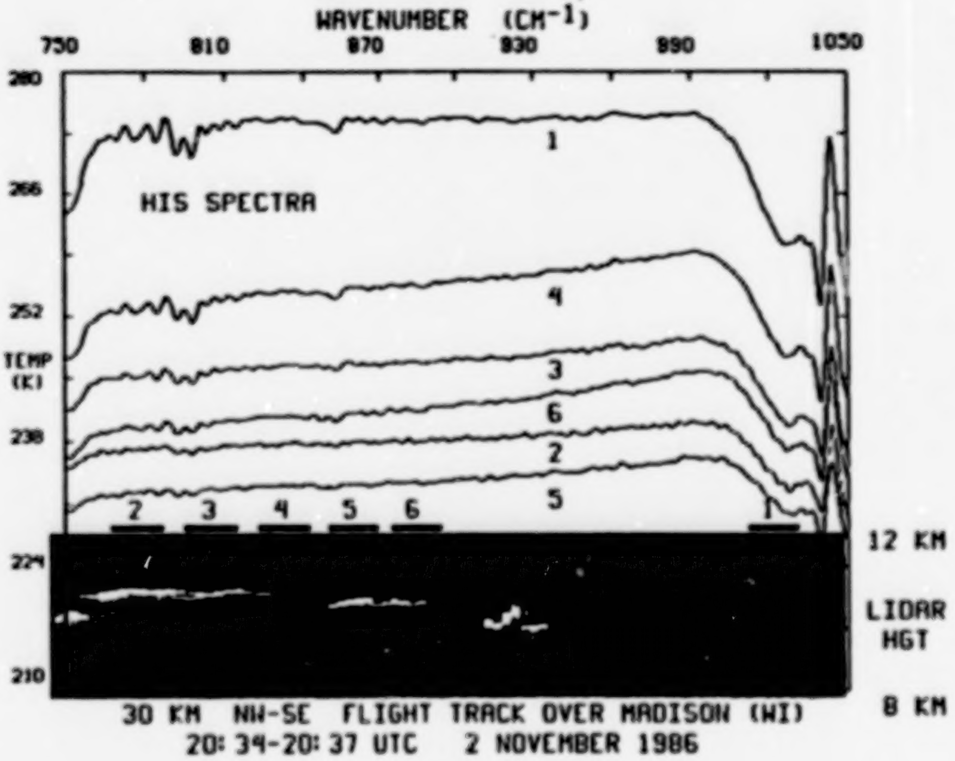

Fig. 1. A set of 10-12μm "window" region cirrus cloud brightness temperature spectral observed from the NASA ER2 on November 2, 1986 near Madison, Wisconsin. Also shown is an image of the cirrus cloud backscatter between 8 and 12 km (no significant return outside this altitude range) of light pulses from a lidar (Spinherne, 1982) also aboard the ER2. The field of view of the HIS corresponding to each spectrum is shown above the lidar.

4. Application to Satellite Observations

Because water vapor absorption is generally larger in the 8-9μm window region than within the 11-12μm region, a positive brightness temperature difference between these two window regions is a definite indicator of the presence of cirrus cloud. This principal is demonstrated using the 8.2 and 11.1μm channel observations of the High Resolution Infrared Radiation Sounder (HIRS) radiometer flying aboard the polar orbiting NOAA satellites.

Figure 2 shows the spectral response of the HIRS 11.1μm (H8) and 8.2μm (H10) channels relative to the volume absorption coefficient for ice. As can be seen, there should be a significant difference

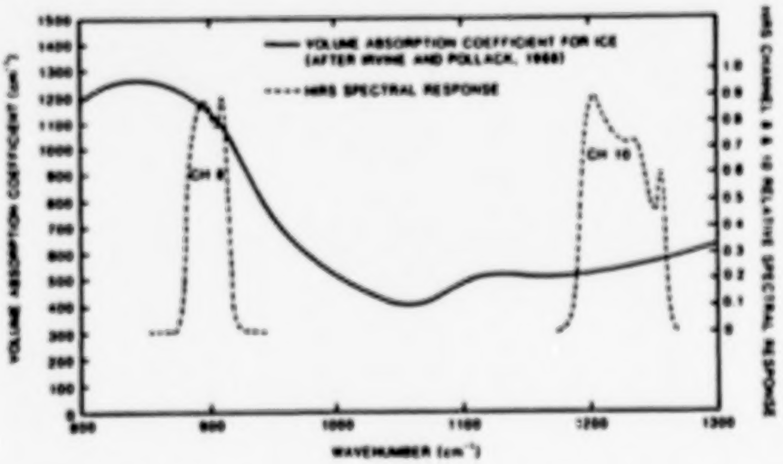

Fig. 2. Volume absorption coefficient for ice and the spectral response of HIRS channels 8 and 10.

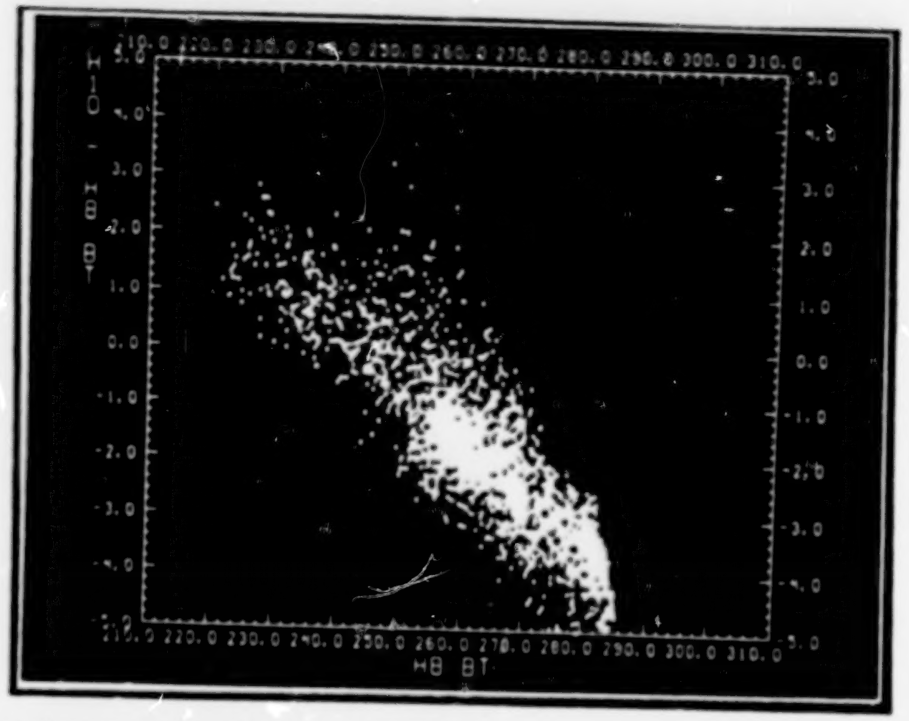

Fig. 3. Scatter diagram of the difference in brightness temperature observed in the HIRS 8.2μm (H10) and 11.1μm (H8) channels as a function of 11.1μm (H8) brightness temperature. Positive differences indicate the presence of semi-transparent cirrus cloud.

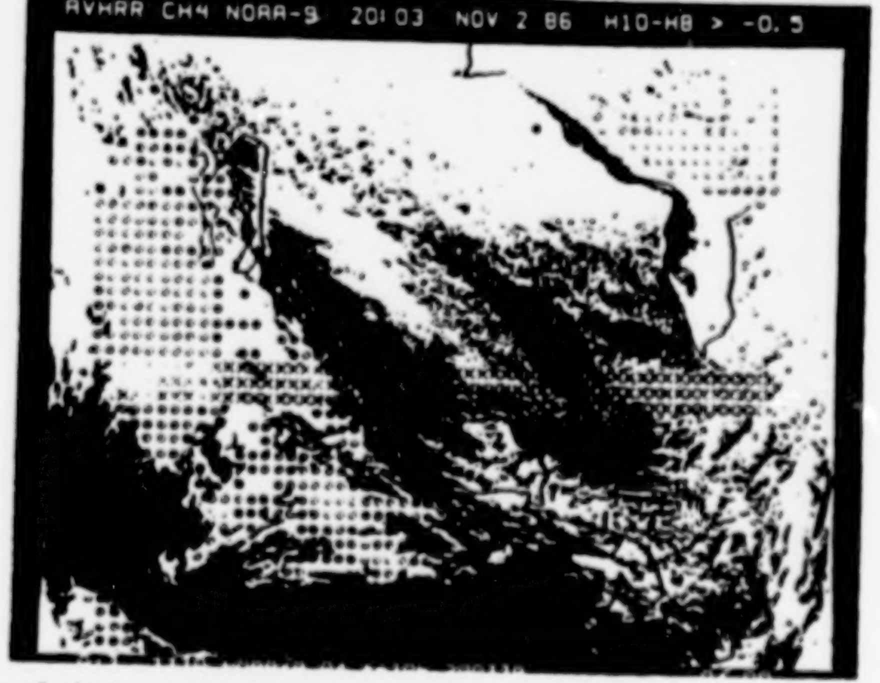

Fig. 4. An image of cloud cover at 20 GMT on November 2, 1986 as observed by the AVHRR 11μm channel (Ch4). Superimposed are circles delineating areas of cirrus cloud detected from the HIRS 8.2 and 11.1μm window channel differences. The crosses denote the gap in earth coverage due to instrumental calibration.

in the brightness temperature observed by these two channels when viewing semi-transparent cirrus cloud. Figure 3 shows a scatter diagram of the difference in brightness temperature observed in the HIRS 8.2μm channel (H10) and the HIRS 11.1μm channel (H8) as a function of the 11.1μm brightness temperature observation over the upper midwest on November 2, 1986 (see Fig. 4). As shown, most of the observations are free of cirrus clouds as indicated by the negative differences. Apparent cirrus cloud conditions, however, do cover a wide range of optical thicknesses as indicated by the wide range

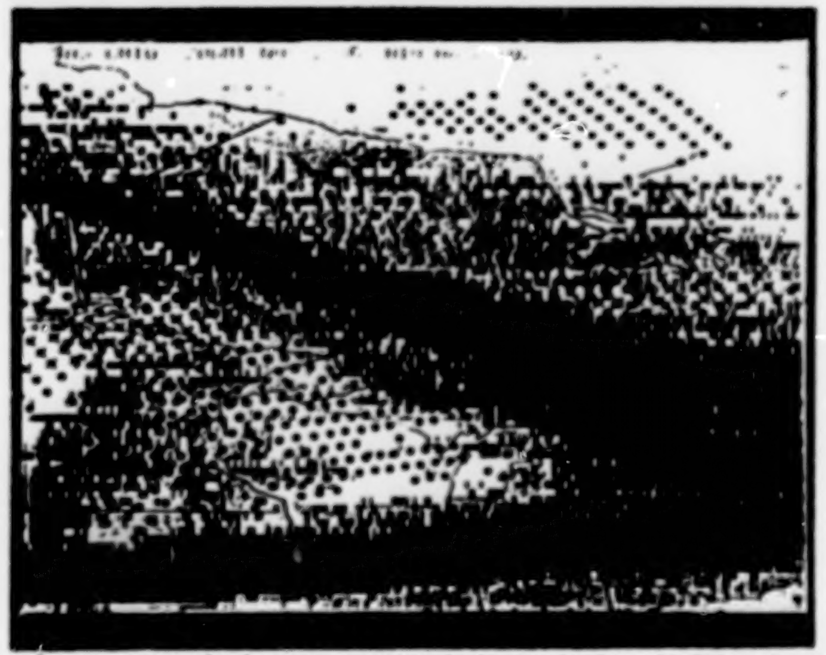

Fig. 5. An image of upper tropospheric water vapor and cirrus cloud at 20 GMT on November 2, 1986 as observed by the GOES-VAS 6.7μm H_2O absorption channel. As in Fig. 4, the circles show regions of cirrus as detected from the NOAA HIRS 8.2μm and 11.1μm brightness temperature difference.

of 11.1μm brightness temperature observations (220-268°K) associated with positive indications of cirrus clouds (i.e., plus H10-H8 brightness temperature differences). Assuming a mean surface skin temperature of 280°K and a probable cirrus cloud temperature of 220°K, the temperature at the 10 km cirrus height depicted by lidar (Fig. 1), the cirrus optical thickness for the 11.1μm channel is as low as 0.2, indicating that cirrus with transmissivities as high as 80% were detected by the HIRS in this case.

Figure 4 shows the location (denote by circles) of HIRS detected cirrus superimposed upon an AVHRR infrared image. Because the instrumental noise of the HIRS is about 0.[illegible]°K for typical cloud temperatures, a threshold of -0.5°K for the difference was used to discriminate cirrus contaminated HIRS fields-of-view. The circles depict the geographical dimension of the 25 km HIRS field-of-view. Based on comparison with the cloud morphology in the AVHRR image, the objective cirrus detection technique seems to work very well, except when the cirrus occupies only a small portion of the HIRS field-of-view.

5. Water Phase Detection

The combination of 6.7um, 8.2um, and 11.1um brightness temperature data can be used to differentiate between upper level moisture in the vapor phase from that which has sublimated into the ice phase. This distinction is very important with regard to the analysis of the "greenhouse effect" on the earth's climate since upper level water vapor is largely transparent to the outgoing radiation to space whereas cirrus cloud produces a very large decrease in the radiation to space.

Upper tropospheric moisture imagery, obtained from 6.7um geostationary satellite measurements is routinely used for the depiction of large scale weather patterns. It would be extremely useful to have an 8.2um channel as part of the geostationary imagery system so that the phase of the upper level moisture depicted by the 6.7um channel could be diagnosed. An example of the results which could be achieved is generated by superimposing HIRS cirrus cloud depictions over a GOES-VAS 6.7μm moisture image obtained at nearly the same time. Figure 5 shows the result. If one had a time sequence of such inferences, the phase change process could be observed, thus providing important measurements of upper tropospheric cloud dynamics as well as the upper tropospheric radiative properties important for weather and climate analyses.

6. Additional Considerations

It is worth noting that cirrus cloud microphysical properties (e.g., partical size distribution) might be deduced from the high resolution HIS spectra and the simultaneous lidar observations conducted from the ER2 aircraft (an example of which is shown in Fig. 1). The optical thickness, τ, of the cloud for "window" wavelengths in between gaseous absorption lines can be shown to be given by

$$\tau_\nu = \beta_\nu \Delta Z = -\ln \left[\frac{I_\nu - B_\nu (T_{cd})}{B_\nu(T_s) - B_\nu (T_{cd})} \right] \qquad (1)$$

where β_ν is the absorption coefficient, ΔZ the geometrical thickness, I_ν is the observed radiance, T_s and T_{cd} are the surface and cloud temperature, respectively, and B is the Planck radiance. The surface skin temperature T_s can be observed from neighboring cloud-free fields-of-view and T_{cd} is taken from a clear sky temperature profile at the cloud altitude depicted by the lidar. The geometric thickness of the cloud ΔZ is also provided by the lidar for optically thin cloud (see Fig. 1). Consequently, the combination of HIS and lidar observations provides a measure of the infrared absorption coefficient spectrum for the cloud. The absorption coefficient is related to the cloud particle properties through the relation

$$\beta_\nu = K(\eta_i \eta_r)\, \nu \int_0^\infty r^3 N(r)\, dr \qquad (2)$$

where $K(\eta_i, \eta_r)$ is a function of the imaginary and real parts of the index refraction for ice, r is the radius of the ice particles (assumed to be effective spheres) and $N(r)$ is the size distribution. If it is assumed that the size distribution can be expressed as a linear combination of Gaussian distributions, i.e.,

$$N(r) = \sum_{i=1} n[r_i(o)] \exp\left(\sqrt{\frac{[r - r_i(o)]^2}{2\sigma_i^2}} \right) , \qquad (3)$$

then estimates of the size distribution might be obtained by solving for those $r_i(o)$ and σ_i values which best satisfy the observed absorption coefficient spectra. This research is the subject of a future paper.

Acknowledgements

We thank H. Woolf of CIMSS for his assistance with the HIS data reduction. J. Spinhirne (NASA/GSFC) graciously provided the ER2 lidar data. Special thanks go to the flight crew of the NASA ER2 for their flawless performance of their difficult mission. L. Beckett and G. Wade are gratefully acknowledged for their help in preparing this manuscript. This research was supported by NASA Contract NAS1-18272.

References

Smith, W. L., 1969: The improvement of clear column radiance determination with a supplementary 3.8μm window channel. ESSA Technical Memorandum NESCTM 16, 17 pp.

Spinherne, J. D., M. Z. Hansen, and L. O. Caudill, 1982: Cloud top remote sensing by airborne lidar. Appl. Optics, 21, 1564-1571.

Arking, A., and J. D. Childs, 1985: Retrieval of cloud cover parameters from multispectral satellite images. J. Clim. Appl. Meteor., 24, 322-333.

Inoue, T., 1985: On the temperature and effective emissivity determinations of semi-transparent cirrus clouds by bi-spectral measurements in the 10um window region. J. Meteor. Soc. Japan, 63, 88-89.

Wu, M.-L. C., 1987: A method for remote sensing the emissivity, fractional cloud cover, and cloud top temperature of high level, thin clouds. J. Clim. Appl. Meteor., 26, 225-233.

Prahahkara, C. P., R. S. Fraser, G. Delu, M.-L. C. Wu, R. J. Curran, and T. L. Styles, 1987: Thin cirrus clouds: seasonal distribution over oceans deduced from Nimbus 4 IRIS. J. Clim. Appl. Meteor.

Cirrus Cloud Statistics: Temperatures and Optical Depths

Francisco P. J. Valero,[1] Thomas P. Ackerman,[2] and Warren J. Y. Gore[1]
[1]NASA Ames Research Center, Moffett Field, CA 94035
[2]Department of Meteorology, Pennsylvania State University, University Park, PA 16802

Measurements of the upwelling infrared radiance at 10.5 μm and 6.5 μm were obtained during the FIRE Cirrus Intensive Field Observations using a radiometer with a 15° cone nadir field-of-view flown on the NASA Ames ER-2. Data is recorded at a frequency of 1 Hertz and the radiometer is continuously calibrated with a liquid nitrogen black-body source, thereby providing a large number of very accurate radiance values during the course of a several hour flight. For this study, we are particularly concerned with the statistical properties of the cirrus deck as deduced from the radiance data. We have focused primarily on the data acquired on 28 October 1986, but also show some data from other flights for comparison purposes.

A histogram of the 10.5 μm brightness temperatures obtained on 28 October between approximately 15:30 and 19:00 GMT is shown in Figure 1. (Brightness temperature is defined as the temperature of a black body that would emit the observed radiance in the same spectral interval.) The distribution shows two distinct peaks. The narrow peak at the higher end represents the range of surface temperatures observed during the flight, with the additional possibility of some observations of very thin cirrus. The broader distribution of colder temperatures represents the distribution of cirrus optical depths ranging from relatively thin to optically thick values. Comparison of cloud heights as deduced from the airborne lidar data (J. Spinhirne, personal communication) and radiosonde profiles (D. Starr, personal communication) show that the actual temperature of the cloud deck was on the order of 235 K. This is quite consistent with the lowest observed brightness temperatures, indicating that the cloud was optically thick in places.

If we neglect any atmospheric emission at 10 μm, we can estimate the cirrus optical depth from the simple relationship:

$$B_E = B_S e^{-\tau} + B_C(1 - e^{-\tau}) + B_S \delta_S - B_C \delta_C.$$

Here B_E is the measured radiance, B_S is the surface emission, B_C is the cloud emission, and τ is the cirrus optical depth. Because ice crystals scatter as well as absorb infrared radiation, correction terms for scatter into the radiometer field of view, δ_S, and for reduced emission from the cloud, δ_C, must be included. These correction terms are calculated with

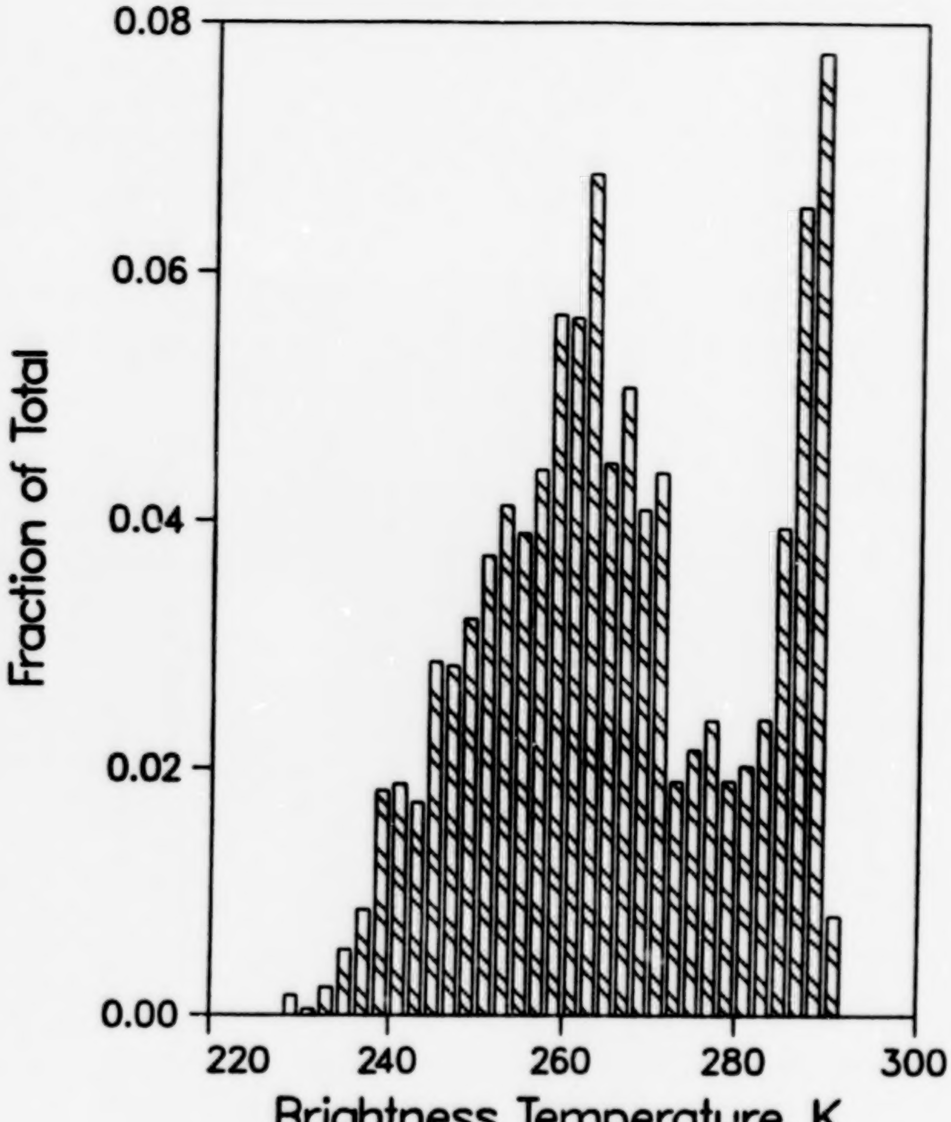

Figure 1: Histogram of 10.5 μm brightness temperatures (in degrees Kelvin) obtained on 28 October, 1986. The bars represent 2K temperature increments and the vertical axis is the fraction of the total observations falling into the given bin.

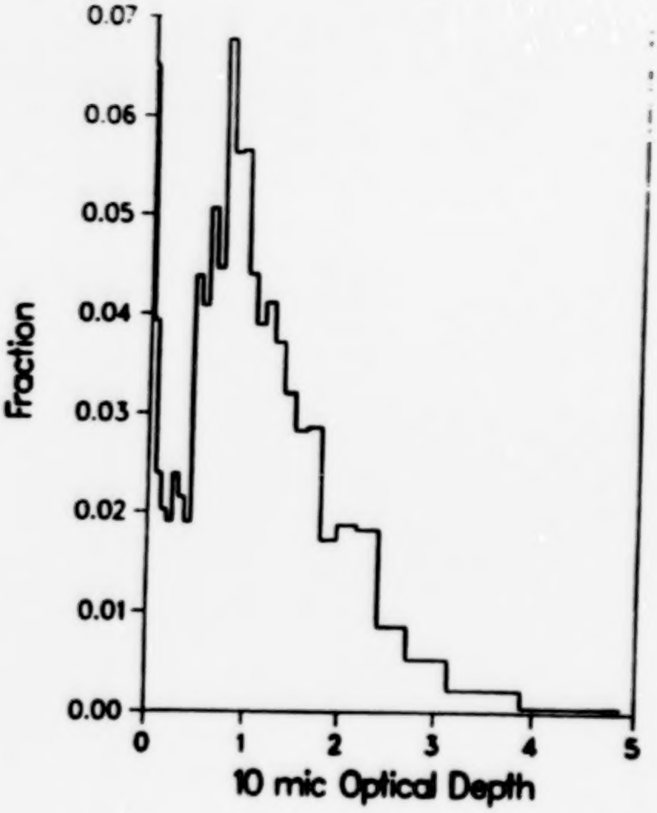

Figure 2: Cirrus 10 μm optical depth inferred from the observed brightness temperature distribution. The vertical axis is the fraction of total observations falling into the given bin.

a simple radiance model incorporating a two-stream source term. A trial value of τ is calculated assuming no scatter and the equation is then solved iteratively and converges in a few iterations.

The results of the optical depth inversion process applied to the distribution in Figure 1 is shown in Figure 2. Here we have assumed that the actual cloud temperature is given by the lowest observed brightness temperature and the actual surface temperature by the highest observed temperature. The latter assumption produces the probably spurious peak of very low optical depths seen in Figure 2. The broad distribution of optical depths appears to be approximately log-normal in shape with a geometric mean of about 0.9. The inversion process is uncertain at large optical depths (since the $e^{-\tau}$ terms tend to 0), so we truncate the distribution at optical depths of about 5.

Given a distribution of optical depths, the atmospheric temperature profile, and the location of the cirrus layer, we can then compute the infrared exchange and atmospheric heating rates. We have used a multi-spectral, two-stream code to compute the broad-band infrared heating rates in the cirrus layer as a function of optical depth. The results of these calculations are compared to the upwelling infrared flux measurements obtained from the ER-2.

Finally, we have carried out similiar analyses for the entire 6.5 μm data record and for sub-sections of the 28 October flight, as well as for some of the other cirrus IFO flights. We show that the distributions of brightness temperature and optical depth vary with time and synoptic situation.

The Radiation Budget of a Cirrus Layer Deduced From Simultaneous Aircraft Observations and Model Calculations

Thomas P. Ackerman,[1] Stefan Kinne,[2] Andrew J. Heymsfield[3], and Francisco P. J. Valero[2]

[1]Department of Meteorology, Pennsylvania State University, University Park, PA 16802
[2]NASA Ames Research Center, Moffett Field, CA 94035
[3]NCAR, Boulder, CO 80307

Several aircraft were employed during the FIRE Cirrus IFO in order to make nearly simultaneous observations of cloud properties and fluxes. We have analyzed a segment of the flight data collected on 28 October 1988 during which the NASA Ames ER-2 overflew the NCAR KingAir. The ER-2 flew at high altitude making observations of visible and infrared radiances and infrared flux and cloud height and thickness. During this segment, the KingAir flew just above cloud base observations of ice crystal size and shape, local meteorological variables, and infrared fluxes. While the two aircraft did not collect data exactly coincident in space and time, they did make observations within a few minutes of each other, which is about the best that can be managed with two such disparate aircraft.

For this case study, we are primarily concerned with the infrared radiation balance of the cirrus layer. Observations of the upwelling 10 μm radiance, made from the ER-2, can be used to deduce the 10 μm optical depth of the layer. The upwelling broad-band infrared flux is also measured from the ER-2. At the same time, the upwelling and downwelling infrared flux at cloud base is obtained from the KingAir measurements. Information on cloud microphysics (size distribution and crystal habit) is also available from the KingAir. Using this data in conjunction with atmospheric temperature and humidity profiles from local radiosondes, the necessary inputs for an infrared radiative transfer model can be developed.

Infrared radiative transfer calculations are carried out with a multi-spectral two-stream model. The model fluxes at cloud base and at 19 km are then compared with the aircraft observations to determine whether the model is performing well. Cloud layer heating rates can then be computed from the radiation exchange.

Lidar and Radiometer Results from the ER-2 for the FIRE Field Experiments

James Spinhirne
NASA Goddard Space Flight Center/617
Greenbelt, MD 20771

I. Introduction

The airborne lidar and radiometers which were flown during the FIRE cirrus and marine stratus field experiments had multiple objectives. Cloud parameters of direct interest, such as cirrus infrared emittance or convective scales for marine stratus, may be derived from the observations and analyzed along with the available cloud physics and meteorological observations. Additionally however a stated goal of the FIRE studies was to validate satellite cloud retrievals. To this end a number of derived products are to be available from the basic lidar and radiometer observations. The characteristics of the derived products will be described, and in addition analysis results for cloud radiometric and structure parameters will be presented. This extended abstract will be used to describe the available data products, and the associated presentation will emphasize case study analysis results.

II. Lidar Observations

A basic parameter from the ER-2 lidar observations is cloud top height and structure, and calculated cloud height and the attenuated backscatter profiles are to be made available as derived products. Calculated cloud height with aircraft navigation is to be available for all days through NCDS. Backscatter files will be made available on request. However,

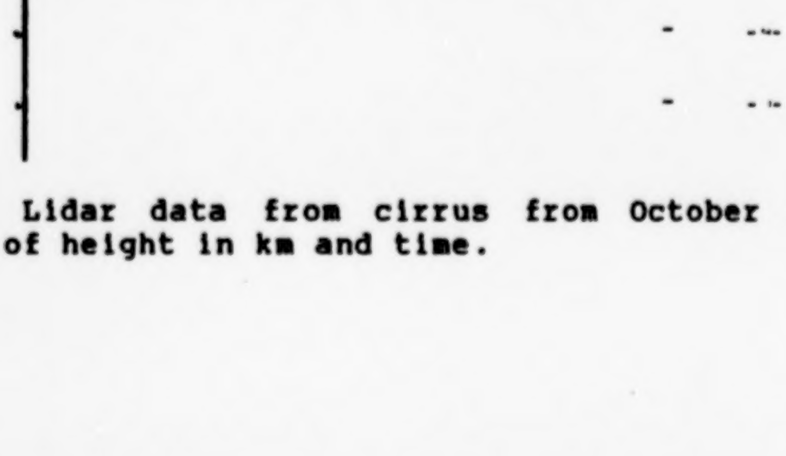

Fig. 1 Lidar data from cirrus from October 22,1988 as a function of height in km and time.

application of the data products requires understanding of the data characteristics and the calculation procedure. In the case of cloud height , for cirrus the height derivation from lidar data is not necessarily unambiguous. Lidar return data is illustrated in Fig. 1 for a partial flight line from October 22, 1988. The gray scale intensity in Fig. 1 represents the log of the return signal. In principle the cloud height may be determined from the discontinuity of the scattered signal. On a shot by shot basis for thin clouds, however, the calculation is not direct. A single laser return at full bandwidth is shown in Fig. 2. The signal is from the beginning

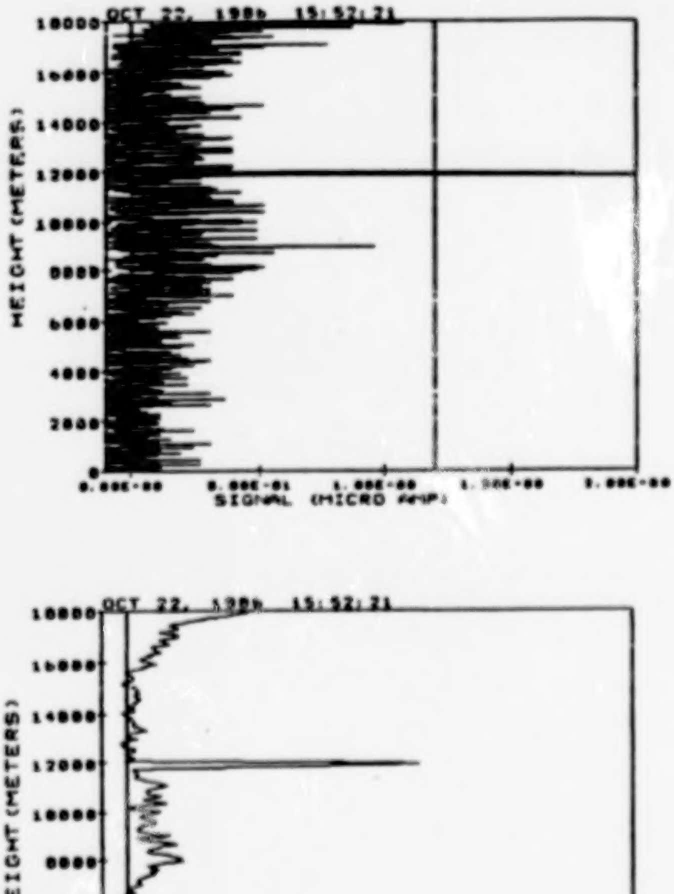

Fig. 2-3 Single laser return signal at full bandwidth and with filtering.

of the flight line in Fig. 1, and contains a dense shallow cloud and diffuse extended cloud. The fluctuations of the signal are due to background signal noise which is proportional to the square root of the bandwidth. A high bandwidth for the received signal is required in order to correctly measure scattering from dense clouds. However thin clouds will be obscured by the noise associated with high bandwidth and filtering is required. In Fig. 3 the signal has been filtered to a 375 m. vertical resolution. The thin lower cloud layer becomes apparent, but the peak signal of the upper dense layer has been distorted.

For the cloud top detection, a simple threshold detection would miss thin layers or produce spurious results. The detection algorithm applies a sequence of smoothing filters each with an associated threshold starting at the greatest smoothing. Both detection of thin clouds and a more accurate top height for dense clouds is obtained. Since both corrections for the aircraft pressure altitude and pitch and roll are applied, absolute height accuracy is less than 15 m for dense clouds such as marine stratus. The minimum scattering discontinuity at which a thin cloud may be detected is approximately at a backscatter cross section five times above molecular scattering. However the height detection does not acquire all cloud tops. The height determination for the

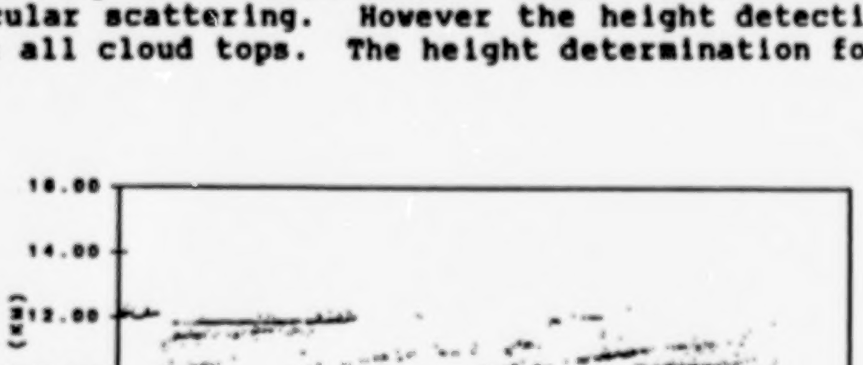

Fig. 4 Derived cirrus cloud top height.

data of Fig. 1 is given in Fig. 4. For the thin extended cloud layer, the height is found as a distribution of values through the layer.

The lidar attenuated backscatter result for a single laser return is in similar form to the signal as shown in the second figure. The total signal is a sum of the scattered signal plus an offset from the ambient background. The signal in Fig. 2 has had the offset subtracted. In order to obtain the attenuated backscatter values with units of (1/km-sr) the scattered signal is scaled by an appropriate constant. The constant is derived from the high altitude molecular scattering. In order to apply the lidar attenuated backscatter for any given application, filtering appropriate to the application must be applied.

III. Radiometer Observations

There were two separate cross track scanning, multi-wavelength radiometers on the ER-2 for the FIRE observation flights. A description of the wavelengths and operating parameters for the Multi-spectral Cloud Radiometer and the Daedalus Cloud Radiometer have been given in the FIRE working documents. The raw data is in the form of intensity proportional digital counts as a function of time and scan angle. The basic derived parameter is the radiometric intensity and the related cloud reflectance which requires a calibration constant for each radiometric channel. For the thermal channels the calibration is directly obtained from on board black bodies. In the case of visible and near infrared channels, the calibration is derived from standard integrating spheres. Initial results from calibration with a single integrating sphere indicated errors as large as 30%. However three separate integrating spheres were involved in the calibrations and an inter analysis could be applied to obtain more correct results. Data from the MCR is processed and available as radiance values with integrated aircraft navigation. Currently DCR observations can be requested as files containing any subset of wavelength channels but must be merged separately with calibration and navigation data.

VI. Analysis

Analysis of results for the cirrus case study of October 28 have been emphasized. The cloud emittance, transmittance, reflectivity and cross sections are derived from combined analysis of the lidar and radiometer data. Parameters are related to height structure and temperature. Some surprising structure for cirrus as been observed, for example the shallow but very dense layers embedded in generally diffuse layers as seen in Fig. 1. Marine stratocumulus cloud top height and liquid water distribution has been analyzed (see abstract by Boers and Spinhirne).

IDENTIFICATION OF CIRRUS OVER WAUSAU DURING THE 1986 FIRE IFO FROM GROUND-BASED RADIOMETER DATA

David A. Robinson

Department of Geography
Rutgers, The State University
New Brunswick, NJ 08903

Allan Frei

Lamont-Doherty Geological Observatory of Columbia University
Palisades, New York 10964

The potential of using irradiation data to indicate episodes of cirrus cloudiness during the day light hours is explored here. Thresholds separating cirrus from other clouds and clear skies are determined using four days of irradiation data, hourly weather observations, sky photographs, sky video and occasional lidar observations. Data were gathered during the First International Satellite Cloud Climatology Program (ISCCP) Regional Experiment (FIRE) Intensive Field Observations (IFO) cirrus project. Thresholds are tested using data from the remaining 17 days of the IFO. Cirrus episodes are defined as intervals when the sky cover is primarily cirrus.

Measurements of incoming shortwave (0.28-2.80µm) and near infrared (0.7-2.80µm) full hemispheric and diffuse irradiation, and atmospheric infrared irradiation (4.0-50.0µm), were made at the Wausau, Wisconsin Municipal Airport. Data were collected between October 13 and November 2, 1986 and are one minute averages of ten second samples. Less than 5% of the data are missing. The Eppley Precision Spectral Pyranometers and the Eppley Pyrgeometer were calibrated with Colorado State University instruments at Madison, WI immediately prior to their installation at Wausau. Pyrgeometer output contains an adjustment for body temperature but not for dome temperature. In addition to the raw irradiances collected, variables derived from these data are analyzed. Ones which proved to be most useful are: shortwave transmissivity, optical depth in the shortwave, fraction of full shortwave which is diffuse, the ratio of near infrared diffuse radiation to visible diffuse radiation, the ratio of full near infrared to full visible, and infrared irradiation.

Data from October 23rd and from October 27-29 were used for threshold determination. On the 23rd skies were heavily overcast. Thin cirrus associated with an approaching warm front covered the sky on the 27th. This episode of cirrus continued through the 28th, however throughout most of this day the cirrus were obscured at the observation site by stratus clouds with bases of approximately 3.5km. Skies were primarily clear on the 29th. Figure 1 shows time series of irradiation data and irradiation-derived variables within two hours of solar noon on these dates. At this preliminary stage of the investigation only midday hours are considered in order to minimize the influence of changes in solar zenith angle on the parameter.

Using weather observations, lidar output, photographs and video, sky conditions were grouped into three categories: non-cirrus cloudy; cirrus and clear. Irradiation data from all periods falling under each of the sky categories were then examined and thresholds denoting a change from one sky category to another were determined. Variables with only a small amount of overlap between sky categories were selected as key indicators. They are listed in Table 1 along with the delimiting thresholds. Variables such as shortwave irradiation, shortwave transmissivity and the ratio of near infrared diffuse to visible diffuse proved inconclusive in terms of distinguishing between cirrus and non-cirrus clouds and/or cirrus and clear conditions. For instance, a shortwave transmissivity threshold of 0.67 separates non cirrus

Figure 1. Mid-day irradiances and associated atmospheric variables at Wausau, WI on October 23 (cloudy), 27 (cirrus), 28 (variable) and 29 (clear), 1986. Time in GMT (local+6). Data are missing after 17:45 on the 27th and before 16:30 on the 28th.

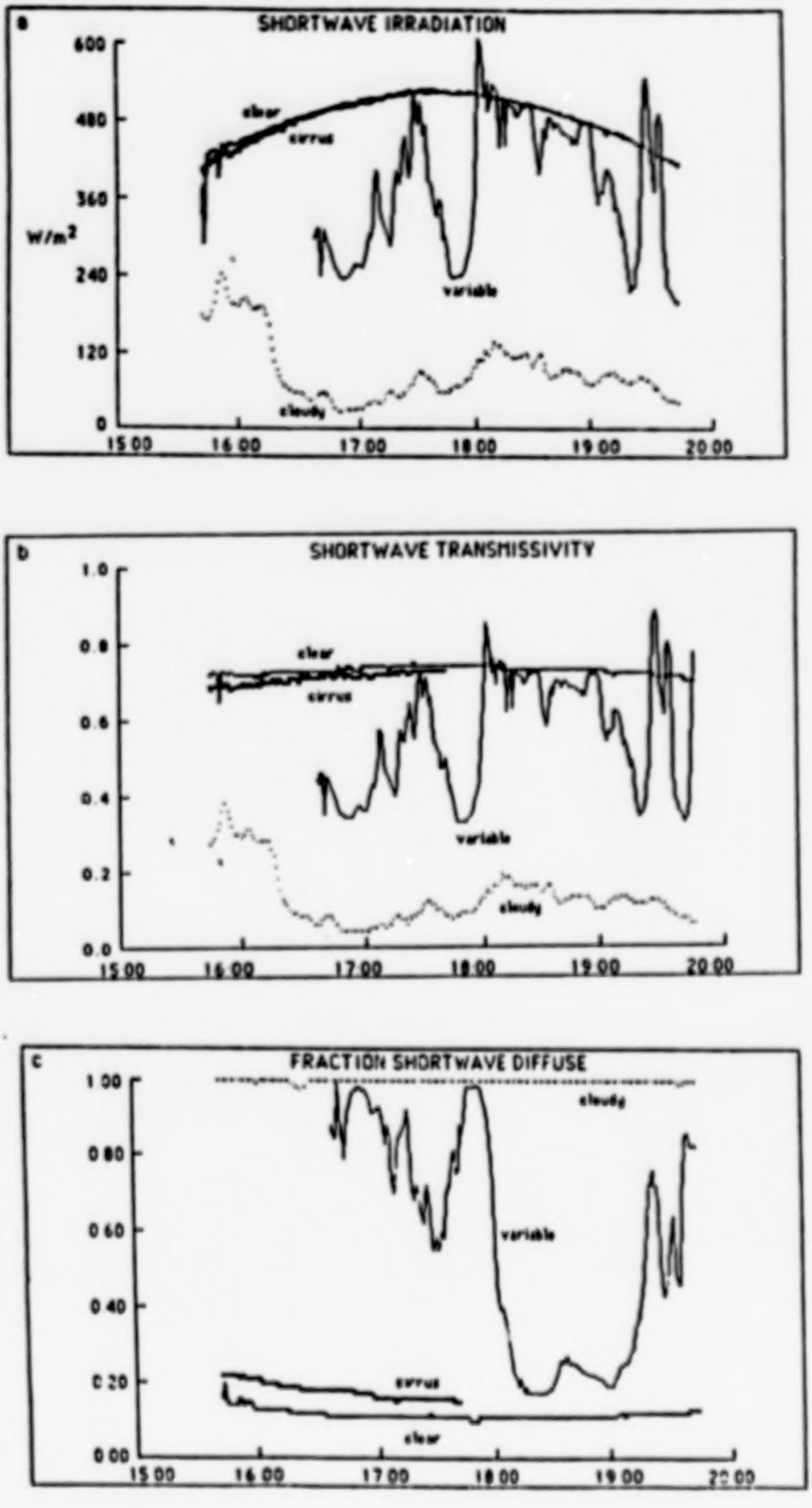

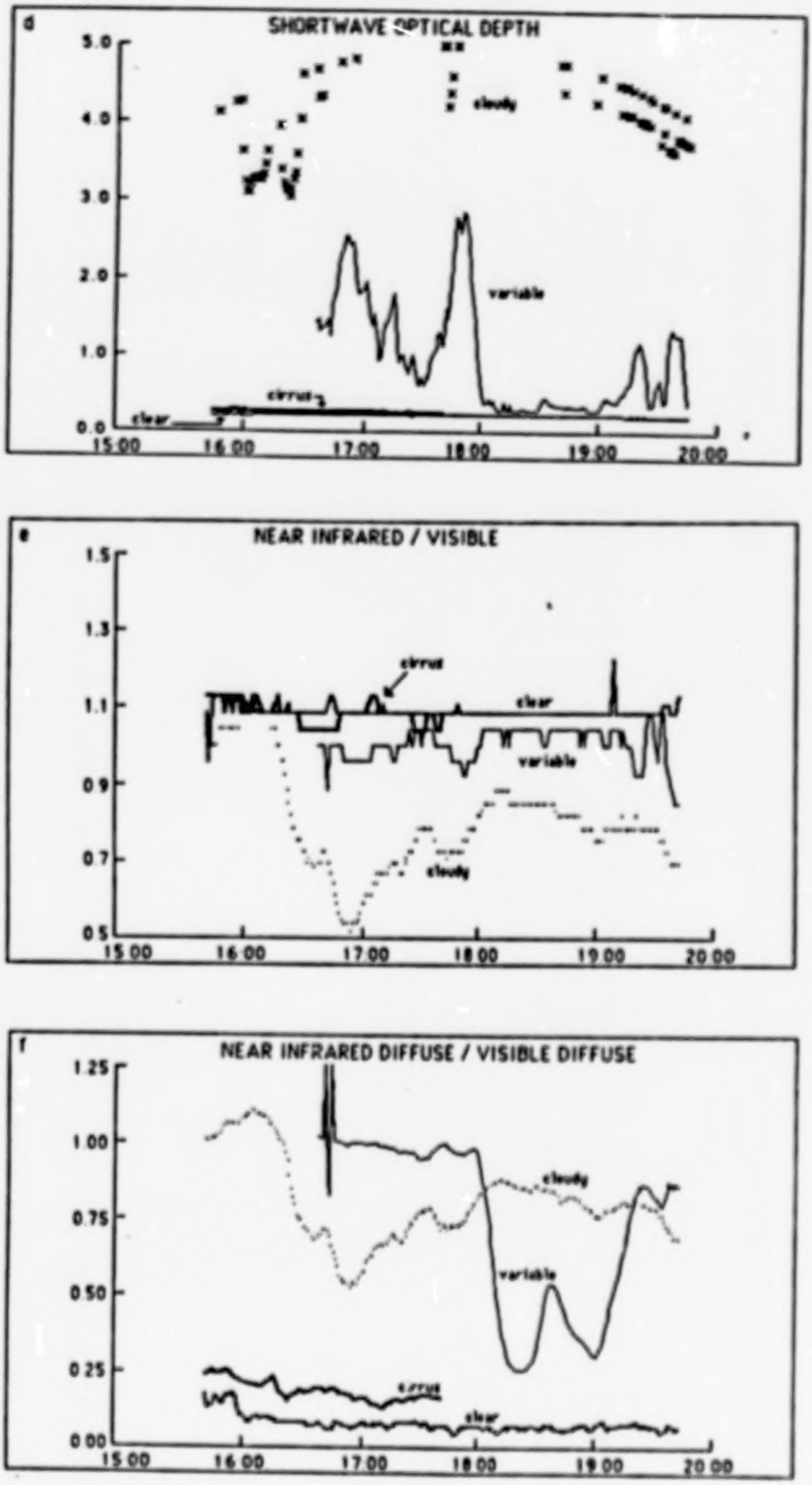
d
SHORTWAVE OPTICAL DEPTH
5.0
4.0
3.0
2.0
1.0
0.0
cloudy
variable
cirrus
clear
15:00
16:00
17:00
18:00
19:00
20:00
e
NEAR INFRARED / VISIBLE
1.5
1.3
1.1
0.9
0.7
0.5
cirrus
clear
variable
cloudy
15:00
16:00
17:00
18:00
19:00
20:00
f
NEAR INFRARED DIFFUSE / VISIBLE DIFFUSE
1.25
1.00
0.75
0.50
0.25
0.00
cloudy
variable
cirrus
clear
15:00
16:00
17:00
18:00
19:00
20:00

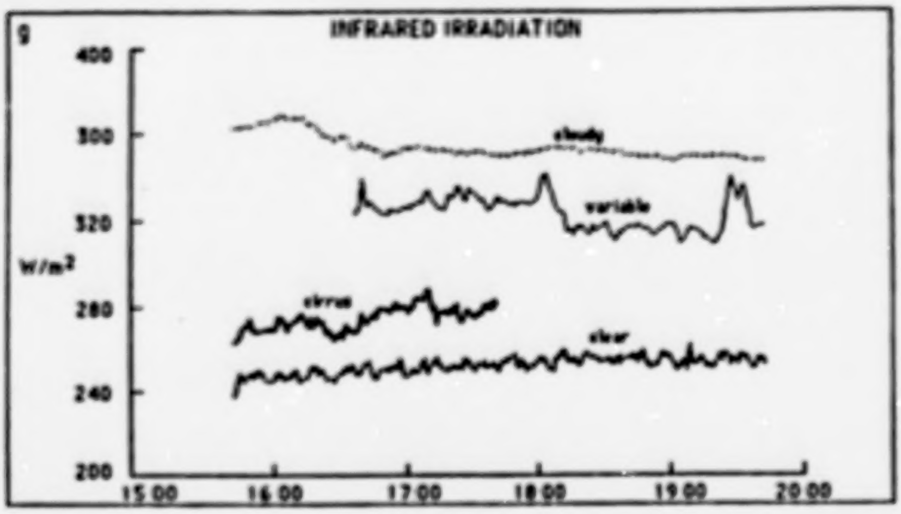

Table 1. Thresholds delimiting non cirrus cloud, cirrus and clear sky conditions.

INDICATOR	CIRRUS / NON-CIRRUS*	CIRRUS/CLEAR*
shortwave transmissivity	≥ 0.67	inconclusive
fraction shortwave diffuse	≤ 0.30	≥ 0.15
shortwave optical depth	≤ 0.30	≥ 0.24
near infrared/visible	≥ 1.00	≤ 1.10
nir diffuse / vis diffuse	inconclusive	≥ 0.12
infrared irradiation	≤ 320 watts/m^2	≥ 260 watts/m^2

*sign refers to what constitutes cirrus

clouds from cirrus quite well, however it is difficult to distinguish cirrus from clear skies using transmissivity. This appears to be due to: difficulties in differentiating between cirrus and clear in the visual observations, photos and video; lack of a specific broad-band shortwave signature which distinguishes cirrus from lower level haze; and to the zenith angle dependance of transmissivity.

Spot checks with other data such as weather service observations, photos, video and lidar indicate that the thresholds listed in Table 1 work quite well on all IFO days. At all times when conclusive evidence from more than one of these sources is available, there is agreement with the threshold-derived results. During the IFO, there were only three or four days with clear episodes, and nine or ten days with at least one short cirrus episode. There were many more hours of overcast conditions than either clear or cirrus. Comparisons of the threshold-derived results with the other types of evidence show that shortwave optical depth, the fraction of shortwave which is diffuse, and shortwave transmissivity seem to be the best indicators for the cloudy/cirrus threshold. The best indicators for the cirrus/clear threshold seem to be the ratio of near-infrared diffuse to visible diffuse radiation, shortwave optical depth, the fraction of shortwave which is diffuse, and infrared irradiation.

The distribution of sky categories as determined by the indicator thresholds is shown for two study days (figure 2). The top graph in each figure shows intervals where clear skies or cirrus were present, the bottom where clear skies occurred. On October 20 there was a non-cirrus cloud episode between approximately 18:00 and 20:00 GMT. Cirrus were prevalent between 15:00 and 18:00 and from 20:00 to 21:00, as suggested by the lack of strong clear indicators throughout these times. The cirrus may occasionally have been thick or obscured by lower-level clouds, as there are breaks in the indicators during the primarily cirrus intervals.

On the 17th skies were cloudy in the morning then cleared up in the afternoon. Most of the indicators in the top portion of the figure (including all of the best ones) show a cloudy morning, with either a cirrus or clear afternoon. The bottom portion of the figure indicates that the afternoon was primarily clear.

Figure 2. Temporal distribution of cirrus or clear skies (top) and clear skies (bottom) at Wausau on October 20 and October 17, 1986 as inferred from key indicators. Intervals when thresholds were exceeded are marked with X's or lines.

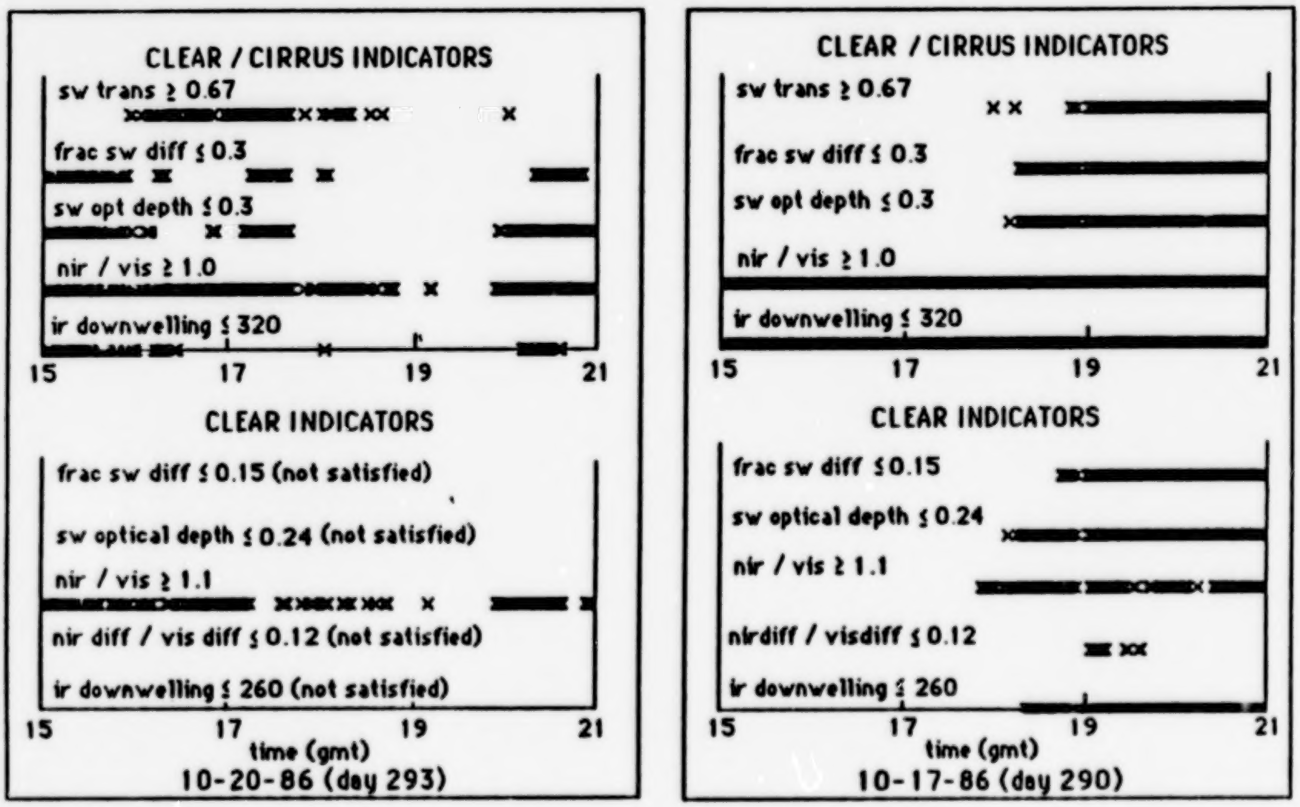

Work is continuing on this evaluative approach. This includes the development of multi-indicator thresholds and extending them to early and late day periods. In the future, data gathered at our Extended Time/Limited Area observation site in Palisades, NY will be used to test the algorithms and make necessary adjustments based on potential site and seasonal differences.

Acknowledgment: This work is supported by NASA grant NAG-1-653.

INTERPRETATION OF SATELLITE-MEASURED BIDIRECTIONAL REFLECTANCE FROM CIRRUS CLOUDY ATMOSPHERES

Y. Takano, K.N. Liou, and P. Minnis
University of Utah
Salt Lake City, Utah 84112

Abstract

The present paper is concerned with the interpretation of the observed bidirectional reflectance from cirrus cloudy atmospheres. We have developed a theoretical model for the computation of the transfer of solar radiation in an anisotropic medium with particular applications to oriented ice crystals in cirrus clouds. In this model, the adding principle for radiative transfer has been used with modifications to account for the anisotropy of scattering particles and the associated scattering phase matrix. We have used the single-scattering properties, including the phase function, single-scattering albedo, and extinction cross-section, for randomly and horizontally oriented hexagonal ice crystals in radiative transfer computations.

Figure 1 shows the reflected and transmitted (diffuse) intensities for randomly oriented ice columns with a length/diameter ratio of 125/50 μm and area-equivalent ice spheres as a function of the zenith angle θ for an overhead sun. Significant differences between the reflected intensities for ice columns and spheres are evident. Ice spheres produce a peak intensity at $\theta = 45^o$, associated with a combination of primary and secondary rainbow features due to single-scattering. However, ice columns have larger reflected intensities in other zenith angle regions. In the transmitted intensity pattern, the 22^o and 46^o halo features produced by ice columns are very distinct for small optical depths, but they disappear when the optical depth is greater than about 16.

We have modified the radiative transfer model devleoped for cirrus clouds to account for the scattering contributions from the atmosphere and the surface. In order to test the relevance and significance of the ice crystal model for the interpretation of observed bidirectional reflectance from satellites, we have selected visible (0.55 - 0.75 μm) radiances collected on the half hour by the GOES series. The data will be calibrated and corrected with the proper filter functions, then navigated to match selected landmark data. A

number of clear and cloudy cases during the cirrus IFO of the FIRE experiment have been chosen for theoretical analyses. The cloud particle shape and size distributions that were taken during satellite overpasses are used in radiative transfer calculations. The sensitivities of the shape, orientation, and size distribution of ice crystals on the reflected intensities at the top of the atmosphere are investigated. Finally, the relative importance of these cloud microphysical properties in the interpretation of satellite bidirectional reflectance are assessed and presented.

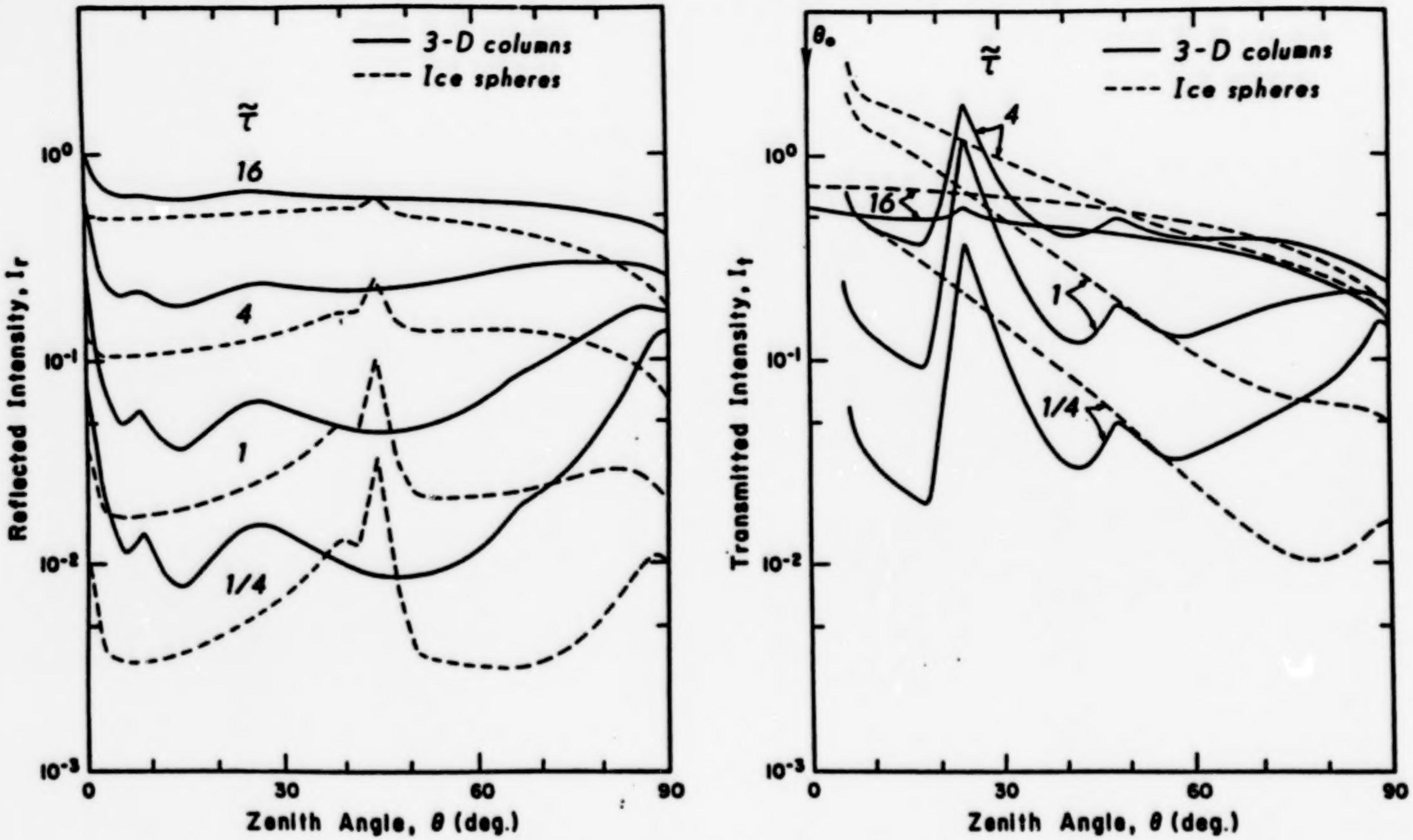

Fig. 1. Intensity reflected and transmitted by randomly oriented hexagonal ice crystals (L/2a = 125 µm/50 µm) and area-equivalent spheres with an overhead sun ($\theta_0 = 0^\circ$) at $\lambda = 0.65$ µm.

FIRE SCIENCE TEAM MEETING
VAIL, COLORADO
JULY 11-15, 1988

CIRRUS

SATELLITE STUDIES - Bruce A. Wielicki Tuesday, July 12, 1988

PAGE

Comparison of NOAA-9 ERBE Measurements with Cirrus IFO Satellite and Aircraft Measurements 117
Ackerman, Steven A.; Hyosang Chung, Stephen K. Cox, Leroy Herman, William L. Smith, and Donald P. Wylie

ERBE and AVHRR Cirrus Cloud FIRE Study 123
Harrison, E. F.; P. Minnis, B. A. Wielicki, P. W. Heck, S. K. Gupta, D. F. Young, and G. G. Gibson

Cloud Parameters from GOES Visible and Infrared Radiances During the FIRE Cirrus IFO, October 1986 129
Heck, Patrick W.; David F. Young, Patrick Minnis, and Edwin F. Harrison

Cloud Altitude Determinations from Infrared Spectral Radiances 135
Smith, William L.; and Richard Frey

AVHRR and VISSR Satellite Instrument Calibration Results for both Cirrus and Marine Stratocumulus IFO Periods 141
Whitlock, C. H.; W. F. Staylor, J. T. Suttles, G. Smith, R. Levin, R. Frouin, C. Gautier, P. M. Teillet, P. N. Slater, Y. J. Kaufman, B. N. Holben, W. B. Rossow, C. Brest, and S. R. LeCroy

Cirrus Cloud Properties Derived from Coincident GOES and Lidar Data During the 1986 FIRE Cirrus Intensive Field Observations 147
Minnis, Patrick; Jose M. Alvarez, David F. Young, Patrick W. Heck, and Kenneth Sassen

COMPARISON OF NOAA-9 ERBE MEASUREMENTS WITH CIRRUS IFO SATELLITE AND AIRCRAFT MEASUREMENTS

Steven A. Ackerman[1], Hyosang Chung[1], Stephen K. Cox[3]

Leroy Herman[1], William L. Smith[1], Donald P. Wylie[2]

Cooperative Institute for Meteorological Satellite Studies[1]

Space Science and Engineering Center[2]

University of Wisconsin-Madison, Madison, WI 53706.

and

Department of Atmospheric Science[3]

Colorado State University

Fort Collins, CO 80523

ABSTRACT

Earth Radiation Budget Experiment measurements onboard the NOAA-9 are compared for consistency with satellite and aircraft measurements made during the Cirrus IFO of October 1986. ERBE scene identification is compared with NOAA-9 TIROS Operational Vertical Sounder (TOVS) cloud retrievals; results from the ERBE spectral inversion algorithms are compared with HIS measurements; and ERBE radiant exitance measurements are compared with aircraft radiative flux measurements.

INTRODUCTION

The Cirrus IFO included measurements made onboard satellites, research aircraft, weather balloons as well as on the ground. An integration of these measurements will be required to fully accomplish the research objectives of the program (Cox *et al.*, 1987). In this paper consistency checks are made between measurements of the Earth Radiation Budget Experiment (ERBE) and measurements made on other Cirrus IFO platforms.

ERBE SCENE ID AND NOAA-9 CLOUD RETRIEVALS

The ERBE includes shortwave (SW) and longwave (LW) radiance measurements by a scanning radiometer. To convert these measurements to radiant exitance at the top of the atmosphere requires knowledge of the scene type (e.g. cloud, ocean, desert, partly cloudy). The ERBE data management system includes 12 scene types. In the first part of this study, scene types from the NOAA-9 ERBE measurements are compared with cloud amount and cloud top pressure retrievals using the NOAA-9 TOVS (Whitlock *et. al*, 1988). The spatial resolution of the ERBE is approximately 44 × 65 km and nadir. Comparisons are made for four ERBE scene identifications (ID); clear (cloud cover $< 5\%$), partly cloud ($5\% \leq$ cloud cover $< 50\%$), mostly cloudy ($50\% \leq$ cloud cover $\leq 95\%$), and overcast ($95\% <$ cloud cover). The NOAA-9 TOVS derived cloud top pressure are categorized into 100 mb intervals (100-200 mb, 200-300 mb ...) and the effective cloud cover is categorized into 10% intervals (0-10%, 10-20%...). Having earth located the TOVS cloud retrieval, the nearest ERBE measurement is found and the scene ID noted. The ERBE and TOVS geographic locations are generally within 0.3° of each other. The TOVS cloud retrieval is then compiled in a cloud top pressure versus effective cloud area histogram. Preliminary analysis of 15 time periods in October 1986 are depicted in figure 1, where the number of counts in the histogram has been normalized with respect to the category with the maximum count. The total count for the clear, partly cloudy, mostly cloudy and overcast scene ID's are 51, 556, 524 and 160 respectively. The ERBE determined clear scenes are most often in agreement with the clear scenes identified with the TOVS. Good agreement is also exhibited in the overcast category, with thin high clouds determined by the ERBE to be overcast. Although the middle level cloud cover seen in the mostly cloudy scene ID, doesn't correspond to an ERBE overcast condition. The partly

CLEAR

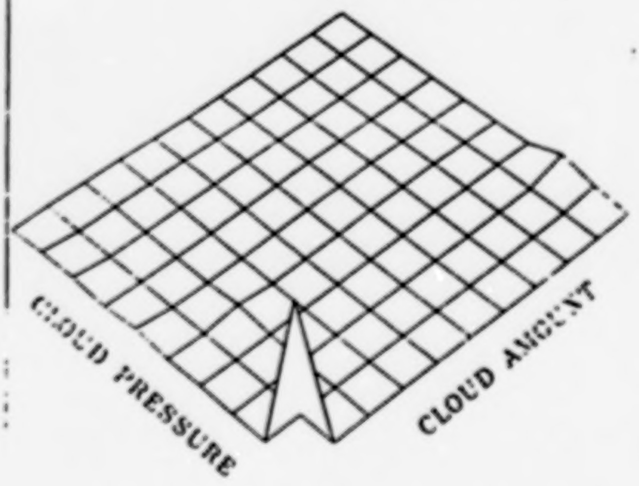

PARTLY CLOUDY

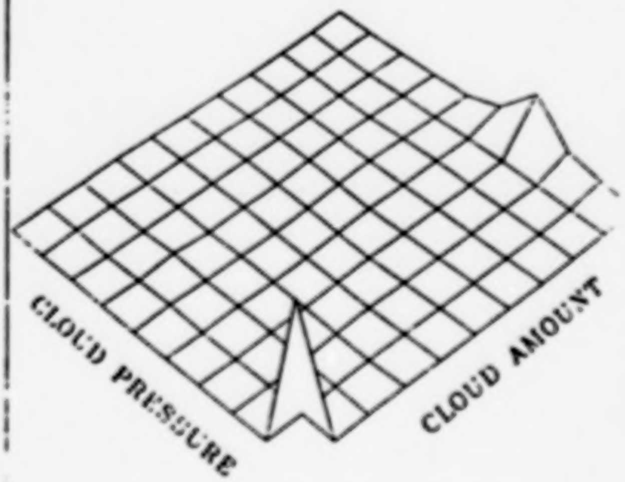

MOSTLY CLOUDY

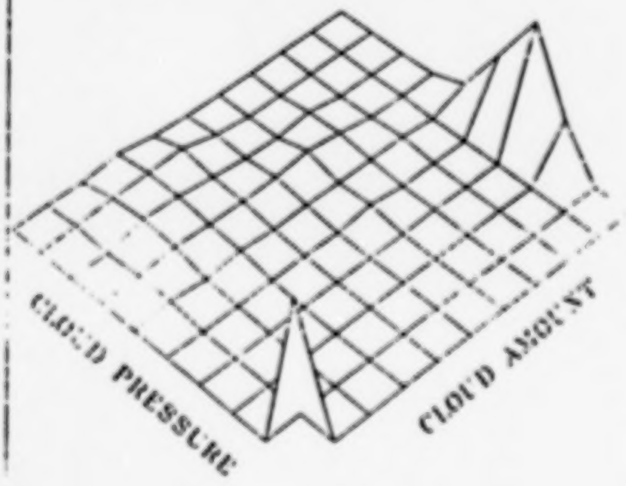

OVERCAST

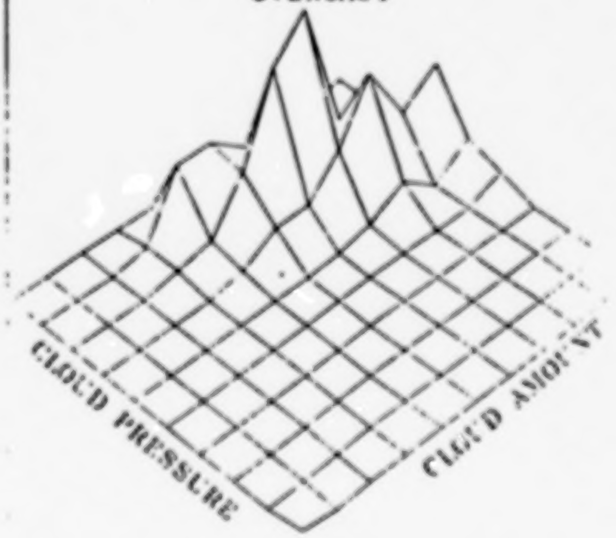

and mostly cloudy ERBE cases do not exhibit the distribution one might expect. A more detailed analysis will be presented at the conference.

ERBE SPECTRAL CORRECTIONS AND HIS MEASUREMENTS

The spectral response of the ERBE SW, LW and total channels are inverted to broadband radiances in a manner described by Avis et al., 1984. In this section results from the LW inversion algorithms are compared with measurements of the High resolution Interferometer Sounder (HIS) (Smith *et al.*, 1988). To compare the data, a ratio of the NOAA-9 ERBE scanner filtered radiance measurements (M_{fil}) to the unfiltered measurements (M_{unfil}) is taken and plotted against the unfiltered measurements. The HIS measurements are then used to simulate an ERBE filtered (H_{fil}) and unfiltered (H_{unfil}) measurements, where

$$H_{fil} = \int_{2000}^{600} I_\nu \phi_\nu d\nu + \int_{600}^{50} B_\nu(T)\phi_\nu d\nu$$

$$H_{unfil} = \int_{2000}^{600} I_\nu d\nu + \int_{600}^{50} B_\nu(T) d\nu$$

where I_ν is the HIS measured radiance and ϕ_ν is the ERBE spectral response function. The ratio H_{fil} to H_{unfil} is then plotted as a function of H_{unfil}. The HIS measures do not include contributions beyond approximately 600 cm^{-1} (16.7 μm). To represent this spectral energy we have assumed the Planck function, $B_\nu(T)$, assuming the average equivalent black body temperature determined from measured over the spectral region 1300-1400 cm^{-1}.

Figure 2 depicts these ratios for the ERBE NOAA-9 (dots) and the HIS (×) measurements. The HIS measurements were made on November 2, 1986 over the FIRE region, while the ERBE region measurements were made over an eight day period for the region 25°-50° N and 75°- 95° E. Both the ERBE and HIS measurements display an increase in the ratio of the filtered to unfiltered radiance with increasing radiant exitance, consistent with the filter response function. The ERBE data display more scatter than the HIS data, particularly at the low radiances, otherwise the agreement is excellent.

ERBE AND SABERLINER BROADBAND FLUX MEASUREMENTS

This comparison study is in progress and will be reported on at the meeting.

REFERENCES

Avis, L. M., R. N. Green, J. T. Suttles and S. K. Gupta, 1984: A robust pseudo-inverse spectral filter applied to the Earth Radiation Budget Experiment scanning channels, NASA TM-[illegible]781, 33 p.

Cox, S. K., D. McDougal, D. Randall, and R. Shiffer, 1987: FIRE- The First ISCCP Regional Experiment. *Bull. Amer. Meteor. Soc.*, 67, 114-118.

Smith, W. L., H. M. Woolf, H. B. Howell, H. L. Huang, and H. E. Revercomb, 1988: High resolution interferometer sounder- the retrieval of atmospheric temperature and water vapor profiles. Proceedings of the Third Conference on Satellite Meteorology and Oceanography, American Meteorological Society, Boston, Mass.

Whitlock, C. H., D. P. Wylie and S. R. LeCroy, 1988:High-spatial- resolution TOVS observations for the FIRE/SRB Wisconsin experiment region from OCtober 14 through November 2, 1986. NASA TM 100522

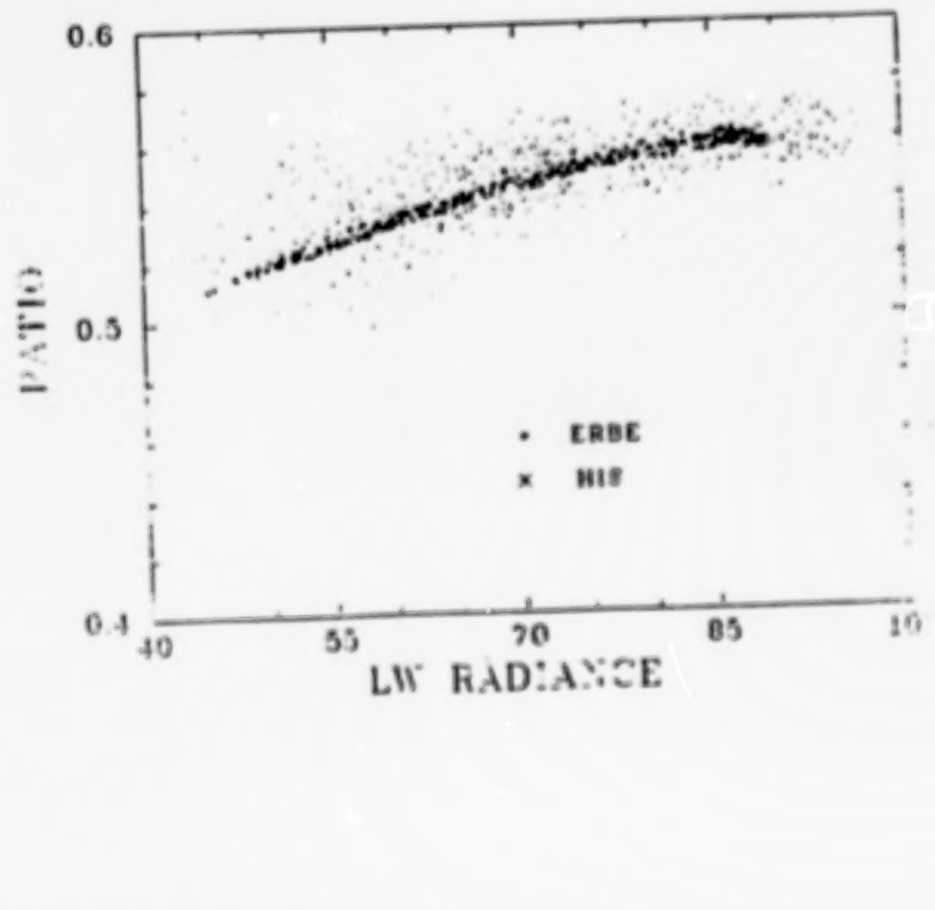

ERBE AND AVHRR CIRRUS CLOUD FIRE STUDY

E. F. Harrison, P. Minnis, and B. A. Wielicki
Atmospheric Sciences Division, NASA Langley Research Center
Hampton, Virginia 23665-5225

P. W. Heck, S. K. Gupta, D. F. Young, and G. G. Gibson
Aerospace Technologies Division, Planning Research Corporaton
Hampton, Virginia 23666

1. Introduction

Understanding the impact of cirrus clouds on the global radiation budget is essential to determining the role of clouds in the process of climate change. The ongoing Earth Radiation Budget Experiment (ERBE) is charged with measuring the global radiation balance at the top of the atmosphere. The International Satellite Cloud Climatology Project (ISCCP) is measuring global cloud amounts and properties over a time frame similar to ERBE. Specific cloud properties are absent from the ERBE program, while ISCCP lacks the broadband radiances necessary to determine the total radiation fields. Together, results from these two global programs have the potential for improving the knowledge of the relationship between cirrus clouds and the Earth radiation balance. The First ISCCP Regional Experiment (FIRE), especially its cirrus Intensive Field Observations (IFO), provides opportunities for studying radiation measurements from the ERBE taken over areas with known cirrus cloud properties (Starr, 1987 and Cox et al., 1987). In this paper, satellite measurements taken during the IFO are used to determine the broadband radiation fields over cirrus clouds and to examine the relationship between narrowband and broadband radiances over various known scenes. The latter constitutes the link between the ERBE and the ISCCP.

2. Analysis

The analysis presented here concentrates on the ERBE and AVHRR (Advanced Very High Resolution Radiometer) data from the NOAA-9 satellite. Both of these instruments are cross-track scanners which allows simultaneous and coincident comparisons. The 4-km AVHRR pixel data can be spatially averaged to match the 40-km ERBE resolution. The other significant difference in these two instruments is their spectral bands. ERBE has broadband channels of 0.2 to 5.0 μm for shortwave, 5.0 to 50 μm for longwave, and 0.2 to 50 μm for total radiation. The three channels allow for spectral consistency checks to be made between channels. The AVHRR has five narrowband channels, three of which were used in this study: the 0.58 to 0.68 μm window for visible radiation and a combination of the 10.3 to 11.3 μm window and the 11.5 to 12.5 μm window for infrared radiation. In this study, the IFO region is defined as a 5° box between 42°N and 47°N and 87°W and 92°W. It is analyzed using a 0.5° grid.

The ERBE broadband radiances are inverted to fluxes at the top of the atmosphere by applying angular directional models for scenes identified using a maximum likelihood estimator technique (Wielicki and Green, 1988). Geographical scenes are classified as ocean, land, desert, coast, or snow with cloud cover categories of clear (0-5%), partly cloudy (5-50%), mostly cloudy (50-95%), or overcast (95-100%). The hybrid bispectral threshold method (HBTM) developed by Minnis et al. (1987) was used to determine cloud amount at low (0-2 km), middle (2-6 km), and high (>6 km) altitudes from the AVHRR visible and infrared measurements.

In order to perform the HBTM analyses, the AVHRR narrowband radiances were converted to broadband fluxes following the approach of Minnis and Harrison (1984). Figure 1 presents the correlations between the ERBE and AVHRR data taken over Wisconsin during seven overpasses within the IFO period. The AVHRR data were averaged to match the larger ERBE footprints. A linear least-squares fit yielded a root-mean-square (RMS) difference of 4.5% in the longwave radiances predicted from the infrared (IR) radiances. An RMS difference of 14.5% was found for the shortwave data using a quadratic fit in visible counts. These results are consistent with Minnis and Harrison (1984) narrowband-broadband correlations of GOES and Nimbus-7 ERB data. The longwave correlations also agree with the narrowband-broadband correlations of Yang et al. (1987). Clear-sky visible reflectance, necessary for application of the HBTM, was predicted for the AVHRR using the clear-sky albedo map given by Heck et al. (1988).

3. Results

The following results were derived from NOAA-9 data taken during the November 2, 1986 overpass of the IFO region. This occurred at approximately 1405 LT. Solar zenith angles ranged from 65° to 70° with satellite viewing zenith angles between 1° and 31°. Figure 2 shows the contours of IR temperature and visible reflectance from the AVHRR. Total and high cloud amounts derived from these data are plotted in Fig. 3. A large area of overcast clouds extends from the northwestern corner to the Green Bay area. Since no emissivity corrections were applied to the results, only the thickest clouds are classified as high-level clouds. Tops of many of the other clouds probably extended above 6 km, but apparently were not dense enough to radiate as blackbodies above the 6-km level. The corresponding broadband shortwave albedos and longwave fluxes derived from the ERBE (Fig. 4) follow the same basic patterns as their narrowband counterparts. IR temperatures from AVHRR range from about 282K over clear areas to 236K over the thickest clouds. Longwave flux varies from about 155 Wm^{-2} to 260 Wm^{-2}. Shortwave albedos generally exceed the visible reflectances.

The inferred broadband shortwave albedos and longwave fluxes derived from the AVHRR data are given in Fig. 5. Although the AVHRR reveals much more structure in the radiation fields than seen in Fig. 4, the large-scale patterns are very similar. On average for this figure, the AVHRR albedos are 1% ± 4% less than the ERBE values. AVHRR longwave fluxes are 7 Wm^{-2} greater than the ERBE values. The standard deviation of the flux difference is 7 Wm^{-2}. These differences may be the result of several factors, such as uncertainties in the correlations, in the scene-type selection, and in the bidirectional models. It appears that the AVHRR albedos are greater over the areas of thick cirrus while they are lower over clear areas and relatively thin cirrus. AVHRR longwave fluxes are much higher than ERBE's over areas with the thickest cirrus. Since the correlations represent average conditions, such differences are to be expected in the resultant fluxes for a given day.

4. Concluding Remarks

The apparent geographical variations of the differences in the fluxes derived from the two different instruments provide encouragement that they are scene-type dependent. Thus it may be possible to improve the methods for inferring broadband radiance from narrowband data by accounting for the scene identification differences. This may be accomplished with additional case studies in combination with radiation measurements taken from other platforms during the IFO.

5. References

Cox, S. K., D. A. McDougal, D. A. Randell, and R. A. Schiffer, 1987: FIRE-The First ISCCP Regional Experiment. Bull. Amer. Meteor. Soc., 68, 114-118.

Heck, P. W., D. F. Young, P. Minnis, E. F. Harrison, 1988: Cloud Parameters from GOES Visible and Infrared Radiances During the FIRE Cirrus IFO, October 1986. FIRE Workshop, Vail, CO, July 11-15.

Minnis, P. and E. F. Harrison, 1984: Diurnal Variability of Regional Cloud and Clear-Sky Radiative Parameters Derived from GOES. J. Climate Appl. Meteor., 23, 993-1051.

Minnis, P., E. F. Harrison, and G. G. Gibson, 1987: Cloud Cover Over the Equatorial Eastern Pacific Derived from July 1983 ISCCP Data Using a Hybrid Bispectral Threshold Method. J. Geophys. Res., 92, 4051-4073.

Starr, D. O'C., 1987: A Cirrus-Cloud Experiment: Intensive Field Obervations Planned for FIRE. Bull. Amer. Meteor. Soc., 68, 119-124.

Wielicki, B. A. and R. N. Green, 1988: Cloud Indentification for ERBE Radiative Flux Retrieval. Submitted to J. Geophys. Res.

Yang, S.-K., A. Gruber, B. Liedmann, A. J. Miller, 1987: Intercomparison of Outgoing Longwave Radiation Obtained from ERBE and NOAA Operational Satellite: A Preliminary Result. Presented at the Third AMS Conference on Satellite Meteorology.

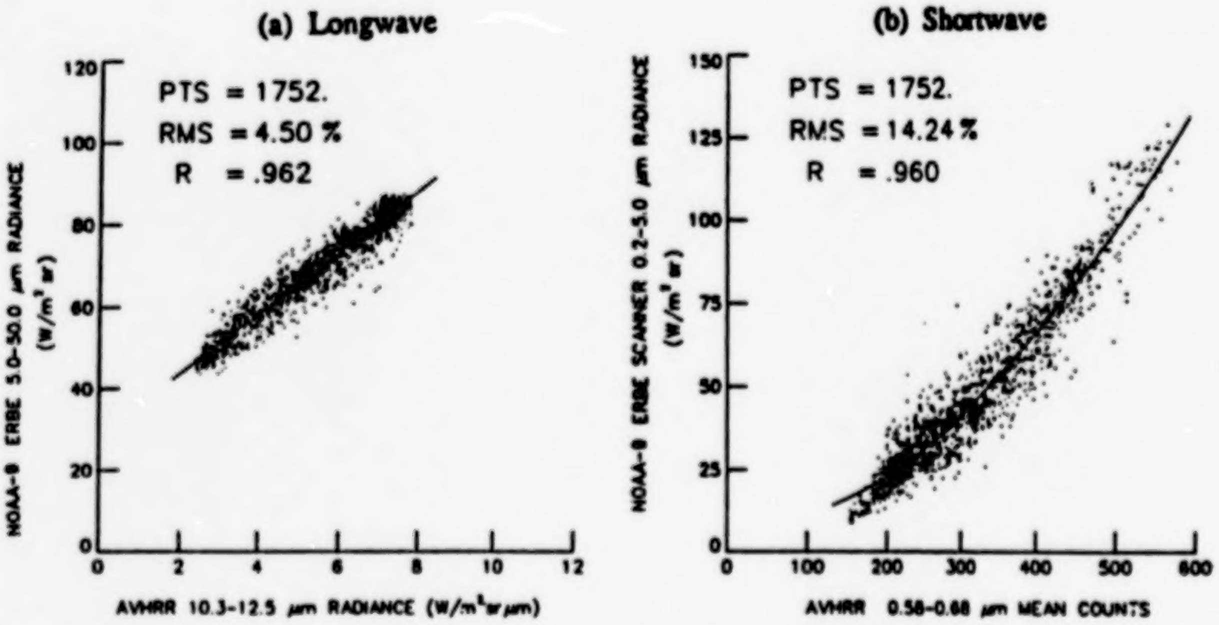

Figure 1. Correlation of ERBE broadband and AVHRR narrowband data for FIRE during October 22 - November 2, 1986.

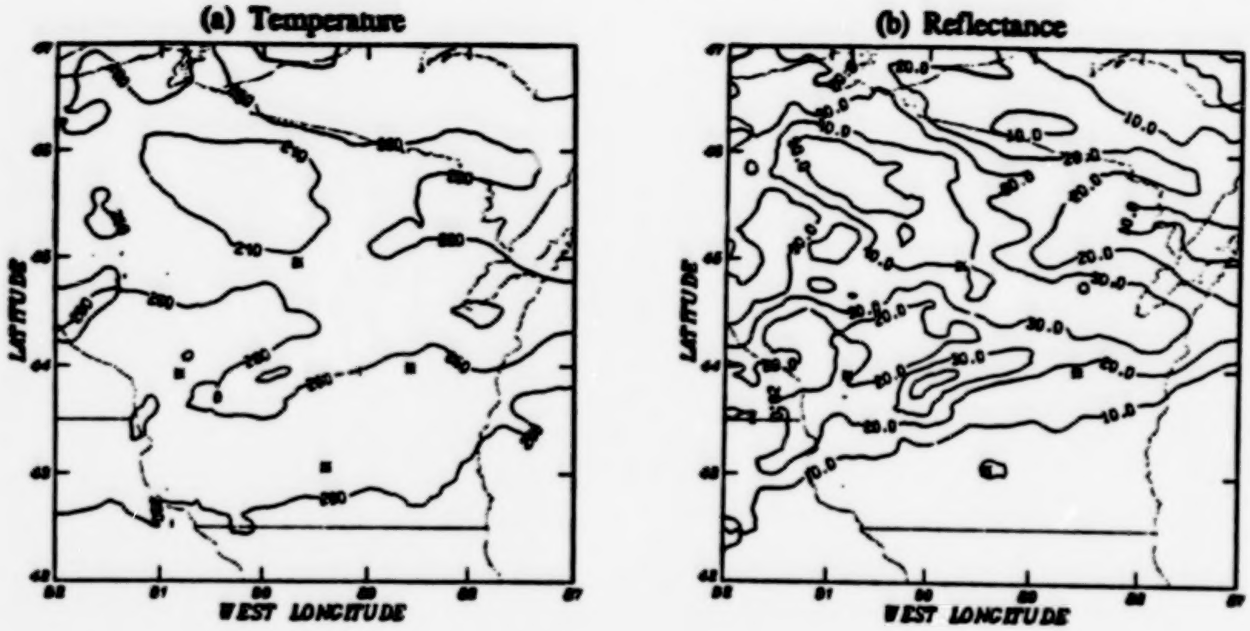

(a) Temperature

(b) Reflectance

LATITUDE
WEST LONGITUDE
210
250
260
20.0
10.0
30.0

Figure 2. AVHRR temperature (K) and reflectance (%) results for November 2, 1986.

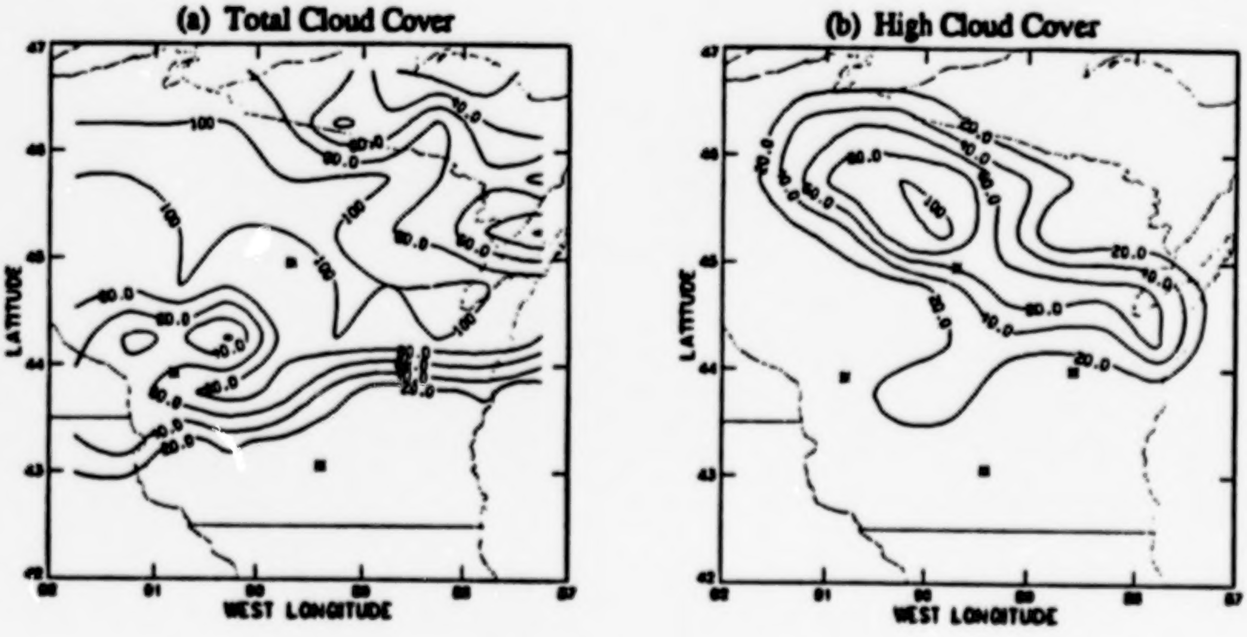

(a) Total Cloud Cover

(b) High Cloud Cover

LATITUDE
WEST LONGITUDE
100
80.0
60.0
40.0
20.0

Figure 3. Cloud cover (%) derived from AVHRR for November 2, 1986.

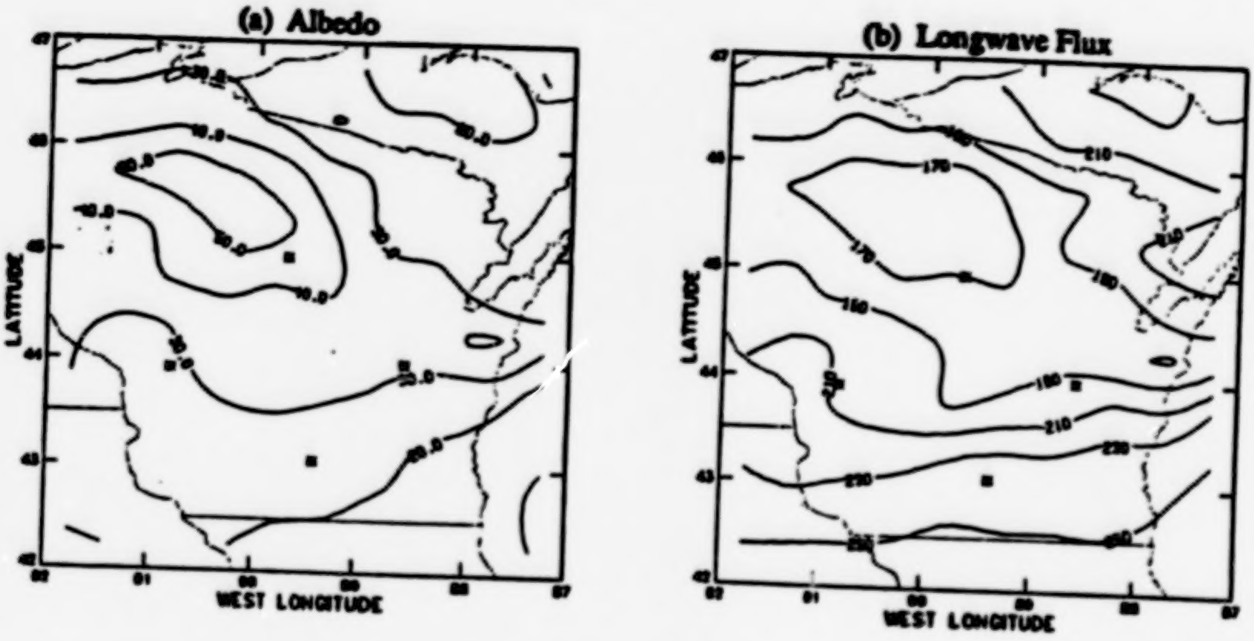

(a) Albedo

(b) Longwave Flux

LATITUDE
WEST LONGITUDE
LATITUDE
WEST LONGITUDE
170
190
210
230
250

Figure 4. ERBE albedo (%) and longwave flux ((Wm^{-2})) for November 2, 1986.

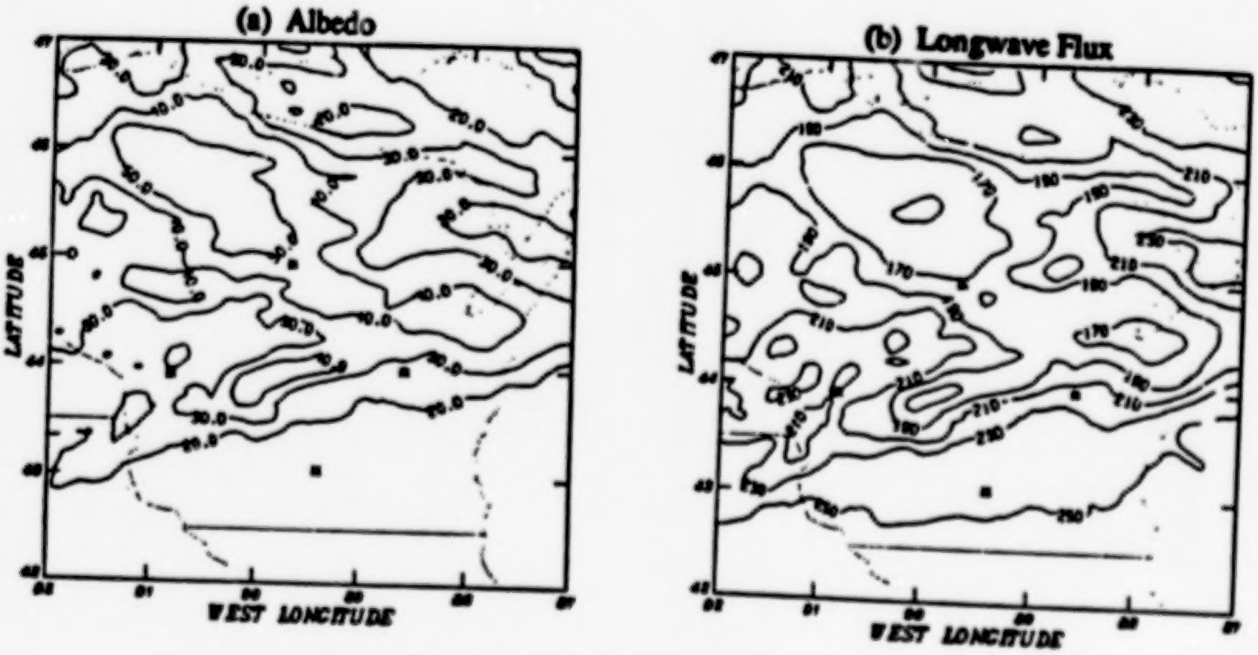

(a) Albedo

(b) Longwave Flux

LATITUDE
WEST LONGITUDE
LATITUDE
WEST LONGITUDE
170
190
210
230
250

Figure 5. AVHRR albedo (%) and longwave flux ((Wm^{-2})) for November 2, 1986.

CLOUD PARAMETERS FROM GOES VISIBLE AND INFRARED RADIANCES DURING THE FIRE CIRRUS IFO, OCTOBER 1986

Patrick W. Heck and David F. Young
Aerospace Technologies Division, Planning Research Corporation
Hampton, Virginia 23666
and
Patrick Minnis and Edwin F. Harrison
Atmospheric Sciences Division, NASA Langley Research Center
Hampton, Virginia 23665-5225

1. Introduction

Visible (VIS, 0.65 μm) and infrared (IR, 10.5 μm) channels on geostationary satellites are the key elements of the International Satellite Cloud Climatology Project (ISCCP). All daytime ISCCP cloud parameters are derived from a combination of VIS and IR data. Validation and improvement of the ISCCP and other cloud retrieval algorithms are important components of the First ISCCP Regional Experiment (FIRE) Intensive Field Observations (IFO). Data from the Cirrus IFO (October 19 - November 2, 1986) over Wisconsin are available for validating cirrus cloud retrievals from satellites. The Geostationary Operational Environmental Satellite (GOES) located over the Equator at approximately 100°W provided nearly continuous measurements of VIS and IR radiances over the IFO area. This paper presents the preliminary results of cloud parameters derived from the IFO GOES data. Cloud altitudes are first derived using an algorithm without corrections for cloud emissivity. These same parameters will then be computed from the same data relying on an emissivity correction algorithm based on correlative data taken during the Cirrus IFO.

2. Data and methodology

A cloud parameter retrieval scheme, the hybrid bispectral threshold method (HBTM) described by Minnis et al. (1987), was applied to the GOES 1-km VIS and 4-km IR radiances taken between 47°N and 42°N and between 87°W and 92°W. This 5° box was divided into a 0.5° grid for analysis. Clear-sky temperature and albedo as well as cloud amount, temperature (height), and cloud albedo were derived over each of the 100 regions at each daylight half hour during the experiment. These cloud properties were also derived for a low-level layer (< 2 km altitude), a middle layer (between 2 km and 6 km), and a high layer (> 6 km). For these preliminary results, a lapse rate of 6.5 °K/km was assumed in order to infer the cloud altitude from the derived cloud temperature.

Both narrowband VIS and broadband shortwave (SW) albedos were derived from the VIS data. The GOES VIS counts (D) were converted to narrowband radiance with the calibration of Whitlock (1987) and then converted to albedo by dividing by the incoming solar radiance at 0.65 μm, the cosine of the solar zenith angle (SZA), and a bidirectional reflectance anisotropic factor (Minnis and Harrison, 1984). Shortwave albedo was determined in a similar fashion except that the incoming radiance covered the entire solar spectrum and the VIS counts were converted to broadband (0.2 μm - 5.0 μm) radiance. Narrowband-broadband conversions were performed in a manner similar to that described by Harrison et al. (1988) except that GOES and NOAA-9 ERBE (Earth Radiation Budget Experiment) data were used. Since these satellites operate in different orbits, only selected data from matching fields of view over the entire GOES field-of-view were used to effect the correlation. The dissimilar scan patterns of the two satellites' instruments dictated more liberal matching constraints than those used by Minnis and Harrison (1984). Broadband longwave (5.0 - 50.0 μm) data were fit to the correlated IR data with a quadratic yielding an RMS difference of 4% over water and 6% over land. With the availability of the varying SZA from the GOES it was determined that a model of the form

$$L_{sw} = a_1 D + a_2 D^2 + a_3 D \ln(\sec(SZA))$$

best described the shortwave radiances, producing RMS differences of 13% over water and 18% over land. This result and the data are shown in Fig. 1.

A critical factor for the HBTM and other algorithms is the accurate specification of clear-sky conditions. With the long time series of GOES data, it was possible to determine the half-hourly clear-sky albedo for the IFO by measuring the minimum VIS counts on days which were predominantly clear. This process was performed utilizing data primarily from Oct. 19 resulting in a 0.1° map of both VIS and SW clear-sky albedo. Clear-sky temperature was derived in the manner given by Minnis et al. (1987).

3. Results

Examples of the clear-sky albedo maps averaged to the IFO grid is given in Fig. 2 for 1800 UT. Values of VIS albedo over the IFO "diamond" (asterisks in the figures) range from 10 - 12%, while the SW albedos vary from 15 - 17%. In the afternoon (not shown), the VIS albedos are much lower than the broadband values which are as high as 29%. The usual trends in daily variation of this parameter are seen in Fig. 3 for the region containing Wausau (top asterisk in Fig.2). A time series of daytime (1500 - 2200 UT) cloud amounts and clear-sky and cloud temperatures are given in Figs. 4 and 5, respectively, for the region containing Ft. McCoy (left asterisk in Fig. 2). The high variability is due to the small size of the region. These plots show that it was clear over the region on Oct. 19 and 21 and overcast on Oct. 22, 31, and from Oct. 24 through 26. Variable cloudiness occurred on the remaining days. These cloud amounts are consistent with surface observations as reported by Hahn et al. (1988). Clear-sky temperatures show a significant diurnal cycle on days with clear or partly cloudy skies. On overcast days, an interpolation scheme was used to obtain clear-sky temperatures. Cloud temperatures suggest low clouds on Oct. 20, 23, 26, 29, and 30 and midlevel clouds on Oct. 22, 25, and 31. The only days with obviously high clouds are Oct. 22, 25, and 31. The nominal HBTM assumes that the clouds can be treated as black bodies so that the mean observed temperature over areas determined to be cloudy is the cloud-top temperature. It is known that many cirrus clouds are non-black and, therefore, the HBTM will probably underestimate their altitudes. Surface and aircraft observations (FIRE, 1987) indicate that high clouds were present over the area on days Oct. 22, 25, and 31 together with lower clouds. High clouds without underlying decks were also reported on days Oct. 27, 28, and 30. Only cirrus was reported on the latter 3 days. Thus, it is apparent that some correction for cirrus emissivity is necessary to correctly identify the true cloud altitudes.

Figure 6 shows the cloud cover derived from GOES data taken at 1500 UT, Oct. 28. Mostly cloudy areas are found in the northern part of the grid. The thickest parts of the cirrus are found in the northern corners and central part of the grid as inferred from the cloud temperatures in Fig. 7. By 2030 UT (Fig. 8), the cloud pattern still shows the most widespread cloudiness over the north with some mostly cloudy areas around Ft. McCoy. Significant high cloudiness was detected west of Green Bay and near Ft. McCoy with the remainder being classified primarily as midlevel clouds. The cloud patterns derived from the AVHRR data (Fig. 9) with the same algorithm (see Harrison et al., 1988) about one-half hour later are very similar but shifted to the east.

4. Concluding remarks

. A preliminary set of cloud parameters derived from GOES data provide a continuous quantification of clouds over the Cirrus IFO. Initial comparisons with the IFO data show that total cloud amount is generally consistent with surface reports. Cloud altitude, however, appears to be substantially underestimated for cirrus. By making use of emissivity computations (Minnis et al., 1988) derived from IFO intercomparisons, it will be possible to greatly improve the techniques for determining cirrus cloud heights.

5. References

FIRE Science Experiment Team Workshop, 1987. Linithicum, MD, Nov. 9-12.

Hahn, C. J., S. G. Warren, and J. L. London, 1988: Surface Synoptic Cloud Reports. FIRE Internal Report, February.

Harrison, E. F., P. Minnis, B. A. Wielicki, P. W. Heck, S. K. Gupta, D. F. Young, and G. G. Gibson, 1988: ERBE and AVHRR Cirrus Cloud FIRE Study. FIRE Workshop, Vail, CO, July 11-15.

Minnis, P. and E. F. Harrison, 1984: Diurnal Variability of Regional Cloud and Clear-Sky Radiative Parameters Derived From GOES. J. Clim. Appl. Meteor., 23, 993-1051.

Minnis, P., E. F. Harrison, and G. G. Gibson, 1987: Cloud Cover Over the Equatorial Eastern Pacific Derived From July 1983 ISCCP Data Using a Hybrid Bispectral Threshold Method. J. Geophys. Res., 92, 4051-4073.

Minnis, P., J. M. Alvarez, D. F. Young, P. W. Heck, and K. Sassen, 1988: Cirrus Cloud Properties Derived From Coincident GOES and Lidar Data During the 1986 FIRE Cirrus Intensive Field Observations. FIRE Workshop, July 11-15.

Whitlock, C. H., 1987: Satellite Calibration Values for the FIRE/SRB Wisconsin Experiment, NASA memo, December 8.

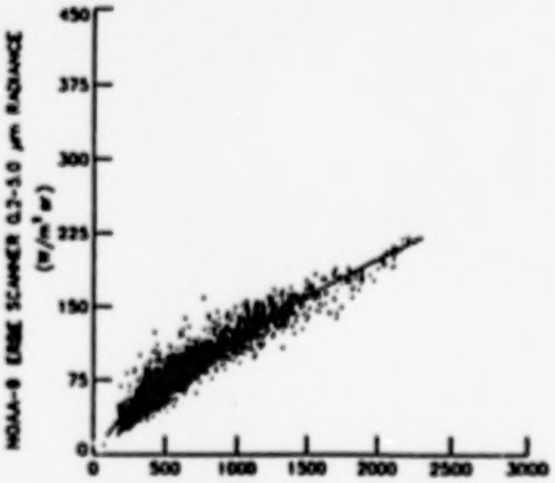

Figure 1. Correlation of ERBE broadband and GOES narrowband shortwave radiances for October, 1986. Curve is for solar zenith of 55°.

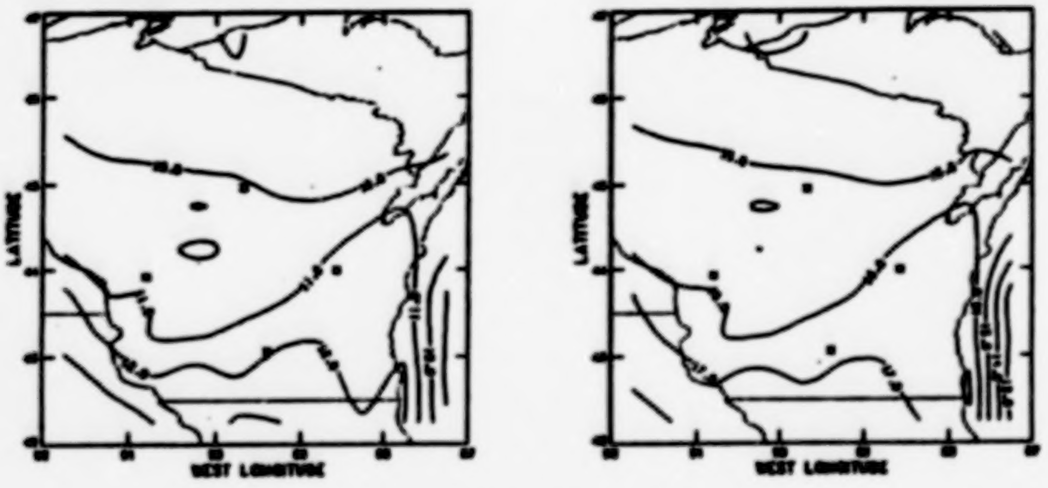
(a) Narrowband albedo

(b) Broadband albedo

LATITUDE
WEST LONGITUDE
LATITUDE
WEST LONGITUDE

Figure 2. Clear-sky albedo(%) for 1800 UT, October 28, 1986.

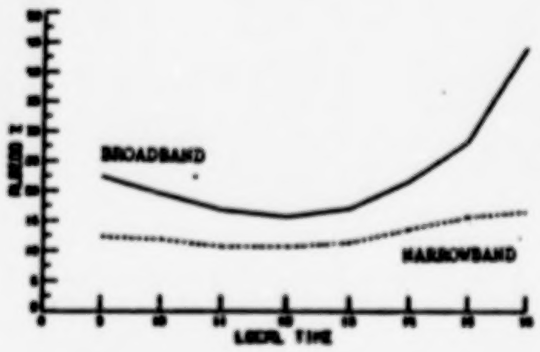

Figure 3. Daytime clear-sky albedo(%) over Wausau for October 28, 1986.

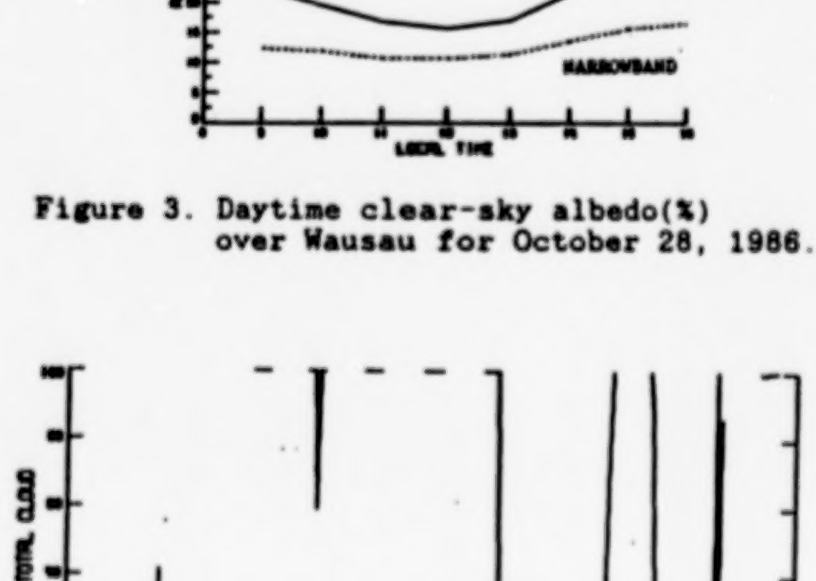

Figure 4. Time series of cloud cover(%) over Ft. McCoy, Oct. 19-31, 1986.

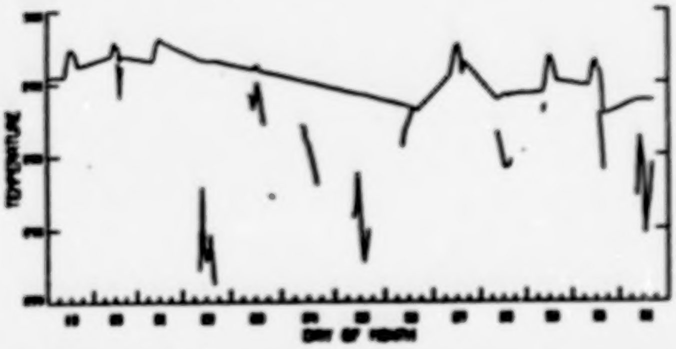

Figure 5. Time series of clear-sky temperature(K, continuous line) and cloud temperature(K) over Ft. McCoy, October 19-31, 1986.

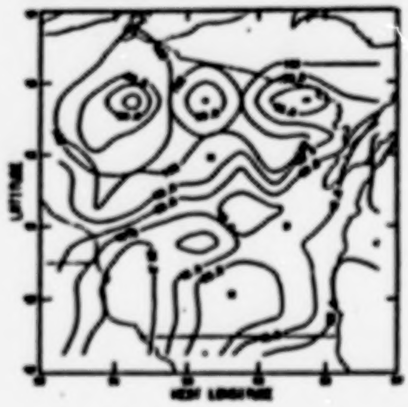
LATITUDE
WEST LONGITUDE

Figure 6. Total cloud cover(%) for 1500 UT, Oct. 28, 1986.

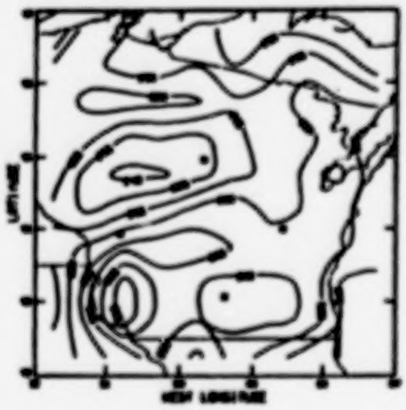
LATITUDE
WEST LONGITUDE

Figure 7. Cloud temperature(K) for 1500 UT, Oct. 28, 1986.

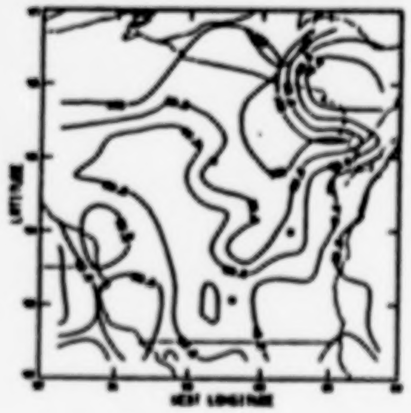
LATITUDE
WEST LONGITUDE

Figure 8. Total cloud cover(%) for 2030 UT, Oct. 28, 1986.

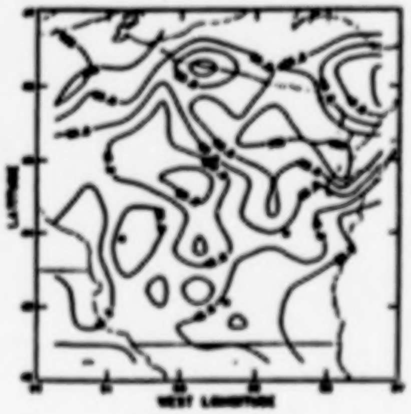
LATITUDE
WEST LONGITUDE

Figure 9. Total cloud cover(%) derived from AVHRR for 2100 UT, Oct. 28, 1986.

Cloud Altitude Determinations from Infrared Spectral Radiances

William L. Smith and Richard Frey

Cooperative Institute for Meteorological Satellite Studies
1225 West Dayton Street
Madison, Wisconsin 53706

Abstract

The "CO_2 slicing" method[1,2,3] is generally recognized as the most accurate means of inferring cloud altitude from passive infrared radiance observations. The method is applicable to semi-transparent and broken cloud. During the cirrus-FIRE and COHMEX field experiments, CO_2 channel radiance data suitable for cloud altitude specification were achieved from moderate spectral resolution satellite sounders (NOAA-TOVS[4] and GOES-VAS[5]) and from a High spectral resolution Interferometer Spectrometer (HIS) flown on the NASA U2/ER2 aircraft. Also aboard the ER2 was a down-looking active lidar unit[6,7] capable of providing cloud top pressure verifications with high accuracy (~5 mb). A third instrument[8], the Multispectral Atmospheric Mapping Sensor (MAMS) provided 50 meter resolution infrared "window" data which is used with radiosonde data to verify the heights of middle and low level clouds. In this paper, comparisons of lidar and MAMS/radiosonde "ground truth" cloud heights are made with those determined from: (a) high resolution (0.5 cm) HIS spectra, (b) HIS spectra degraded to the moderate resolution (15 cm) of the VAS/TOVS instruments, and (c) spectrally averaged HIS radiances for individual pairs of VAS spectral channels. The results show that best results are achieved from high resolution spectra; the RMS difference with the "ground truth" is 23 mb. The RMS differences between the infrared radiance determination and ground truth increase by 35% when the spectral resolution is degraded to the moderate spectral resolution of the VAS/TOVS instruments and by 52% to 183%, depending upon channel combination, when only two spectral channels at VAS/TOVS spectral resolution are used.

1. Introduction

The working equation of the CO_2 slicing method[3] is

$$\frac{I_1(\nu) - I_2(\nu)}{I_1(\nu_o) - I_2(\nu_2)} = \frac{\int_{P_c}^{P_s} \tau(\nu,P)\,\frac{\partial B(\nu, T(p))}{\partial \ln p}\, d\ln p}{\int_{P_c}^{P_s} \tau(\nu_o,P)\,\frac{\partial B(\nu_o, T(p))}{\partial \ln p}\, d\ln p} = C(p_c) \tag{1}$$

where I is an observed spectral radiance at wavenumber (or spectral channel) ν, subscripts 1 and 2 refer to geographically independent fields of view, and the subscript o refers to a reference wavenumber (or spectral channel). It is assumed that the cloud radiates as a "greybody" (i.e., the cloud emissivity is the same for wavenumbers ν and ν_o). $B(\nu,T(p))$ is the Planck radiance corresponding to the temperature T, p is pressure, P_s is surface pressure, and $\tau(\nu,p)$ is the atmospheric transmittance of the atmosphere between the instrument and the pressure p. The cloud top pressure (p_c) which yields the minimum difference between the left-hand side and the right-hand side of Eq. (1) is the cloud pressure estimate. Note that the solution is independent of cloud amount and cloud emissivity.

The CO_2 slicing method assumes that one can find two spatially different radiances due to different cloud amounts and/or cloud emissivity with the cloud emissivity assumed to be independent of spectral wavenumber. In practice, it is attempted to utilize a "clear" air radiance which is representative of the cloudy area of interest together with a cloudy radiance to define the left-hand side of Eq. (1). When using a clear sky reference, the signal-to-noise ratio is maximized and the cloud height need only be constant over a single field of view.

2. The HIS Instrument

The HIS[9,10] is a Michelson interferometer which measures upwelling radiation (3.5-17.0um) at high spectral resolution (λ/Δλ > 1000/1). The spectral range of the instrument is partitioned into three bands. Band 1 (9.1-17.0um or 600-1100 cm), band 2 (5.0-9.1um or 1100-2000 cm), and band 3 (3.5-5.0um or 2000-2800 cm). The maximum spectral resolution is 0.28 cm . One calibration cycle consists of two cold blackbody views, two hot blackbody views and six earth views followed by two more cold and hot blackbody views. During 1986, the HIS was flown aboard NASA U2/ER2 aircraft at a 65,000 foot altitude during the First ISCCP Regional Experiment (FIRE) and the Cooperative Huntsville Meteorological Experiment (COHMEX). The instrument was nadir viewing during the FIRE and COHMEX aircraft flights.

The high spectral resolution of the HIS in the 700-900 cm^{-1} region makes it ideal for application of the CO_2 slicing method. At a 0.5 cm resolution there is available a very large number of spectral "channels". As will be shown, the high resolution enables accurate cloud height estimates. Figure 1a shows a typical radiance spectrum measurement from the HIS in the 600-1100 cm^{-1} region with the spectral bands of the VAS superimposed. Figure 1b shows two CO_2 channel weighting functions for the HIS compared with those for the VAS. The superior vertical resolving power of the HIS is readily apparent and enables more accurate cloud altitude determinations using the CO_2 slicing method.

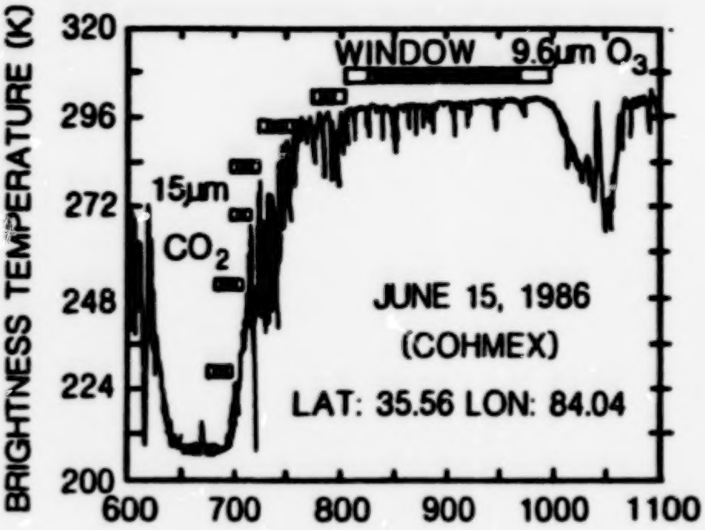

Fig. 1a: HIS long wavelength band spectrum with VAS spectal intervals shown.

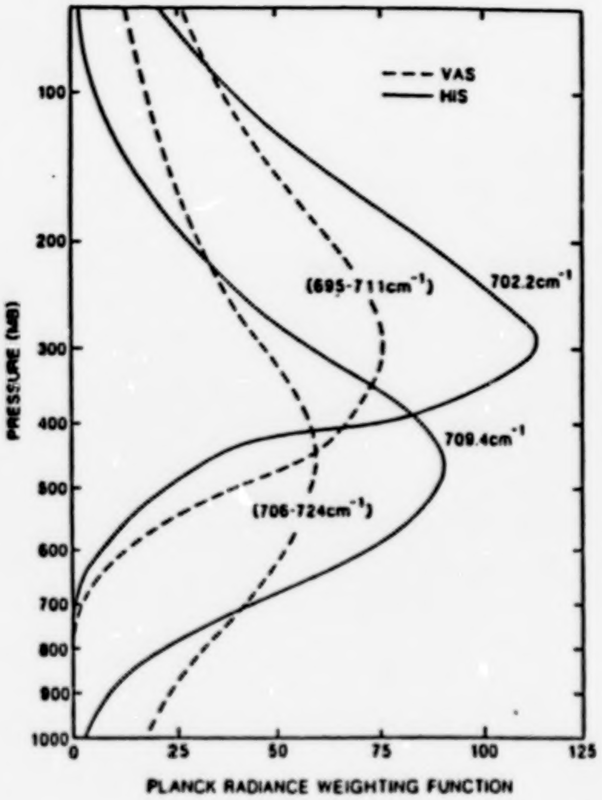

Fig. 1b: Planck radiance weighting functions at HIS and VAS resolutions.

3. Methodology

The first step in the application of the CO_2 slicing method is determining a representative "clear" radiance. "Clear" is in quotes since it refers to the clearest field of view of those corresponding to a geographical sample of radiance spectra. During Project FIRE, a down-looking lidar unit[6,7] was mounted on the NASA U2/ER2 aircraft. This provided a means of locating clear and cloudy regions as well as defining the cloud top pressure "ground truth" with high accuracy (∿5 mb). An average of the largest radiances from among those near the time of interest was chosen as the "clear" reference radiance. Next, differences between the "clear" and cloudy radiances were calculated for each point on the spectrum between 675 and 920 cm^{-1}. The spacing between points was .275 cm^{-1}. The result was normalized by dividing the spatial difference at each point on the spectrum by the value of the spatial difference at a reference wavenumber, chosen to be 899.7 cm^{-1}. This result was compared to the cloud pressure function (the right-hand side of Eq. (1) evaluated from the surface pressure to 50 mb for every point on the spectrum. Atmospheric transmittances were calculated using the line-by-line algorithm "FASCOD"[13] (Clough et al., 1986) while temperature and water vapor profiles were obtained from rawinsonde soundings. (Alternatively, the temperature and water vapor profiles could be obtained by sounding retrieval from the HIS spectra.[12] The value of the cloud pressure function (p_c) for which a minimum difference existed between the left-hand and right-hand sides of Eq. (1) was adopted as the cloud pressure estimate. In this way, a cloud height estimate was obtained for every point on the spectrum.

A reasonable procedure to achieve a single cloud top pressure estimate from a range of frequencies is to form a weighted average over the frequency range. Thus,

$$P_c = \Sigma\, p_c(\nu)\, w^2(\nu) / \Sigma\, w^2(\nu) \qquad (2)$$

is used where the weight "w" represents the sensitivity to cloud height and is given by the derivative of the cloud pressure function, $C(P_c)$, with respect to the natural log of pressure (proportional to height). Mathematically,

$$w = \frac{\partial C(p_c)}{\partial \ln p} = C^1(p_c) \; ,$$

where $C(p_c)$ is defined as the right-hand side of Eq. 1. In our application of Eq. (2), if $w(\nu)$ is not at least one-half the value of the largest $w(\nu)$ within the spectral range used, it is assigned a value of zero.

Figure 2 shows a spectrum of $C^1(p_c)$ for cloud pressures of 300 mb, 500 mb, and 850 mb. The amplitude can be interpreted as the sensitivity of spectral radiance to cloud top pressure variations at these levels. Notice the many sharp peaks along the spectrum. The frequencies of these peaks are ones which should produce the best estimates of the cloud top pressure. Notice that the highest sensitivities are shifted toward larger wavenumbers with lower values of $C(p_c)$ (i.e., higher values of cloud pressure). This is consistent with the fact that in this portion of the 15µm CO_2 absorption band, larger wavenumbers are generally more sensitivity to upwelling radiation from lower levels of the atmosphere. Note the extremely low sensitivity in the opaque region near 720 cm^{-1}. One can see that the highest sensitivities to high clouds (300 mb) are near 710 cm^{-1} and 740 cm^{-1} with generally lower values elsewhere. It is also apparent that spectral smearing causes a reduction of cloud height sensitivity, particularly for low level clouds.

4. Cloud Height Verification Results

HIS determinations of cloud height were obtained from U2/ER2 flights on November 2, 1986 (a FIRE flight), July 5, 1986 (a COHMEX flight), and June 15, 1986 (a COHMEX flight). The November 2 flights were above widespread CIRRUS over north central Wisconsin. The July 5 flight was above middle and upper tropospheric altocumulus clouds associated with a warm front over New England. The June 15 flight was over boundary layer cumulus cloud over northern Alabama and central Tennessee. The November 2 cirrus cloud height verifications were achieved using the ER2 lidar, which is believed to provide cloud top altitudes to an accuracy of 100 meters. The July 5 and June 15, middle and low level cumulus cloud verifications were achieved using time coincident window channel radiance data from the 50 meter resolution MAMS instrument and nearby radiosonde temperature and moisture profiles. A complete description of the "ground truth" cloud height data used to verify the "CO_2 slicing" determinations for these three days can be found in the thesis of Frey.[14]

Table I shows the RMS differences between the "CO_2 slicing" determinations and the ground truth for three categories of cloud height. Scatter diagrams of the results are shown in Fig. 3. As can be seen from Fig. 3, a large part of the RMS difference is due to a systematic tendency for the

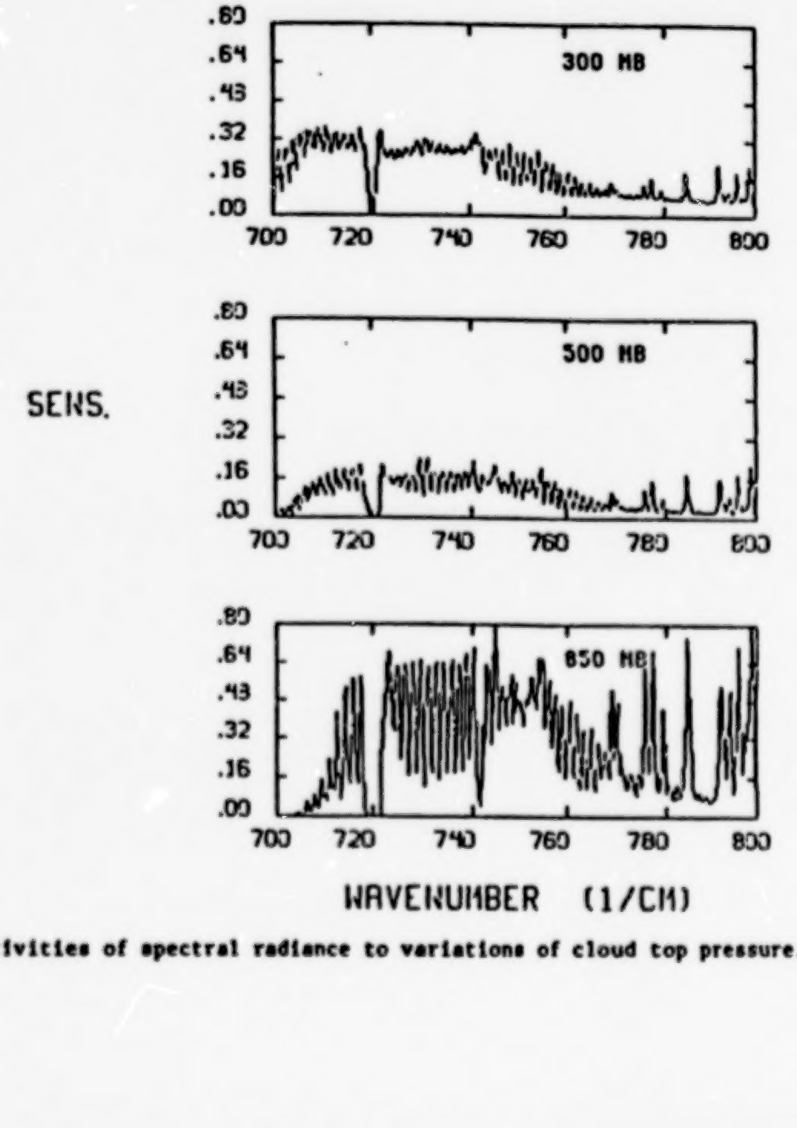

Fig. 2: Sensitivities of spectral radiance to variations of cloud top pressure.

infrared cloud pressures to be higher (low heights) than the ground truth. This tendency which is seen to be spectral resolution dependent is due to the semi-transparency of the cloud.[2] Referring to Table I, the most accurate results are achieved when the determinations are based upon high resolution HIS spectra. The discrepancies increased by 35% when the HIS spectral resolution is degraded to that of the VAS/TOVS sounding instruments. When the determinations are made using pairs of infrared spectral channels pertaining to the VAS, as opposed to using the continuous spectrum, the discrepancies increase by as much as 183%, depending upon the channel combination used. In general, best results for VAS channel combinations are achieved when a "window" channel is used as a reference; the discrepancy in this case is less than a factor of two poorer than that achieved with high resolution HIS spectra.

Table I. RMS differences (mb) between cloud top pressure estimates from HIS and simulated VAS data with lidar and MAMS/radiosonde ground truth.

	RMS Error (mb)			
Method	**High Cloud (N=30)**	**Middle Cloud (N=6)**	**Low Cloud (N=16)**	**All Clouds[3] (N=52)**
HIS at high resolution	26	13	26	23
HIS at VAS/TOVS resolution	31	14	42	31
VAS Channels[1] (simulated from HIS, window channel reference)				
3/8	46	18	NA	35
4/8	49	20	NA	37
5/8[2]	34	31	44	37
VAS Channels[1] (simulated from HIS, near channel reference)				
3/4	45	54	NA	50
3/5[2]	48	17	NA	36
4/5	54	74	NA	65

---

[1] The half bandwidth spectral limits of VAS channels are: (1) Channel 3, 695-711 cm^{-1}; (2) Channel 4, 706-724 cm ; (3) Channel 5, 742-758 cm ; and, (4) Channel 8, 822-960 cm .

[2] Considered to be the "optimum" channel combination.

[3] Computed from the average of the error variance for each height category.

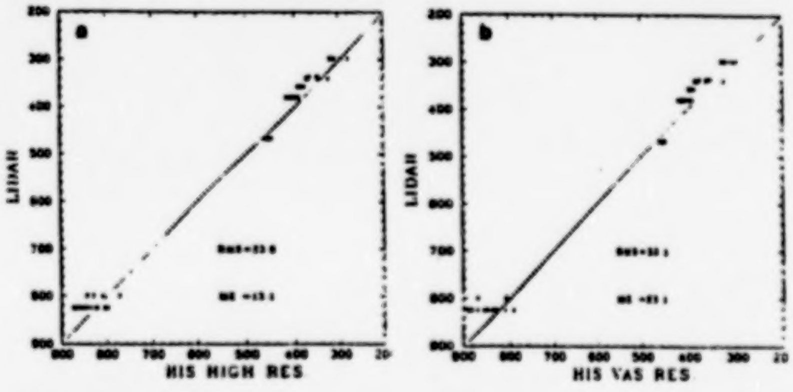

Fig. 3: Scatter diagrams of ground truth (lidar) versus CO_2 slicing infrared cloud pressure heights (mb) for (a) HIS high resolution spectra, (b) moderate (VAS) resolution spectra, (c) VAS channels using a window channel (8) as a reference, and (d) VAS channels using a CO_2 channel (5) as a reference.

Acknowledgments

We wish to thank Henry Revercomb, Harold M. Woolf, H. B. Howell, and H.-L. Huang for their assistance with the HIS data processing required for this research. We gratefully acknowledge Jim Spinhirne for providing the lidar data used to verify the radiometric cloud height determinations. Our thanks to Laura Beckett and Steve Ackerman for their help in the preparation of this manuscript. This research was supported by NASA under contract NAS1-18272.

References

[1] Smith, W. L., H. M. Woolf, P. G. Abel, C. M. Hayden, M. Chalfant and N. Grody, 1974: Nimbus-5 sounder data processing system, Part 1: measurement characteristics and data reduction procedures. NOAA Tech. Memo. NESS 57, 99 pp.

[2] Smith, W. L., and C. M. R. Platt, 1978: Comparison of satellite-deduced cloud heights with indications from radiosonde and ground-based laser measurements. J. Appl. Meteor., 17, 1796-1802.

[3] Menzel, W. P., W. L. Smith and T. R. Stewart, 1983: Improved cloud motion wind vector and altitude assignment using VAS. J. Appl. Meteor., 22, 377-384.

[4] Smith, W. L., H. M. Woolf, C. M. Hayden, D. Q. Wark and L. M. McMillin, 1979: The TIROS-N vertical sounder. Bull. Amer. Meteor. Soc., 60, 1177-1187.

[5] Smith, W. L., V. E. Suomi, W. P. Menzel, H. M. Woolf, L. A. Sromovsky, H. E. Revercomb, C. M. Hayden, D. N. Erikson and F. R. Mosher, 1981: First sounding results from VAS-D. Bull. Amer. Meteor. Soc., 62, 232-236.

[6] Spinhirne, J. D., M. Z. Hansen and L. O. Caudill, 1982: Cloud top remote sensing by airborne lidar. Appl. Optics, 21, 1564-1571.

[7] Spinhirne, J. J., M. Z. Hansen and J. Simpson, 1983: The structure and phase of cloud tops as observed by polarization lidar. J. Appl. Meteor., 22, 1319-1331.

[8] Jedlovec, G. J., W. P. Menzel, R. J. Atkinson and G. S. Wilson, 1986: The Multispectral Atmospheric Mapping Sensor (MAMS): instrument description, calibration and data Quality. NASA TM-86565, Marshall Space Flight Center, Huntsville, AL, 37 pp.

[9] Revercomb, H. E., H. Buijs, H. B. Howell, D. D. LaPorte, W. L. Smith, and L. A. Sromovsky, 1987: Radiometric calibration of IR Fourier transform spectrometers: solution to a problem with the High-resolution Interferometer Sounding (HIS). Submitted to Applied Optics, December 11.

[10] Revercomb, H. E., H. Buijs, H. B. Howell, R. O. Knuteson, D. D. LaPorte, W. L. Smith, L. A. Sromovsky, and H. M. Woolf, 1987: Radiometric calibration of IR interferometers: experience from the High-resolution Interferometer Sounder (HIS) aircraft instrument. Proceedings of the International Workshop on Remote Sensing Retrieval Methods, Williamsburg, VA.

[11] Smith, W. L., H. M. Woolf, H. B. Howell, H.-L. Huang, and H. E. Revercomb, 1987: The simultaneous retrieval of atmospheric temperature and water vapor profiles - application to measurements with the High spectral resolution Interferometer Sounder (HIS). Presented at the International Workshop on Remote Sensing Retrieval Methods, Williamsburg, VA, December 15-18.

[12] Smith, W. L., H. M. Woolf, H. B. Howell, H.-L. Huang, and H. E. Revercomb, 1988: High resolution interferometer sounder - the retrieval of atmospheric temperature and water vapor profiles. Proceedings of the Third Conference on Satellite Meteorology and Oceanography, American Meteorological Society, Boston, MA.

[13] Clough, S. A., F. X. Kneizys, E. P. Shettle, G. P. Anderson, 1986: Sixth Conference on Atmospheric Radiation, AMS, Boston, MA, p. 141.

[14] Frey, R., 1988: "On the determination of cloud altitude using infrared spectral radiances." MS thesis, University of Wisconsin-Madison.

AVHRR AND VISSR SATELLITE INSTRUMENT CALIBRATION RESULTS FOR BOTH CIRRUS AND MARINE STRATOCUMULUS IFO PERIODS

C. H. Whitlock, W. F. Staylor, and J. T. Suttles
Atmospheric Sciences Division, NASA Langley Research Center
Hampton, Virginia 23665-5225

G. Smith and R. Levin
Satellite Research Laboratory, NOAA/NESDIS
Washington, D.C. 20233

R. Frouin and C. Gautier
California Space Institute, Scripps Institution of Oceanography
La Jolla, California 92093

P. M. Teillet and P. N. Slater
Optical Sciences Center, University of Arizona
Tucson, Arizona 85721

Y. J. Kaufman and B. N. Holben
Laboratory for Atmospheres, NASA Goddard Space Flight Center
Greenbelt, Maryland 20771

William B. Rossow and Chris Brest
NASA Goddard Institute for Space Sciences
New York, New York 10025

LeCroy, S. R.
Planning Research Corporation
Hampton, Virginia 23666

INTRODUCTION - Accurate characterizations of some cloud parameters are dependent upon the absolute accuracy of satellite radiance measurements. Visible-wavelength measurements from both the AVHRR and VISSR instruments are often used to study cloud characteristics. Both of these instruments were radiometrically calibrated prior to launch, but neither has an onboard device to monitor degradation after launch. During the FIRE/SRB cirrus Intensive Field Operation (IFO), a special effort was made to monitor calibration of these two instruments onboard the NOAA-9 and GOES-6 spacecraft. In addition, several research groups have combined their efforts to assess the long-term performance of both instruments. These results are presented, and a limited comparison is made with the ERBE calibration standard.

DATA - Figures 1 and 2 show calibration results for NOAA-9 AVHRR channels 1 and 2. Figure 3 presents the same information for the GOES-6 VISSR instrument. On each figure, the equation for radiance in terms of instrument gain is shown at the top of the figure. Increasing gain means that instrument sensitivity is decreasing, and the system is deteriorating. All indirect methods are based on radiative transfer calculations from various combinations of model inputs and produce absolute calibration values like the U-2 method. As noted on the figures, the relative methods are anchored to the October 1986 NOAA U-2 absolute results and symbol size indicates the authors' estimates of uncertainty. For sake of brevity, details of the various methods cannot be discussed here but most are generally described in the literature. The NOAA/NESDIS U-2 method and the Scripps indirect method are described in references 1 and 2, respectively. The University of Arizona indirect method is discussed in references 3 and 4. The NASA/GSFC indirect method is based on reference 5. The NASA/LaRC indirect method has not been published, but it uses the radiative transfer model and atmospheric analysis techniques described in reference 6 in combination with surface reflectance and atmospheric measurements made over the Sonora Desert during May 1985 (see reference 7). The ISCCP relative approaches are described in references 8, 9, and 10, and the NASA/LaRC relative method is described in reference 11. Estimated uncertainties in the various methods are summarized below:

METHOD	UNCERTAINTY PERCENT
NOAA/NESDIS U-2	± 5
U. AZ. INDIRECT	± 5
NASA/LaRC INDIRECT	± 7
SCRIPPS INDIRECT	± 8
NASA/GSFC INDIRECT	± 11
NASA/LaRC RELATIVE ANCHORED TO DAY 682 U-2 VALUE	± 2 + (U-2 ERROR)
ISCCP RELATIVE ANCHORED TO DAY 682 U-2 VALUE	± 2 + (U-2 ERROR)

RESULTS - Figure 1 suggests that channel 1 of the NOAA-9 AVHRR instrument degraded by approximately 28 percent over the first 1200 days from launch. Both the NASA/LaRC and ISCCP relative methods appear to give reasonable trends when applied over an extended time period of 2 or more years. When the relative methods are anchored to periodic absolute values, the result is a continuous calibration history that can be used with confidence.

In the period from days 152-257 (May-August 1985), all of the indirect and anchored relative methods agree within estimated uncertainties. One question of some concern is why the channel 1 U-2 results at day 257 do not fall in line with the other methods during that period. (Reference 1 actually reports a slight positive instrument enhancement rather than the usual degradation for that day.) Some insight into this problem may be gained by examining the NASA/LaRC indirect results taken during days 152-159. During that period, the U-2 overflew the Mohawk Valley region, and the NASA/LaRC method was applied using reference 7 data. Figure 4 shows that both the U-2 and NASA/LaRC indirect methods were in reasonable agreement for the channel 1 wavelength range during the May time period. There is a tendency for the indirect method to give slightly higher values at near-infrared wavelengths, however. [Reference 7 describes a deficiency in NBS testing of the field reflectance standard that is the probable cause of this bias at wavelengths either higher or lower than 0.65 micrometers for this particular experiment.] The trend to slight overprediction was confirmed when broad-band results from the indirect method were found to be 7 percent high compared to broad-band ERBE/ERBS values (figure 5). If one compensates for the near-infrared bias, the NASA/LaRC indirect method applied to visible wavelengths is apparently consistent with the ERBE calibration standard. This in turn gives additional confidence in all of the indirect and anchored relative results for the days 152-257 period. For this reason, it is believed that the U-2 point at day 257 is in error by a larger amount than the quoted 5 percent uncertainty.

Figure 2 suggests that channel 2 of the NOAA-9 AVHRR instrument may have been as much as 10 percent degraded immediately after launch and that degradation increased to 28 percent by day 1200. Those values are based on an assumed fit, however, since neither the ISCCP nor the NASA/LaRC relative methods have analyzed AVHRR channel 2.

Figure 3 suggests a sinusoidal degradation of the GOES-6 VISSR instrument. In this case, the ISCCP VISSR values are computed using AVHRR channel 1 gain values in combination with the ISCCP slope ratio in the following equation:

$$G_{8(G-6)} = 0.01966*A*G_{10(N-9,CH\ 1)} \qquad (1)$$

where: $G_{8(G-6)}$ = GOES-6 VISSR gain in terms of 8-bit counts.

$G_{10(N-9,CH\ 1)}$ = NOAA-9 AVHRR channel 1 gain in terms of 10 bit counts.

A = ISCCP slope ratio.

It is believed that the sinusoidal characteristic is partly caused by the fact that the gain often changed weekly by NOAA to correct for banding effects in the cloud images. Additional investigation of GOES degradation is desirable.

The following calibration equations are recommended for satellite data analysis during the FIRE IFO periods:

CIRRUS IFO

NOAA-9/AVHRR CH 1: RAD = - 22 + [0.6060*(10-BIT COUNTS)] (2)
NOAA-9/AVHRR CH 2: RAD = - 16 + [0.4000*(10-BIT COUNTS)] (3)
GOES-6/VISSR: RAD = - 8 + [0.01015*(8-BIT COUNTS^2)] (4)

MARINE STRATOCUMULUS IFO

NOAA-9/AVHRR CH 1: RAD = - 22 + [0.6338*(10-BIT COUNTS)] (5)
NOAA-9/AVHRR CH 2: RAD = - 16 + [0.4150*(10-BIT COUNTS)] (6)
GOES-6/VISSR: RAD = - 8 + [0.01000*(8-BIT COUNTS^2)] (7)

The following filter bandpass and filtered solar constants are recommended:

	BANDPASS VALUES ....microns....	SOLAR CONSTANTS W/(m^2 sr micron) @ 1 AU
NOAA-9/AVHRR CH 1:	0.117	519.4
NOAA-9/AVHRR CH 2:	0.240	335.2
GOES-6/VISSR:	0.187	526.9

REFERENCES

1. Smith, G. R., Levin, R. H., Able, P., and Jacobowitz, H.: Calibration of the Solar Channels of the NOAA-9 AVHRR Using High Altitude Aircraft Measurements. Journal of Atmospheric and Oceanic Technology, vol. 5, no. 5, October 1988, pp. 631-639.

2. Frouin, R. and Gautier, C.: Calibration of NOAA-7 AVHRR, GOES-5, and GOES-6 VISSR/VAS Solar Channels. Remote Sensing of Environment, vol. 22, no. 1, June 1987, pp. 73-101.

3. Slater, P. N., Biggar, S. F., Holm, R. G., Jackson, R. D., Mao, Y., Moran, M. S., Palmer, J. M., and Yuan, B.: Reflectance- and Radiance-Based Methods for the In-Flight Absolute Calibration of Multispectral Sensors. Remote Sensing of the Environment, vol. 22, no. 1, June 1987, pp. 1-37.

4. Teillet, P. M., Slater, P. N., Mao, Y., Ding, Y., Yuan, B., Bartell, R. J., Biggar, S. F., Santer, R. P., Jackson, R. D., and Moran, M. S.: Absolute Radiometric Calibration of the NOAA AVHRR Sensors. Proc. SPIE, Vol. 924, Recent Advances in Sensors, Radiometry, and Data Processing for Remote Sensing, 1988.

5. Fraser, R. S., and Kaufman, Y. J.: Calibration of Satellite Sensors After Launch. Applied Optics, vol. 25, no. 7, April 1, 1986, pp. 1177-1185.

6. Whitlock, C. H., Suttles, J. T., Sebacher, D. I., Fuller, W. H., and LeCroy, S. R.: Interpretation of Spectral Radiation Experiments Using Finite-Difference Radiative Transfer Theory. IRS84: Current Problems in Atmospheric Radiation. A Deepak Publishing, 1985, pp. 293-296.

7. Whitlock, C. H., Purgold, G. C., and LeCroy, S. R.: Surface Bidirectional Reflectance Properties of Two Southwestern Arizona Deserts for Wavelengths Between 0.4 and 2.2 Microns. NASA TP 2643, 1987.

8. Rossow, W. B., Kinsella, E., Wolf, A., and Garder, L.: International Satellite Cloud Climatology Project (ISCCP) Description of Reduced Resolution Radiance Data. WMO/TD-58, 1987.

9. International Satellite Cloud Climatology Project (ISCCP) Working Group on Data Management - Sixth Session. WMO/TD-210, January 1988, pp. 19-28.

10.Brest. C. L., and Rossow, W. B.: Radiometric Calibration and Monitoring of NOAA AVHRR Data for ISCCP. International Journal of Remote Sensing, 1989 (in press).

11.Staylor, W. F.: Degradation Rates of the AVHRR Visible Channel for the NOAA 6, 7, and 9 Spacecraft. Journal of Atmospheric and Oceanic Technology, 1989 (in press).

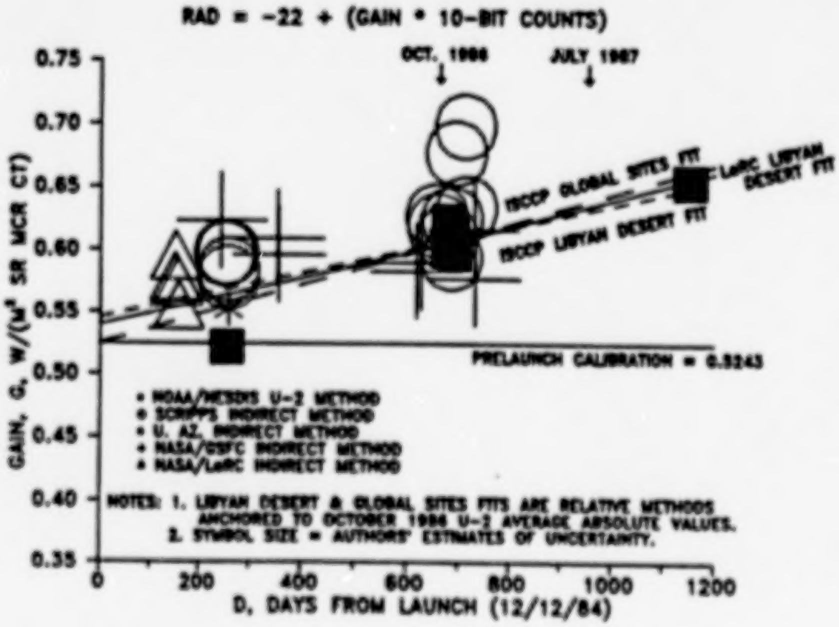

Fig. 1. NOAA-9 AVHRR channel 1 gain.

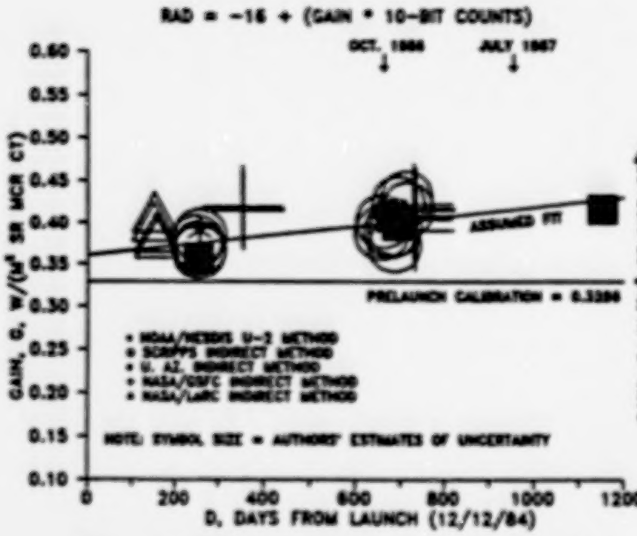

Fig. 2. NOAA-9 AVHRR channel 2 gain.

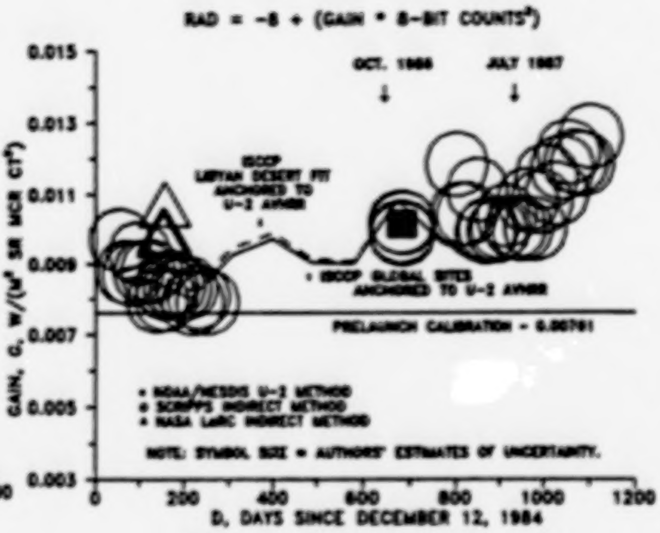

Fig. 3. GOES-6 VISSR gain.

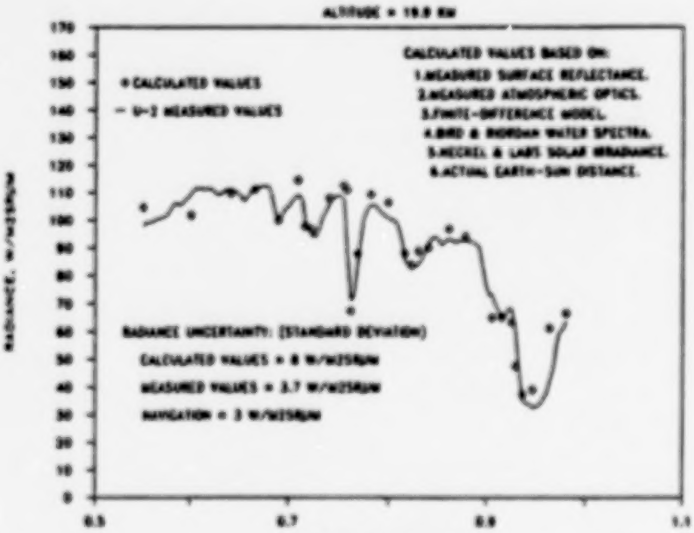

Fig. 4. Comparison of NASA/LaRC indirect method with NOAA U-2 method in May 1985.

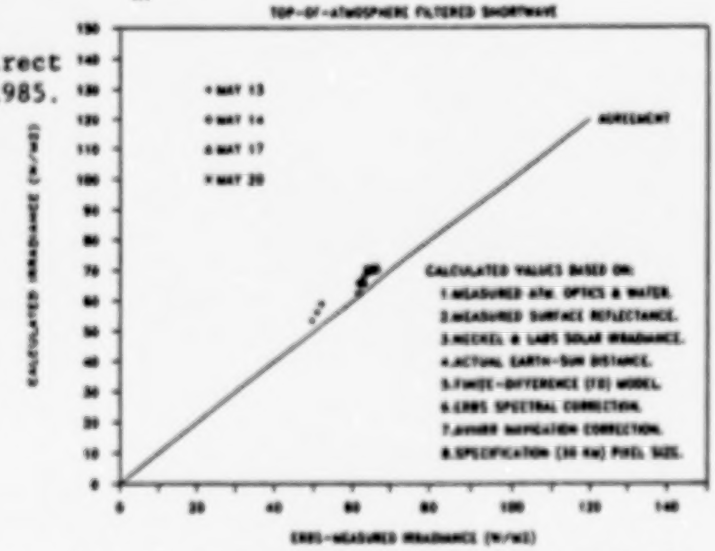

Fig. 5. Comparison of NASA/LaRC indirect method with ERBE/ERBS top of atmosphere irradiances in May 1985.

CIRRUS CLOUD PROPERTIES DERIVED FROM COINCIDENT GOES AND LIDAR DATA DURING THE 1986 FIRE CIRRUS INTENSIVE FIELD OBSERVATIONS

Patrick Minnis and Jose M. Alvarez
Atmospheric Sciences Division, NASA Langley Research Center
Hampton, Virginia 23665-5225

David F. Young and Patrick W. Heck
Aerospace Technologies Division, Planning Research Corporation
Hampton, Virginia 23666
and
Kenneth Sassen
Department of Meteorology, University of Utah
Salt Lake City, Utah 84112

1. Introduction

One of the main difficulties in detecting cirrus clouds and determining their correct altitude using satellite measurements is their non-blackness. In the present algorithm (Rossow et al., 1985) used by the International Satellite Cloud Climatology Project (ISCCP), the cirrus cloud emissivity is estimated from the derived cloud reflectance using a theoretical model relating visible (VIS, 0.65 μm) optical depth to infrared (IR, 10.5 μm) emissivity. At this time, it is unknown how accurate this approach is or how the derived cloud altitude relates to the physical properties of the cloud. The First ISCCP Regional Experiment (FIRE) presents unique opportunities for determining how the observed radiances depend on the cloud properties. During the FIRE Cirrus Intensive Field Observations (IFO, see Starr, 1987), time series of cloud thickness, height, and relative optical densities were measured from several surface-based lidars. Cloud microphysics and radiances at various wavelengths were also measured simultaneously over these sites from aircraft at specific times during the IFO (October 19 - November 2, 1986). Satellite-observed radiances taken simultaneously can be matched with these data to determine their relationships to the cirrus characteristics. In this paper, a first step is taken toward relating all of these variables to the satellite observations. Lidar-derived cloud heights are used to determine cloud temperatures which are used to estimate cloud emissivities from the satellite IR radiances. These results are then correlated to the observed VIS reflectances for various solar zenith angles.

2. Data and approach

Half-hourly 1-km VIS and 4-km IR radiances from the Geostationary Operational Environmental Satellite (GOES) taken during the IFO are used to determine cloud reflectance and effective blackbody temperatures over two sites, Ft. McCoy and Wausau, Wisconsin. The VIS counts are converted to reflectances using the calibration parameters given by Whitlock (1987). All of the data found within 0.35° longitude and 0.25° latitude of the ground sites are assumed to be representative of the radiances directly above the ground site during a 30-minute interval. Thus, spatial variations near the station replace the time variations in the clouds as they advect over the station. This assumption also minimizes the effects of navigational errors.

In this initial study it is assumed that the pixels are entirely clear or cloud-filled. Therefore, given an equivalent blackbody, clear-sky temperature, TS, a measured IR temperature, T, and a cloud temperature, TC, it is possible to estimate the cloud emissivity as

$$\epsilon = [B(T) - B(TS)]/[B(TC)-B(TS)],$$

where B represents the Planck blackbody function. This simple model treats the cloud as a homogeneous mass radiating at some effective temperature TC. The dependence of ϵ on viewing zenith angle, VZ, is ignored here because all of the measurements are taken at $51° < VZ < 52°$. Since the VIS data are discretized to 6 bits, there are only a few values of reflectance, ρ, which will be observed at a given hour. In order to determine ϵ as a function of ρ, the emissivities measured for some given value of ρ are averaged to yield a single value for each reflectance value. This averaging process tends to smooth out some of the inhomogeneities found in real clouds.

A first guess value of TS was taken from the time series results for clear-sky temperature derived by Heck et al. (1988). This value was reset to the highest observed temperature over the site whenever a negative average emissivity was found. Cloud temperature was determined in the following manner. First, a density center for the cloud in terms of altitude was estimated from time series plots of lidar relative backscatter intensities. These intensities were taken by the NASA Langley ground lidar system operating at Ft. McCoy (Alvarez et al., 1988) and by the University of Utah mobile polarization lidar at Wausau (Sassen, 1987). An initial guess of TC was taken from the nearest available radiosonde data using the temperature corresponding to the density center height. This process assumes that this inferred "center of mass" is the radiating core of the cloud. Whenever any of the derived emissivities exceeded unity, TC was reset to the coldest observed temperature. Underestimates of TC may be detected from a flattening of the emissivity curve long before $\epsilon = 1$.

3. Results and discussion

A plot of the Ft. McCoy lidar returns for 1500 - 2200 UT, Oct. 28, 1986 is shown in Fig. 1 with the selected values of cloud height and TC. In the morning, the cloud altitude was lower and the clouds described as "mackerel" indicative of alto- or cirrocumulus. By 1900 UT, a cirrus deck of variable thickness advected over the area between 8 and 11 km. Before 2030 UT, the clouds were generally described as thin and variable. Between 2030 and 2200 UT, the cloud deck was described as uniform with some "bluish" areas in the clouds. Cloud emissivities over Ft. McCoy for 1500 UT, 1930 UT, and 2100 UT are plotted as functions of VIS reflectances in Fig. 2. These results appear to be consistent with the surface descriptions. At 1500 UT, the points yield a smooth curve indicating a relatively homogeneous cloud deck, while at 1930 UT the values of ϵ do not vary monotonically with ρ, suggesting the presence of some lower-level clouds or partially-filled pixels. The curve for 2100 UT is also relatively smooth.

Some values of ρ in Fig. 2 are actually less than the nominal clear-sky reflectance. Since this occurs for $\epsilon > 0.1$, this phenomenon may be due to either shadowing of a lower part of the cloud by a thick part or due to the transmission properties of the clouds. The 3-km altitude variation in the cells around 2100 UT seen in Fig. 1 indicates that such a shadowing effect is possible for that hour. Additional examination of the pixel maps will help determine the reasons for the decreased reflectances.

Figure 3 shows the emissivities derived from data over both sites for hours 1500 UT and 2130 UT on Oct. 28. The solar zenith angles are about 68°

at 1500 UT and 78° at 2130 UT. Relative azimuth angles are approximately 130° in both cases. The variation of ϵ with ρ appears to be consistent between the sites but differs from the morning to the afternoon. Emissivity increases rapidly until a value of $\epsilon = 0.8$ is reached in Fig. 3a, then it increases with a decreasing slope. In Fig. 3b, the slope appears to increase gradually up to $\rho = 25\%$, then more rapidly, at least for the Ft. McCoy data. The clouds are 1-2 km higher in the afternoon, but the slope at 2100 UT (Fig. 2c) is very similar to the 1500 UT case. Although there may be enhanced shadowing at 2130 UT, it is not immediately apparent why this large difference occurs.

Emissivities derived over Ft. McCoy on three different days at 2030 UT are given in Fig. 4. Variations in their dependence on VIS reflectance probably result from variations in the cloud microphysics and morphologies. The lidar returns indicate that the clouds are thickest on Oct. 28. On Oct. 27 the clouds are only about 1 km thick with no obvious precipitating cells. All three cloud decks were between 9 and 10 km. The dip in the emissivity at the highest reflectances may correspond to views of the sides of the cirrus clouds. Since these data are taken in a backscattering geometry with a low sun and satellite, the cloud sides would be intercepting and reflecting a considerable fraction of the incident radiation. Viewing of the cloud sides would tend to increase the observed IR radiance since both the top and lower portions of the clouds are seen.

4. Concluding remarks

The analysis of combined satellite and lidar data will help improve our understanding of how to interpret radiances observed over cirrus cloud fields. Examples given here show significant variability in the relationship between VIS reflectance and IR emissivity. Other complicating factors such as shadows, finite cloud geometry, and partially cloud-filled pixels are also apparent in these initial results. The similarities in some of the cases reported here, however, show potential for some empirical modeling. Further study of these and other cases with additional correlative FIRE data will be required to develop parameterizations for interpreting these radiances for cirrus cloud quantification from satellites.

5. References

Alvarez, J. M., M. P. McCormick, J. D. Moore, W. H. Hunt, B. R. Rouse, L. R. Poole, and B. D. Poole, 1988: A Synopsis of Langley Research Center's Lidar Effort for the 1986 FIRE IFO. FIRE Workshop, Vail CO, July 11-15.

Heck, P. W., D. F. Young, P. Minnis, E. F. Harrison, 1988: Cloud Parameters From GOES Visible and Infrared Radiances During the FIRE Cirrus IFO, October 1986. FIRE Workshop, Vail CO, July 11-15.

Rossow, W. B., F. Mosher, E. Kinsella, A. Arking, M. Desbois, E. Harrison, P. Minnis, E. Ruprecht, G. Seze, C. Simmer, and E. Smith, 1985: ISCCP Cloud Algorithm Intercomparison. J Clim. Appl. Meteor., 24, 877-903.

Sassen, K., 1987: The Structure of Cirrus Clouds. FIRE Experiment Team Workshop, Linithicum, MD, Nov. 9-12, 91-104.

Starr, D. O'C., 1987: A Cirrus-Cloud Experiment: Intensive Field Observations Planned for FIRE. Bull. Amer. Meteor. Soc., 68, 119-124.

Whitlock, C.H., 1987: Satellite Calibration Values for the FIRE/SRB Wisconsin Experiment. NASA memo, December 8.

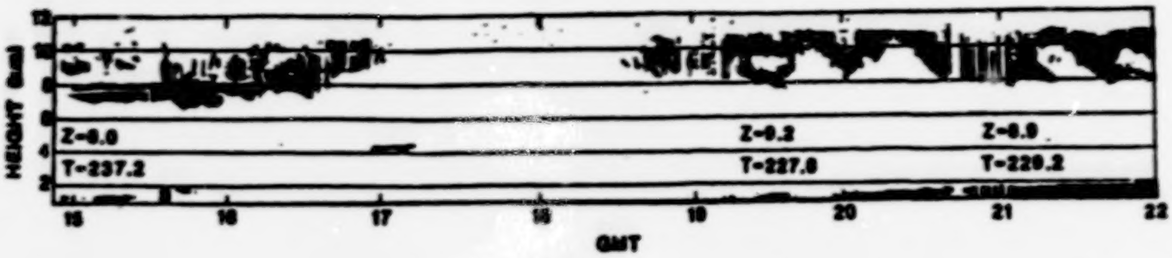

Figure 1. Time series of Ft. McCoy returned lidar power for 1500 UT - 2200 UT, Oct. 28. Estimated height (Z) and temperature (T) for the "center of mass" of the cirrus are given for 1500, 1930, and 2100 UT

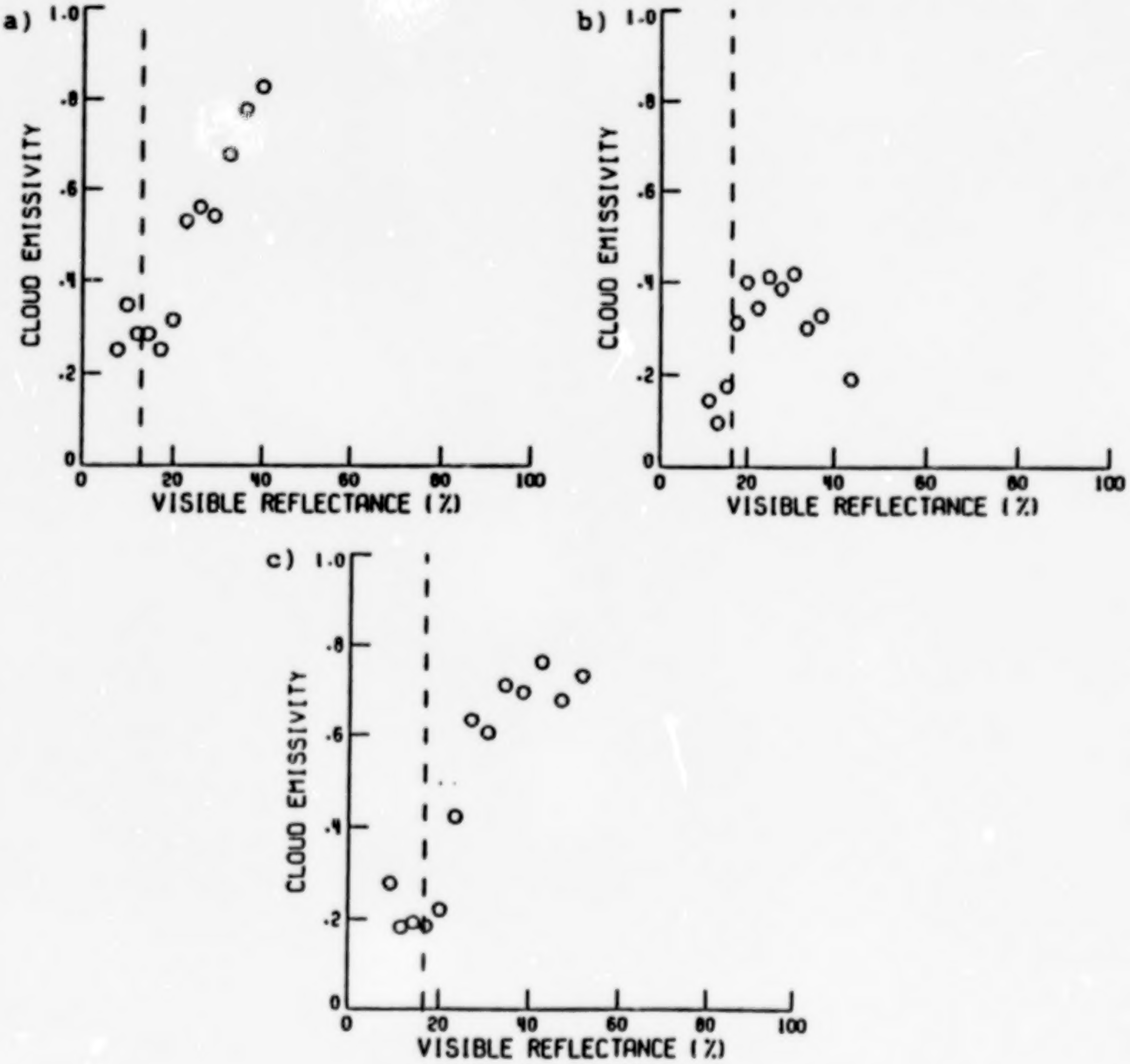

Figure 2. Variation of cirrus cloud emissivity with visible reflectance for a) 1500 UT, b) 1930 UT, and c) 2100 UT for Oct. 28. The dashed line represents the nominal clear-sky reflectance

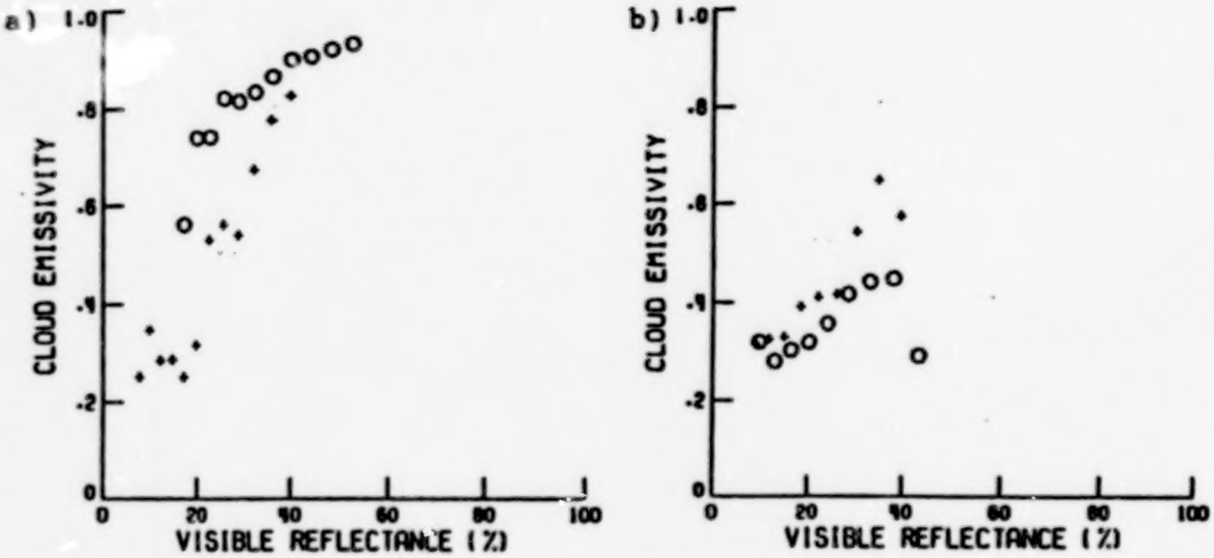

Figure 3. Comparison of Wausau (○) and Ft. McCoy (+) emissivity curves for a) 1500 UT and b) 2130 UT, Oct. 28.

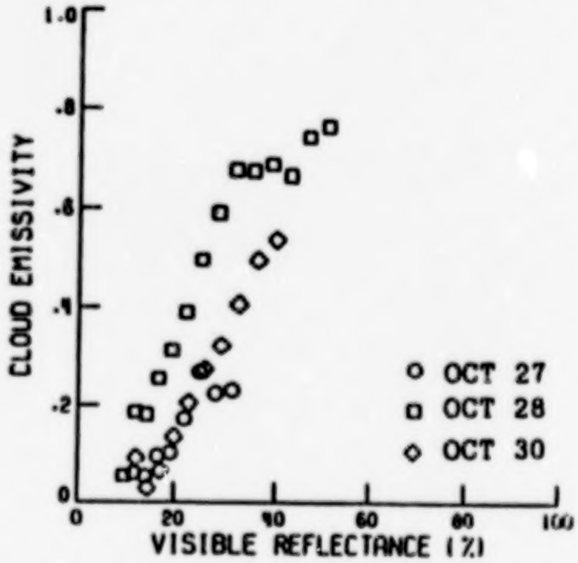

Figure 4. Comparison of Ft. McCoy emissivity curves for Oct. 27, 28, and 30.

FIRE SCIENCE TEAM MEETING
VAIL, COLORADO
JULY 11-15, 1988

CIRRUS

CASE STUDY OF OCTOBER 27-28, 1986 - Kenneth Sassen   Tuesday, July 12, 1988

PAGE

Overview of the 27-28 October FIRE Cirrus IFO Case: Meteorology and Cloud Fields 155
Starr, David O'C.; and Donald P. Wylie

A Four-Lidar View of Cirrus from the FIRE IFO: 27-28 October 1986 157
Sassen, Kenneth.; Christian John Grund, Jose M. Alvarez, and Freeman F. Hall

Radiative Properties of Cirrus Clouds: FIRE IFO Case 10/28/86 159
Hein, Paul F.; William L. Smith, Jr., and Stephen K. Cox

FIRE Cirrus on 10/28/86: Landsat; ER-2; King Air; Theory 163
Wielicki, Bruce A.; John T. Suttles, Andrew J. Heymsfield, Ronald M. Welch, James D. Spinhirne, Lindsay Parker, and Robert F. Arduini

Surface Radiation Observations for October 27-28, 1986 During the Wisconsin FIRE/SRB Experiment 169
Whitlock, C. H.; L. R. Poole, S. R. LeCroy, and D. A. Robinson

ABSTRACT

Overview of the 27-28 October FIRE Cirrus IFO Case: Meteorology and Cloud Fields

by

David O'C. Starr
NASA Goddard Space Flight Center
Greenbelt, Maryland 20771

and

Donald P. Wylie
Space Science and Engineering Center
University of Wisconsin
Madison, Wisconsin 53706

A detailed description of the meteorology of the 27-28 October FIRE Cirrus IFO case will be presented. The progression of synoptic scale events over the region will be reviewed including the the evolution of surface and upper air features, i.e., the surface cyclone that formed to the west over Montana on the 27th and moved through Wisconsin late on the 28th and the associated short wave ridge aloft. A summary of the corresponding cloud conditions observed over the area of aircraft operations will be given including characterization of the cloud forms and cloud heights based on information derived from debriefings of the aircrews, surface observations, airborne (ER-2) and surface lidars observations and satellite imagery (GOES). The correspondence between the resolved meteorological features (subsynoptic rawinsonde network) and the development of cloud layers will be illustrated. In particular, the discussion will emphasize the relationship between vertical thermodynamic structure and the character and vertical structure of the cloud fields. The role of the larger scale in maintaining the observed vertical structure will be quantified both with respect to its control via forced ascent and advective processes. Based on results of these analyses, conclusions will be drawn with respect to the design of future field missions. A handout will be provided.

A FOUR-LIDAR VIEW OF CIRRUS FROM THE FIRE IFO:

27-28 OCTOBER 1986

Kenneth Sassen
Meteorology Department, University of Utah
Salt Lake City, UT 84112

Christian John Grund
Meteorology Department, University of Wisconsin
Madison, WI 53706

Jose M. Alvarez
NASA Langley Research Center
Hampton, VA 23665

Freeman F. Hall
NOAA Wave Propagation Laboratory
Boulder, CO 80303

The four ground-based lidar systems that participated in the 1986 FIRE IFO were configured in a diamond-shaped array across central and southern Wisconsin. Using the analogy of a baseball diamond, the base paths were 125 km long. Stationed at home plate at Madison was the University of Wisconsin High Spectral Resolution Lidar (HSRL) with a 0.51 μm wavelength; first base at Oshkosh, the NOAA/WPL scanning CO_2 Doppler lidar (10.6 μm); second base at Wausau, the University of Utah polarization ruby lidar (0.69 μm); and third base at Ft. McCoy, the NASA/LRC polarization cloud lidar (frequency-doubled Nd YAG at 0.53 μm). Data were generally collected in the zenith-pointing mode, except for the Doppler lidar, which regularly operated in a scanning mode with intermittent zenith observations.

As a component of the cirrus case study of 27-28 October 1986 selected for initial analysis, data collected by the remote sensor ensemble from 1600 (on the 27th) to 2400 UTC (on the 28th) will be described and compared. Data were collected nearly continuously over this period by the HSRL, but night operations at the three other sites were suspended for operator rest periods, and fog and low stratus cloud conditions occasionally interrupted data collection at Wausau and Oshkosh. Nonetheless, the 32-h dataset provided an interesting and fairly comprehensive view of the movement of cirrus clouds over the central Wisconsin area. Note that the average cirrus level winds were ~30 m s^{-1} out of the northwest late on the 27th, changing to westerly on the 28th, such that cloud advection was approximately orthogonal to the north-south axis of the lidar field site grid.

In general, the cirrus studied on the 27th consisted of intermittent layers of thin and subvisual cirrus clouds. Particulary at Wausau, subvisual cirrus was detected from 11.0-11.5 km MSL, just below the tropopause. At lower levels, occasional cirrus clouds between ~8.0-9.5 km were detected from all ground sites. These layers were thickest at Ft. McCoy and Oshkosh. Although measurements are only available for the Madison lidar between 0200-0800 UTC, these data reveal the passage of an exceptionally well-defined Mesoscale Uncinus Complex (MUC) from 0500-0630 UTC. Although this structure attained a maximum cloud depth of nearly 4 km and was ~150 km in horizontal extent, the high resolution view provided by the HSRL provides evidence for the ~1 km scale of numerous cirrus uncinus generating cells and fallstreaks. Subsequently, as the full complement of lidars was restored, the develoment of a ~5 km-thick cirrus cloud system was observed. Initially, rather thin cloud layers were intermittently present at about 8.0 and 11.0 km. Laser depolarization data indicate that the lower layer was an altocumulus cloud containing supercooled cloud droplets, which produced virga. With continued upper level cloud develoment, however, it appears that the altocumulus cloud became incorporated in the cirrus ice cloud system. Following the passage at Wausau of a well-defined cloud band, all sites recorded little or no cirrus from 1800-1900 UTC, before clouds again began developing from cirrus generating cells located near the tropopause.

In summary, preliminary analysis of the four-lidar dataset reveals the passage of surprisingly consistent cloud features across the experiment area. A variety of types and amounts of middle and high level clouds occurred, ranging from subvisual cirrus to deep cloud bands. It is expected that the ground-based lidar measurements from this case study, as well as the airborne observations, will provide an excellent data base for comparison to satellite observations.

Acknowledgments. Support for the university-based research programs has come primarily from NSF Grant ATM-85 13975 (Utah), and ARO Grant DAA G29-84-K-0069 and ONR Contract N00014-85-K-0581 (Wisconsin).

RADIATIVE PROPERTIES OF CIRRUS CLOUDS: FIRE IFO CASE 10/28/86

PAUL F. HEIN, WILLIAM L. SMITH, JR., AND STEPHEN K. COX

Department of Atmospheric Science, Colorado State University, Fort Collins, CO 80523

1. Data Analysis Procedures

A description of the radiative properties of two cirrus clouds sampled on 10/28/86 in the FIRE cirrus IFO is presented. The clouds are characterized in terms of the broadband infrared effective emittance, cloud fractional absorptance, shortwave (.3-2.8μ m) heating rate, cloud albedo and vertical velocity. The broadband fluxes used in these calculations were obtained from measurements made by pyranometers and pyrgeometers manufactured by Eppley Laboratories Inc. For a description of these radiometers and calibration procedures, see Albrecht and Cox (1976), Albrecht and Cox (1977) and Smith Jr. *et al.* (1988). In addition, the shortwave irradiances were corrected to a horizontal plane and normalized to the same time by taking into account Sabreliner flight information (i.e. pitch, roll, heading and angle of attack), as well as sun-earth geometry considerations (Ackerman and Cox, 1981; hereafter AC).

Since only one aircraft was used, broadband fluxes at different levels in the cloud were not measured simultaneously. As a result, sampling errors may occur due to the nonsteady state of the cloud field or due to the possibility that the flight legs were not flown directly above or below each other. To minimize these errors and to simplify the analysis, the necessary variables were averaged and the averages used in the calculations. The averaging for each flight leg was done in the following ways:

(1) Average the appropriate variables using every data point along a flight leg to determine a mean value for the cirrus cloud field.

(2) Average some percentage of the data to stratify the cloud into separate regimes (i.e. optically thicker or thinner than average).

The downwelling shortwave and longwave irradiances were used as selection criteria to remove cloud free data encountered along the data sampling leg.

(a) Shortwave Stratification

Find the lowest 30% of the downwelling shortwave irradiance values along each flight leg and average all irradiance variables corresponding to these points.

(b) Longwave stratification

Find the highest 30% of the downwelling longwave irradiance values along each flight leg and average all irradiance variables corresponding to these points.

The effective emittance (ϵ^*) is the ratio of the observed change in irradiance through a cloud layer to the change that would have occurred had the cloud been black. ϵ^*, as derived from the downward irradiance may defined as:

$$\epsilon^*(\downarrow) = \frac{H_B(\downarrow) - H_T(\downarrow)}{\sigma T_B^4 - H_T(\downarrow)}$$

where H( ) refers to the observed downwelling infrared irradiance, T is the mean temperature along the flight leg, the subscripts T and B refer to the top and bottom of the cloud layer, respectively, and σ is the Stefan Boltzman constant.

The cloud fractional absorptance (CFA) is described by AC and is defined as:

$$CFA = \frac{(H\downarrow - H\uparrow)_T - (H\downarrow - H\uparrow)_B - \sum_i H_{S_i}}{H\downarrow_T},$$

where

$(H\downarrow - H\uparrow)_T \equiv$ net irradiance at cloud top,
$(H\downarrow - H\uparrow)_B \equiv$ net irradiance at cloud base,
$\sum_i H_{S_i} \equiv$ net energy gain or loss through cloud sides (i.e., $\partial Hx/\partial x + \partial Hy/\partial y$),
$H\downarrow_T \equiv$ incoming irradiance at cloud top.

In seeking ways to quantitatively express the spatial variability of the observed variables, two techniques have been applied: a histogram analysis and a cumulative variance summary.

The histograms were created by applying thresholds to detrended data and calculating the size (in kilometers) of each section that exceeded the threshold. These sizes were then combined to form the histograms. In Figure 1, an example graph, the +1 SD (standard deviation) threshold is exceeded between points F and G. The distance between F and G is then the size used in creating the histogram with the threshold of +1 SD. The count of the appropriate bin size will then be incremented. Similarly, the distance between E and H is the size used to increment the count of the appropriate bin for the +0.0 threshold. For the negative thresholds, -0.0 and -1 SD, the values must be less than the threshold (instead of being greater than for the positive thresholds) for the threshold to be exceeded. Thus, the section between points B and E, and the section between H and K, exceed the -0.0 threshold. Similarly, the section between points C and D, and the section between points I and J, exceed the -1 SD threshold. Sections of the graph at the ends of the data set that exceed a threshold (*i.e.* section to the left of point B for the +0.0 threshold) are not used because the size is unknown. Each histogram contains several different heights to increase the total number of sizes. Since the thresholds are based on standard deviations and not absolute values, the distribution of sizes at each height is expected to be similar.

The cumulative variance graphs were created by first using Fast Forrier Transforms to create a variance spectra. The variances were then summed in a cumulative fashion from the largest scalelengths (wavelengths) to the smallest. No detrending was done to the original data and no smoothing or averaging was done to the spectral points. Also, no points were removed due to the effect of the finite length of the file. This means that the spectral points at scalelengths larger than about 4000 m (especially greater than 8000 m) may only be qualitatively correct. The cumulative variance at the smaller scalelengths should be correct because a more accurate representation of the variance at the larger scalelengths should only redistribute the energy amongst the larger scalelengths.

2. Flight Description

The Sabreliner flight on the morning of 28 October 1986 was flown over the western shore of Lake Michigan. There was a shortwave (pressure) ridge over the region with a trough approaching from the west.

The cirrus, the Sabreliner flew through, was thin and had a banded structure. Cloud base of the upper cloud deck varied from about 8.8 km to 9.2 km with broken undercast beneath. Cloud top was at about 11.0 km.

The Sabreliner flew a racetrack pattern with the flight legs being oriented about 30 degrees off of the mean wind direction WNW. Because of the racetrack pattern, it became apparent that the cloud on the NW side had different characteristics than the cloud on the SE side of the racetrack. Therefore the data from each racetrack side were treated separately. "Cloud 1", on the SE side of the racetrack pattern, included the flight legs at heights: 11.3 km, 10.0 km, and 8.8 km. "Cloud 2", the NW side of the racetrack, was sampled at heights: 10.7 km, 9.4 km, and 8.5 km. Tables 1a and 1b show the times, positions and headings of the flight legs for each of the designated clouds.

Table 1a. Cloud 1 flight leg times, positions and headings.

Table 1a. Cloud 1 flight leg times, positions and headings.

Height (km)	Time (GMT)	Start Lat	Long	Time (GMT)	End Lat	Long	Heading
11.3	15:45:48	44.29	-87.89	15:48:08	44.45	-87.41	130
10.0	16:00:56	44.27	-87.89	16:04:31	44.45	-87.36	118
8.8	16:16:47	44.28	-87.93	16:20:41	44.44	-87.36	113

Table 1b. Cloud 2 flight leg times, positions and headings.

Table 1b. Cloud 2 flight leg times, positions and headings

Height (km)	Time (GMT)	Start Lat	Long	Time (GMT)	End Lat	Long	Heading
10.6	15:36:23	44.37	-87.44	15:41:54	44.13	-88.14	292
10.7	15:53:20	44.06	-87.86	15:57:17	44.54	-87.91	288
9.4	16:07:45	44.65	-87.21	16:12:20	44.65	-87.93	289
8.5	16:24:44	44.12	-87.36	16:30:04	44.48	-88.11	275

3. Results

Cloud fractional absorptance values were deduced from pyranometer measurements in the .3-2.8 μ m spectral region with a correction made for sampling of finite cloud effects in the manner described by AC.

Figure 2 shows a plot of the solar cloud fractional absorptance vs the infrared emittance for the two, two layer cloud samples defined in Table 1. The lower values represent a layer with a 1.3 km geometric thickness while the higher values represent a 2.5 km thick layer. Values derived from both the SW stratification and the LW stratification are shown. As we mentioned above, the stratification of the data was necessary to eliminate the banded structure of cirrus cloud within each data leg. In essence, both clouds for both stratifications show very similar radiative properties with emittances between .48 and .55 for the thicker layers and .28 and .30 for the thinner layers; similarly the SW fractional absorptance varies from .08 to .09 for the thicker layers and .05 to .06 for the thinner layers. Within the errors of the observations, the slopes of the lines connecting these points for the two clouds are essentially the same.

Layer SW heating rates for these same cloud layers are given in tables 2 and 3. The heating rates for the two layers are encouragingly similar as would be expected from the previous figure; for the top 1.3 km layer they vary between .23 and .29 ° C/hr and for the lower layer between .15 and .17 ° C/hr.

Figure 3 represents the SW reflectance observed at cloud top for Cloud 2 for three spectral bandpasses. This is an example of the structure of the observations in the raw data.

Figures 4 shows the results of the histogram analysis of scale size variation on the measured vertical velocity. It is notable that most of the vertical velocity "cells" have horizontal dimensions less than 3 km. Figure 5 shows that the downward visible irradiance shows essentially the same structure as the vertical velocity.

Figure 6 shows the cumulative variance analysis for the albedo at the top of cloud 2. The continuous line is a fit to the plotted data points. This graphs may be interpreted to show the per cent variance explained by scale lengths larger than a given value. For example, this figure suggests that 85% of the variance arises from features whose horizontal scale is greater than 10 km. Figure 7 illustrates the cumulative variance analysis for vertical velocity applied to each of the flight levels in the sample of cloud 2. The solid curve represents the 10.6 km height, the dashed curve - 9.4 km, and the dotted curve - 8.5 km. Notable is the narrowing of the scale length with increasing height. Fifty percent of the variance is explained by features larger than 13 km at the 10.6 km height, larger than 22 km at the 9.4 km level and larger than 50 km at the 8.5 km level.

4. Acknowledgements

This research has been supported by the National Science Foundation under Grant ATM-8521214 and by the National Aeronautics and Space Administration under Grant NAG 1-554.

REFERENCES

Ackerman, S. A., and S. K. Cox, 1981: Aircraft observations of the shortwave fractional absorptance of non-homogeneous clouds. *J. Appl. Meteor.*, **20**, 0128-0133.

Albrecht, B., and S. K. Cox, 1977: Procedures for improving pyrgeometer performance. *J. Appl. Meteor.*, **16**, 188-197.

Albrecht, B., and S. K. Cox, 1976: Radiation data reduction procedures for Sabreliner, C-130 and DC-6 aircraft during the GARP Atlantic Tropical Experiment. Colorado State University *Atmospheric Science Paper No. 244*, Fort Collins, CO., 100 pp.

Smith, Jr., W. L., S. K. Cox and V. Glover, 1988: Temperature sensitivity of Eppley broadband radiometers. Colorado State University *Atmospheric Science Paper No. 432*, Fort Collins, CO., 12 pp.

Table 2. Layer heating rates (.3-2.8 µm) in degrees/hr. for Cloud 1

Z = 11.2 Km	MEAN	IR STRATIFICATION	SW STRATIFICATION
Z = 10.0 Km	*	.335 (.710)	.361 (.309)
Z = 8.8 Km	.171 (.310)	.162 (.360)	.172 (.351)
	Values in parentheses uncorrected for cloud inhomogeneities		

*indicates heating rate indeterminate

Table 3. Layer heating rates (.3-2.8 µm) in degrees/hr. for Cloud 2

Z = 10.7 Km	MEAN	IR STRATIFICATION	SW STRATIFICATION
Z = 9.4 Km	*	.300 *	.288 (.431)
Z = 8.5 Km	.159 (.158)	.160 (.161)	.148 (.158)
	Values in parentheses uncorrected for cloud inhomogeneities		

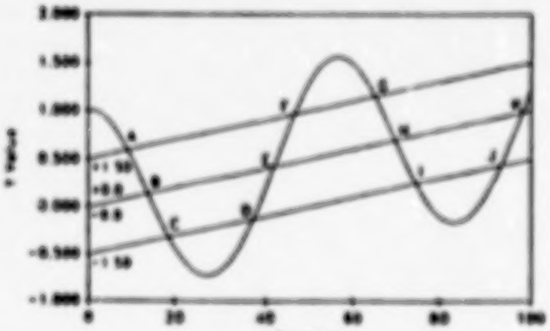

Figure 1. Example plot illustrating procedure for generation of size histogram plots (figs. 4 and 5).

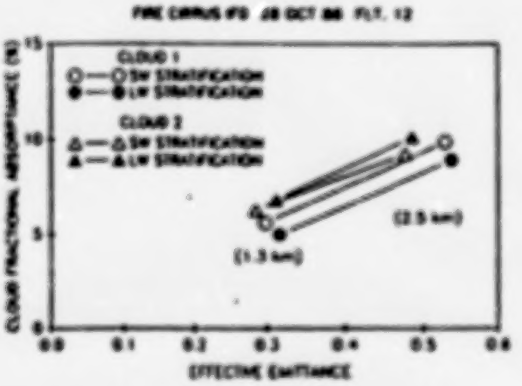

Figure 2. .3-2.8 μ m CFA vs. effective emittance for Cloud 1 and Cloud 2.

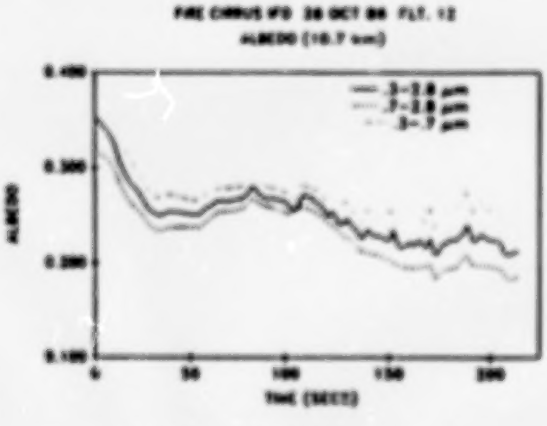

Figure 3. Albedo for Cirrus Cloud 2.

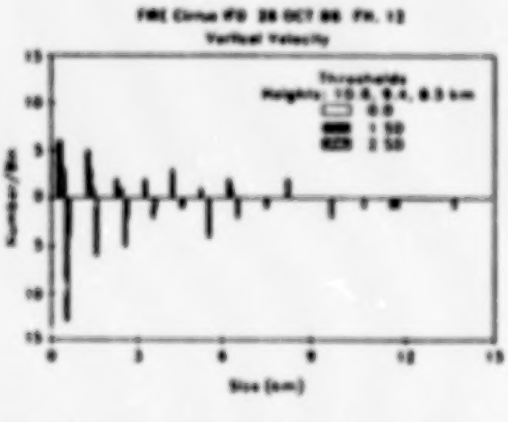

Figure 4. Histogram illustrating observed vertical velocity scale sizes (SD is standard deviation from detrended mean).

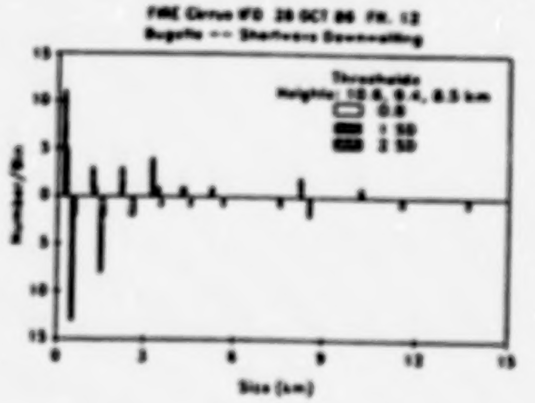

Figure 5. Same as Figure 4 but for downwelling shortwave irradiance.

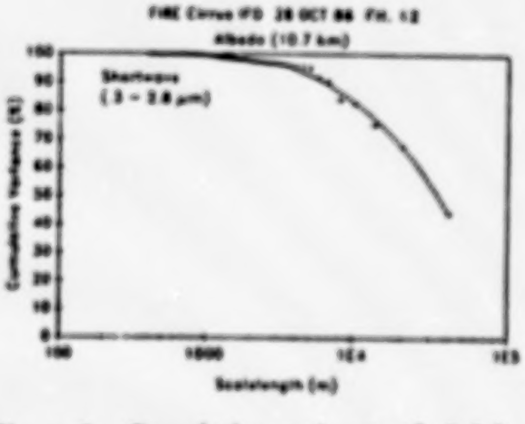

Figure 6. Cumulative variance of .3-2.8 μ m albedo for Cloud 2.

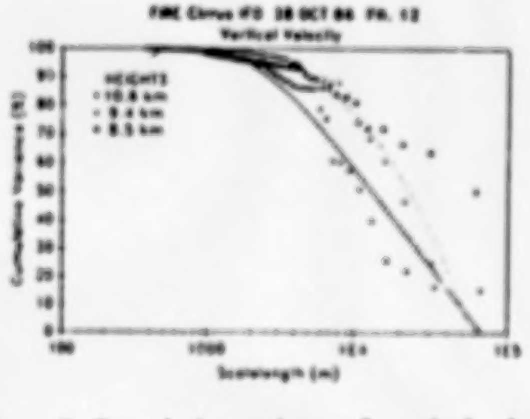

Figure 7. Cumulative variance of vertical velocity at different heights in Cloud 2.

FIRE CIRRUS ON 10/28/86: LANDSAT; ER-2; KING AIR; THEORY

Bruce A. Wielicki and John T. Suttles
Atmospheric Sciences Division
NASA Langley Research Center
Hampton, VA. 23665-5225

Andrew J. Heymsfield
National Center for Atmospheric Research
Boulder, CO. 80302

Ronald M. Welch
South Dakota School of Mines and Technology
Rapid City, SD. 57701

James D. Spinhirne
NASA Goddard Space Flight Center
Greenbelt, MD. 20771

Lindsay Parker and Robert F. Arduini
Planning Research Corporation
Hampton, VA. 23602

I. INTRODUCTION

The purpose of this study is to conduct a simultaneous examination of cirrus clouds in the FIRE Cirrus IFO-I on 10/28/86 using a multitude of remote sensing and in-situ measurements. The focus of the study is cirrus cloud radiative properties and their relationship to cloud microphysics. A key element of this study is the comparison of radiative transfer model calculations and varying measured cirrus radiative properties (emissivity, reflectance vs. wavelength, reflectance vs. viewing angle). As the number of simultaneously measured cloud radiative properties and physical properties increases, more sharply focused tests of theoretical models are possible.

II. CALIBRATION AND NAVIGATION

The area of interest is shown in Figure 1 using the Landsat 11.5μm brightness temperature. The region shown is 2048 by 2048 pixels with a length of 58.4 km on a side. Time of the Landsat overpass is 1553 GMT on 10/28/86. Calibration for all Landsat channel radiances is taken from Markham and Barker (1986). Absolute accuracy of solar reflectance bands is estimated as 10 percent of any radiance value.

Figure 1 also gives the aircraft tracks of the ER-2 and King Air aircraft. Nominal navigation accuracy for Landsat and aircraft is 1 km. The King Air track (curved in Figure 1) has been advected using the King Air wind measurements (7.3 km altitude), in order to compensate for the cloud motion between the time of the aircraft observations and the time of the Landsat overpass. Typical wind speeds are 16 m sec^{-1} from the west (270°), giving a largest advection distance of 15 km for the King Air data at 1536 GMT shown at the top of Figure 2. The opposite end of the King Air track required a correction of 1 km.

The ER-2 observations are taken within ± 2 minutes of 1553 GMT and require maximum wind corrections of 2 km. For all multiple platform intercomparisons, radiance data from the ER-2 and Landsat are spatially averaged to 1 km resolution in order to reduce the effect of noise from limitations in navigation accuracy and time simultaneity.

III. NADIR REFLECTANCE VERSUS 11.5μm EMISSIVITY

Figure 2 gives the observed nadir reflectance R versus 11.5μm effective emissivity ϵ using the Landsat radiances along the ER-2 groundtrack (data given as points). Nadir reflectance is calculated as an equivalent Lambertian reflectance, $R = \pi L/S_0 \cos\theta_0$, where L is spectral radiance ($Wm^{-2}sr^{-1}\mu m^{-1}$), S_0 is solar spectral flux ($Wm^{-2}\mu m^{-1}$) averaged over the narrow spectral bandpass, and θ_0 is the solar zenith angle (63°). Effective emissivity is calculated following Platt et al (1980), $\epsilon = (L_{clr} - L_m)/(L_{clr} - L_{cld})$ where L_m is the measured 11.5μm radiance, L_{clr} is the clear-sky 11.5μm radiance determined using the apparently clear area in the lower right of Figure 2, and L_{cld} is the blackbody radiance which would be emitted by an optically thick cloud at the altitude of the cirrus layer. Cloud altitude is determined using the ER-2 lidar data.

Backscatter crossections from the ER-2 downlooking lidar give two cloud layers beneath the ER-2. The lower cloud layer is between 6.9 and 8.0 km altitude, while the upper layer is between 8.9 and 11.2 km altitude. An examination of optically thick portions of the cloud field (nadir 0.83μm reflectance between 50% and 60%) using the Landsat 10.8μm channel data gave an emitting temperature of 231K, which the Green Bay radiosonde places at an altitude of 9.0 km. This would place an optically thick cirrus cloud layer at an altitude where no cirrus was visible in the lidar backscatter, a puzzling result. One possibility for the discrepancy in these results is that the optically thick brightness temperature measured by the Landsat (and ER-2) radiometers was produced by a combination of an optically thick lower layer with cloud top at 8 km and an optically thin overlying cirrus at 9-11 km. In this initial work, an 9.0 km cloud height is used for emissivity calculations. If the appropriate cloud altitude were in fact 7.5 km, or 10.0 km, an error of ± 15% in 11μm emissivity would occur.

Figure 2 compares the measured 0.83μm reflectance vs 11μm emissivity to theoretical calculations. In order to make the model and measurements more directly comparable, the first order reflectance of the surface (Lake Michigan) has been removed as described in Platt et al (1980). This correction causes the data to tend to zero reflectance and zero emissivity as cloud optical depth tends to zero. The correction is approximately 4% in nadir reflectance for small optical depths, decreasing to no correction for large optical depths. The theoretical results are shown for calculations of cloud albedo using a Delta-Eddington approximation with single scattering albedo = 1.0; asymmetry factor g = 0.88 for spherical drops and g = 0.73 for cylindrical ice particles; and the ratio of scattering optical depth at 0.83μm $\tau_s(0.83)$ to absorption optical depth at 11.4μm $\tau_a(11.4)$ is taken as $\tau_a(11.4)/\tau_s(0.83) = 0.57$ for spheres and 0.50 for cylinders. These parameters are those used in Platt et al (1980). In all modeled results, emissivity is absorption emissivity. Wielicki (1980) showed that effective nadir emissivity is within 1% of absorption emissivity for 11.5μm radiation in spherical ice clouds 20μm mode radius, using ATRAD adding doubling calculations (Wiscombe, 1975). Finally, multiple scattering calculations were performed using the Finite Difference method (Barkstrom, 1976) as extended by Suttles (1986). The Finite Difference method produced estimates of nadir relfectance meant to be directly comparable to the Landsat reflectance. The Finite Difference code was run using a single scattering albedo of 1.0 and a double Heyney-Greenstein phase function with parameters b=0.98, g_1=0.9, and

g_2= -0.5. Figure 3 compares this phase function with a single H-G phase function (g=0.9) and with two phase functions from Liou, 1973 for Mie calculations of spherical water drops, and for theoretical calculations for randomly oriented cylinders. In general, the cylinders exhibit much more side scattering (60 to 120° scattering angles) than do spheres. The double H-G phase function is intermediate between the sphere and cylinder phase functions. Note that for single scatter, radiation scattered from the solar zenith angle of 63° to nadir for Landsat would have a scattering angle of 117°, where large differences in the three phase functions occur. Figure 2 indicates that the measured nadir reflectances are much larger than those predicted using the double H-G, indicating larger side scattering, more consistent with the cylindrical phase function. Figure 2 also demonstrates the large anisotropy of reflected radiation for thin cirrus. Albedo is much larger than nadir reflectance (Finite Difference albedo is very similar to the Delta-Eddington values for spheres), indicating the importance of using multiple-scattering calculations capable of determination of viewing zenith and azimuth variations of reflected radiation (see also King, 1987). Future work will investigate Mie calculations using the observed King Air microphysical measurements, and hexagonal ice crystal phase functions.

IV. MULTIPLE ANGLE VIEWS OF CIRRUS

Given the large differences between nadir reflectance and albedo for optically thin cloud, an additional independent test of theoretical calculations is their ability to predict the reflectance anisotropy as a function of viewing zenith angle and viewing azimuth angle. A particularily useful test is the determination of the ratio of reflectance at two viewing angles of the same cloud. This ratio eliminates sensitivity to uncertainties in the absolute gain calibration of the radiometer. The ER-2 flight path on 10/28/86 was chosen to provide observations as a function of angle in the solar plane (i.e. viewing azimuth angle of 0° (forward scatter) while scanning to the right of the aircraft, and 180° (backward scatter) while scanning to the left of the aircraft). Figure 4 gives a schematic of the geometry for the Landsat/ER-2 intercomparison.

The first step in this process is to use the nadir ER-2 observations to intercalibrate the ER-2 and Landsat radiometers. After navigation, a regression of 1-km averaged ER-2 and Landsat radiances gave R(ER-2) = 0.779*R(Landsat) - 1.61 (units of nadir reflectance) with a 2σ uncertainty in the gain of ± .025 and correlation coefficient of 0.993. While the final agreement between the radiometers is good, the relative gain differences in these two radiometers at 0.83μm is larger than expected. More careful calibrations of narrowband radiometers are recommended for future work.

Having navigated and intercalibrated the Landsat and ER-2 radiometer data at nadir, off nadir observations at 30° were examined. In view of the presence of two cloud layers, and lack of lidar data for off nadir viewing, the 30° viewing zenith data was navigated using test cloud altitudes between 6.5 and 12.5 km. Spatial variations in the 30° viewing zenith ER-2 data matched those in the nadir Landsat view when cloud height was set to 7.5 km, in the center of the lower cloud layer. Poor correlations were found assuming cloud heights within the upper cloud layer. This test indicates that the shortwave radiative properties are dominated by the lower cloud level, consistent with microphysical measurements showing increasing ice water content with decreasing cloud height.

After subtracting off the surface reflectance contribution as in section III, measured cloud reflectance ratios $R(\theta=30,\phi=0)/R(\text{nadir})$ ranged from 1.3 to 1.5, where θ is viewing zenith angle and ϕ is viewing azimuth angle relative to the solar plane ($\phi=0$ is forward scatter). Cloud reflectance ratios for backscattered radiation $R(\theta=30,\phi=180)/R(\text{nadir})$ ranged from 0.8 to 1.2. Theoretical calculations for the reflectance ratios using the Finite Difference model discussed in section III are shown in Figure 5, and show more anisotropy in both forward and backscatter ratios than the data. Recall that the scattering optical depth given in Figure 5 is approximately twice the absorption optical depth at 11.4μm, so that scattering optical depth 1 is approximately an emissivity at 11.4μm of $1-\exp(-0.5) = 0.39$, typical of the data shown in Figure 2. Note that the reflectance ratio is a strong function of optical depth in Figure 5, indicating the importance of cloud optical depth when using radiance (i.e. bidirectional reflectance) to estimate flux. This might impact the accuracy of ERBE derived fluxes for optically thin cirrus cloud.

V. NADIR REFLECTANCE: VISIBLE AND NEAR-INFRARED WAVELENGTHS

Theoretical calculations predict that cloud reflectance in near-infrared windows such as those at 1.6μm and 2.2μm should give lower reflectances than at visible wavelengths. The reason for this difference is that ice and liquid water show significant absorption at these wavelengths, in contrast to the nearly conservative scattering at visible wavelengths. In addition, because the amount of absorption scales with the thickness of the particle, increasing cloud particle size should lead to decreasing reflectances at 1.6μm and 2.2μm. Measurements of these wavelengths have to date, however, given unpredicted results (Twomey, 1982; Curren et al, 1982).

The Landsat satellite has channels with central wavelengths at 0.83μm, 1.65μm, and 2.21μm which cover this range of variation in cloud absorption. Figure 6 gives the ratio R(2.21μm)/R(0.83μm) for the Nadir Landsat data along the King Air ground track. At 153830GMT (at 13.7 km on the distance scale in Figure 6, the King Air aircraft took a direct sample of the cloud particles and found almost entirely water droplets, approximately 5-10μm in radius. This corresponds to the large anisotropic ratio (near 0.75) found in the Landsat data. A second direct cloud particle sample was collected at 1552GMT, consisting strictly of ice particles (broken spatial plates and some columns, 20 to 300μm in length). This second sample corresponds to a distance of 88 km in Figure 6 and shows a low measured reflectance ratio (≈0.5).

Figure 7 compares theoretical calculations using the Finite Difference radiative transfer model with the measured nadir reflectance at 0.82 and 2.2μm along the King Air groundtrack. It is evident that there are two distinct populations of cloud particles along the 88 km track. The high reflectance ratio values in Figure 6 appear along the diagonal of nearly equal reflectance at the two wavelengths and are consistent with water or ice droplets with mode radius of 7.5μm or less. The remaining data indicates larger particles of about 30μm mode radius. Examination of the 1.6μm versus 2.2μm data indicate that the 7.5μm particles are water as opposed to ice. Further work using the King Air microphysical data along this groundtrack will allow determination of the effective particle size of the ice crystals in the lower cloud. The Sabreliner will provide microphysical data for the upper cirrus level, although on a different flight path.

VI. CONCLUSIONS

The 10/28/86 data provides a unique opportunity to compare measured and theoretical cloud properties for cirrus clouds. Overall impressions from the present analysis are:

1. The cirrus clouds produced more side-scattered radiation (scattering angle 60°-120°) than predicted by spherical particles. Cylindrical particle scattering appears to better describe the cirrus properties.

2. Variation of measured cloud reflectance at 0.82μm versus 2.21μm was consistent with King Air cloud particle samples, and in reasonable agreement with theoretical calculations.

3. The lower cirrus layer (7-8 km) appeared to dominate the cloud radiative properties as viewed by the ER-2 and Landsat. Initial indications from King Air and Sabreliner microphysics confirm the larger ice water contents in the lower cloud layer.

4. Better calibrations of narrowband shortwave radiometry are desired.

Future work will test use measured cirrus microphysical properties to determine phase functions used in the radiative transfer calculations, and to compare measured particle size to ratios of visible and near-infrared reflected solar radiation.

VII. REFERENCES

Barkham, B. L. and J. L. Barker, 1986, Landsat Technical Notes, August 1986.

Barkstrom, B. R., 1976: JQSRT, 16, 725-739.

Curren, R. J. and M. L. C. Wu, 1982. JAS, 39, 635-647.

King, M. D., 1987: JAS, 44, 1734-1751.

Liou, K. N., 1973: JGR, 78, 1409-1418.

Platt, C. M. R., et al., 1980: MWR, 108, 195-204.

Suttles, J. T., 1985: In Radiative Transfer in Scattering and Absorbing Atmospheres. Edited by J. Lenoble, A. Deepak Publishing.

Twomey , S. and T. Cocks, 1982: JMSJ, 60, 583-592.

Wiscombe, W., 1975: Climate of the Arctic, G. Weller and S. Bowling, Eds., University of Alaska Press, 245-254.

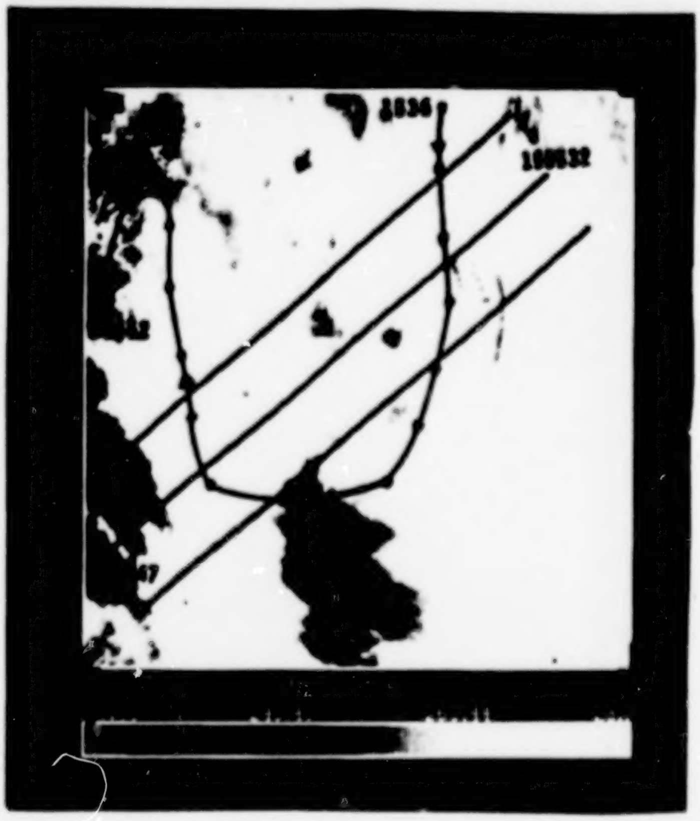

Figure 1

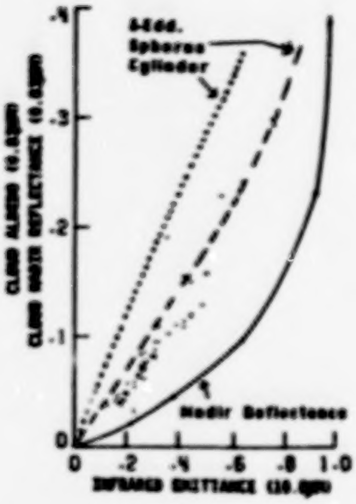

Figure 2

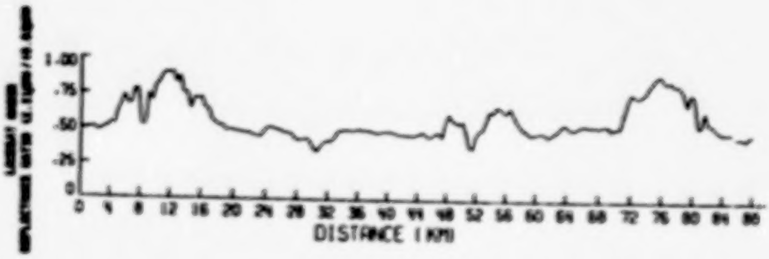

Figure 6

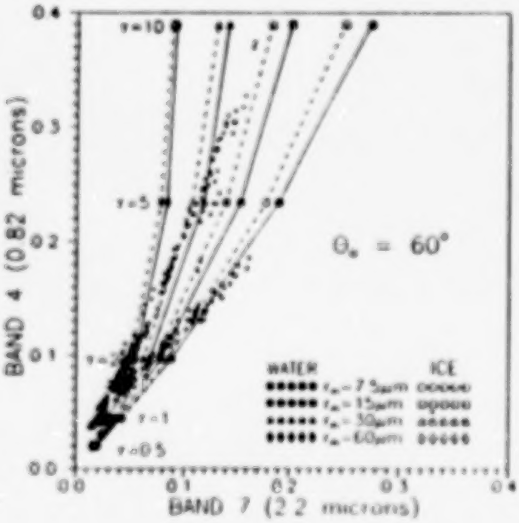

Figure 7

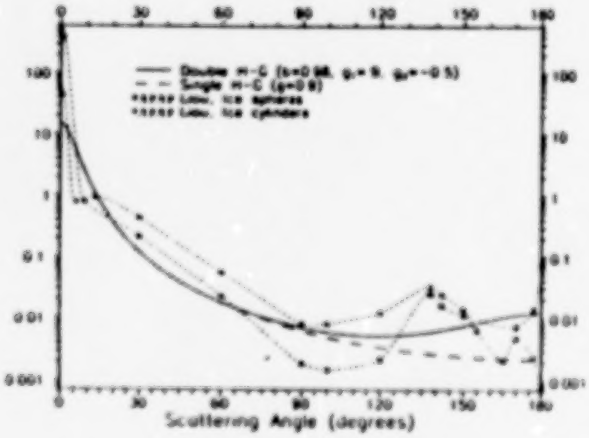

Figure 3

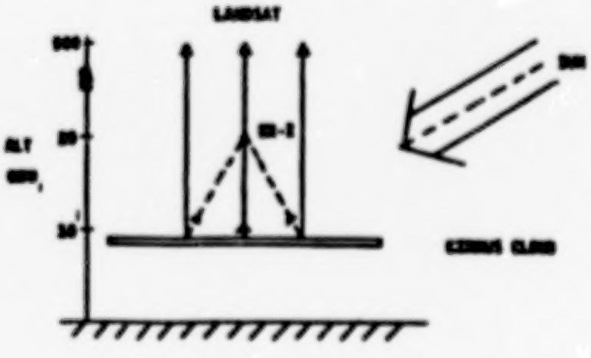
LANDSAT
SUN
CIRRUS CLOUD

Figure 4

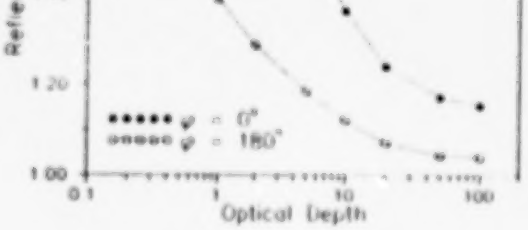

Figure 5

SURFACE RADIATION OBSERVATIONS FOR OCTOBER 27-28, 1986 DURING THE WISCONSIN FIRE/SRB EXPERIMENT

C. H. Whitlock, and L. R. Poole
Atmospheric Sciences Division,
NASA Langley Research Center
Hampton, Virginia 23665-5225

LeCroy, S. R.
Planning Research Corporation,
Hampton, Virginia 23666

D. A. Robinson
Lamont-Doherty Geological Observatory,
Palisades, New York 10964

The purpose of this paper is to present a portion of both the shortwave and longwave surface radiation data measured during the combined FIRE (First ISCCP Regional Experiment) and SRB (Surface Radiation Budget) experiments conducted in central Wisconsin from October 14 to November 2, 1988. Figures 1 and 2 summarize the time periods from which high quality measurement values were obtained. Data gaps exist because of either equipment malfunctions or electrical power failures. Intercomparison of pre-experiment measurements by the various organizations involved suggests that all stations are accurate (relative to each other) to within about 10 W/m^{-2} on a 24-hour daily average basis. Most of the instruments were calibrated by the National Radiation Centers in either the U.S. (National Oceanic and Atmospheric Administration) or Canada (Atmospheric Environment Service).

October 27-28, 1986 have been selected for detailed case study because a large amount of cirrus clouds existed over the experiment region on those days. Figures 3 and 4 show downwelled irradiance values at each surface station at the times of afternoon NOAA-9 overpasses. Unfortunately, October 27th was a day in which a number of the sites experienced unexpected problems. Values shown are 10-minute averages centered about each overpass time, but minute-average data are available. Similar data will be presented for both GOES and Landsat overpasses. In addition, time histories of each site will be available for synchronization with aircraft overpasses which occurred during those two days. Downwelled shortwave irradiance values will be correlated with narrow-band cloud optical depth values from Ft. McCoy in order to determine if there is a reasonable quantitative relationship between Eppley-measured surface shortwave irradiance and cirrus cloud optical depth.

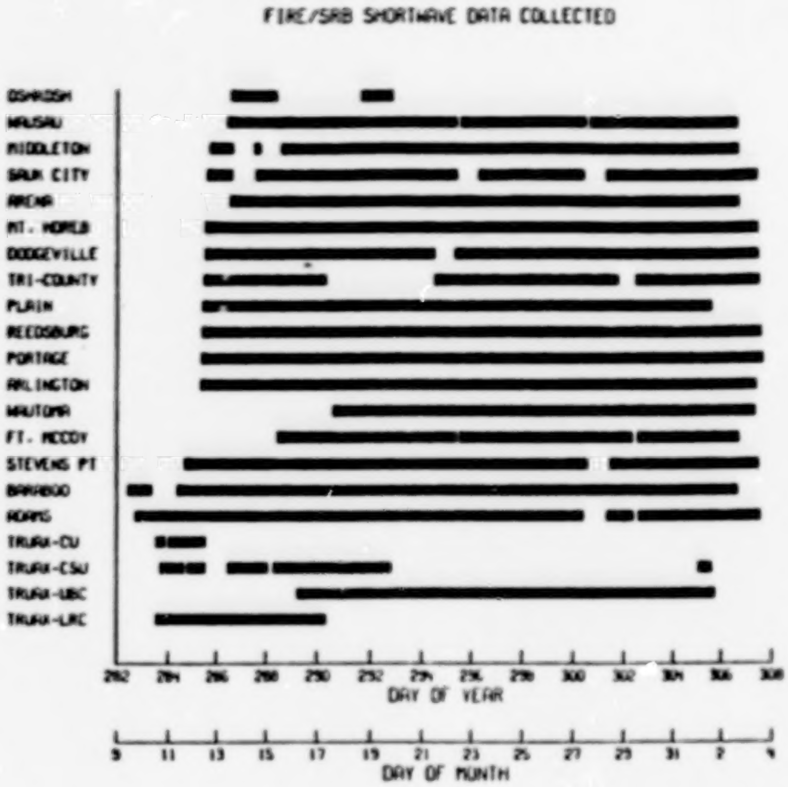

Figure 1. Wisconsin FIRE/SRB shortwave data periods.

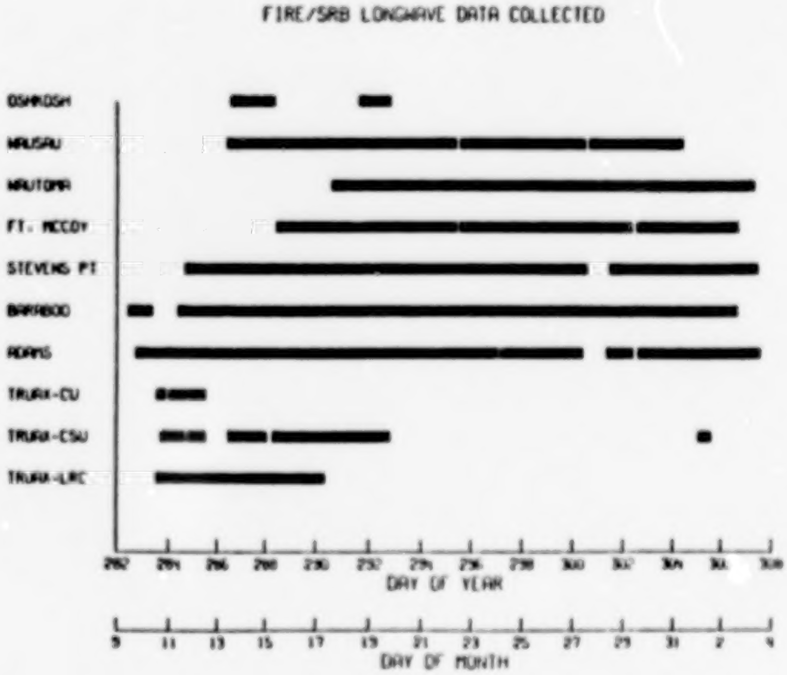

Figure 2. Wisconsin FIRE/SRB longwave data periods.

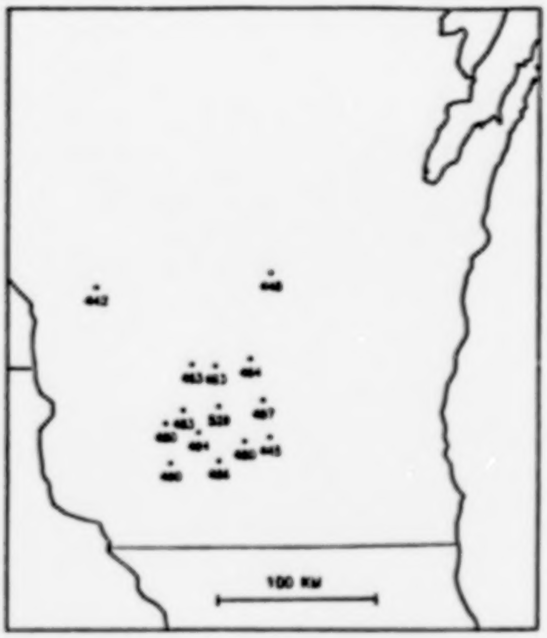

(a) October 27, 1986.

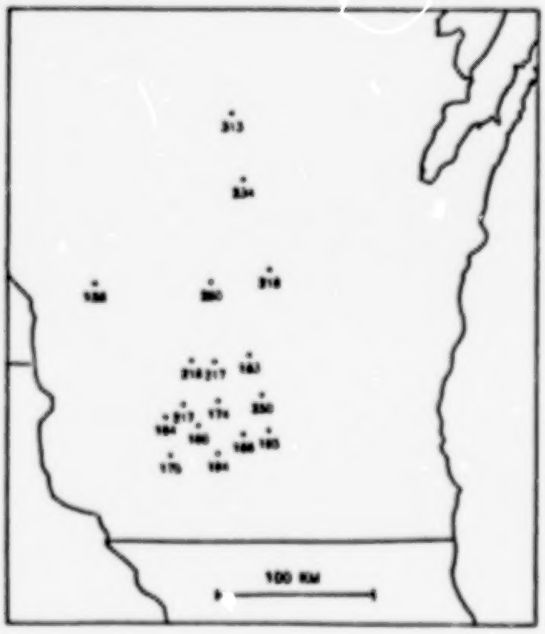

(b) October 28, 1986.

Figure 3. Downwelled shortwave surface irradiance (W/m²) at time of afternoon NOAA-9 overpass.

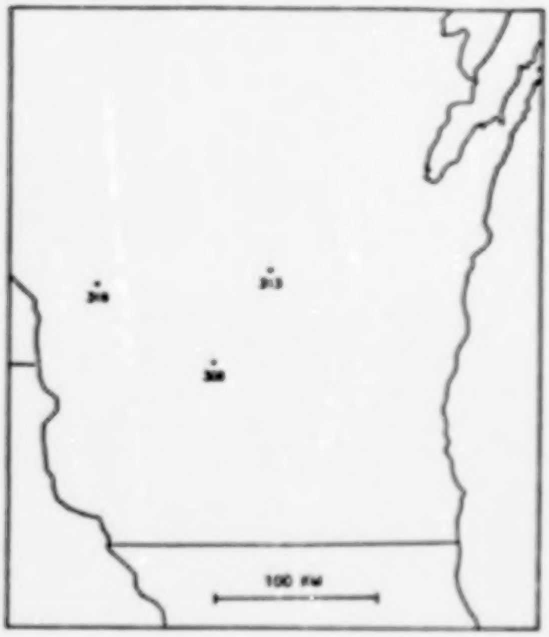

(a) October 27, 1986.

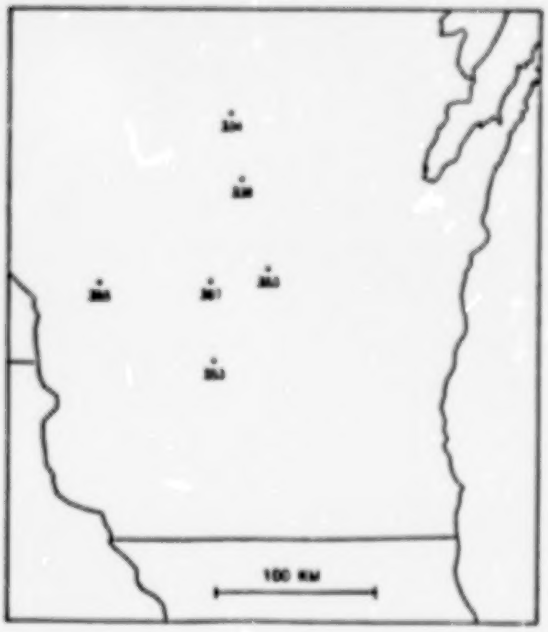

(b) October 28, 1986.

Figure 4. Downwelled longwave surface irradiance (W/m^2) at time of afternoon NOAA-9 overpass.

FIRE SCIENCE TEAM MEETING
VAIL, COLORADO
JULY 11-15, 1988

CIRRUS

CIRRUS POSTER SESSION - Stephen K. Cox Tuesday, July, 12, 1988

PAGE

The New FIRE Cloud Lidar at Langley Research Center 175
Alvarez, J. M.; M. P. McCormick, M. A. Vaughan, G. Kent, W. H. Hunt, W. H. Fuller, B. R. Rouse, and R. Dubinsky

Interpretation of the Optical and Morphological Properties of Cirrus Clouds from Lidar Measurements 177
Grund, Christian J.; and Edwin W. Eloranta

Temperature Sensitivity of Eppley Broadband Radiometers 183
Smith, Jr., William L.; Stephen K. Cox, and Vince Glover

Both Sides Now 187
Wylie, Donald

Sub-Visual Cirrus Detection and Characterization 191
Schmidt, E.; G. Grams, and E. Patterson

Cloud Atlas for the FIRE Cirrus Intensive Field Observation: October 5 - November 10, 1986 193
Arking, Albert; Jeffrey D. Childs, John Merritt, and Sharen L. Williams

Optical and Morphological Properties of Cirrus Clouds Determined by the High Spectral Resolution Lidar and Volume Imaging Lidar ***
Grund, Christian

Joint HSRL-HIS Lidar-IR Radiometer Experiment: June 13-17, 1988 ***
Grund, Christian

Satellite Measurements Over the Cirrus IFO, October 28, 1986 ***
Harrison, Edward F.; Patrick Minnis, and Paul Heck

Radiative Properties of Cirrus Clouds? FIRE IFO Case 10/28/86 ***
Hein, Paul F.; William L. Smith, Jr., and Stephen K. Cox

Cirrus Microphysics and Radiative Transfer: A Case Study on 10/28/86 ***
Kinne, S.; Thomas P. Ackerman, and A. J. Heymsfield

Climate Data Systems Supports FIRE ***
Olsen, Lola M.

FIRE Extended Time/Limited Area Observations at Palisades, NY ***
Robinson, David; George Kukla, and Allan Frei

FIRE SCIENCE TEAM MEETING
VAIL, COLORADO
JULY 11-15, 1988

CIRRUS

CIRRUS POSTER SESSION (Cont'd) - Stephen K. Cox Tuesday, July, 12, 1988

PAGE

FIRE Cirrus on 10/28/86; LANDSA; ER-2; King Air; Theory ***
Wielicki, Bruce A.; John T. Suttles, Andrew J. Heymsfield, Ronald M. Welch, James D. Spinhirne, Lindsay Parker, and Robert F. Arduini

Evidence for Asymmetric Inertial Instability in the FIRE Satellite Data ***
Stevens, Duane; and Paul Ciesielski

Lidar Measurements of Antarctic Polar Stratospheric Clouds in Support of Ozone Hole Studies ***
Uthe, Edward

Airborne/Lidar/Radiometric Study of Cirrus in Support of DOD Sensor Test Programs ***
Uthe, Edward

Operational Results for Surface Radiation Observations for October 27-28, 1986 During The Wisconsin FIRE/SRB Experiment ***
Whitlock, C. H.; L. R. Poole, S. R. LeCroy, and D. A. Robinson

Cirrus Radiation Parameters 10/28/86 ***
Spinhirne, J.

THE NEW FIRE CLOUD LIDAR AT LANGLEY RESEARCH CENTER

by

J. M. Alvarez[1], M. P. McCormick[1], M. A. Vaughn[2], G. Kent[3], W. H. Hunt[4], W. H. Fuller[1], B. R. Rouse[1], and R. Dubinsky[3]

Using the Langley 14" Aircraft Lidar for cirrus cloud observations at Langley Research Center in Hampton, Virginia is overkill both in terms of the actual lidar and the people required to run the system. A small lidar system to be used specifically for cloud probing was designed and constructed at Langley in 1987. This lidar is presently being used to collect the FIRE ETO (Extended Time Observation) data at Langley.

A description of the new FIRE Cloud Lidar System will be presented at this workshop. The data collected by this lidar will be discussed as well as some of the cloud statistics emerging from the data. A brief synopsis of system performance will also be given.

---

[1]NASA Langley Research Center, Atmospheric Sciences Division,
Hampton, VA 23665-5225
[2]Christopher Newport College, Newport News, VA 23601
[3]Science and Technology Corporation, 101 Research Drive, Hampton, VA 23666
[4]Wyle Laboratories, Hampton, VA 23666

Interpretation of the Optical and Morphological Properties of Cirrus Clouds from Lidar Measurements

Christian J. Grund and **Edwin W. Eloranta**
University of Wisconsin, Department of Meteorology
1225 W. Dayton St., Madison, Wi. 53706

I. Introduction

Lidar measurements can provide a great deal of information about the structure, location, and scattering properties of cirrus clouds. However, caution must be used when interpreting raw lidar backscatter profiles in terms of relative or absolute extinction distribution, internal cloud structure, and, at times, cloud location. The problem arises because the signal measured from a range by any monostatic lidar system depends on the backscatter cross section at that range and the 2-way optical thickness to the scattering volume. Simple lidar systems, however, produce only one measurement of attenuated backscatter from each range. It is the purpose of this paper to aid the general FIRE research community in interpretation of lidar measurements, and to explain the special capabilities of the High Spectral Resolution Lidar (HSRL). Some examples will be given of conditions under which direct interpretation of cirrus cloud morphology from simple lidar profiles could be misleading.

II. Lidar Theory

Simple lidar systems cannot separate the extinction and backscatter components of the lidar signal without additional information or significant assumptions about the atmosphere and/or scattering properties of the particles. This may be readily seen from the lidar equation

$$P(R) = \frac{E_0 \xi \frac{\beta_\pi(R)}{4\pi} e^{-2\int_0^R \beta_\varepsilon(r')\,dr'}}{R^2} + M(R) \qquad (1).$$

Here, $P(R)$ is the power incident upon the receiver from range R, E_0 is the energy of the transmitted pulse, $\xi = A_r \cdot c / 2$ where A_r is the receiver area and c is the speed of light, $\beta_\pi(R)$ is the backscatter cross section per unit volume, $\beta_\varepsilon(R)$ is the extinction cross section per unit volume, and $M(R)$ is the contribution from multiple scattering. The most frequently reported lidar measurement is $P(R) \cdot R^2/E_0$, the energy normalized and R^2 corrected backscatter. Both $\beta_\pi(R)/4\pi$ and $\beta_\varepsilon(R)$ are due to the effects of particles *and* molecules. The factor of 2 in the exponential term accounts for the extinction along the 2-way path between the lidar and the backscattering volume.

As can be seen, $P(R)$ depends upon both the local value of $\beta_\pi(R)/4\pi$ and upon the integral of $\beta_\varepsilon(R)$. Only a single measurement of $P(R)$ is provided at each range by simple lidar systems leading to ambiguities in the direct evaluation of $\beta_\pi/4\pi$ or β_ε. The problem is severe enough so that with certain $\beta\varepsilon(R)$ profiles or certain penetration angles, it is possible that the clouds could be rendered invisible to simple lidar systems[1]. This can occur whenever $\beta_\varepsilon(R)$ increases with penetration in such a way that the increase in backscattered energy with range is just offset by the increase in 2-way path attenuation. In addition the multiple scattering contribution M(R) can further complicate matters by effectively increasing P(R) in a way which depends upon the unknown spatial distributions of the scattering phase function and optical thickness between the lidar and the sensed volume[2].

While several techniques have been employed to untangle β_π from β_ε[3,4,5,6], each method requires significant assumptions about the distribution of scatterers and about the nature and profile of the particulate backscatter to extinction ratio. The multiple scattering contribution, which can become large in returns from cirrus clouds, may be minimized by a narrow field of view (fov) design for the lidar system. This solution is often difficult to achieve and is therefore not frequently implemented; however, narrow fov (~.32 mrad) is a necessary requirement for the high resolution spectrometer employed in the HSRL, thus the uncertainties caused by the effects of multiple scattering processes are greatly reduced in the cirrus cloud data acquired with this system[7].

III. HSRL Technique

The HSRL differs from simple lidar systems in that it separates the particulate backscatter component from the molecular backscatter component of the lidar return. Extinction is directly and unambiguously determined from the separated molecular backscatter return and an atmospheric density profile. This is possible because the atmospheric density determines the molecular backscatter cross section, thereby establishing a known target available at every range.

The HSRL achieves the separation of the molecular and particulate backscatter by utilizing spectral distribution differences in the scattered energy. Rapid thermal motion of molecules Doppler-broadens the molecular backscatter spectrum. Particulates are more massive than molecules and are thus characterized by relatively slow Brownian drift velocities which produce insignificant Doppler broadening of the particulate scattered spectrum. Using a multi-etalon pressure-tuned Fabry-Perot spectrometer, the HSRL simultaneously observes the lidar return in two channels[8,9]. The spectrally narrow (~.6 pm FWHM) "particulate channel", centered on the transmitted wavelength (510.6 nm), is most sensitive to particulate scattering and to the central region of the Doppler-broadened molecular spectrum. With a prominent notch in the center of its bandpass, the spectrally wider (~5 pm FWHM) "molecular channel" accepts the entire Doppler-broadened molecular spectrum while rejecting much of the particulate scatter. Thus, the signal in each channel represents a different linear combination of the aerosol and molecular scattering contributions to P(R). Complete separation of the two channel signals requires the determination of a 2X2 matrix of linear inversion coefficients. These coefficients are determined by diffusely filling the receiver telescope with attenuated laser light and observing the response of the two channel signals to a spectral scan of the receiver[7].

Because the HSRL separately measures molecular and particulate backscatter, two lidar equations may be written which are coupled by a common extinction term. Assuming M(R) is negligible, the molecular and particulate lidar equations may be written

$$P_m(R)\,R^2 = E_0\,\xi\,\beta_m(R)\,\frac{3}{8\pi}\,e^{-2\int_0^R \beta_\varepsilon(r)\,dr}$$

(2), and,

$$P_a(R)R^2 = E_0 \xi \beta_a(R) \frac{\mathbb{P}_a(\pi,R)}{4\pi}\, e^{-2\int_0^R \beta_\varepsilon(r')\,dr'} \tag{3}$$

The subscripts a and m denote particulate and molecular scattering quantities. The term particulate includes both aerosol particles and cirrus cloud particles, and the subscript notation , a, is retained to preserve continuity with cited references. In addition, the backscatter cross section has been expanded into its component parts

$$\beta_\pi(R)/4\pi = \beta_a(R)\, \mathbb{P}_a(R,\pi)/4\pi + \beta_m(R)\ 3/8\pi \tag{4}$$

where $\mathbb{P}_a(\pi)$ denotes the particulate backscatter phase function and $\beta_{a,m}$ denote the respective scattering cross sections per unit volume, and the molecular backscatter phase function has been replaced with its analytic value, $3/8\pi$.

With knowledge of the profile of atmospheric density from a convenient radiosonde (or from climatology), eq. (2) is completely defined, and may be solved *explicitly* for the extinction. Thus, the underdetermination ambiguity in eq. (1) has been eliminated in the HSRL by effectively calibrating the system at each range with the known molecular backscatter cross section. The particulate backscatter cross section is also unambiguously determined from the ratio of eq. (3) to eq. (2).

$$\beta_a(R)\, \frac{\mathbb{P}_a(\pi, R)}{4\pi} = \beta_m(R)\, \frac{3}{8\pi}\, \frac{P_a(R)}{P_m(R)} \tag{5}$$

In the absence of particulate and gaseous absorption, $\beta_a = \beta_\varepsilon - \beta_m$; therefore, the backscatter phase function is uniquely determined from (5) and the atmospheric density profile

$$\frac{\mathbb{P}_a(\pi, R)}{4\pi} = \beta_m(R)\, \frac{3}{8\pi}\, \frac{P_a(R)}{[\beta_\varepsilon(R) - \beta_m(R)]\, P_m(R)} \tag{6}$$

IV. Example

Fig. 1 shows an example of the raw R^2 corrected backscatter from cirrus clouds ahead of a warm front. This data is a plot of 10 minute averaged, un-inverted HSRL returns, and is similar to the expected output from a simple lidar system. After calibrating the HSRL and separating the particulate and molecular scattering profiles, the extinction corrected backscatter cross section was plotted in fig. 2. Note the significant altitude differences in the centers of scattering activity between the extinction corrected and un-corrected plots, particularly in the latter half of the record. Cloud tops could easily be mispositioned to a lower altitude in the uncorrected plot because extinction has attenuated the upper-cloud-scattered energy.

The layer optical thickness and backscatter phase function plots for this day[10] have indicated that a substantial portion of the structural details evident in fig. 2 may, in fact, be due to modulations in the backscatter phase function, and not simply due to changes in extinction. Because of this effect, one must use caution in interpreting relative changes in backscatter as changes in extinction. Changes in backscatter may be related to changes in scatterer phase and habit as well changes in the number density or radiative effects of particles.

V. Summary

We have explained some of the potential pitfalls of casual application of simple lidar data to the determination of cloud morphology and optical parameters. In optically thick clouds, correction for extinction may be important for the determination of cloud boundaries, and for the realistic rendering of structural details. Interpretation of relative backscatter changes as modulations in cloud extinction may not be valid for rapidly evolving cloud systems.

The unique capabilities of the HSRL have been explained and have been used to illustrate the potential problems with direct interpretation of one-channel lidar system retrievals. The HSRL has several disadvantages when compared to simple lidar systems. In its current state of development, the HSRL is complicated and time consuming to maintain, align, operate, and calibrate. Because of the many optical surfaces in the receiver, much of the backscattered light is lost before measurement. The spectral purity and stability of the transmitter must meet stringent requirements, reducing the choice of lasers. With the current $CuCl_2$ laser transmitter, output power is limited to 50 mW. Nevertheless, successful measurements of optical thickness, backscatter phase function and backscatter cross section have been achieved in cirrus clouds with 10 minute time resolution. Internal cloud details of backscatter phase function, and time resolution sufficiently short as to allow angle scanning (possibly volume scanning), will await integration of a new laser transmitter. The new transmitter will decrease averaging times by at least a factor of 40 and will hopefully be ready for operation by the time of this meeting.

Support for this work has been provided under ARO grant DAAG29 - 84 - 0069 and ONR contract N00014 - 85 - K - 0581.

References

1) C.J. Grund and E.W. Eloranta, Optically Significant Cirrus Clouds may be Rendered "Invisible" to Space-borne Simple Lidar Systems, Technical Digest, Topical Meeting on Laser and Optical Remote Sensing: Instrumentation and Techniques, 75, (1987).
2) E.W. Eloranta and S.T. Shipley, A Solution for Multiple Scattering, Atmospheric Aerosols: Their Formation, Optical Properties and Effects, Ed. A. Deepak, 227, (1982).
3) Klett, J.D. (1981) Stable analytical inversion solution for processing lidar returns. Appl.Opt, 20, pp 211-220.
4) Spinhirne, J.D., J.A. Reagan, B.M. Herman (1980) Vertical distribution of aerosol extinction cross section and inference of aerosol imaginary index in the troposphere by lidar technique. J.Appl.Meteor., 19, pp 426-438.
5) Eloranta, E.W., and D.K. Forrest (1986) Generation of attenuation corrected images from lidar data: in Thirteenth International Laser Radar Conference, NASA conference publication 2431, pp. 291-294.
6) Weinman, J.A. (1984) Tomographic lidar to measure the extinction coefficients of atmospheric aerosols. App.Opt., 23, pp 3882-3888.
7) C.J. Grund, Measurement of Cirrus Cloud Optical Properties by High Spectral Resolution Lidar, Ph.D. Thesis, U.Wisconsin-Madison, (1987).
8) Shipley, S.T., D.H. Tracey, E.W. Eloranta, J.T. Trauger, J.T. Sroga, F.L. Roesler, and J.A. Weinman (1983) High spectral resolution lidar to measure optical scattering properties of atmospheric aerosols. 1: Theory and instrumentation. App.Opt., 22, pp 3716-3724.
9) Sroga, J.T., E.W. Eloranta, S,T. Shipley, F.L. Roesler, and P.J. Tryon (1983) High spectral resolution lidar to measure optical properties of atmospheric aerosols. 2: Calibration and analysis. Appl.Opt., 22, pp 3725-3732.
10) C.J. Grund and E.W. Eloranta (1988) Cirrus Cloud Optical and Morphological Properties Observed by the High Spectral Resolution Lidar During FIRE. Elsewhere in this volume.

Fig. 1 Raw BACKSCATTER

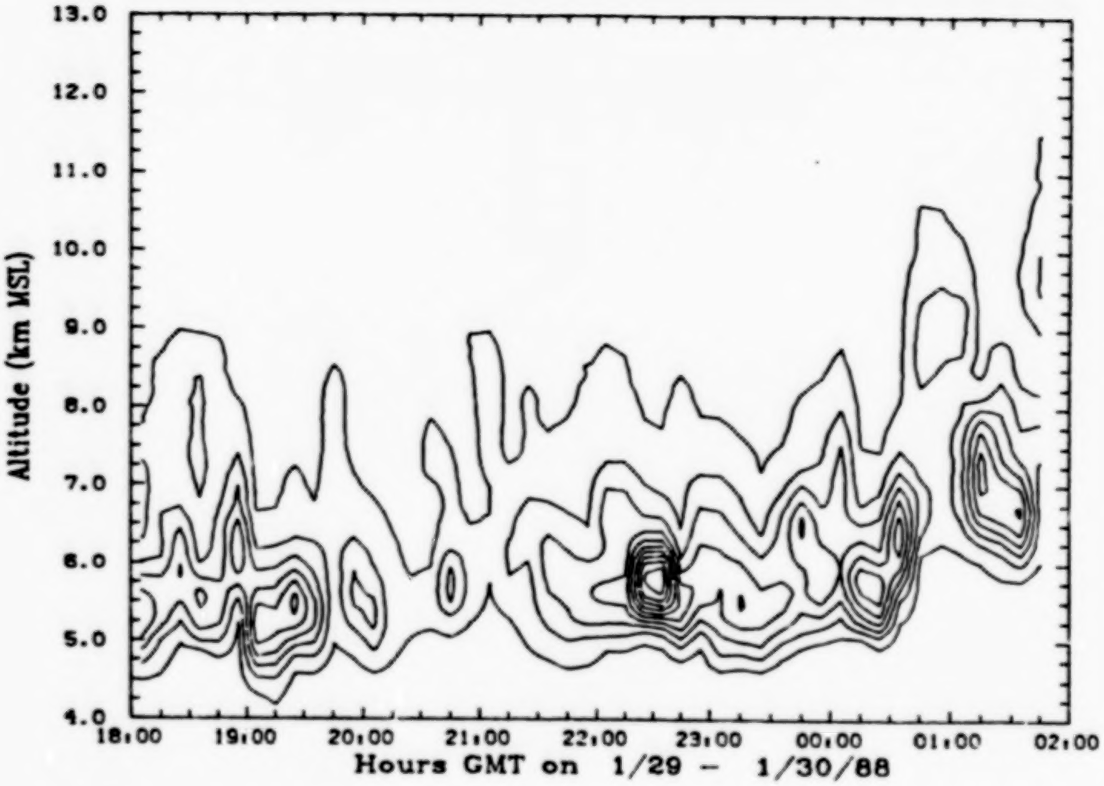

Fig. 2 Backscatter Cross Section $(10^{-6} m^{-1} sr^{-1})$

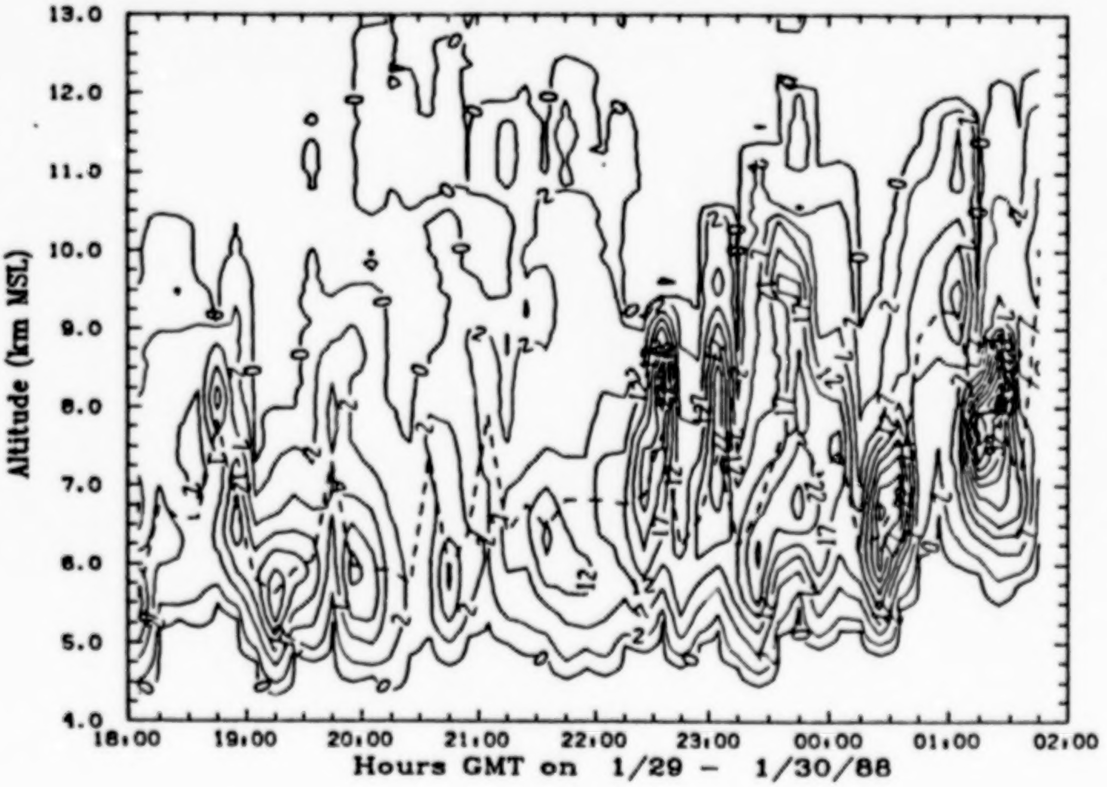

TEMPERATURE SENSITIVITY OF EPPLEY BROADBAND RADIOMETERS

William L. Smith, Jr., Stephen K. Cox

Department of Atmospheric Science, Colorado State University, Fort Collins, CO 80523

Vince Glover

Research Aviation Facility of the Atmospheric Technology Division, National Center for Atmospheric Research, Boulder, CO 80307

Eppley Laboratory Inc. model PIR pyrgeometers and model PSP pyranometers have built in temperature compensation circuitry designed to limit relative errors in the measurement of radiation to ± 2% for a temperature range of -20 C to +40 C. A procedure developed to verify this specification and to determine the relative sensitivity to temperatures below -20 C is described. Results of this calibration and application to data correction are also presented.

1. INTRODUCTION

Broadband radiometers manufactured by Eppley Laboratories Inc. are commonly used to measure irradiance from both ground-based and aircraft platforms. Namely, the pyranometer (Model PSP) measures irradiance in the .3-3 micron spectral region while the pyrgeometer (Model PIR) senses energy in the 4-50 micron region. The two instruments have a similar thermopile construction but different filters to achieve the appropriate spectral selection.

The precision pyranometer has been described by Albrecht and Cox (1976) and Robinson (1966). These instruments are typically sent to the manufacturer for calibration relative to a group of reference standards. Calibration of the pyrgeometer is more complex and can be performed following the procedures of Albrecht and Cox (1977). For a description of this instrument, see Albrecht *et al.* (1974). Several other authors have made contributions in assessing the performance of pyrgeometers. For example, see Weiss (1981), Bradley and Gibson (1982) and Ryzner and Weber (1982). Foot (1986) points out that the main problem with achieving accurate irradiance measurements from the pyrgeometer is associated with errors caused by temperature gradients within the instrument itself. He suggests minimizing these errors by utilizing a newly constructed pyrgeometer which demonstrates a markedly reduced sensitivity to temperature gradients.

During the fall of 1986, the First ISCCP (International Satellite Cloud Climatology Project) Regional Experiment (FIRE) commenced with the first cirrus Intensive Field Observation (IFO) conducted in central Wisconsin. Due to the nature of this field project, pyranometers and pyrgeometers manufactured by Eppley were flown on NCAR's high altitude research aircraft, the Sabreliner. Inherent in the construction of these radiometers is temperature compensation circuitry designed to make the instrument sensitivity nominally constant (within ± 2%) over a temperature range from -20 C to +40 C. Because the Sabreliner flew at high altitudes where temperatures were as cold as -70 C, it was necessary to determine the radiometers relative sensitivity to temperatures below -20 C and apply appropriate corrections to the FIRE radiation data set. A procedure to perform this calibration is outlined below. It is meant to serve as a supplement to the calibration procedures referenced above.

2. LABORATORY SET UP

Six Eppley Laboratory Inc. manufactured radiometers were flown on the NCAR Sabreliner during the FIRE first cirrus IFO. Of these six, only three were available for this particular calibration at NCAR's Research Aviation Facility (RAF) and included two pyranometers and one pyrgeometer. Because this calibration is concerned with radiometer thermopile characteristics only, the calibration procedure can be simplified by converting them all to visible radiometers. This conversion only requires that the domes be visibly clear. The three radiometers were mounted inside an environment chamber at NCAR's RAF so that they faced, and were encompassed in the field of view of, a plated glass window in the door. A light source was mounted directly in front of the radiometers but on the outside of the chamber. In addition, an extra pyranometer was mounted on the outside of the chamber to monitor any changes in the light source output. Signal wires connected to the radiometers were passed through a datalogger to a computer where thermopile output, chamber temperature, room temperature and the sink temperature of the pyrgeometer were recorded and monitored in real-time. For a more visual depiction of the laboratory set up, see figure 1.

3. CALIBRATION PROCEDURE

The temperature of the insulated environment chamber was controlled so that data could be sampled every 5 C from +26 C to -63 C. Again, because we are concerned with thermopile characteristics only, the calibration procedure can also be simplified by ensuring that the radiometers are in thermal equilibrium when data is recorded. The sink temperature of the pyrgeometer is the best indication of the temperature of the thermal mass of the radiometer. So, at each calibration point (i.e. each 5 C chamber temperature increment), the sink temperature of the pyrgeometer was monitored with respect to the chamber temperature to determine when the pyrgeometer was in thermal equilibrium. While the temperature of the chamber's environment could be changed rather rapidly, it was found to take nearly an hour for the thermal mass of the pyrgeometer to achieve thermal stability. Since the pyranometers and pyrgeometer are nearly identical in construction and thermal mass, it was assumed that all radiometers reached thermal equilibrium at the same time.

The instrument output was sampled at 1 Hz and recorded in 10 second averages. The source was chopped at each calibration point by covering the plated glass window, thus shielding the radiometers from all shortwave radiation. This provided information concerning the dark current of the instruments. Because of the time it took for thermal equilibrium to be reached at each calibration point, it took several days to cover the entire temperature range from +26 C to -63 C in 5 degree intervals. At the beginning of each day, a room temperature calibration data point was recorded. This data relates the output voltage of each radiometer being calibrated to the output voltage of the pyranometer monitoring the source while all radiometers are at the same room temperature. So, for each instrument being calibrated,

$$V_m(T_r) = p(T_r)[V_c(T_r) - V_d(T_r)]$$

where T_r = room temperature

V_m = voltage output of source monitor at T_r

V_c = voltage output of radiometer being calibrated at T_r

V_d = dark voltage of radiometer

p = function relating V_c to V_m at T_r.

Then, for each subsequent calibration point,

$$V_m(T_r) = q(T)[V_c(T) - V_d(T)]$$

where T = temperature of chamber and of the thermal mass of the radiometers being calibrated

q = function relating V_c at T to V_m at T_r

and the relative sensitivity is

$$K(T,T_r) = p(T_r)/q(T).$$

Thus, the relative sensitivity $K(T,T_r)$ is normalized to express the temperature dependence of each radiometers thermopile given a constant source of energy and with respect to some reference temperature, taken here to be the room temperature (T_r) of 26 C.

4. RESULTS

Results of this calibration for the available radiometers are shown in figure 2. Within the electronically compensated temperature range from +40 C to -20 C, our results depict nominal instrument sensitivity within about 2.5%, close to Eppley Laboratory Inc. ± 2% specification. Outside of this range (i.e. below -20 C), errors could be as large as 7% at -63 C. A third order polynomial proved to provide the best fit to these data. These curves are also shown in figure 2. The corresponding coefficients for these curves have been used to correct the data collected on board the Sabreliner during FIRE. Since two of the pyranometers flown on the Sabreliner were unavailable for this post mission calibration, an average was taken of the two curves that were developed and this third curve used to correct the data collected by the uncalibrated instruments. Similarly, one pyrgeometer was also unavailable, so the curve developed from the calibrated pyrgeometer was also applied to data collected by the uncalibrated pyrgeometer.

5. APPLICATION TO DATA CORRECTION

The application of this calibration to data correction is straight-forward because the original calibrations were done at room temperatures near the 26 C reference temperature used in this calibration. Eppley Laboratory Inc. states in their calibration documentation that the adopted calibration temperature for the pyranometer is 25 C. For the pyrgeometers, the calibration procedure following the methods of Albrecht and Cox (1977) dictates that the temperature of the radiometer thermopile is near the room temperature of the laboratory. Albrecht *et al.* (1974) report that the sink temperature is representative of the thermopile sensor temperature. This is because the temperature difference between the hot and cold junctions of the thermopile is, at most, 0.5 C for typical irradiance measurements in the atmosphere.

The relative sensitivity (K) can be applied directly to the pyranometer measurements to get the corrected value. For example,

$$SW_{CORR} = 1/K(T_s) \cdot C \cdot V$$

where V = thermopile output voltage of pyranometer

C = calibration constant supplied by Eppley Laboratory Inc. to convert thermopile voltage output to units of irradiance (i.e. W/M^2)

$K(T_s)$ = the relative sensitivity at a temperature T_s which is the sink temperature of an adjacent pyrgeometer

SW_{CORR} = the corrected irradiance.

For the pyrgeometer, an equation derived by Albrecht *et al.* (1974) and Albrecht and Cox (1977) of the form

$$E = \frac{V}{\eta} + \epsilon\sigma T_s^4 - \beta\sigma(T_d^4 - T_s^4)$$

where
ϵ - emissivity of the thermopile (usually taken to be unity)
σ = Stefan Boltzmann constant
T_d, T_s = dome temperature and sink temperature, respectively
η, β = calibration constants
V = thermopile voltage
E = incoming irradiance

can be further corrected for temperature sensitivity by applying K(Ts) to the first term such that

$$E_{CORR} = \frac{1}{K(T_s)} \cdot \frac{V}{\eta} + \epsilon\sigma T_s^4 - \beta\sigma(T_d^4 - T_s^4)$$

where E_{CORR} is E but corrected for temperature sensitivity.

However, because the infrared irradiance (from the pyrgeometer) is a function of the summation of several terms, the effect of the temperature sensitivity correction will be somewhat less for the pyrgeometer data than for the pyranometer data. Several FIRE data sets were analyzed to determine the magnitude of error between corrected and uncorrected pyranometer and pyrgeometer measurements. Irradiance errors for the pyrgeometer were found to be, at most, 2-3 W/m^2 which is within the noise of the instrument. Because the temperature sensitivity correction is applied directly to the pyranometer measurements, errors could be as large as 7% of the uncorrected measurement at -63 C. In addition, errors as large as 10% were found in cloud fractional absorptance (CFA) calculations (See Ackerman and Cox (1981) for a description of CFA).

6. SUMMARY

A calibration procedure to correct Eppley Laboratory Inc. broadband radiometers for thermopile temperature sensitivity has been presented. This calibration should be performed prior to field work where radiometers of this type, particularly the pyranometer, may be exposed to temperatures beyond the range of the temperature compensation circuit.

7. ACKNOWLEDGEMENTS

This research has been supported by the National Science Foundation under Grant ATM-8521214 and by the National Aeronautics and Space Administration under Grant NAG 1-554.

REFERENCES

Ackerman, S. A., and S. K. Cox, 1981: Aircraft Observations of the Shortwave Fractional Absorptance of Non-Homogeneous Clouds. *J. Appl. Meteor.*, 20, 0128-0133.

Ackerman, S. A., M. Poellot and S.K. Cox, 1974: Pyrgeometer measurements from aircraft. *Rev. Sci. Instrum.*, 45, 33-38.

Albrecht, B., and S. K. Cox, 1976: Radiation data reduction procedures for Sabreliner, C-130 and DC-6 aircraft during the GARP Atlantic Tropical Experiment. Colorado State University *Atmospheric Science Paper No. 244*, Fort Collins, CO., 100 pp.

Albrecht, B., and S. K. Cox, 1977: Procedures for improving pyrgeometer performance. *J. Appl. Meteor.*, 16, 188-197.

Bradley, S.G., and R.G. Gibson, 1982: On the use of pyrgeometers in cloud. *J. Appl. Meteor.*, 21, 1155-1159.

Foot, J.S., 1985: A new pyrgeometer. *J. Atmos. Oceanic Technol.*, 3, 363-370.

Robinson, N., 1966: *Solar Radiation*, Elsevier, 347 pp.

Ryzner, E., and M.R. Weber, 1982: Comments "On the performance of pyrgeometers with silicon domes." *J. Appl. Meteor.*, 21, 1208-1210.

Weiss, A., 1981: On the performance of pyrgeometers with silicon domes. *J. Appl. Meteor.*, 20, 962-965.

Figure 1

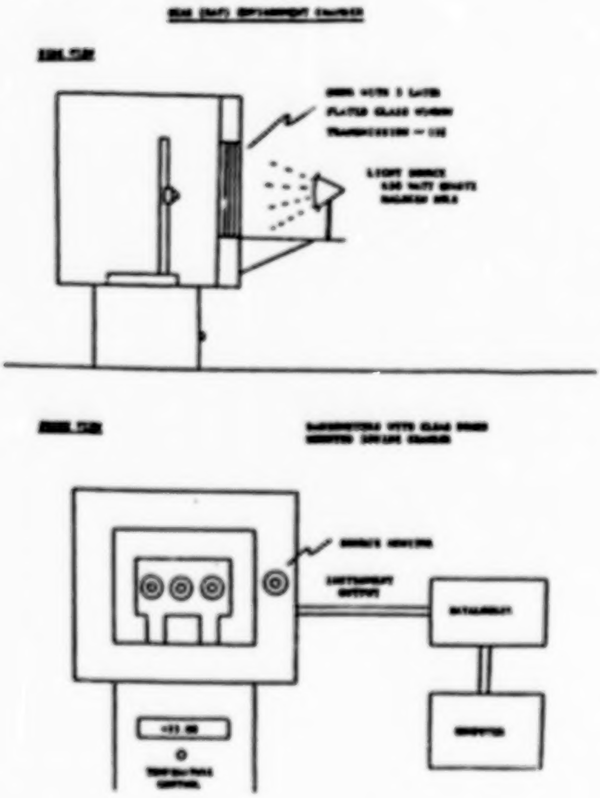

Figure 2

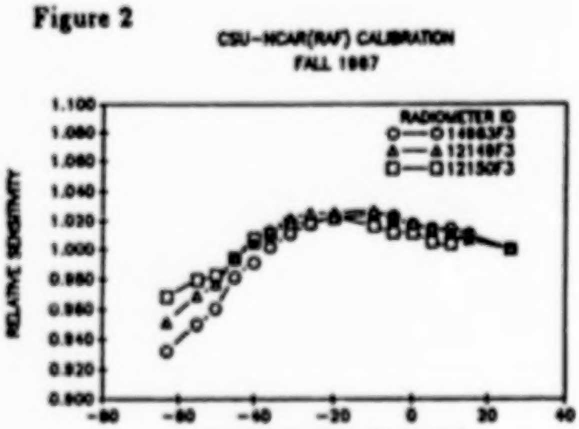

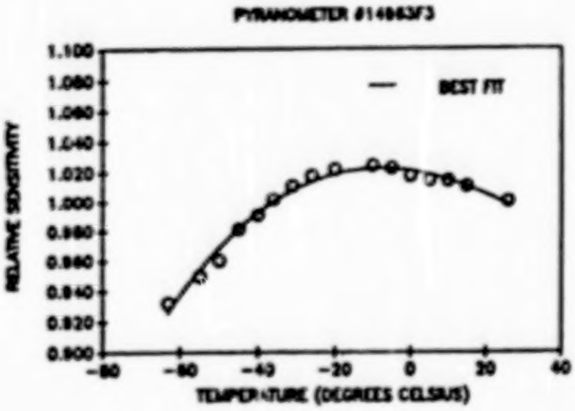

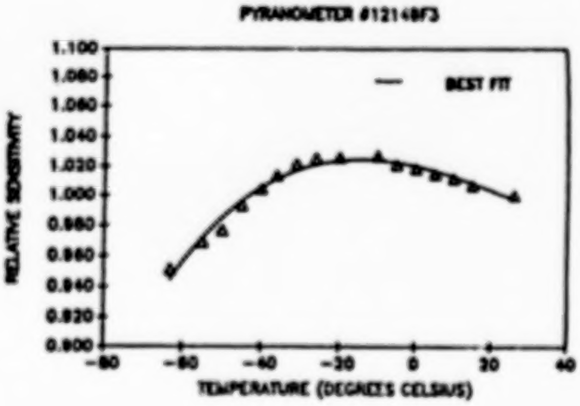

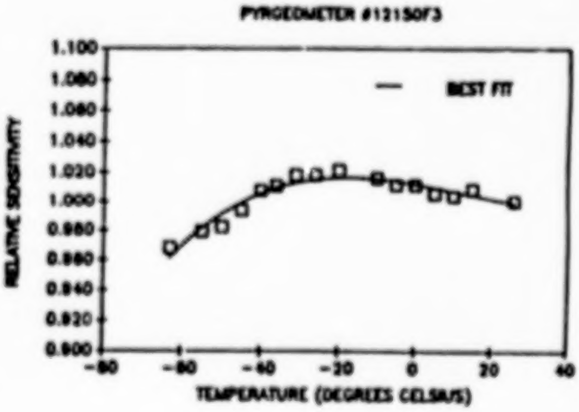

Poster Exhibit

BOTH SIDES NOW

Donald Wylie
Space Science and Engineering Center
University of Wisconsin-Madison

On November 2, 1986 of the cirrus Intensive Field Observations, cirrus clouds were observed from both ground-based and aircraft lidar. The NASA ER2 aircraft carrying a lidar, crossed Madison three times and Wausau five times during its mission. Ground-based lidars from the University of Wisconsin in Madison and the University of Utah in Wausau were operating during the ER2 overpasses. This gave FIRE unique lidar observations of cirrus clouds from both sides.

Cloud cover on November 2 was absent from most of the FIRE observation area at the start of the ER2 mission (Fig. 1). There was a long line of cirrus and alto stratus clouds south of Madison. This cloud line was over Madison on the previous day and had moved south. Southern Wisconsin experienced very dry and cloudy skies. Cirrus clouds encroached upon the FIRE study area from the northwest. The clouds in northwestern Wisconsin were generally multi-layered cirrus clouds from 5 to 10 km altitude. The cloud layers were thin in central Wisconsin and thickened to the northwest. These clouds proceeded the warm from which approached Wisconsin from Canada.

The movement of these cirrus clouds into Wisconsin is depicted by the time section of lidar data from Wausau (Fig. 2). Two separate layers of clouds were observed in the morning at 6-7 km and 10-11 km. After local noon (1800 GMT), the cloud layers thickened into one nearly solid cloud mass from 5 to 11 km.

The NASA ER2 aircraft initially flew over the cloud band in Illinois south of Madison. Lidar tracks were taken going south into the cloud band along the band flying west, and flying north toward Madison away from the band. The aircraft crossed Madison at 18:49 GMT when there were no clouds present and extremely clear skies. It then proceeded north to Wausau at 19:00 GMT crossing first on a northward track and the four additional east-west tracks. The last lidar cross section over Wausau is shown in Fig. 3 (19:59 GMT).

The ER2 lidar vividly depicts the cloud top altitudes. A return from the ground also can be seen part of the time. Cloud interval structure and intermediate layers are sometimes visible to the lidar. The variable height of the cloud top is most apparent in Figs. 2 and 3. There appeared to be a high layer over Wausau (AUW) at 10.8 km. This gave a strong lidar return to the ER2 from 19:00 to 19:30 GMT. This was near the cloud tops found earlier by the ground-based lidar. A second lower layer at 7.6 to 9.2 km also is partially visible on the last ER2 crossing of Wausau and to the west (Fig. 3). The lidar picked up variable and broken cloud tops. Another high layer was apparent at the end of the track.

The height of the highest cloud layers found by the ER2 lidar are indicated on the time section from the Wausau ground-based lidar as thick horizontal bars (Fig. 2). It is apparent that the cloud tops remained at 10.7 to 11 km until 19:45 GMT. The ground-based lidar is unable to define the cloud top after 19:00 GMT because of obstructing thicker cloud layers from below. Many variations in the cloud top height and cloud density were found by the ER2. At 19:50 GMT, the ground-based lidar appeared to correctly identify some of the heights reported from the ER2. The heights of the lower layers seen on the ER2 data are depicted on the time section as horizontal bars connected by a thin line. The positions of the bars in time were drawn assuming advection of the broken cloud top over Wausau. The height of the broken cloud layers appear to match some of the cloud tops found by the ground-based lidar.

These lidar cross section show the layered and broken structure of the cirrus clouds. At least two layers were observed during the morning. Later during the afternoon, the layers were not easily discernible. The special structure indicated several breaks in the cloud top ranging from 5 to 50 km in width. Similar scales also were found on the Madison lidar as the edge of the cloud mass moved south during the day.

Satellite cloud top analyses also indicated variable cloud top heights (Fig. 4). The GOES/VAS cloud top analysis was made at 20:18 GMT, approximately 25 minutes after the ER2 cross section. Satellite-derived cloud top heights were generally lower than the cloud tops visible from the ER2. This relationship has been commonly observed in other comparisons of the GOES/VAS cloud analyses to lidar data. Less variable cloud top heights were found by the GOES/VAS analysis to the north of Wausau. More radiatively dense clouds were found in this region by the GOES/VAS system.

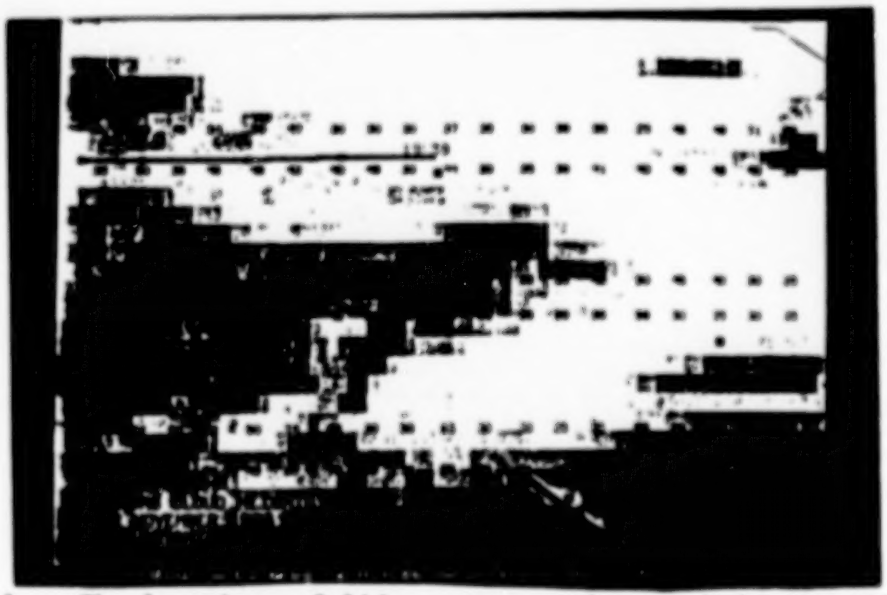

Figure 1: The locations of lidar cross sections made by the ER2 on November 2, 1986.

GOES-VAS satellite multi-spectral infrared analysis of cloud top heights for 20:18 GMT (25 minutes after the lidar cross section shown in Fig. 4).

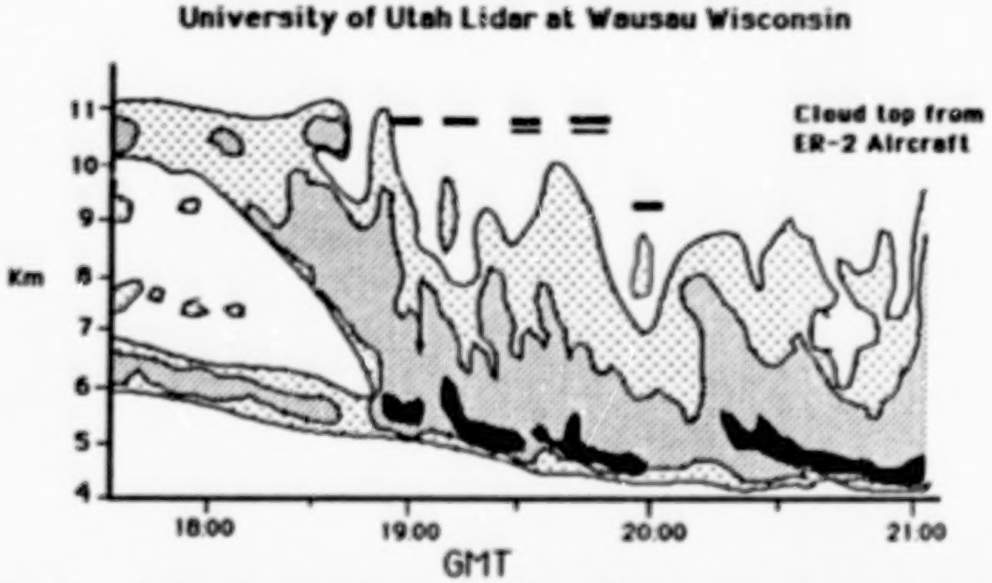

Figure 2: Composite picture of the ground-based University of Utah lidar (operated by Dr. K. Sassen) time section from Wausau, Wisconsin. Shaded areas indicate the strength of the backscattered return (uncalibrated). The mean height of the highest cloud tops from ER2 lidar crossing over Wausau are depicted as

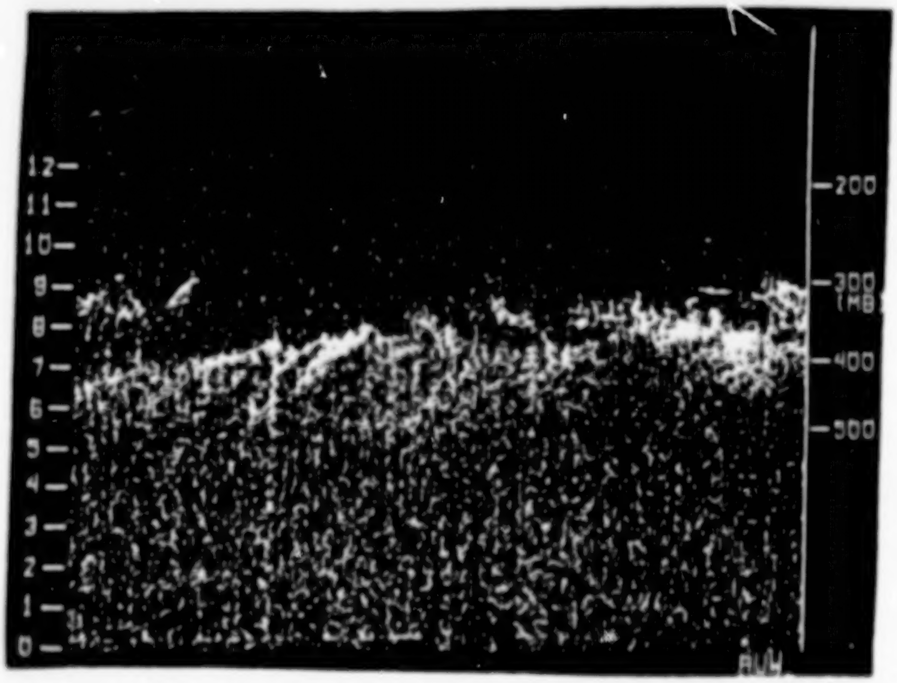

Figure 3: Cross section of lidar returns from the ER2. Brightness (white) indicate the strength of the return (uncalibrated).

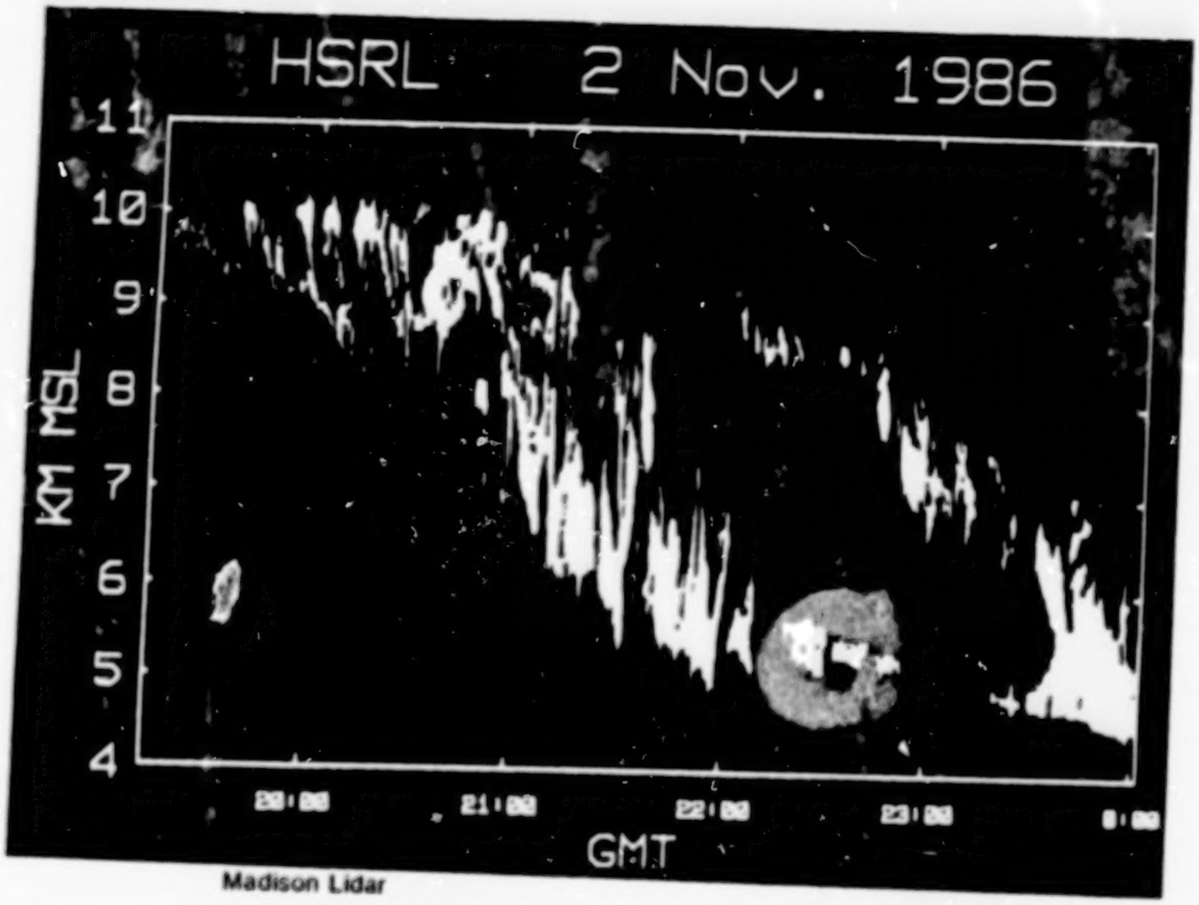

Madison Lidar

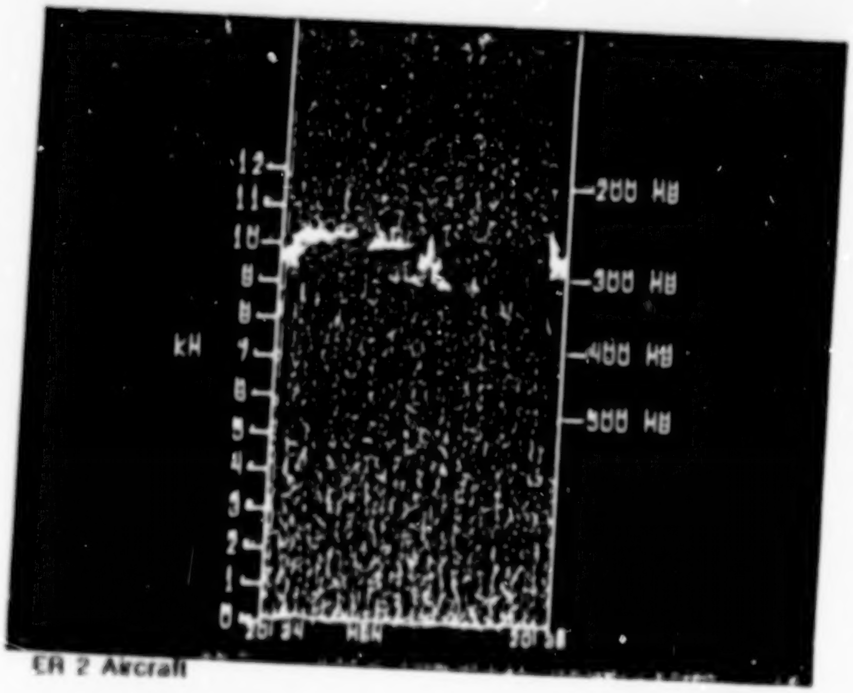

ER 2 Aircraft

Figure 3 Continued

SUB-VISUAL CIRRUS DETECTION AND CHARACTERIZATION

E. Schmidt, G. Grams, E. Patterson
Georgia Institute of Technology, School of Geophysical Sciences
Atlanta, Ga 30332

Analysis of archived cold optics (COR) radiometer data is yielding useful information on the diurnal, geographic, seasonal and altitude variability of atmospheric background radiance levels in the 11 micron window region. This database is a compilation of Kuiper Infrared Technology Experiment (KITE) and Atmospheric Radiance Study (ARS) observations under a wide variety of conditions. Correlating the measurements from these two studies with the LOWTRAN model code has revealed several important results. First, the 11 micron window appears to be "filled-in," i.e., the troughs on either side of the nitric acid peak are shallower than expected. Second, the amplitude of the background radiances measured exceeds the model predictions by a factor of 2-3 or more. This is thought to be due to the existence of thin, high altitude cirrus clouds (sub-visual cirrus) above the sensor platform. These high background levels are observed under quiescent conditions in the south Pacific (Marshall Islands), as well as over the continental United States (the west coast). In the tropics, there appears to be little diurnal variability, a plausible seasonal variation and a linear dependence between 7.2 and 11.4 micron band data, indicating possible multi-spectral approaches to detection of sub-visual cirrus clouds.

Theoretical analysis of the magnitude of the effects of a sub-visual cirrus cloud on atmospheric background radiances measured by a near-horizontal sensor is in progress. Fine tuning of the radiative transfer calculations requires characterization of sub-visual cirrus cloud properties, specificaly total optical depth, altitude, vertical structure, and persistence. The scattering of thermal emissions from the Earth and low-lying warm clouds by non-spherical hexagonal ice crystals that are non-randomly oriented is suggested as a possible explanation for the elevated window measurements (emission from the cloud itself is considered.) Calculation of phase functions to specificaly address these conditions requires information on particle size distribution and orientation, as well as shape.

Further efforts underway include work at Wright-Patterson Air Force Base using the 100-inch collimator as the receiver for a powerful lidar system, the "MEGALIDAR." The MEGALIDAR facility will ultimately provide profiles of atmospheric density and temperature up to 100 km. Other experiments planned rely on coordination of lidar techniques with sky background observations. Under a project sponsored by the USAF Summer Research Program, we plan to correlate simultaneous visible and infrared (8-12 micron) spectral sky measurements with lidar observations of altitude, vertical structure, total optical thickness and persistence of sub-visual cirrus at the MEGALIDAR site. This information, along with satellite and rawindsonde support data, should provide a useful "snapshot" of the subvisual cirrus and allow proper analysis of the effects of sub-visual cirrus.

Information on the spatial extent and characteristics of sub-visual and high altitude cirrus clouds will not be available from the planned program; however, it is hoped that useful information might be gathered from the FIRE data and included in our analysis.

CLOUD ATLAS

for the

FIRE Cirrus Intensive Field Observation

October 5 - November 10, 1986

An Intensive Field Observation (IFO) of cirrus clouds was conducted over the mid-western U.S. during the period October 13 - November 2, 1986. This activity, part of the First ISCCP Regional Experiment (FIRE), included measurements made from specially deployed instruments on the ground, balloons, and aircraft as well as observations from existing operational and experimental satellites. The satellite observations were collected for the purposes of the IFO beginning 1 week prior to and ending 1 week after the IFO period. In addition, there were satellite observations collected on the 5th to the 10th and 20th to the 25th of each calendar month as part of the FIRE Extended Time Observations, which cover a region that encompasses the Cirrus IFO area. As a result, the collected satellite data include daily coverage over a 37-day period from October 5 to November 10, 1986.

One of the sets of satellite observations was the radiance measurements made with the 5-channel AVHRR radiometer on the NOAA 9 polar orbiting meteorological satellite. These data were collected from NOAA ground stations at Wallops Island, Virginia, and Redwood City, California, during satellite overpasses. The ground resolution of the measurements at nadir is approximately 1 km. It is these measurements, made once each day at approximately 2:30 p.m. local time, that were used in determining the present cloud atlas. The area covered by the atlas is slightly larger than the area specified for the IFO, in order to be in alignment with the grid that will be used in a forthcoming atla for the larger, ETO region. The present atlas covers the area from 37.5 - 47.5 N and 80 - 105 W, which includes 8 x 15 *analysis boxes* out of the 16 x 48 boxes that constitute the ETO region. Each *analysis box* covers 1.25° latitude by 1 2/3° longitude, which is an area approximately 140 km square. There are from 5,000 to 22,000 pixels within each box (except where there is missing data), the amount depending on the position of the box with respect to the satellite track.

The retrieved parameters for each pixel include:

f fraction of pixel covered by cloud
τ cloud optical thickness
T_c cloudtop temperature
M cloud microphysical model

The three parameters are retrieved from the visible [Ch. 1] and thermal infrared [Ch. 4] channels using the *maximal clustering method*, described in Arking and Childs (1985), with some refinements that will be described in a forthcoming publication. A fourth parameter, the microphysical model (MPM) index *m*, represents information concerning the particle size and phase of the cloud particle, which is assumed to be spherical with a size distribution given by

$$\frac{dN(r)}{dr} \alpha \; r^6 \exp[-6 \; r/r_o]$$

where $N(r)$ is the number of particles per unit volume with radii smaller than r, and r_o is the mode radius. For this distribution the mean radius is 7/6 r_o, and the effective radius is 3/2 r_o .

The MPM index is retrieved as a single parameter for the *analysis box* as a whole, representing the best fit for all points to the observed 3.7 μm [Ch. 3] radiance measurements, as described in Arking and Childs (1985). There are five possible values of *m*, representing the following combinations of particle size (mode radius r_o) and phase (water/ice):

m	MPM
1	4 μm water
2	4 μm ice
3	8 μm water
4	8 μm ice
	16 μm water
5	32 μm ice

The atlas contains four pages of information for each satellite pass. The satellite pass is identified at the top of each page by date, time (GMT) at which the satellite crosses 40° N latitude, satellite (NOAA 9 in each case), and orbit number. The 1st page of each group shows the distribution of measured radiances in channel 1 (normalize to the incoming solar flux multiplied by the cosine of the solar zenith angle) and in channel 4 (expressed as a brightness temperature in degrees) for the area as a whole and for each *analysis box*. The 2nd page shows t images in: channels 1 and 2, combined to form a color image as described in Arking, Childs, and Merritt (1987); channel 3R, which represents channel 3 after subtracting out the emitted radiance based upon the channel 4 brightness temperature and normalizing to the incoming solar flux multiplied by the cosine of the solar zenith angle; and channel 4, the 11 μm brightness temperature. The 3rd page shows the retrieved parameters in *graphical* form for the region as a whole and for each *analysis box*, where cloud fraction appears as a contour plot with respect to optical thickness and cloudtop temperature. The 4th page provides a statistical summary of the retrieved parameters in *numerical* form for each *analysis box*.

The entries are as follows:

Cloud Amount

Total cloud amount is shown for all values of f and for f restricted to the range $0.9 \leq f \leq 1$. A large difference between the two values indicates that most of the cloud cover is associated with sub-pixel resolution clouds, thus suggesting greater uncertainty in the results.

Optical Thickness

The optical thickness, in the visible channel (0.63 µm), mean and standard deviation, based upon plane parallel radiative transfer theory. (For any pixel, it is inversely related to cloud amount.)

Cloudtop Temperature

Cloudtop temperature, mean and standard deviation, based upon a cloud infrared emissivity derived from the visible channel optical thickness using Mie theory.

Surface Parameters

The mean visible channel reflectance and infrared channel equivalent blackbody temperature associated with clear-sky conditions. An asterisk indicates that the algorithm failed to identify clear-sky conditions and used default values.

Number of Pixels

The number of pixels in the analysis, which is affected by viewing geometry.

Number of Clusters

The number of clusters that were found by the cluster detection algorithm and used in the analysis. An asterisk indicates failure to detect any clusters (other than the surface cluster) and consequent use as default the clusters derived from analyzing the entire region as one box.

Cosine of Satellite Zenith Angle (μ)

Mean value of the cosine of the satellite zenith angle measured from the target point. Values less than 0.5 or 0.6 indicate poor viewing geometry.

Model Index

The mode value of the MPM distribution. Note that all pixels associated with a single cluster are assigned the same MPM.

Prepared: July 8, 1988

Albert Arking
Jeffrey D. Childs[1]
John H. Merritt[2]
Sharen L. Williams[2]

Climate and Radiation Branch
Laboratory for Atmospheres
NASA/Goddard Space Flight Center

References

Arking, A., and J. D. Childs, 1985: Retrieval of cloud cover parameters from multispectral satellite images. J. Climate Appl. Meteor., 23, 322-333.

Arking, A., and J. D. Childs, and J. H. Merritt, 1987: Remote sensing of cloud cover parameters. Atmospheric Radiation Progress and Prospect. Proceedings of the Beijing International Radiation Symposium, ed. by K.-N. Liou and Z. Xiuju, 473-488, Science Press, Beijing.

---

[1] Systems and Applied Science Corporation, Vienna, Virginia

[2] Applied Research Corporation, Landover, Maryland.

FIRE SCIENCE TEAM MEETING
VAIL, COLORADO
JULY 11-15, 1988

CIRRUS

PANEL DISCUSSION OF CIRRUS "NEXT" - David O'C Starr Wednesday, July 13, 1988

PAGE

Panel and Audience Discussions •••

FIRE SCIENCE TEAM MEETING
VAIL, COLORADO
JULY 11-15, 1988

MARINE STRATOCUMULUS

LARGE SCALE ENVIRONMENT AND MODELING - David A. Randall Wednesday, July 13, 1988

PAGE

Extended Time Observations of California Marine Stratocumulus Clouds from GOES for July 1983-1987 201
Minnis, Patrick; Edwin F. Harrison, and David F. Young

The Relationship of Marine Stratus to Synoptic Conditions 207
Wylie, Donald; Barry Hinton, Peter Grimm, and Kevin Kloesel

Analysis of Diurnal Variation of SCu Layer Using 2 Days of CLASS Soundings on San Nicolas Island 213
Betts, Alan K.

Diurnal Variation of Marine Stratocumulus over San Nicholas Island During the FIRE IFO 215
Davies, R.; and M. Blaskovic

Analysis of Tethered Balloon, Ceilometer, and Class Sounding Data Taken on San Nicolas Island During the FIRE Project 221
Schubert, Wayne H.; Paul E. Ciesielski, Thomas A. Guinn, Stephen K. Cox, and Thomas B. McKee

Radiative Control on Tropical Convective Boundary Layer Equilibrium 225
Betts, A. K.; and W. Ridgway

A GCM Parameterisation for the Shortwave Radiative Properties of Water Clouds 227
Slingo, A.

Preliminary Mixed-Layer Model Results for FIRE Marine Stratocumulus IFO Conditions 229
Barlow, R.; and S. Nicholls

Simulations and Observations of Cloudtop Processes 231
Siems, S. T.; C. S. Bretherton, and M. B. Baker

A Cloud Classification Scheme Applied to the Breakup Region of Marine Stratocumulus 237
Khalsa, Siri Jodha S.; and Catherine Gautier

Fractional Cloudiness in Shallow Cumulus Layers 243
Randall, David A.

Studying Marine Stratus with Large Eddy Simulation 249
Moeng, Chin-Hoh

EXTENDED TIME OBSERVATIONS OF CALIFORNIA MARINE STRATOCUMULUS CLOUDS FROM GOES FOR JULY 1983-1987

Patrick Minnis and Edwin F. Harrison
Atmospheric Sciences Division, NASA Langley Research Center
Hampton, Virginia 23665-5225
and
David F. Young
Aerospace Technologies Division, Planning Research Corporation
Hampton, Virginia 23666

1. Introduction

One of the goals of the First ISCCP Regional Experiment (FIRE) is to relate the relatively small scale (spatial and temporal) Intensive Field Observations (IFO) to larger time and space domains embodied in the Extended Time Observations (ETO) phase of the experiment. The data analyzed here as part of the ETO are to be used to determine some climatological features of the limited area which encompasses the Marine Stratocumulus IFO which took place between 29 June and 19 July 1987 off the coast of southern California (Kloessel et al., 1988).

2. Data and methodology

The primary data for this study are 3-hourly, 8-km visible (0.65 μm) and infrared (10.5 μm) radiances taken by the series of Geostationary Operational Environmental Satellites (GOES) which operated at various longitudinal positions between 1983 and 1987. Analysis of the data was confined to the month of July during each year. Table I lists the satellite, subsatellite longitude, dates of analysis, and satellite viewing zenith angle, VZ, relative to the center of the stratocumulus limited area. The latter is defined by 140°W and 115°W longitudes and 40°N and 25°N latitudes. These bounds were selected to ensure that IFO flight tracks would fall in the domain and that areas with stratocumulus presumably free from continental influences would be included.

The data were analyzed on a 2.5° grid with the hybrid bispectral threshold method described by Minnis et al. (1987). Resulting parameters include cloud amount, cloud-top temperature, cloud albedo, and clear-sky temperature and albedo for each region. All of the cloud parameters were derived for total, low (< 2 km), middle (2-6 km), and high (> 6 km) clouds. Because of the extremely high values (up to 79°) of VZ, the 1987 cloud amounts were adjusted to the viewing angles found for the 1985 data using the technique outlined by Minnis (1988). This correction lowered the cloud amounts by 2-4% absolute cloud amount.

Albedo here refers to the mean top-of-the-atmosphere broadband shortwave (0.2 - 5.0 μm) albedo over clear or cloudy areas. The narrowband visible radiances are converted to broadband radiances using the same conversion formula and coefficients as Minnis et al. (1987) for 1983, 1985, and 1986. That calibration produced good estimates of clear-sky reflectance and consistent mean cloud albedos for all 3 years. The offset voltage remained the same throughout the period.

A different approach was applied for the 1987 GOES-East data since its instruments were different from the previous years (see Table I) and the offset voltage was much lower. The clear-sky visible count (proportional to the square root of radiance) was estimated using the ocean bidirectional model of Minnis and Harrison (1984) calibrated with the same formula used for the previous years. Clear-sky counts over the limited area were also derived from the 1987 GOES-East data. These data were plotted against the calibrated model results and used to fit the GOES-East radiances by forcing the line through the pair of known offset counts. This "calibration" is very uncertain for high radiances but it provides a reasonable estimate of clear-sky reflectance essential for derivation of the cloud parameters. The approach to the calibrations taken here is necessitated by the lack of a consistent calibration source at the present time.

3. Results

All of the results presented here exclude the results for 1984 and 1987 GOES-West since they were unavailable at the time of printing. Figure 1 shows the mean total and layer cloud amounts for the entire period. Mean total cloudiness is less than 70% within 5° of the California coast with the minimum occurring north of 35°N. Cloud cover increases to a maximum between 125°W and 130°W south of 30°N before decreasing to the southwest. Most of the clouds are found in the lowest layer (Fig. 1b), especially in the southern half of the domain. Midlevel and high clouds constitute less than 10% of the total over all marine areas except in the northwest corner (Figs. 1c and 1d). Total cloudiness over the adjacent land areas is less than 30%. The interannual standard deviations of the monthly mean total cloudiness for the period range from 3% in the southwest to nearly 12% over the areas of maximum cloudiness.

The clear-sky temperatures (Fig. 2) over the ocean range from 285K in the north to 290K in the southeast corner of the region. The interannual standard deviations of these temperatures are less than 1K over most of the ocean areas. Values greater than 1K are found over some of the western regions of the grid. Mean equivalent blackbody cloud-top temperatures in Fig. 3 also show a general north-south decrease. The cloud-top isotherms, however, are skewed to the north ridging near the coast while the clear isotherms are more parallel with latitude troughing near the coast. This results in a 1K to 2K east-west gradient in the difference between the two quantities. This difference is about 6K on average indicating that the clouds are confined to the boundary layer as expected. Interannual standard deviations of mean cloud-top temperature range from 0.5K to 1.5K over areas with less than 5% midlevel cloud cover.

Mean clear ocean albedos (Fig. 4) range between 0.10 and 0.12 with standard deviations generally < 0.01. Cloud albedos (Fig. 5) over the ocean regions are typically around 0.35. Maximum marine cloud albedos occur near the coast and along a line southwestward from 35°N, 122°W. Minimum cloud albedo (0.32) is found over the southeastern corner of the region. Interannual standard deviations of cloud albedo vary from less than 0.01 over the northwest corner to 0.06 over the southeastern regions.

Cloud cover over both the marine and land areas undergoes distinct diurnal variations. Over all of the ocean regions, cloud amount peaks between 0300 LST and 0900 LST with a minimum during the afternoon. Two special regions have been defined to determine if any significant differences exist between the diurnal variations of the stratocumulus clouds near the coast and far from the coast. The pacific (PAC) region is a 7.5° box between 32.5°N and 25°N and 140°W and 132.5°W; the IFO region is bordered by 35°N and 30°N and 125°W and 120°W, with an additional 2.5° region to the east centered at 31.3°N and 118.8°W. Figure 6 compares the 3-hourly means for the IFO and PAC. The diurnal range over the PAC is 25%

greater than that near the shore. Minimum cloudiness appears to occur earlier over the PAC and remain longer than it does over the IFO region.

4. Discussion

Cloud amount patterns are similar to those compiled by Sadler et al. (1976). The slightly higher values here may be the result of including night and morning hours in the analysis. Climatological values of sea surface temperatures over the area (Reynolds, 1983) are between 2K and 4K lower than the clear-sky results shown here. The differences which increase from the coast toward the southwest are primarily due to water vapor attenuation and some cloud contamination. Atmospheric moisture variations are probably responsible for the difference gradient. The differences between clear-sky and cloud-top temperatures may be related to the strength of the inversion over the marine boundary layer. Except for the area of maximum albedo extending from the coast, cloud albedos are within 1 - 2% of those found in previous studies (e.g., Minnis et al., 1987) over areas of stratocumulus over the open ocean. The cloud albedo maximum could result from an infusion of continental aerosols near the coast. Diurnal variations of cloudiness are also similar to those found over other parts of the Pacific (e.g., Minnis et al., 1987). Coastal-open ocean differences in the diurnal range may be tied to variations in the strength of the inversion and liquid water content.

5. Concluding remarks

The preliminary results described in this paper provide a long-term perspective of the large-scale cloudiness over the stratocumulus IFO region. Inclusion of data from GOES-West taken during 1984 and 1987 will complete this 5-year climatology of July marine stratocumulus over the IFO limited area. Measurements taken during the IFO will improve our understanding of the behavior of the various parameters observed in this study and over larger time and space scales. This analysis and similar ETO results will provide the link between the IFO and stratocumulus over the rest of the globe and other seasons.

6. References

Kloessel, K. A., B. A. Albrecht, and D. P. Wylie, 1988: FIRE Marine Stratocumulus Observations -- Summary of Operations and Synoptic Conditions. FIRE TR No. 1, 171 pp.

Minnis, P., 1988: Viewing Zenith Angle Dependence of Cloudiness Determined from Coincident GOES-East and GOES-West Data. Submitted to *J. Geophys. Res.*

Minnis, P. and E. F. Harrison, 1984: Diurnal Variability of Regional Cloud and Clear-Sky Radiative Parameters Derived from GOES Data. Part III: November 1978 Radiative Parameters. *J. Clim. Appl. Met.*, 23, 1033-1051.

Minnis, P., E. F. Harrison, and G. G. Gibson, 1987: Cloud Cover Over the Equatorial Eastern Pacific Derived from July 1983 ISCCP Data Using a Hybrid Bispectral Threshold Method. *J. Geophys. Res.*, 92, 4051-4073.

Reynolds, R. W., 1983: A Comparison of Sea Surface Climatologies. *J. Appl. Met.*, 22, 447-459.

Sadler, J. D., L. Oda, and B. J. Kilonsky, 1976: Pacific Ocean Cloudiness from Satellite Observations. UHMET 76-01, Univ. of Hawaii, Honolulu, 137 pp.

Satellite	Longitude (deg W)	Dates	VZ (deg)
GOES-6	135.0	July 17–31, 1983	30
GOES-6	135.0	July 1–31, 1984	30
GOES-6	108.7	July 1–31, 1985	46
GOES-6	108.7	July 1–31, 1986	46
GOES-7	75.0	July 2–31, 1987	67
GOES-6	135.0	July 1–31, 1987	30

Table 1. Satellite data characteristics. (Note that GOES–6 and GOES–7 are also referred to as GOES–West and GOES–East.)

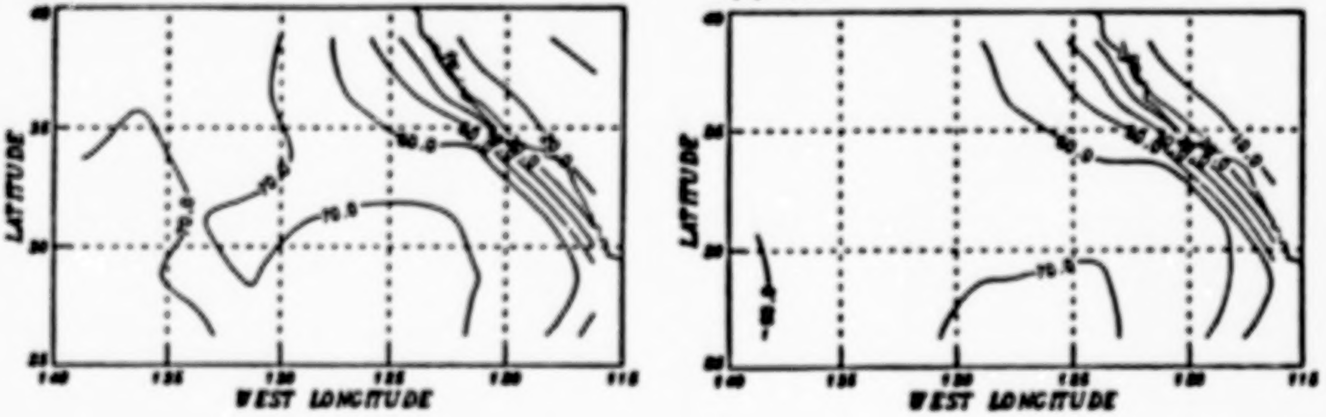

(a) Total (b) Low

LATITUDE
WEST LONGITUDE
40
35
30
25
140
135
130
125
120
115
70.0
80.0

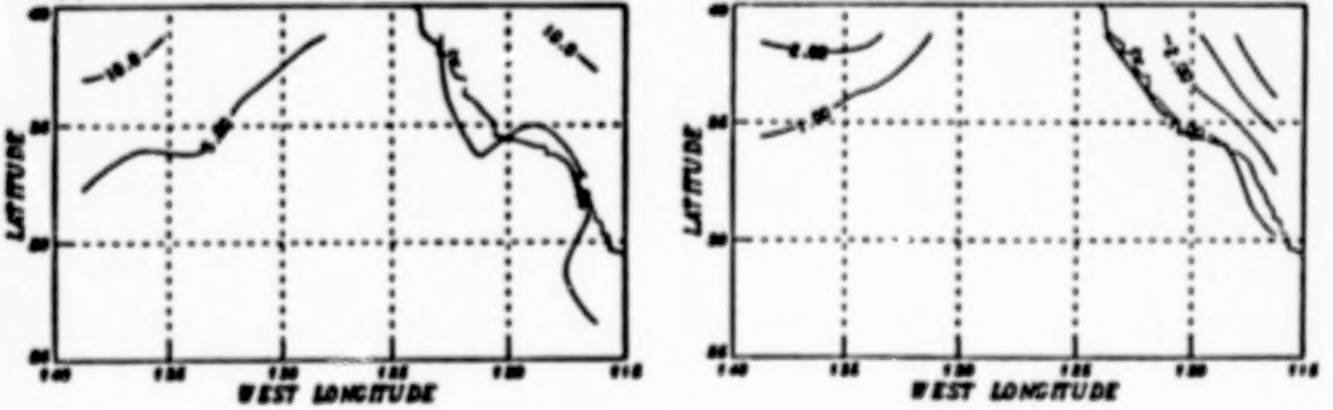

(c) Middle (d) High

LATITUDE
WEST LONGITUDE
40
35
30
25
140
135
130
125
120
115
10.0
1.00

Figure 1. Mean cloud amounts for July (1983 - 1987).

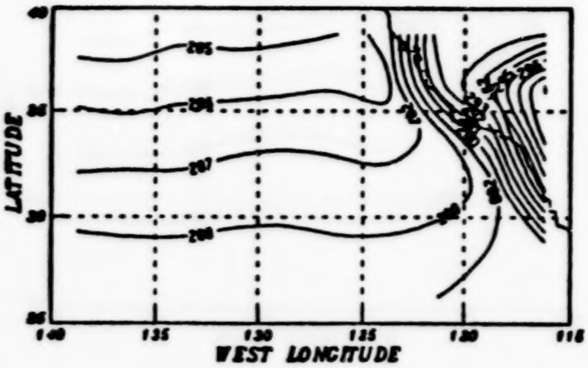
40
35
30
25
LATITUDE
140
135
130
125
120
115
WEST LONGITUDE
285
286
287
288

Figure 2. Mean clear-sky temperatures for July (1983 - 1987).

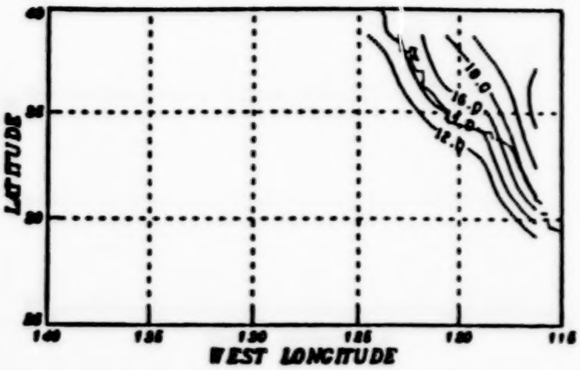
40
35
30
25
LATITUDE
140
135
130
125
120
115
WEST LONGITUDE
10.0
16.0
14.0
12.0

Figure 4. Mean clear-sky albedos for July (1983 - 1987).

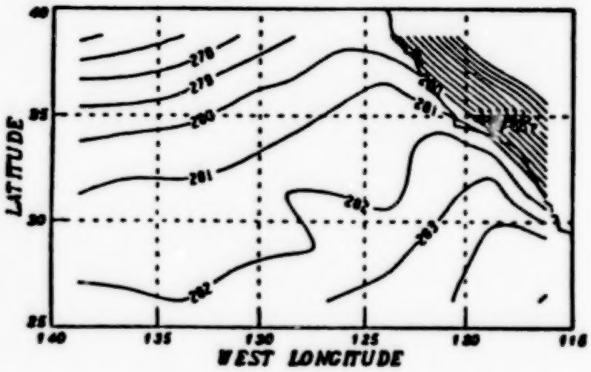
40
35
30
25
LATITUDE
140
135
130
125
120
115
WEST LONGITUDE
278
279
280
281
282
283

Figure 3. Mean cloud-top temperatures for July (1983 - 1987).

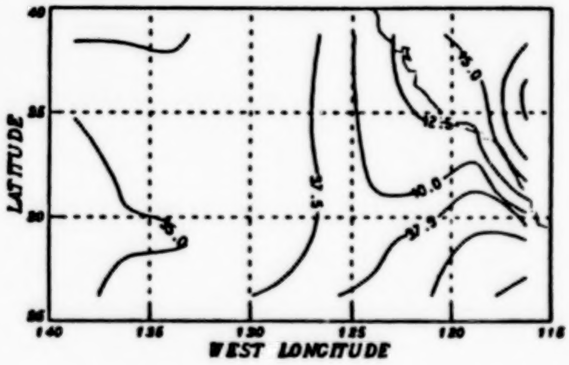
40
35
30
25
LATITUDE
140
135
130
125
120
115
WEST LONGITUDE
15.0
12.5
10.0

Figure 5. Mean cloud albedos for July (1983 - 1987).

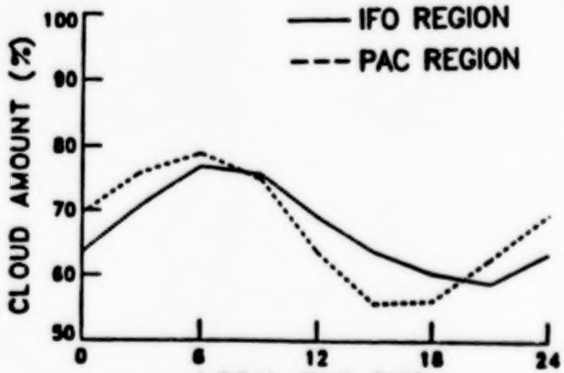

Figure 6. Diurnal variation of cloud cover for July (1983 - 1987).

THE RELATIONSHIP OF MARINE STRATUS TO SYNOPTIC CONDITIONS

Donald Wylie, Barry Hinton, Peter Grimm
University of Wisconsin-Madison

Kevin Kloesel
The Pennsylvania State University

1. Introduction

The marine stratus which persistently covered most of the eastern Pacific Ocean, Had large clear areas during the FIRE Intensive Field Operations (IFO) in 1987. Clear zones formed inside the large oceanic cloud mass on almost every day during the IFO (Figure 1). The location and size of the clear zones varied from day to day implying that they were related to dynamic weather conditions and not to oceanic conditions. Forecasting of cloud cover for aircraft operations during the IFO was directed towards predicting when and where the clear and broken zones would form inside the large marine stratus cloud mass.

The clear zones often formed to the northwest of the operations area and moved towards it. However, on some days the clear zones appeared to form during the day in the operations area as part of the diurnal cloud burn off. The movement of the clear zones from day to day were hard to follow because of the large diurnal changes in cloud cover. Clear and broken cloud zones formed during the day only to distort in shape and fill during the following night.

The field forecasters exhibited some skill in predicting when the clear and broken cloud patterns would form in the operations area. They based their predictions on the analysis and simulations of the models run by NOAA's Numeric Meteorological Center. In this paper, we will discuss how the atmospheric conditions analyzed by one NOAA/NMC model related to the cloud cover.

2.Background

The forecasters knew before the IFO that the positions of the subtropical high at the surface and the upper air troughs could be used for predicting breaks and clear zones in the marine stratus. Clear and broken zones were observed prior to the IFO as upper air troughs reached the California coast. Clearing occurred when the trough axis crossed the coast moving east. At the surface, the subtropical high formed a nose that protruded into northern California (see Figure 2). Clear and broken zones often formed to the west of San Diego. When the subtropical high was farther offshore west of North America, the marine stratus cloud cover had fewer and smaller clear and broken areas.

After the FIRE IFO, we decided to quantify the relationship between the cloud cover and synoptic weather patterns. Before the IFO, we knew that the best meteorological information over the ocean was the analyses made for the model initializations by NOAA NMC. The surface analysis made by NOAA National Weather Service only pertained to continental conditions since few marine observations were available. The pressure patterns poorly depicted the subtropical high or the wind conditions observed offshore. Because of this problem, the forecasters exclusively used the NOAA/NMC model analyses for predicting wind directions and cloud cover changes.

3. Statistical Analysis of Model Fields

A statistical test was made to see if the model fields were related to marine stratus cloud cover. For this test, we extracted some standard dynamic and thermodynamic parameters from the model fields during the IFO. They were the 1000 mb wind components (U_{1000} and V_{1000}), temperature (T), dew point (T_d), dew point depression ($T-T_d$), 1000 mb height (Z_{1000}), 50 mb height (Z_{500}), 500 mb wind components (U_{500} and V_{500}), 1000 mb temperature advection ($V \bullet \nabla T$), and dew point advection ($V \bullet \nabla T_d$). Time series of these parameters were formed from the initial model fields at 00 and 12Z. The two values each day were averaged together to form a time series that could be correlated with one cloud cover analysis per day.

Seven locations in the eastern Pacific were chosen for this correlation test. They are shown in Figure 3. Each location was a grid point of the Global Circulation Model of NOAA/ NMC. At each location, cloud cover was defined as the fraction of a 100 line by 100 element box with brightness above two threshold levels on the GOES-West visible image at 20:00 Z (local noon). The two thresholds used were 15 counts (0-63 scale) for defining general cloud fraction and 30 counts for defining bright cloud fraction. These thresholds were arbitrarily chosen from a visual inspection of the images. An obvious brightness difference between cloud and clear could be seen on the images. We choose only images at local noon over a restricted part of the season to avoid the affects of changing illumination of the area. Cirrus and other cloud forms were absent during this 21-day period, so all satellite derived cloud cover fractions are indicative of marine stratus cloud cover.

These brightness levels tracked the changes in cloud cover for each box. The FIRE IFO aircraft flew in the general area of box 1. This area had nearly 100% cloud cover, except for three major clearing events. The cloud fraction in the box decreased after the first day. The lowest cloud fraction was reached on 4 July. Cloud cover rebuilt and a second major clearing event happened on 8 July. A decrease in bright cloud fraction occurred on 11 July with little change in the general cloud cover (lower brightness threshold). Nearly solid cloud cover followed until 18 July when a third major clearing event started and continued to the end of the IFO.

The difference between the cloud cover fraction at high and low brightness levels indicates the ranges in the pattern of the clouds on the satellite images. Cells or broken cloud patterns were present when the low brightness cloud fraction fell below 90%. This was indicative of cellular type clouds with nearly black areas in between. We assume the black areas were clear, However, higher resolution imagery form other satellites indicated that some small clouds were possibly present in these areas.

Cellular structure also was commonly observed when totally overcast conditions were present. These cells were bright spots inside solid cloud fields. The low brightness threshold cloud fraction was usually near 100% while the high brightness cloud fraction was lower. We generally interpret the low brightness cloud fraction as indicative of the general cloud cover while the high brightness cloud fraction followed the changes in bright cells. The bright cells being an indication of the more intense convection in the marine stratus.

A summary of our correlation between model fields and cloud fraction is given in Table 1. We had 21 days in our time series. A correlation of 0.36 was found to have a 90% confidence that a real correlation (non-zero) existed. These correlations are designated by the bold type in Table 1. We will note where correlations of this level or higher were found as being indicative of relationships.

U_{1000} and $V \bullet \nabla T_d$ correlated with cloud fraction in five out of seven boxes. Z_{1000} and T_d also had strong correlations in some boxes.

The relationships between $V\cdot\nabla T_d$ and cloud fraction also had one unusual factor. A negative correlation was found in five out of seven boxes. This indicated that cloud fraction increased with negative dew point advection $(-V\cdot\nabla t_d)$, which would be expected. Negative dew point advection implies that advection is moistening the boundary layer. However, along the California coast in boxes 1 and 3 the opposite relationship was found, a positive correlation coefficient. This implied that cloud fraction decreased with $(-V\cdot\nabla T_d)$ negative dew point advection. Boxes 1 and 3 appear to have other factors controlling marine stratus cloud formation. The dew points themselves (T_d) had very small correlations with cloud cover where as in the western boxes (5 and 7) the dew points had high correlations. Temperature advection $(V\cdot\nabla T)$ correlations also followed the same signs as the dew point advection correlations in all boxes. This indicates the the cloud cover increased when advection attempted to lower the temperature and dew point along the northern California coast while to the west, the cloud cover decreased when advection acted to lower both T and T_d. The cloud cover obviously was controlled by different factors along the California coast than farther out in the open ocean. This difference is also evident by the high brightness cloud fraction. Boxes 1 and 3 had lower high brightness clouds fractions during most of the 21-day period than the other boxes. There was a general absence of bright cells in the marine stratus cloud fields. Boxes 1 and 3 are closer to the origin of the wind fetch acrossed the ocean. The marine stratus cloud fields had smaller and possibly thinner clouds while to the west in boxes 5 and 6. the cellular structure was better developed. Cloud top temperatures were also colder indicating a growth in cloud top heights. This is the area where marine stratus cloud fields began to transform into cumulus convective groups more closely related to trade wind cumulus. In the beginning of the wind fetch (boxes 1 and 3), the clouds may be related to mixing processes with the cold underlying ocean, a stable boundary layer situation. As the air moves southwest over warmer ocean temperatures, the boundary layer became less stable and more convection develops in the marine clouds.

4. Conclusion

Marine status cloud cover is predictable using NOAA NMC Global Circulation Model analyses. The forecasters observed patterns in the 1000 mb and 500 mb height fields that related to cloud cover changes. At the same time we have been able to statistically correlate atmospheric parameters analyzed by the model with observed cloud cover changes. This indicates that there is information in the model that can be used for parameterizing marine stratus clouds. The effects of these clouds on radiative heating and cooling can thus be developed.

Table 1: Correlation of the cloud cover defined by the low brightness threshold (15 counts on a 0-63 scale) with variables from NOAA/NMC's Global Model

	BOX NUMBER						
VARIABLE	1	2	3	4	5	6	7
Low vs High Brightness	**0.8**	**0.6**	**0.8**	**0.7**	**0.7**	**0.6**	**0.7**
$V\cdot\nabla T$	0.2	-0.3	0.3	-0.3	**-0.5**	-0.1	**-0.5**
$V\cdot\nabla T_d$	**0.5**	**-0.4**	**0.5**	-0.3	**-0.4**	-0.3	**-0.7**
Z_{1000}	**-0.4**	-0.2	0.0	0.3	-0.3	0.3	-0.2
Z_{500}	0.2	0.2	0.2	0.2	**0.4**	0.3	**0.6**

	BOX NUMBER						
VARIABLE	1	2	3	4	5	6	7
T	-0.1	-0.3	0.1	0.0	0.3	**0.4**	**0.6**
T_d	-0.0	-0.0	0.2	0.1	**0.8**	-0.0	**0.7**
$(T-T_d)$	-0.1	-0.1	-0.3	-0.1	**0.8**	0.3	**-0.5**
U_{1000}	0.3	0.2	**-0.4**	**-0.4**	**-0.5**	**-0.5**	**-0.7**
V_{1000}	0.1	-0.3	0.3	-0.3	-0.3	-0.1	-0.1

A

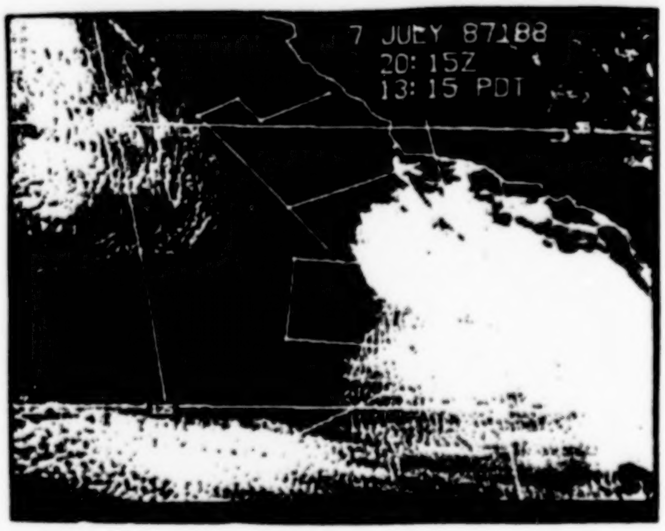
7 JULY 87188
20:15Z
13:15 PDT

Figure 1

GOES satellite imagery for 7 July 1987.
(A) Visible 2015Z,

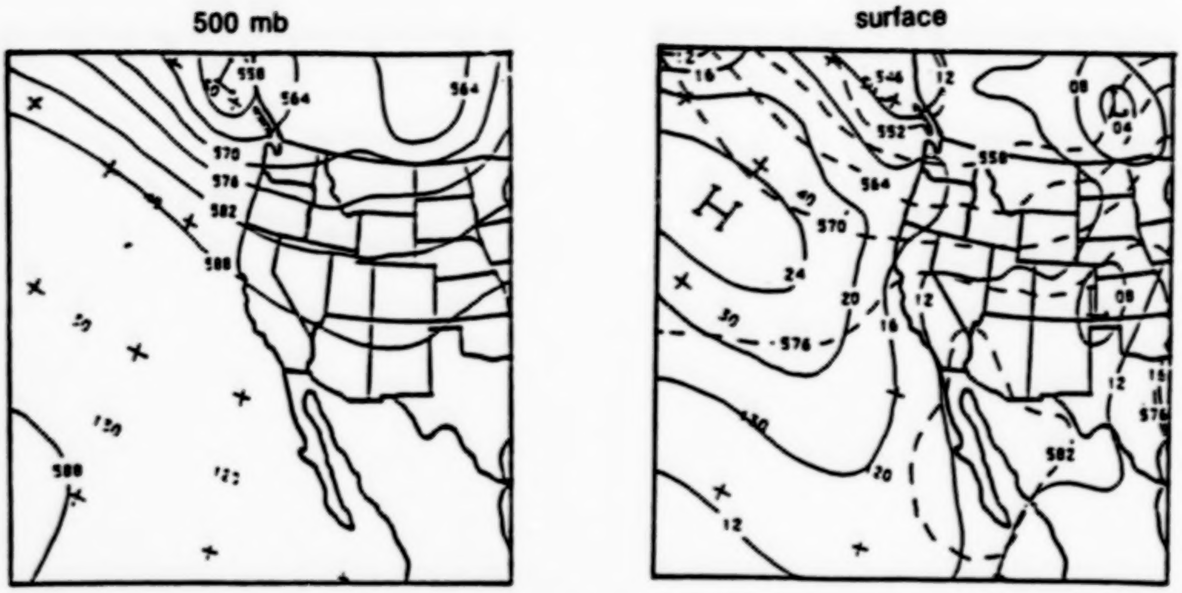

500 mb

surface

558
564
570
576
582
588
H
L
570
576
582
16
12
20
24
08
04

Figure 2: NGM analysis of surface pressure and 500 mb heights for 12:00 GMT 7 July 1987

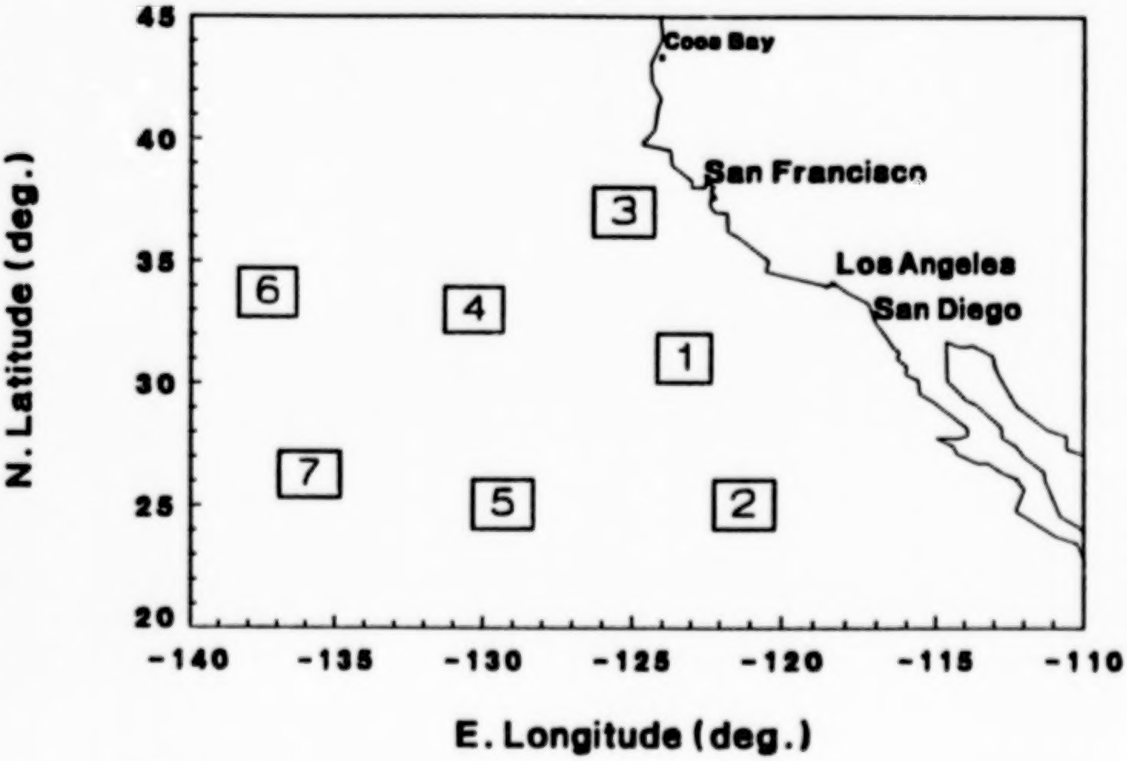

Coos Bay
San Francisco
Los Angeles
San Diego
1
2
3
4
5
6
7
45
40
35
30
25
20
-140
-135
-130
-125
-120
-115
-110
N. Latitude (deg.)
E. Longitude (deg.)

Figure 3: The locations of the boxes used in correlating cloud cover with atmospheric parameters shown in Table 1.

FIRE Abstract: July 11-15, 1988

Analysis of diurnal variation of SCu layer using 2 days of CLASS soundings on San Nicolas Island

Alan K. Betts
RD2, Box 3300
Middlebury, VT 05753
(802) 545-2492

Sixty-nine soundings were taken at San Nicolas Island during the FIRE marine stratocumulus experiment (Schubert et al, 1987a). The archived thermodynamic data at 5mb vertical resolution were reduced to 25mb vertical resolution by averaging. Ceilometer data showed the time variation of cloud-base. (Schubert et al, 1987b)

A subset of 20 soundings taken during a 2 day period of light winds (04L on July 10 to 07L on July 12) were analyzed. The soundings are grouped into 6 hr. averages (with 5 soundings in each category) to examine the diurnal variation of the thermodynamic structure. Consistent with the solar heating during the daytime, cloud-base rises during the daytime hours and the cloud layer thins. The subcloud layer also becomes more stable, suggesting some uncoupling of the cloud layer from the surface.

Acknowledgements: This work was supported by NSF under grant ATM87-05403 and NASA-GSFC under contract NAS5-28800

References:

Schubert, W.H., P.E. Ciesielski, T.B. McKee, J.D. Kleist, S.K. Cox, C.M. Johnson-Pasqua, and W.L. Smith 1987a: An analysis of boundary layer sounding data from the FIRE marine stratocumulus experiment. Atmos. Sci. Paper No 419, Dept. of Atmos. Sci., CSU, Ft. Collins, CO 80523. 101pp.

Schubert, W.H., S.K. Cox, P.E. Ciesielski and C.M. Johnson-Pasqua, 1987b: Operation of a ceilometer during the FIRE marine stratocumulus experiment. Atmos. Sci. Paper No 420. Dept. of Atmos. Sci., CSU, Ft. Collins, CO 80523. 34pp.

Diurnal Variation of Marine Stratocumulus over San Nicolas Island during the FIRE IFO

R. Davies and M. Blaskovic

Department of Meteorology, McGill University,

Montreal, Quebec H3A 2K6, Canada

1. Introduction

Preliminary analysis has been made of data collected at San Nicolas Island during the Intensive Field Observation (IFO) phase of the First International Satellite Cloud Climatology Program's Regional Experiment (FIRE). Of particular interest has been an examination of a distinct diurnal variation in the cloud properties, despite an apparent absence of diurnal forcing from the surface. Direct or indirect radiative modulation of such clouds, as proposed by Fravalo *et al.* (1981) and Turton and Nicholls (1987) indeed seems likely.

In this paper, preliminary observational evidence for diurnal change in the marine stratocumulus adjacent to San Nicolas Island is presented. A comparison is then made between the observed behavior and predictions from theoretical models of the interactive effect of radiation on boundary layer clouds.

2. Data Analysis

Preliminary analysis of the data collected by the San Nicolas Island participants[1] during the IFO period of July 1–19, 1988 indicates the presence of a relatively persistent stratocumulus cloud deck, modified by mild synoptic-scale variations. The first order effect of these variations on the values presented below has been removed by considering the local time departures from 24-hr running means. Error bars indicate the expected error in the mean local time departure at the 1 σ level, based on the observed natural variability during the data collection period.

Column liquid water, determined from the NOAA/WPL radiometer (Hogg *et al.*, 1983), is shown as a function of local time in Fig. 1. A diurnal signature is clearly discernible, with a maximum value of 0.13 mm in early morning falling steadily to a minimum of 0.02 mm in late afternoon before rising again to its early morning maximum.

Equally evident is the systematic diurnal variation in the cloud base height, obtained from the CSU ceilometer (Schubert *et al.*, 1987), shown in Fig. 2. Coincidental with maximum column liquid water, the cloud base drops to a minimum height of about 450 m above sea level in early morning and rises to a maximum of about 630 m by late afternoon.

Continuous time series of cloud top height had not been released at the time of this writing, so that cloud top height had to be determined from the much sparser CLASS radiosonde data. These are shown similarly in Fig. 3, and give the appearance of a consistent diurnal variation, with cloud top reaching a maximum height of about 820 m in early morning and a minimum of about 660 m in late afternoon.

Despite the noise present in the derived values of cloud thickness, presented in Fig. 4, the data are consistent with the presence of a diurnal trend in cloud thickness. Consistent with Fig. 1, maximum cloud thickness of about 400 m occurs in early morning and reduces to a minimum of about 150 m by late afternoon.

---

[1] see acknowledgments for a list of data sources.

Similarly, the average liquid water density within the cloud, obtained by dividing the column amount by the cloud thickness, as shown in Fig. 5, is too noisy to unequivocally confirm a diurnal variation. However Fig. 5 is consistent with an average liquid water density ranging from 0.5 g m^{-3} in early morning to 0.2 g m^{-3} in late afternoon.

The relationship between average liquid water density and cloud thickness may be clearer in Fig. 6, which shows strong positive correlation between these variables.

3. Discussion

The clear diurnal signature in column liquid water content of the marine stratocumulus adjacent to San Nicolas Island during the FIRE IFO indicates some degree of radiative modulation of the cloud. Despite noisy values of cloud top height that will be improved once more data is released to the FIRE science team, estimates of the diurnal variation of cloud thickness can be made. The initial analysis reveals a systematic lowering of cloud top and raising of cloud base from around sunrise to around sunset, with the reverse during nighttime. As the cloud thickness decreases during the day, so too does the mean liquid water density in the cloud, and together these effects combine to produce the observed signature in column liquid water.

We are presently examining explanations for this behavior, in conjunction with theoretical models of cloud-radiative interaction, and will relate the model predictions to measurements of drop size distributions within the cloud once these also are made available.

Acknowledgments. We are pleased to acknowledge the following data sources: Dr. Jack Snider, NOAA/WPL for the radiometer determinations of integrated liquid water; Dr. Wayne Schubert, Colorado State University for ceilometer measurements of cloud base; Mr. B. Syrett, The Pennsylvania State University, for the radiosonde data. Funding for this research is provided in part by NASA grant NAG 1-552, NSERC, and AES.

References

C. Fravalo, Y. Fouquart, and R. Rosset, 1981: The sensitivity of a model of low stratiform clouds to radiation, *J. Atmos. Sci.*, *38*, 1049–1062.

D.C. Hogg, F.O. Guiraud, J.B. Snider, M.T. Decker, and E.R. Westwater, 1983: A steerable dual-channel microwave radiometer for measurement of water vapor and liquid in the troposphere, *J. Clim. Appl. Meteor.*, *22*, 789–806.

W.H. Schubert, S.K. Cox, P.E. Ciesielski, and C.M. Johnson-Pasqua, 1987: Operation of a ceilometer during the FIRE marine stratocumulus experiment, Atmos. Sci. paper No. 420, Colorado State University (FIRE Vol. 3).

J.D. Turton and S. Nicholls, 1987: A study of the diurnal variation of stratocumulus using a multiple mixed layer model, *Quart. J. Roy. Meteor. Soc.*, *113*, 969–1009.

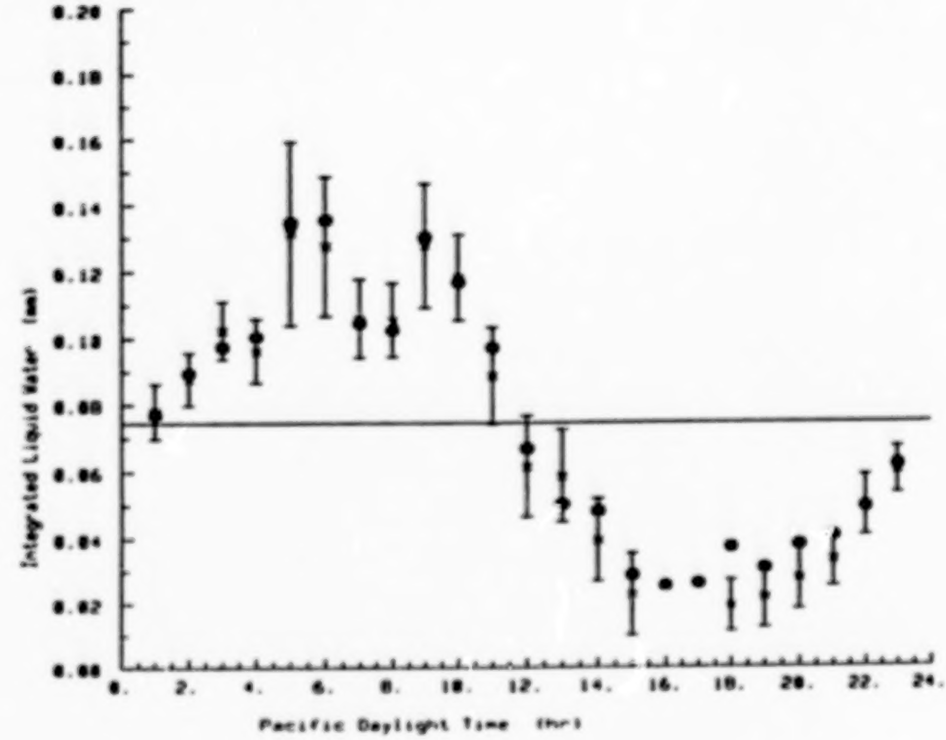

FIG. 1. Column liquid water versus local time, determined from the NOAA/WPL radiometer on San Nicolas Island. Circles - averages over the observing period. Crosses - averages after removing synoptic trends. Error bars indicate uncertainty in individual mean values based on natural variability.

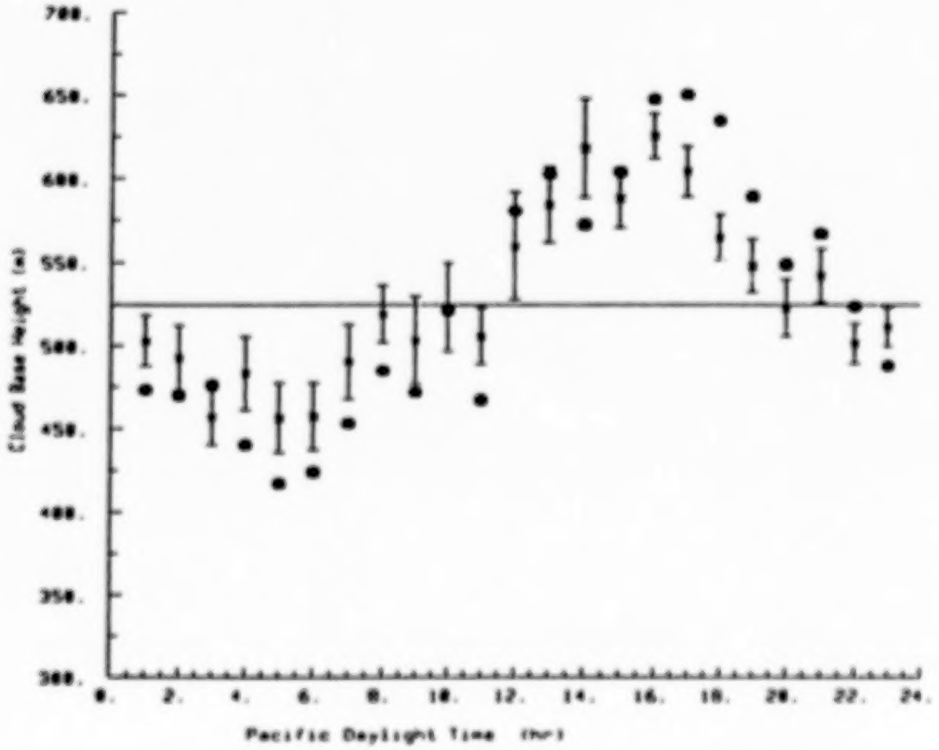

FIG. 2. Cloud base height versus local time. Symbols as in Fig. 1.

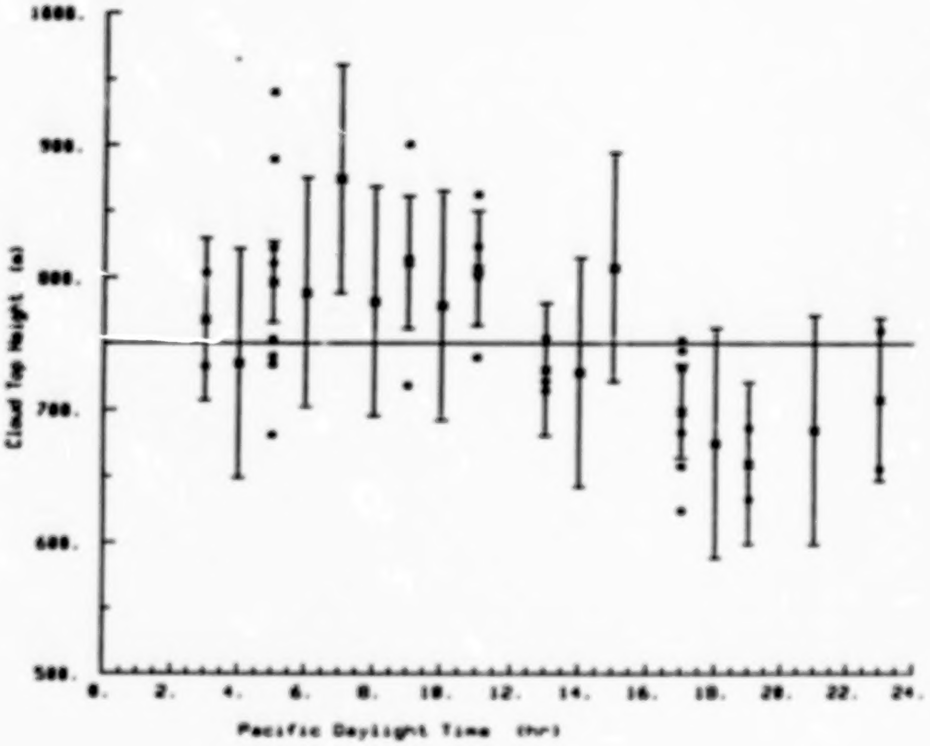

FIG. 3. Cloud top height from radiosonde data, after removal of synoptic trends. Open circles- individual data points. Crosses- mean values. Error bars indicate uncertainty in mean values based on variance of data at 0500 PDT.

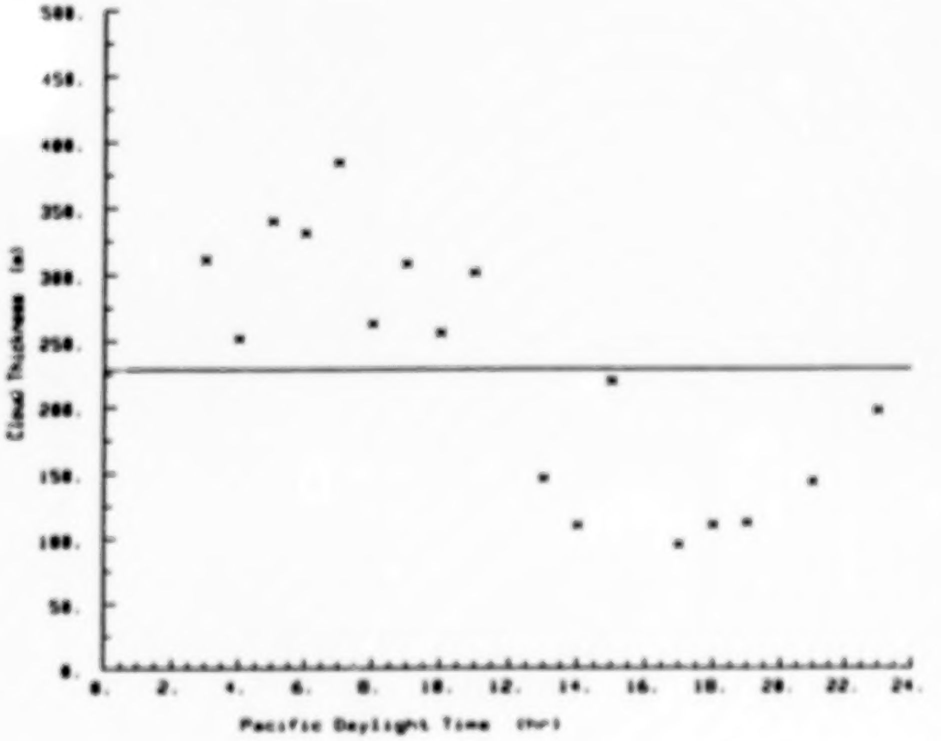

FIG. 4. Cloud thickness versus local time, obtained by differencing Fig. 3 and Fig. 2.

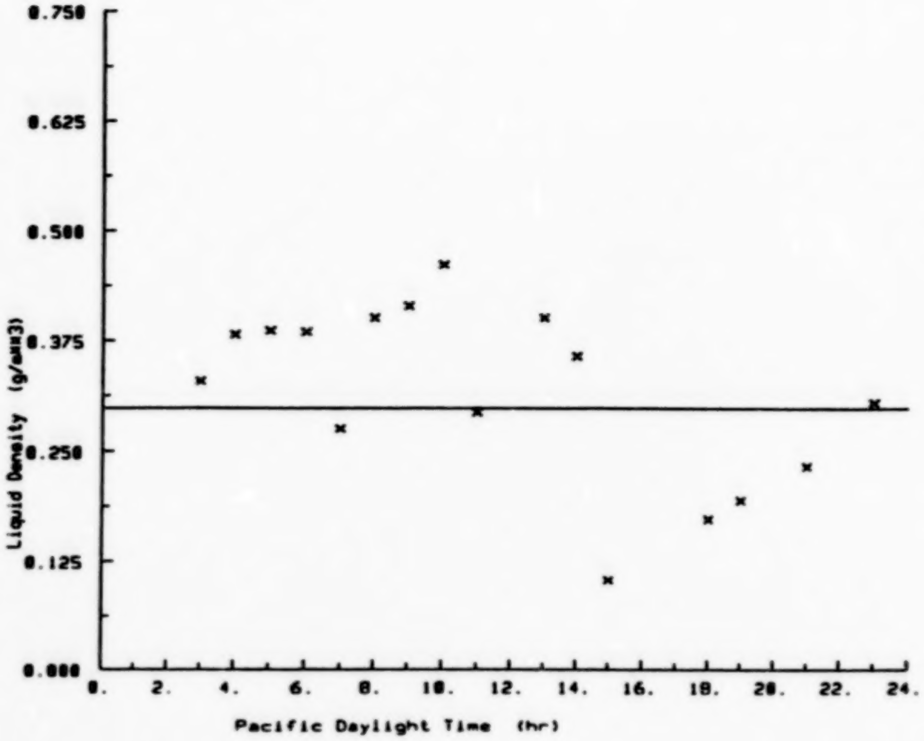

FIG. 5. Average cloud liquid water density versus local time, obtained by combining data from Fig.1 and Fig. 4.

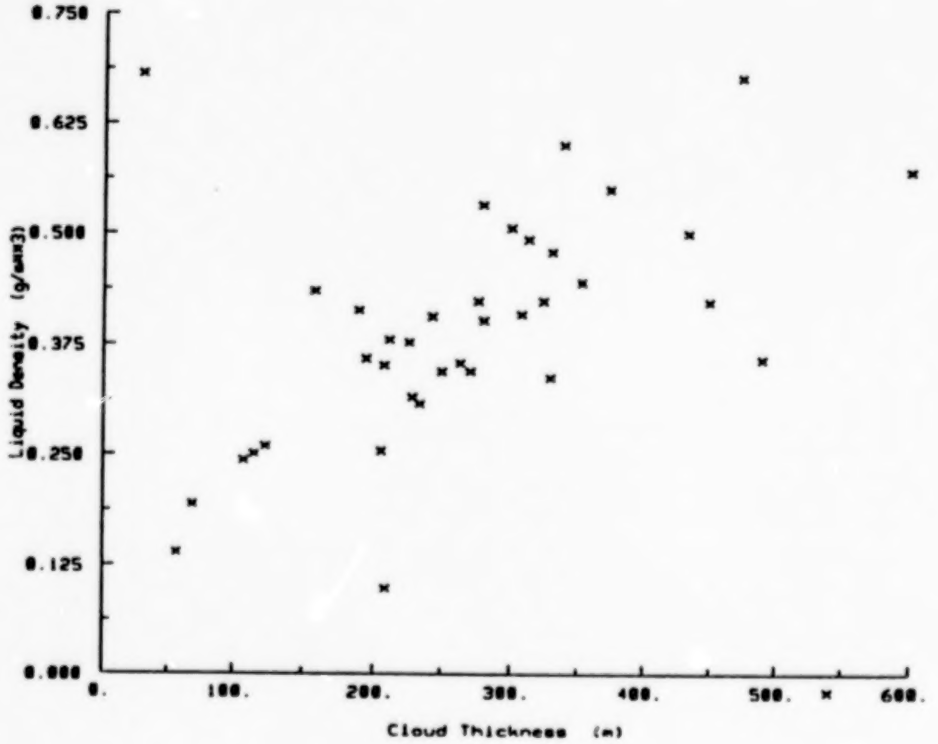

FIG. 6. Scatter diagram of average cloud liquid water density versus cloud thickness, using data coincident with radiosonde determination of cloud top height.

ANALYSIS OF TETHERED BALLOON, CEILOMETER AND CLASS SOUNDING DATA TAKEN ON SAN NICOLAS ISLAND DURING THE FIRE PROJECT

Wayne H. Schubert, Paul E. Ciesielski, Thomas A. Guinn, Stephen K. Cox and Thomas B. McKee
Department of Atmospheric Science, Colorado State University, Fort Collins, CO 80523

During the FIRE Marine Stratocumulus Program on San Nicolas Island, Colorado State University (CSU) and the British Meteorological Office (BMO) operated separate instrument packages on the NASA tethered balloon. The CSU package contained instrumentation for the measurement of temperature, pressure, humidity, cloud droplet concentration, and long and short wave radiation. Eight research flights, performed between July 7 and July 14, are summarized in the attached table. We have assigned an analysis priority to the July 7, 8, and 11 flights for the purposes of comparing the CSU and BMO data. Results will be presented at the conference.

In addition, CSU operated a laser ceilometer for the determination of cloud base, and a CLASS radiosonde site which launched 69 sondes. We are in the process of analyzing data from all of the above systems. Reports have so far been prepared on the ceilometer and on the CLASS sounding data (see attached references). According to the ceilometer record, 55 of the 69 CLASS soundings were released with stratocumulus overhead. For each of these 55 soundings we have determined the cloud top total water jump Δr as follows. We first compute the vertically averaged water vapor mixing ratio in the layer which extends from 60 m to 240 m above cloud top. We then subtract from this the average water vapor mixing ratio in the layer which extends from 65 m to 165 m above sea level (the island sounding site being 38 m above sea level). This water vapor mixing ratio difference should be equivalent to the cloud top jump in total water if the boundary layer is well-mixed. The procedure for determining $\Delta\theta_e$ is identical. In this way each of the fifty-five soundings was characterized by a point in the $(\Delta r, \Delta\theta_e)$ plane as shown in Fig. 1. As can be seen, 40 of the 55 points lie on the stable side of the Randall (1980) stability line (the line labeled $\Delta\theta_e = kL\Delta r/c_p$), and 15 lie on the unstable side. According to the ceilometer record, 7 of the unstable cases show cloud break-up within 12 hours while 4 of the stable cases show break-up within 12 hours. The cases exhibiting break-up are indicated in Fig. 1 by the partially blackened symbols, with the fraction of blackening indicating the fraction of 12 hours before cloud disappearance. The occurrence of partially blackened symbols on the stable side of the critical stability line indicates that cloud top evaporative instability is not the only mechanism for break-up. For further discussion the reader is referred to Kuo and Schubert (1988), who report on model experiments designed to understand the existence of persistent cloud decks with soundings which are unstable according to theory.

Acknowledgments

We want to thank John Kleist, Christopher M. Johnson-Pasqua, William Smith Jr. and Hung-Chi Kuo for their valuable contributions to this work. Our participation in the FIRE project has been supported by the Marine Meteorology Program of the Office of Naval Research under contract N00014-87-K-0228 and by the National Aeronautics and Space Administration under contract NAG1-554.

REFERENCES

Kuo, H.-C., and W. H. Schubert, 1988: Stability of cloud-topped boundary layers. *Quart. J. Roy. Meteor. Soc.*, **114**, in press.

Randall, D.A., 1980: Conditional instability of the first kind upside-down. *J. Atmos. Sci.*, **37**, 125–130.

Schubert, W. H., P. E. Ciesielski, T. B. McKee, J. D. Kleist, S. K. Cox, C. M. Johnson-Pasqua and W. L. Smith Jr., 1987: Analysis of boundary layer sounding from the fiire marine stratocumulus project. Colorado State University Atmospheric Science Paper No. 419.

Schubert, W. H., S. K. Cox, P. E. Ciesielski and C. M. Johnson-Pasqua, 1987: Operation of a ceilometer during the FIRE marine stratocumulus experiment. Colorado State University Atmospheric Science

CSU – TETHERED BALLOON RESEARCH SUMMARY

DATE:	REMARKS:
July 7 1987	9.8 hours – daytime; launch at 07:45 PDT. BMO attach 6 packages as balloon is taken to about 2400 ft. BMO does four 68 minute runs while CSU package is above cloud. At 13:25 PDT CSU begins two soundings with 5 minute legs at each 300 ft level.
July 8 1987	6.5 hours – daytime; launch at 07:30 PDT. Four BMO packages deployed at 100 ft intervals just below CSU package. Four 20 minute constant level runs with packages near cloud top (which was about 935 mb). Balloon brought down in 200 ft steps with 20 minutes at each level.
July 9 1987	4.0 hours – daytime; launch at 08:31 PDT. Very deep cloud with top near 950 meters. Some drizzle. Flight shortened because BMO could not get highest package above cloud top. No turbulence data but good sounding data.
July 10 1987	10.0 hours – daytime; launch at 08:34 PDT. Very deep boundary layer (1000 meters) so BMO stands down in light of previous day. CSU package steps upward in 300 ft intervals with 20 minutes at each level. Many 15 minute legs at 50 ft intervals near cloud top on descent.
July 11 1987	9.5 hours – evening; launch at 13:35 PDT. Some difficulty in getting the balloon above cloud top. BMO deploys 6 packages but takes the lowest one off. BMO does two 64 minute runs. CSU then steps down with eleven 20 minute legs.
July 12 1987	1 hour – night time; launch at 03:40 PDT. BMO put on four packages. At about 930 mb slack suddenly developed in the cable and everything was brought down in a hurry.
July 13 1987	11.5 hours – daytime; launch at 09:20 PDT. Only CSU is operating today. Cloud top near 960 mb. Ran about 16 twenty minute legs in the cloud layer and 9 in the subcloud layer.
July 13–14 1987	6.5 hours – night time; launch at 21:45 PDT without BMO. Low cloud top still. Performed 20 constant level legs in the boundary layer.

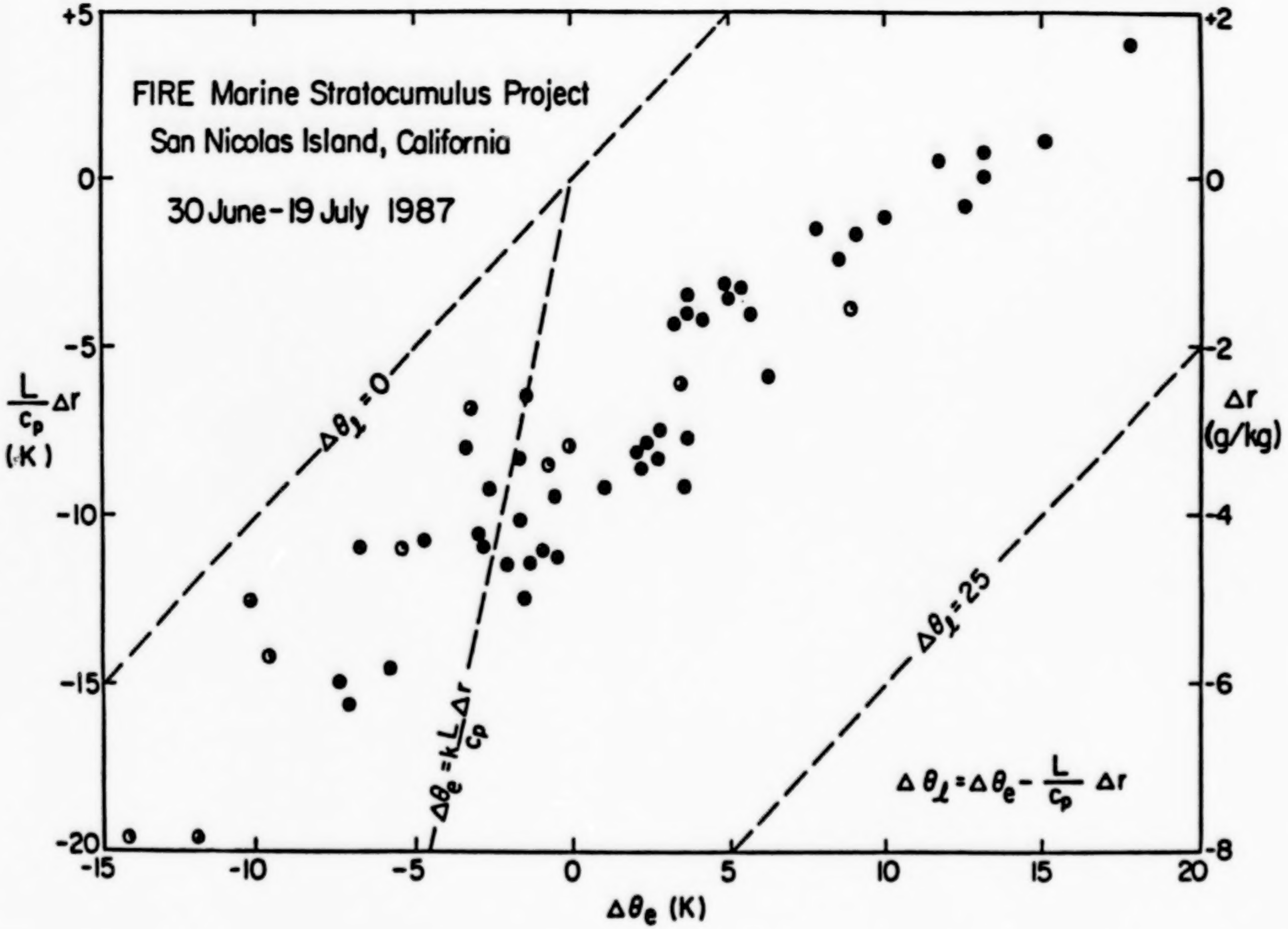
FIRE Marine Stratocumulus Project
San Nicolas Island, California
30 June-19 July 1987
$\frac{L}{c_p}\Delta r$ (K)
Δr (g/kg)
$\Delta\theta_e$ (K)
$\Delta\theta_l = 0$
$\Delta\theta_l = 25$
$\Delta\theta_e = k\frac{L}{c_p}\Delta r$
$\Delta\theta_l = \Delta\theta_e - \frac{L}{c_p}\Delta r$
+5
0
-5
-10
-15
-20
+2
0
-2
-4
-6
-8
-15
-10
-5
0
5
10
15
20

Figure 1

FIRE Abstract: July 11-15, 1988

Radiative control on tropical convective boundary layer equilibrium.

A.K. Betts
RD2 Box 3300
Middlebury, VT 05753
(802) 545-2492

and W. Ridgway
Applied Research Corp.
Landover, MD

This paper, an extension of Betts and Ridgway(1988), discusses how the near-balance between the radiative cooling and the surface fluxes in the tropics controls boundary layer θ_E, the height of cloud-base and the top of the convective boundary layer over the tropical oceans. The impact of boundary layer cloudiness and upper level moisture on the equilibrium solutions is explored.

Acknowledgements: This work was supported by NSF under Grant ATM87-05403 and NASA-GSFC under contract NAS5-28800.

Reference: Betts, A.K. and W. Ridgway, 1988: Coupling of the radiative convective and surface fluxes over the equatorial Pacific. J. Atmos. Sci. **45**, 522-536.

A GCM Parameterisation for the Shortwave Radiative Properties of Water Clouds

A. Slingo

National Center for Atmospheric Research [1]
Boulder, Colorado 80307

A new parameterisation has been developed for predicting the shortwave radiative properties of water clouds, suitable for inclusion in general circulation models (GCMs). The parameterisation makes use of the simple relationships found by Slingo and Schrecker (Quarterly Journal of the Royal Meteorological Society, **108**, 407-426, 1982), giving the three input parameters required to calculate the cloud radiative properties (the optical depth, single scatter albedo and asymmetry parameter) in terms of the liquid water path and equivalent radius of the drop size distribution. The input parameters are then used to derive the cloud radiative properties, using standard two-stream equations for a single layer. The relationships were originally derived for fairly narrow spectral bands (for example Slingo and Schrecker used 24 bands across the solar spectrum) but it has been found that it is possible to average the coefficients so as to use a much smaller number of bands, without sacrificing accuracy in calculating the cloud radiative properties. This makes the parameterisation fast enough to be included in GCMs.

The parameterisation has been programmed into the radiation scheme used in the U.K. Meteorological Office GCM. This scheme and the 24 band Slingo/Schrecker scheme have been compared with each other and with observations, using a variety of published datasets. There is good agreement between the two schemes for both cloud albedo and absorption, even when only four spectral bands are employed in the GCM.

The explicit separation of the dependence of the predicted cloud radiative properties on the liquid water path and equivalent radius is new. Previous attempts to generate parameterisations for large-scale models have not included such a separation, which limits their usefulness in climate change experiments.

FIRE data, particularly those from the stratocumulus field phase, should prove to be extremely useful in further testing of this parameterisation. This should establish a valuable link with the GCM community in this important area of climate research.

---

[1] The National Center for Atmospheric Research is sponsored by the National Science Foundation.

Preliminary Mixed-Layer Model Results for FIRE Marine Stratocumulus IFO Conditions

R Barlow and S Nicholls

Cloud Physics Branch
Meteorological Office, London Road, Bracknell, Berks RG12 2SZ, UK

Some preliminary results from the Turton & Nicholls (1987) mixed layer model using typical FIRE boundary conditions will be presented. The model includes entrainment and drizzle parametrizations as well as interactive long and shortwave radiation schemes. A constraint on the integrated turbulent kinetic energy balance ensures that the model remains energetically consistent at all times.

The preliminary runs have been used to identify the potentially important terms in the heat and moisture budgets of the cloud layer, and to assess the anticipated diurnal variability. These will be compared with typical observations from the C130.

Sensitivity studies have also revealed the remarkable stability of these cloud sheets: a number of negative feedback mechanisms appear to operate to maintain the cloud over an extended time period. These will also be discussed.

The degree to which such a modelling approach can be used to explain observed features, the specification of boundary conditions and problems of interpretation in non-horizontally uniform conditions will also be raised.

Simulations and Observations of Cloudtop Processes

S. T. Siems*, C. S. Bretherton*, and M. B. Baker**
*Applied Mathematics Department **Geophysics Program
University of Washington
Seattle WA 98195

Turbulent entrainment at zero mean shear stratified interfaces has been studied extensively in the laboratory and theoretically for the classical situation in which density is a passive tracer of the mixing and the turbulent motions producing the entrainment are directed toward the interface (see Turner, 1986, for a comprehensive review). For gases at high Reynolds number, the entrainment velocity w_e at the interface separating a lower turbulent fluid of mean virtual potential temperature $\overline{\theta}_v$ from a nonturbulent fluid of virtual potential temperature $\overline{\theta}_v - \Delta\theta_v$ depends only on a Richardson's number, which can be defined as

$$Ri = \frac{g \Delta\theta_v h}{w^2 \overline{\theta}_v} \tag{1.1}$$

where w and h are turbulent velocity and length scales. Carruthers and Hunt (1986), Linden (1973), Stull (1976), and others have described the entrainment mechanism at intermediate Ri in terms of eddies impinging on the interface and dragging down wisps of upper layer fluid. Lidar pictures (Atlas et al., 1986) show evidence of dome-wisp like entrainment in the inversion topping the dry atmospheric boundary layer.

In the layer cloud situation, radiative and evaporative cooling tend to drive convective motions away from the interface, instead of toward it as in the classical flows. Moreover, the function $\theta_v(F)$ is piecewise linear in the cloud case, where F is the fraction of cloudy air in a parcel formed by mixing cloud and upper air. This behavior introduces another parameter into the problem, which we define as D_*:

$$D_* = \frac{\Delta_*}{\Delta\theta_v F_*} \tag{1.2}$$

where $\Delta_* = \theta_v(F_*) - \overline{\theta}_v$ and F_* is the mixing fraction of exactly saturated air.

The effects of these properties of the cloud-clear interface on the entrainment process are not well understood. Observations (Nicholls and Leighton, 1986; Caughey et al., 1985) in stratocumulus show that evaporative cooling enhances entrainment over that expected in the dry, linearly mixing case, even if $D_* > 0$. On the other hand, observations (for example, Hanson, 1984) show that even in cases for which the "cloudtop entrainment instability," or CEI, criterion holds ($D_* < 0.0$), clouds do not necessarily thin or breakup, as had been suggested by Deardorff (1980), Randall (1980) and others. This suggests that kinetic energy due to evaporative cooling is a secondary effect in determining cloudtop motions in these cases.

It has been suggested (Caughey et al., 1985; Nicholls and Leighton, 1986) that detachment of small, cooled parcels from the base of the optically active layer below cloudtop gives rise to convective circulations which result in turbulent motions at cloudtop and thus in turbulent entrainment. Mahrt and Paumier (1982) showed that, in the case of some mean shear at cloudtop, mixing of cloud and clear air was in the main confined to the downwind side of penetrative cloudy elements. They found significant heat fluxes carried by non-cloudy, yet mixed, air parcels.

It is the purpose of our numerical simulations and data analysis to investigate these processes and, specifically, to focus on the following questions.

(1) Can local cooling below cloudtop play an important role in (a) setting up convective circulations within the cloud, and (b) bringing about entrainment?

(2) Can CEI alone lead to runaway entrainment under geophysically realistic conditions?

(3) What are the important mechanisms of entrainment at cloudtop under zero or low mean shear conditions?

II. Numerical Simulations

We have numerically simulated the stratocumulus inversion layer by a two-dimensional fluid dynamic representation of a Boussinesq layer. We use the following set of governing equations:

$$\frac{\partial \zeta}{\partial t} = -(\vec{U}\cdot\nabla)\zeta + \nu\nabla^2\zeta - b_x \tag{2.1}$$

$$\zeta = \nabla^2\Psi \tag{2.2}$$

$$\vec{U} = (-\partial\Psi/\partial z, \partial\Psi/\partial x) \tag{2.3}$$

$$b = f(\gamma_1, \gamma_2) \tag{2.4}$$

$$\frac{\partial \gamma}{\partial t} = -(\vec{U}\cdot\nabla)\gamma + \nu\nabla^2\gamma \tag{2.5}$$

where ζ is the vorticity, Ψ is the stream function, $\vec{U}$ is the velocity, ν is an eddy diffusivity, and b is the buoyancy, which is a linear function of the two conserved quantities γ_1, γ_2 (the equivalent potential temperature and total water content or saturation point temperature and pressure (Betts, 1982; Bretherton, 1987)). These equations are solved with a finite differencing scheme in time and space. Periodic boundary conditions are assumed in x and Dirichlet boundary conditions in z. The two-layer stratified fluid is initially at rest, and at $t = 0$ we apply a small perturbation in the conserved variables. This stratified flow would remain stable without the incorporation of additional physics to the model. We discuss here simulations in which evaporative cooling drives the circulations. Note that all mixing, turbulent and diffusive, is represented by the eddy diffusivity term $\nu\nabla^2$. Values used here are orders of magnitude larger than values appropriate for thermal and molecular diffusion. Stability considerations prevented use of lower values; thus the simulated flow is laminar rather than turbulent. While the upper boundary did not appear to have an important effect, the lower boundary forced an artificial circulation in the fluid and gave rise to spurious fluxes of the conserved quantities.

Figure 1 displays $\theta_v(F)$ for three cases: namely, the measurements discussed below and two situations we have simulated. Preliminary results of our simulations are shown in Figures 2 and 3. In the right hand figure of each pair, we show contours of a variable which is proportional to the difference between the saturation point pressure (Betts, 1982) and the actual pressure; thus the zero contour indicates cloudtop and the most dense mixtures of the upper and lower fluids. The area below this contour represents the cloud; small contour values represent mixtures which are close to saturation and, therefore, relatively dense. The left hand figure of each pair shows the stream function. Initially, the inversion layer is at height 1, and the fluid is at rest. The simulations represent the situation at later times, when the circulations are established.

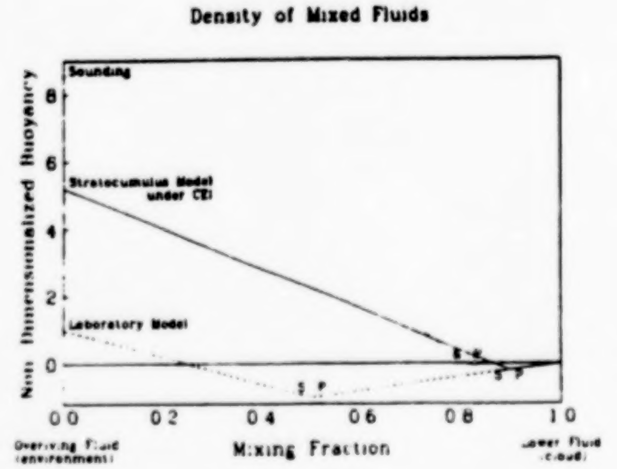

Figure 1. $\theta_v(F)$, where F is the fraction of cloudbase air in a mixture of cloudbase and upper level air. Solid and dashed lines: numerical simulations (see text); dotted line: computed from 19:06 sounding, July 5, 1987.

Figure 2 shows a geophysically realistic case (solid curve, Figure 1; $D_* = -0.04$.) The initial cooling at cloudtop has led to the formation of a steady circulation within the moist, cool cloud, indicating that evaporative cooling is a significant source of turbulent kinetic energy. The dry, lighter, inversion fluid is affected only by diffusion. The circulation produces "cool pools" of unsaturated air of approximately the same buoyancy as the cloud. Penetrative plumes with high evaporation rates form under these pools. A sharp interface between layers was maintained by the circulation, instead of the gradient layer predicted by Turner and Yang (1963). Under these physically reasonable initial conditions satisfying the CEI condition, no indication of runaway entrainment evolves.

Figure 3 corresponds to a laboratory simulation (Shy and Breidenthal, personal communication) in which CEI is a greater effect (dashed curve, Figure 1; $D_* = -2.$). Under these extreme conditions runaway entrainment occurs. The contamination of the lower fluid with the newly created mixed fluid becomes important before a semi-steady circulation is established.

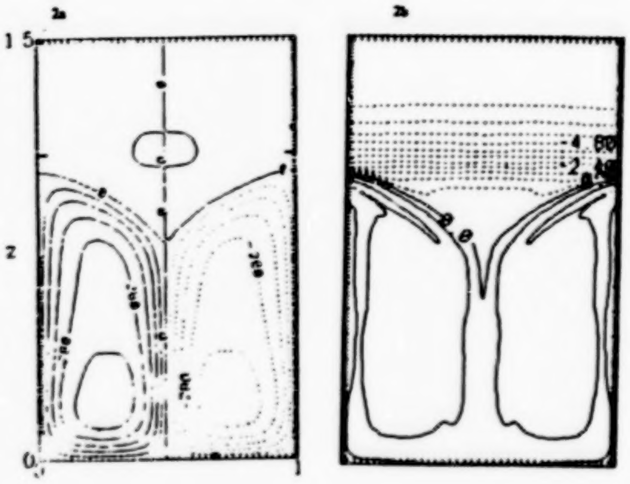

Figure 2. Vertical cross section of simulated stratocumulus deck $D_* = -.04$, at a time when steady circulation has developed. a) Stream function. b) Negative values of the contoured variable correspond to positive buoyancy: zero contour is cloudtop.

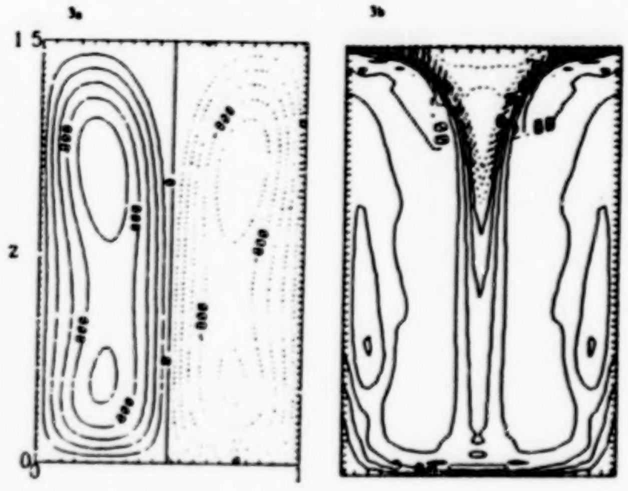

Figure 3. As in Figure 2, but for "laboratory" sounding, $D_* = -2.0$.

III. Data Analysis

We report here on a preliminary analysis of high resolution measurements made aboard the NCAR Electra on July 5, 1987, as part of the FIRE project. For averaged 1-Hz thermodynamic measurements we used the static (fuselage) pressure, temperature measured by the the Rosemount thermometer, liquid water from the Johnson-Williams device, and vapor content computed by averaging, filtering and applying a 2-second lag (Austin, personal communication) to the signal from the dewpoint sensors, and we used the 20 Hz FSSP and Lyman α records as high resolution tracers of the presence of cloud and pockets of moistened air.

Figure 4 displays the sounding made at 19:06-19:10 GMT in saturation point coordinates (Betts, 1982), showing the thermodynamic structure of the cloud and above cloud layers. The mixing line lies close to a θ_e isopleth. There was some mean shear within the layer, permitting the identification of air parcel origin by horizontal velocity, as well as thermodynamic properties. The sounding values at 950 and 910 mb were used to calculate the dotted curve in Figure 1. The CEI criterion is marginally met; $D_* = -.006$ and the cloud was quite solid.

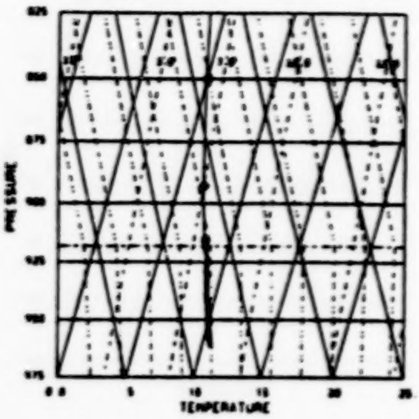

Figure 4. 19:06-19:10 GMT, July 5 sounding computed in saturation point coordinates. Dotted lines are θ_e isopleths computed at cloudtop, 920 mb.

Figure 5 shows portions of the time series of liquid water, w, θ, and the buoyancy flux (calculated as the simple covariance, unfiltered, of w and θ_v) over an in-cloud segment at about 936 mb. The cloud was highly turbulent and the most notable features of the traces are the distinct events, tens of meters in scale, at intervals of about 4-5 kilometers in which the liquid water decreased sharply and there were large excursions in vertical velocity. This is the scale of the major undulations in cloudtop shown by lidar measurements later on this flight. Examination of the radiative fluxes and vapor content (not shown) suggests that the events were passage through columns of clear, and in some cases unsaturated, air. Note the highly intermittent character of the buoyant fluxes; convection is driven from below as well as from the top, and the breaks between cloud segments appear to play an important dynamic role.

Cloudtop rose before the cloudtop traverse, a segment of which is shown in Figure 6. The aircraft flew in and out of cloudy segments at about 912 mb. The cloudy segments, which were more turbulent than the intervening clear air but much less turbulent than the cloud at lower levels, consist of regions of high liquid water content, separated by shorter, more dilute regions referred to by Mahrt and Paumier as "wisps." Note the high turbulence levels marking small turbules of cloudy air and the high vapor content in some of the "wisps." Mixing appears fairly localized to the edges of the cloudy segments, as evidenced by the spikes in horizontal and vertical velocity there. Evaporative cooling is probably responsible for the velocity spikes at these interfaces. The spatial scales of these mixing regions are comparable with the scales of the liquid-free regions seen at lower levels, but the cooling is not sufficient to explain the descent of cloudtop air to the lower level without some dynamic forcing. The nonturbulent air between the cloudy segments is the result of prior mixing of cloud and upper level air, and may represent evidence of "cool pools" as shown in the calculations. (See Fig. 2).

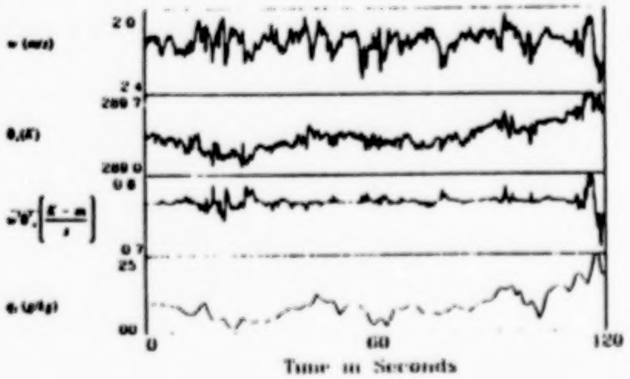

Figure 5. In-cloud measurements made at 936 mb, 18:40-18:45 GMT, Average aircraft velocity about 105 m/s. See text.

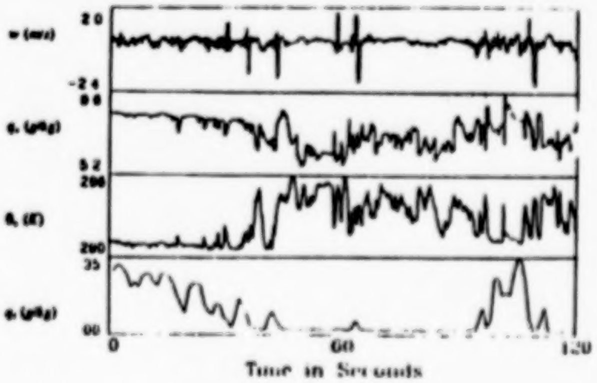

Figure 6. Cloudtop measurements made at 912 mb, 19:20-19:25 GMT. See text.

IV. Discussion

From these preliminary results, it appears that mixing of cloudy and clear air takes place primarily in highly localized regions, both at the edges of large cloudy segments, and in the vicinity of small cloudy turbules rising into the cloudtop region. The descent of the mixed air is apparently accelerated by evaporative cooling. However, our simulations, as well as the observations, show that relatively quiescent, mixed, clear air accumulates between the upward penetrating cloud elements, and they suggest that it is not sufficiently negatively buoyant to be efficiently drawn down into the cloud. Moreover, it appears from the simulations that, under physically realistic conditions, evaporative cooling alone does not lead to runaway entrainment, even when the CEI criterion is met, unless D_* is a very large negative number.

The relatively low efficiency of evaporative cooling in generating turbulent kinetic energy at the interface may be due partially to the fact that $\theta_v(F) < \theta_v(1)$ only for relatively high F values. Parcels with these mixture ratios are probably characteristic only of air at the base of the inversion layer. The displacement of the accleration due to evaporative cooling from the upper layer fluid, and thus from the region at which it could most efficiently promote entrainment, is further suggested by recent laboratory experiments (Johari, 1988), showing that no molecular mixing occurs in a buoyant (or in this case, negatively buoyant) thermal until it has moved a distance comparable to its diameter. The evaporatively cooled parcels seen at cloudtop have dimensions on the order of tens of meters, so they may be roughly that far from their first encounter with upper level fluid before they receive the additional downward acceleration due to the evaporation. For small D_*, the mixed fluid simply accumulates at cloudtop, reshaping the density profile and thus slightly facilitating further entrainment there.

Acknowledgement: This research was supported by NSF grant ATM-8620165.

References

Atlas, D., B. Walter, S. Chou and P. Sheu (1986), *J. Atmos. Sci. 43*, 1301-1317.
Betts, A. (1982), *J. Atmos. Sci. 39*, 1484-1505.
Bretherton, C. (1987), *J. Atmos. Sci. 44*, 1869-1874.
Carruthers, D. and J. Hunt (1986), *J. Fluid Mech. 165*, 475-502.
Caughey, S., B. Crease, and W. Roach, (1982), *Q. J. Roy. Met. Soc. 108*, 125-144.
Deardorff, J. (1976), *Q. J. Roy. Met. Soc. 102*, 563-582.
Deardorff, G. (1980), *J. Atmos. Sci. 37*, 131-147.
Hanson, H. (1984), *J. Atmos. Sci. 41*, 1226-1234.
Johari, H. (1988), AMS Conference on Turbulence and Diffusion.
Linden, P. (1973), *J. Fluid Mech. 60*, 467-480.
Mahrt, L. and J. Paumier (1982), *J. Atmos. Sci. 39*, 622-634.
Nicholls, S. and J. Leighton (1986), *Q. J. Roy. Met. Soc. 112*, 431-460.
Nicholls, S. and J. Turton (1986), *Q. J. Roy. Met. Soc. 112*, 461-480.
Randall, D. (1980), *J. Atmos. Sci. 37*, 125-130.
Rogers, D. and J. Telford (1986), *J. Atmos. Sci. 37*, 481-500.
Stull, R. (1976), *J. Atmos. Sci. 33*, 1260-1267.
Turner, J. S. (1986), *J. Fl. Mech. 173*, 431-471.
Turner, J. and I. Yang (1963), *J. Fluid Mech. 17*, 212-224.

A CLOUD CLASSIFICATION SCHEME APPLIED TO THE BREAKUP REGION OF MARINE STRATOCUMULUS

Siri Jodha S. Khalsa

Cooperative Institute for Research in
Environmental Sciences, CB-449
University of Colorado
Boulder, CO 80303

and

Catherine Gautier

California Space Institute, A-021
Scripps Institution of Oceanography
La Jolla, California 92038

1. Introduction

A major goal of the marine stratocumulus (MSc) segment of FIRE is to describe and explain the temporal and spatial variability in fractional cloud cover. The challenge from a theoretical standpoint is to correctly represent the mechanisms leading to the transitions between solid stratus, stratocumulus and trade wind cumulus. The development and testing of models accounting for fractional cloudiness require an observational data base that will come primarily from satellites. This, of course, is one of the missions of the ISCCP.

There are a number of satellite cloud analysis programs that are being undertaken as part of FIRE. One that has already produced data from the FIRE MSc experiment is the spatial coherence method (Coakley and Baldwin, 1984). This method produces information on fractional cloud coverage and cloud heights. It may be possible, however, to extract more information on cloud structure from satellite data that might be of use in describing the transitions in the marine stratocumulus cloud deck. The purpose of this research is to explore potential applications of a cloud analysis scheme relying on more detailed analysis of visible and infrared cloud radiance statistics.

For this preliminary study we examine data from three days during the 1987 FIRE MSc field work. These case studies provide a basis for comparison and evaluation of the technique. Later studies will involve a more extensive data set.

2. Satellite Data Set

The data used in this analysis came from the AVHRR instrument aboard the NOAA polar orbiting satellites. Daytime passes of NOAA-9 over the eastern Pacific between approximately 20° and 40° N were selected for 7 July, 10 July and 13 July. A wide variety of cloud conditions are represented in these days.

A nearly solid status deck is found on the 13th. A wide spectrum of broken cloud conditions is found on the 10th and the 7th was chosen because of coincident LANDSAT and SPOT passes on this day.

Visual (AVHRR Chan. 2, 0.8 μm) and IR (AVHRR Chan. 4, 11 μm) data are used, both having a horizontal resolution of 1.1 km at the subsatellite point.

3. Cloud Classification Method

Parikh (1977) demonstrated that spectral and textural features of visible and infrared satellite images could be used for cloud classification. Tournadre and Gautier (1988) have developed a method that uses a set of ten spectral and textural parameters to classify subscenes according to the cloud features that they contain.

For the FIRE data the method is applied to scenes of 512 by 512 pixels. Each scene is divided into subscenes of 8 x 8 pixels. The ten parameters are then derived from the visible and IR data for each subscene.

There are six spectral parameters and four textural parameters derived for each subscene. The spectral parameters are the minimum, maximum and mean for both visible and IR channels. The textural parameters are based only on the visible data. They are derived from the statistics of the differences between adjacent pixels within the subscene. The parameters are: the first and second moments of the differences (the "mean distribution" and "contrast"), and the angular second momentum (ASM) and entropy of the distribution of differences. The first two textural parameters measure the magnitude of the differences within a subscene while the latter two textural parameters are functions only of the frequency distribution of the differences.

Each parameter is normalized by the respective mean and standard deviation computed over all subscenes. The set of ten normalized parameters then defines a "profile" that may be used to classify the subscene. For display purposes the ten parameters are ordered as follows: 1-minimum value visible, 2-maximum value visible, 3-mean value visible, 4-mean distribution visible, 5-contrast visible, 6-ASM visible, 7-Entropy visible, 8-minimum value IR, 9-maximum value IR, 10-mean value IR.

A principal component analysis is then performed on all the profiles for a given scene. The method used follows that of Jalickee and Ropelewski (1978) who developed the technique for classifying atmospheric temperature profiles. Their method, which they call Typical Shape Function (TSF) analysis, is equivalent to a rotated Empirical Orthogonal Function (EOF) analysis. It produces a set of independent eigenvectors or TSFs that best represent the various profiles occurring within the scene.

After the TSFs have been found, each profile is classified by finding which TSF it is best correlated with. Each subscene is assigned a number corresponding to the TSF for which its profile matches best. Because information on the magnitudes of the variations in the parameters relative to each other has been lost in the process of normalization, it is only the "shape" of the profile that matters in the process of classification.

The classification procedure outlined above was repeated for several scenes on a given day. The TSFs from one scene are not in general identical to the TSFs from another scene. Therefore, in order to compare the classifications of multiple scenes, a common set of TSFs is required. This is accomplished by finding which TSFs are most highly correlated and therefore probably representative of the same cloud type. The regrouped TSF set consists of averages of these common types. Each scene is then reclassified on the basis of this new set of TSFs.

4. Results

The discussion here will focus on data from 10 July 1987. The area chosen for analysis (Fig. 1) was selected for its wealth of different cloud types and range of fractional cloudiness. Within the four 512 x 512 pixel scenes that make up the area, both open and closed cell clouds are evident (Fig. 2). What we seek to determine from this preliminary analysis is how well the TSF cloud classification scheme can discriminate these various cloud types.

The results are displayed in image format where each subscene is shaded according to the TSF that its profile most closely matches. A monochrome rendition of the regrouped classification of Fig.2 is given in Fig. 3.

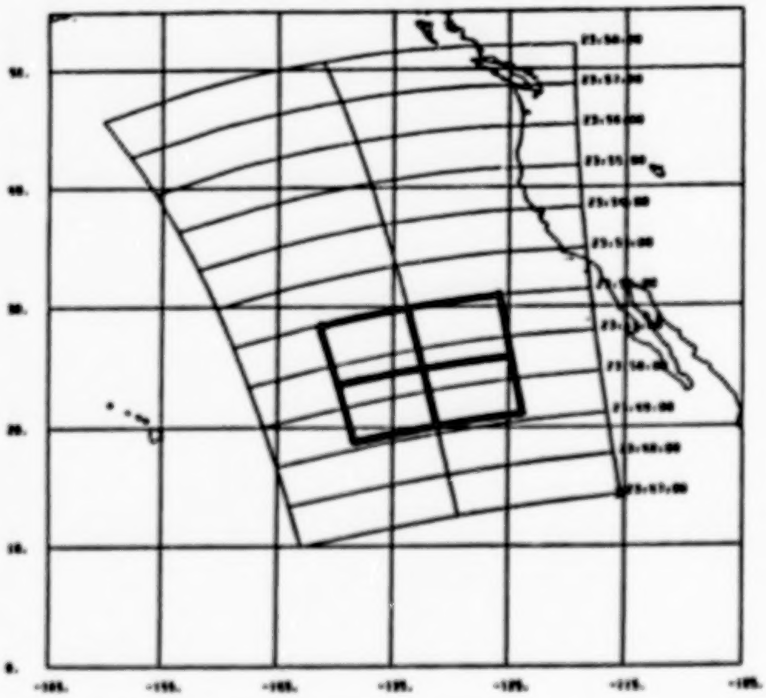

Figure 1. Location of the four scenes (bold boxes) used in the analysis for 10 July 1987.

There are nine classes in the regrouped classification. The TSFs for 3 of these classes are shown in Fig. 4. Regions of unbroken low cloud are shaded white in Fig. 3 and correspond to TSF class 1. There appears to be a band that is clear of clouds running horizontally in the lower half of Fig. 2. From Fig. 3 we see that this corresponds to class 4. Class 3 occupies a large fraction of the upper right quadrant. Examination of Fig. 2 shows that these are partly cloudy regions with small cloud sizes.

The class 1 profile (Fig. 4) has high visible spectral parameters and low IR parameters, as expected for radiation from a solid cloud. The texture parameters all indicate relatively homogeneous conditions. Class 4 has low visible and high IR spectral parameters as would be expected for radiation

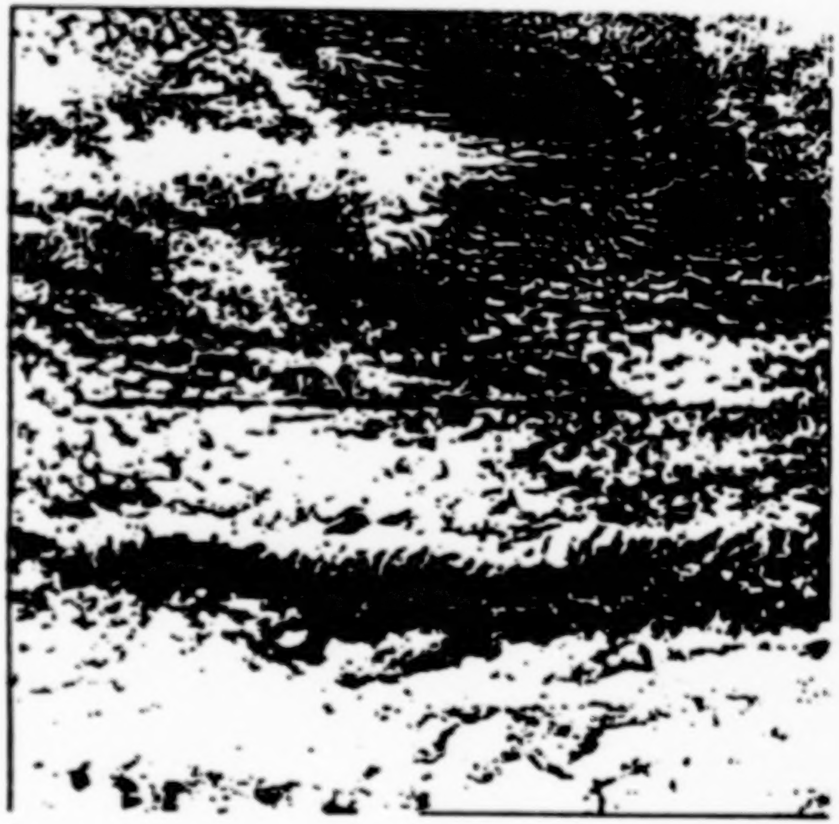

Figure 2. Channel 4 (IR) imagery for the four scenes shown in Fig. 1.

Figure 3. Regrouped TSF classifications for 8 x 8 pixel subscenes of the region shown in Fig. 1. The shading corresponding to the 9 classes is indicated in the bar at the right.

from the ocean surface. The textural parameters indicate even more homogeneous conditions than for the unbroken cloud case (very high ASM and very low entropy). Class 3, the small broken cloud cover case, has a low normalized visible minimum like the clear case, but higher normalized maximum and mean, comparable to the unbroken cloud case. IR spectral parameters are midway between the clear and unbroken case. What most distinguishes this class from the other two is the magnitude of the textural parameters. In all, this profile indicates a subscene containing some clear areas but one that is largely filled with low inhomogeneous clouds of small size.

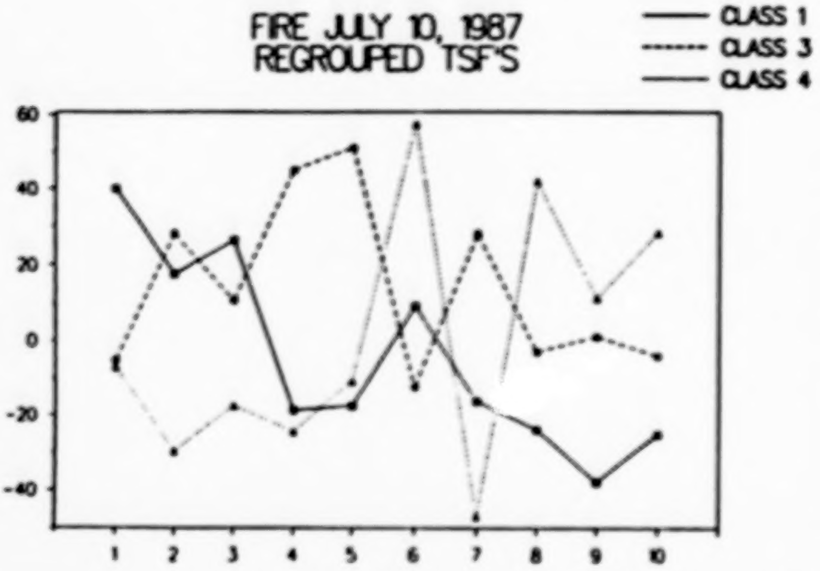

Figure 4. Profiles of the TSF parameters for three of the classes in Fig. 3. Class 1 is solid low cloud, class 3 is small broken cloud and class 4 is clear.

5. Summary

The marine stratocumulus regime, as represented in the small sample examined for this study, contains a sizable number of distinctly different cloud types. We have demonstrated that a TSF analysis can objectively discriminate a number of these cloud types on the basis of spectral and spatial statistics.

One application of this technique that we foresee is a description of the stages that the cloud layer goes through as it breaks up. Such a description will help in developing models of this process. Through intercomparisons with in situ measurements it may be possible to relate these cloud types to the thermodynamic properties of the cloud layer.

In the future we plan to incorporate observations from FIRE aircraft and other satellites in refining the technique. Eventually, the TSF cloud signatures identified in this study will be added to a TSF data base being developed from analyses done with data from various cloud regimes around the globe.

6. Acknowledgments

This work is support by the Marine Meteorology Program of the Office of Naval Research. We wish to thank P. Collard, J. McPherson and D. Hooper for their assistance.

7. References

Jalickee, J. B., and C. F. Ropelewski, 1978: An objective analysis of the boundary-layer thermodynamic structure during GATE. Part I: Method. Mon. Wea. Rev., 107, 68-76.

Parikh, J., 1977: A comparative study of cloud classification techniques. Rem. Sens. of the Environ., 6, 76-81.

Tournadre, J. and C. Gautier, 1988: Automatic cloud field analysis based on spectral and textural signatures, Proceedings of the International Workshop on Remote Sensing Retrieval Methods, A. Deepak ed.

FRACTIONAL CLOUDINESS IN SHALLOW CUMULUS LAYERS

David A. Randall
Department of Atmospheric Science
Colorado State University
Fort Collins, Colorado 80523

1. Introduction. Fractional cloudiness influences the planetary boundary layer by controlling the cloud-top radiative cooling rate, and regulating the buoyant production and consumption of turbulence kinetic energy. Betts, Hanson, and Albrecht have modeled partly cloudy PBLs by assuming a single family of convective circulations. The same idealized model has been used in observational studies, based on conditional sampling and/or joint distribution functions, by Lenschow, Albrecht, and others. This approach is extended in the present paper. None of these authors has proposed a method to determine σ, the fractional area covered by rising motion; finding such a method has been a key objective of the present study.

2. Model formulation. As a starting point, we adopt Lilly's mixed-layer model. It is assumed that in the interior of the PBL, the turbulent fluxes are entirely due to the convective circulations, with rising branches covering fractional area σ, and sinking branches covering fractional area $1 - \sigma$. The vertical flux of an arbitrary scalar ψ due to the convective circulations is given by

$$F_\psi = -\frac{\omega_*}{g}(\psi_u - \psi_d),$$

(2.1)

where g is the acceleration of gravity; ω_* is the "convective mass flux"; and subscripts u and d denote upward and downward branches, respectively. Near the lower boundary is a "ventilation layer" (essentially the same as the surface layer) within which the turbulent fluxes have to be carried by small eddies, since the organized vertical motions associated with the convective circulations must vanish there. The ventilation layer is assumed to be thin in the sense that the turbulent fluxes at its top are approximately equal to those at the surface. The surface fluxes are assumed to satisfy the usual bulk aerodynamic formula,

$$(F_\psi)_S = V(\psi_g - \psi_S),$$

(2.2)

where V is the "ventilation mass flux." Here subscripts g and S denote the earth's surface and a level in the ventilation layer, respectively. At level S, the parcels rising away from the lower boundary must be "charged" with the properties of the boundary. We cannot assume, however, that the properties of the updrafts at level S are the same as the those of the boundary, because there can be very strong gradients across the ventilation layer. The small eddies of the ventilation layer rapidly dilute air that has been in contact with the boundary, by mixing it with air that has recently descended from the interior of the PBL. In order to take this mixing into account, we introduce a nondimensional parameter, M_V, such that

$$(\psi_u)_S - \psi_S = M_V(\psi_g - \psi_S);$$

(2.3)

in case $M_V = 1$, we get $(\psi_u)_S = \psi_g$. Smaller values of M_V indicate stronger mixing by the small eddies of the ventilation layer. We expect $0 < M_V << 1$. By combining (2.1-3), we find that

$$-M_V \omega_{*S} = gV(1-\sigma).$$

(2.4)

This is a kind of "continuity equation" for the eddies, expressing a relationship between the convective mass flux and the ventilation mass flux.

Near the PBL top is an "entrainment layer" within which the organized vertical motions associated with the convective circulations become negligible, and smaller eddies carry the turbulent fluxes. The entrainment layer is assumed to be thin in the sense that the turbulent fluxes at its base are approximately equal to those at the PBL top. We can show that

$$-M_E \omega_{*B} = gE\sigma_B.$$

(2.5)

This is another "continuity equation", analogous to (2.4). Here subscript B denotes a level in the entrainment layer, and M_E is another mixing parameter, analogous to M_V. We expect $0 < M_E << 1$.

We now assume that σ is independent of height between the top of the ventilation layer and the base of the entrainment layer. This allows us to drop the subscripts B and S from σ. Comparing (2.4) and (2.5), we find that

$$\sigma = \frac{1}{1 + \frac{E\omega_{*S} M_V}{V\omega_{*B} M_E}}.$$

(2.6)

The form of (2.6) ensures that σ is between zero and one, so long as the ratio in the denominator is positive. To develop a useful expression for σ, a logical next step would be to introduce parameterizations for M_E and M_V. Because M_E and M_V represent the effects of small eddies with brief lifetimes, they should be highly amenable to parameterization. Unfortunately, however, no such parameterization currently exists.

As an alternative to parameterizing M_E and M_V, we assume that the expression in the denominator of (2.6) is equal to one. This implies that an increase in the convective mass flux at B or S is accompanied by more vigorous mixing there. Using this assumption, we find that

$$\sigma = \frac{1}{1 + \frac{E}{V}}.$$

(2.7)

According to (2.7), σ decreases as the entrainment mass flux increases relative to the ventilation mass flux. *Rapid entrainment implies small σ.*

3. Flux profiles in a partly cloudy well mixed layer. Lilly showed that, in a well mixed layer, the turbulent fluxes of conservative variables are linear with pressure, and also vary linearly with the entrainment rate. He further showed that in a mixed layer of horizontally uniform cloudiness the fluxes of liquid water and buoyancy have simple dependencies on height and the entrainment rate, even though liquid water and buoyancy are not conservative. In this Section we generalize Lilly's results to include the case of partly cloudy layers, by drawing on the results of Randall (*J. Atmos. Sci.*, 1987, pp. 850-858; hereafter referred to as R87), and using (2.7). An example is used for clarity.

We assume that $(F_r)_S$ satisfies a bulk aerodynamic formula, and $(F_r)_B$ satisfies Lilly's "jump" relation. The effects of drizzle are neglected for simplicity. As an example, we consider the following parameters: $\delta p_M = 70$ mb, $r_M = 7.5$ g kg^{-1}, $T_S = 21$ °C, gV = 2.2 mb hr^{-1}, $R_0 = 70$ W m^{-2}, $\Delta\sigma_d = 2$ K, $\Delta\sigma_m = -2$ K, $p_S = 1020$ mb. Here $\Delta\sigma_d$ and $\Delta\sigma_m$ are the usual dry and moist inversion stability parameters. Fig. 1 shows how the latent heat flux varies with σ. At the earth's surface, the latent heat flux is always equal to its prescribed surface value. Near the PBL top, F_r varies strongly with E. Since E and σ are related by (2.7), $(F_r)_B$ increases rapidly as σ decreases for $\sigma \ll 1$.

We assume that $(F_h)_S$ satisfies a bulk aerodynamic formula, and $(F_h)_B$ satisfies Lilly's "jump" formula. (Distributed radiative cooling is neglected for simplicity.) The area-averaged radiative cooling obviously depends on the fractional cloudiness. We assume for simplicity that when only the updrafts are saturated

$$\overline{\Delta R} = \sigma Q_v \Delta R_0. \tag{3.1}$$

Here ΔR_0 denotes the radiative cooling that occurs above a fully overcast optically thick cloud layer. The factor Q_v is introduced to allow continuous transitions as clouds form and dissipate; for thick clouds, $Q_v = 1$. The details are omitted here for brevity.

For the case in which only the updraft is saturated, the radiative cooling depends explicity on σ through (3.1), and the turbulent fluxes also depend on σ implicitly because the entrainment rate satisfies (2.7). The radiative cooling rate and the entrainment rate depend on the cloudiness, but to find the cloudiness we need to know the turbulent flux. *In short, we have to solve simultaneously for the cloudiness, the radiative cooling rate, and the moist static energy flux.*

Fig. 1 shows how the updraft cloud depth varies with σ, for the parameters given above. For σ greater than about 0.7, no cloud occurs. For smaller values of σ, the updrafts are cloudy, but the downdrafts remain cloud-free. Fig. 2 shows how $\overline{\Delta R}$ varies with σ . The maximum value of $\overline{\Delta R}$ occurs for $\sigma \cong 0.3$; for larger values of σ the cloud is absent or thin, and for smaller values it covers little of the area.

Up to this point, we have not had to consider latent heat effects, since both the total mixing ratio and the moist static energy are conserved under both dry adiabatic and moist adiabatic processes. Virtual temperature is not conserved under moist processes, however. As shown by R87, *for the case in which only the updrafts are saturated* the convective mass flux model implies that the buoyancy flux satisfies

$$F_{sv} = (1-\sigma)(F_{sv})_{CLD} + \sigma)(F_{sv})_{CLR} - \frac{m_c}{g}[1-(1+\delta)\epsilon]\, L\Gamma . \tag{3.2}$$

where $\tilde{\Gamma}$ is a measure of the relative humidity of the mean state. In (3.2), the forms of F_{sv} for the clear-sky and overcast cases are denoted by $(F_{sv})_{CLR}$ and $(F_{sv})_{CLD}$, respectively; L is the latent heat of condensation; and δ and ϵ are the usual positive nondimensional thermodynamic parameters. Notice that in (3.2) the "cloudy" flux is paradoxically weighted by the "clear-sky" fractional area, and vice versa. A derivation and interpretation of (3.2) is given by R87.

Fig. 3 shows how the fluxes of moist static energy, total water, and liquid water vary with with σ, at the PBL top level. All three fluxes increase rapidly as σ decreases for $\sigma << 1$. This is due to the rapid increase in the entrainment rate as σ decreases, which follows from (2.7). As σ decreases, the liquid water mixing ratio of the updrafts increases, while that of the downdrafts remains constant (at zero). This favors an increase in the liquid water flux near the PBL top. Further discussion is given by R87.

Fig. 4 shows the variation of F_{sv} with σ, at the surface, the updraft cloud base, and the PBL top. Of course,the surface value is independent of σ. For $\sigma \leq 0.5$, F_{sv} decreases upward from the surface to cloud base, and increases upward continuously above cloud base. As E increases and σ decreases, the vertical profile of F_{sv} responds to several competing factors. First, increasing E tends to reduce F_{sv} below cloud base, because of the inversion at the PBL top. There is a similar but weaker tendency for Fσv to decrease above cloud base, unless cloud-top entrainment instability occurs. A second factor is that cloudiness leads to radiative cooling for $\sigma \leq 0.5$. For $0.3 < \sigma < 0.5$, $\overline{\Delta R}$ increases as σ decreases because the cloud gets thicker, even though its fractional area decreases. This increase in $\overline{\Delta R}$ tends to increase F_{sv} at all levels above the surface. For $\sigma \leq 0.3$, $\overline{\Delta R}$ decreases as σ decreases, and this tends to reduce F_{sv} at all levels.

4. Plans for comparisons with FIRE data. There are many ways in which the FIRE data can be used to test the assumptions on which the present model is based. Lenschow, Greenhut and others have demonstrated that conditional sampling methods can be used with aircraft data to determine the convective mass flux profile, and the updraft and downdraft properties, including the fractional area covered by rising motion. Using such methods, it should be possible to determine M_E and M_V. This can best be done by using (2.4) for M_V and the analogous definition for M_E, with measured values of the updraft and downdraft properties. The values of M_E and M_V so determined should be independent of "species;" they should be the same for water vapor and ozone, for example.

The ventilation and entrainment mass fluxes can also be determined observationally, using standard methods. It then becomes possible to check (2.5) and (2.6), which are the key equations used in the derivation of our method to determine σ. In addition, the assumption that σ is independent of height can be tested. This assumption leads to (2.6), which is the most general form of our prescription for σ. In addition, we can check (2.7), which has been used to determine σ in this paper.

5. Concluding Remarks. The fractional cloudiness parameterization described here is suitable, with minor modifications, for use in a general circulation model. It represents a break with earlier cloudiness parameterizations, because in the present parameterization, the cloud amount is partly determined by the turbulence. Of course, the more familiar couplings among clouds, radiation, and turbulence are retained. The cloud, turbulence, and radiation parameterizations give rise, therefore, to a coupled system of equations that must be solved simultaneously. Dealing with this added complexity is a challenge for the future.

Acknowledgements: Support has been provided by NASA's Climate Program. Drs. Alan Betts and Phil Austin made useful comments. References have been made informally to save space.

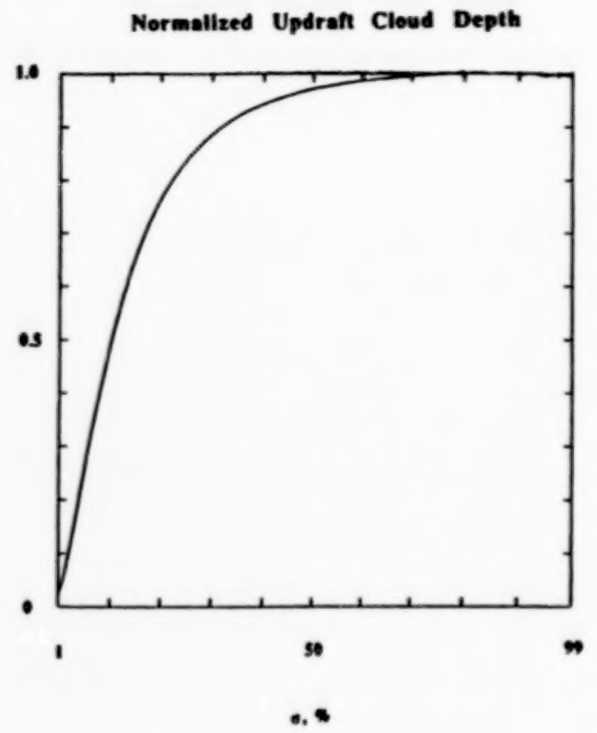

Normalized Updraft Cloud Depth

Figure 1

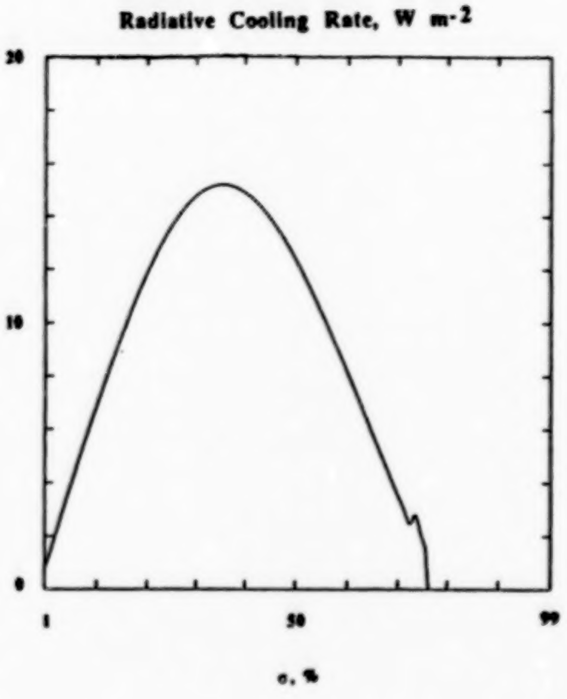

Radiative Cooling Rate, W m^{-2}

Figure 2.

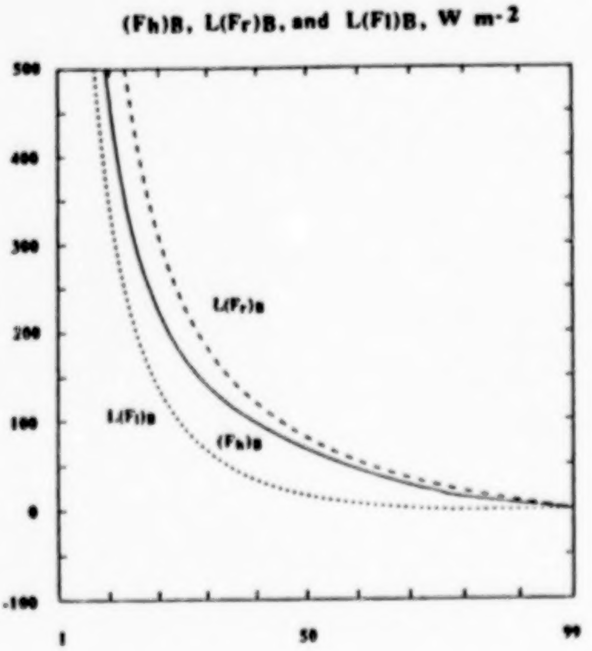

(Fh)B, L(Fr)B, and L(Fl)B, W m^{-2}

Figure 3.

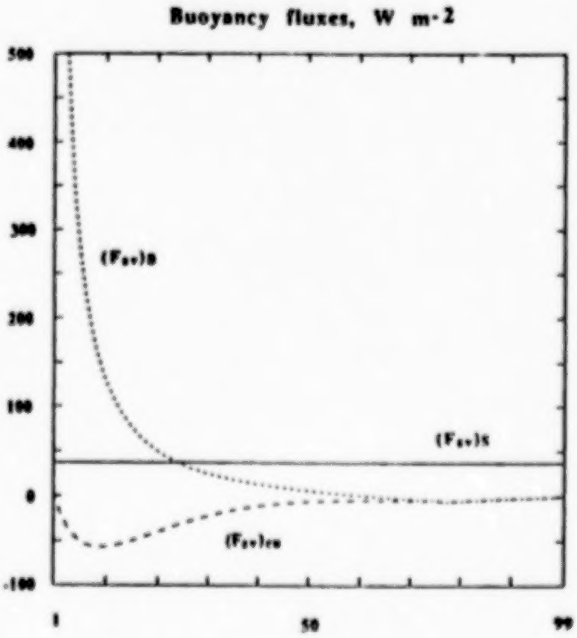

Buoyancy fluxes, W m^{-2}

Figure 4.

STUDYING MARINE STRATUS WITH LARGE EDDY SIMULATION

by

Chin-Hoh Moeng

National Center for Atmospheric Research *
P. O. Box 3000, Boulder, CO 80307

April 1988

Data sets from field experiments over the stratocumulus regime may include complications from larger scale variations, decoupled cloud layers, diurnal cycle, or entrainment instability, etc. On top of the already complicated turbulence-radiation-condensation processes within the cloud-topped boundary layer (CTBL), these complexities may sometimes make interpretation of the data sets difficult.

To study these processes, we need to have a better understanding of the basic processes involved in the prototype CTBL. For example, is cloudtop radiative cooling the primary source of the turbulent kinetic energy (TKE) within the CTBL? Curry et al. (1987) pointed out that the vertical gradient of the mean virtual potential temperature is almost always positive at cloud top and hence suggested that the mean radiative cooling does not generate TKE in the upside-down sense analogous to heating from the surface. Furthermore, from the analysis of the buoyancy-flux budgets, we found that the radiation term, which is proportional to the correlation between the radiative cooling and vertical velocity fluctuations, is small. This implies that the radiative cooling is not the primary source of buoyancy flux in the TKE budget.

Historically, laboratory measurements have played an important role in addressing the turbulence problems. The CTBL is a turbulent field which is probably impossible to generate in laboratories. Large eddy simulation (LES) is an alternative way of "measuring" the turbulent structure under controlled environments, which allows us to systematically examine the basic physical processes involved (Moeng, 1984; Moeng, 1986; Moeng, 1987).

However, there are problems with the LES approach for the CTBL. The LES data need to be consistent with the observed data. In the talk, I will discuss the LES approach, and show results which provide some insights into the simulated turbulent flow field. Problems with this approach for the CTBL and information from the FIRE experiment needed to justify the LES results will be discussed.

---

* The National Center for Atmospheric Research is sponsored by the National Science Foundation.

REFERENCES

Curry, J. A., G. F. Herman, and E. E. Ebert, 1987: Mean and turbulence structure of the summertime arctic cloudy boundary layer. (Submitted to *Quart. J. Roy. Met. Soc.*)

Moeng, C.-H., 1984: A large-eddy-simulation model for the study of planetary boundary-layer turbulence. *J. Atmos. Sci.*, 41, 2052-2062.

Moeng, C.-H., 1986: Large-eddy simulation of a stratus-topped boundary layer. Part I: Structure and budgets. *J. Atmos. Sci.*, 43, 2886-2900.

Moeng, C.-H., 1987: Large-eddy simulation of a stratus-topped boundary layer. Part II: Implications for mixed-layer modeling. *J. Atmos. Sci.*, 44, 1605-1614.

FIRE SCIENCE TEAM MEETING
VAIL, COLORADO
JULY 11-15, 1988

MARINE STRATOCUMULUS

SATELLITE STUDIES - James A. Coakley, Jr. Thursday, July 14, 1988

PAGE

Cloud Spatial Structure During the FIRE MS IFO 253
Cahalan, Robert F.

Reflectivities of Uniform and Broken Marine Stratiform Clouds 259
Coakley, Jr., James A.

Marine Stratocumulus Cloud Characteristics from Multichannel Satellite Measurements 265
Durkee, Philip A.; and Gary M. Mineart

Structures Observed on the SPOT Radiance Fields During the FIRE Experiment 271
Seze, Genevieve; Leonard Smith, and Michel Desbois

Analysis of Stratocumulus Cloud Fields using LANDSAT Imagery: Size Distributions and Spatial Separations 277
Welch, R. M.; S. K. Sengupta, and D. W. Chen

Cloud Parameters Derived from GOES During the 1987 Marine Stratocumulus FIRE Intensive Field Observation Period 279
Young, David F.; Patrick Minnis, and Edwin F. Harrison

Cloud Spatial Structure During the FIRE MS IFO

ROBERT F. CAHALAN
(1) Laboratory for Atmospheres, Goddard Space Flight Center, Greenbelt, MD 20771

EXTENDED ABSTRACT

This abstract summarizes work being done at the Goddard Laboratory for Atmospheres on the fractal properties of clouds observed during the FIRE Marine Stratocumulus Intensive Field Observations (MS IFO) and their effects on the large-scale radiative properties of the atmosphere. This involves three stages: (a) analysis of LANDSAT Thematic Mapper (TM) cloud data to determine the scaling properties associated with various cloud types; (b) simulation of fractal clouds with realistic scaling properties; (c) computation of mean radiative properties of fractal clouds as a function of their scaling properties. The focus here is on the empirical work, which is being done with the assistance of Mark Nestler of Science Applications Research.

Thirty-three LANDSAT scenes were acquired As part of the FIRE Marine Stratocumulus IFO in July 1987. They exhibit a wide variety of stratocumulus structures. Analysis has so far focused upon the July 7 scene, in which the NASA ER-2, the BMO C130 and the NCAR Electra repeatedly gathered data across a stratocumulus-fair weather cumulus transition.

Before discussing our conclusions about cloud structure based upon observations of cloud reflectivity, we should first note that what we really wish to know is how the cloud liquid water is distributed, since the reflectivity is computable from the distribution of liquid water, traditionally by specifying microscopic properties like drop sizes, and macroscopic properties like optical depth, etc.. The radiation field provides a kind of low-pass spatial filter, so that there may be small-scale variations of liquid water to which the LANDSAT data is completely insensitive. However, the LANDSAT data does reveal considerable small-scale structure not included in our usual plane-parallel assumptions. Interpretation of this structure in terms of the three-dimensional distribution of liquid water will be an important result of coordinating the satellite and aircraft data analysis.

brightness histograms

The LANDSAT TM has 3 visible reflected bands, 3 near-infrared bands and the thermal water vapor window band. The July 7 stratocumulus clouds have a maximum reflectance of about 0.5, which saturates two of the visible and one of the near-infrared TM bands. Table 1 shows the typical maximum reflectance required to saturate each band. Bands 1, 3 and 5 are all saturated at a reflectance of less then 0.5, and thus are saturated by the July 7 stratocumulus. Band 2 (0.52-0.60) is saturated at 0.5, so that only the few brightest pixels are saturated. Bands 4 and 7 are well below saturation.

Band	Wavelength(µ)	Rsat	saturated?
1	0.45-0.52	0.22	√
2	0.52-0.60	0.50	
3	0.63-0.69	0.46	√
4	0.76-0.90	0.63	
5	1.55-1.75	0.41	√
7	2.08-2.35	0.60	

The histogram of the thermal band (Band 6, 10.4-12.5 microns) for July 7 shows two narrow peaks separated by about 8°C, which corresponds to a cloud top at about 800 meters if we assume a dry adiabatic lapse rate.

Plots of temperature versus brightness (band 6 vs band 7, for example) show the usual scatter of points extending up from the warm dark surface cluster to the cold bright cloud cluster. At 1 km resolution the points are all concentrated at the two extremes, but as the resolution is refined to 120 m, narrowing the field-of-view to keep the number of pixels the same, the points spread out uniformly between the cloudy and clear clusters. This is due to the fact that the field-of-view is focusing in on the stratocumulus boundary, where a high percentage of partially cloudy pixels occur.

spatial distributions

The wavenumber spectra and cloud size distributions are approximately power-law, but the stratocumulus clouds conform to a single power more closely than do the fair weather cumulus, which exhibit a clear change in the fractal dimension at a diameter of about 0.4 km. The fractal dimension also changes with the reflectivity threshold. As the threshold is raised from cloud base to cloud top, the perimeter fractal dimension increases, perhaps indicative of the increased turbulence at cloud top. The aircraft and island data from FIRE will allow us to relate the spatial structure of the LANDSAT brightnesses to that of the liquid water, drop sizes, vertical motion and entrainment rate.

The fact that the larger clouds are less probable and more irregular in shape suggests a random coincidence hypothesis. That is, the smaller clouds are generated by a scaling fractal process up to some maximum cell size of about 0.5 kilometers, and larger clouds occur only as accidental coincidences of the smaller ones. One test of this picture is to see if the smaller cloud areas have a simpler distribution of cloud brightnesses within each cloud area. Visual inspection of a few cases seems to bear this out, since we observe that the smaller cloud areas have a single brightness maximum, while larger ones invariably have multiple brightness maxima.

Raising the threshold to a high level allows the determination of the fractal dimensions of the bright regions. The brighter regions were found to have higher perimeter dimensions for both fair weather cumulus and stratocumulus. In the case of fair weather cumulus it may be that the thicker, and therefore brighter, cloud regions are more irregular because they arise from the random coindidence of the smaller cells. On the other hand, in the case of stratocumulus this may be associated with increased turbulence at the cloud top, where the convection is driven by radiative cooling. Note that there is a limit to the increase of the perimeter dimension with threshold, since the brighter regions cover a successively smaller area as the threshold is raised.

Stratocumulus dimensions are intermediate between the smaller and larger fair weather cumulus, and the break in slope is less pronounced. Since stratocumulus convection is driven by cooling at the cloud top, rather than heating from below as in fair weather cumulus, the stratocumulus downdraft regions are of more interest. These take the form of long, irregular leads, not unlike those observed in sea ice.

Simulations of fair weather cumulus and stratocumulus clouds have been developed which take these properties into account. The simulations depend upon two scaling parameters which determine the distributions of cloud sizes and spacings, respectively, and also upon a maximum characteristic cell size. The fair weather cumulus simulations begin with an initially cloud free scene and add liquid water associated with updraft regions, while the stratocumulus simulations begin with a uniform liquid water distribution and remove liquid water in downdraft regions. The simulations may be run until a given total liquid water is generated, or each updraft and downdraft may be assigned a "lifetime" from some probability distribution, and the resulting time-dependent simulation run to a steady state.

The initial Monte Carlo radiative transfer computations have been carried out with a highly simplified model in which liquid water is redistributed in an initially plane-parallel cloud while cloud height and mean optical depth are held fixed at each step. Redistribution decreases the mean albedo from the plane parallel case, since the albedo of optically thick regions saturates as optical depth is increased. The albedo of each homogeneous region may be computed from the thickness of each region independently only when the horizontal optical depth is large compared to the photon mean free path. The albedo of a region comparable in horizontal optical depth to the photon mean free path depends upon radiation from the sides. The mean albedo is insensitive to variations in optical depth on horizontal scales much smaller than the photon mean free path. These concepts have been illustrated with a simple one-parameter fractal model.

JULY 7, 1987 NAVIGATION
for FIRE marine statocumulus intensive field observations

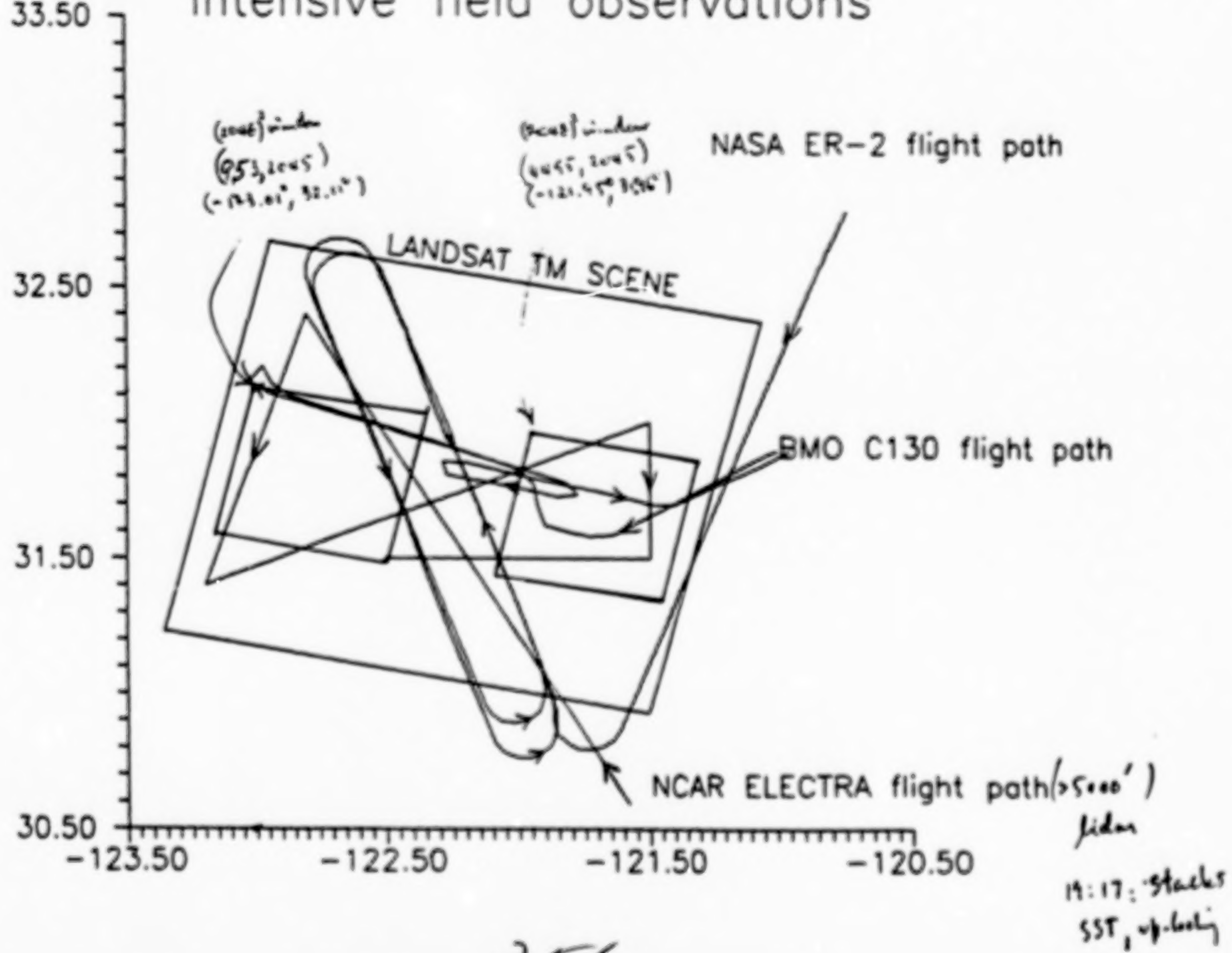
33.50
32.50
31.50
30.50
-123.50
-122.50
-121.50
-120.50
window
(953, 2045)
(-123.01°, 32.11°)
window
(4455, 2045)
(-121.45°, 32.56°)
LANDSAT TM SCENE
NASA ER-2 flight path
BMO C130 flight path
NCAR ELECTRA flight path (>5000')
lidar
19:17: stacks
SST, up-looking

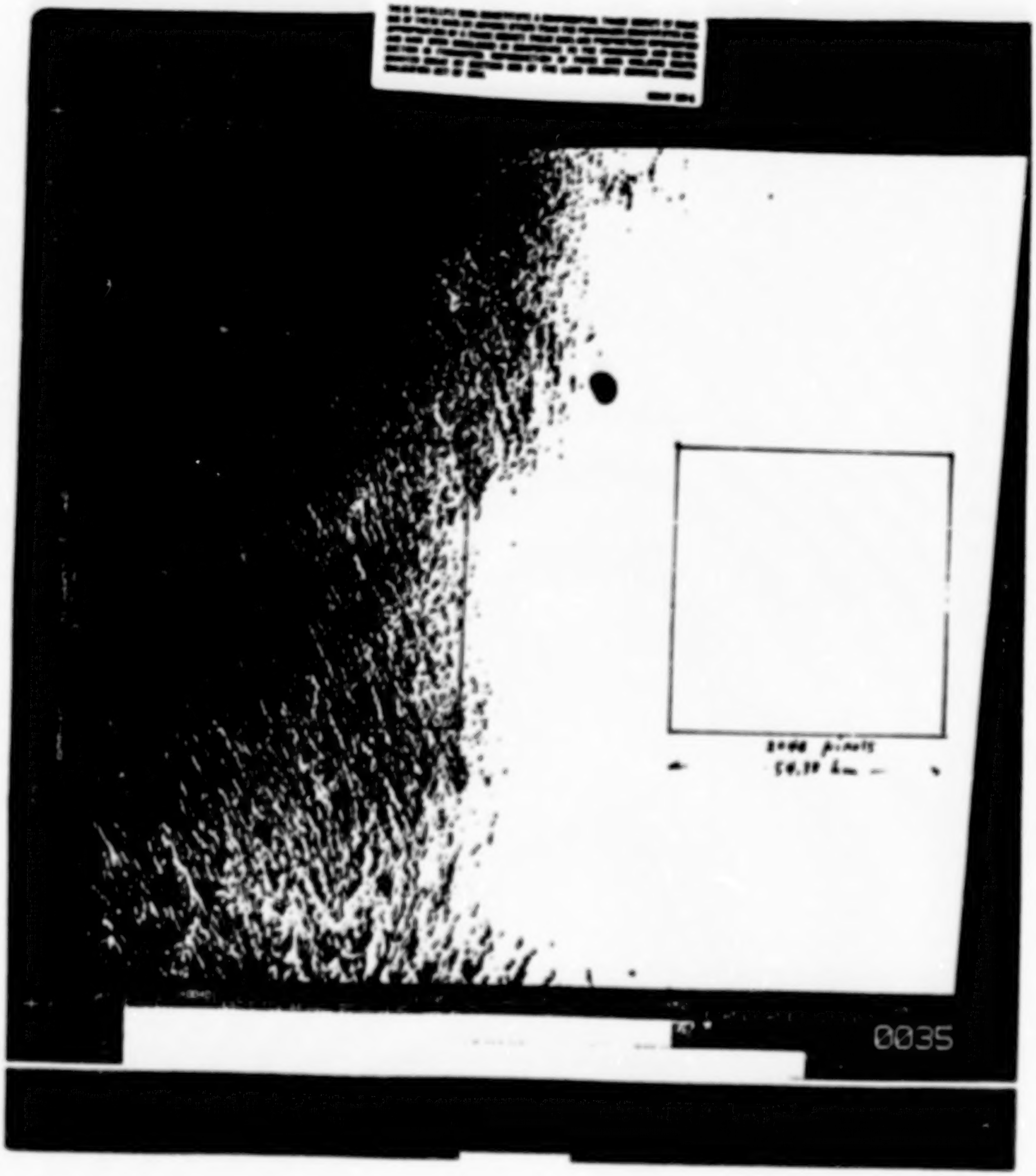
2048 pixels
50.30 km
0035

Reflectivities of Uniform and Broken Marine Stratiform Clouds

James A. Coakley, Jr.
National Center for Atmospheric Research
Boulder, CO 80307

1. Introduction

Plane-parallel radiative transfer models are often used to estimate the effects of clouds on the earth's energy budget and to retrieve cloud properties from satellite observations. Here an attempt is made to assess the performance of such models by using $(1\ \mathrm{km})^2$ AVHRR data collected during the FIRE Marine Stratus IFO to determine the reflectivities and, in particular, the anisotropy of the reflected radiances for the clouds observed during the field experiment. The intent is to determine the anisotropy for conditions that are overcast and to compare this anisotropy with that produced by the same cloud when broken. The observations will thus be used to quantify aspects of the differences between reflection by plane-parallel clouds and non-planar clouds expected on the basis of theoretical studies (McKee and Cox, 1974; Davies, 1978; Welch and Wielicki, 1984 and others).

The results reported are from the 10 daytime passes analyzed during the field experiment (Coakley and Beckner, 1988). These passes coincided with major aircraft missions. The IFO provided a large sample of overcast conditions as is illustrated in Figure 1. The figure shows the frequency of cloud cover occurrence for all of the $(60\ \mathrm{km})^2$ subregions included in the $(500\ \mathrm{km})^2$ regions typically analyzed for each overpass. The predominant condition was overcast. Furthermore, the IFO presented a narrow range of sun-earth-satellite viewing geometries as is illustrated in Figure 2. The figure shows the scattering angle, which is the angle between the direction of the incident sunlight and the reflected radiation observed at the satellite, as a function of the AVHRR scan position. For the IFO radiation undergoes a smoothly varying transition in scattering geometry as a function of the AVHRR scan spot number. At small scan spot numbers radiation is invariably backscattered; at large scan spot numbers it is invariably forward scattered. Reflectivities are reported as a function of AVHRR scan spot position for both uniform and broken clouds and for 0.63 μm, where scattering is nearly conservative, and 3.7 μm where liquid water is moderately absorbing.

2. Data Analysis

To study the properties of uniform clouds and their broken counterparts, cases must be selected for which there is considerable confidence that the cloud is single-layered and either recognizably overcast or clearly broken. The results of the spatial coherence analysis of the AVHRR data are screened following procedures described by Coakley and Davies (1986) to ensure these condition. Furthermore, to ensure that the properties are reported for the same clouds, and to ensure that the properties are representative of the clouds, observations are restricted to $(60\ \mathrm{km})^2$ subframes containing a single cloud layer, and having at least 20% of the area completely overcast while at the same time having at least 20% covered by broken cloud from the same layer. To obtain reflectivities representative

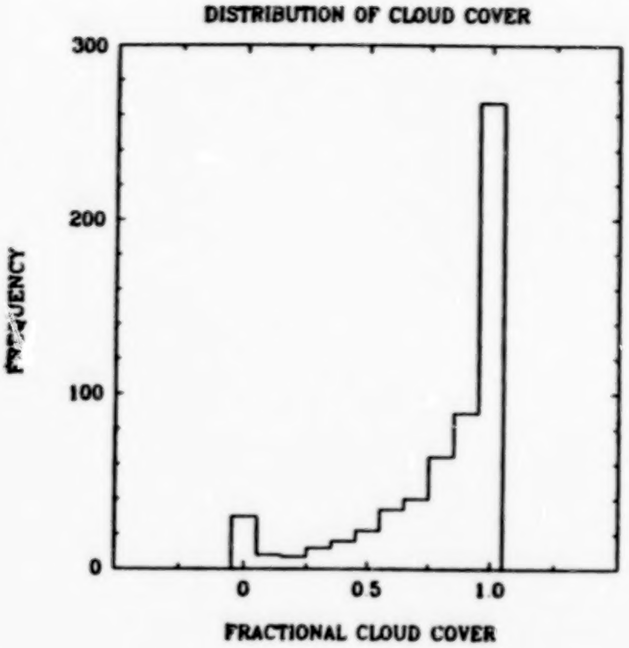

Figure 1. Frequency of cloud cover occurrence for (60 km)^2 subregions derived from the daytime NOAA overpasses analyzed during the FIRE Marine Stratus IFO.

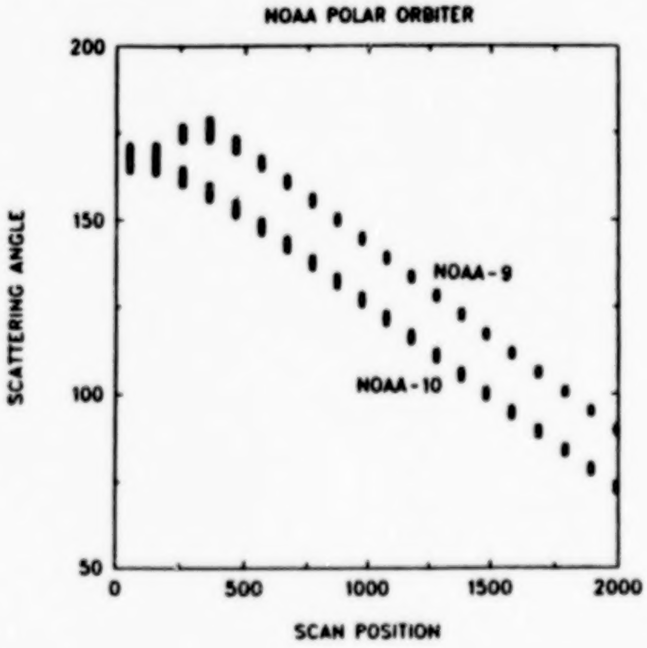

Figure 2. Scattering angle as function of AVHRR scan position for the IFO region and period.

of the broken cloud, allowance is made, to first order, for the fractional cloud cover, which is obtained by the spatial coherence method. That is, the reflectivity associated with broken clouds, r_C, is given by

$$r_C = \frac{r - (1 - A_C)}{A_C} \tag{1}$$

where r is the reflectivity for the portion of the (60 km)^2 subframe for which the fields of view are partially cloud covered and A_C is the fractional cloud cover for these fields of view.

3. Results

Figure 3 shows 0.63 μm reflectivities for overcast (open circles-solid line) and broken cloud conditions (dots-dashed line). It is immediately obvious that broken clouds reflect less radiation per unit cloud fraction than do overcast clouds. The decrease is approximately 12% of the overcast reflectivity. This reduction in reflectivity can also be deduced from visible-infrared scatter diagrams. The reduction could be due to either smaller optical depths for the broken clouds or to the effects of cloud geometry (Schmetz, 1984).

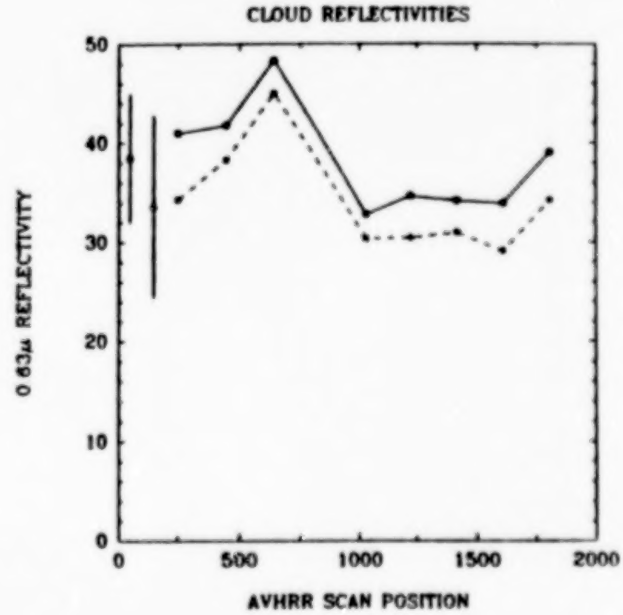

Figure 3. 0.63 μm reflectivities as a function of scan position for overcast (open circles-solid line) and broken clouds (dots-dashed line). Observations for both overcast and broken clouds were taken from the same (60 km)^2 subregions. The two data points at the left side of the figure give the mean of all the points and the typical variability of the data points for each recorded scan position.

There is considerable scatter in the reflectivities reported for the various scan positions as is indicated by the error bars in Figure 3. With such variability it is difficult to deduce a trend in the anisotropy. Nevertheless, if a trend exists (that is, the observations are not an idiosyncrasy of the AVHRR or the sparse sample of data), it is for higher reflectivities at forward and backward scattering angles and lower reflectivities at intermediate angles or near nadir viewing. There is no discernible difference in the anisotropy of the radiance fields for overcast and broken clouds.

At 3.7 μm liquid water becomes a moderate absorber. The single scattering albedo for marine stratus cloud droplets is approximately 0.9. Figure 4 shows the reflectivities for 3.7 μm radiation. To obtain the reflectivities, estimates of emission at 3.7 μm were removed from the observed radiances (Coakley and Davies, 1986). As with the visible reflectivities, the reflectivities at 3.7 μm show considerable scatter. If there is a trend, it is for higher reflectivities at forward and backward scattering angles and lower reflectivities at intermediate scattering angles. Unlike the visible reflectivities, the reflectivities at 3.7 μm for broken clouds are comparable in magnitude, if not greater than those for overcast conditions. The comparable magnitudes is a result of the absorption. With the absorption, the clouds become optically thick at 3.7 μm and the resulting reflected radiation is thus unaffected by optical depth or leakage of radiation through the cloud boundaries. Coakley and Davies (1986) also note that the enhancement of reflectivities for broken clouds may

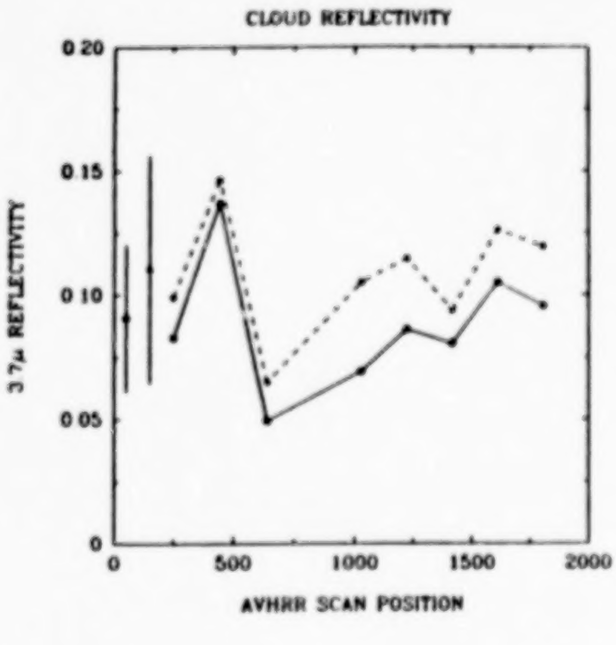

Figure 4. Same as Fig. 3 but for 3.7 μm.

be due to a systematic shift in cloud droplet size to smaller droplets at cloud edges or to the increased frequency of sun-cloud surface-satellite viewing geometries yielding high reflectivities for the broken clouds.

4. Summary and Conclusions

Reflectivities at visible wavelengths for broken clouds are 88% of the reflectivities of the same clouds under overcast conditions. The decrease in reflectivity for broken clouds may be due to smaller optical depths or to cloud geometrical effects. There is no discernible difference in the anisotropy of the reflectivities between broken and overcast cloud conditions. At 3.7 μm where liquid water is a moderate absorber, the reflectivities of broken clouds are comparable to and even greater than those observed for overcast conditions. The lack of a difference at this wavelength is attributed to the amount of absorption, but may also be due to enhancements in the reflectivities for broken clouds that result from the microphysical structure of the cloud and the effects of cloud geometry on reflected radiation.

When data received from PCDS for the IFO period is processed, the results will be added to those presented here. It is anticipated that the increased number of data points will clarify the anisotropy of the reflected radiation and will reveal any differences in the anisotropy for broken and overcast cloud conditions. To remove concerns about a scan dependent response to the AVHRR sensor, correlations of AVHRR reflectivities to those obtained with the ERBE scanner will be made when the ERBE data becomes available. Finally, calculations will be made using plane-parallel cloud models to determine the extent to which such models predict the observed anisotropy for conservative and nonconservative scattering.

Acknowledgement

This work was supported in part by AFGL and AFOSR through transfer of funds to NASA, GLH6-6031 and by NASA Grant L-79877B.

References

Coakley, J.A., Jr. and M.H. Beckner, 1988: Spatial coherence retrievals of cloud properties for the FIRE Marine Stratocumulus IFO, June 29 - July 19, 1987. NCAR/TN-307+STR, 205 pp.

Coakley, J. A., Jr., and R. Davies, 1986: The effect of cloud sides on reflected solar radiation as deduced from satellite observations, *J. Atmos. Sci.*, **43**, 1025-1035.

Dav[illegible]., 1978: The effect of finite geometry on the three-dimensional transfer of solar irradiance in clouds. *J. Atmos. Sci.*, **35**, 1712-1725.

McKee, T.B. and S.K. Cox, 1974: Scattering of visible radiation by finite clouds, *J. Atmos. Sci.*, **31**, 1885-1892.

Schmetz, J., 1984: On the parameterization of the radiative properties of broken clouds, *Tellus*, **36A**, 417-432.

Welch, R.M. and B.A. Wielicki 1984: Stratocumulus cloud field reflected fluxes: The effect of cloud shape. *J. Atmos. Sci.*, **41**, 3085-3103.

Marine Stratocumulus Cloud Characteristics from Multichannel Satellite Measurements

PHILIP A. DURKEE AND GARY M. MINEART

Department of Meteorology
Naval Postgraduate School
Monterey, California 93943

INTRODUCTION

Understanding the effects of aerosols on the microphysical characteristics of marine stratocumulus clouds, and the resulting influence on cloud radiative properties, is a primary goal of FIRE. The effect of aerosols on clouds and the impact on climate processes have recently been discussed by several authors (Twomey et al., 1984; Coakley et al., 1987, Charlson et al., 1987). Of particular concern in this presentation is the potential for observing variations of cloud characteristics that might be related to variations of available aerosols. Some results from theoretical estimates of cloud reflectance will be presented. We also present here the results of comparisons between aircraft-measured microphysical characteristics and satellite-detected radiative properties of marine stratocumulus clouds. These results are extracted from Mineart (1988) where the analysis procedures and a full discussion of the observations are presented. Due to the space available, only a brief description of the procedures and the composite results will be presented.

The satellite data used here are from the National Oceanic and Atmospheric Administration (NOAA) Advanced Very High Resolution Radiometer (AVHRR) collected at the Scripps Satellite Oceanography Facility. The AVHRR channel 1 (0.63 μm), channel 3 (3.7 μm), and channel 4 (11 μm) data were used in the analysis. Cloud microphysical data were obtained by instruments on the NCAR Electra during MABL cloud-penetrating missions in support of the IFO from 29 June - 19 July 1988.

RESULTS

Theoretical Reflectance Estimates

Cloud reflectance can be estimated from cloud droplet distributions that represent anticipated conditions in marine stratocumulus clouds. Model cloud droplet distributions were generated using the modified gamma distribution after Deirmendjian (1969). Modal radii of 4 and 8 μm were used to show the effects of change in droplet size. The results presented here are for a constant liquid water content of 0.4 g m^{-3}. Three distributions at each mode radius were chosen to illustrate the effects of distribution width. The droplet size distribution curves for the two mode radii are shown in Fig. 1. The optical properties of the cloud droplet distributions were calculated using Mie calculations after Wiscombe (1980). Reflectance was calculated using the delta-Eddington approximation from

Joseph et al. (1976), applied at 45° solar zenith angle and cloud thickness ranging from 10 to 750 meters.

Fig. 2 illustrates the dependency of reflectance on cloud droplet size distribution, at a constant liquid water content (LWC) of 0.4 g m^{-3}, for 0.63 μm (AVHRR channel 1 3) and 3.7 μm wavelength (AVHRR channel 3). Reflectance decreases as droplet size increases for both wavelengths.

Fig. 3 shows reflectance dependence on cloud thickness. Channel 1 reflectance increases sharply in the first few hundred meters and then asymptotically approaches a value of 1.0 with increasing cloud thickness. Channel 3 reflectance rises quickly at cloud thickness below 0.1 km and then remains constant. Therefore, reflectance in channel 3 does not vary with cloud thickness once the cloud is greater than about 100 m thick. This is due to the moderate absorption by water droplets at 3.7 μm wavelength.

FIRE IFO Aircraft/Satellite Comparisons

Mineart (1988) presents four case studies that show a consistent relationship between cloud microphysical characteristics and radiative properties. Here we present only the composite results. The results of comparisons between coincident aircraft and satellite observations are displayed in Figs. 4 and 5.

The 3.7 μm (AVHRR channel 3) reflectance in Fig. 4 displays an excellent correlation with cloud droplet size. The outlying data point at 3 μm represents an observation of a cloud edge (about 80 m thick), where the decrease in cloud thickness dominates the drop size effect on reflectance. Fig. 4 also compares the channel 3 results with the model cloud reflectance data shown in Fig. 2. The variations closely match the expected values from simple theoretical estimates. Also, the shift toward model distribution D1 (broadest distribution) at large droplet sizes and the shift toward model distribution D2 (narrow distribution) at the smaller droplet sizes is consistent with the shift in distribution shape observed in the aircraft measurements (not presented here, see Mineart, 1988).

Fig. 5 relates 0.63 μm (AVHRR channel 1) reflectance to cloud thickness. Cloud thickness values are estimated from APN-159 radar altimeter and PMS-King LWC data. The vertical and horizontal bars indicate the 95% confidence intervals. The data show increasing channel 1 reflectance with increasing cloud thickness, which is consistent with the dependence shown in Fig. 3. Although channel 1 reflectance should vary as a function of droplet radius with constant cloud thickness and LWC, we have not analyzed enough cases to separate variations due to drop size from variations due to LWC and cloud thickness.

CONCLUSIONS

Relationships between cloud reflectance and cloud characteristics have been illustrated by comparing AVHRR satellite data and aircraft measurements. At 0.63 μm (AVHRR channel 1) reflectance variations relate strongly to cloud thickness. Also, The expected relationship of higher reflectances from smaller cloud droplet size spectra is confirmed for 3.7 μm wavelength (AVHRR channel 3). This dependence is closely approximated by model cloud reflectance estimates. Although not presented here, Mineart (1988) showed that a primary source of droplet size variations is related to continental/marine air mass differences. Continental air masses are generally have higher concentrations of aerosols, higher concentrations of cloud droplets, and a shift towards a smaller mean cloud droplet radius. The strong dependence of channel 3 reflectance on cloud droplet size distribution allows inference of cloud composition characteristics from satellite observations.

REFERENCES

Charlson, R. J., J. E. Lovelock, M. O. Andreae, and S. G. Warren, 1987: Oceanic phytoplankton, atmospheric sulphur, cloud albedo and climate. *Nature*, **326**, 655-661.

Coakley, J. A., Jr., R. L. Bernstein and P. A. Durkee, 1987: Effect of ship-stack effluents on cloud reflectivity. *Science*, **237**, 953-1084.

Deirmendjian, D., 1969: *Electromagnetic scattering on spherical polydispersions.* Elsevier, New York, 290pp.

Joseph, J. H., W. J. Wiscombe and J. A. Weinman, 1976: The delta-Eddington approximation for radiative flux transfer. *J. Atmos. Sci.*, **33**, 2452-2459.

Twomey, S., M. Piepgrass and T. L. Wolfe, 1984: An assessment of the impact of pollution on global cloud albedo. *Tellus*, **36B**, 356-366.

Wiscombe, W. J., 1980: Improved Mie scattering algorithms. *Applied Optics*, **19**, 1505-1509.

FIGURES

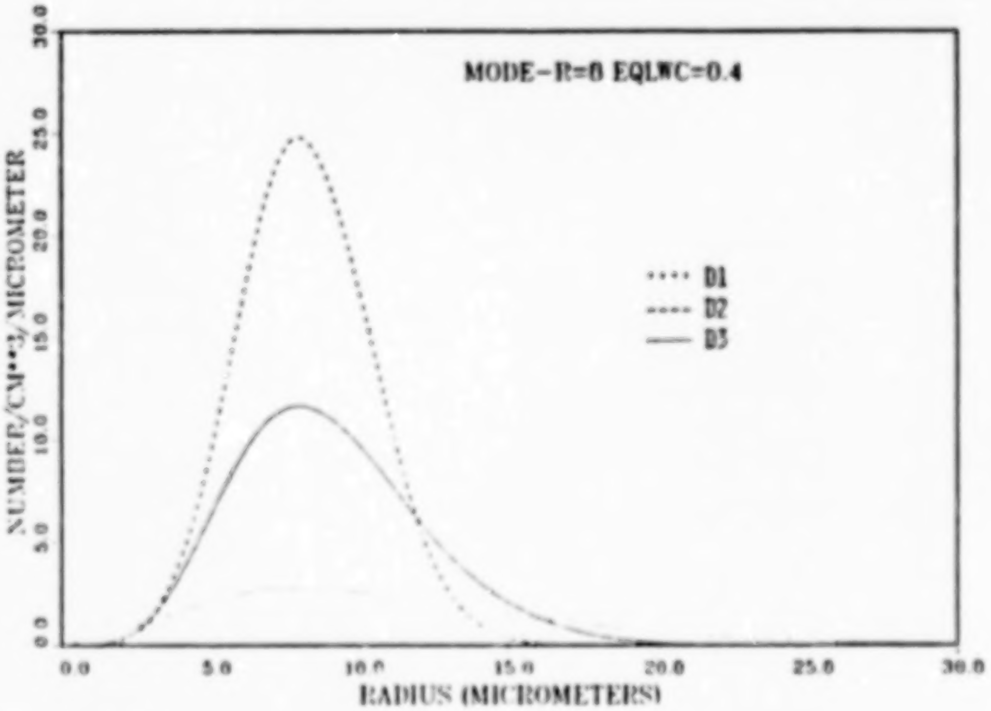

FIG. 1. Model Cloud Droplet Distributions for a modal radius = 4 μm, LWC=0.4 g m^{-3}. D1, D2, and D3 represent three modified gamma distributions of varying width.

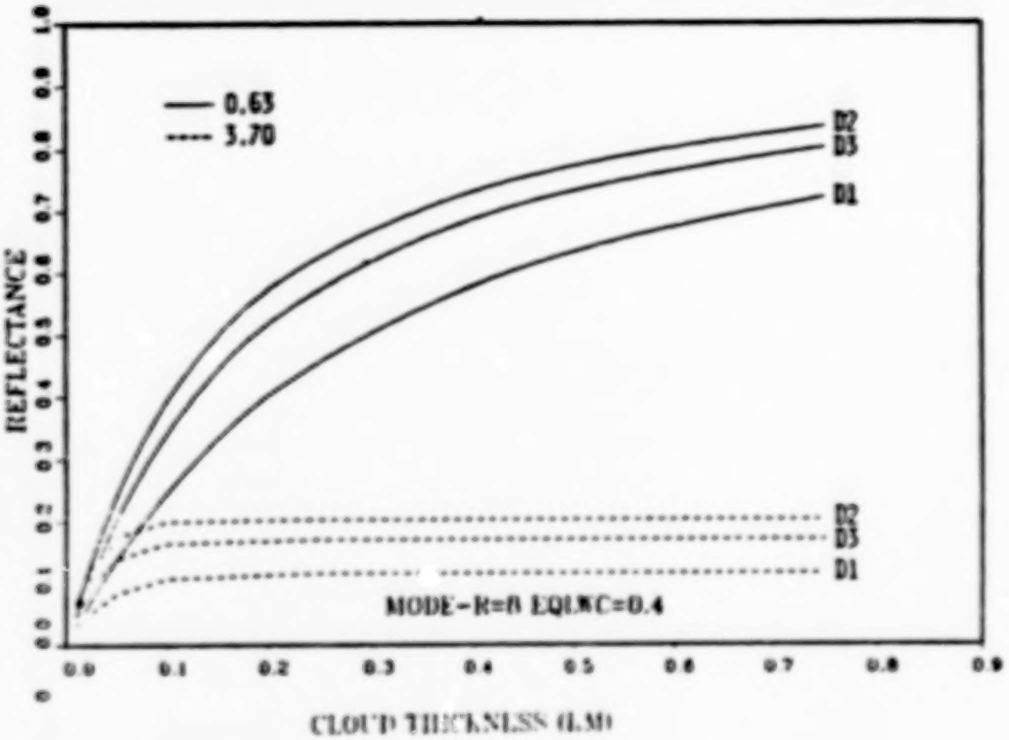

FIG. 2. Reflectance verses cloud thickness for solar zenith angle=45°, modal radius=8 μm, LWC=0.4 g m^{-3} and at the three modified gamma distributions (D1, D2, and D3).

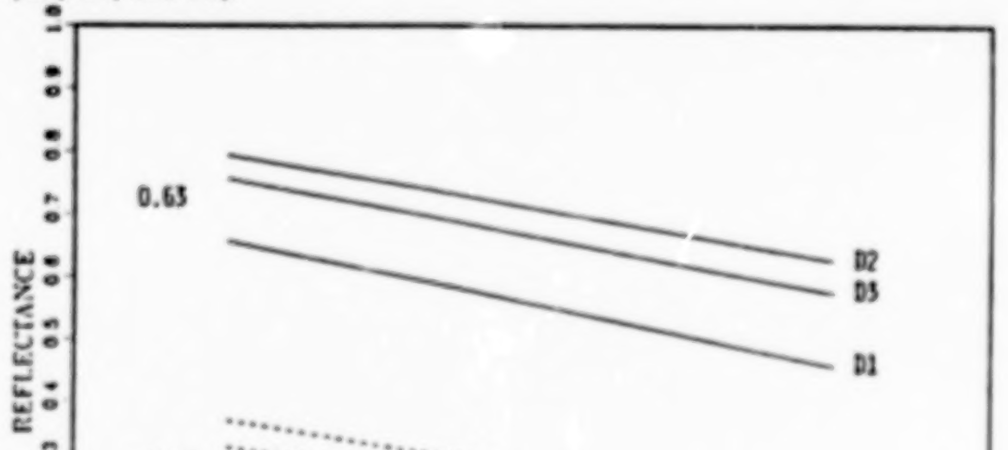

FIG. 3. Reflectance verses droplet radius for z=0.25 km, solar zenith angle=45°, LWC=0.4 g m^{-3} and at the three modified gamma distributions (D1, D2, and D3).

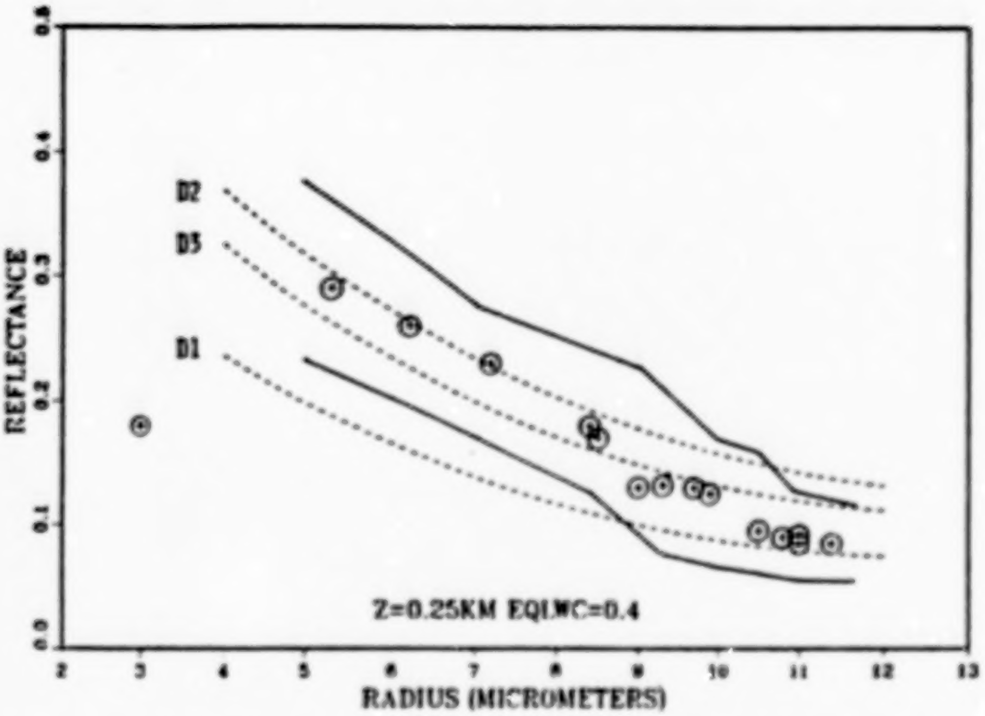

FIG. 4. Reflectance at 3.7 μm wavelength from AVHRR analysis versus droplet radius from NCAR Electra measurements. Solid lines indicate the 95% confidence interval for the data points. Dashed lines indicate model cloud reflectance estimates for droplet distributions D1, D2, and D3.

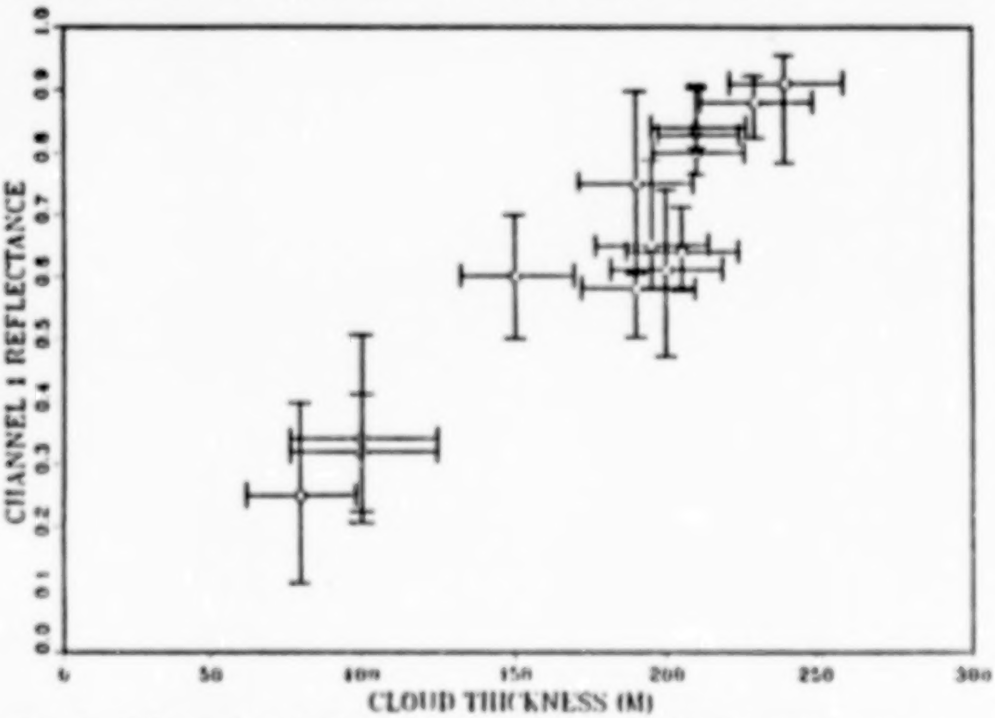

FIG. 5. Reflectance at 0.63 μm wavelength from AVHRR analysis versus cloud thickness from NCAR Electra measurements. Brackets indicate 95% confidence intervals for reflectance and cloud thickness.

Structures Observed on the Spot Radiance Fields During the FIRE Experiment

Genevieve Seze[*], Leonard Smith[**] and Michel Desbois[*]
[*]LMD/Ecole Polytechnique 91128 Palaiseau Cedex (France)
[**]DAMTP, Cambridge University (UK)

Introduction

Three Spot images taken during the FIRE experiment on stratocumulus (july 1987) have been analysed. From this high resolution data detailed observations of the true cloud radiance field may be made. The structure and inhomogeneity of these radiance fields hold important implications for the radiation budget, while the fine scale structure in radiance field provides information on cloud dynamics. Wieliki and Welsh (1986) and Parker et al. (1986) have quantified the inhomogeneities of the cumulus clouds through a careful examination of the distribution of cloud (and hole) size as functions of an effective cloud diameter and radiance threshold. Cahalan (1988) has compared for different cloud types (stratocumulus, fair wheather cumulus, convective clouds in the ITCZ) the distributions of clouds (and holes) sizes, the relation between the size and the perimeter of these clouds (and holes), and examining the possibility of scale invariance. We extended these results from Landsat resolution (57m and 30m) to the Spot resolution (10m) resolution in the case of boundary layer clouds. Particular emphasis is placed on the statistics of zones of high and low reflectivity as a function of a threshold reflectivity.

Data

Each Spot instrument returns one panchromatic images (10m resolution) and three multispectral images (20m resolution). These images are obtained from the measure of solare enery in a large spectral band (0.51-0.73) and three narrower bands at visible and infrared wavelengths. The saturation is reached in the panchromatique band for 30% of reflectivity and in the multispectral bands respectively for 50%, 60% and 80% of reflectivity. Data are discretized in digital count comprised between 0 and 255. In the panchromatic image the sea reflectivity corresponds to about 25 counts.

Three different Spot scenes have been recorded during the FIRE experiment: One 60km by 80km scene on the 7th of july both in panchromatic mode and multispectral mode, one double scene of 120km by 120km on the 8th of july in panchromatic mode and on 60km by 66km scene on the 19th both in panchromatic and multispectral mode. The 7th and 8th are very cloudy. However, inspite of the small variability in radiances, different structures appear. The scene for the 19th of july is on the opposite characterized by the presence of very small clouds. From these data sets, three regions of 1024 by 1024 pixels (10km by 10km) have been extracted (Fig. 1). The first region is composed of a mixing of high reflectivity and low reflectivity structures. The second region has increasing reflectivity from the center to the edges. Scene 3 is a almost clear sky with sparse small clouds of various size but low reflectivity.

Radiance field analysis

For each of the three scenes, binary images have been constructed in order to study the size distribution of the high reflectivity and low reflectivity regions and their spatial dispersion. The images are constructed by using radiance threshold: for a certain threshold R, pixels having a radiance larger than R in the original image, are assigned the value 1 in the binary image while the other pixels are assigned the value 0. The pixels with value 1 will be called high reflectivity pixels or "bright" pixels, whereas pixels with value 0 will be called low reflectivity pixels or "dark" pixels. The fraction of pixels in each state will vary with the chosen threshold; for scene 1 and scene 2, thresholds have been chosen so as to obtain a "dark" ("bright") pixel percentage : 10%, 30%, 50%, 70%, 90%. For the clear scene on the 19th (scene 3), more than 93% of the pixels are clear sky. In this case, four thresholds have been chosen as to have 93%, 95%, 97%, 98% of the pixels darker than the threshold.

As the radiance threshold is increased the binary images of the first scene more and more resembles an open cell or cumulus cloud field. In binary images of scene 2, the interior hole becomes sucessively better defined, the similarity with an open cell is enhanced. For images of the third scene, the effect of increasing the threshold is first to mask noise over the sea, then to decrease the cloud surface area. For each threshold-related binary image, the number of "dark" and "bright" regions have been determined; then for each of these regions various parameters have been computed. We will concentrate only on two of them: the surface area or the number of pixels forming the region and the so called "perimeter" or the number of pixel edges which are at boundary between a "dark" and a "bright" pixel. From the surface area an equivalent diameter has been computed (see Wieliki and Welsh, 1986). To study their distributions the "dark" ("bright") surface areas have been gathered in classes of equal step of ln(2) in ln(D). Boundary between class increase by factor of 2 (10m, 20m, 40m ...) Figure 2 show these distributions for scene 2 and the 5 thresholds on a log/log plot.

For scene 1 and 2, the observed dependence in the number of regions, and the distribution of the surface area of these regions versus thresholds indicates that as the percentage of "bright"("dark") pixels increases, the number of areas increases first and then decreases; at first as the "bright" ("dark") pixel percentage increases the number of new regions which appear is larger than the number of regions which are gathered, then the reverse situation occurs. The magnitude of these increases and decreases and the percentage value for the break point are related to the spatial organisation of the bright and dark areas. For a given percentage, the number of small "dark" regions (10m to 160m in equivalent diameter) is larger than the number of small "bright" regions. Especially, the darkest pixels are wider spread in small regions than the brightest pixels. For scene 1 the number of "bright"("dark") regions for a certain percentage is higher than for scene 2; the spatial mixing of the "bright" and "dark" regions of various area surface is larger in scene 1.

For a given percentage of "bright" ("dark") pixels, the number of region decrease versus surface area increase is obvious; this increase is relatively uniform on the log/log plot (Fig. 2) for surface area larger than 10m and smaller than 1280m. Exceptions are 90% cases of "bright"/"dark" regions, the number of regions and specially of small regions consequently decreases. The relatilly uniform decrease observed, is in agreement with previous results found by Cahalan (1988) for Landsat cloudy scenes; these results show that distributions of surface areas of clouds (or holes) often decrease versus surface area increase as a power law; the exponent is related to the cloud field beiing studied. This exponent is defined as the area exponents by Lovejoy and Shwertzer (1988). For boundary layer clouds, Cahalan finds an exponent value of 1.5 for low thresholds, and observes an increase of this exponent for increasing thresholds. In the present study, when the power law aproximation seems reasonable (a percentage of pixels smaller than 90% and generally surface areas between 20m and 1240m), the exponent value found ranges between 1. and 1.3.

The length of the boundary has also been computed, it appears that in the case of a small threshold the number of boundary pixel is larger than in the case of a high threshold, because of the larger spatial dispersion of the darkest pixels as compared to the brightest pixels. In order to have a measure of the complexity of the boundary of these "bright" ("dark") regions, we have plotted for each region its perimeter value versus the root mean square of its surface area on a log/log scale. The same linear relationship as found by Lovejoy (1982) on Goes images and by Cahalan (1988) on Lansat appears on these graphs; the fitted slope is close to 1.3.

For scene 3 the number of "bright" or "cloud" regions is small, and the diameter of these clouds is generally between 10m and 360m. The large decrease of the number of regions (1135 to 562) occurs for thresholds between 29 and 31 which only correspond to about 0.4% reflectivity difference. This decrease is due to the disparition of noisy sea pixels. As for scene 1 and 2 the decrease of the distribution slope with surface area increase (for surface area between 20m and 320m) is relatively uniform. The slopes observed range between -.8 and -.7.

On the other hand, a box counting technic on a regular grid has been used to study the spatial distribution of these "bright" ("dark") regions. Box counting technics have been developped as a way to estimate the dimension of fractal sets (Lovejoy and Shertzer, 1988). It has also been used to study the effect of sensor resolution (Shenk and Salomonson 1972). To apply this technic, different resolution grids are defined, for resolution elements varying from a quarter of the image (lowest resolution), to one pixel (highest resolution) and dividing at each step the resolution element by 4; then for each resolution the percentage of "bright" ("dark") coverage is determined by counting the number of resolution elements containning at least one "bright" ("dark") pixel. For each scene and each threshold, the percentages of "bright" and "dark" coverages in function of the resolution (Eps) have been plotted. For each curve several parameters have been extracted. The first parameter is the exponent d0 which for a fractal set equal its dimension. d0 is obtained by fitting a a power law (M(Eps)=Eps**d0) through the scatter. The other parameters M0, Beta and A are obtained by fitting a function F (F=M0+A*Eps**Beta). F is an empirical scaling law to determine the "true area" of assumed "fat fractal" set (Farmer and Umberger, 1985; Smith, 1986).

These different parameters vary in function of the increase of the "bright" ("dark") pixel percentage and of the scene studied. They are related to the surface area distribution of the "bright" and "dark" regions and to their relative spatial disposition. For high percentages, d0 is close to 2, the fractal dimension of an area beling 2. However as the percentage of "bright" ("dark") pixels decreases d0 decreases due to the region increasing scatter. Correlatively, A and Beta increase. For a given percentage of "dark" and "bright" pixels, the value of d0 for "dark" regions is smaller than for "bright" regions, especially for the lowest percentages (1.5 and 1.7); On the opposite A and Beta are larger in the case of "dark" regions. These differences between the "dark" and "bright" cases are related to the larger number of regions found for the darkest image than for the brightest image. Differences are observed between scene 1 and scene 2 in these parameter values and are related to the spatial organisation of the "bright" and "dark" region in these regions; especially, the differences between the parameters associated to the "dark" areas and to the "bright" areas are larger for scene 1 than scene 2.

Conclusion

Some results found are in agreement with previous studies on satellite high resolution data; the number of "bright" and "dark" region decrease versus surface area increase can be in some cases aproximated by a power law; the perimeter and the surface area are found to be a power law related with an exponent close to 1.3. However, our study focussed, at least for two of the scenes, on the change in the scales of variability versus the percentage of pixels declared "thick" ("thin"). This shows the possibility for differentiating spatial structures in an apparently homogeneous cloud field. The parameters obtained from the fat fractal scaling can give usefull indications on these structures, and allow to aproximate the error in cloud cover estimation from coarse resolution data; further studies must be pursued to check the conditions for which fat fractal scaling can be applied to the cloud radiance field. The third scene shows the existence of very small and low refectivity clouds and the importance of noise in the data for the choice of a cloud/no cloud detection threshold. This study has to be continued on more scenes; the comparison between the 10m and 20m resolution images has to be developped and simultaneously the effect of a spatial sampling or averaging of the data must be tested. Comparison of these 60km by 60km Spot scenes with the corresponding 1km resolution Goes radiance field has to be done.

References

R. F. Cahalan, 1988: Landsat observations of fractal cloud structure. Non Linear Variability in Geophysics. S.L Eds, Reidel.

D.K. Umberger and Farmer J.D. , 1985: Fat fractals on the enery of surface. Phys. Rev. Lett. 55, 661-664.

S. Lovejoy, 1982: Area-perimeter relation for rain and cloud areas. Science, 26, 185-187.

S. Lovejoy and Shertzer D., 1988: Multifractal analysis techniques and geophysical applications. Non Linear Variability in Geophysics. S.L Eds, Reidel.

L. Parker, Welsh R.M. and Musil D.J., 1986: Analysis of spatial inhomogeneities in cumulus clouds using high spatial resolution Lansat data. J. Climate Appl. Meteor., 25, 1301-1314.

William E. Shenk and Salomonson V. V., 1972: A simulation study exploring the effects of sensor spatial resolution on estimates of cloud cover from satellites. J. Appl. Meteor., 11, 214-220.

L. Smith, 1986: Fat fractal scaling of cloud areas. Conference on Nonlinear Variability in Geophysics. 25-29 august 1986. McGill University, Montreal.

Bruce Wieliki and Welch R. W., 1986: Cumulus cloud properties using Landsat satellite data. J. Climate Appl. Meteor., 25, 261-276.

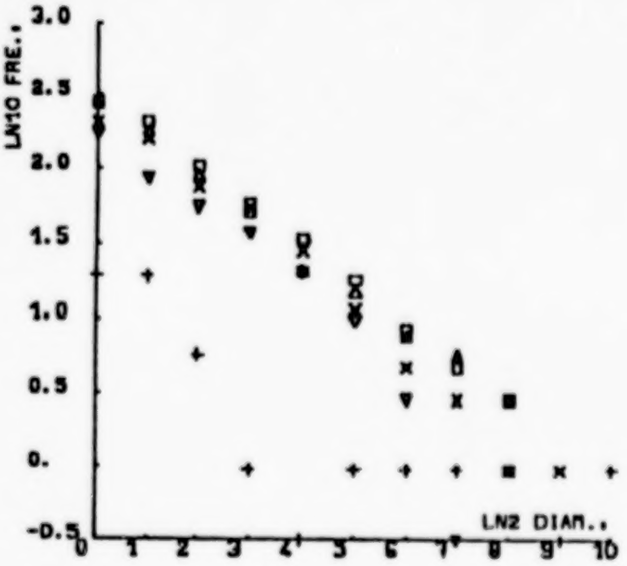

Figure 2: Distributions of the surface areas of the "thick" regions in scene 2 for 5 thresholds; the , , , , , correspond to thresholds 10%,30%,50%,70%,90%.

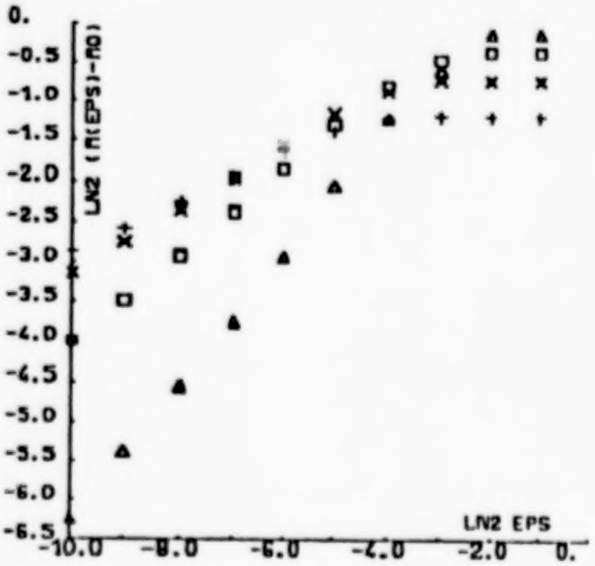

Figure 3: For scene 1, difference of the "thick" pixel percentage (M(Eps)) with the estimated percentage M(0) versus resolution Eps for 4 thresholds; the , , , , correspond to thresholds 10%/30%/50%/70%.

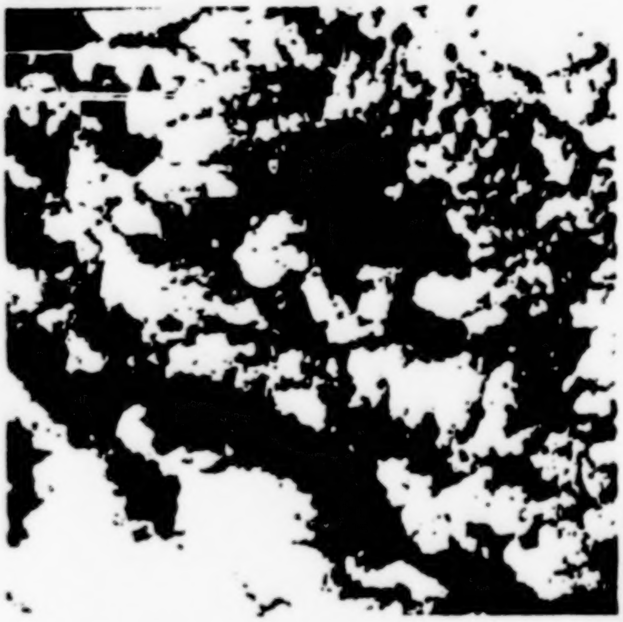

a) 2048 by 2048 pixel square Centered on region 1; the black (white) represents the radiance 100 (255).

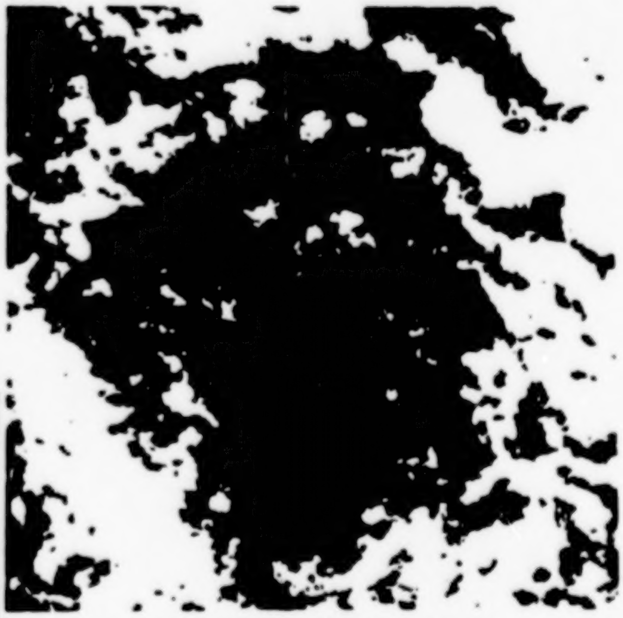

b) 1024*1024 pixel square corresponding to region 2; the black (white) represents the radiance 60 (255).

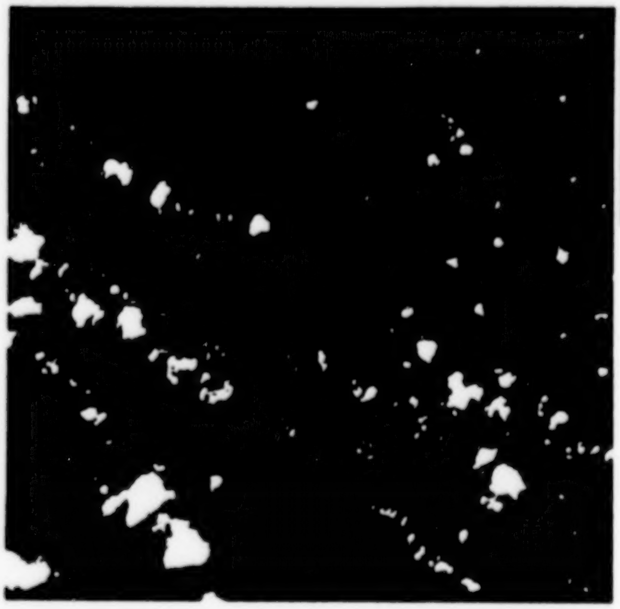

c) 2048 by 2048 pixel square; region 3 is a 1024 by 1024 pixel square placed on the middle left part of the scene. the black (white) represents the radiance 25 (80).

Figure 1: Spot panchromatique images.

Analysis of Stratocumulus Cloud Fields Using LANDSAT Imagery: Size Distributions and Spatial Separations

by R. M. Welch[1], S. K. Sengupta[2] and D. W. Chen[2]

[1]Institute of Atmospheric Sciences
[2]Department of Mathematics and Computer Science
South Dakota School of Mines and Technology
501 East St. Joseph Street
South Dakota School of Mines and Technology
Rapid City, SD 57701-3995

Stratocumulus cloud fields in the FIRE IFO region are analyzed using LANDSAT Thematic Mapper imagery. Structural properties such as cloud cell size distribution, cell horizontal apsect ratio, fractional coverage and fractal dimension are determined. It is found that stratocumulus cloud number densities are represented by a power law. The slope of the power law α is about $\alpha = 1.5$ for cell diameters $D < 1$ km and about $\alpha = 2.5$ for cell diameters $D > 1$ km. Cell horizontal aspect ratio has a tendency to increase at large cell sizes, and cells are bi-fractal in nature. Using LANDSAT Multispectal Scanner imagery for twelve selected stratocumulus scenes acquired during previous years, similar structural characteristics are obtained.

Cloud field spatial organization also is analyzed. Nearest-neighbor spacings are fit with a number of functions, with Weibull and Gamma distributions providing the best fits. Poisson tests show that the spatial separations are not random. Second order statistics are used to examine clustering.

CLOUD PARAMETERS DERIVED FROM GOES DURING THE 1987 MARINE STRATOCUMULUS FIRE INTENSIVE FIELD OBSERVATION PERIOD

David F. Young
Aerospace Technologies Division, Planning Research Corporation
Hampton, Virginia 23666
and
Patrick Minnis and Edwin F. Harrison
Atmospheric Sciences Division, NASA Langley Research Center
Hampton, Virginia 23665-5225

1. Introduction

The Geostationary Operational Environmental Satellite (GOES) is well suited for observations of the variations of clouds over many temporal and spatial scales. For this reason, GOES data taken during the Marine Stratocumulus Intensive Field Observations (IFO) (June 29 - July 19, 1987, Kloessel et al., 1988) serve several purposes. One facet of the First ISCCP Regional Experiment (FIRE) is improvement of our understanding of cloud parameter retrievals from satellite-observed radiances. This involves comparisons of coincident satellite cloud parameters and high resolution data taken by various instruments on other platforms during the IFO periods. Another aspect of FIRE is the improvement of both large- and small-scale models of stratocumulus used in general circulation models (GCMs). This may involve, among other studies, linking the small-scale processes observed during the IFO to the variations in large-scale cloud fields observed with the satellites during the IFO and Extended Time Observation (ETO) periods. This paper presents preliminary results of an analysis of GOES data covering most of the IFO period. The large-scale cloud-field characteristics are derived, then related to a longer period of measurements. Finally, some point measurements taken from the surface are compared to regional scale cloud parameters derived from satellite radiances.

2. Data and methodology

The data used in this study are hourly GOES-East, 8-km visible (0.65 μm) and infrared (10.5 μm) radiances and half-hourly GOES-West 1-km visible and 4-km infrared radiances. Analysis of the data is the same as that described by Minnis et al. (1988). The cloud parameters were derived for 2.5° regions between 140°W and 115°W longitudes and 40°N and 25°N latitudes. They include cloud amount, cloud-top temperature, cloud albedo, and clear-sky temperature and albedo for each region. All of the cloud parameters were derived for total, low (< 2 km), middle (2-6 km), and high (> 6 km) clouds. GOES-East cloud amounts were corrected for viewing zenith angle as described by Minnis et al. (1988). Albedo here refers to the mean top-of-the-atmosphere broadband shortwave (0.2 - 5.0 μm) albedo over clear or cloudy areas. Details of its determination from the visible radiances are given in Minnis et al. (1988). Means are computed in the same fashion noted by Minnis et al. (1987).

3. Large-scale cloud features

At the time of this writing, only the cloud analyses from a 3-hourly subset of the July, 1987 GOES-East data were completed. All results shown here refer to July 2-19, 1987 GOES-East data, unless specified otherwise. Mean total cloudiness, shown in Fig. 1a, is less than 70% along the California coast reaching a maximum of more than 90% near 34°N and 132°W.

Total cloudiness is < 70% in the southeastern and southwestern corners of the grid. Except over land areas and the northwestern corner, more than 95% of the total cloud cover consists of low-level clouds (Fig. 1b).

The clear-sky temperatures (Fig. 2) over the ocean range from about 285K in the north to 290K in the southeastern corner of the region. Mean oceanic, equivalent blackbody, cloud-top temperatures in Fig. 3 vary from 276K in the northwestern corner to about 286K in the southeastern corner. Mean clear ocean albedos range between 0.10 and 0.12 while cloud albedos (Fig. 4) over the ocean regions are between 0.30 and 0.40. Maximum cloud albedos occur within much of the IFO region southwest of Los Angeles. Minimum cloud albedo (0.31) occurs over the southeastern and southwestern corners of the region.

Diurnal variability of total cloud cover is plotted in Fig. 5 for each 2.5° region. Maximum cloudiness occurs around 0600 LT over all of the ocean regions while the minimum is found during the afternoon. Two large areas assumed to represent near-coast and midocean conditions are defined as the pacific (PAC) region between 25°N and 32.5°N and 140°W and 132.5°W and the IFO region bordered by 35°N and 30°N and 125°W and 120°W with an additional 2.5° region to the east centered at 31.3°N and 118.8°W. The 3-hourly means for these two regions are shown in Fig. 6. Maximum cloudiness occurs at the same time for both of these regions, while minimum cloudiness appears to occur earlier over the PAC than it does over the IFO region. The diurnal range over the PAC is significantly higher than over the IFO region.

Although cloud amounts during the 18-day period are from 0 to 20% greater than the July 2-31 mean value, the remaining parameters are very close to the corresponding monthly means. These results appear to be relatively typical of the cloud properties observed over this same grid during earlier years. A comparison with the data of Minnis et al. (1988) reveals very similar patterns in cloud-top temperature, cloud albedo, clear-sky temperature, cloud amounts, and diurnal cloud variability. The slightly lower values of cloud albedo may be due to uncertainties in the calibration procedures. The extreme viewing zenith angles in these data may also affect some of the parameter values. Despite these potential limitations, these results indicate that the IFO period represents fairly typical conditions over the California marine stratocumulus region.

4. Comparisons with surface observations

Most of the comparisons with other analyses will attempt to match the spatial domain of the correlative data to a reasonable degree. In this section, however, point measurements of cloud properties taken from San Nicolas Island are compared to large-area averages derived from the GOES results over a 2.5° region, designated R39, centered at 31.3°N and 118.8°W which is just south of the island. (The region containing the island is partially land-covered, introducing some complications). This comparison is shown to demonstrate how the surface and/or aircraft data may be related to the satellite cloud retrievals. The point measurements are the values of cloud-top height and cloud base, cloud liquid water density, and solar irradiance measured between 1200 UT July 12 and 0600 UT July 15 as well as the hourly averages of liquid water for July 2-19, 1987 (FIRE, 1987).

Figure 7 shows the time series of cloud cover over R39, while the corresponding clear-sky and cloud-top temperatures are given in Fig. 8 with the San Nicolas Island cloud base and top heights. Clear-sky temperature changes by less than 1K over the period. Cloud-top temperature and cloud-top altitude vary in a negative correspondence. Significant breaks in the clouds over the island also occur during the lowest cloud amounts over R39 late on July 12 and early on July 13. The values of cloud albedo shown in Fig. 9 reveal sparse sampling, but also vary with the liquid water density over the island. Cloud albedo normally increases with increasing solar zenith angle because of increased air mass. If the cloud properties are constant, then the cloud albedo variation should be symmetrical about local noon and the same each day. Local noon occurs at approximately 1955 UT. Thus, aside from the increasing albedo from July 12 to July 14, a morning bias in cloud albedo is also evident. These two patterns apparently reflect the variations in cloud liquid water density. This correspondence is clearer in the comparison of the 18-day means of albedo and liquid water which show a morning bias in both quantities (Fig. 10). Similar cloud albedo variations have been reported over other regions covered by large-scale stratocumulus cloud fields (e.g., Minnis and Harrison, 1984). Eighteen-day averages of cloud amount and cloud-top temperature (Fig. 11) also suggest that the variations in stratocumulus cloud properties seen during this small window are fairly representative of the clouds in this area during July.

5. Concluding remarks

The preliminary results presented here have led to several conclusions. It appears that the large-scale cloud properties observed during the 1987 IFO are very similar to the climatological (i.e., 1984-1987) means. Thus, the results of this experiment should be very representative of the California marine stratocumulus during July. Regional-scale satellite measurements appear to correspond closely to island-observed quantities suggesting that the island observations are representative of cloud property variations on a much larger scale. These results also indicate that the satellite retrieval is producing a reasonable estimate of stratocumulus characteristics. Much additional research is anticipated using the GOES-West satellite with higher temporal and spatial sampling. This should allow for improvements in defining cloud structure and in matching the satellite observations to those on other platforms.

6. References

FIRE Science Experiment Team Workshop, 1987. Linithicum, MD, Nov. 9-12, pp. 24-25.

Kloessel, K. A., B. A. Albrecht, and D. P. Wylie, 1988: FIRE Marine Stratocumulus Observations -- Summary of Operations and Synoptic Conditions. FIRE TR No. 1, 171 pp.

Minnis, P. and E. F. Harrison, 1984: Diurnal Variability of Regional Cloud and Clear-Sky Radiative Parameters Derived from GOES Data. J. Clim. Appl. Met., **23**, 993-1051.

Minnis, P., E. F. Harrison, and G. G. Gibson, 1987: Cloud Cover Over the Equatorial Eastern Pacific Derived from July 1983 ISCCP Data Using a Hybrid Bispectral Threshold Method. J. Geophys. Res., **92**, 4051-4073.

Minnis, P., E. F. Harrison, and D. F. Young, 1988: Extended Time Observations of California Marine Stratocumulus Clouds from GOES for 1983-1987. FIRE Workshop, Vail, CO, July 11-15.

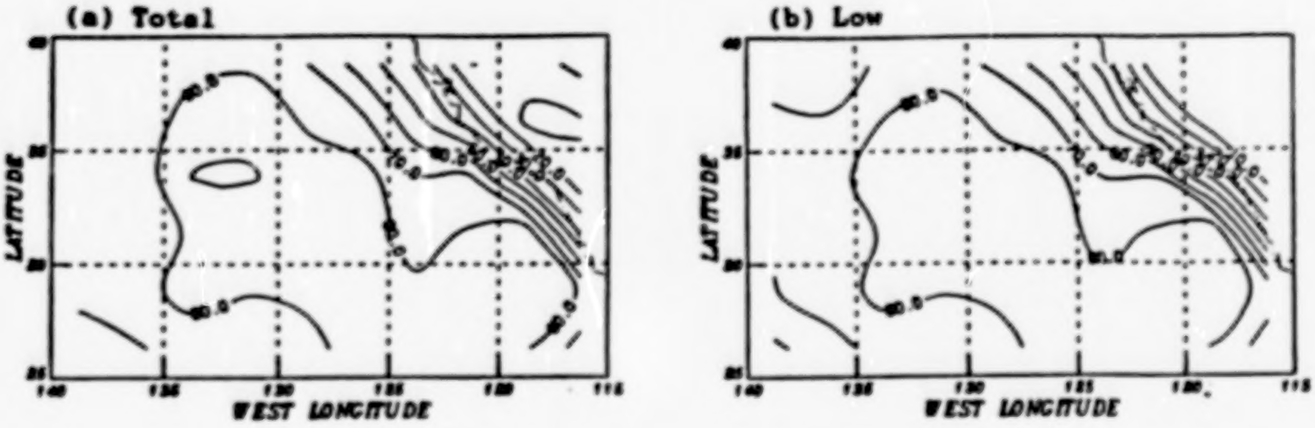
(a) Total
(b) Low
LATITUDE
WEST LONGITUDE
40
35
30
25
140
135
130
125
120
115

Figure 1. Mean cloud amounts (%) for July 1987.

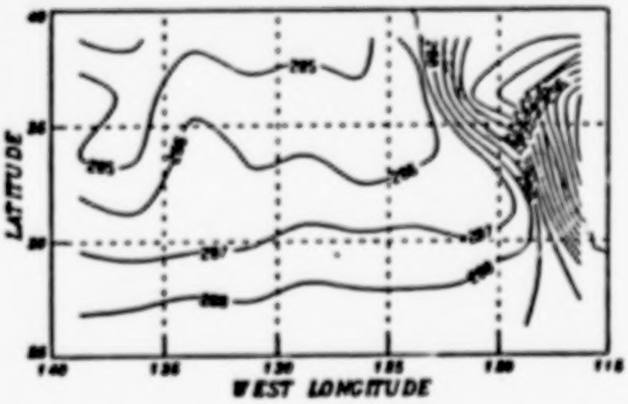
LATITUDE
WEST LONGITUDE
295
297
298
140
135
130
125
120
115

Figure 2. Mean clear-sky temperatures for July 1987.

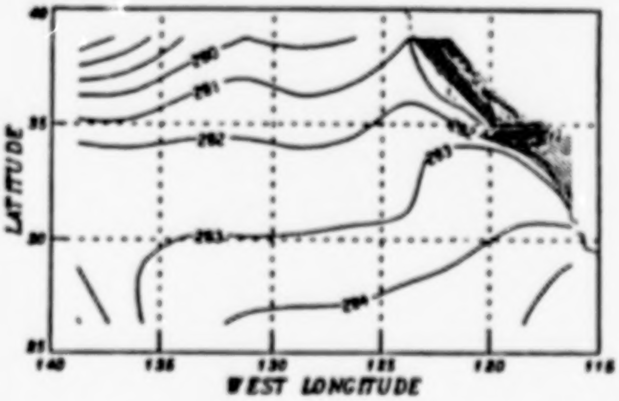
LATITUDE
WEST LONGITUDE
290
291
292
293
294
140
135
130
125
120
115

Figure 3. Mean cloud-top temperatures for July 1987.

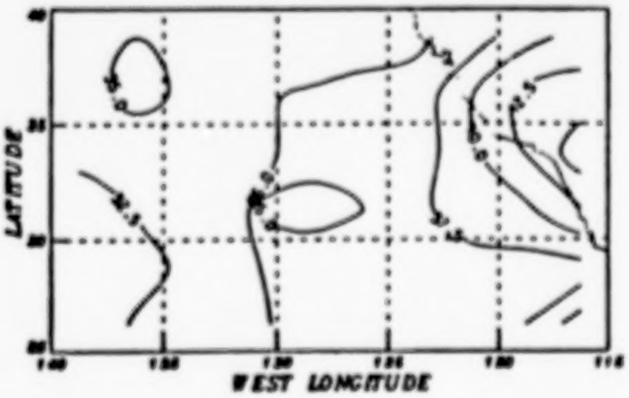
LATITUDE
WEST LONGITUDE
140
135
130
125
120
115

Figure 4. Mean cloud albedo (%) for July 1987.

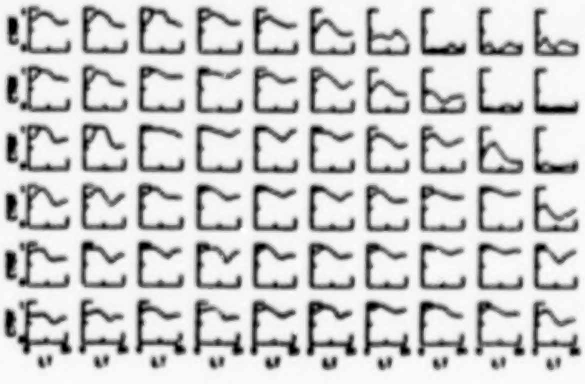

Figure 5. Diurnal variability of total cloud amount (%).

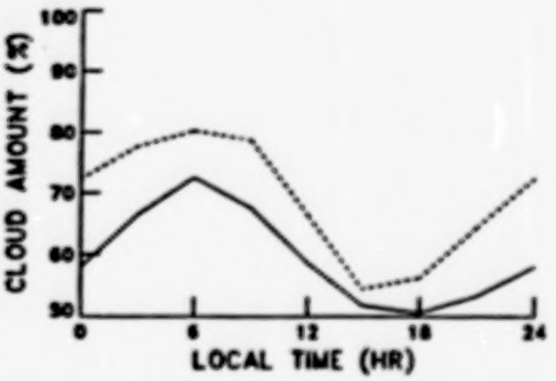

Figure 6. Diurnal variability of total cloud amount (%) for the IFO and PAC regions.

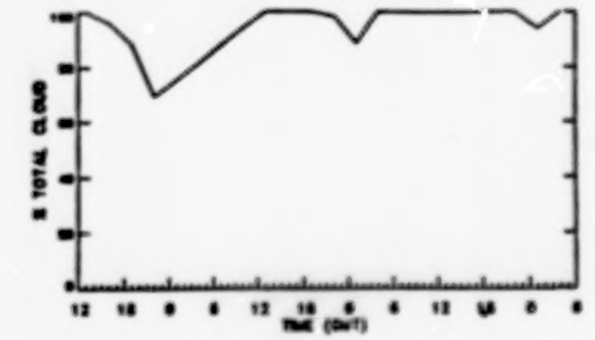

Figure 7. July 12-14 time series of Region 39 cloud amount (%).

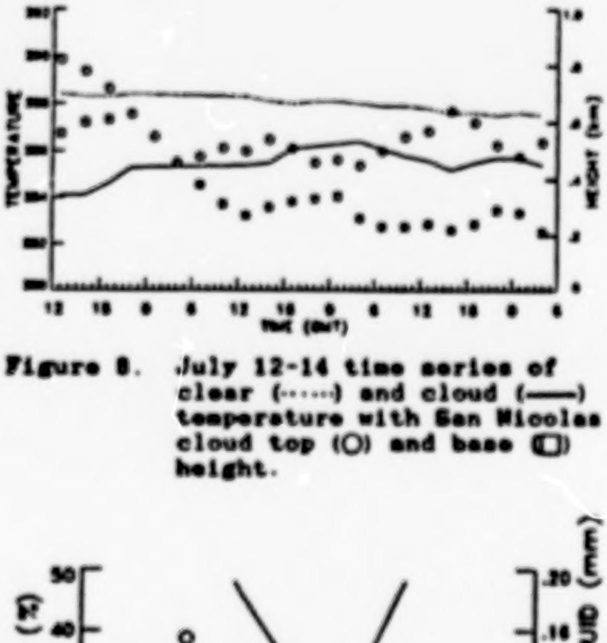

Figure 8. July 12-14 time series of clear (······) and cloud (——) temperature with San Nicolas cloud top (○) and base (□) height.

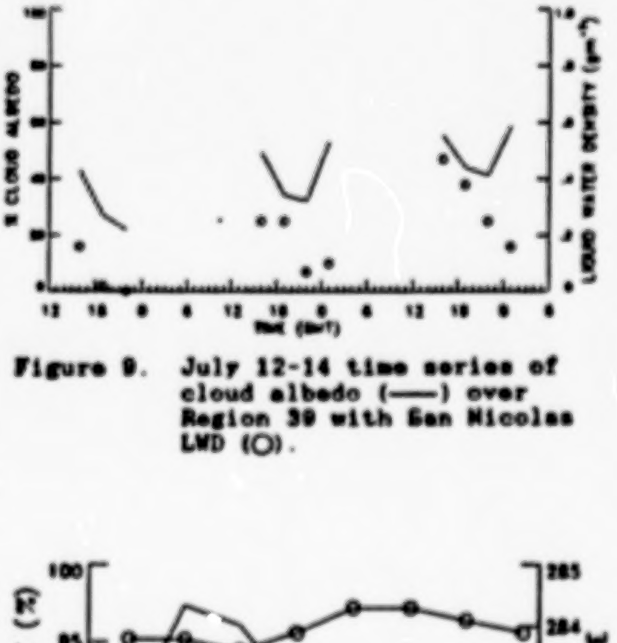

Figure 9. July 12-14 time series of cloud albedo (——) over Region 39 with San Nicolas LWD (○).

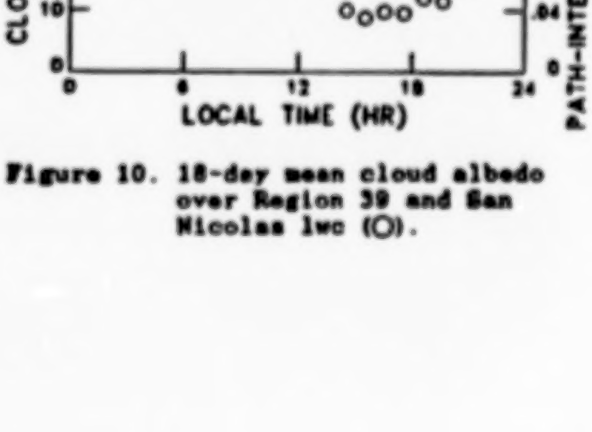

Figure 10. 18-day mean cloud albedo over Region 39 and San Nicolas lwc (○).

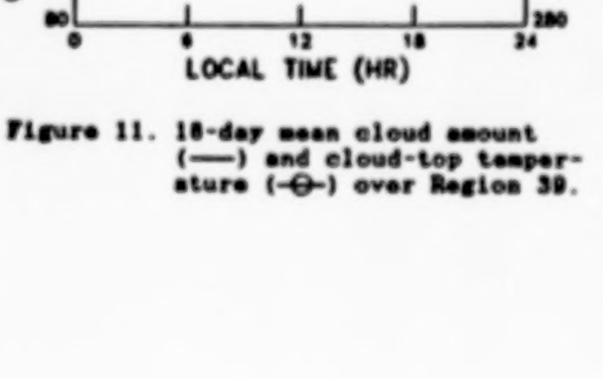

Figure 11. 18-day mean cloud amount (——) and cloud-top temperature (-⊖-) over Region 39.

FIRE SCIENCE TEAM MEETING
VAIL, COLORADO
JULY 11-15, 1988

MARINE STRATOCUMULUS

LIDAR/RADIATIVE PROPERTIES/MICROPHYSICAL - Philip H. Austin   Thursday, July 14, 1988

PAGE

Aerosol Measurements in the Stratocumulus Project 287
Hudson, James G.

In Situ Measurements of "Ship Tracks" 29[illegible]
Radke, Lawrence F.; Jamie H. Lyons, and Peter V. Hobbs

Estimated Accuracy of Ground-Based Liquid Water Measurements During FIRE 295
Snider, J. B.

NRL Tethered Balloon Measurements at San Nicholas Island During FIRE IFO 1987 299
Gerber, Hermann; Stuart Gathman, Jeffrey James, Mike Smith, Ian Consterdine, and Scott Brandeki

Aerosol measurements in the stratocumulus project

by James G. Hudson
Desert Research Institute
University of Nevada System
P.O. Box 60220
Reno, Nevada 89506

Cloud Condensation Nuclei (CCN) and Condensation Nuclei (CN) were measured from the NCAR Electra throughout the marine stratocumulus project. The total particle concentration was measured with a TSI 3020 condensation nucleus counter. The CCN were measured with the DRI instantaneous CCN spectrometer (Hudson, 1986). This instrument simultaneously measures the concentration of aerosol active at up to 100 different critical supersaturations, Sc. This is accomplished by exposing the sample to a fixed supersaturation field and using the size of the droplets produced in this cloud chamber to deduce the Sc of the nuclei upon which they have grown. Droplet size is associated with Sc through a calibration which is accomplished by passing soluble aerosols of known size and composition through the cloud chamber. This procedure results in a calibration curve of Sc vs. droplet size. This then allows the channel number to be directly associated with Sc. Thus number concentration vs. Sc is obtained and this is a CCN spectrum. Since the instrument operates continuously the measurements at all Sc's are available simultaneously. Sample is drawn directly from the ambient air and data is displayed in nearly real time. Samples were integrated over times of about 10 seconds so that substantial spatial resolution is available. Calibrations performed once or twice a day and were found to be consistent.

Preliminary results are shown in the figures 1-4. Figure 1 shows the rather surprizing but consistent result that the particle concentration below cloud is lower than the concentrations above cloud. This was true for all measurements on the Electra. Therefore it appears that continental or polluted air was advected out over the ocean at these levels. Figures 2 and 3 exhibit differential CCN spectra above and below cloud. This differential display of the CCN spectrum is now possible because of the great number of Sc channels which are now available with this new instrument. It is much more useful than the traditional cumulative CCN spectra because, for instance, it readily reveals the higher concentrations of small particles (CN and high Sc CCN) above cloud (fig. 3). This can be contrasted with the flatter spectrum seen below cloud (fig. 2). The steeper spectrum is indicative of more recent particle production whereas the flatter spectrum seen in figure 2 is characteristic of a more aged aerosol where the smaller particles have coagulated into larger particles. There is a preliminary indication that the feature exhibited in figure 1 and further explained in figures 2 and 3 is not as prominent at night. If so it would indicate photochemical particle production in the air above cloud.

At any rate the higher conctrations above cloud are very important when it is considered that the droplet spectrum in the upper layers of a cloud determines the cloud albedo. If the high CCN concentrations are indeed influencing the cloud microphysics and producing a cloud with more numerous small droplets then this could be an example of widespread anthropogenic influence on cloud albedo (i.e. Twomey et al., 1984) which could produce a climatic effect as large (but in the opposite direction) as the possible carbon dioxide effect.

Fig. 4 shows that ships are a source of CCN. Thus this hypotheses for the explanation of shiptrails first proposed by Conover (1966) is not contradicted. Although shiptrails themselves do not pose a threat to climate they are an indication of the sensitivity of maritime clouds to anthropogenic and continental influences on microphysics. These aerosol measurements indicate that the U.S. westcoast stratus may already exhibit the cloud microphysical effects which could have profound climatic implications. Shiptrails were not encountered by the Electra. However the high concentrations of CCN shown in figure 1 reveal that the clouds in this vicinity have already had microphysical alterations to the extent that the increase in concentration due to the ship exhaust may have only a minor effect on cloud microphysics. Therefore these widespread cloud decks may already be experiencing anthropogenic effects due to transport of air from the continent. This is consistent with the fact that shiptrails are rarely observed close to shore.

References

Conover, J.H, 1966: Anomalous cloud line. J. Atmos. Sci., 23, 778-785

Hudson, J.G. 1986: Measurements with an airborne instantaneous CCN spectrometer, Preprints, Conference on Cloud Physics, Snowmass, Colorado, 22-26 September J309-312.

Twomey, S., M. Piepgrass, and T.L. Wolfe, 1984: An assessment of the impact of pollution on global cloud albedo. Tellus, 36b, 356-366.

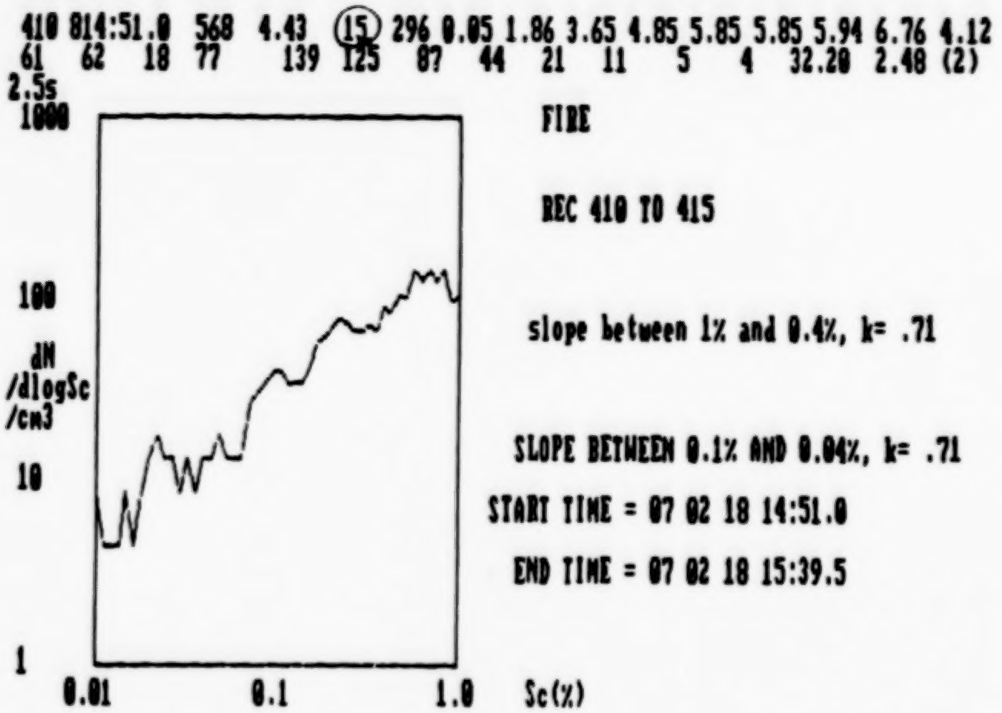

Fig. 2 Differential CCN spectrum in the air below cloud base. The cumulative CCN concentration is given in the second line from the top beginning with 25 and ending with 4. The CN or total aerosol concentration in this case was 78 per cubic centimeter.

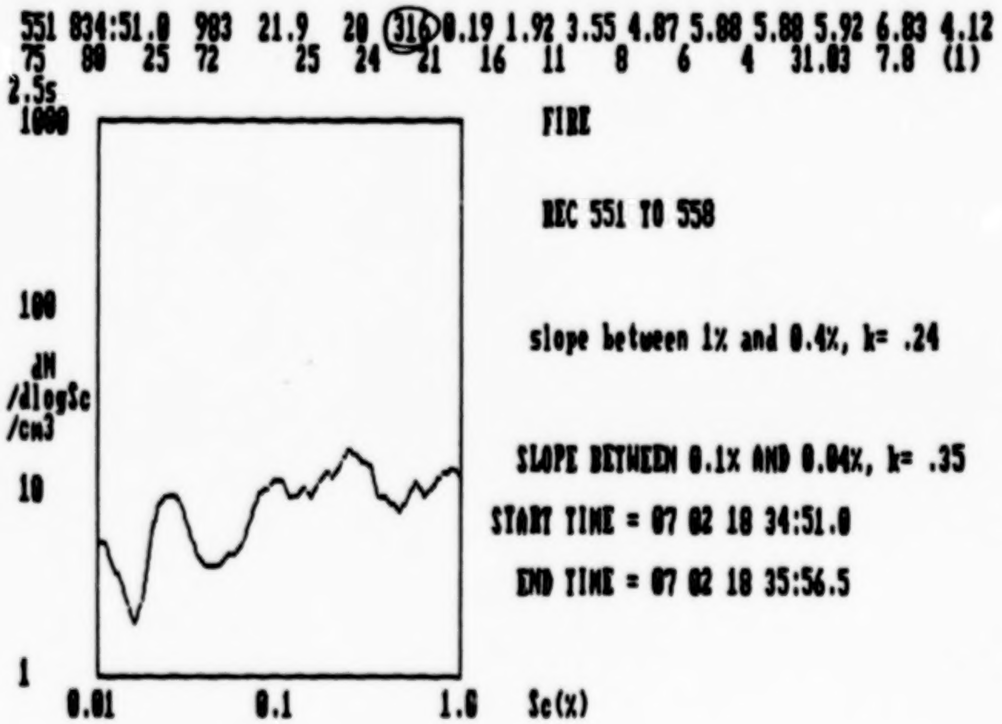

Fig. 3. As fig. 2 but above cloud where the total concentration was 248 and the total CCN concentration was 139.

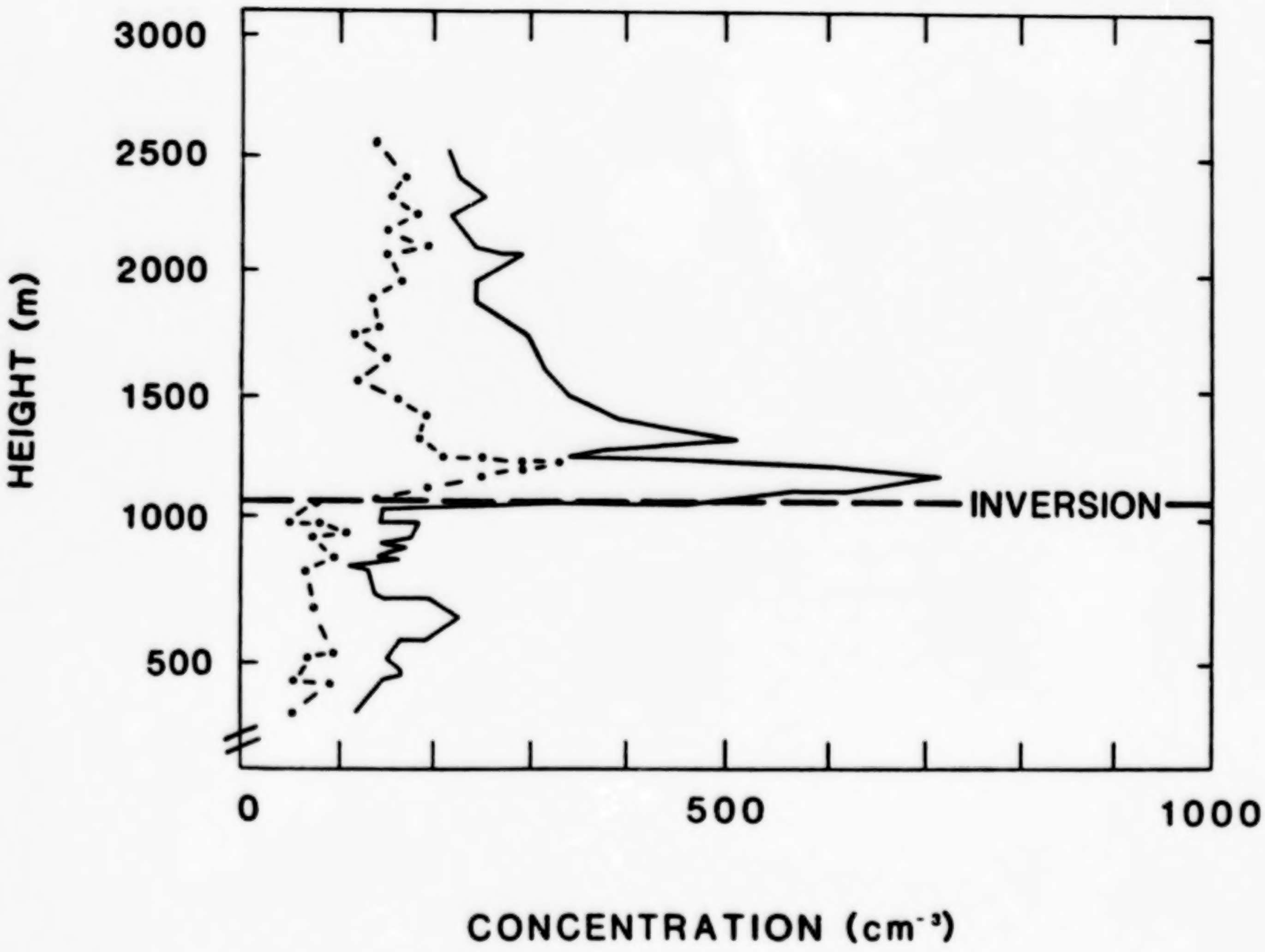

Fig. 1 Total particle (solid line) and CCN (dot-dash line) concentration measured as a function of height above sea level.

IN SITU MEASUREMENTS OF "SHIP TRACKS"

Lawrence F. Radke, Jamie H. Lyons and Peter V. Hobbs
Atmospheric Sciences Department, University of Washington
Seattle, Washington 98195 USA
and
James E. Coakley
National Center for Atmospheric Research
Boulder, Colorado 80307 USA

1. INTRODUCTION

It has long been known that cloud droplet concentrations are strongly influenced by cloud condensation nuclei (CCN) (Twomey and Warner, 1967) and that anthropogenic sources of pollution can affect CCN concentrations (Radke and Hobbs, 1976). More recently it has been suggested that CCN may play an important role in climate through their effect on cloud albedo (Twomey et al., 1984; Charlson et al., 1987).

An interesting example of the effect of anthropogenic CCN on cloud albedo is the so-called "ship track" phenomenon. Ship tracks were first observed in satellite imagery when the ship's emissions were evidently needed for the formation of a visible cloud (Conover, 1966). However, they appear more frequently in satellite imagery as modifications to existing stratus and stratocumulus clouds. The tracks are seen most clearly in satellite imagery by comparing the radiance at 3.7 µm with that at 0.63 and 11 µm (Coakley et al., 1987). To account for the observed change in radiance, droplet concentrations must be high, and the mean size of the droplets small, in ship tracks.

In this note we describe what we believe to be the first *in situ* measurements in what appears to have been a ship track.

2. OBSERVATIONS

During the FIRE study of marine stratus off the coast of California in the summer of 1987, a number of ship-tracks were detected with 3.7 µm satellite radiance measurements. Interceptions of ship track-like features by the University of Washington's C-131A research aircraft were made on July 2, 7 and 10. The July 10 case is described here.

On July 10 a ship track-like feature (hereafter referred to as "the feature") was penetrated by the aircraft between 1557 and 1615 UTC in the vicinity of 32°N and 120°W. The surface synoptic situation was dominated by a subtropical high off the California Coast with the winds from the N-NW. The GOES satellite imagery showed rather uniform stratocumulus in the area. Several ship track-like features are visible in the GOES 2015 UTC imagery. The satellite image that is closest in time to our aircraft observations is the NOAA-10 satellite imagery for 1537 UTC. This shows a linear track near the feature that we intercepted, however, there is a possibility that the feature on the satellite imagery is a mesoscale cloud boundary.

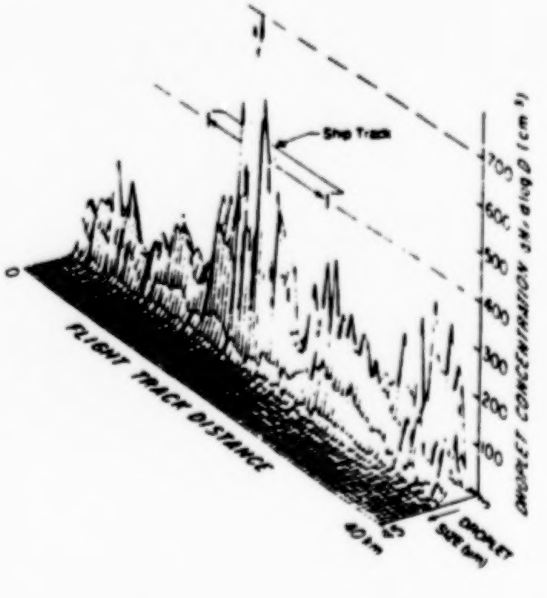

Figure 1: Cloud drop size distributions in 3-D perspective across the ship track-like feature on 10 July 1987.

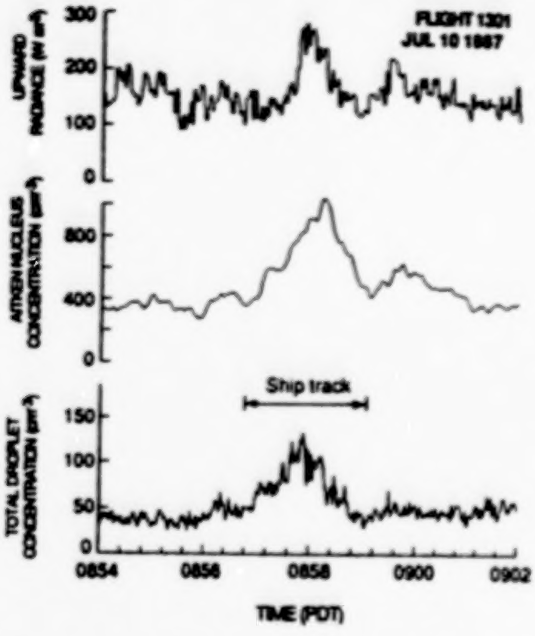

Figure. 2: Total cloud drop concentrations, Aitken nucleus concentrations and broadband upward radiance measurements across the ship track-like feature on 10 July 1987.

The first aircraft penetration of the ship track-like feature was made at 1557 UTC; when the aircraft was located about midway between the top and bottom of a stratocumulus layer about 500 m thick. The change in the drop size distribution across the feature is clearly revealed by the microphysical measurements shown in Fig. 1. The feature can also be seen in Fig. 2, where total drop concentrations are shown. The increase in liquid water content in the feature was about 30%.

Also shown in Fig. 2 are measurements of Aitken nucleus concentrations, which show a sharp increase across the feature. The Aitken nucleus measurements were made within the cloud and represent mainly the cloud interstitial aerosol (Radke, 1983). However, a fraction of these nuclei may be the evaporated residues of cloud drops. Hence, while in cloud, a modest correlation is to be expected between drop and Aitken nucleus concentrations. Nevertheless, the sharp increase in Aitken nuclei in the feature must have been due to a dramatic increase in interstitial particles, particles that did not serve as CCN in the cloud. Such particles could well have been combustion products from a ship's engine.

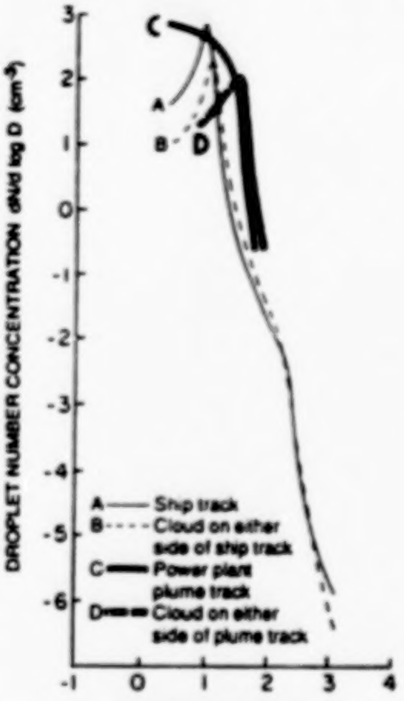

Figure 3: Cloud droplet size distributions averaged across (A) and on either side of (B) the ship track-like feature on 10 July 1987. Overprinted are corresponding data showing the effect on a cloud of the emissions from a coal-fired electric power plant (from Hobbs et al., 1980).

Coincident with the feature was an average increase of ~ 16% in upward radiance detected by the Eppley broad-band radiometer aboard the aircraft (Fig. 2). Coakley et al. (1988) show that the change in upward radiance, ΔR, is related to a change in cloud drop concentration ΔN by:

$$\Delta R \simeq \frac{1}{12} \frac{\Delta N}{N} \tag{1}$$

Substituting the value of $\frac{\Delta N}{N}$ $(= \frac{100}{50})$ from our measurements into (1) yields $\Delta R \simeq 17\%$.

3. DISCUSSION

Is it feasible that the modifications to the cloud structure described above could have been produced by emissions from a ship? In Fig. 3 we show the drop size distributions measured in and on either side of the feature. Also shown in Fig. 3 for comparison, are measurements of the effect on the cloud drop size distribution of the emissions from a 1000 MW coal-fired electric power plant on a cloud 13 km downwind of the plant (data from Hobbs et al., 1980). It can be seen that the two effects are similar. Hobbs et al. calculated that the flux of CCN active at 0.2% supersaturation from the coal power plant, including gas-to-particle conversion in the plume, was ~ 10^{16} - 10^{17} s^{-1}. This is a large source of CCN, comparable to the emissions from a large urban area or industrial complex (Radke and Hobbs, 1976).

Assuming a ship speed of 10 m s^{-1}, and using the measurements of 16 km and ~ 500 m for the width and depth, respectively, of the feature, and an increase in droplet concentration in the feature of 100 cm^{-3}, we calculate that in order for a ship to produce the observed changes in drop concentrations it would have had to produce ~ 10^{16} CCN s^{-1}. This requires the ship to be a very large (perhaps unreasonably large) source of CCN. However, in addition to fuel combustion, a ship can cause CCN to be lofted into the atmosphere by generating sea-salt particles through cavitation, splashing and bubble bursting. Particle production by these processes can produce substantial numbers of particles in the 0.1 - 1 µm size range (Radke, 1977). Since these particles serve as very efficient CCN, they could augment the combustion products from a ship and thereby play a role in the formation of ship tracks. Also, the dynamic effects suggested by the increase in liquid water content in the feature would increase the supersaturation in the cloud and thereby activate additional CCN. A ship might also loft additional water vapor through emissions and/or stirring of the boundary layer.

Despite these various means by which ships might modify clouds, we have to conclude that ship tracks are a surprising phenomenon that is not yet fully explained.

Acknowledgments. This work was supported by National Science Foundation Grant ATM-86153[illegible]4.

4. REFERENCES

CHARLSON, R. J.; LOVELOCK, J. E.; ANDREAE, M. O.; WARREN, S. G.: Oceanic phytoplankton, atmospheric sulfur, cloud albedo and climate. *Nature*, 326 (1987), 655-661.

COAKLEY, J. A.; BERNSTEIN, R. L.; DURKEE, P. A.: Effect of ship-track effluents on cloud reflectivity. *Science*, 237 (1987), 1020-1022.

COAKLEY, J. A.; BERNSTEIN, R. L.; DURKEE, P. A.: Effect of ship-stack effluents on the radiative properties of marine stratocumulus: Implications for man's impact on climate. In *Aerosols and Climate* (Eds. P. V. Hobbs and M. P. McCormick). Hampton, VA: A. Deepak Publishing. 1988.

CONOVER, J. H.: Anomalous cloud lines. *J. Atmos. Sci.*, 23 (1966), 778-785.

HOBBS, P. V.; STITH, J. L.; RADKE, L. F.: Cloud active nuclei from coal-fired electric power plants and their interactions with clouds. *J. Appl. Meteor.*, 19 (1980), 439-451.

RADKE, L. F.; HOBBS, P. V.: Cloud condensation nuclei on the Atlantic seaboard of the United States. *Science*, 193 (1976), 999-1002.

RADKE, L. F.: Marine aerosol: simultaneous size distributions of the total aerosol and the sea-salt fraction from 0.1 to 10 µm diameter. In *Atmospheric Aerosols and Nuclei* (Eds. A. F. Roddy and T. C. O'Conner). Galway, Ireland: Galway University Press. 1977.

RADKE, L. F.: Preliminary measurements of the size distribution of cloud interstitial aerosol. In *Precipitation Scavenging, Dry Deposition and Resuspension* (Eds. H. R. Pruppacher, R. G. Semonin and W. G. N. Slinn). New York: Elsevier. 1983.

TWOMEY, S. A.; PIERGRASS, M.; WOLFE, T. L.: An assessment of the impact of pollution on global cloud albedo. *Tellus*, 36B (1984), 356-366.

TWOMEY, S. A.; WARNER, J.: Comparisons of measurements of cloud droplets and cloud nuclei. *J. Atmos. Sci.*, 24 (1967), 702-703.

ESTIMATED ACCURACY OF GROUND-BASED LIQUID WATER MEASUREMENTS DURING FIRE

J. B. Snider
NOAA/ERL/WPL
325 Broadway
Boulder, CO 80303

Remote measurements of path-integrated liquid water and precipitable water vapor were made continuously during the Marine Stratocumulus Intensive Field Observations (IFO) from 1 - 19 July 1987. Observations were made with a three-channel (20.6, 31.65 and 90.0 GHz) microwave radiometer whose antenna was directed toward the zenith. As a result, the radiometer provided a continuous record of the total vertical moisture substance, i. e. both liquid and vapor, passing overhead. Fig. 1a shows hourly averages of the vapor and liquid amounts passing over the radiometer during the three week experiment. As expected, amounts of vertically-integrated liquid water contained in the marine stratocumulus were relatively small but highly variable (see table I). An example of the typical variation observed during a day's time is shown in figure 1b.

Since one goal of the FIRE project is to improve our understanding of the relationships between cloud microphysics and cloud reflectivity, it is important that the accuracy of remote liquid measurements by microwave radiometry be thoroughly understood. The question is particularly relevant since the uncertainty in the absolute value of the radiometric liquid measurement is greatest at low liquid water contents (<0.1 mm). However, it should be stressed that although uncertainty exists in the absolute value of liquid, it is well known that the observed radiometric signal is proportional to the amount of liquid in the antenna beam. As a result, changes in amounts of liquid are known to greater accuracy than the absolute value, which may contain a bias. In this paper, an assessment of the liquid measurement accuracy attained at San Nicolas Island (SNI) is presented.

The vapor and liquid water data shown in Fig. 1 were computed from the radiometric brightness temperatures using statistical retrieval algorithms (Hogg et al.,1983). The regression coefficients in the algorithms are customarily derived from _a priori_ radiosonde data for the area where the measurements are performed. However, for the data reported here, the retrieval coefficients were derived from the 69 soundings made by Colorado State University during the SNI observations. Sources of error in the vapor and liquid measurements include cross-talk in the retrieval algorithm (not a factor at low liquid contents), uncertainties in the brightness temperature measurement, and uncertainties in the vapor and liquid attenuation coefficients. The relative importance of these errors is discussed. For the retrieval of path-integrated liquid water, the greatest uncertainty is caused by the temperature dependence of the absorption at microwave frequencies. As a result, the accuracy of statistical retrieval of liquid depends to large measure upon how representative the _a priori_ radiosonde data are of the conditions prevailing during the measurements.

In an attempt to clarify this question, the microwave radiometer measurements at SNI were supplemented by an infrared (IR) radiometer modified for measurement of cloud-base temperature. Thus, the IR system provides the means to incorporate continuous measurements of the liquid temperature into the retrieval process. The method involves separation of the contributions to the total absorption due to water vapor and liquid water through an empirical relationship between absorption by vapor and the integrated water vapor obtained at SNI during clear weather. The excess attenuation caused by the liquid water is converted to the amount of path-integrated liquid using recent formulations for dielectric constant (Liebe, 1988) at the liquid temperature indicated by the IR radiometer. Table II presents calculations of amounts of liquid water calculated by (1) statistical inversion, and (2) taking into account the temperature of the liquid. Although comparative liquid amounts do not differ greatly, values obtained using the liquid temperature are about 5 percent higher. In the remainder of this paper, the trend for the entire data set is examined.

Acknowledgement:

Wave Propagation Laboratory participation in the FIRE experiment at San Nicolas Island was partially supported by the Office of Naval Research and Colorado State University.

References:

Hogg, D. C., F. O Guiraud, J. B. Snider, M. T. Decker, and E. R. Westwater, 1983: A steerable dual-channel microwave radiometer for measurement of water vapor and liquid in the troposphere. J. Climate Appl. Meteor., 22, 789-806.

Liebe, Hans J., 1988: private communication.

Table I - Statistical Summary of Precipitable Water Vapor and Vertical Integrated Liquid Water Recorded at San Nicolas Island, 1-19 July 1987

Quantity	Mean	Std. Dev.	Coeff. of Var.
Water Vapor	1.903 cm	0.538 cm	28.84 %
Liquid Water	0.077 mm	0.108 mm	114.30 %

Table II Comparison of Integrated Liquid Water Calculated by Statistical Inversion and by Taking Liquid Temperature into Account

Date	Time(UTC)	Integrated Liquid (mm) Stat. Inversion	Temp. Dependence
870703	0400	0.051	0.060
870709	1000	0.319	0.320
870714	1800	0.201	0.215
870715	1700	0.217	0.231
870715	2200	0.060	0.068
870717	1200	0.487	0.490

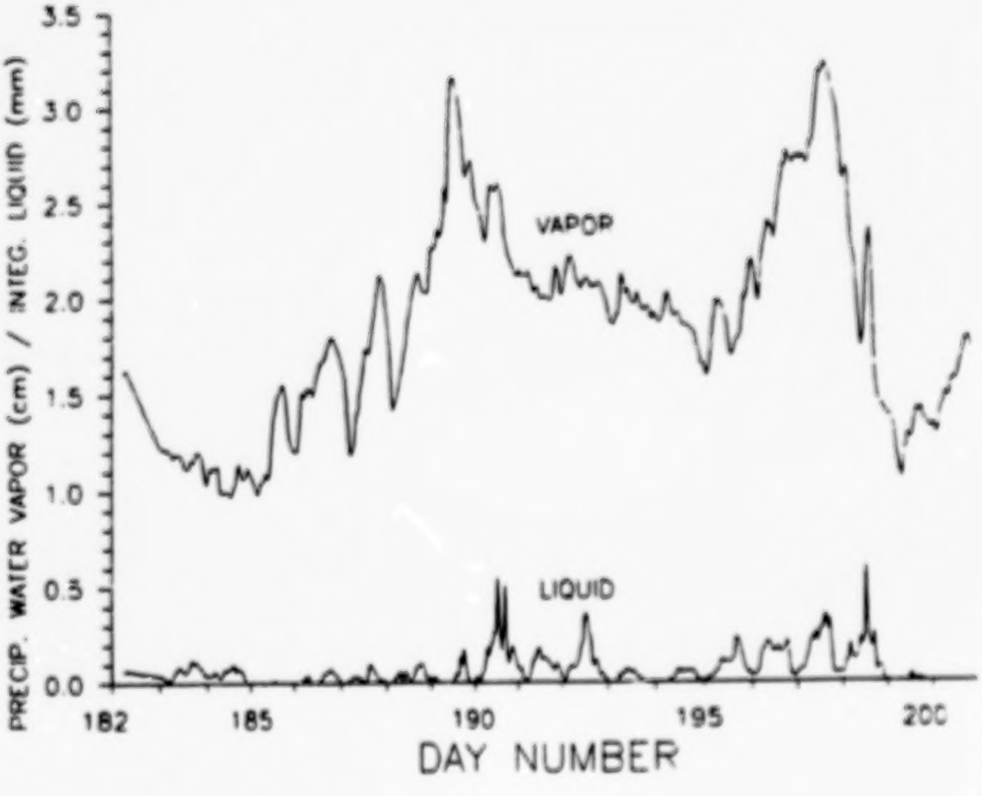

Figure 1a. Hourly averages of precipitable water vapor and vertical integrated liquid water measured at San Nicolas Island, 1-19 July 1987.

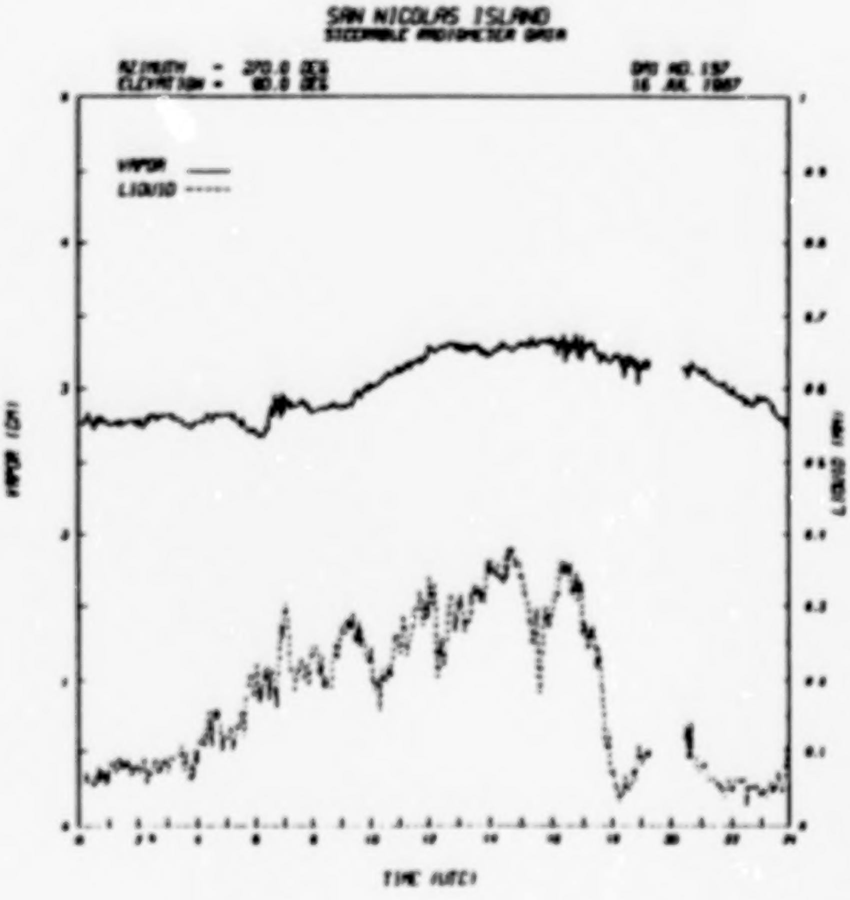

Figure 1b. Variation of precipitable water vapor and liquid water for 16 July 1987. Data values are one minute averages.

NRL TETHERED BALLOON MEASUREMENTS AT SAN NICOLAS ISLAND DURING FIRE IFO 1987

Hermann Gerber(1), Stuart Gathman(1), Jeffrey James(1)
Mike Smith(2), Ian Consterdine(2), Scott Brandeki(3)

1. Introduction

This presentation gives an overview of the tethered balloon measurements made during the FIRE marine stratocumulus IFO at San Nicolas Island in 1987. The instrumentation utilized on the balloon flights, the 17 flights over a 10 day period, the state of the data analysis, and some preliminary results are described.

A goal of the measurements with the NRL balloon was to give a unique and greatly improved look at the microphysics of the clear and cloud-topped boundary layer. For this goal, collocated measurements were made of turbulence, aerosol, cloud particles, and meteorology. Two new instruments which were expected to make significant contributions to this effort were the saturation hygrometer (Gerber, 1980), capable of measuring 95% < RH < 105% (with an accuracy of 0.05% near 100%), and used for the first time in clouds; and the forward scatter meter (Gerber, 1987) which gives in situ LWC measurements at more than 10 Hz.

Due to technical problems the tethered balloon was not functional until 15 July, near the end of the IFO period. This permits only several days of intercomparisons with the measurements collected by other FIRE investigators at SNI (Davidson, Pt. Sur; Hanson, Electra; Fairall, wind profiler and photometers; Snider, microwave radiometer). Balloon measurements were made for an additional week after the other FIRE investigators had left. Several flights were made upwind of SNI by the NOSC aircraft during that week.

The meteorology during the additional week following 19 July was characterized by several episodes of fractional Sc cloud cover, which were mostly missing earlier in the IFO period. Two such episodes occurred on the morning flight of 23 July when the cloud cover was rapidly decreasing, and on the morning flight of 24 July when the opposite trend occurred. A study of the relationship between turbulence and microphysics for these two fractional-cloudy cases would address a goal of FIRE: to understand the factors which cause the formation and evolution of fractional Sc cloud cover.

(1) Naval Research Laboratory, Washington, DC 20375-5000
(2) University of Manchester, Manchester M60 1QD, England
(3) University of Denver, Denver, CO 80208

2. Experimental Aspects

The instrumentation which was flown on the tethered balloon is listed in Fig. 1, and the method by which it was attached to the balloon is shown. Most instrumentation was mounted on a pallet hung 35m below the balloon. The motion of the pallet was not constrained, except for being pointed into the wind with a large wind vane. Two flux gate magnetometers, two inclinometers, and altimeter form a positioning system with which an orthogonal transformation of the velocity vector measured by the bivane can be made to correct for the motion of the pallet. The motion of the pallet during flight was well behaved. With a high degree of persistence, the intermittent motion of the pallet was perpendicular to the direction of the wind with a period of oscillation of 11.8 s.

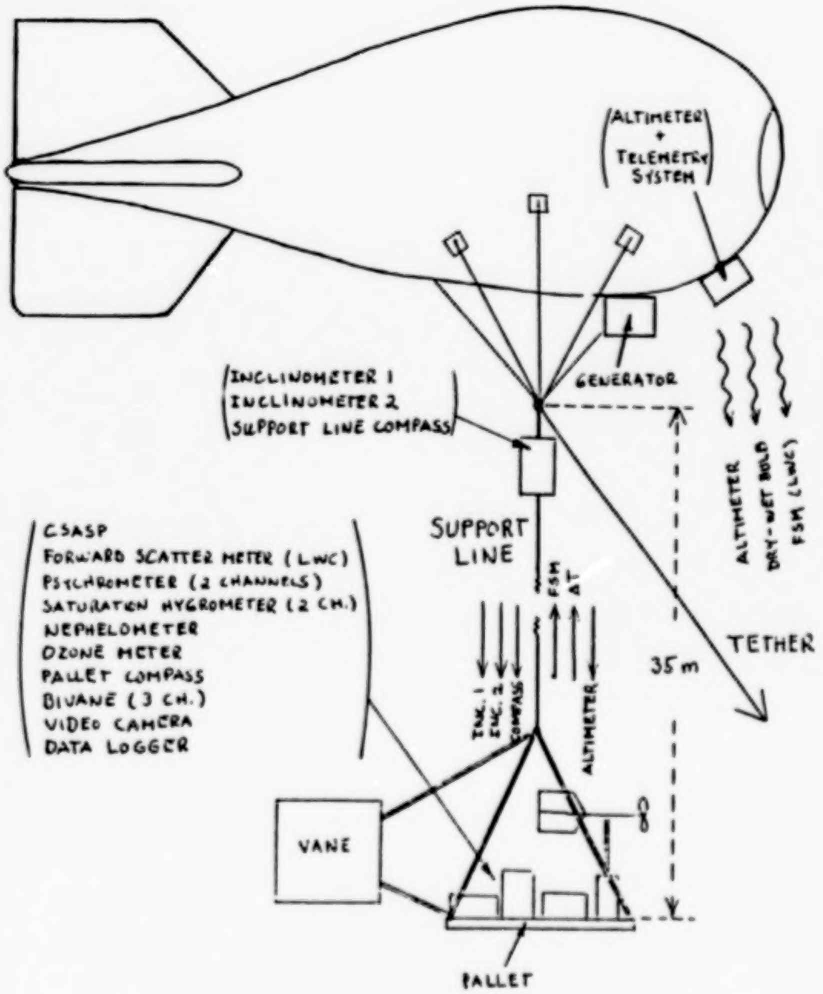
ALTIMETER + TELEMETRY SYSTEM
INCLINOMETER 1
INCLINOMETER 2
SUPPORT LINE COMPASS
GENERATOR
ALTIMETER
DRY-WET BULB
FSM (LWC)
CSASP
FORWARD SCATTER METER (LWC)
PSYCHROMETER (2 CHANNELS)
SATURATION HYGROMETER (2 CH.)
NEPHELOMETER
OZONE METER
PALLET COMPASS
BIVANE (3 CH.)
VIDEO CAMERA
DATA LOGGER
SUPPORT LINE
FSM
AT
INC. 1
INC. 2
COMPASS
ALTIMETER
TETHER
35 m
VANE
PALLET

Fig. 1 - List and mounting locations of instrumentation carried on the tethered balloon. Arrows indicate data flow.

Data was collected at either 5 Hz or 1 Hz. Several data channels were in addition telemetered to the surface where they were logged at 0.3 Hz.

The typical flight of the balloon lasted 3 hrs., with an initial ascent of 0.5 m/s to the free atmosphere above the boundary layer, and with a stepwise descent consisting of about 25 min. holds at several levels to obtain turbulence statistics. The 17 flights are summarized in Table 1.

Table 1. Balloon Flight Date, Time, Duration, and Local Meteorology.

No.	Date (July)	Duration of Flight	Cloud Cover	Wind Dir.	Sfc. Wind (m/s)	Inversion Ht. (m)
1	15	1511-1707	10/10	NW	7	640
2	16	0900-1140	10/10	W	2	760
3	16	1737-1930	10/10	W	2	-
4	17	1100-1415	10/10-5/10 (d)	NW	9	1070
5	18	0735-1115	1/10	WNW	2	670
6	18	1407-1552	0/10	NW	5-7	400
7	19	0522-0706	<1/10	NW	5-7	335
8	19	1332-15559	<<1/10	NW	2-4	460
9	20	0817-1013	6/10-1/10 (d)	WNW	5-7	640
10	20	1803-1945	0/10	WNW	5	-
11	21	1305-1535	0/10	WNW	<2	-
12	22	1744-1946	0/10	NW	7	380
13	23	0952-1225	8/10-1/10 (d)	NW	9	640
14	23	1518-1648	0/10	NW	9-13	-
15	24	0756-1101	6/10-10/10 (i)	NW	7-9 (d)	550
16	24	1723-1945	1/10-4/10	NW	9	360
17	25	0815-1026	1/10-5/10	NW	7	400

(d = decreasing, i = increasing)

3. Data Reduction and Quality

This large raw data set has been reduced to a stage where analysis of any variables for any of the flights is practical. Algorithms have been developed for use during analysis, and the variables have been stored in separate data files for easy access. The data files are stored in compressed form on 1.2 Meg floppy disks which can be ready by IBM PCs of compatibles; copies of the disks are available to FIRE investigators.

Use of the data requires careful attention to its quality, because not all instruments operated properly all the time: No useful data resulted from the ozone meter. For condensing conditions RF interference caused the data channels which are both telemetered and logged on the pallet to be noisy on the pallet logger. The forward scatter meter was over ranging on the first several flights. During flight 4 where a great deal of drizzle occurred the saturation hygrometer failed, and on some other flights drift in the sensor was noticed; however, useful data was collected. Only a limited record was obtained with the video camera, the best was for flight 13. The CSASP particle spectrometer and other sensors functioned properly throughout. On flight 2 all data except that telemetered was inadvertently lost.

4. Results

The data analysis is just commencing so that very few results are presently available. Examples of the measurements are shown in Figs. 2 and 3 which give respectively the 5 Hz data for LWC from the forward scatter meter, and the RH from the saturation hygrometer. Both profiles are for the ascent of flight 13 when a fractional cloud cover of Sc was in the process of dissipating. Figure 2 shows the cloud layer extended from 500m to 650m, and that the LWC profile was very different from the adiabatic LWC profile. Figure 3, as well as the other data, shows that RH within the cloudy air ranges from about 99.5% to 100.2%, and that deep layers of subsiding air exist in the clouds where RH < 100%. The large sub- and supersaturated conditions suggested by Curry (1986) for Arctic stratus were not seen in the marine Sc. In Figure 3 the supersaturation peak at the top of the main cloud at 625m is consistent with radiation-forcing calculations of Davies (1985); although, the cause of the peak due to a strong updraft cannot be ruled out until the w field is analyzed.

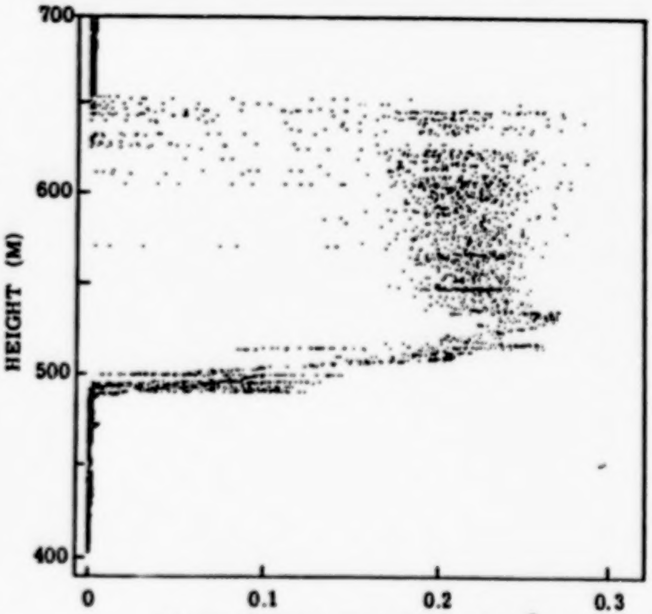

Fig. 2 - Liquid water content on the ascent of flight 13 during Sc dissipation.

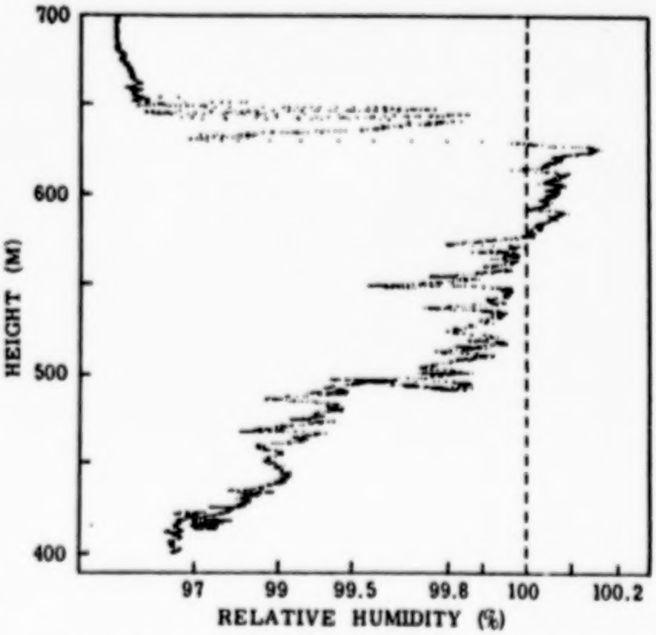

Fig. 3 - Relative humidity profile measured with the saturation hygrometer on the ascent of flight 13.

5. Conclusions

This data set, while unfortunately only partially simultaneous with the bulk of the FIRE stratocumulus observations, is unique and worthwhile in its own right. For the first time accurate RH measurements near 100% have been made in-cloud; although, the use of the saturation hygrometer reflected a learning experience which will result in substantially better performance the next time. These measurements were made in conjunction with other microphysical measurements such as aerosol and cloud droplet spectra, and perhaps most important of all, they were all collocated with bivane turbulence measurements thus permitting flux calculations. Thus the analysis of this data set which consisted of about 50% stratocumulus cases including increasing and decreasing partial cloud cover, should lead to new insights on the physical mechanisms which drive the boundary-layer/cloud/turbulence system.

Addressing the entrainment mechanism at the top of the clouds should be especially amenable with this data set. In addition to the listed authors, investigators associated with Fire and located at the following institutions are looking at portions of this data: McGill University, NASA Goddard, U. of Washington, Colorado State University, and CIRES.

References

Curry, J.A., 1986: Interaction among turbulence, radiation and microphysics in Arctic stratus clouds. J. Atmos. Sci., 43, 90-106.

Gerber, H., 1980: A saturation hygrometer for the measurement of relative humidity betwen 95% and 105%. J. Appl. Meteoro., 19, 1196-1208.

Gerber, H., 1987: Forward-scatter meter for estimating 10.6-um aerosol extinction. Applied Optics, 26, 539-544.

Davies, R., 1985: Response of cloud supersaturation to radiative forcing. J. Atmos. Sci., 42, 2820-2825.

FIRE SCIENCE TEAM MEETING
VAIL, COLORADO
JULY 11-15, 1988

MARINE STRATOCUMULUS

RADIATIVE PROPERTIES - Michael D. King Thursday, July 14, 1988

PAGE

Estimating Integrated Cloud Liquid Water from Extended Time Observations of Solar Irradiance 307
Fairall, C. W.; Raja El-Salem Rabadi, and J. Snider

A Study of Marine Stratocumulus using Lidar and other FIRE Aircraft Observations 313
Jensen, Jorgen B.; and Donald H. Lenschow

Cloud Absorption Properties as Derived from Airborne Measurements of Scattered Radiation within Clouds 319
King, Michael D.; Teruyuki Nakajima, Lawrence F. Radke, and Peter V. Hobbs

Cloud Optical Parameters as Derived from the Multispectral Cloud Radiometer 327
Nakajima, Teruyuki; and Michael D. King

Estimating Integrated Cloud Liquid Water from Extended Time Observations of Solar Irradiance

C.W. Fairall and Raja El-Salem Rabadi
Department of Meteorology
Pennsylvania State University
University Park, PA 16802

and

J. Snider
NOAA/ERL/WPL
325 Broadway
Boulder, CO 80303

INTRODUCTION

Extended time observations (ETO) were made at San Nicolas Island (SNI) from March to October, 1987. A small ground station was installed at the NRL trailer (Site B). Hourly averages of air temperature, relative humidity, wind speed and direction, solar irradiance, and downward longwave irradiance were recorded. The radiation sensors were standard Eppley pyranometers (shortwave) and pyrgeometers (longwave). Data records of SNI rawinsonde launches for this period have been requested from the Pacific Missile Test Center (PMTC).

This data will be processed in a variety of was to deduce properties of the stratocumulus covered marine boundary layer (MBL). From the temperature and humidity the lifting condensation level, which is an estimate of the height of the cloud bottom, can be computed. Combinations of shortwave and longwave irradiance statistics can be used to estimate fractional cloud cover parameters.

This paper describes an analysis technique used to estimate the integrated liquid water content (W) from the measured solar irradiance. The cloud transmittance is computed by dividing the irradiance measured at some time by a clear sky value obtained at the same time on a cloudless day. From the transmittance and the zenith angle, the cloud LWC is computed using the radiative transfer parameterizations of Stephens et al. (1984). The results are compared with 17 days of mm-wave (20.6 and 31.65 GHz) radiometer measurements made during the FIRE IFO in July of 1987.

CLOUD RADIATIVE TRANSFER COMPUTATIONS

Stephens (1978) has developed a simple parameterization of cloud albedo (Re), transmittance (Tr), and absorption (Ab) in terms of the cloud optical thickness (T) and the zenith angle (θ). The parameterization is based on the two-stream approximation of Coakley and Chylek (1975). A look-up table of values for single scattering albedo (w) and backscatter fraction (β) is given as a function of T and $\mu=\cos(\theta)$. The values are based on results of sophisticated 10-layer, 15-band radiative transfer computations. The revised look-up table (Stephens et al., 1984) was used for the work presented here. Non absorbing ($\lambda<0.7$ μm) and absorbing ($\lambda>0.7$ μm) wavelength regions are considered. The two-stream model is as follows:

(i) Non absorbing, $w=1$

$$Re = \beta T/\lambda/(1 + \beta T/\lambda) \qquad (1a)$$

$$Tr = 1 - Re \qquad (1b)$$

(ii) Absorbing, $\omega < 1$

$$Re = (u^2 - 1)[\exp(Tef) - \exp(-Tef)]/R \qquad (2a)$$

$$Tr = 4u/R \qquad (2b)$$

$$Ab = 1 - Re - Tr \qquad (2c)$$

where

$$u^2 = (1 - \omega + 2\beta\omega)/(1 - \omega) \qquad (3a)$$

$$Tef = SQRT[(1 - \omega)*(1 - \omega + 2\beta\omega)]T/\mu \qquad (3b)$$

$$R = (u + 1)^2 \exp(Tef) - (u - 1)^2 \exp(-Tef) \qquad (3c)$$

The optical thickness is calculated from the cloud W using a parameterization obtained from a number of measured cloud properties.

$$\log_{10}(T) = 0.2633 + 1.7095 \log_e[\log_{10}(W)], \quad \lambda < 0.7 \qquad (4a)$$

$$\log_{10}(T) = 0.3492 + 1.6518 \log_e[\log_{10}(W)], \quad \lambda > 0.7 \qquad (4b)$$

Since the Stephens parameterization was developed to apply to some 15 cloud types, we decided to compare it to a model with microphysics specific to the marine stratocumulus, which we shall refer to as the DFBS (Davidson et al., 1984) model. The DFBS model is a 15-band, delta-Eddington radiative transfer model that assumes a linear liquid water profile in the cloud with a log-radius gaussian cloud droplet distribution where the mode radius is determined from the liquid water assuming a constant number of cloud droplets (100/cc). Figure 1 shows a comparison of transmittances for the two models at three different zenith angles for a generic California stratocumulus with cloudtop at 600 m and total water (liquid plus vapor) mixing ratio of 8 g/kg. Optical thickness was varied by varying the cloud thickness from 50 m to 450 m. The comparison is very good but the Stephens parameterizations (Eqs. 4) appear to underestimate the optical thickness at low values of W, which are at the lower limit of his fit. Since marine stratocumulus often have low values of W, we used the parameterization given below for $W < 100$ g/m^2 (see Fig. 2), which is obtained from the DFBS model:

$$\log_{10}(T) = -0.35 + 0.91 \log_{10}(W) \qquad (5)$$

Using this slightly modified form of the Stephens model, a nomogram can be constructed in terms of contours of transmittance versus zenith angle and integrated liquid water path (Fig. 3).

RESULTS

Using the clear sky irradiance, the cloud transmittance was computed for each day from July 1 to July 18 for the times 1600 to 0100 GMT. Low incidence angles ($\mu < .4$) were not used because of the potential for large errors. For the same reason, transmittances greater than 0.9 were not considered. For a given value of Tr and μ, the value of W was iterated until the Stephens model gave the measured transmittance. This computed value of W is compared with the values from the NOAA radiometer (Fig. 4).

The mm-wave radiometer values of W are on average about 50% greater than the values estimated from the transmittance. The rms scatter is about 35%. The NOAA radiometer is believed to be accurate to 20%, but a 50% fractional bias is not out of the question. Some of the rms scatter is due to differences in sampling geometry, since the pyranometer has a hemispherical field of view and the radiometer has a narrow field of view. These differences in field of view are somewhat moderated by averaging for one hour. Another source of error is the use of a single clear sky irradiance for the entire 17 day period, which ignores variability in the meteorological conditions above the mixed-layer. Once these issues are sorted out, we expect to use this method to analyze the entire data base.

REFERENCES

Coakley, J.A. and P. Chylek, 1975: The two stream approximation in radiative transfer: Including the angle of the incident radiation. J. Atmos. Sci., 32, 409-418.

Davidson, K.L., C.W. Fairall, P. Jones Boyle and G.E. Schacher, 1984: Verification of an atmospheric mixed-layer model for a coastal region. J. Clim. Appl. Met., 23, 617-636.

Stephens, G.L., 1978: Radiation profiles in extended water clouds. II: Parameterization schemes. J. Atmos. Sci., 35, 2123-2132.

Stephens, G.L., S. Ackerman, and E.A Smith, 1984: A shortwave parameterization revised to improve cloud absorption. J. Atmos. Sci., 41, 687-690.

Acknowledgements . This work is supported by NASA grant NAG 1-652. Part of this work was performed while CWF was a visiting scientist at the Naval Environmental Prediction and Research Facility. The authors wish to express special thanks to Richard Dixon and Carl Otten of PMTC for aiding and abetting the installation and maintainence of the ETO system at SNI and to Dick Thompson of the Department of Meteorology, PSU, who put the system together and kept the data flowing.

Fig. 1 Comparison of transmittance versus integrated cloud LWC at zenith angles of 0, 60, and 80 degrees for the Stephens (circles) and DFBS (line) models.

Fig. 2 Optical thickness versus integrated cloud LWC for the Stephens parameterization of Eq. 4a (solid line), the DFBS calculations (circles), and Eq. 5 (dotted line).

Fig. 3 Contours of transmittance as a function of solar zenith angle and integrated cloud LWC from the modified Stephens parameterization.

Fig. 4 Integrated cloud LWC: the vertical axis is computed from solar irradiance versus W from the NOAA radiometer measurements.

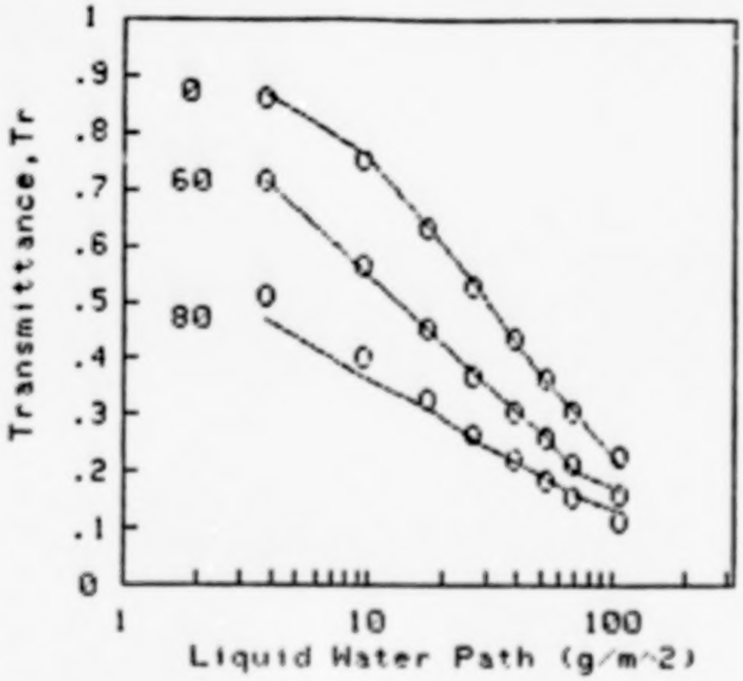

Fig. 1 Comparison of transmittance versus integrated cloud LWC at zenith angles of 0, 60, and 80 degrees for the Stephens (circles) and DFBS (line) models.

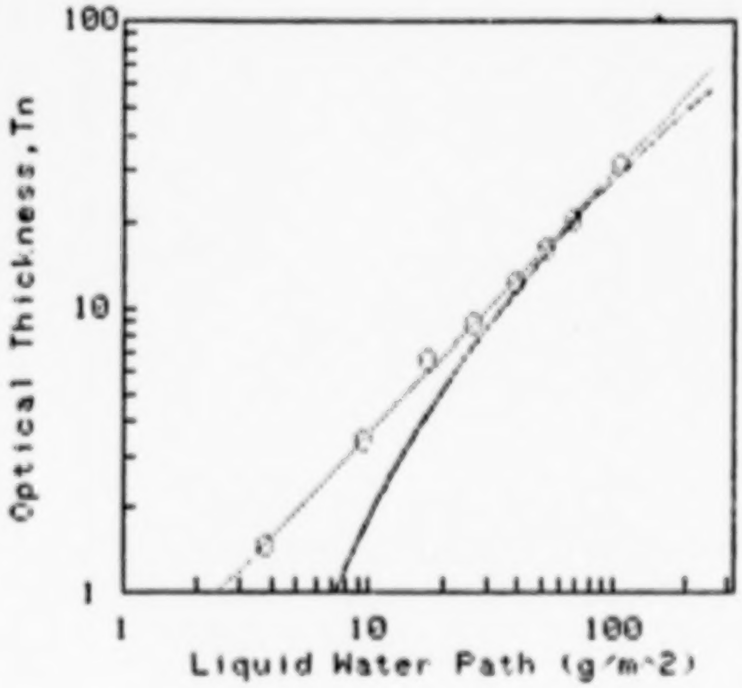

Fig. 2 Optical thickness versus integrated cloud LWC for the Stephens parameterization of Eq. 4a (solid line), the DFBS calculations (circles), anc Eq. 5 (dotted line).

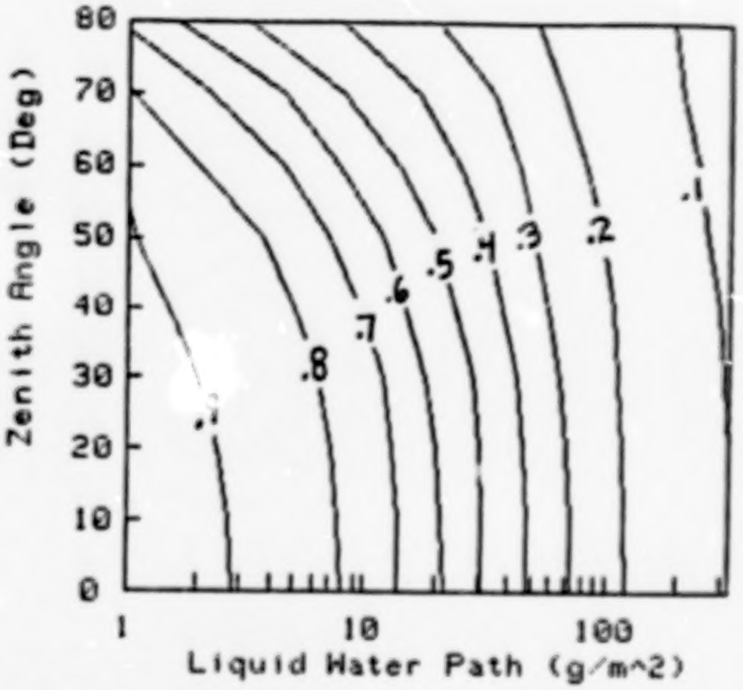

Fig. 3 Contours of transmittance as a function of solar zenith angle and integrated cloud LWC from the modified Stephens parameterization.

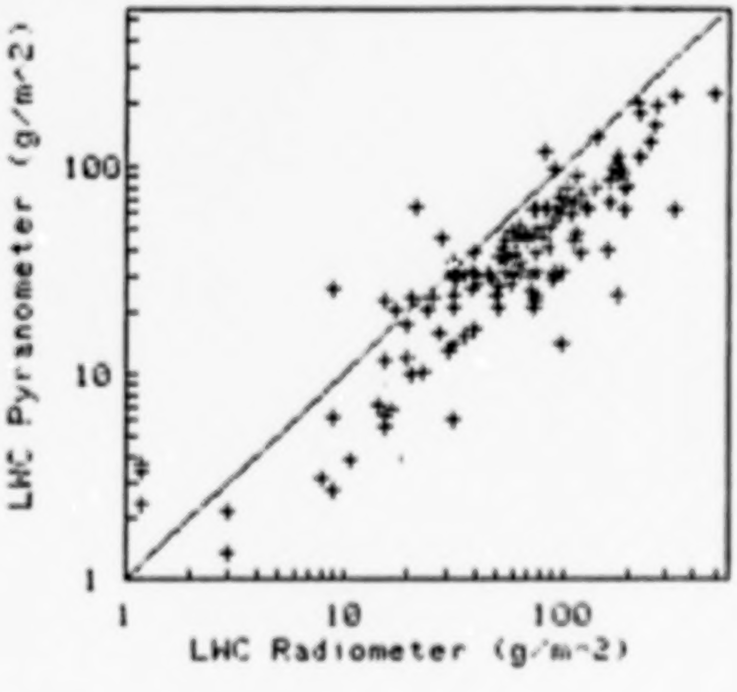

Fig. 4 Integrated cloud LWC: the vertical axis is computed from solar irradiance versus W from the NOAA radiometer measurements.

A STUDY OF MARINE STRATOCUMULUS USING LIDAR AND OTHER FIRE AIRCRAFT OBSERVATIONS

Jørgen B. Jensen and Donald H. Lenschow

National Center for Atmospheric Research [1]

Boulder, Colorado 80307

1. BACKGROUND

In order to understand the distribution and evolution of marine stratocumulus, we need to determine how variables such as radiation divergence, surface heat and moisture fluxes, wind shear, subsidence, and lapse rate control the dynamical and microphysical structure of the clouds through processes such as entrainment and mixing, and in turn, how the cloud structure affects these variables. A key to studying entrainment is to be able to resolve the structure of the cloud at and near cloud-top. Ideally, we would like to be able to resolve both the motion field as well as some tracer that allows us to distinguish well-mixed boundary-layer air from that originating in the free atmosphere and entrained into the boundary layer. At the top of the stratiform-capped boundary layer, the cloud itself can be a tracer of boundary-layer air. Entrained parcels, or regions of mixed boundary-layer and free air are clear. The NCAR Airborne Infrared Lidar (NAILS, Schwiesow, 1987) is a tool for distinguishing the interface between the clear and cloudy parcels.

Some progress has already been made in studying the characteristics of the entrainment region of marine stratocumulus. Jensen and Lenschow (1978), for example, investigated the sizes of turbulent eddies at the top of a cloud-capped mixed layer using data from an aircraft flight leg at cloud-top. They found two peaks in the vertical velocity spectrum at cloud-top—one with a wavelength of about 1.5 times the depth of the mixed layer, and the other with a wavelength of 200 to 300 m that likely was associated with entrainment and mixing near cloud-top. Mahrt and Paumier (1982) looked in more detail at the entrainment process at cloud top for the same experiment, and estimated a scale of 100 to 200 m for the eddies involved in cloud-top entrainment. These results have been confirmed in subsequent observational studies by Caughey and Kitchen (1984) for nocturnal stratocumulus over land using tethered balloon observations.

A theoretical analysis of the preferred wavelengths and frequencies of vertical velocity fluctuations in the inversion layer capping a clear-air mixed layer and the interactions of waves and turbulence at the top of the mixed layer has been carried out by Carruthers and Hunt (1985 and 1986), and related numerical simulations are reported by Carruthers and Moeng (1987). Again, these analyses suggest vertical velocity wavelengths of a few hundred meters in the vicinity of the mixed-layer top. From the standpoint that clouds offer a visible tracer of the interface between the free atmosphere and the boundary layer, the cloud-capped boundary layer has an advantage over a clear boundary layer. [We note, however, that occasionally a thin cloud-free layer has been observed just below the capping inversion (e.g. Rogers and Telford, 1986). This situation, although possibly not common, warrants further study to see if differences in cloud-top structure are also detectable with NAILS; we recall, on the basis of our inflight observations, that one or more cases of this situation exist in the FIRE data set.]

---

[1] The National Center for Atmospheric Research is funded by the National Science Foundation.

Thus far, most of the observational evidence for studies of the eddy size and structure in the vicinity of cloud top has come from direct measurements of vertical velocity, temperature and cloud droplet size distributions. Recently, however, Boers and Spinhirne (1987) have reported lidar observations of cloud top which illustrate some of the potential that this technique has to offer. They show, for example, a frequency distribution and spectrum of cloud-top height for a marine stratocumulus case, and indicate that in situ measurements in cloud were obtained concurrently on a second airplane; the in situ observations are discussed in Boers and Betts (1988).

In addition to investigations in the vicinity of cloud top, the NAILS was also pointed up at cloud base while flying below the stratocumulus. In this way, it is possible to look at cloud-base structure to see how it correlates with measurements in the lower boundary layer. A couple of interesting and important questions that can be addressed are: is the scale of cloud organization seen in cloud-base height detectable in variables measured at aircraft height? How well can the lidar detect multiple cloud layers which, as discussed by Nicholls (1984) and Hanson et al. (1988), are indicative of decoupling of the main cloud layer from the boundary layer, and if detected, can they also be related to variables measured at aircraft height? As Nicholls (1984) points out, this decoupling can make a significant difference in the subsequent evolution of the cloud cover, and therefore significantly affect the radiation budget of the cloud-capped mixed layer.

2. NAILS

The NCAR airborne infrared lidar system (NAILS) used in the 1987 FIRE experiment off the coast of California is a 10.6 μm wavelength CO_2 lidar system constructed by Ron Schwiesow and co-workers at NCAR/RAF. The lidar is particularly well suited for detailed observations of cloud shape; i.e. height of cloud top (when flying above cloud and looking down) and cloud base (when flying below cloud and looking up) along the flight path. Schwiesow *et al.* (1988) have presented some examples of NAILS lidar data from FIRE.

A detailed discussion of the lidar design characteristics is given by Schwiesow (1987), and only a brief summary is listed here (Table 1). The lidar height resolution of ± 3 m allows for the distance between the aircraft and cloud edge to be determined with this accuracy; however, the duration of the emitted pulse is approximately 3 μs, which corresponds to a 500 m pulse length. Therefore, variations in backscatter intensities within the clouds can normally not be resolved. Hence the main parameter obtainable from the lidar is distance to cloud; in some cases we may also be able to determine the cloud depth.

During FIRE the lidar was operational on 7 of the 10 Electra flights, and data were taken when the distance between cloud and aircraft (minimum range) was at least 500 m. The lidar was usually operated at 8 Hz, which at a flight speed of 100 m s^{-1} translates into a horizontal resolution of about 12 m.

TABLE 1

NAILS Lidar Characteristics (modified from Schwiesow, 1987)

Operating wavelength	10.6 μm
Beam width	16 $\times 10^{-5}$ radians
Lidar return sampling rate	100 MHz
Height resolution	± 3 m
Track resolution (variable*)	$\sim$ 10 m
Design backscatter coefficient	5×10^{-9} (m^{-1} sr^{-1})
Maximum range from aerosols	2 km
Maximum range from cloud	5 km
Minimum range (dead zone)	500 m
Signal channels (polarization)	2

*Depending upon pulse frequency and flight speed.

The backscatter as function of time (equivalent to distance) for each laser pulse is stored in digital form on magnetic tape. Currently, three independent variables are available to the investigators on the FIRE Electra data tapes: lidar range to cloud, strength of return (relative power) and pulse width of return, which is related to penetration depth.

The values of these variables should currently be interpreted with some caution. In the future we hope (i) to test the detection algorithm in order to insure that the actual cloud edge is detected, (ii) to determine under what circumstances the lidar is able to detect the heights of both cloud base and cloud top, and (iii) to correct the data for pitch and roll errors.

3. EXAMPLES OF NAILS DATA

The following example illustrates only one of many ways the lidar can be used in conjunction with other sensors in order to study stratocumulus clouds. Schwiesow *et al.* (1988) present time series of lidar-derived cloud top height and radiation temperature at cloud top from the Barnes PRT-5 sensor. Fig. 1 shows the cloud top height, z_c, measured by the Electra from 211100 to 211400 PDT on June 30, 1987. The lidar shows numerous variations in the cloud top height on scales of hundreds of meters. In the following we will examine the association between the variation of cloud top height and cloud top temperature.

In Fig. 1 we have selected a segment of the cloud top for calculating a reference value of entropy. If we assume a moist adiabatic temperature gradient in the cloud, then we can calculate the temperature of the cloud surface based on the lidar measured cloud top height. This lidar-derived cloud top temperature, T_l, can then be compared with the PRT-5 temperature, T_r; see Fig 1, center panel. Differences between these two, $\Delta T = T_r - T_l$, are shown in the bottom panel of Fig. 1 and they can be due to several effects:

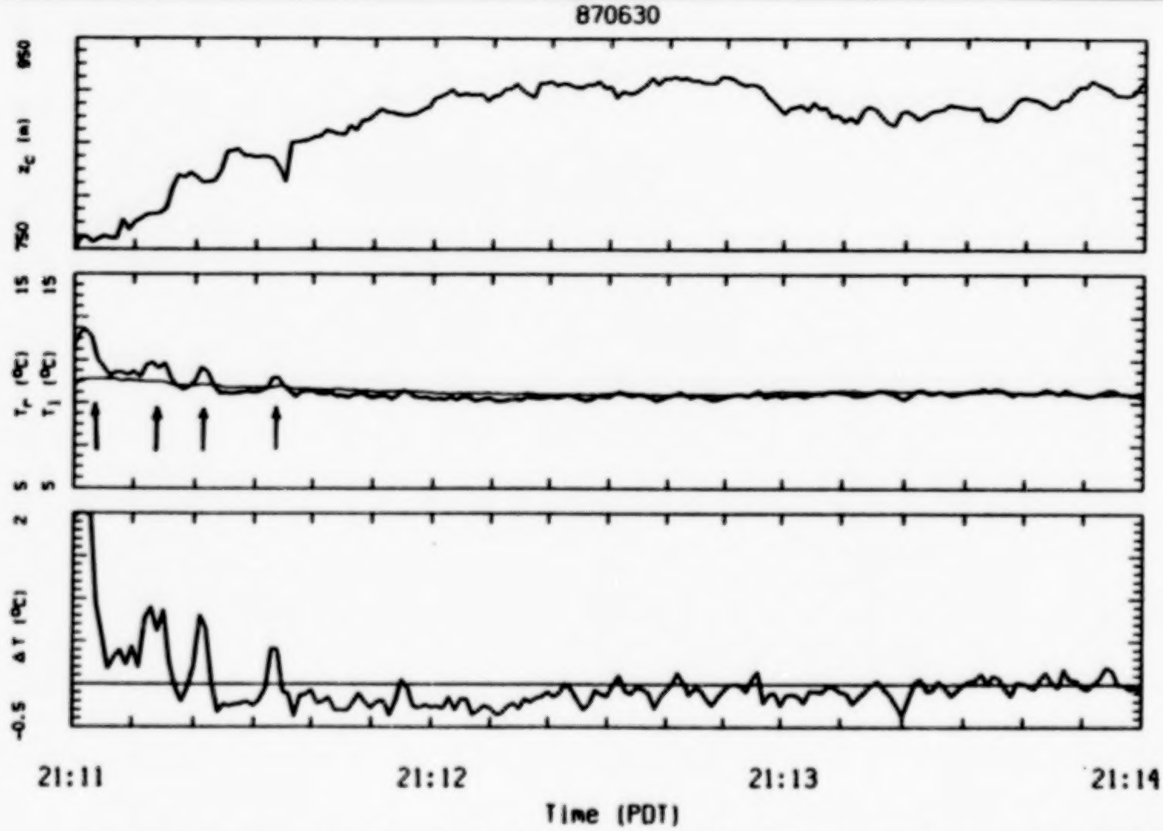

Fig. 1. Top panel: Lidar-derived cloud top height (z_c) averaged to 1 s^{-1}. Middle panel: PRT-5 radiation temperature (T_r, bold line) and lidar-derived cloud top temperature (T_l, thin line). See text for explanation of arrows. Bottom panel: Temperature difference, $\Delta T = T_r - T_l$. The thin line shows $\Delta T = 0$. The distance between tick marks on the abcissa is ≈ 1 km.

(1) Radiative cooling and the subsequent formation of cold pools may lead to a pattern in which local depressions in the cloud top surface have predominantly negative ΔT.

(2) Entrainment and the ensuing evaporative cooling may likewise lead to local depressions in the cloud top surface with negative ΔT.

(3) It is not clear to what extent the lidar-derived cloud edge coincides with the region which dominated the PRT-5 signal. If the cloud is very thin, then the PRT-5 temperature may include contributions from a substantial cloud depth, whereas the lidar may detect the actual cloud edge. This would lead to regions of positive ΔT.

(4) The approximation of moist adiabatic temperature gradient may not be valid for the cloud.

An examination of Fig. 1 does not result in obvious correlations between z_c and ΔT; hence without further investigation we can not conclude that "domes" contain warm air, whereas depressions between them contain cooled air. Examples of "thin" cloud appear likely in at least four segments, as indicated by the arrows in Fig. 1.

REFERENCES

Boers, R. and A.K. Betts, 1988: Saturation point structure of marine stratocumulus clouds. Preprint Volume, Seventh Conference on Ocean-Atmosphere Interactions of the AMS, 1–5 February 1988, Anaheim, CA. American Meteorological Society, Boston, MA, 166–169.

Boers, R. and J.D. Spinhirne, 1987: High altitude lidar observations of marine stratocumulus clouds. Topical Meeting on Laser and Optical Remote Sensing: Instrumentation and Techniques Technical Digest Series, 1987 Volume 18, (Optical Society of America, Washington, D.C.) 84–87.

Carruthers, D.J. and J.C.R. Hunt, 1985: Turbulence and wave motions near an interface between a turbulent region and a stably strafified layer. *Turbulence and Diffusion in Stable Environments*, edited by J.C.R. Hunt, Clarendon Press, Oxford, 319 pp.

Carruthers, D.J. and J.C.R. Hunt, 1986: Velocity fluctuations near an interface between a turbulent region and a stably stratified layer. *J. Fluid Mech.*, 165, 475–501.

Carruthers, D.J. and C.-H. Moeng, 1987: Waves in the overlying inversion of the convective boundary layer. *J. Atmos. Sci.*, 44, 1801–1808.

Caughey, S.J. and M. Kitchen, 1984: Nocturnal stratocumulus. *Quart. J. Roy. Met. Soc.*, **110**, 13-34.

Hanson, H.P., G.K. Greenhut and V.E. Derr, 1988: An investigation of the climatology and mechanics of the California stratocumulus cloud deck. Submitted to *Bull. Amer. Meteor. Soc.*

Jensen, N.O. and D.H. Lenschow, 1978: An observational investigation of penetrative convection. *J. Atmos. Sci.*, 35, 1924–1933.

Lenschow, D.H., I.R. Paluch, A.R. Bandy, R. Pearson, Jr., S.R. Kawa, C.J. Weaver, B.J. Huebert, J.G. Kay, D.C. Thornton and A.R. Driedger III: Dynamics and Chemistry of Marine Stratocumulus (DYCOMS) Experiment. Submitted to *Bull. Amer. Meteor. Soc.*

Mahrt, L and J. Paumier, 1982: Cloud-top entrainment instability observed in AMTEX. *J. Atmos. Sci.*, 39, 622–634.

Nicholls, S., 1984: The dynamics of stratocumulus: Aircraft observations and comparisons with a mixed layer model. *Quart. J. Roy. Meteor. Soc.*, 110, 783–820.

Rogers, D. and J. Telford, 1986: Metastable stratus tops. *Quart. J. Roy. Met. Soc.*, **112**, 481-500.

Schwiesow, R.L., 1987: *The NCAR Airborne Infrared Lidar System (NAILS) Design and Operation*, NCAR Technical Note NCAR/TN-291+1A, Available from NCAR, P.O. Box 3000, Boulder CO, 80307, 38 + xiii pp.

Schwiesow, R.L., V.M. Glover and D.H. Lenschow, 1988: Measurements with airborne lidar: an example from FIRE and potential applications to turbulence and diffusion. Preprint Volume, Eighth Symposium on Turbulence and Diffusion of the American Meteorological Society, 26–29 April 1988, San Diego, CA.

Cloud Absorption Properties as Derived from Airborne Measurements of Scattered Radiation within Clouds

Michael D. King and Teruyuki Nakajima[†]

Laboratory for Atmospheres, Goddard Space Flight Center, NASA,
Greenbelt, MD 20771, USA

Lawrence F. Radke and Peter V. Hobbs

Department of Atmospheric Sciences, University of Washington,
Seattle, WA 98195, USA

1. Introduction

A multiwavelength scanning radiometer has been developed for measuring the angular distribution of scattered radiation deep within a cloud layer (King *et al.*, 1986). The purpose of this instrument is to provide measurements from which the similarity parameter of clouds can be derived as a function of wavelength, where the similarity parameter is a function of cloud single scattering albedo and asymmetry factor. The cloud absorption radiometer flew on the University of Washington's Convair–131A aircraft during the marine stratocumulus intensive field observation component of the First ISCCP Regional Experiment (FIRE), conducted off the coast of San Diego, California during July 1987. The instrument was flown as one of a group of instruments that included upward and downward looking pyranometers, cloud microphysics probes for measuring the cloud particle size distribution and liquid water content, and an air batch sampler for measuring the cloud interstitial aerosol size distribution (Radke, 1983).

The cloud absorption radiometer has been built, flight tested and flown on the University of Washington C-131A aircraft during 8 flights of the marine stratocumulus intensive field observation phase of FIRE. We have thus far concentrated our attention on aspects of three of these flights, two of which were flown in coordination with the UK Meteorological Research Flight C-130 aircraft and one in coordination with the NASA ER-2 aircraft. The C-130 contained a 16 channel, fixed-angle, multispectral cloud radiometer, with 8 channels in the visible and near-infrared region and 8 channels in the thermal infrared (Foot, 1988), while the ER-2 contained a 7 channel scanning radiometer for the purpose of deriving the cloud optical thickness, effective particle radius, and cloud top altitude (Curran *et al.*, 1981; King, 1987).

[†] Permanent affiliation: Upper Atmosphere and Space Research Laboratory, Faculty of Science, Tohoku University, Sendai 980, Japan.

In this paper, we briefly review the diffusion domain method for deriving the cloud similarity parameter and present preliminary analyses of the results thus far obtained. Our presentation will concentrate on the following points:

(1) Intercomparison of calibrated reflected intensities between the cloud absorption radiometer and the UK multispectral cloud radiometer,

(2) Quality control tests required to select those portions of an aircraft flight for which measurements are obtained within the diffusion domain,

(3) Case studies of the spectral similarity parameter of marine stratocumulus clouds,

(4) Comparisons of the experimentally-derived similarity parameter spectrum with that expected theoretically from the cloud droplet size distribution obtained from *in situ* observations.

2. Calibration

The Goddard Space Flight Center multispectral cloud radiometer (MCR) and cloud absorption radiometer (CAR) were calibrated using a laboratory calibration facility consisting of a 6 ft integrating sphere and a 4 ft integrating hemisphere. The absolute calibrations of the integrating sphere and hemisphere are determined about once every 6 months by a calibration branch at Goddard and somewhat less frequently by an outside laboratory (Optronic Laboratories). After considerable examination of the experimental data from these two instruments and the absolute lamp intensities from both laboratories, we were able to determine our best estimate of the absolute calibration coefficients for both instruments at their respective wavelengths (13 for the CAR and 6 near-infrared channels for the MCR). Thus the first quantitative examination of the radiation data from the FIRE flights centered on comparing the absolute reflected intensities of the CAR and the UK multispectral cloud radiometer during three simultaneous wing-tip intercomparisons during two flights.

Figs. 1-3 illustrate the nadir reflected intensities as measured by the UK multispectral cloud radiometer and the GSFC cloud absorption radiometer on each of these intercomparison flights. Since the gains of the CAR were adjusted for internal cloud radiation measurements, some of the filter wheel channels (channels 8-13, $1.55 \leq \lambda \leq 2.29$ µm) were saturated. By careful examination of these figures, especially Fig. 2, one can see the spectral reflection signature of the clouds quite clearly. The C-130 radiometer has channels in a couple of water vapor bands (1.33 and 1.85 µm), whereas the Goddard CAR has all channels in waver vapor window regions. Thus, in combination, the entire reflected spectrum of these clouds is quite apparent.

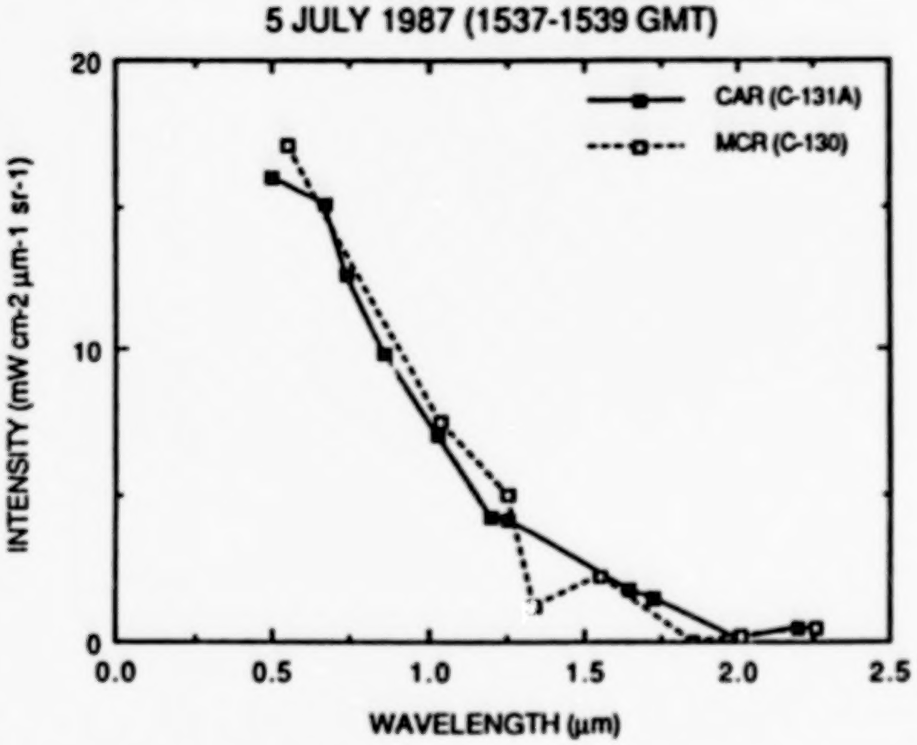

Fig. 1. Intercomparison of the nadir reflected intensity of marine stratocumulus clouds as measured by the UK multispectral cloud radiometer and the GSFC cloud absorption radiometer on 5 July 1987 (1544-1546 GMT).

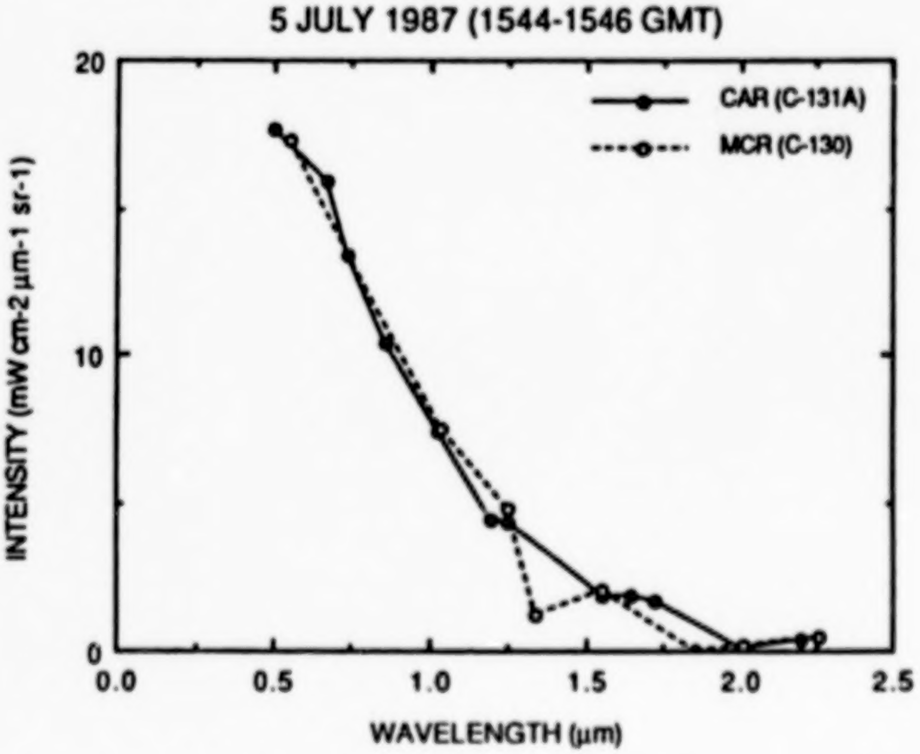

Fig. 2. As in Fig. 1 except for 1544-1546 GMT.

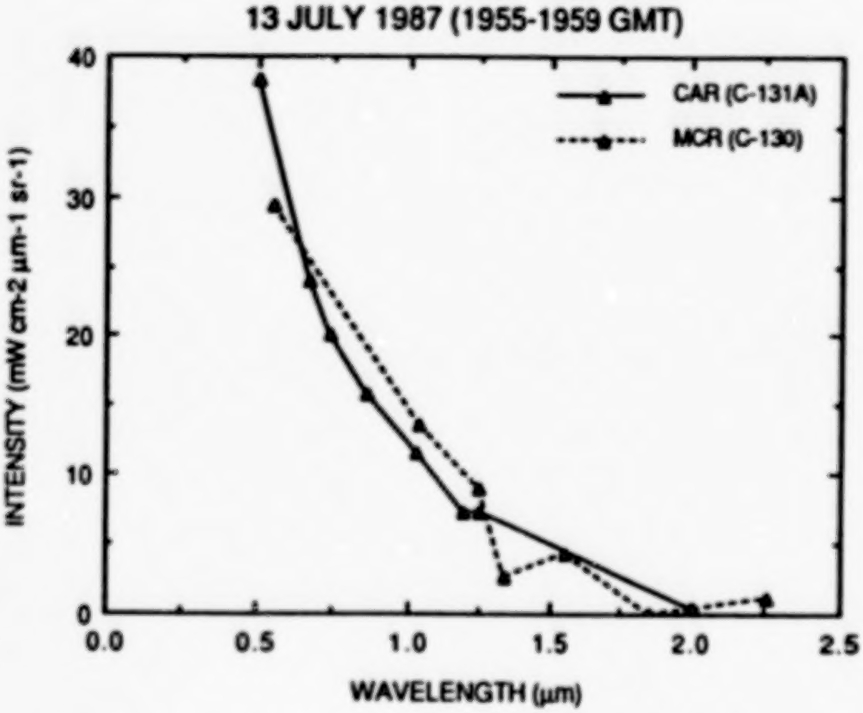

Fig. 3. As in Fig. 1 except for 13 July 1987 (1955-1959 GMT).

The longest intercomparison occurred on 13 July 1987, for which the C-130 and C-131A flew wing-tip to wing-tip for 3.41 min (16.4 km). Fig. 4 illustrates the zenith (skylight) and nadir (reflected) intensities as a function of time for channel 2 ($\lambda = 0.67$ µm), where the dashed curve corresponds to the reflected intensity that was averaged and presented in Fig. 3. Since the solar zenith angle was 10.2° at the time of these measurements, the zenith intensity measurement was influenced by the solar aureole and was often saturated.

3. Diffusion domain measurements

On 10 July 1987 the C-130 flew a tightly coordinated mission with the ER-2 aircraft, consisting of continually flying legs of 130 km in length. The C-130 was primarily making cloud radiation and cloud microphysics measurements deep within the clouds. The determination of the cloud similarity parameter, defined as $s = [(1 - \omega_0)/(1 - \omega_0 g)]^{1/2}$, where g is the asymmetry factor and ω_0 the single scattering albedo, is based on making measurements of the ratio of the nadir to zenith intensity within the diffusion domain of a cloud. We have developed a comprehensive set of tests to which the CAR data are subjected in order to identify those portions of the flight for which measurements were obtained within the diffusion domain. On this particular day, our tests showed that a staggering 5380 scans (53.8 min, 266 km) met these criteria.

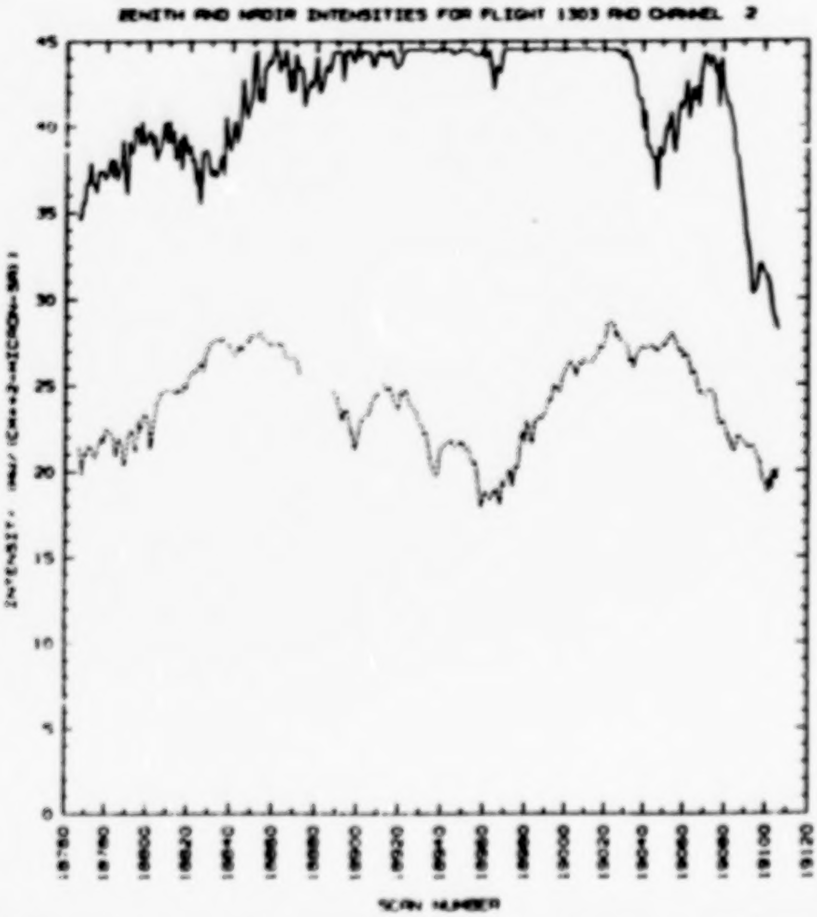

Fig. 4. Zenith and nadir intensities as measured by the cloud absorption radiometer for the wing-tip intercomparisons presented in Fig. 3. The solid curve represents the zenith (downward propagating) intensity and the dashed curve the nadir (reflected) intensity from the marine stratocumulus clouds. The abscissa is the CAR scan number (100 scans min^{-1}) and thus the time scale runs for 341 scans (3.41 min, 16.8 km).

Although we have not yet quantitatively analyzed these data to derive the similarity parameter spectrum, the time series of the zenith and nadir intensities for 1000 scan lines (10 min) of data, illustrated in Fig. 5 for $\lambda = 0.67$ µm, show that the zenith and nadir intensity field was quite uniform within these clouds. The method of analysis, described in detail by King (1981) and summarized by King et al. (1986), will be applied to these data and discussed in detail at the meeting.

REFERENCES

Curran, R. J., H. L. Kyle, L. R. Blaine, J. Smith and T. D. Clem, 1981: Multichannel scanning radiometer for remote sensing cloud physical parameters. *Rev. Sci. Instrum.*, **52**, 1546-1555.

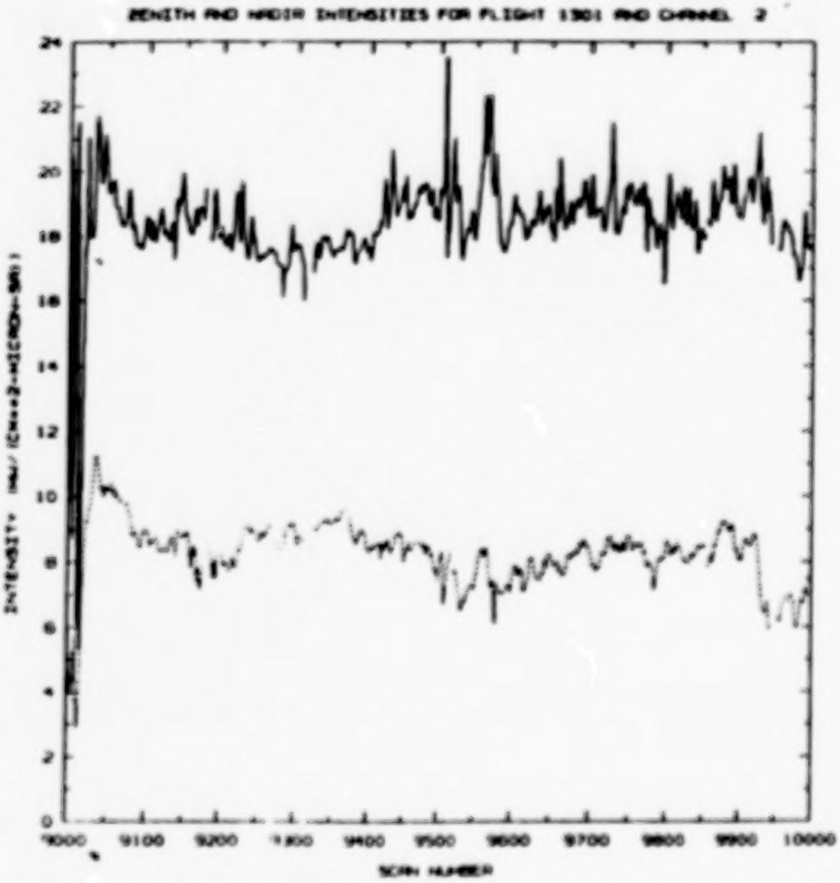

Fig. 5. As in Fig. 4 except for measurements within the diffusion domain of optically thick clouds as measured by the cloud absorption radiometer on 10 July 1987. The abscissa is the CAR scan number and runs for 1000 scans (49.4 km).

Foot, J. S., 1988: Some observations of the optical properties of clouds. I: Stratocumulus. *Quart. J. Roy. Meteor. Soc.*, **114**, 129-144.

King, M. D., 1981: A method for determining the single scattering albedo of clouds through observation of the internal scattered radiation field. *J. Atmos. Sci.*, **38**, 2031-2044.

_____, M. G. Strange, P. Leone and L. R. Blaine, 1986: Multiwavelength scanning radiometer for airborne measurements of scattered radiation within clouds. *J. Atmos. Oceanic Tech.*, **3**, 513-522.

_____, 1987: Determination of the scaled optical thickness of clouds from reflected solar radiation measurements. *J. Atmos. Sci.*, **14**, 1734-1751.

Radke, L. F., 1983: Preliminary measurements of the size distribution of cloud interstitial aerosol. *Precipitation Scavenging, Dry Deposition and Resus-*

pension, H. R. Pruppacher, R. G. Semonin and W. G. N. Slinn, Eds., Elsevier, 71-78.

Cloud Optical Parameters as Derived from the Multispectral Cloud Radiometer

Teruyuki Nakajima[†] and Michael D. King

Laboratory for Atmospheres, Goddard Space Flight Center, NASA,
Greenbelt, MD 20771, USA

1. Introduction

There are several studies on the simultaneous determination of cloud optical thickness and mean droplet size as derived from multispectral radiometers (Twomey and Cocks, 1982; Curran and Wu, 1982; Arking and Childs, 1985). These studies are very important to elucidate the cloud microphysical structure. As pointed out by many investigators (e. g. Rossow *et al.*, 1985; Wu, 1985), however, many factors bother the successful retrieval when we apply these methods to real data. Therefore, many ground truth experiments are required in order to test the validity of these methods. Here, we have analyzed the data taken in the marine stratocumulus intensive field observation component of the First ISCCP Regional Experiment (FIRE), conducted off the California coast in July, 1987 using the Multispectral Cloud Radiometer (MCR).

The MCR has six near-infrared channels and one 10.7 μm-channel (Curran *et al.*, 1981). The first channel (λ = 0.754 μm) has proven to be very useful for estimating the cloud optical thickness (King, 1987). Adding the additional two wavelengths (λ = 1.645, 2.160 μm), we are able to estimate the mean droplet size (Curran and Wu, 1982). Arking and Childs (1985) also studied a similar problem using the 0.73 and 3.7 μm channels of the NOAA/AVHRR. In spite of these pioneering works, there seem to be insufficient systematic studies of the efficiency of the algorithms. For this purpose, we have performed numerous simulations of the reflected radiation from clouds using an improved radiation calculation algorithm (Nakajima and Tanaka, 1988). Results of the simulation and an application of our algorithm to the MCR data are presented in Sections 2 and 3, respectively.

2. Retrieval algorithm

For the purpose of analyzing the three MCR near-infrared channels outside water vapor and oxygen absorption bands (λ= 0.754, 1.645 and 2.160 μm), we investigated the characteristics of the numerically simulated bidirectional reflectivity of plane-parallel earth-cloud systems. The variables we examined were the optical thickness (τ) and the mode radius of cloud droplets (r_m), defined by the following log-normal cross-section spectrum:

[†] Permanent affiliation: Upper Atmosphere and Space Research Laboratory, Faculty of Science, Tohoku University, Sendai 980, Japan.

$$\frac{dC}{d\ln r} = C_0 \exp\left[-(\ln r - \ln r_m)^2/(2\sigma^2)\right], \tag{1}$$

where C is the geometric cross section of droplets; r is the particle radius; σ is the log-dispersion of the spectrum. Investigating the first and second moments of several model size spectra of cloud droplets, it is found that σ can be fixed at 0.35 for most problems even including aerosol polydispersions. The following points are clarified as a results of the numerical simulation:

(1) As a first approximation, the cloud optical thickness τ at $\lambda = 0.754$ µm can be determined from the reflected radiation at this wavelength. The retrieval is stable, because the cloud reflectivity increases monotonically with increasing optical thickness and the dependence on the droplet size is relatively small.

(2) Using the cloud optical thickness determined in step (1), the cloud droplet mode radius r_m is estimated from an absorbing channel, i.e., 1.645 or 2.160 µm radiation. The optical thickness dependence is small as absorption increases.

(3) Iterating steps (1) and (2) or investigating these steps for several pre-assumed particle radii, we can have an optimum set of τ and r_m. We have developed two methods for the simultaneous retrieval of cloud optical thickness and mode radius, a bispectral method and a multispectral method. The bispectral method uses the two channels of 0.754 and 2.160 µm. This method is hardly affected by the vertical inhomogeneity of the cloud microphysics, but tends to be marred by noise in the absorbing channel. Also, this method can have multiple-solutions of r_m, as demonstrated in Fig. 1. For simplicity we show in Fig. 1 a mode radius dependence of the cloud spherical albedo at $\lambda = 2.16$ µm for $\tau = 8$, 16 and 32. Figure 1 shows that the profiles are a peaked function of mode radius with a peak around $r_m = 2$–3 µm. Thus, for example, a measured reflectance at 2.16 µm, given an optical thickness derived from the 0.754 µm channel, could be produced by one of two possible mode radii. Therefore, it is very important to set a suitable minimum droplet radius for the algorithm. On the other hand, the multispectral method uses all three channels. The optimum value of r_m is determined in this method so as to minimize the following root mean square deviation between the observed and theoretical values:

$$\chi^2 = \sum_{n=2}^{3}\left[\frac{R_n^c(\tau,r_m)}{R_n^m} - 1\right]^2, \qquad (2)$$

where $n = 2$ stands for the second channel (1.645 µm) and $n = 3$ for the third channel (2.160 µm); superscripts c and m stand for theoretical (computed) and measured values, respectively. In the above equation, τ is determined from the first channel (0.754 µm), as in the bispectral method. This method is relatively insensitive to noise in any individual channel and we can have a unique solution for r_m, potentially different from the bispectral method. But this method fails in some case of vertical inhomogeneity. We have adopted both methods for the sake of diagnosing the soundness of the retrieval.

(4) The error involved in the retrieval increases in the backward portion of the scattering. The error in r_m increases with decreasing r_m; the errors in τ and r_m increase in the region $\tau < 6$ or $\tau > 100$.

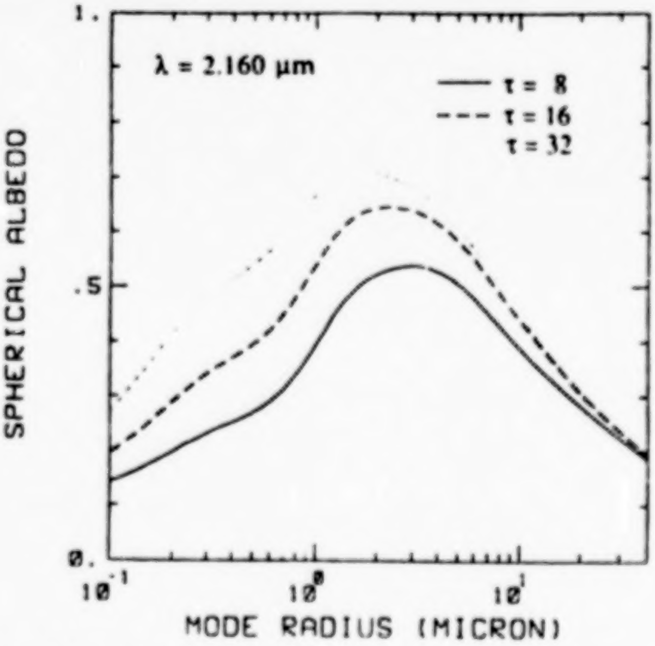

Fig. 1. Spherical albedo of a plane-parallel cloud versus the droplet mode radius at λ= 2.16 µm.

3. Analysis of MCR-data

Since the MCR can produce a 2-D image of the upwelling radiation, we tried to develop a retrieval scheme computationally very efficient. We have generated four tables of bidirectional reflectivity for the scaled cloud optical thickness $\tau^* = (1-g)\tau = 0.4, 0.8, 1.2$ and ∞, where g is the cloud asymmetry factor. Using asymptotic theory for $\tau^* \geq 1.8$ (King, 1987) and computations for $\tau^* < 1.8$, we can interpolate the bidirectional reflectivity with errors less than 2%. Since our intention is to derive effective parameters to describe the radiative characteristics of clouds, we assume homogeneous and plane-parallel stratification for the analysis. According to numerical simulations, τ can be estimated with an error less than 20% and r_m can be estimated at the effective depth of radiation unless the optical thickness and particle radius are too small.

Figure 2 shows contours of the cloud optical thickness derived for the first half of the fourth ER-2-flight line of July 10, 1987 (about 1000 scan lines, 60 km). A photographic print of the original data for this example shows that a band of τ~15 was the edge of a large flat cloud deck spreading ahead of the flight course. The optical thickness varied from 5 to 20 around this edge.

Figure 3 shows the horizontal distributions of τ and r_m along a constant pixel line (solid lines for pixel number 84 and dotted lines for pixel number 252, where the total number of profiles in an active scan is typically 336). Although r_m showed a small monotonic decrease from left to right, the value was remarkably constant with values around 15 μm, in spite of the large change of τ from 5 to 15 around the horizontal distance of 30 km (solid line) and large hole around 40–50 km (dotted line). Although we showed the value of r_m derived by the multispectral method, there was no large difference from the bispectral method except for small optical thickness < 6. For small optical thickness, however, there were some cases when the algorithm selected the smaller branch of the solution depending on the viewing direction, as shown by several steep dips of the mean radius. Since we had a large difference between the results of the multispectral and bispectral methods in this case, there may be large uncertainties in the retrieved value of r_m around these dips (as expected by item (4) in the preceding section). We show the minimized χ^2-value in the multispectral method in the uppermost section of Fig.3. The *rms*-difference between the measured and theoretical values was less than 5%.

4. Concluding remarks

We have installed an efficient retrieval scheme for deriving the cloud optical thickness and droplet mode radius; and we have described the behavior of the retrieval error. Generally the scheme can retrieve the optical thickness and mode radius adequately unless they are too small; the use of the forward scattering region is more sound than the use of the backscattering portion.

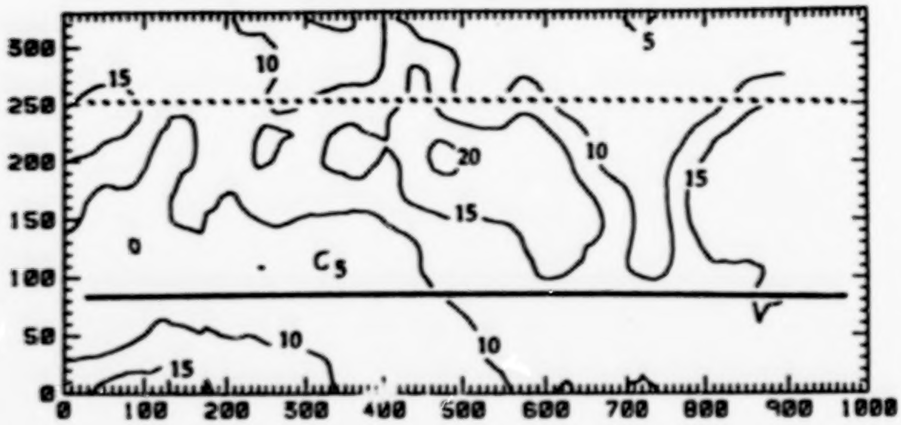

Fig. 2. Cloud optical thickness distribution for the fourth flight line of July 10, 1987. Horizontal and vertical axes are for scan-line and pixel numbers. Bold solid and dotted lines shows the sampling lines for Fig. 3.

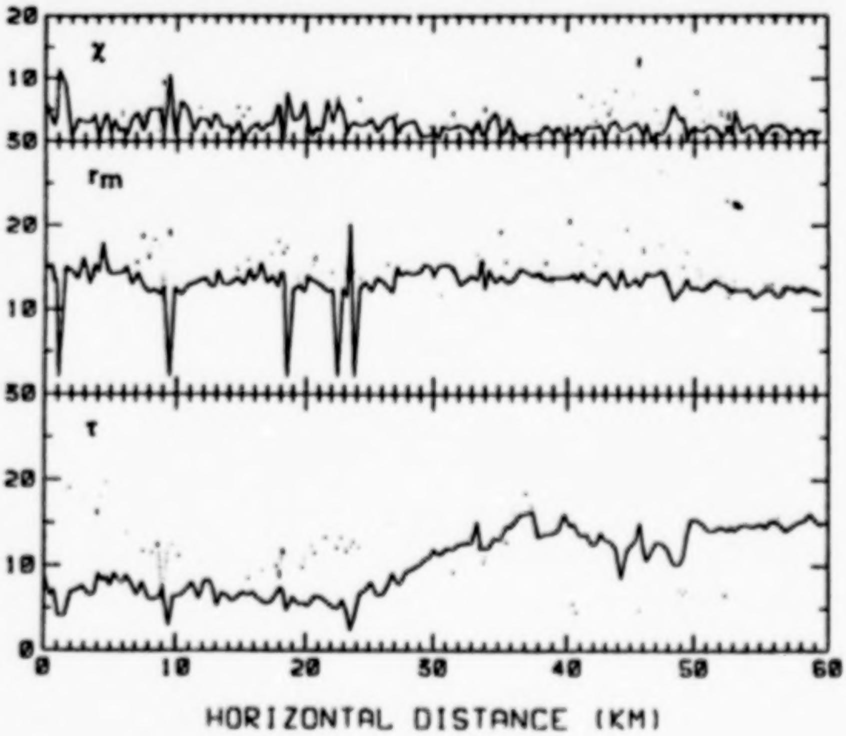

Fig. 3. Cloud optical thickness (τ), droplet mode radius retrieved by the multispectral method (r_m), and χ along the bold solid and dotted lines in Fig. 2.

Applying our method to real data, we have derived the two-dimensional distribution of optical thickness and mode radius for a portion of one of the FIRE marine stratocumulus missions. In this case study, the droplet size showed a more uniform distribution than optical thickness with some correlation between large droplet size and small optical thickness. Although we can find microphysical reasons for these tendencies, we are suspecting that the remotely sensed droplet size may be overestimated. As a future problem, we will compare our results with *in situ* data of the droplet size distribution. Also it will be very important to check several reasons why the droplet radius might be overestimated, e.g., soot contamination, effect of escaping photons from the lateral sides of broken clouds, and so on.

REFERENCES

Arking, A. and J. D. Childs, 1985: Retrieval of cloud cover parameters from multispectral satellite images. *J. Climate Appl. Meteor.*, **24**, 322–333.

Curran, R. J., H. L. Kyle, L. R. Blaine, J. Smith and T. D. Clem, 1981: Multichannel scanning radiometer for remote sensing cloud physical parameters. *Rev. Sci. Instrum.*, **52**, 1546–1555.

Curran, R. J., and M-L. C. Wu, 1982: Skylab near-infrared observations of clouds indicating supercooled liquid water droplets. *J. Atmos. Sci.*, **39**, 635–647.

King, M. D., 1987: Determination of the scaled optical thickness of clouds from reflected solar radiation measurements. *J. Atmos. Sci.*, **44**, 1734–1751.

Nakajima, T., and M. Tanaka, 1988: Algorithms for radiative intensity calculations in moderately thick atmospheres using a truncation approximation. *J. Quant. Spectrosc. Radiat. Transfer* (in press).

Rossow, W. B., F. Mosher, E. Kinsella, A. Arking, M. Despois, E. Harrison, P. Minnis, E. Ruprecht, G. Seze, C. Simmer and E. Smith, 1985: ISCCP cloud algorithm intercomparison. *J. Appl. Meteor.*, **24**, 877-903.

Twomey, S., and T. Cocks, 1982: Spectral reflectance of clouds in the near-infrared: Comparison of measurements and calculations. *J. Meteor. Soc. Japan*, **60**, 583–592.

Wu, M.-L., 1985: Remote sensing measurements of cloud physical parameters in the cooperative convective precipitation experiment. *J. Geophys. Res.*, **90**, 10551–10562.

FIRE SCIENCE TEAM MEETING
VAIL, COLORADO
JULY 11-15, 1988

MARINE STRATOCUMULUS

THERMODYNAMIC AND DYNAMIC PROPERTIES - Bruce A. Albrecht

Thursday, July 14, 1988

PAGE

Aircraft Measurements of the Mean and Turbulent Structure of Marine Stratocumulus Clouds During FIRE 335
Albrecht, Bruce A.; Kevin A. Kloesel, Kerry A. Moyer, Jefferey J. [illegible]ucciarone, and George Young

Cloud and Boundary Layer Structure Over San Nicolas Island During FIRE 337
Albrecht, Bruce A.; Christopher W. Fairall, William J. Syrett, Wayne H. Schubert, and Jack B. Snider

Thermodynamic Structure of the Stratocumulus-Capped Boundary Layer on 5 July, 1987 339
Austin, Philip H.; Reinout Boers, and Alan K. Betts

Analysis of Tethered Balloon Data from San Nicolas Island on 8 July 1987 341
Cox, Stephen K.; David P. Duda, Thomas A. Guinn, Christopher M. Johnson-Pasqua, Wayne H. Schubert, and Jack B. Snider

Turbulence Measurements using Tethered Balloon Instrumentation During FIRE '87 357
Hignett, Phillip

Horizontal Variability of the Marine Boundary Layer Structure Upwind of San Nicolas Island During FIRE, 1987 359
Jensen, Douglas R.

An Overview of UK C130 Observations from the FIRE Marine Stratocumulus IFO 365
Nicholls, S.; J. Leighton, and R. Barlow

Boundary Layer Roll Circulations During FIRE 367
Shirer, Hampton N.; and Tracy Haack

Winds and Turbulence above San Nicolas Island During FIRE 371
White, Allen B.; William J. Syrett, Christopher W. Fairall, and Dennis W. Thomson

Aircraft Measurements of the Mean and Turbulent Structure of Marine Stratocumulus Clouds during FIRE

Bruce A. Albrecht, Kevin A.Kloesel, Kerry A. Moyer,
Jefferey J. Nucciarone, and George Young

Department of Meteorology
Penn State University
University Park, PA 16802

The mean and turbulent structure of marine stratocumulus clouds is defined from data that were collected from 10 flights made with the NCAR Electra during FIRE. The number of cases sampled is sufficiently large that we can compare the boundary layer structure obtained a) for solid and broken cloud conditions, b) for light and strong surface wind conditions, c) for different sea-surface temperatures and d) on day and night flights. We will describe the cloud and synoptic conditions present at the time of the Electra flights and show how those flights were coordinated with the operations of other aircraft and with satellite overpasses. Mean thermodynamic and wind profiles and the heat, moisture, and momentum fluxes obtained from data collected during these flights will be compared. Variations in the cloud-top structure will be quantified using LIDAR data collected during several of the Electra flights. The spatial structure of cloud-top height and the cloud-base height will be compared with the turbulent structure in the boundary layer as defined by spectra and cospectra of the wind, temperature and moisture.

Cloud and Boundary Layer Structure Over San Nicolas Island During FIRE

Bruce A. Albrecht, Christopher W. Fairall, William J. Syrett

Penn State University
Department of Meteorology
University Park, PA 16802

Wayne H. Schubert

Department of Atmospheric Science
Colorado State University
Fort Collins, CO 80523

Jack B. Snider

NOAA/ERL/WPL
Boulder, CO 80303

The temporal evolution of the structure of the marine boundary layer and of the associated low-level clouds observed in the vicinity of San Nicolas Island (SNI) is defined from data collected during the FIRE Marine Stratocumulus IFO (July 1-19). Surface, radiosonde, and remote-sensing measurements are used for this analysis. Soundings from the Island and from the ship Point Sur, which was located approximately 100 km northwest of SNI, are used to define variations in the thermodynamic structure of the lower-troposphere on time scales of 12 hours and longer. Time-height sections of potential temperature and equivalent potential temperature clearly define large-scale variations in the height and the strength of the inversion and periods where the conditions for cloud-top entrainment instability (CTEI) are met. Well-defined variations in the height and the strength of the inversion were associated with a Catalina Eddy that was present at various times during the experiment and with the passage of the remnants of a tropical cyclone on July 18 (Fig. 1). The large-scale variations in the mean thermodynamic structure at SNI correlate well with those observed from the Point Sur.

Cloud characteristics are defined for 19 days of the experiment using data from a microwave radiometer, a cloud ceilometer, a sodar, and longwave and shortwave radiometers. The depth of the cloud layer is estimated by defining inversion heights from the sodar reflectivity and cloud-base heights from a laser ceilometer. The integrated liquid water obtained from NOAA's microwave radiometer is compared with the adiabatic liquid water content that is calculated by lifting a parcel adiabatically from cloud base. In addition, the cloud structure is characterized by the variability in cloud-base height and in the integrated liquid water. The laser ceilometer is used to estimate the relative fraction of clear and cloudy periods during the experiment. Mean and variances of the solar and longwave fluxes are computed from pyranometer and pyrgeometer measurements.

The time-height sections of equivalent potential temperature are used to identify times during the experiment when conditions for CTEI exist for a day or longer. Our initial analysis shows that CTEI conditions are met over SNI from July 1-4 and over both SNI and the Point Sur July 10-13. From July 6-9 and from July 13-16 the the conditions at the inversion are very unfavorable for CTEI. The cloud characteristics for these different periods will be studied in detail to evaluate the effects of CTEI on cloud structure.

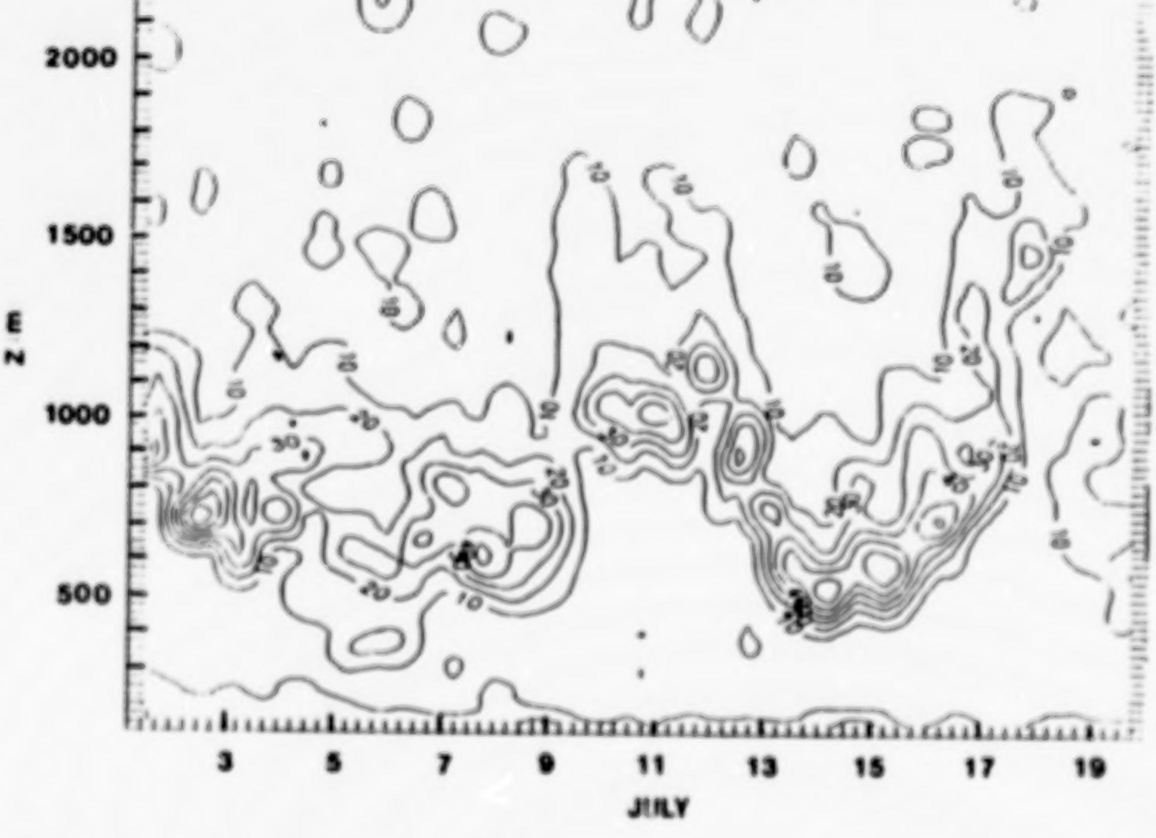

Figure 1. Time height section of [illegible] calculated from CLASS soundings made from San Nicolas Island during FIRE.

Thermodynamic structure of the stratocumulus-capped boundary layer on 5 July, 1987

Philip H. Austin[1], Reinout Boers[2], and Alan K Betts[3]

[1]Code 613 and [2]Code 617
Nasa Goddard Space Flight Center
Greenbelt, MD 20771
and
[3]RD2, Box 3300, Middlebury, VT 05753

The NCAR Electra flew a single aircraft mission on July 5 in comparatively uniform stratocumulus cloud (80 - 100% cloud coverage). The flight pattern, a series of north-south doglegs centered at (32N, -122W), included 15 full or partial soundings to examine layer vertical structure between altitudes of 150 and 5000 m.

In contrast to the July 7 case study (see Boers et al., this conference), the air below the inversion was well-mixed in moist static energy, total water, and ozone. The inversion base measured by the aircraft ranged from 920 to 938 hPa, while the thickness of the cloud layer varied between 30 and 10 hPa. Maximum cloud liquid water contents approached 0.3 g kg^{-1} (as measured by the Johnson-Williams and King probes.). Comparison of soundings made in the same location show a strengthening of the inversion and increasing shear at cloud top over the observation period (16:50 - 00:22 UT). Typical windspeeds below the inversion were ~ 10 m s^{-1}, decreasing to 6 m s^{-1} 8 hPa above cloud top.

A thermodynamic budget for this case is in preparation; it will provide a comparison and contrast with the more complicated July 7 case.

ANALYSIS OF TETHERED BALLOON DATA FROM SAN NICOLAS ISLAND ON 8 JULY 1987

STEPHEN K. COX

DAVID P. DUDA

THOMAS A. GUINN

CHRISTOPHER M. JOHNSON-PASQUA

WAYNE H. SCHUBERT

Department of Atmospheric Science, Colorado State University, Fort Collins, Colorado 80523

JACK B. SNIDER

NOAA/ERL/Wave Propagation Laboratory, Boulder, Colorado 80303

(June 1988)

1. Introduction

This paper summarizes our analysis of the 8 July 1987 (Julian Day 189) tethered balloon flight from San Nicolas Island. The flight commenced at about 14:30 UTC (7:30 Pacific Daylight Time) and lasted six and one-half hours. The position of the CSU instrument package as a function of time is shown in Fig. 1. For the purpose of presentation of results we have divided the flight into the 13 legs indicated in Fig. 1. These legs consist of 20 minute constant level runs, with the exception of leg 1, which is a sounding from the surface to just above 930 mb. The laser ceilometer (Schubert et al., 1987) record of cloud base is also shown in Fig. 1. The cloud base averaged around 970 mb during much of the flight but was more variable near the end.

Before the tethered balloon flight commenced, a CLASS sounding (Schubert et al., 1987) was released at 12:11 UTC (5:11 PDT). Temperature and moisture data below 927 mb for this sounding is shown in Figure 2. The sounding indicates a cloud top around 955 mb at this time.

2. Some Basic Theory

In order to interpret the tethered balloon data, some basic theory is required. Define the saturation moist static energy as $h^* = c_pT + gz + Lq^*$, where q^* is the saturation mixing ratio. The moist adiabatic lapse rate is derived by setting $\partial h^*/\partial z = 0$, which leads directly to

$$\frac{\partial T}{\partial z} + \frac{g}{c_p} = -\frac{L}{c_p}\frac{\partial q^*}{\partial z}. \tag{2.1}$$

Since q^* is a function of T and p, we have

$$\frac{\partial q^*}{\partial z} = \left(\frac{\partial q^*}{\partial T}\right)_p \frac{\partial T}{\partial z} + \left(\frac{\partial q^*}{\partial p}\right)_T \frac{\partial p}{\partial z}. \tag{2.2}$$

Using the hydrostatic approximation, this can be written

$$\frac{L}{c_p}\frac{\partial q^*}{\partial z} = \gamma\frac{\partial T}{\partial z} + \frac{g}{R}\frac{Lq^*}{c_pT}, \tag{2.3}$$

where

$$\gamma = \frac{L}{c_p}\left(\frac{\partial q^*}{\partial T}\right)_p. \tag{2.4}$$

Eliminating $\frac{\partial q^*}{\partial z}$ between (2.1) and (2.3) we obtain the moist adiabatic lapse rate

$$-\frac{\partial T}{\partial z} = \frac{g}{c_p}\left(\frac{1 + \frac{Lq^*}{RT}}{1 + \gamma}\right). \tag{2.5}$$

Since the dry adiabatic lapse rate is g/c_p, the last factor in (2.5) gives the ratio of the moist and dry adiabatic lapse rates. Using $g = 9.80$ m s^{-2}, $c_p = 1004.5$ J kg^{-1} K^{-1}, $L = 2.47 \times 10^6$

J kg^{-1}, $R = 287$ J kg^{-1} K^{-1}, $q^* = 9.5$ g kg^{-1}, $T = 285.65$ K and $\gamma = 1.34$, we obtain

$$-\frac{\partial T}{\partial z} = \begin{cases} 0.00536 K\mathrm{m}^{-1} & \text{in cloud layer,} \\ 0.00976 K\mathrm{m}^{-1} & \text{in subcloud layer,} \end{cases} \tag{2.6}$$

or

$$\frac{\partial T}{\partial p} = \begin{cases} 0.0448 K\mathrm{mb}^{-1} & \text{in cloud layer,} \\ 0.0816 K\mathrm{mb}^{-1} & \text{in subcloud layer.} \end{cases} \tag{2.7}$$

Eliminating $\partial T/\partial z$ between (2.1) and (2.3), and assuming that the total water $q^* + \ell$ is mixed in the cloud layer we obtain

$$\frac{\partial \ell}{\partial z} = -\frac{\partial q^*}{\partial z} = \frac{g}{L}\left(\frac{\gamma - \frac{Lq^*}{RT}}{1+\gamma}\right) \approx 0.00179 \mathrm{g\,kg^{-1}m^{-1}} \tag{2.8}$$

If the liquid water mixing ratio ℓ is a linear function of height in the cloud layer, then

$$\int_{z_C}^{z_B} \ell \rho dz = \frac{\partial \ell}{\partial z}\frac{\rho}{2}(z_B - z_C)^2, \tag{2.9}$$

where $(z_B - z_C)$ is the depth of the cloud. Solving for $(z_B - z_C)$ we obtain

$$z_B - z_C = \left(\frac{\int \ell \rho dz}{\frac{\partial \ell}{\partial z}\frac{\rho}{2}}\right)^{\frac{1}{2}}. \tag{2.10}$$

3. Thermodynamic Data

Figure 3 shows profiles of dry bulb and wet bulb temperatures taken on leg 1 of Figure 1. Note that the brief constant level section of leg 1 at 935 mb was partially in and partially out of cloud; this leads to the large variance in temperature at 935 mb in Figure 3. The laser ceilometer reported a cloud base of 970 mb during the sounding, and this is indicated in Figure 3 by the kink between the dry and the moist adiabatic lapse rates. The fact that the wet bulb temperature increases with height just above cloud top indicates that the cloud layer is stable for evaporative instability processes. An interesting feature of Figure 3 is that the subcloud layer lapse rate is less than dry adiabatic, which is inconsistent with mixed layer theory; the value found from Figure 3 is about 7K/100m. If the boundary layer were warming at a rate of 1.8 K/hour, the time required for the balloon to reach cloud base would explain the difference between the apparent lapse rate and the dry adiabatic lapse rate. Another (perhaps more likely) explanation is that there was evaporative cooling in the subcloud layer due to drizzle, which was quite noticable at the surface at 17:30 UTC but was probably also present at earlier times.

A measurement of path-integrated liquid water (i.e. the numerator in (2.10)) was made by a microwave radiometer (Snider, 1988; Hogg et al., 1983). The data for 8 July is shown in Fig. 4. Using (2.8) and (2.10) the path integrated liquid water can be converted to cloud depth with 0.05, 0.10, 0.15, 0.20, 0.25 mm of liquid corresponding to cloud depths of 214, 303, 370, 428, 478 m respectively. Since the spike at 17:30 UTC in Fig. 4 would correspond to a cloud thickness of over 500 m, the transformation of path-integrated liquid water to cloud thickness is probably not valid at this particular time. Indeed, at 17:30 UTC drizzle was reported at the ground, which indicates there was probably considerable liquid in the subcloud layer.

4. Cloud Physics Data

a. instrumentation

Cloud droplet sizes and concentrations were measured with a PMS Forward Scattering Spectrometer Probe (FSSP) mounted on the front of the instrument platform. The FSSP operated in the diameter range between 2 and 47 μm. However, due to a problem in the data collection equipment, the values from two adjacent bins were stored in one bin, resulting in seven channels which are six microns in width and one channel 3 microns in width (44 - 47 μm). The values collected from the probe were from five second samples.

b. data reduction

From the raw FSSP data, liquid water content (LWC), mean droplet diameter (d_m) and number density (N) were calculated for each leg of the flight. The FSSP counts particles which sweep through a variable sampling area, which is based on the number of the total counts accepted by the velocity averaging circuitry in the instrument. The effective sampling area is

$$A_e = A \times AC \div TC,$$

where A is the measured sampling area (2.8×10^{-7}m^2), AC the total accepted counts, and TC the total counts (accepted + rejected). The sampling volume is

$$V = A_e v \delta t,$$

where v is the true airspeed and δt the sampling interval (5 seconds). Thus, the concentration of particles in one channel is

$$n_j = \frac{C_j}{V}$$

where C_j is the number of droplets counted in the j^{th} channel and the total number density is the summation of the particle concentrations in each channel,

$$N = \sum_{j=1}^{15} n_j.$$

The average droplet diameter in each of the channels is

$$d_j = \begin{cases} (6j-1) \text{ for } 1 \le j \le 7 \\ 45.5 \text{ for } j = 8 \end{cases}$$

where d_j is expressed in microns. The mean diameter of the particles was computed from

$$d_m = \frac{1}{N} \sum_{j=1}^{15} n_j d_j$$

and the liquid water content was calculated from

$$LWC = \frac{\pi}{6} \rho_L \sum_{j=1}^{15} n_j d_j^3,$$

where ρ_L is the density of water.

c. results

Figures 5–7 present the liquid water content, the mean radius and the total number density respectively, which were measured during leg 5 of the balloon flight. This leg measured the microphysical properties near the top of the cloud at a level of 928.8 mb. At the start of the leg, it appears the instruments are above the cloud, but at 17:03 UTC the rapid increases in LWC and number density indicate the package has entered the cloud. The time series of the number density indicates the number density is 11 particles·cm^{-3} in this part of the cloud. The average concentration remains fairly constant during the leg, although there are large peaks at 17:13 UTC and 17:24 UTC which are over two times the average value. These peaks probably indicate problems with the data collection system.

The liquid water content near cloud top averages near 0.08 g·m^{-3}, although there is some variability in the data. The measured liquid water content at this level is much lower than the values observed lower in the cloud, and it is suggested that the entrainment of the dry air above the cloud is producing the low LWC at this pressure. The points in the LWC curve follow the shape of the number density curve, and thus the sharp peaks result from the same problems which affect the number density data.

Figure 8 presents a profile of the liquid water content throughout the boundary layer. The points on the graph represent the average LWC in each of the twenty minute legs. The liquid water contents in the cloud were generally equal to the adiabatic LWC, with a peak value of 0.38 g·m^{-3} during leg 6 (947.7 mb). At the bottom of the cloud there is a peak of 0.30 g·m^{-3} but in the subcloud layer the LWC was near zero g·m^{-3}. The number density and mean radius profiles are shown in Figure 9. The maximum concentrations occur in the top of the cloud, with values up to 130 particles·cm^{-3} during leg 6. As reflected in the LWC data, the number density in leg 9 is extremely high. The presence of such numerous particles is puzzling. It is not certain whether these particles are real or a problem with the FSSP counts.

Figure 10 shows a normalized droplet size distribution during leg 1 at 994.3 mb, which is in the subcloud layer. A majority (65%) of the particles are smaller than 8 μm in diameter, which suggests they may be haze particles. The small particles, however, appear to be dominant not only in the sub-cloud layer, but also inside and above the cloud.

5. Radiation Data

Figure 11 shows the net near infrared and longwave radiative fluxes measured during leg 1. Inside the cloud layer, from roughly 300 m to 600 m, the net longwave flux is nearly constant and approximately zero. At the top of the cloud layer there is strong longwave flux divergence, nearly -60 W m^{-2}. Inhomogeneties in the cloud structure produced variabilities in the net near IR flux inside the cloud. The variability is greatest near the top of the cloud deck, where the instrument platform passed through an uneven cloud top. Near the top of the cloud there is a convergence of shortwave radiation.

Table 1 presents radiation statistics for legs 2, 3 and 4 of the flight. Leg 2 (929 mb) and leg 3 (935 mb) were taken above cloud top. In both cases the net longwave flux is high and the standard deviation of measured downwelling shortwave flux is low. Leg 4 (942 mb) was taken just below cloud top. At this height the standard deviation in downwelling shortwave flux is much higher than in the other legs and the net longwave flux is nearly zero. It should be noted that the total albedo above the cloud (at 929 mb) is 71.0 %, while the near IR albedo is 67.5 % and the visible albedo is 74.2 %.

Acknowledgments. Our participation in the FIRE project has been supported by the Marine Meteorology Program of the Office of Naval Research under contract N00014-87-K-0228 and by the National Aeronautics and Space Administration under contract NAG1-554.

REFERENCES

Hogg, D.C., F.O. Guiraud, J.B. Snider, M.T. Decker, and E.R. Westwater, 1983: A steerable dual-channel microwave radiometer for measurement of water vapor and liquid in the troposphere. J. Climate Appl. Meteorol., 22, 789- 806.

Particle Measuring Systems, Inc, 1984: Foward scattering spectometer probe PMS model fssp-100, Operating and servicing manual, 58 pp.

Schubert, W.H., P.E. Ciesielski, T.B. McKee, J.D. Kleist, S.K. Cox, C.M. Johnson-Pasqua, and W.L. Smith, Jr., 1987: Analysis of boundary layer sounding data from the FIRE marine stratocumulus project. Atmos. Sci. Paper No. 419, Dept. of Atmos. Sci., Colorado State University.

Schubert, W.H., S.K. Cox, P.E. Ciesielski, and C.M. Johnson-Pasqua, 1987: Operation of a ceilometer during the FIRE marine stratocumulus experiment. Atmos. Sci. Paper No. 420, Dept. of Atmos. Sci., Colorado State University.

Snider, J.B., 1988: Radiometric observations of cloud liquid water during FIRE. Preprint.

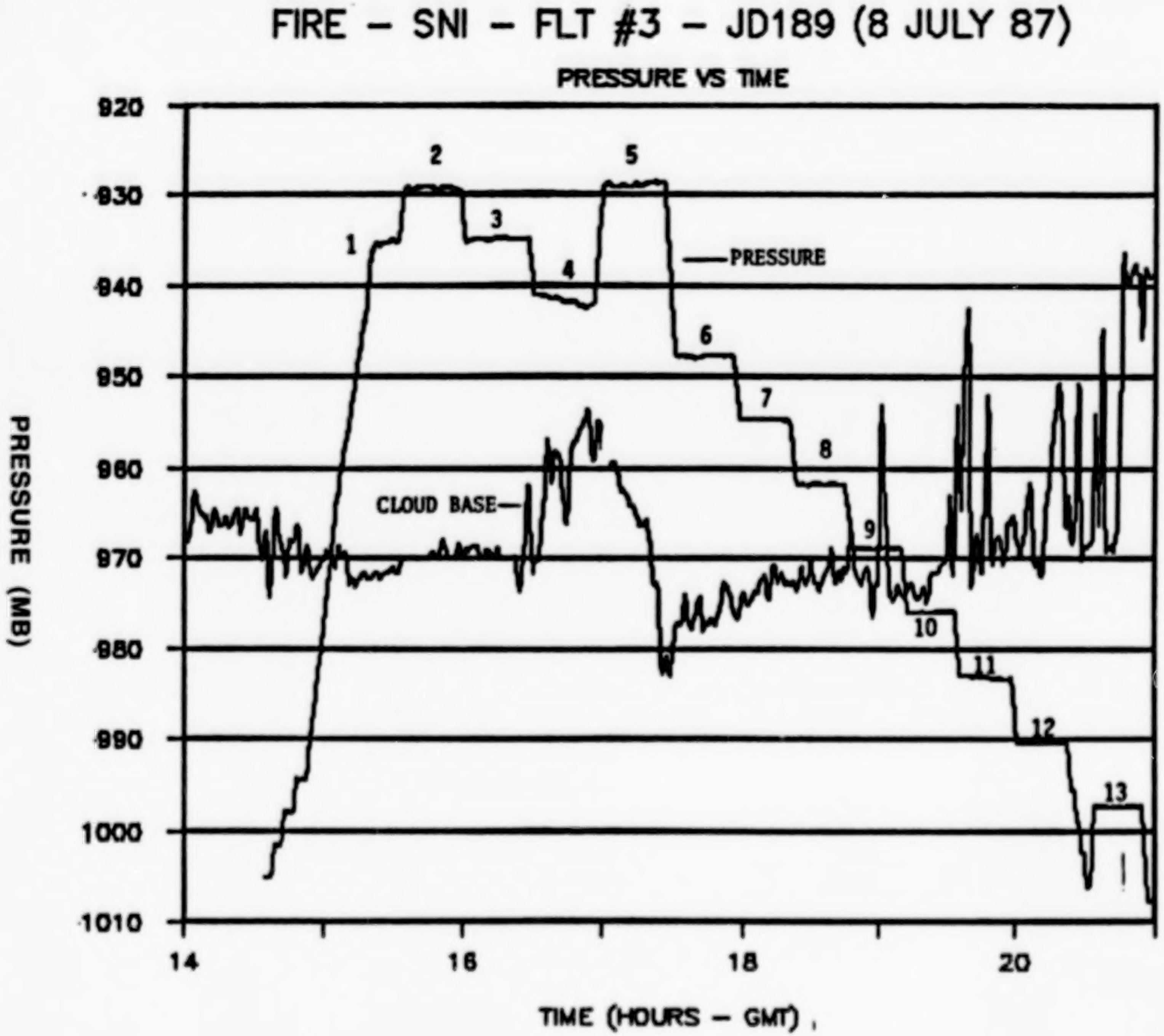
FIRE - SNI - FLT #3 - JD189 (8 JULY 87)
PRESSURE VS TIME
920
930
940
950
960
970
980
990
1000
1010
PRESSURE (MB)
14
16
18
20
TIME (HOURS - GMT)
1
2
3
4
5
6
7
8
9
10
11
12
13
PRESSURE
CLOUD BASE

Figure 1

FIRE - SNI - JD189 1211Z (8 JULY 87)

CLASS SOUNDING PRESSURE VS TEMPERATURE

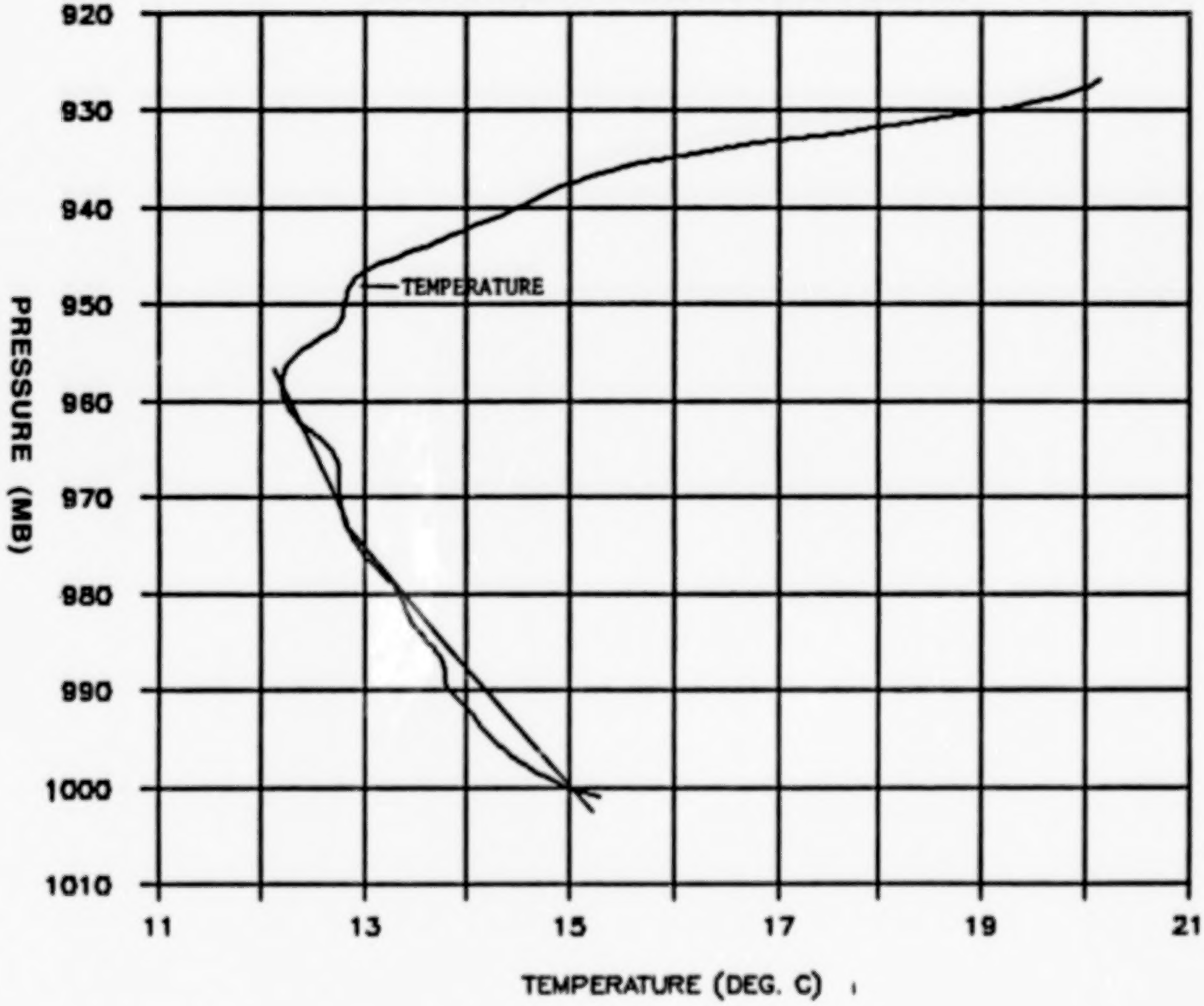

Figure 2a

346

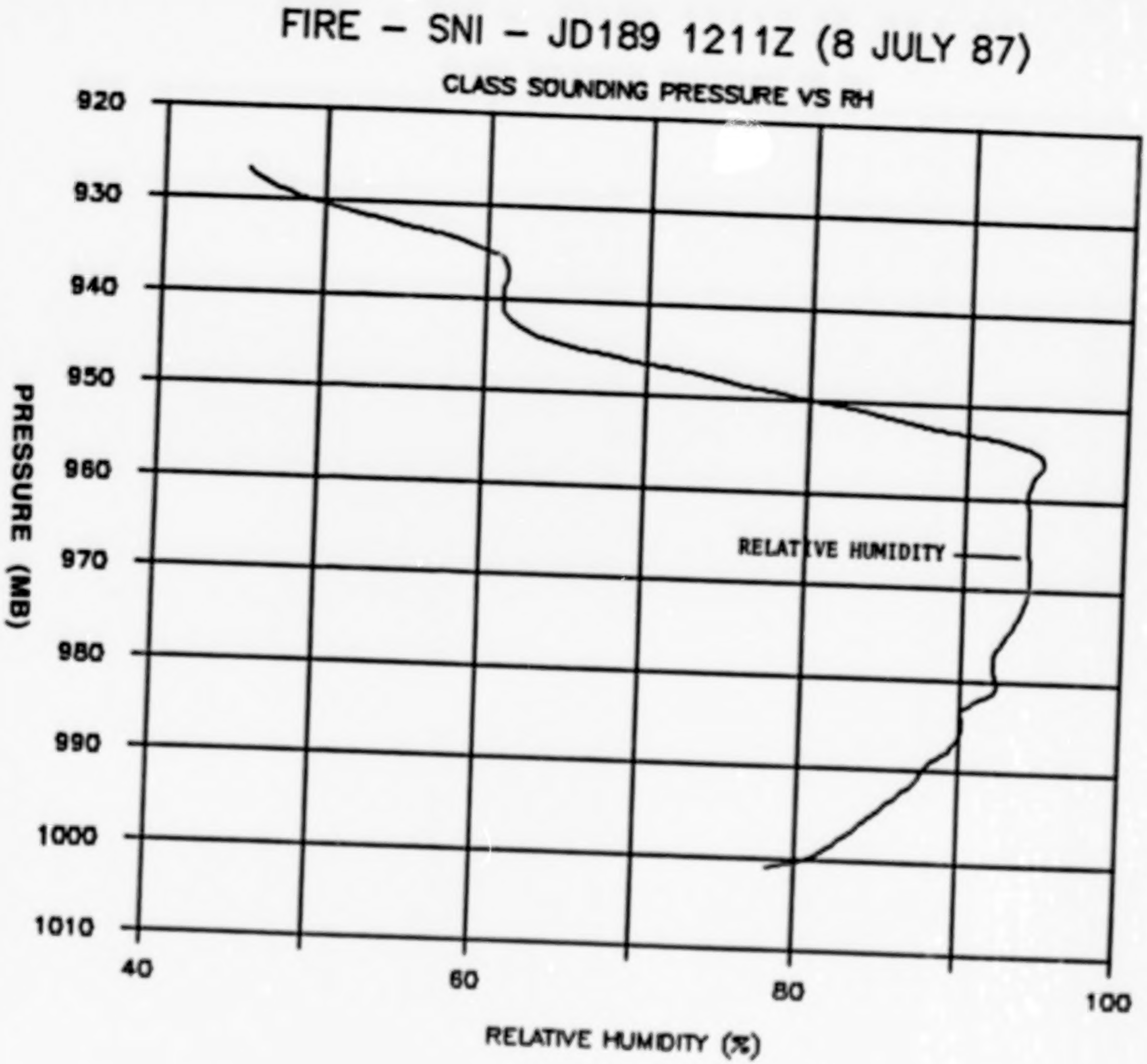
FIRE - SNI - JD189 1211Z (8 JULY 87)
CLASS SOUNDING PRESSURE VS RH
PRESSURE (MB)
920
930
940
950
960
970
980
990
1000
1010
40
60
80
100
RELATIVE HUMIDITY (%)
RELATIVE HUMIDITY

Figure 2b

FIRE – SNI – FLT #3 – JD189 (8 JULY 87)

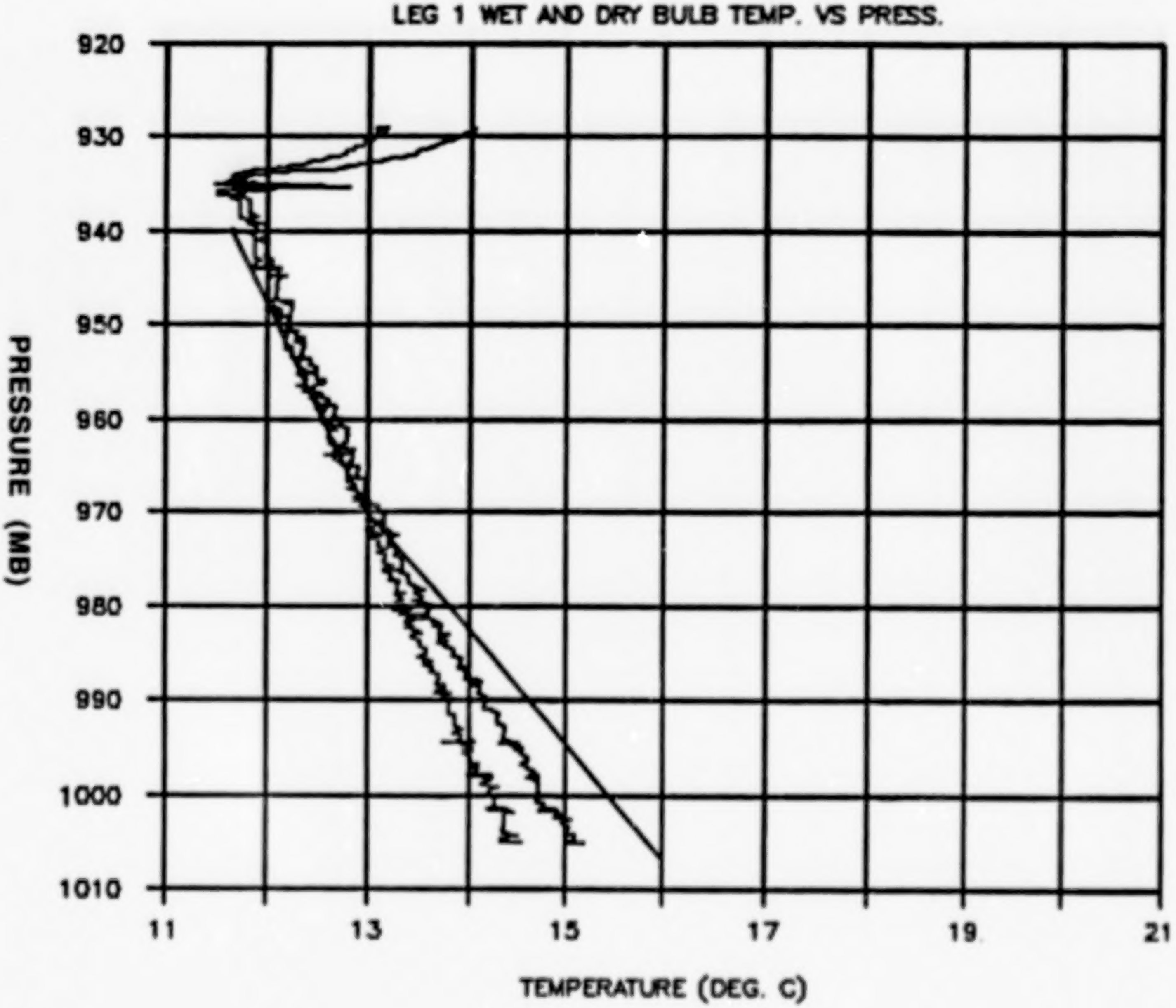

Figure 3

348

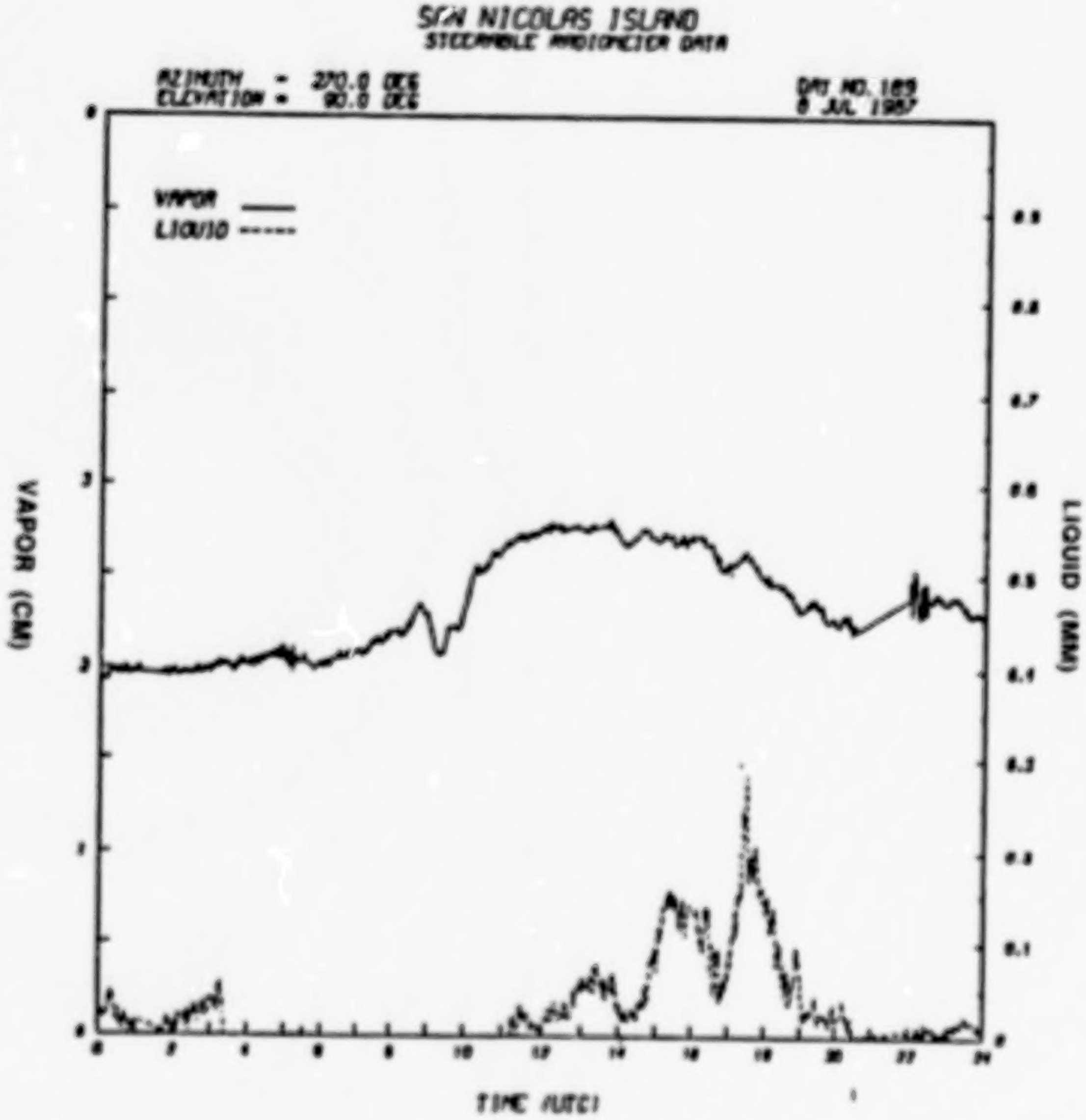
SAN NICOLAS ISLAND
STEERABLE RADIOMETER DATA
AZIMUTH = 270.0 DEG
ELEVATION = 90.0 DEG
DAY NO. 189
8 JUL 1987
VAPOR
LIQUID
VAPOR (CM)
LIQUID (MM)
TIME (UTC)
0
1
2
3
0.1
0.2
0.3
0.4
0.5
0.6
0.7
0.8
0.9
0
2
4
6
8
10
12
14
16
18
20
22
24

Figure 4

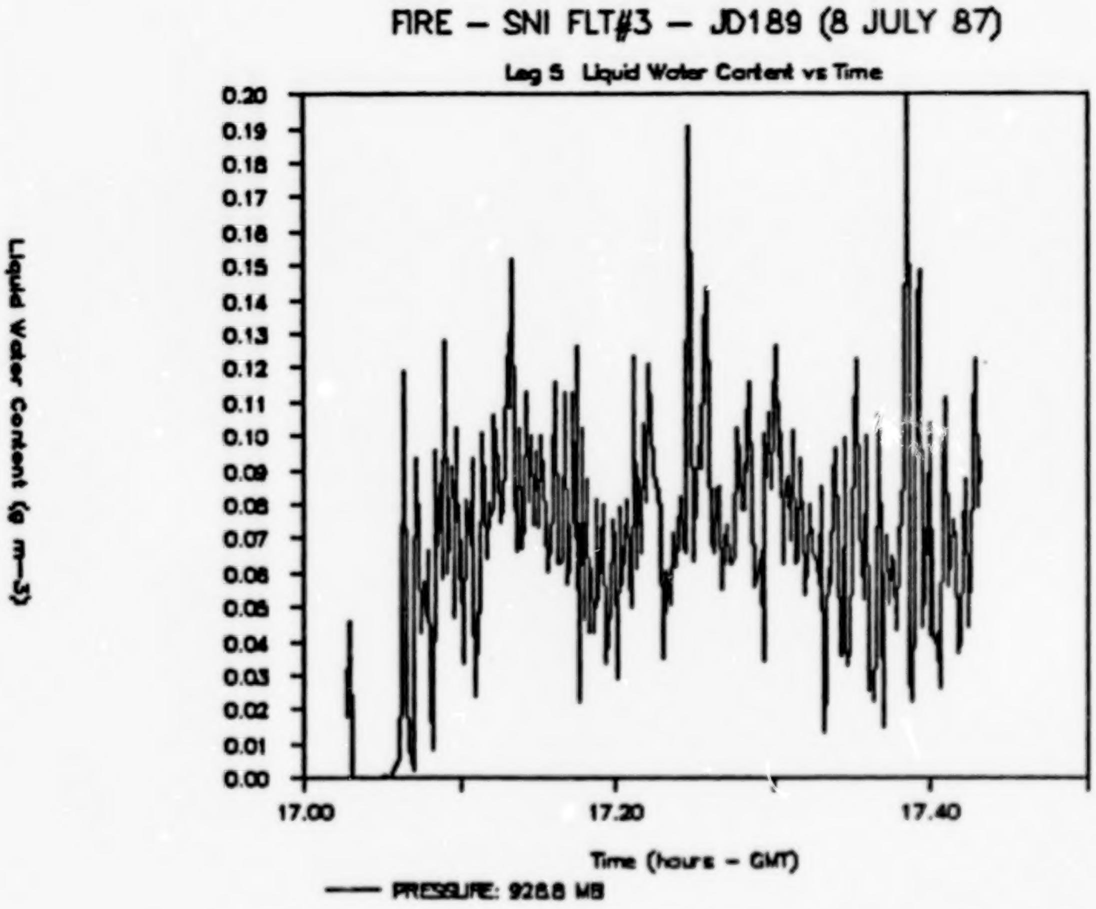
FIRE – SNI FLT#3 – JD189 (8 JULY 87)
Leg 5 Liquid Water Content vs Time
Liquid Water Content (g m−3)
0.20
0.19
0.18
0.17
0.16
0.15
0.14
0.13
0.12
0.11
0.10
0.09
0.08
0.07
0.06
0.05
0.04
0.03
0.02
0.01
0.00
17.00
17.20
17.40
Time (hours – GMT)
—— PRESSURE: 928.8 MB

Figure 5

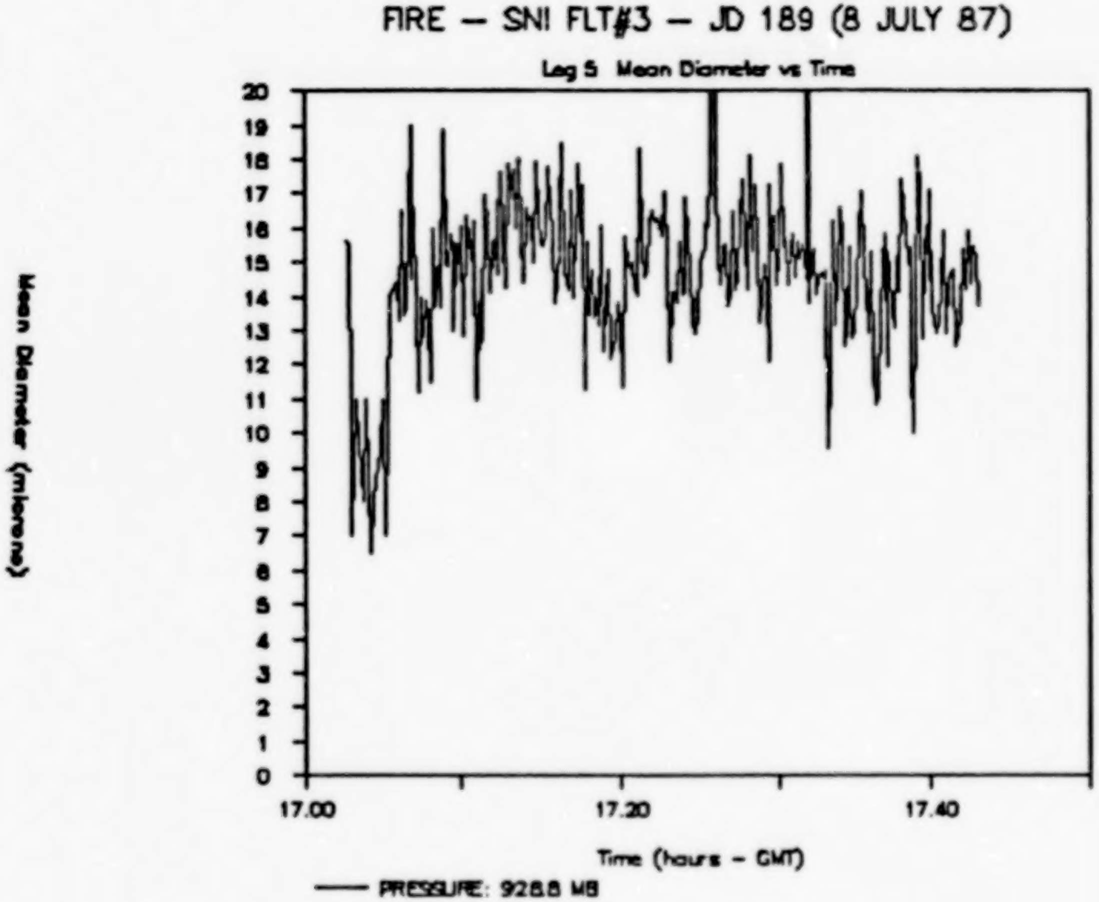
FIRE — SNI FLT#3 — JD 189 (8 JULY 87)
Leg 5 Mean Diameter vs Time
Mean Diameter (microns)
0
1
2
3
4
5
6
7
8
9
10
11
12
13
14
15
16
17
18
19
20
17.00
17.20
17.40
Time (hours - GMT)
PRESSURE: 928.8 MB

Figure 6

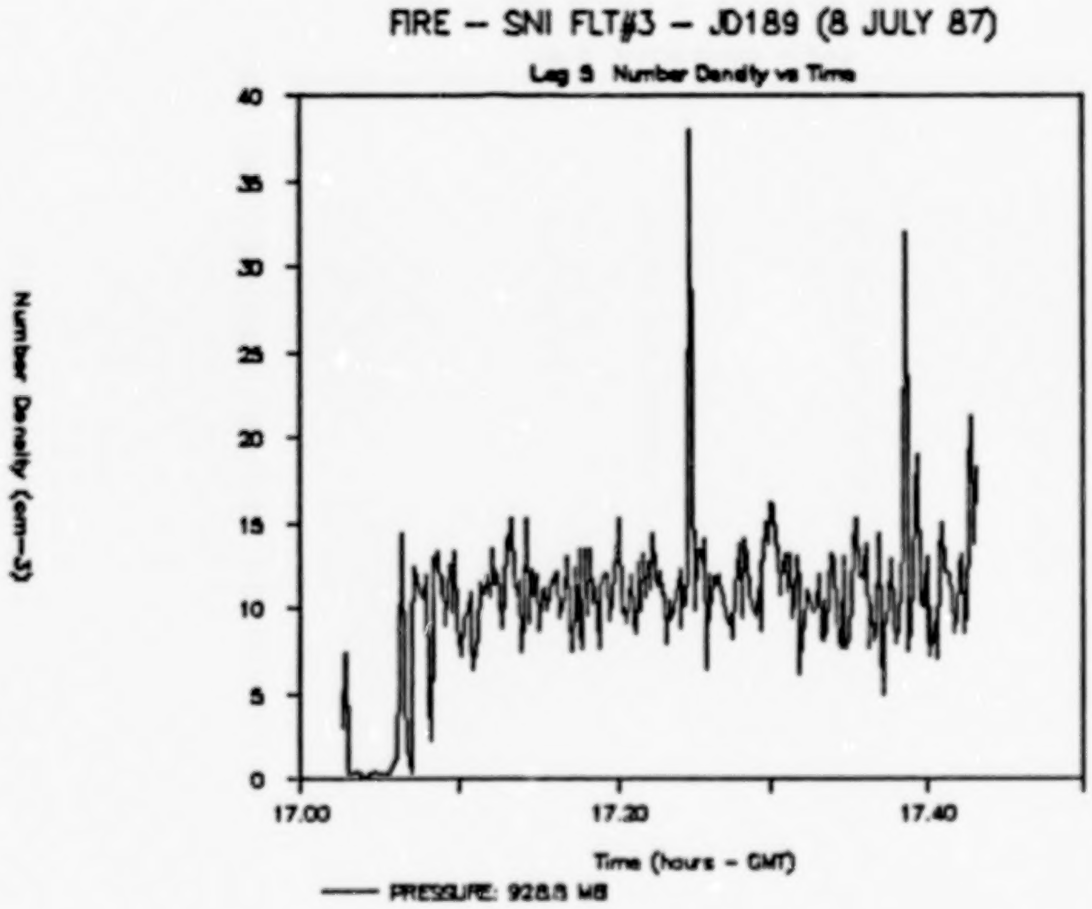
FIRE – SNI FLT#3 – JD189 (8 JULY 87)
Leg 5 Number Density vs Time
Number Density (cm−3)
40
35
30
25
20
15
10
5
0
17.00
17.20
17.40
Time (hours – GMT)
PRESSURE: 928.5 MB

Figure 7

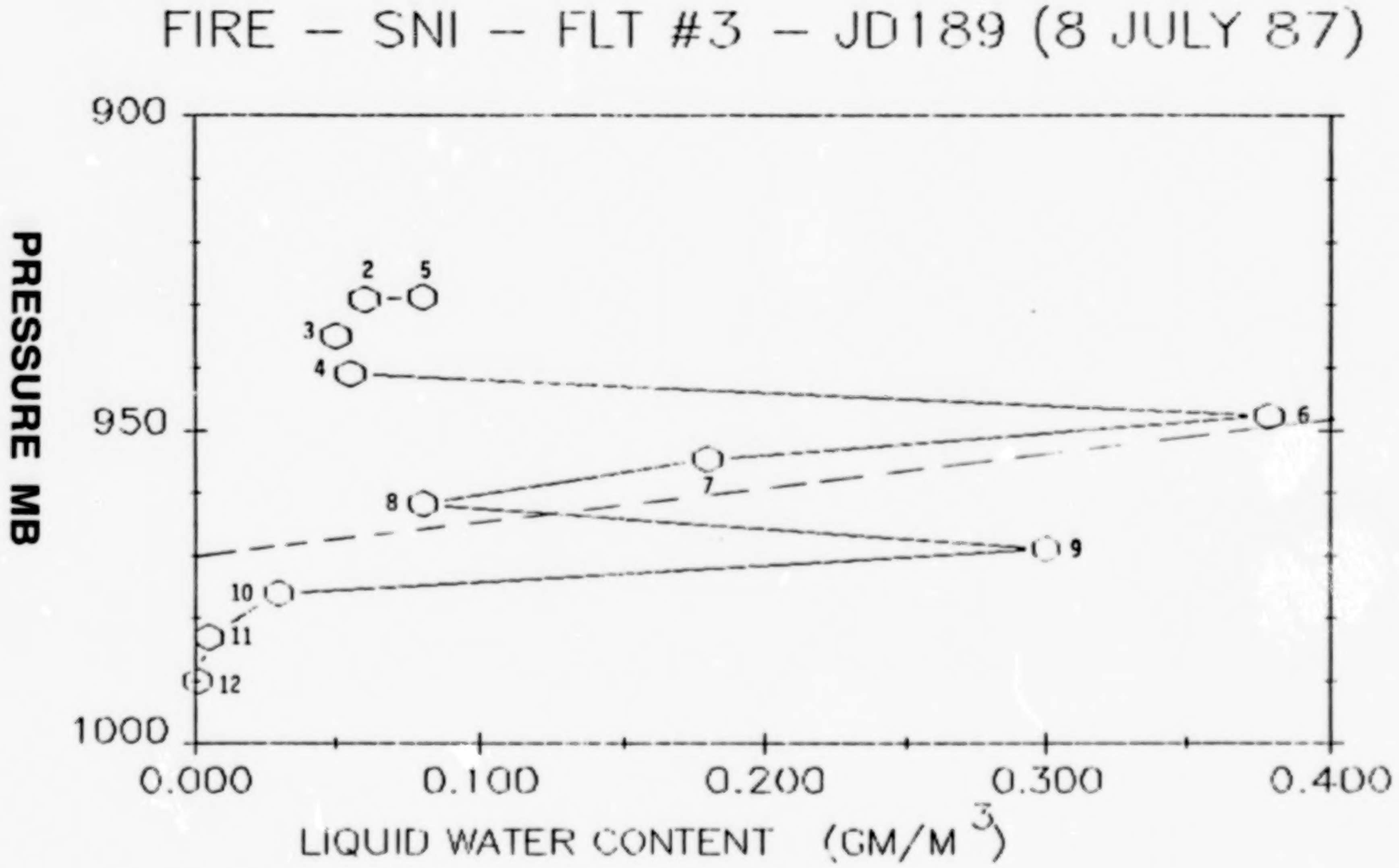
FIRE – SNI – FLT #3 – JD189 (8 JULY 87)
PRESSURE MB
900
950
1000
0.000
0.100
0.200
0.300
0.400
LIQUID WATER CONTENT (GM/M^3)
2
5
3
4
6
7
8
9
10
11
12

Figure 8

35-3

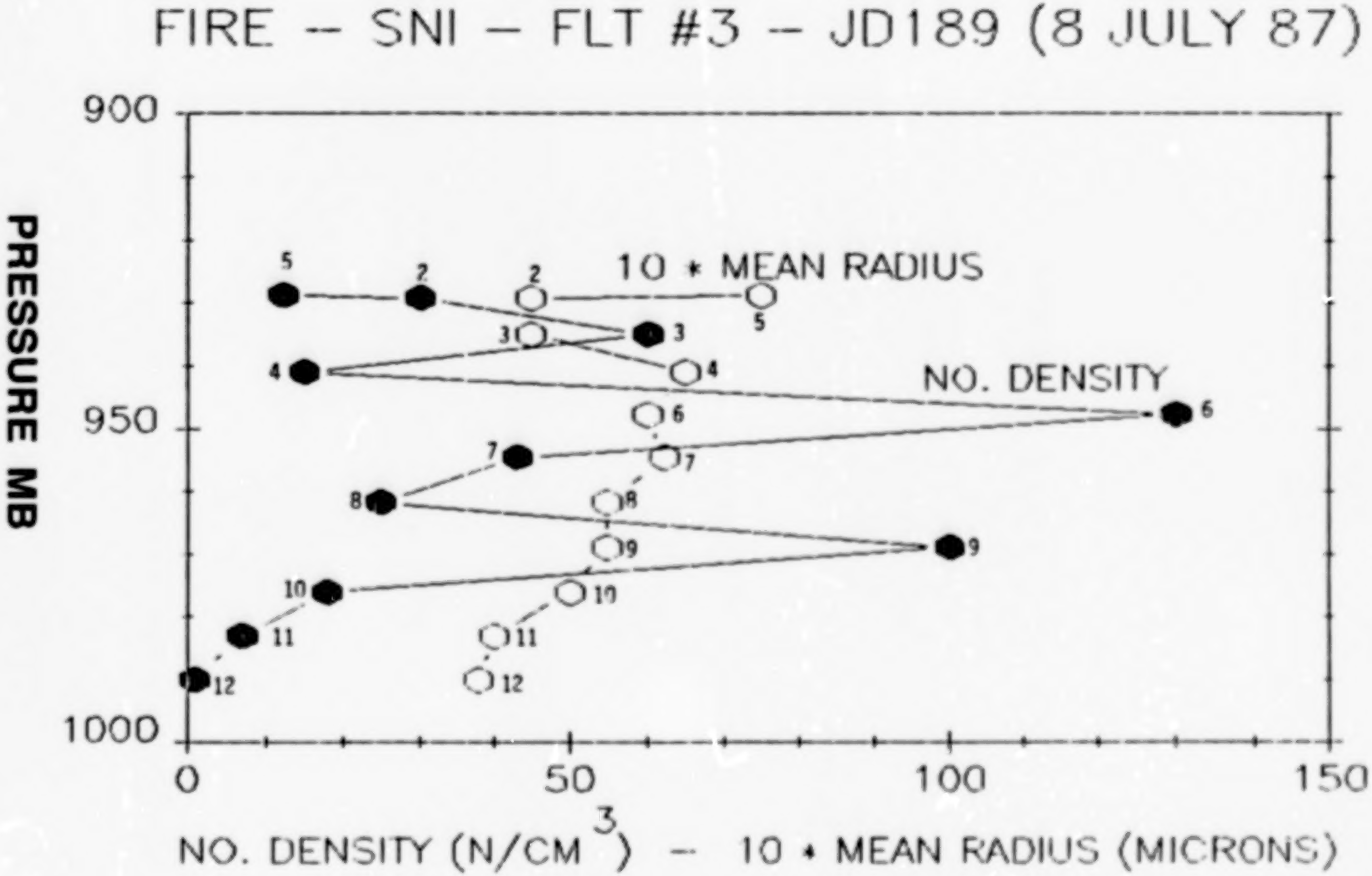
FIRE -- SNI - FLT #3 - JD189 (8 JULY 87)
PRESSURE MB
900
950
1000
0
50
100
150
NO. DENSITY (N/CM^3) - 10 * MEAN RADIUS (MICRONS)
10 * MEAN RADIUS
NO. DENSITY
2
3
4
5
6
7
8
9
10
11
12

Figure 9

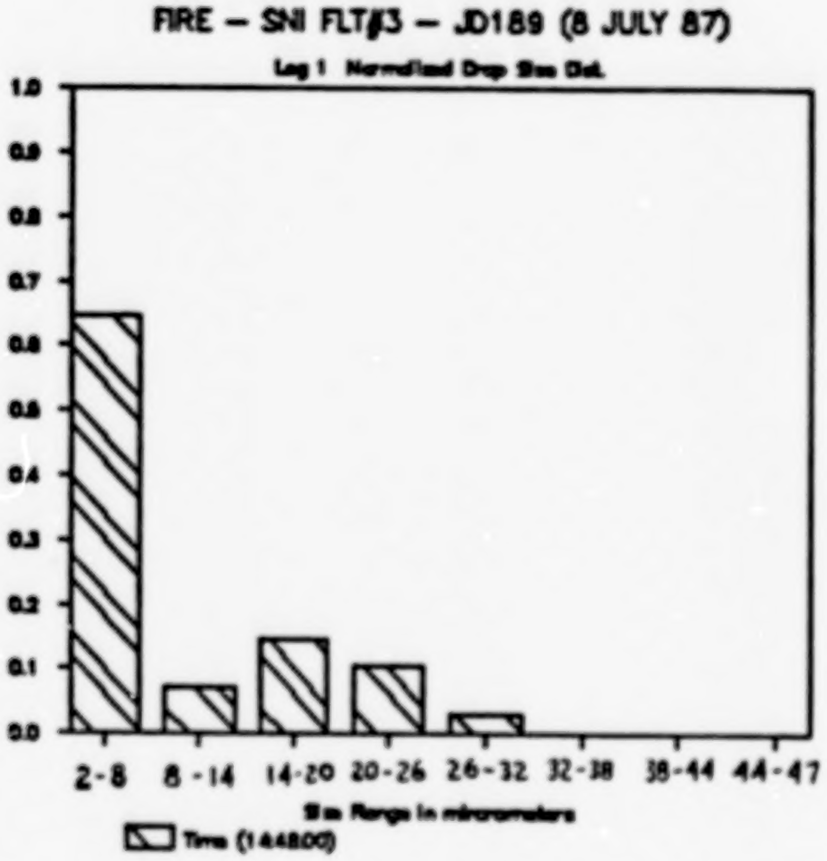
FIRE – SNI FLT#3 – JD189 (8 JULY 87)
Leg 1 Normalized Drop Size Dist.
1.0
0.9
0.8
0.7
0.6
0.5
0.4
0.3
0.2
0.1
0.0
2-8
8-14
14-20
20-26
26-32
32-38
38-44
44-47
Size Range in micrometers
▨ Time (144800)

Figure 10

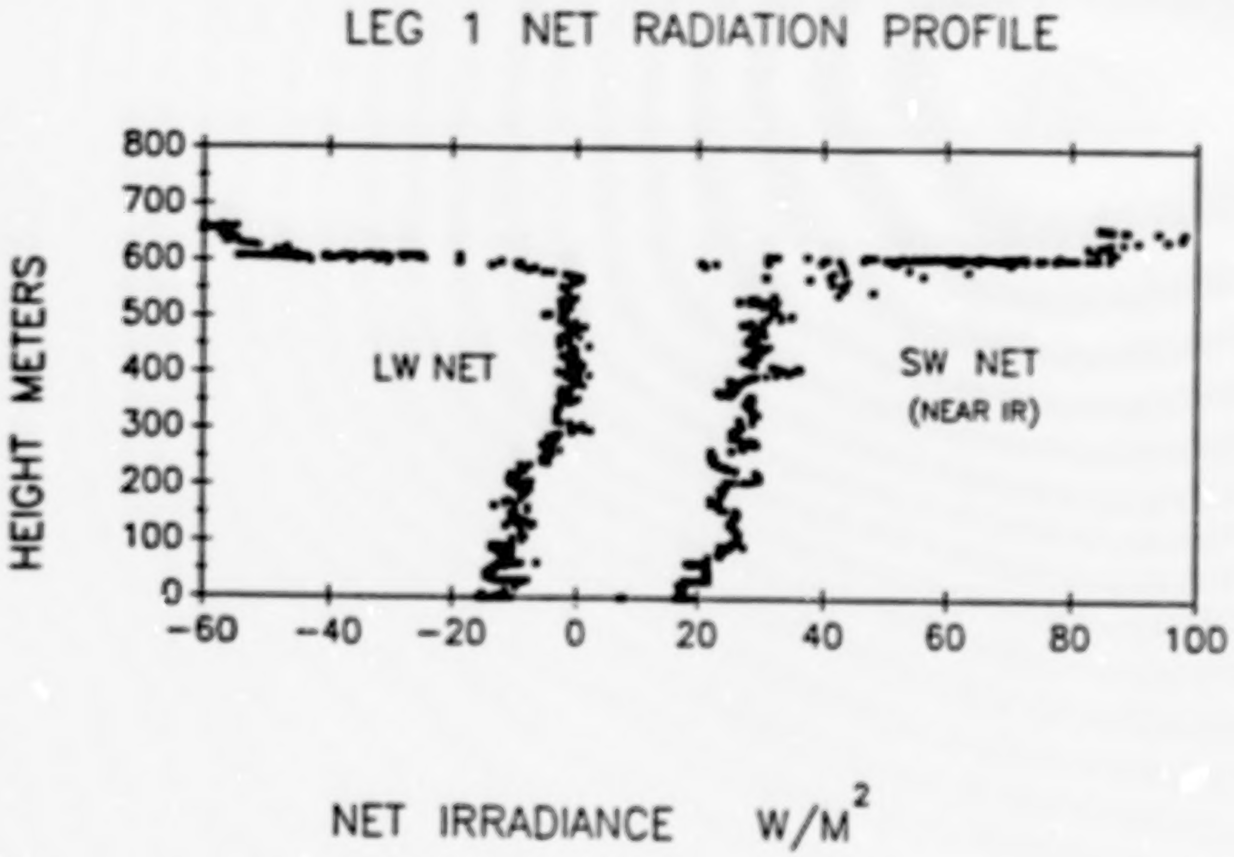

Figure 11

Table 1

RADIATION STATISTICS FOR DATA LEGS 2, 3 AND 4

Pres. mb		SW DN Wm^{-2}	SW UP Wm^{-2}	NIR DN Wm^{-2}	NIR UP Wm^{-2}	ALB TOT %	ALB NIR %	ALB VIS %	SW TOT NET Wm^{-2}	LW NET Wm^{-2}
920	Ave	616.0	437.0	296.2	199.8	71.0	67.5	74.2	179.0	-56.8
	SD	23.7	22.9	12.1	10.8	2.2	2.2	2.2	14.4	2.1
930	Ave	711.0	519.2	344.0	241.0	73.1	70.1	75.9	191.8	-53.5
	SD	30.0	25.1	15.0	12.4	2.7	2.6	2.8	23.4	5.1
942	Ave	618.0	364.0	294.7	173.1	59.4	59.3	59.6	253.9	0.1
	SD	85.8	57.0	42.5	27.0	9.2	8.8	9.5	78.0	4.3

TURBULENCE MEASUREMENTS USING TETHERED BALLOON INSTRUMENTATION

DURING FIRE '87

Phillip Hignett
Meteorological Research Unit
RAF Cardington
Bedfordshire MK42 0TH
U.K.

As part of the surface-based observations conducted on San Nicolas Island the U.K. Meteorological Office operated a set of turbulence probes attached to a balloon tether cable. Typically six probes were used, each capable of measuring momentum, heat and humidity fluxes. Two probes were fitted with net radiometers, one positioned above cloud and the other below; a third probe carried a Lyman-alpha hygrometer fitted with a pre-heater for the measurement of total water content.

Some preliminary results will be presented from the 14th July describing the variation in structure of the cloudy boundary layer during the daytime. This day was characterised by a complete cloud cover, an inversion height of ≈ 600m. and north-westerly winds of ≈ $6 m.s.^{-1}$. As an illustration the equivalent potential temperature derived from a profile ascent made between ≈ 0830 and 0930 (PDT) is shown in figure 1. The data has been smoothed to a height resolution of about 4 metres. At this time the cloud base was ≈ 200m. and very light drizzle was reaching the surface. In figure 2 are shown the vertical velocity variance and potential temperature flux for two periods; the first (shown by full lines) immediately follows the profile and the second (shown by dashed lines) is central around 1400 (PDT). The data have been normalised by their maximum values in the first period. Cloud base has now risen to ≈ 300m. There is a marked variation during the morning, particularly in sigma w. The net radiative flux above cloud top has by now reached its maximum value.

BLANK PAGE

Figure 1

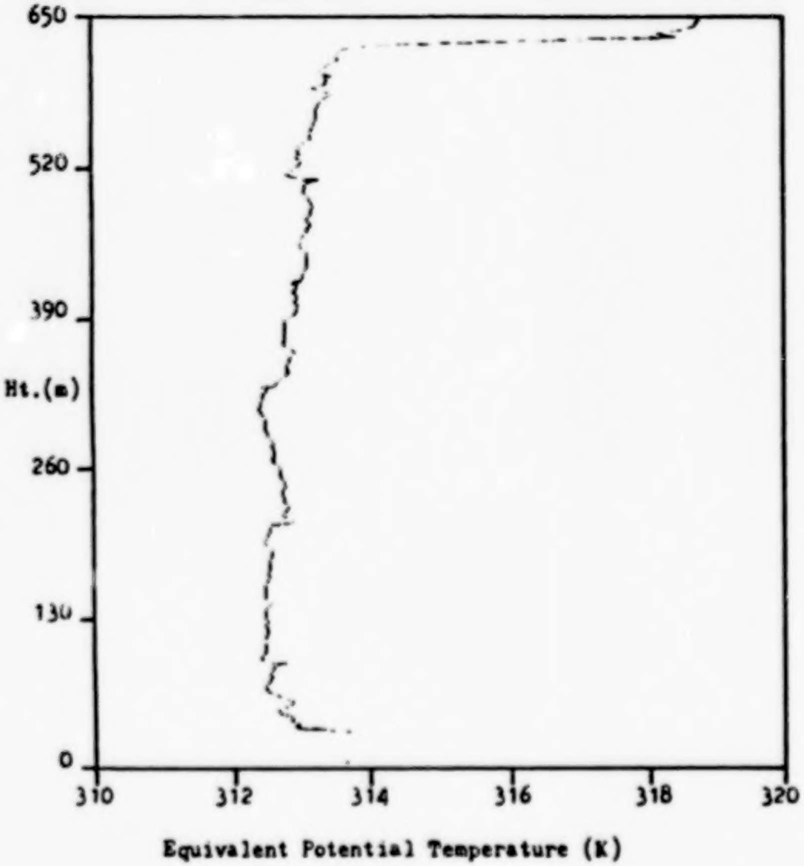

Figure 2

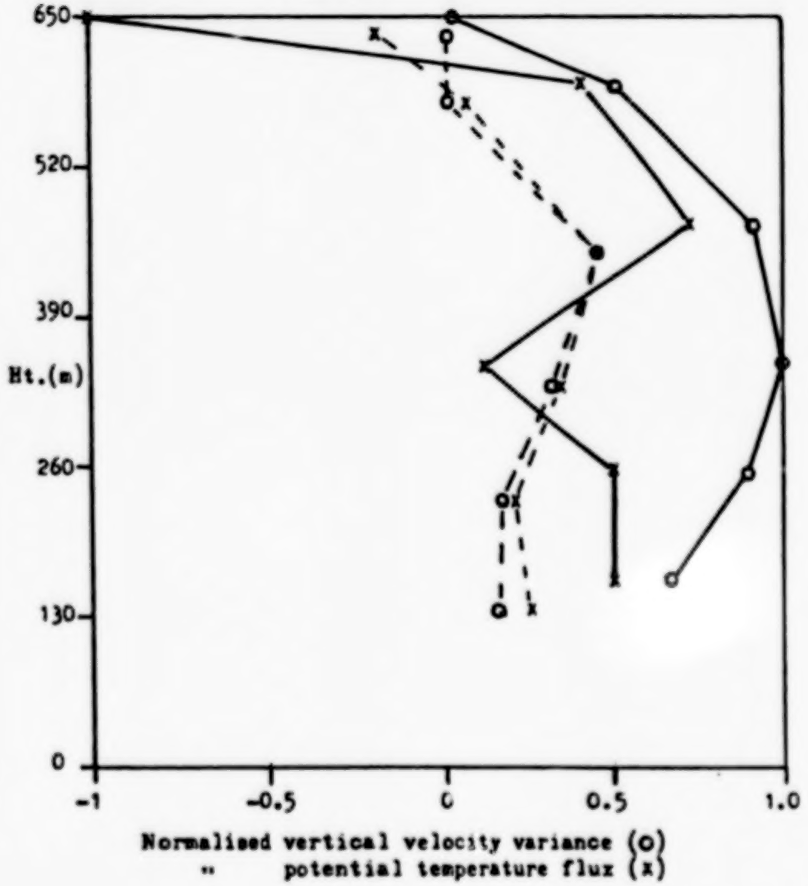

HORIZONTAL VARIABILITY OF THE MARINE BOUNDARY LAYER STRUCTURE UPWIND OF SAN NICOLAS ISLAND DURING FIRE, 1987

Douglas R. Jensen
Code 543
Naval Ocean Systems Center
271 Catalina Blvd.
San Diego, CA 92152

INTRODUCTION

During the months of June and July 1987 the Marine Stratocumulus Intensive Field Observation Experiment of FIRE was conducted in the Southern California offshore area in the vicinity of San Nicolas Island. The Naval Ocean Systems Center (NOSC) airborne platform was utilized during FIRE to investigate the upwind low level horizontal variability of the marine boundary layer structure to determine the representativeness of SNI-based measurements to upwind open ocean conditions. The NOSC airborne meteorological platform made three flights during FIRE, two during clear sky conditions (19 & 23 July), and one during low stratus conditions (15 July). This paper addresses the boundary layer structure variations associated with the stratus clouds of 15 July 1987.

The prescribed flight pattern for the NOSC aircraft consisted of two upwind radial legs as shown in Figure 1. On each of the radials constant altitude flights were made at altitudes of 100ft and at 4000ft with spirals at each radial end point and midpoint. Parameters recorded by the NOSC aircraft included air temperature (AT), relative humidity (RH), sea surface temperatures (SST), cloud top temperatures (CTT), and aerosol extinction profiles. All flights were coordinated with the SNI ground based platforms and the NPS Research Vessel Point Sur to ensure simultaneous measurements.

MEASUREMENTS

Air temperature profiles taken at the four spirial locations (WP#1-4, Figure 1) are shown in Figure 2. The surface AT at SNI was lower than those measured upwind and did not increase linearly with upwind distance from SNI. Above 300m (within the haze/cloud layer) the AT at the island was bounded above and below by the upwind profiles. The inversion heights at all four locations were essentially the same. A sharper inversion did exist however at SNI.

Profiles of relative humidity are shown in Figure 3. The highest surface RH existed at SNI (97%) with the minimum (90%) at WP#2. These corresponded to the lowest and highest AT's respectively. Above 200m and below the stratus tops the SNI RH profile is bounded above and below by the upwind profiles. Just below the stratus tops the RH's at all spiral locations were within a few percent of each other.

Figure 4 shows the average weighted aerosol radius (RBAR) as a function of altitude for the aerosol profiles taken at each waypoint. At the surface the upwind RBAR values were between 0.3 and 0.4 m while at SNI RBAR was an order of magnitude higher. Above 300m and below the stratus tops the SNI RBAR profile is bounded by upwind profiles. The corresponding extinction coefficients calculated using MIE theory (0.53 m), Figure 5, shows a surface extinction coefficient at SNI to be one hundred times greater than that at the other upwind waypoints. This difference is strictly a SNI surface related phenomena since the RBAR versus altitude profiles show a rapid decrease in extinction with altitude. Within the stratus cloud deck (above 300m) the cloud aerosol extinction varied by as much as a factor of ten between waypoints. The variation was not necessarily in any wind related pattern.

The total integrated optical depth for 0.53 m as a function of altitude is shown in Figure 6 for each waypoint. The higher optical depths occurred upwind of SNI at waypoints 3 and 4. At SNI where the surface aerosol extinction was the highest, the total optical depth was next to the lowest. The major contribution to the optical depth occurred within the top 100 meters of the stratus deck. Aerosols below this height did contribute but not as significantly as did the stratus top. This is evidenced by the slight increase in the optical depth at the bottom of the SNI profile which resulted from a large increase in the number of surface based aerosols (Figures 5 and 6).

Horizontal profiles of sea surface temperatures, example in Figures 7, showed a general trend toward warmer water upwind of SNI. Large fluctuations of SST's were superimposed on this general warming trend with scale sizes in the order of 5 to 10 nmi. In general the sea surface temperatures were warmer than the air temperatures.

Cloud top temperature profiles showed CTT's decreasing upwind of SNI in contrast to the SST observations. This decrease in upwind CTT's was thought to be caused by vertical mixing (SST warmer than the AT) thus resulting upwind stratus tops being at a higher elevation. However, stratus tops were within 100ft over the entire flight pattern.

CONCLUSIONS

Profiles of AT and RH taken 'at' and 'upwind' of SNI do show differences between the so called open ocean conditions and those taken near the island. However, the observed difference cannot be uniquely identified to island effects, especially since the upwind fluctuations of AT and RH bound the SNI measurements.

Total optical depths measured at SNI do not appear to be greatly effected by any surface based aerosol effects created by the island and could therefore realistically represent open ocean conditions. However, if one were to use the SNI aerosol measurements to predict ship to ship EO propagation conditions, significant errors could be introduced due to the increased number of surface aerosols observed near SNI which may not and were not characteristic of open ocean conditions.

Sea surface temperature measurements taken at the island will not in general represent those upwind open ocean conditions. Also, since CTT's varied appreciably along the upwind radials, measurements of CTT over the island may not be representative of actual open ocean CTT's.

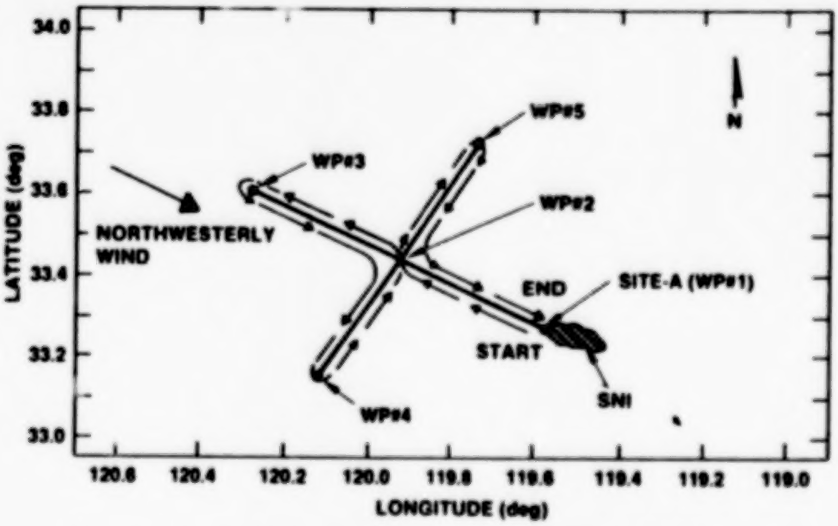
34.0
33.8
33.6
33.4
33.2
33.0
LATITUDE (deg)
WP#5
N
WP#3
WP#2
NORTHWESTERLY WIND
END
SITE-A (WP#1)
START
SNI
WP#4
120.6
120.4
120.2
120.0
119.8
119.6
119.4
119.2
119.0
LONGITUDE (deg)

Figure 1. NOSC prescribed flight pattern.

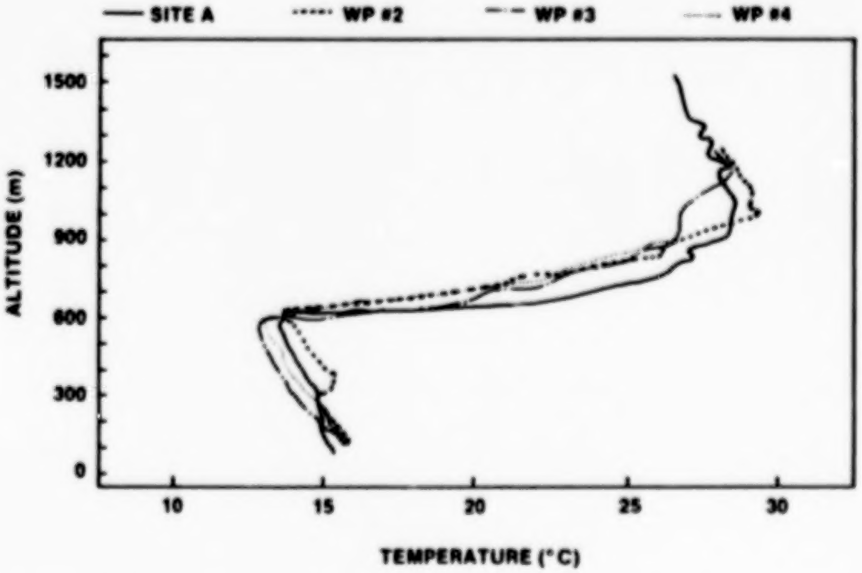

Figure 2. Air temperature profiles.

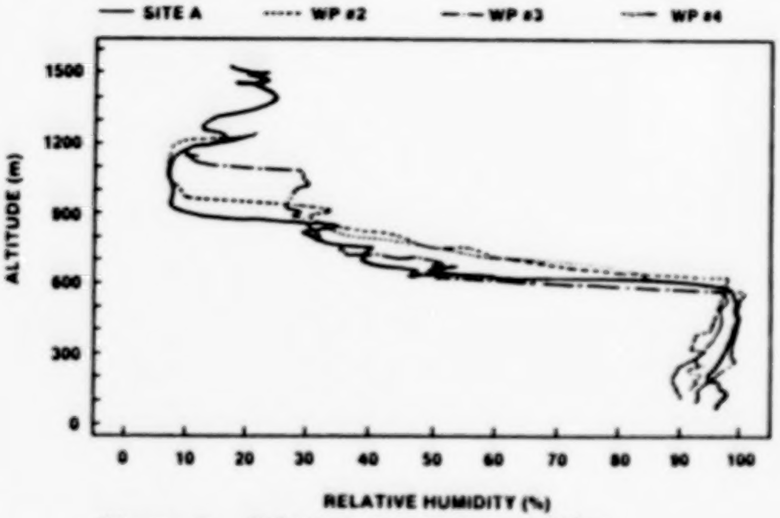

Figure 3. Relative Humidity profiles.

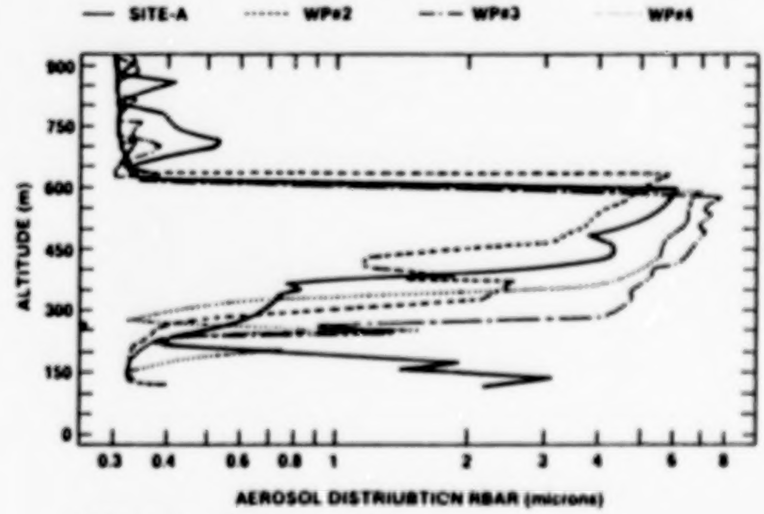

Figure 4. RBAR profiles.

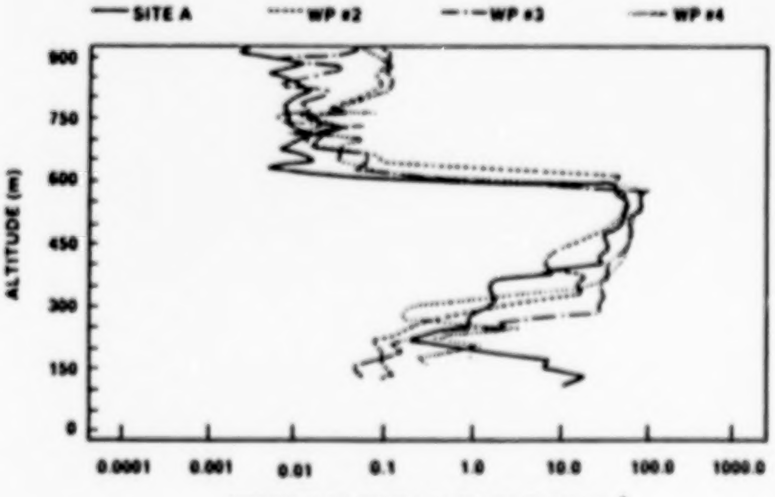

Figure 5. Aerosol extinction profiles.

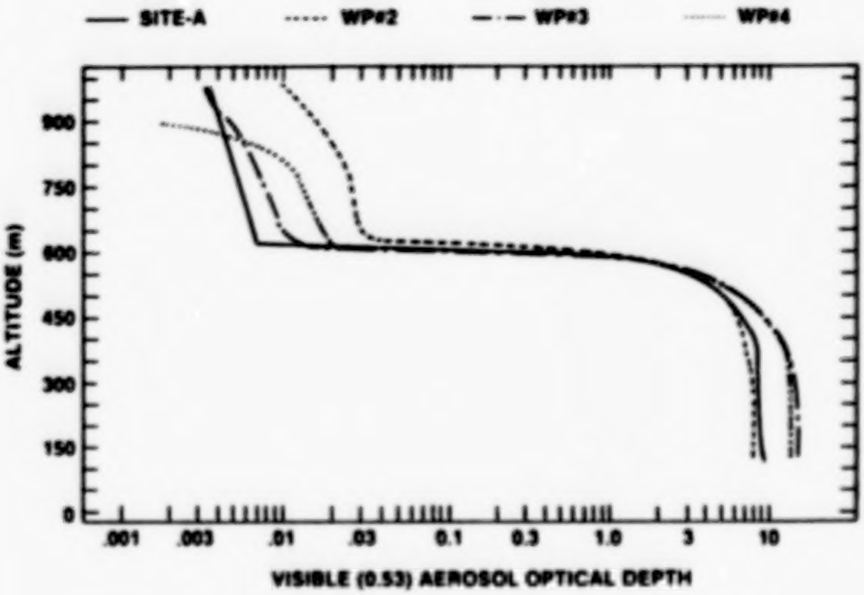

Figure 6. Optical depth profiles.

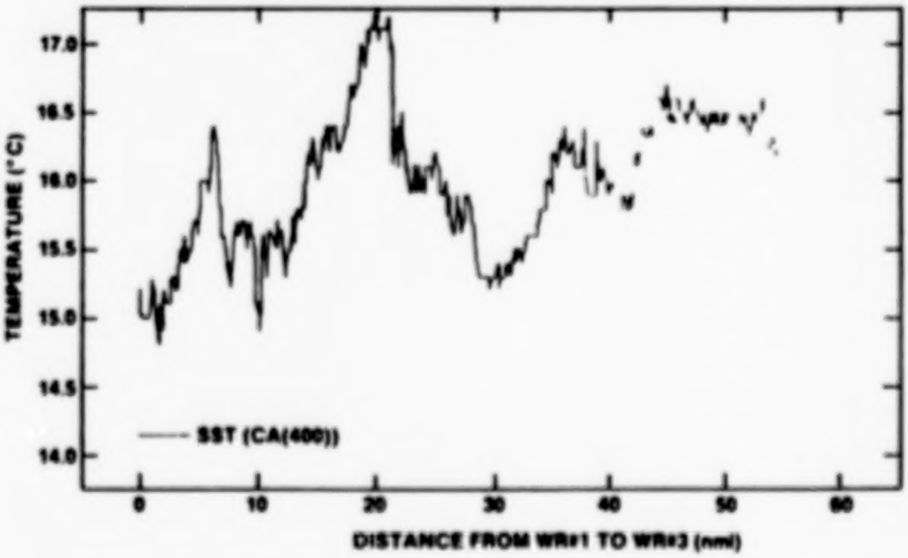

Figure 7. Sea surface temperature profiles.

An Overview of UK C130 Observations from the FIRE Marine Stratocumulus IFO

S Nicholls, J Leighton, R Barlow

Cloud Physics Branch
Meteorological Office, London Road, Bracknell, Berks RG12 2SZ, UK

An overview of the characteristics of the ten flights made by the C130 during the IFO will be presented. An indication of data quality will be given. Comparisons of the CO_2 radiation thermometer and the Rosemount suggest there may be potentially serious wetting problems with the latter, especially close to cloud base.

The main features of the cloud layers sampled by the C130 will be summarized, including microphysical parameters. Many of the results shown will be derived from a first order analysis of turbulence quantities. The gross vertical variation of heat, vapour and liquid water fluxes from case to case, together with the observed vertical velocity variance, a good indicator of convective activity, will be discussed. Preliminary results suggest that the different cases can be usefully categorized using these data. The relationship between these and the measured boundary conditions will also be mentioned. Similarities and differences between the various cases will be highlighted, and interpreted in terms of our current understanding of stratocumulus. Attention will be given to particular features of the various flights which may deserve more intensive study.

The degree to which our present understanding can explain the observed features will be discussed and outstanding problems eg the inversion layer structure, spatial variability and broken cloud cases will be briefly addressed.

BOUNDARY LAYER ROLL CIRCULATIONS DURING FIRE

Hampton N. Shirer and Tracy Haack
Department of Meteorology
The Pennsylvania State University
University Park, PA 16802

The probable mechanisms underlying the development of boundary layer roll circulations are studied using wind and temperature profiles measured by the NCAR Electra during the stratocumulus phase of the FIRE experiment. The expected, or preferred, roll orientations, horizontal wavelengths and propagation periods are determined by finding the minimum values of the dynamic and thermodynamic forcing parameters, which here are the eddy Reynolds number Re and moist Rayleigh number Ra_m. These minimum values depend on the height z_T of the capping temperature inversion and on the values of the Fourier coefficients of the background height-dependent vector wind profile. As input to our nonlinear spectral model, descent and ascent runs by the Electra provide good initial estimates of the inversion height and the wind profiles. In the first phase of the investigation presented here, a mechanism is said to be a probable contributor to the development of roll circulations within the stratocumulus-topped boundary layer if the modeled roll orientations and wavelengths agree with their observed values.

Possible mechanisms for roll development are the well-known thermal and inflection point instability mechanisms (e.g. Brown, 1980) and the recently identified shear instability mechanism of Haack-Hirschberg (1988). The first mechanism leads to thermal modes dominated by one wavenumber in the vertical, while the second two lead to dynamic modes requiring two wavenumbers in the vertical. Several low-order spectral models that are capable of accepting observed data for determination of the expected modes have been developed at Penn State; these include the pure thermal model of Shirer (1986), the pure inflection point model of Stensrud and Shirer (1988), and the mixed thermal/dynamic model of Haack-Hirschberg (1988). Linear analyses of the solutions to these models produce estimates of the preferred values of the orientation angles, horizontal wavelengths, and dimensionless frequencies for the above three modes, and these values can be readily compared with observations.

Preliminary results using the 14-coefficient model of Haack-Hirschberg (1988) are discussed for the 7 July 1987 Electra Mission 188-A (Flight 5). This mission was flown across a sharp cloud boundary that was within a Landsat/SPOT scene (Kloesel et al., 1988). The stratocumulus deck was relatively solid in the eastern part of the scene, while there was a rapid decrease in cloud cover to scattered cumulus clouds aligned in streets to the west. These cloud streets were oriented nearly parallel to the mean wind direction in the layer, which was approximately 340°. The hypothesis that roll circulations occurred in both the relatively clear and the cloudy regions is investigated using as model input a descent profile obtained in the relatively clear air and an ascent profile obtained in the cloudy air. Initial results for the clear air case are that the pure inflection point mode is not possible and the pure thermal mode was oriented 35° to the right of the mean wind direction. The origin of this unacceptably large discrepancy between the observed and modeled results will be investigated further and the conclusions reported at the next FIRE workshop.

The results for the cloudy case are more promising. In Fig.1 are shown the measured cross-roll U_M and along-roll V_M wind components (jagged curves), together with the fit to the data implied by the model representation (smooth curves). Clearly the limited resolution of the 14-coefficient model is able to represent the observations rather well. As shown by the solid and dashed lines in Fig. 2, two thermal modes are possible in this case. The quadrilateral in Fig. 2 encloses the estimated range of observed values of Re and Ra_m, where $Re = |\underline{V}(z_T)|z_T/(\pi\nu)$, $Ra_m = g z_T^3 \Delta_z T/(\nu\kappa T_{00}\pi^4)$, $|\underline{V}(z_T)|$ is the wind at the inversion base z_T, ν and κ are the eddy viscosity and thermometric conductivity respectively, and $\Delta_z T$ is a combined measure of the sea surface/air temperature difference and the environmental lapse rate of equivalent potential temperature. The mode whose transition curve passes to the left of the estimated range of observed values for Ra_m and Re is associated with orientations that are 10^0 to the right of the mean wind direction (335°); this preferred orientation angle β_p is 75° south of east, or -75°. The expected aspect ratio a_p of 0.6 corresponds to a horizontal roll wavelength $L = 2z_T/a_p$ of approximately 2500 m. This value of L is consistent with the wavelengths found from preliminary vertical velocity spectra for the horizontal flight leg between the descent and ascent profiles. Finally the dimensionless frequency ω_p of 31.7 corresponds to a propagation period of approximately 30 minutes. Thus, the model results suggest that a thermally driven roll circulation supported the stratocumulus clouds observed on 7 July 1987.

Acknowledgments. Mark Laufersweiler helped us read the FIRE data tapes using a program written by Jeff Nucciarone, who also computed the preliminary vertical velocity spectra. The research reported here was partially supported by the National Science Foundation through Grant ATM- 8619854 and by the Office of Naval Research through Contract N000014-86-K-06880.

References

Brown, R.A., 1980: Longitudinal instabilities and secondary flows in the planetary boundary layer. A review. Rev. Geophys. Space Phys., 18, 683-697.

Haack-Hirschberg, 1988: Boundary layer roll circulations in a stratified atmosphere. M.S. Thesis, Department of Meteorology, Penn State University, 161 pp.

Kloesel, K.A., B.A. Albrecht, and D.P. Wylie, 1988: FIRE marine stratocumulus observations--summary of operations and synoptic conditions. FIRE Technical Report Number 1, Department of Meteorology, Penn State University, 171 pp.

Shirer, H.N., 1986: On cloud street development in three dimensions: Parallel and Rayleigh instabilities. Contrib. Atmos. Phys., 59, 126-149.

Stensrud, D.A. and H.N. Shirer, 1988: Development of boundary layer rolls from dynamic instabilities. J. Atmos. Sci., 45, 1007-1019.

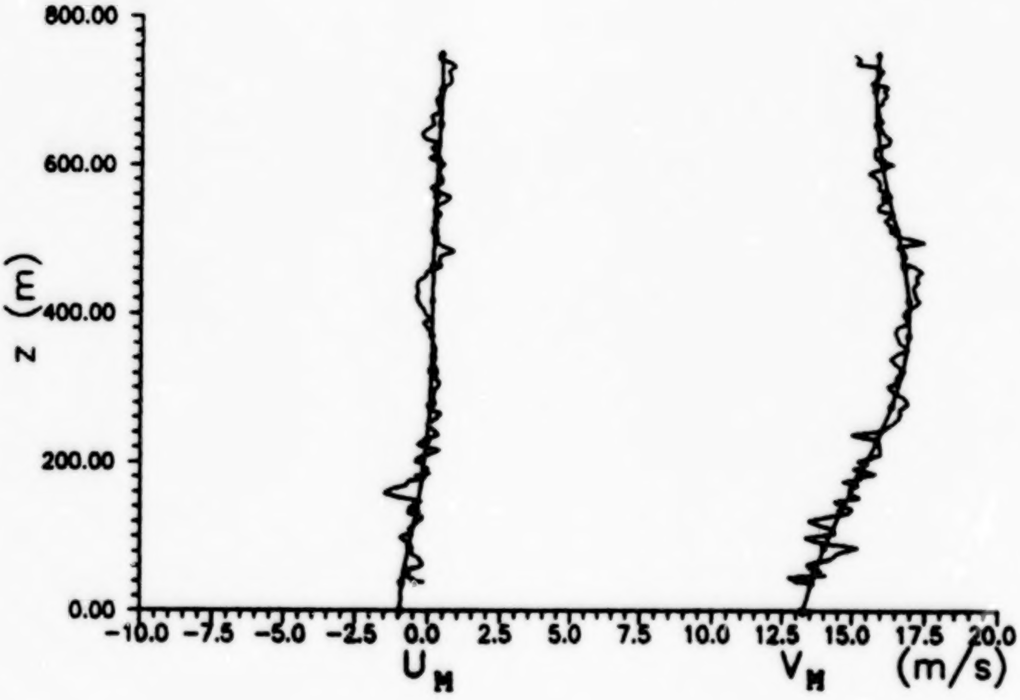

Figure 1. Cross-roll U_M and along-roll V_M wind profiles (jagged curves) measured by the NCAR Electra in the stratocumulus region on 7 July 1987 (Flight 5) between 2154:43 and 2156:49 UTC. The cross-roll, or x-, direction is 65° (~ENE), so that negative values correspond to winds having directions less than 335°. The representation of the data by the model is shown by the smooth curves.

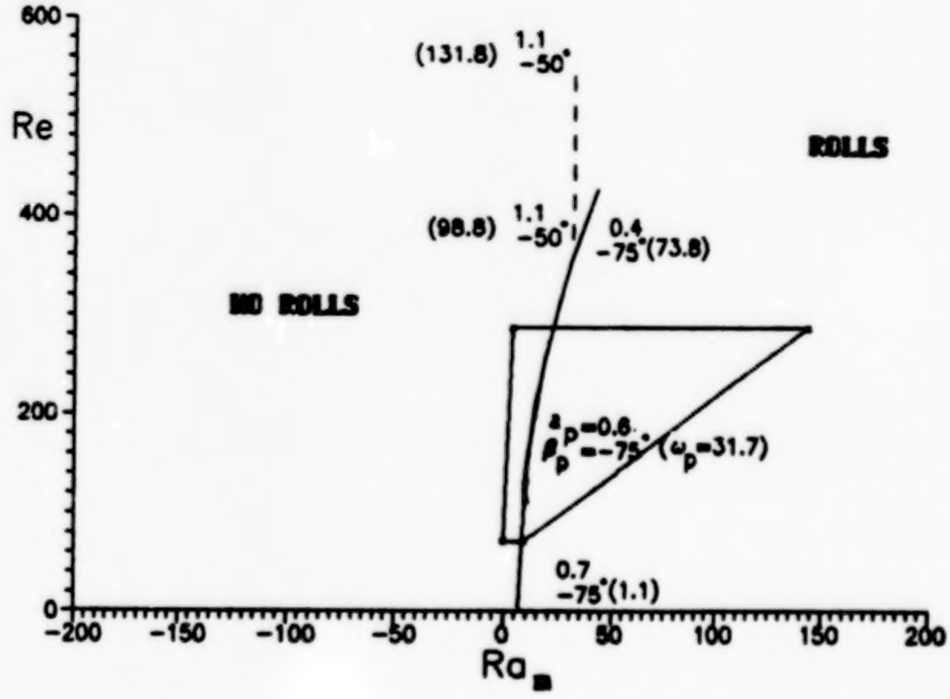

Figure 2. Results from the model analysis. The solid and dashed lines denote the transition curves for the two thermal modes supported by the observed wind profile given in Fig. 1. The numbers next to these curves denote the preferred orientation angle β_p, the aspect ratio a_p and the dimensionless frequency ω_p (in parentheses). The quadrilateral encloses the values of the moist Rayleigh number Ra_m and Reynolds number Re that are estimated to characterize the observed stratocumulus regime. These vertices are given approximately by $(Ra_m, Re) = (0,70)$; $(10,70)$; $(145,285)$; $(5,285)$. Here $z_T = 750$ m and ν and κ vary between 10 m^2/s and 50 m^2/s.

Winds and Turbulence above San Nicolas Island during FIRE

Allen B. White, William J. Syrett, Christopher W. Fairall
and Dennis W. Thomson

Penn State University
Department of Meteorology
University Park, PA 16802

Winds and turbulence above San Nicolas Island were continuously monitored during FIRE with a Doppler sodar (1600 Hz) and UHF (400 MHz) wind profiler. Individual profiles were logged from 1 through 19 July 1987 at 30 sec to 2 min intervals; preliminary processing of hourly averaged winds from 100 to 2300 m is complete. These wind profiles have been combined with intermittent radiosonde profiles to construct time-height sections of parameters such as the Richardson Number. Analysis now in progress includes interpretation of the sodar (C_T^2) and profiler (C_N^2, C_q^2) reflectivity profiles. These profiles are being combined with radiometric and ceilometer data for investigations of vertical transport and cloud base/top entrainment processes. Finally, by using the SNI data in conjunction with soundings made from the research vessel Pt. Sur, the relationship between changes in the SNI winds and mesoscale and synoptic-scale weather features is being investigated.

FIRE SCIENCE TEAM MEETING
VAIL, COLORADO
JULY 11-15, 1988

MARINE STRATOCUMULUS

MARINE STRATOCUMULUS POSTER SESSION - David A. Randall Thursday, July 14, 1988

PAGE

ER-2 Lidar Measurements of Stratocumulus Cloud Top Structure on July 14, 1987 375
Boers, Reinout; and James D. Spinhirne

Dependence of Marine Stratocumulus Reflectivities on Liquid Water Paths 377
Coakley, Jr., J. A.; and J. B. Snider

Near Infra-red Radiances Observed by the UK C130 Multi-channel Radiometer During the Marine Stratocumulus IFO and Preliminary Comparison with Model Calculations 383
Foot, J. S.

Plume Mechanics and Stratocumulus Convection 393
Hanson, Howard P.

FIRE Extended Time/Limited Area Observations at Palisades, New York 397
Robinson, David A.; George Kukla, and Allan Frei

Measurements of the Light-Absorbing Material Inside Cloud Droplets and its Effect on Cloud Albedo 403
Twohy, C. H.; A. D. Clarke, S. G. Warren, L. F. Radke, and R. J. Charlson

Preliminary Results of Radiation Measurements from the Marine Stratus FIRE Experiment 409
Valero, Francisco P. J.; Philip D. Hammer, Thomas P. Ackerman, Warren J. Y. Gore, and Melinda L. Weil

Third Generation Earth Radiation Budget Measurements; ERBE in the Context of Earlier Systems 411
Vonder Harr, Thomas H.

San Nicolas Island Surface Radiation - Meteorology Data 417
Johnson-Pasqua, Christopher M.; and Stephen K. Cox

A Cloud Classification Scheme Applied to FIRE Stratocumulus Data ***
Khalsa, Siri Jodha Singh; and Catherine Gautier

Determination of Cloud Radiative and Microphysical Parameters from Airborne Radiation Measurements ***
King, M. D.; T. Nakajima, J. D. Spinhirne, P. V. Hobbs, and L. F. Radke

Mean and Turbulent Boundary Layer Measurements for a Tethered Balloon ***
Hignett, Phil

Marine Stratocumulus Cloud Characteristics from Multichannel Satellite Measurements ***
Durkee, P. A.; and G. M. Mineart

FIRE SCIENCE TEAM MEETING
VAIL, COLORADO
JULY 11-15, 1988

MARINE STRATOCUMULUS

MARINE STRATOCUMULUS POSTER SESSION (Cont'd) - David A. Randall Thursday, July 14, 1988

PAGE

Initial Analyses of GOES VISSR Data for Marine Stratocumulus IFO and ETO ***
Minnis, Patrick; Edwin F. Harrison, and D. F. Young

Analysis of Tethered Balloon Data from San Nicholas Island on 8 July 1987 ***
Cox, Stephen K.; David P. Duda, Christopher M. Johnson-Pasqua, Wayne H. Schubert, and Jack B. Snider

ER2-lidar measurements of stratocumulus cloud top structure on July 14, 1987

Reinout Boers and James D. Spinhirne

NASA/Goddard Space Flight Center
code 617
Greenbelt, MD 20771

On July 14, 1987 NASA's ER2-high altitude aircraft flew a mission to measure the structure of stratocumulus clouds off the coast of California. A flight pattern was executed so that the two-dimensional variability of the clouds could be detected.
The technique of analysis of the lidar data to measure cloud tops is as follows: First each signal is searched for its maximum in return strength. This maximum is caused by scattering of the laser light off cloud particles or from the ocean surface. Next the variance of the signal return above the level of maximum backscatter is determined. Cloud top is assigned to a level (above the level of maximum backscatter) where the backscatter exceeds the average variance. This two-step process is necessary because the level of maximum backscatter does not correspond to the cloud top. Ocean surface returns are easily separated from cloud returns in this process, descibed in detail by Boers, Spinhirne and Hart (1988).
Analysis of the data so far has shown that there were very few breaks in the clouds. Furthermore the layer top was very flat with local oscillations not exceeding 30 m. Such small cloud top variations are still well within the range of detectability, because the precision of our technique of cloud top detection has previously been established to be 13-15 m. Figure 1 shows a detailed linescan recording of the stratocumulus clouds, near one of the few breaks in the clouds. The small cloud top variability is evident, except near the break, where the sea surface return is also visible. The scale on the left is in km. The thick mark indicating the surface does not entirely correspond to the level of the surface return. This reflects the inaccuracies of determining the exact altitude based on the pressure-altitude scale.
This data is presently being analyzed to compute cloud top distributions and fractional cloudiness. The aim of this research is to relate the fractional cloudiness to the mean thermodynamic structure of the boundary layer. We plan to compute spectral scales of the cloud top variability in two dimensions to determine the orientation of the clouds with respect to the mean wind. Furthermore the lidar derived cloud top distribution will be used in the computation of the thermodynamic and radiation budget of the boundary layer.

Reference: R.Boers, J.D.Spinhirne and W.D.Hart, 1988: Lidar observations of the fine scale variability of marine stratocumulus clouds. J.Appl.Meteor, 27, June.

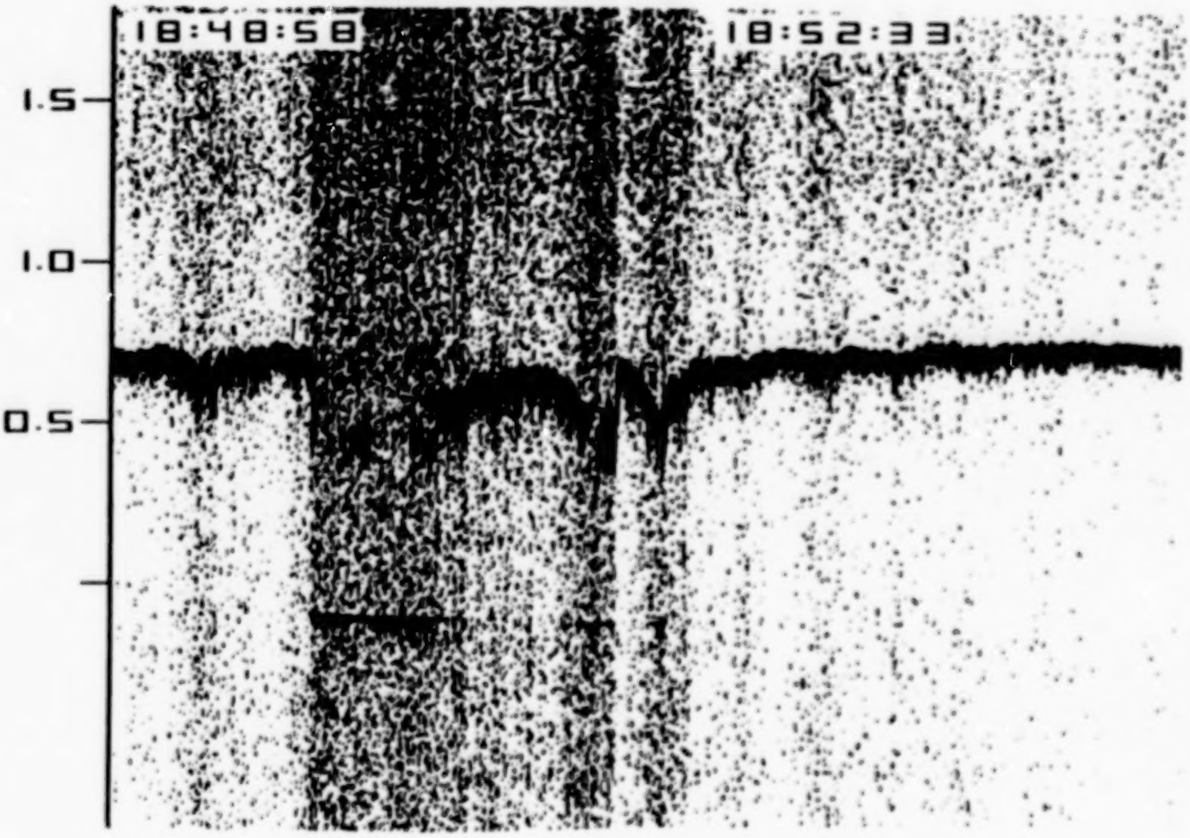

Figure 1. Linescan recording of backscatter profiles taken aboard the ER2-aircraft on July 14, 1987. The ER2 was flying at a nominal altitude of 18 km. Both cloud and sea surface reflections are visible. Pressure altitude scale is offset with respect to the ocean surface level (visible from the surface signal return).

Dependence of Marine Stratocumulus Reflectivities on Liquid Water Paths

J. A. Coakley, Jr.
National Center for Atmospheric Research

J. B. Snider
NOAA/ERL/WPL

1. Introduction

Simple parameterizations that relate cloud liquid water content to cloud reflectivity are often used in general circulation climate models to calculate the effect of clouds on the earth's energy budget. Such parameterizations have been developed by Stephens (1978) and by Slingo and Schrecker (1982) and others. Here we seek to verify the parametric relationship through the use of simultaneous observations of cloud liquid water content and cloud reflectivity. The column amount of cloud liquid water was measured using a microwave radiometer on San Nicolas Island following techniques described by Hogg et al. (1983). Cloud reflectivity was obtained through spatial coherence analysis of AVHRR imagery data (Coakley and Beckner, 1988). We present the dependence of the observed reflectivity on the observed liquid water path. We also compare this empirical relationship with that proposed by Stephens (1978).

2. Data Analysis

Estimates of the column amount of cloud liquid water or the cloud liquid water path were obtained from microwave radiometry data taken continuously on San Nicolas Island July 3-18, 1987. The data was averaged and recorded at one minute intervals. The cloud liquid water path generally shows considerable fluctuation as is shown in Fig. 1 for July 3. To allow for this variability in comparing liquid water path to satellite observed reflectivity we have used the average of the liquid water path in the hour bin associated with the satellite overpass. On most of the days for which results are reported the satellite observations indicate mostly overcast conditions for San Nicolas Island and thus the average of the near simultaneous liquid water path observations is taken to be typical of overcast conditions at the time of the overpass.

The reflectivities obtained from the 0.63 μm channels of the AVHRRs on NOAA-9 and NOAA-10 were used to derive reflectivities representative of overcast conditions. The spatial coherence method was used to identify fields of view that were completely cloud covered by the marine stratus. Average reflectivities were calculated for overcast fields of view extracted from the $(60\ \mathrm{km})^2$ subframes surrounding and including the island. These averages were taken to be representative of the clouds in the vicinity of the liquid path observations. Like the cloud liquid water path obtained from the microwave radiometer, the cloud reflectivity derived from the satellite radiances also exhibited considerable fluctuation at the $(1\ \mathrm{km})^2$ resolution of the AVHRR.

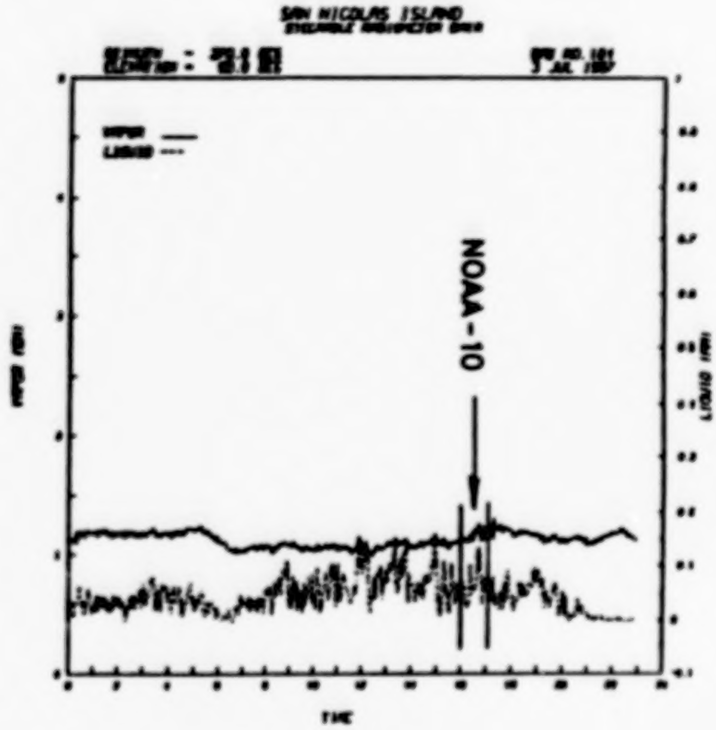

Figure 1. Column amounts of cloud liquid water and water vapor as obtained from a microwave radiometer on San Nicolas Island, July 3, 1987. Time is UTC.

3. Results

Simple two-stream and Eddington approximations to the transfer of radiation in a conservatively scattering medium show that the reflectivity, R, is given by

$$R = \frac{\beta(\tau,\mu_0)\tau/\mu_0}{1+\beta(\tau,\mu_0)\tau/\mu_0} \tag{1}$$

where, for clouds having moderate optical depths, $\beta(\tau,\mu_0)$ is a slowly varying function of τ and μ_0 (Stephens, 1978); τ is the optical depth and μ_0 is the cosine of the solar zenith angle. Comparisons of the reflectivities given by (1) with those obtained through accurate numerical methods indicate that (1) provides a rather good approximation. Neglecting for the time being the dependence of optical depth on droplet size, we take the optical depth, τ, to be linearly proportional to the cloud liquid water path, W. Thus, from the observations we expect to find the reflectivities and liquid water paths to be given by

$$1/R = A + B\mu_0/W \tag{2}$$

Fig. 2 shows $1/R$ as a function of μ_0/W for the times of the satellite overpasses when clouds were present over San Nicolas. The observations follow the expected linear relationship reasonably well. A least squares fit gives $A = 1.69$ and $B = 0.019$ with W given in precipitable millimeters.

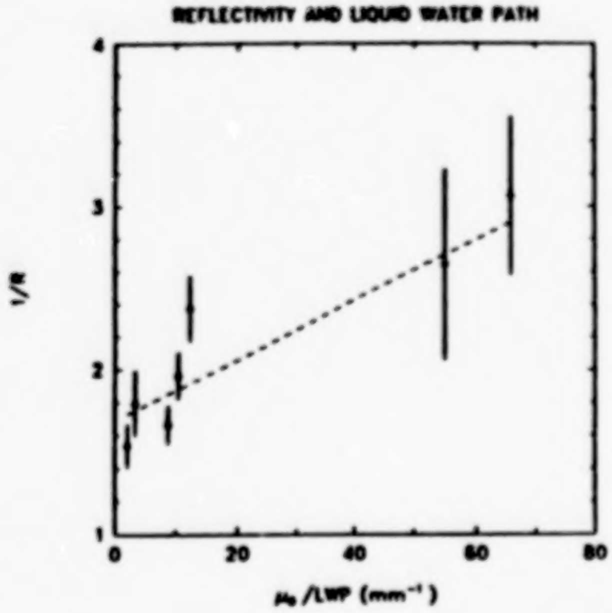

Figure 2. Reflectivities and cloud liquid water paths. The error bars on the reflectivities indicate the standard deviation of the reflectivities for overcast fields of view in the vicinity of San Nicolas Island. The dashed curve is a least squares fit to (2).

Theory also indicates that the reflectivities observed from satellites should depend strongly on the sun-cloud-satellite geometry at the time of the observations. Attempts to correct for the anisotropy of the radiance field using the results of radiative transfer calculations for plane-parallel cloud models (Coakley and Kobayashi, 1988) produced considerable scatter about the linear relationship given by (2). As a result, the AVHRR data itself was used to determine the anisotropy of the reflected radiances. The observed anisotropy showed little if any distinct trends, and as a result corrections for the viewing geometry were deemed unnecessary for the current study. Finally, theory indicates that when the cloud is thin, reflection by the underlying surface can significantly alter the reflectivities measured above the cloud. In the cases reported here, these corrections are small and thus also neglected.

Fig. 3 shows a comparison of the observed reflectivities and those predicted by Stephens (1978) for the observed liquid water paths and the solar zenith angles at the time of the observations. While the reflectivities obtained from the parameterization correlate well with those observed the paucity of points and the uncertainty in the calibration of the AVHRR prevent a critical assessment of the parameterization.

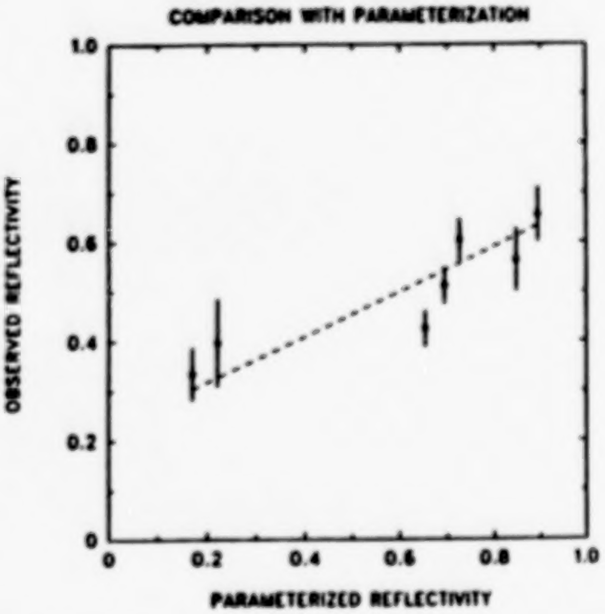

Figure 3. Observed and parameterized reflectivities. The parameterization is by Stephens (1978). The dashed curve is a least squares fit.

4. Summary and Conclusions

We have found that by taking clouds to be isotropic reflectors, the observed reflectivities and observed column amounts of cloud liquid water are related in a manner that is consistent with simple parameterizations often used in general circulation climate models to determine the effect of clouds on the earth's radiation budget. Attempts to use the results of radiative transfer calculations to correct for the anisotropy of the AVHRR derived reflectivities resulted in a greater scatter of the points about the relationship expected between liquid water path and reflectivity. The anisotropy of the observed reflectivities proved to be small, much smaller than indicated by theory.

To critically assess parameterizations, more simultaneous observations of cloud liquid water and cloud reflectivities and better calibration of the AVHRR sensors are needed. More points for comparison will be obtained when data from PCDS for days not included in this study are analyzed. Better calibration of the AVHRR sensor might be afforded through simultaneous observations with the ERBE scanner on NOAA-10 when the ERBE data become available.

Acknowledgment

This work was supported in part by AFGL and AFOSR through transfer of funds to NASA, GLH6-6031, by NASA Grant L-79877B and by ONR.

References

Coakley, J.A., Jr. and M.H. Beckner, 1988: Spatial coherence retrievals of cloud properties for the FIRE Marine Stratocumulus IFO, June 29 - July 19, 1987. NCAR/TN-307+STR, 205 pp.

Coakley, J.A., Jr., and T. Kobayashi, 1988: Broken cloud biases in albedo and surface insolation derived from satellite imagery data. Submitted to *J. Climate*.

Hogg, D.C., F.O. Guiraud, J.B. Snider, M.T. Becker and E.R. Westwater 1983: A steerable dual-channel microwave radiometer for measurement of water vapor and liquid in the troposphere. *J. Climate Appl. Meteor.* **22**, 789-806.

Slingo, A. and H.M. Schrecker, 1982: On the shortwave radiative properties of stratiform water clouds. *Quart. J. R. Met. Soc.*, **108**, 407-426.

Stephens, G.L. 1978: Radiation profiles in extended water clouds. II: Parameterization schemes. *J. Atmos. Sci.*, **35**, 2123-2132.

Near Infra-red Radiances Observed by the UK C130 Multi-channel Radiometer during the marine stratocumulus IFO and preliminary comparison with model calculations

Foot J S

Meteorological Office, Meteorological Research Flight, Y46 Building,
Royal Aerospace Establishment, Farnborough, Hampshire GU14 6TD, UK.

Poster presentation to FSET meeting July 1988

1. Introduction

This paper presents a preliminary analysis of some of the narrow band radiance data measured on the UK Meteorological Office's C130 aircraft during the marine stratocumulus intensive field observation of FIRE, San Diego 29 June to 18 July 1987. The data are compared with Monte Carlo calculations of the reflectance and transmittance of the cloud based upon the observed droplet size distribution. The main scientific question being addressed is whether there is any evidence of anomalous absorption within the cloud which has been observed in similar measurements (Rozenberg et al 1974; Twomey and Cocks 1982; Foot 1988). The measurements also indicate the potential for remotely sensing cloud properties.

2. Introduction

A full description of the multi-channel radiometer (MCR) fitted to the C130, its calibration and performance during FIRE '87 is given by Barrowcliffe, Dewey and Foot (1988). The instrument is essentially the same as used on another aircraft and described by Doherty and Houghton (1984) and Foot (1988). Table 1 shows the filter fit of the visible and near infra-red channels (denoted by channel numbers B1, B2, B3, B4, D1, D2, D3 and D4), additionally there was an 11.0µm (A1) channel operative during FIRE. Channels with the same number (eg. B2 and D2) make simultaneous measurements.

Table 1 Filter Characteristics

No	50% peak	Transmission	Gaseous absorption	Refractive index: real imaginary			
	µm			Liquid Water		Ice	
B1	0.534	0.574	O_3+ Rayleigh	1.334	2.0×10^{-9}	1.310	3.1×10^{-9}
B2	2.240	2.281	Window	1.290	3.3×10^{-4}	1.277	2.0×10^{-4}
B3	1.031	1.052	Window	1.325	1.5×10^{-6}	1.301	2.7×10^{-6}
B4	1.331	1.354	H_2O edge	1.320	2.0×10^{-5}	1.296	1.5×10^{-5}
D1	1.229	1.256	Window	1.332	8.9×10^{-6}	1.297	1.4×10^{-5}
D2	1.994	2.027	CO_2	1.304	1.1×10^{-3}	1.291	1.6×10^{-3}
D3	1.536	1.562	Window	1.317	1.2×10^{-4}	1.294	5.8×10^{-4}
D4	1.838	1.875	H_2O	1.311	1.4×10^{-4}	1.292	6.3×10^{-5}

The visible and near infra-red channels are calibrated in flight using a diffusing shutter to scatter sunlight into the instrument. Radiances are converted into normalised reflectances and transmittances on the basis that the observed layer in a perfect Lambertian diffuse reflector or transmitter, as was carried out in the earlier work, Foot (1988). Details of the atmospheric transmission for the B1, B4 and D2 channels which are applied are given in Barrowcliffe, Dewey and Foot (1988). The D4 channel being centrally placed in a water vapour band is strongly absorbed and produces no valuable information for FIRE. The estimated absolute accuracy of the reflectance or transmittance is 6% for the window channels and slightly poorer for the other channels. Some of the intercomparison data during FIRE between the MCR and the University of Washington's C-131, radiometer (CAR) is being presented by King et al (1988) at this meeting.

The other principal instrument used in this study is the PMS FSSP used to provide droplet size spectra on the level runs or profiles through the cloud.

3. Data

Details of the C130's flight patterns during FIRE are given in FIRE Technical Report No 1 (Kloesel et al 1988). The flights were conducted over fixed ground patterns on either a fixed straight leg or an L pattern. Levels flown include runs just above the stratocumulus and beneath the main base providing vertical reflectance and transmittance of the cloud. Runs in cloud, particularly near cloud top, and profiles through the cloud provide the droplet size distributions and liquid water contents. Although the MCR did take some measurements at angles other than the vertical, these are not treated in this paper. The normalised vertical reflectances and transmittances are denoted by the channel number, thus $B1\uparrow$ is the reflectance of the cloud at 0.55μm and $D1\downarrow$ is the transmittance of the cloud at a wavelength of 1.25μm.

4. Model

A Monte Carlo model, as used in the earlier work, has been used to simulate the observations. Various simplifications have been made in this initial analysis which will be explored later in sensitivity studies. All these simplifications were found to be satisfactory in the earlier work although the cloud studied then was optically much thicker ($\tau \sim 48$). The assumptions are:-

(1) The observed size distributions have been fitted to a single analytic expression which provides a reasonable fit to the observations allowing only one variable, the effective radius, r_e. Mie calculations have been performed on this analytic function.

(2) The observed variation of r_e with height in the cloud is ignored. A value appropriate to the top quarter (where most of the liquid water is present) is used for the whole cloud.

(3) The optical depth, τ, is assumed to be identical for all the channels.

5. Results

Figure 1 shows the variation of the average reflectance of three cloud layers plotted against the absorption coefficient of liquid water. The examples shown have similar reflectances at 0.55 μm, a similar solar zenith angle but different values of r_e near cloud top. The reflectance is mainly constant where the absorption of water is $<10^2 m^{-1}$, the variation may not be significant bearing in mind the absolute accuracy is 6%. The reflectance decreases where water is a stronger absorber and is lower for the cloud with larger droplets.

It is instructive to study the individual synchronised measurements, ie D1/B1, D2/B2 and D3/B3, rather than averaged data over a cloud with variable optical depth. Plots of reflectance (and transmittance) ratios of D/B have been made against the reflectance (or transmittance) B. An example is shown in Figure 2. This run was over a very variable cloud which gradually became thicker at one end; the maximum optical depth is estimated to be 24. As B3↑ increases, ie the optical depth increases, so the ratio D3↑/B3↑ has decreased because of increased absorption. This result is unlike the earlier work Foot (1988) where the optical depth was very high but there was considerable variation in a single run in the ratio which could be attributed to variation in r_e or variation in cloud top structure.

Variation between the ratio plots using D1/B1, where absorption is weak, for different flight occasions is small. Small changes could result from variations in the daily amounts of ozone and particle above the cloud. Variation in the ratio plots for D2/B2 and D3/B3 are however larger and seem correlated with the value of r_e. Both the observations and calculations suggest that variation in solar zenith angle between 10 to 30° do not significantly change these plots.

Figure 3 and 4 show the D3/B3 ratio plots for the reflectance and transmittance of the cloud. The lines are best fits to individual values as (Figure 2). There is clearly a separation with occasion with large r_e showing the strongest absorption. The points plotted are a first attempt to model the variations: two optical depths and four values of r_e having been used. The variations on a single day in the observations are consistent with variation in optical depth without any change in effective radius. The data from flight H804 seems to substantiate this in that the variation of r_e near cloud top between the thicker and thinner ends of the layer was small. The agreement between the observations and calculations for both transmission and reflection tend to indicate that the measurements show stronger absorption than the calculated values, particularly for the largest r_e value. Further work is needed to quantify any disagreement.

Figure 5 shows the reflectance ratio at the other pair of channels D2↑/B2↑ for the same clouds as Figure 3 and 4. These separate out in a similar way. The two flights with similar r_e values show similar behaviour in Figure 4 and 5 but the reflectance data in Figure 3 do show a systematic difference.

6. Discussion

The data and method of presentation discussed here clearly separates out clouds in terms of the size of the cloud droplets. All of the daytime C-130 FIRE flights have been studied and are consistent with the data presented in this short paper. There appears to be no peculiarities that might arise, for example if pollution were to be a significant factor in determining cloud absorption. Variation in the inferred size parameters, r_e, along runs are also very small; this is unlike previous results Foot (1988) and Twomey and Cocks (1982). Further calculations and sensitivity studies are required before we can confidently state whether or not the observations presented here are consistent with our model.

As well as this narrow band work there are also broad band observations which we are just starting to interpret. There is also a limited amount of data on the optical properties of cloud water and interstitial aerosol collected during FIRE: a report on this will be issued soon.

Attendants at the FSET meeting wishing further details may request information through Mr R Barlow, UK Met Office who is attending this meeting.

References

Barrowcliffe R, Dewey K J and Foot J S	1988	The Multi-Channel Radiometer fitted to MRFs C130. Description and calibration methods before and during FIRE 87 Experiment. MRF Internal Note No 42. (Available from UK National Meteorological Library Bracknell, Berks)
Doherty G M and Houghton J T	1984	Some observations of the optical properties in clouds in the near infrared. Infrared PHys. 24, 15-20
Foot J S	1988	Some observations of the optical properties of clouds. I: Stratocumulus. Quart. J.R. Met. Soc. 114, 129-144.
King M D, Nakajima T, Radke L R and Hobbs P V	1988	Cloud absorption properties as derived from airborne measurements of scattered radiation within clouds. FSET meeting July 1988.
Kloesel K A, Albrech B A and Wylie D P	1988	FIRE marine stratocumulus observations - summary of operations and synoptic conditions. FIRE Technical Report No 1.
Rosenberg G V, Malkevich M S, Malkova V S and Syachinov V I	1974	Determination of the optical characteristics of clouds from measurements of reflected solar radiation on the KOSMOS 320 satellite. Atmos. Ocean. Phys. 10, 14-24.
Twomey S and Cocks T	1982	Spectral reflectance of clouds in the near infrared: comparisons of measurements and calculations. J. Meteorol. Soc. Japan 60, 583-592.

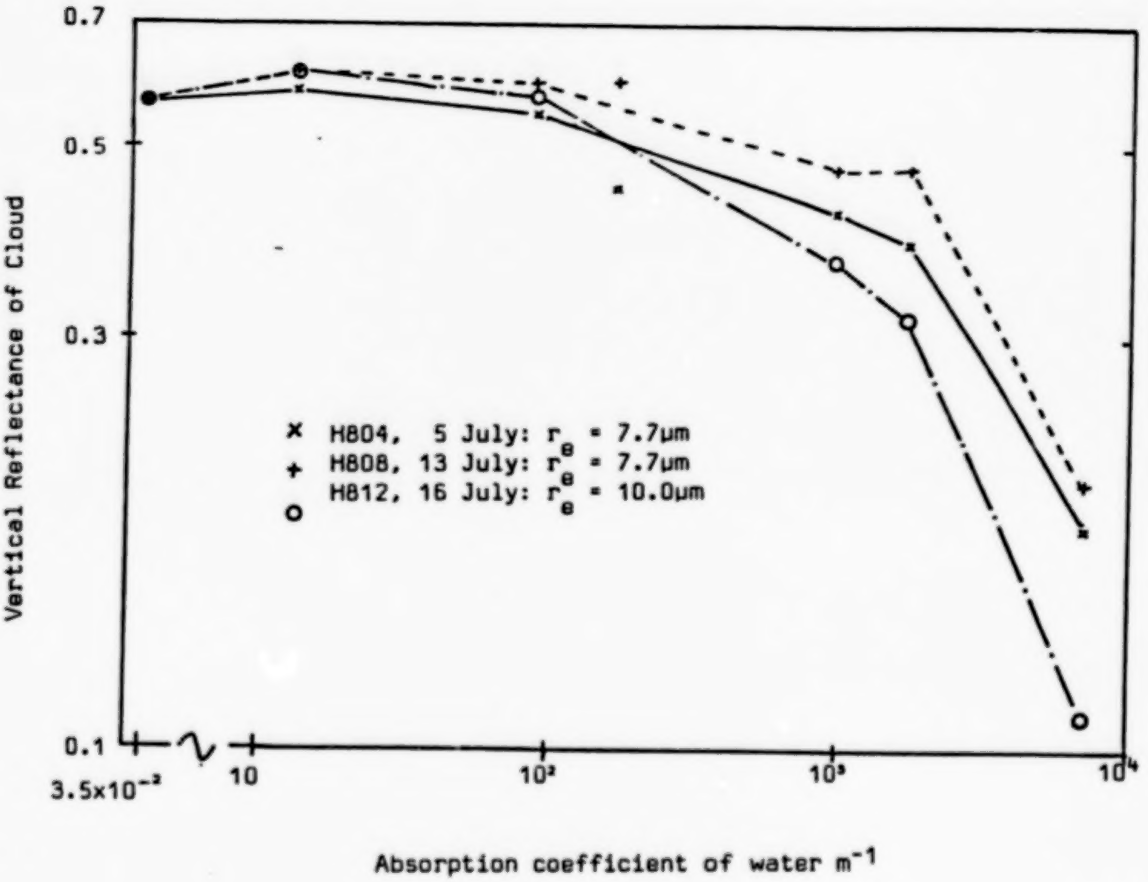

Figure 1

Average Vertical Reflectance of three cloud layers as a function of cloud water absorption.

(Lines are drawn to join points for the same flight excluding the B4 channel because of the extra uncertainty of calculating the atmospheric transmission in the water vapour band.)

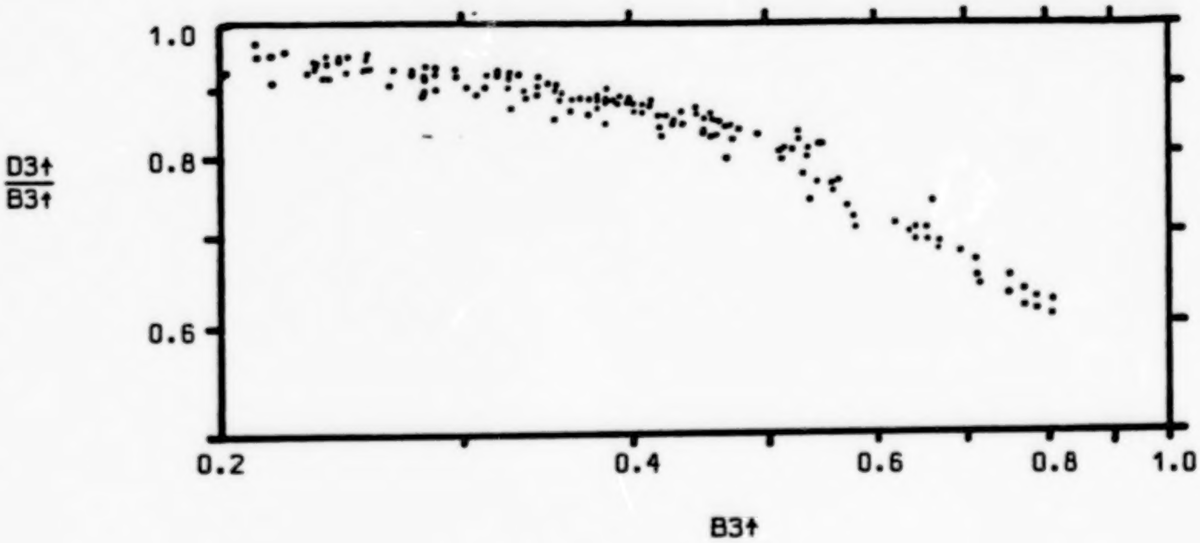

Figure 2

Individual observations of reflectance ratio D3↑/B3↑.
Data from flight H804, 5 July 1987
Solar zenith angle 30°.

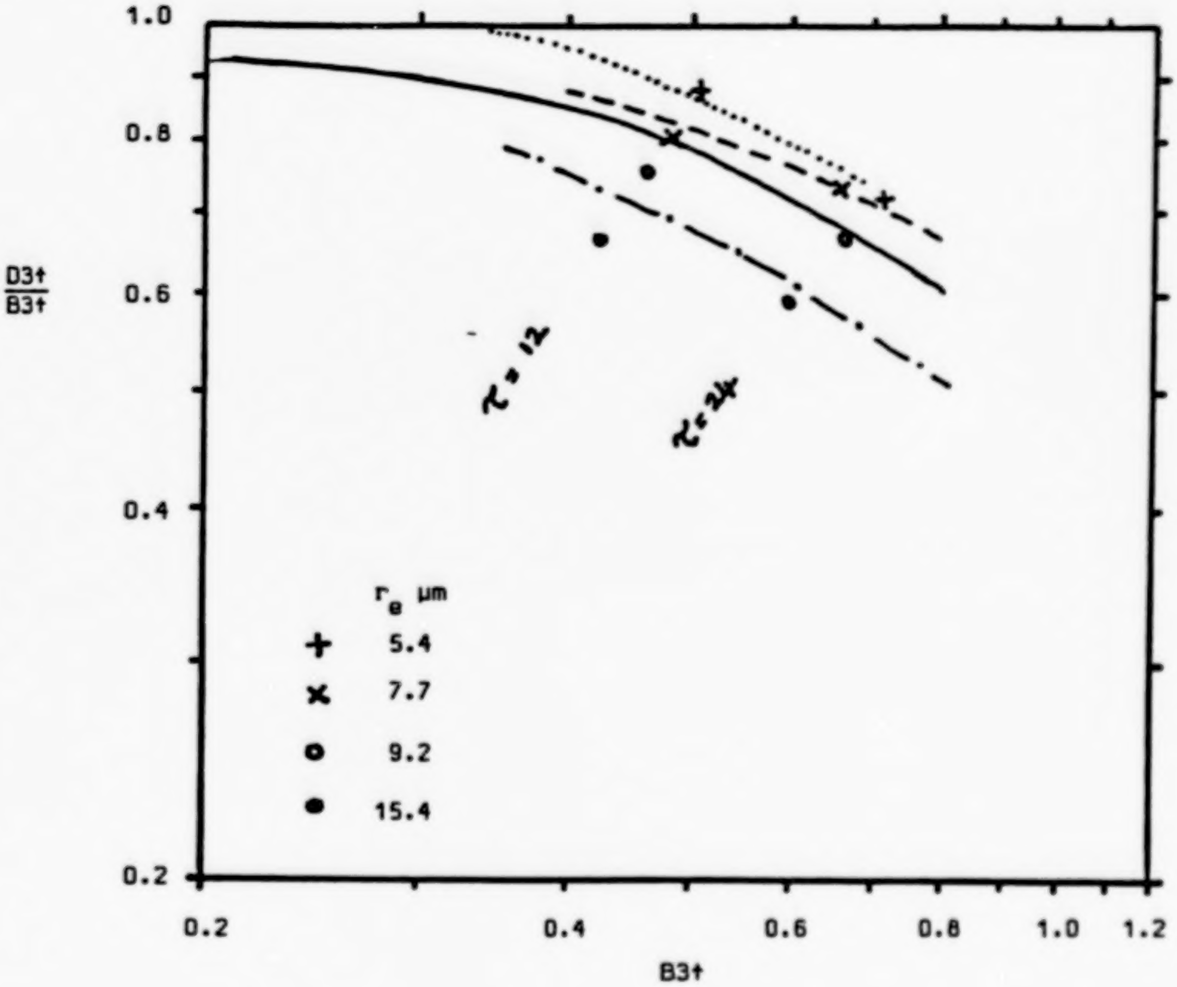

Figure 3 Comparison between observed and calculated reflectance ratio D3↑/B3↑. Lines represent observations and points are calculations.

Dotted line	Flight H813	18 July	r_e = 5.4 μm
Solid line	Flight H804	5 July	r_e = 7.7 μm
Dashed line	Flight H808	13 July	r_e = 7.7 μm
Dashed/Dotted line	Flight H812	16 July	r_e = 10.0 μm

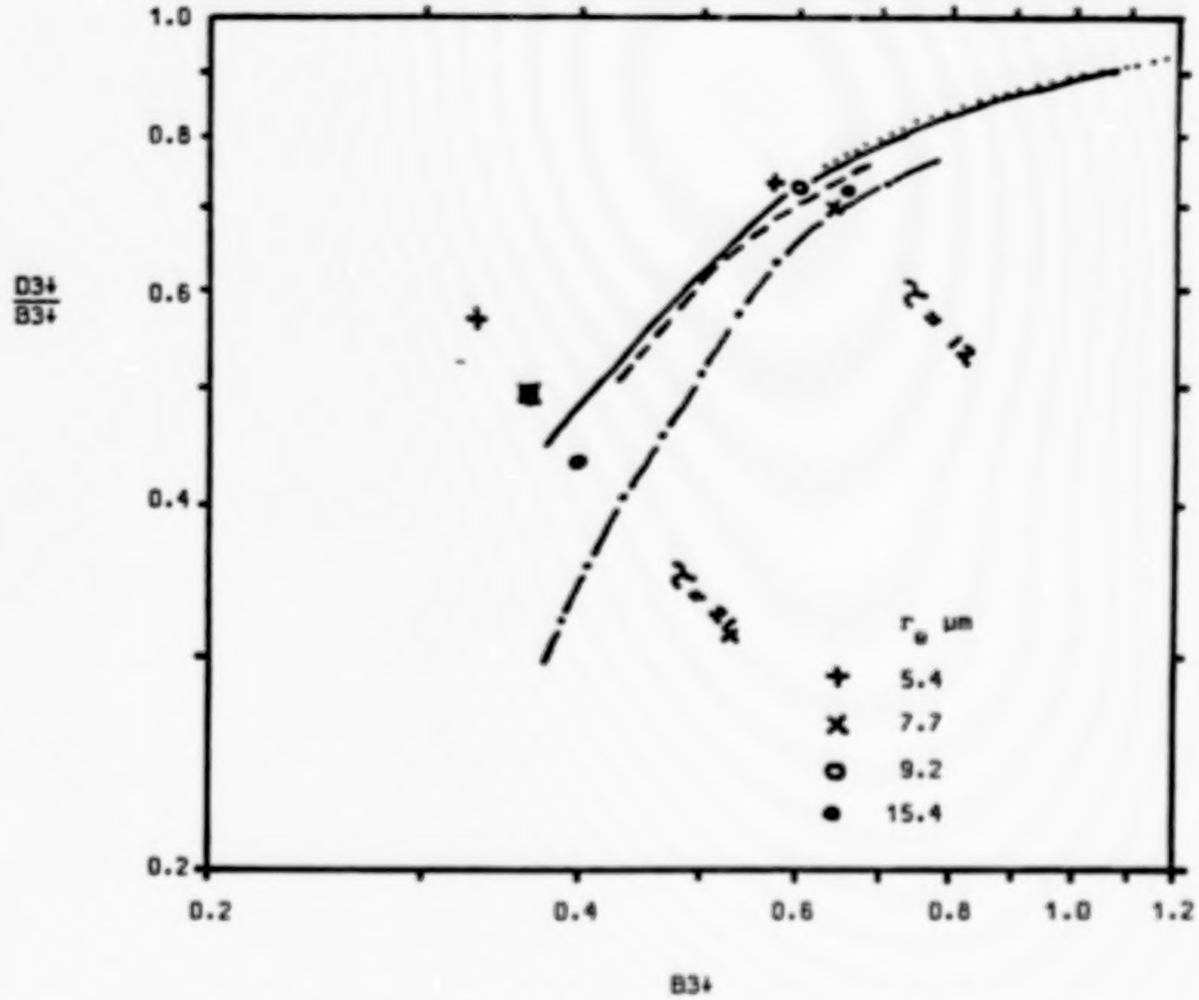

Figure 4 Comparison between observed and calculated transmittance ratio D3↓/B3↓. Key as Figure 3.

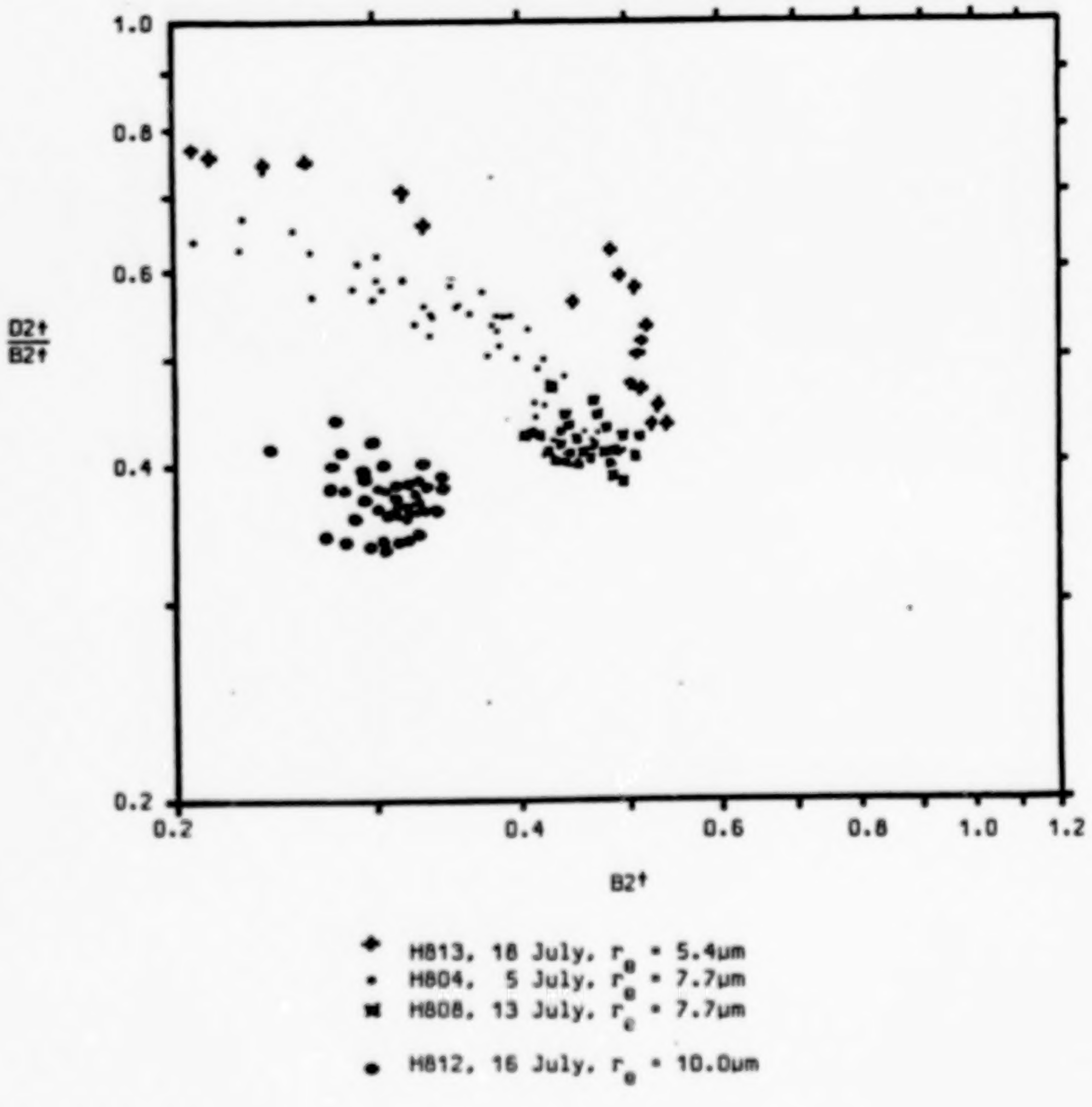

Figure 5

Individual observations of reflectance ratios D2↑/B2↑ for four flights

PLUME MECHANICS AND STRATOCUMULUS CONVECTION

HOWARD P. HANSON

Cooperative Institute for Research in Environmental Sciences
University of Colorado/NOAA, Boulder, CO 80309-0449

1. Introduction

The FIRE marine stratocumulus IFO held in July, 1987 produced a data set that is far more comprehensive than data sets from previous stratocumulus experiments. One exciting new development was the use of the 10.6μm lidar system for cloud-top mapping that was available on the NCAR Electra. This system provided a unique look at the small scales of the turbulence in the clouds, images of the turbulent structures that are quantitatively revealed by conditional sampling (e.g., Khalsa and Greenhut, 1987).

The behavior of these updrafts and downdrafts is central to the dynamics of the stratocumulus-topped marine boundary layer. FIRE's objectives of understanding cloud dynamics and how they affect the cloud optical depth — which, in turn, is the crucial factor in determining the clouds' albedo — therefore require the investigation of these drafts. This poster discusses initial results from a simple model capable of simulating moist, entraining plumes that are subject to water phase changes and radiative heating and cooling. The results discussed here are limited to plumes that are not affected by condensation and evaporation but are subject to radiative heating and cooling. These results correspond, therefore, to the "dry cloud" case discussed by Lilly and Schubert (1980). The model's simplicity limits the realism of the results — the plumes are assumed not to interact, for example — but the role of radiative processes in influencing the plume dynamics is clear. Also revealed is the role the plumes play in maintaining the cloud-top inversion.

This poster abstract presents the model equations and methodology used, and discusses qualitative results.

2. Model

The plume model discussed here is based on the work of Telford (1966, 1972) and is basically a simplification of the model discussed by Chai and Telford (1983). The main simplification in the present work concerns the neglect of downdrafts that are explicitly associated with the modeled updrafts. In the Telford (1972) model of a field of convective plumes, updrafts are surrounded by downward (compensating) flow; here, drafts are completely independent.

In the complete model, the physical processes of the drafts include adiabatic expansion, lateral entrainment, buoyant acceleration (due to virtual temperature perturbations induced by boundary conditions, condensation and radiative heating) and parameterized friction. The heating from condensation is the most non-intuitive aspect of the model equations, and this is discussed in detail by Chai (1978) and more briefly in Chai and Telford (1983). Here, it is ignored.

Dependent variables in the model are the plume radius r, vertical velocity w, rms turbulent velocity i, total density ρ, and water content ρ_w. Because condensation is neglected here, the equation for the conservation of water is not needed, and therefore the four equations represent conservation of volume, mass, (vertical) momentum and turbulence kinetic energy. Each plume is assumed to be in a steady state, and therefore these dependent variables are functions of height z. Boundary conditions are applied at the surface or at the inversion, for updrafts and downdrafts, respectively. The plumes are embedded in an environment specified by mean temperature profiles $\overline{T}(z)$ which, hydrostatically, determines the pressure distribution $p(z)$; pressure perturbations associated with the plumes are ignored. The system of equations for the dependent variables is first order and highly non-linear; it is solved numerically using a Runge-Kutta procedure.

The equations can be written as

$$\mathbf{L}(\Gamma)\frac{d\Gamma}{dz} = \mathbf{F}(\Gamma)\,, \qquad (1)$$

where

$$\Gamma(z) \equiv \begin{bmatrix} r(z) \\ w(z) \\ \rho(z) \\ i^2(z) \end{bmatrix} . \qquad (2)$$

Assuming a quiescent (non-turbulent) environment and using $\overline{T}(z)$ and $p(z)$ to calculate an environmental density profile $\overline{\rho}(z)$ allows the right-hand side of (1) and the nonlinear operator $\mathbf{L}$ to be written as

$$\mathbf{F} \equiv \begin{bmatrix} 2\lambda i + (1-\kappa)wr^2p^{-1}dp/dz \\ 2\lambda i\overline{\rho w} + rg(\overline{\rho}-\rho) - rw^2\dot{\rho} \\ 2\lambda i\overline{\rho} + r\dot{\rho} \\ 2\lambda i\overline{\rho}\left[(w-\overline{w})^2+i^2\right] - ri^2\dot{\rho} - A/2\,\rho i^3 \end{bmatrix} ; \qquad (3)$$

$$\mathbf{L} \equiv \begin{bmatrix} 2w & r & 0 & 0 \\ 2w^2\rho & 2rw\rho & rw^2 & 0 \\ 2w\rho & r\rho & rw & 0 \\ 2w\rho i^2 & r\rho i^2 & r^2wi^2 & r^2w\rho \end{bmatrix} . \qquad (4)$$

The environmental vertical velocity $\overline{w}$ can be deduced from the continuity equation, provided the area of the affected environment is specified. Here, it is assumed to be so much larger that the plume that $\overline{w} \to 0$. The parameter λ is an entrainment coefficient (~0.08, according to Telford, 1966), and A is a dissipation coefficient, taken to be equal to unity. κ is the ratio of the gas constant to the specific heat at constant pressure. The non-adiabatic sources of mass are denoted by $\dot{\rho}$.

In principle, the solution to (1) is given simply by

$$\Gamma(z) = \int_{z_0}^{z} \mathbf{L}^{-1}\mathbf{F}\,dz; \qquad (5)$$

since $|\,\mathbf{L}\,| = 2r^4w^4\rho$, the problem is well-posed except for plumes of vanishing radius or density, or plumes that stop. Accordingly, given an environmental temperature profile and boundary conditions, the system (1) can be integrated until the vertical velocity vanishes, at which point, to cite an example in physical terms, an updraft either disappears or becomes a downdraft.

In practice, integration of (1) must be accomplished numerically because of the nonlinearity of F and L. This is simplified by defining a *density perturbation* (which is also a temperature perturbation, due to the hydrostatic assumption and neglect of pressure perturbations within the plume)

$$\delta \equiv (\overline{\rho}/\rho - 1) = (T/\overline{T} - 1), \qquad (6)$$

where T is the plume temperature. Defining an entrainment (inverse) length scale $\Lambda \equiv \dfrac{2\lambda i}{rw}(1+\delta)$; a static stability

$S \equiv (g/c_p + d\overline{T}/dz)/\overline{T}$; and the parameters $\beta \equiv g\delta/w^2$ and $\sigma \equiv -(1-\kappa)p^{-1}dp/dz$, where g and c_p are gravitational acceleration and the specific heat of air at constant pressure, respectively; and the appropriate heating rate Q (this is discussed further below), the equations take the form

$$\frac{d(r^2)}{dz} = \left[\Lambda\frac{2+\delta}{1+\delta} + \sigma - \beta\right]r^2 \; ; \tag{7a}$$

$$\frac{dw}{dz} = \left[-\Lambda + \beta\right]w \; ; \tag{7b}$$

$$\frac{d\delta}{dz} = -\Lambda\delta - (S - Q/w)(1 + \delta) \; ; \tag{7c}$$

$$\frac{d(i^2)}{dz} = -\left[\Lambda(1-\frac{w^2}{i^2}) + \frac{A}{2}\,\frac{i}{rw}\right]i^2 \, . \tag{7d}$$

The parameter σ acts as an adiabatic expansion term, and β represents a sort of Bernoulli effect, through which accelerating plumes become smaller. The heating Q is related to the radiative flux divergence by

$$Q \equiv -\frac{1}{\overline{\rho}c_p\overline{T}}\,\frac{dF_{rad}}{dz} . \tag{8}$$

In deriving (7c), it has been assumed that the radiative heating is horizontally homogeneous, a reasonable first-orcer approximation for stratocumulus clouds. In the case of isolated cumulus, this is clearly invalid, and future work with stratocumulus convection will also use differential heating rates. It is important to stress that radiative heating has a distinct influence on the plume's perturbation temperature (and therefore its dynamics, through the coupled system) *even though the heating rates are assumed to be horizontally homogeneous*. The results discussed in this poster use radiative fluxes calculated with the parameterizations developed by Hanson and Derr (1987). Various assumptions about the (implicit) cloud liquid water and solar zenith are used to investigate the sensitivity of plumes to the heating.

3. Discussion

The main purpose of this abstract is to present the equations of the plume model and briefly to discuss the model's behavior in qualitative terms. Numerical solutions will be presented on the poster itself. Even without integrating the set of equations (7), however, it is possible to infer several aspects of the model's behavior from the governing equations.

Note, first, that, with the exception of the term $-(S-Q/w)$ on the right-hand-side of (7c), the equations are homogenous and, further, take the general form

$$\frac{d\ln\hat{\mathbf{\Gamma}}}{dz} = \hat{\mathbf{F}}(\hat{\mathbf{\Gamma}}) \, , \tag{9a}$$

where $\hat{\mathbf{\Gamma}}$ and $\hat{\mathbf{F}}$ are analogous to $\mathbf{\Gamma}$ and $\mathbf{F}$ in (2) and (3). This suggests, in cases of neutral stability* with no heating, that small departures from boundary conditions can by deduced analytically with

$$\hat{\mathbf{\Gamma}}(z) = \hat{\mathbf{\Gamma}}_0 \exp\left[-\hat{\mathbf{F}}_0(z-z_0)\right] \, , \tag{9b}$$

where $(\;)_0$ is a boundary value. For realistic plumes, $|\delta| \ll 1$ and $|w| < i$, and w and δ can take both positive and negative values. The behavior of the solutions (9b) can then be classified entirely according to the energetics of the plume in question. Energy-producing plumes — that is, *direct circulations* — behave identically, be they (warm) updrafts or (cold) downdrafts. Similarly, energy consuming plumes (*indirect circulations*) exhibit the same symmetry.

The behavior of a warm updraft that encounters an abrupt increase in stability is also apparent from Eqs. (7). The term $-S(1+\delta)$ on the right-hand-side of (7c) will immediately cause the temperature perturbation to decrease, eventually to become negative. When this happens, β changes sign and the plume decelerates and widens [see (7a) and (7b)]. The point at which $w \to 0$ signals the termination of the integration.

Note also that the effect of radiative cooling on updrafts will be exacerbated tremendously by this behavior within an inversion. As the plume slows, the term Q/w in (7c) will become disproportionately large and will apply positive feedback to the the deceleration. The role of radiative cooling in decelerating updrafts in the presence of clouds may thus explain the relatively sharper inversion structure observed atop the cloud-topped boundary layer when compared to the un-cloudy boundary layer. In the latter case, updrafts are slowed by lack of positive buoyancy, and this causes them to spread out and stop. In the cloud-topped case, the radiative cooling acts as a braking mechanism for the updrafts, stopping them nearer the inversion base. The net effect of this on many plumes is a thinner inversion layer.

Finally, it can be seen that, in cool downdrafts, this behavior works in the opposite sense, to accelerate the downdraft, but with *negative* feedback. This suggests that, near the cloud top, at least, the role of energetic downdrafts should be much stronger in stratocumulus than in the clear boundary layer. It also suggests that solar heating will affect the different drafts in quite different fashions. It is this assymetry of updrafts and downdrafts of the same sense of circulation (i.e., both direct) in the presence of radiative heating that causes the dynamics of stratocumulus convection to differ so dramatically from the clear boundary layer heated from below. Further discussion, with quantitative results of the cases discussed here, will be included on the poster.

Acknowledgements: The research leading to this contribution is supported by the Office of Naval Research, Marine Meteorology Program Contract No. N000-14-84-K-0405 and by the National Aeronautics and Space Administration, Langley Research Center Contract No. NAG-1-651.

REFERENCES

Chai, S.K., 1978: Lowering stratus cloud in surface driven convection over the sea. Ph.D. Dissertation, University of Nevada, Reno, 146pp.

Chai, S.K. and J.W. Telford, 1983: Convection model for stratus cloud over a warm water surface. *Boundary-Layer Meteor.*, **26**, 25-49.

Hanson, H.P., and V.E. Derr, 1987: Parameterization of radiative flux profiles within layer clouds. *J. Climate Appl. Meteor.*, **26**, 1511-1521.

Khalsa, S.J.S., and G.K. Greenhut, 1987: Convective elements in the marine atmospheric boundary layer. Part II: Entrainment at the capping inversion. *J. Climate Appl. Meteor.*, **26**, 824-836.

Lilly, D.K., and W.H., Schubert, 1980: The effects of radiative cooling in a cloud-topped mixed layer. *J. Atmos. Sci.*, **37**, 482-487.

Telford, J.W., 1966: The convective mechanism in clear air. *J. Atmos. Sci.*, **23**, 652-666.

Telford, J.W., 1972: Convective plumes in a convective field. *J. Atmos. Sci.*, **27**, 347-358.

FIRE EXTENDED TIME/LIMITED AREA OBSERVATIONS AT PALISADES, NEW YORK

David A. Robinson

Department of Geography
Rutgers, The State University
New Brunswick, NJ 08903

George Kukla and Alan Frei

Lamont-Doherty Geological Observatory of Columbia University
Palisades, NY 10964

Downwelling shortwave and longwave irradiation are being continuously monitored at Palisades, New York as part of the First International Satellite Cloud Climatology Project (ISCCP) Regional Experiment (FIRE) Extended Time/Limited Area initiative. In addition, fisheye (180°) sky photographs are taken at the times of NOAA 9 and Landsat satellite overpasses on select days, particularly when cirrus clouds are present.

Measurements of incoming shortwave (0.28-2.80µm) hemispheric and diffuse, hemispheric near infrared (0.7-2.80µm) and downwelling hemispheric infrared (4.0-50.0µm) irradiation have been made from a rooftop location on the grounds of the Lamont-Doherty Geological Observatory since December 1986. The three Eppley Precision Spectral Pyranometers and the Eppley Pyrgeometer used to measure these variables were calibrated with Colorado State University instruments at Madison, Wisconsin as part of the FIRE Intensive Field Observations project in October 1986. They were recently recalibrated by the Eppley Laboratory. Pyrgeometer output contains an adjustment for body temperature but not for dome temperature. Data are transmitted to a Campbell CR-21 Digital Recorder, where one minute averages of ten second samples are stored and subsequently dumped to a cassette recorder. Using a Campbell C-20 Cassette Interface, these data are transferred to an Apple Macintosh computer for analysis and for archiving on floppy disks.

In addition to the raw irradiances collected, variables derived from these data are generated and stored. These include: 1) the ratio of near infrared irradiation to visible irradiation and 2) the fraction of the full shortwave irradiation which is diffuse; and will soon include: 3) shortwave (sw) transmissivity (equation 1) and 4) optical depth in the shortwave (equation 2).

$$\text{transmissivity} = \frac{\text{sw irradiation at the surface}}{\text{incoming sw at top of atmosphere}} \qquad (1)$$

$$\text{optical depth} = \text{cos zenith angle} \quad \ln \frac{\text{top of atmosphere insolation}}{\text{sw irradiation - sw diffuse irradiation}} \qquad (2)$$

Sky photographs are taken with an Olympus OM2-N 35mm camera and are timed to be coincident with overpassing NOAA 9 and Landsat satellites. Palisades is within the field of view of the NOAA 9 daily in the middle to late afternoon. The satellite viewing angle is within 45° of nadir over Palisades on approximately half of the passes.

Graphs showing measurements of irradiances and several of the derived products are shown in figure 1 for November 24, 1987. Cirrus of varying thickness was present throughout the day. Excluding the 16:30-18:30 GMT interval, this is indicated by the rough nature of the temporal march of irradiation, yet its relatively high values, from the relatively low infrared irradiation, from the high near infrared to visible ratio and from the shortwave diffuse ranging between approximately 0.2 to 0.7. Clouds were lower and thicker during the mid-day period (16:30-18:30), as seen by rises in the shortwave diffuse and the downwelling infrared. The lack of a noticeable decrease in the near infrared to visible ratio and the continued presence of 10-20% direct radiation indicates that these clouds were not opaque. Compare this to a thicker stratus event at approximately 20:10, when the near infrared to visible ratio fell significantly. This thick patch of stratus apparently covered only a small region near the sun, as some direct radiation, or at least radiation close to the sun's direct beam continued to be recorded.

Figure 1 a-d. Irradiances and associated atmospheric variables on November 24, 1987 at Palisades, New York. Time is GMT, which is local time plus 5 hours. Local noon is at 16:45. See the text for a description of sky conditions.

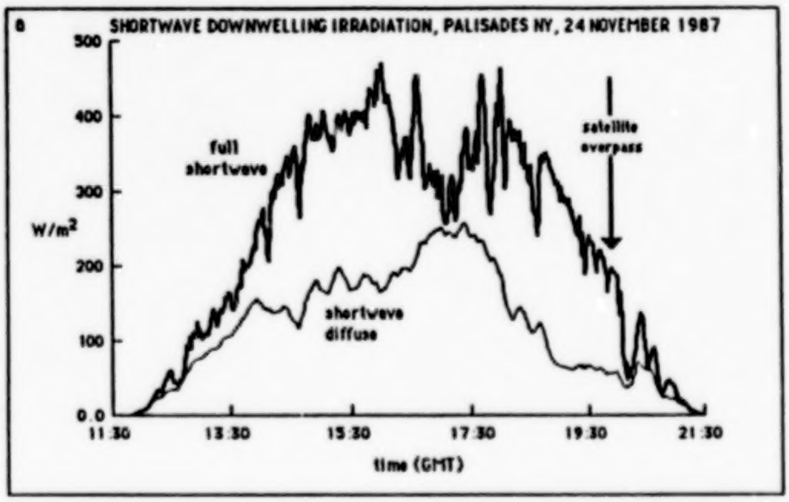

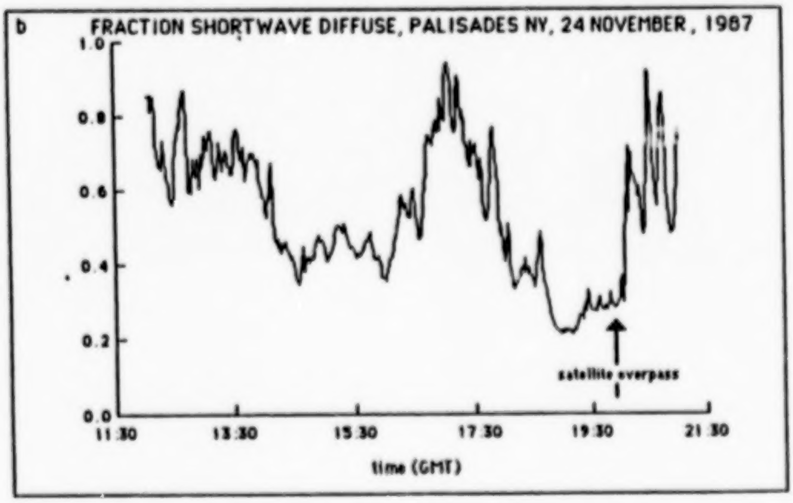

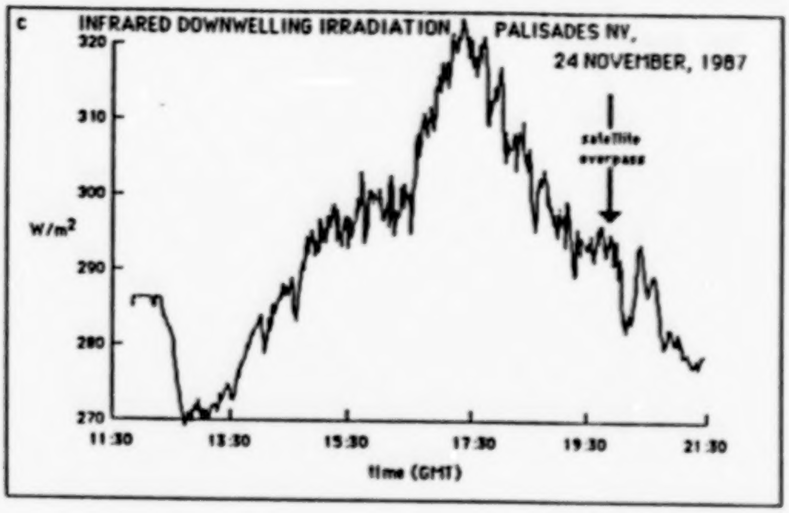

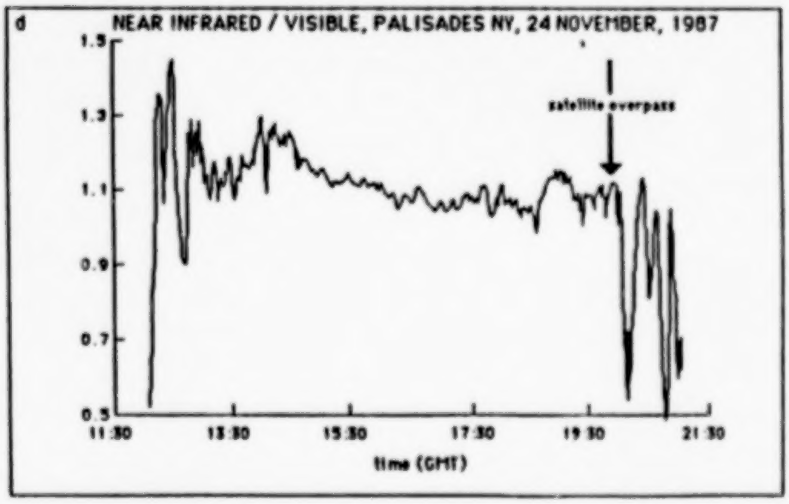

Details of conditions for 30 minutes on either side of the NOAA 9 overpass on the 24th are shown in figure 2. The satellite image was taken with cirrus over the station and in the direction of the sun. About ten minutes after the overpass, the previously discussed thick stratus passed in front of the sun. At this point, in a late-afternoon situation such as this, one would expect the shortwave signal to decrease and the infrared to remain relatively stable at first and later increase as the cloud passed from west to east over the station. In this case, however, the shortwave and infrared decreased simultaneously. This suggests that the approximate 10 W/m^2 decrease in the infrared was the result of dome cooling in the absence of direct shortwave insolation. Also, the lack of an increase in the infrared to values greater than those preceding its decrease suggests that either: a) this cloud never passed directly over the station or b) if the cloud passed overhead it had a high base. This situation is indicative of the difficulties inherent in looking at station records in detail with respect to both time and absolute irradiances.

Figure 2 a-d. Detailed view of a portion of figure 1 around the time of the NOAA 9 overpass.

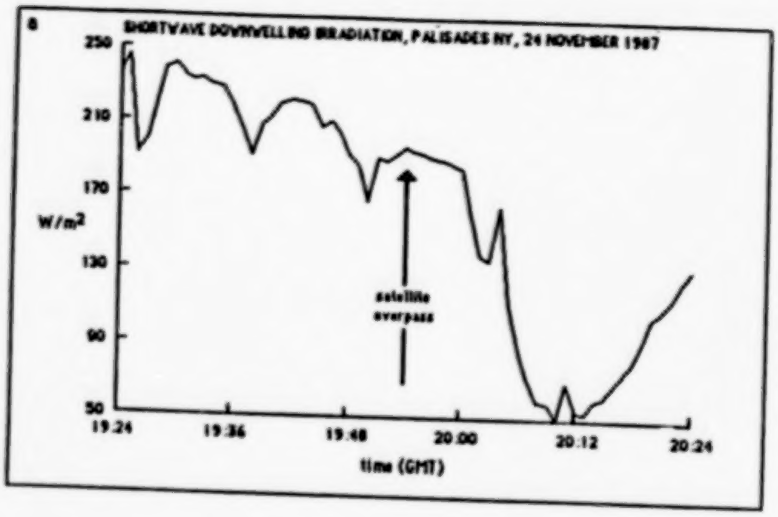

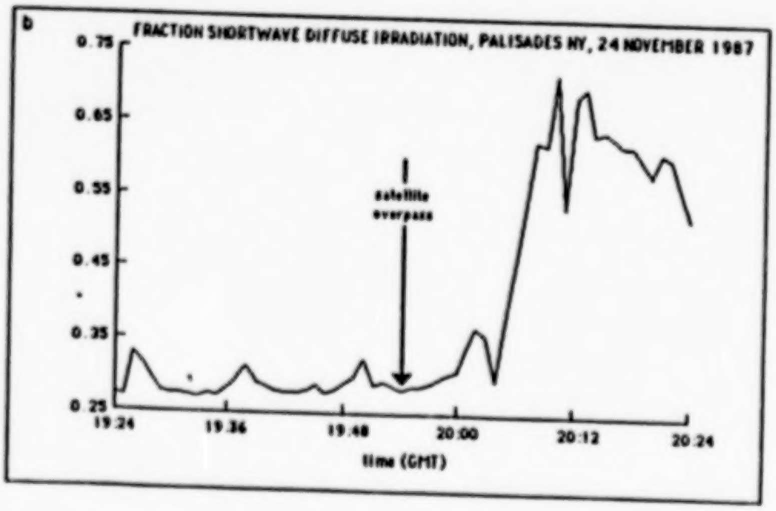

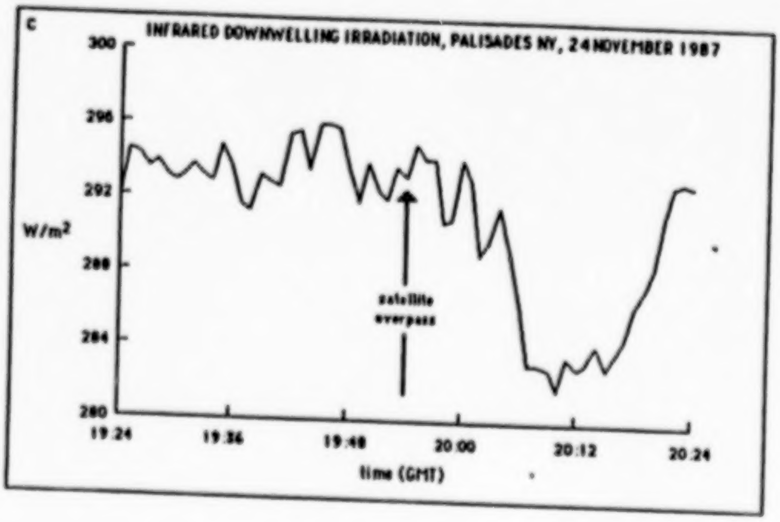

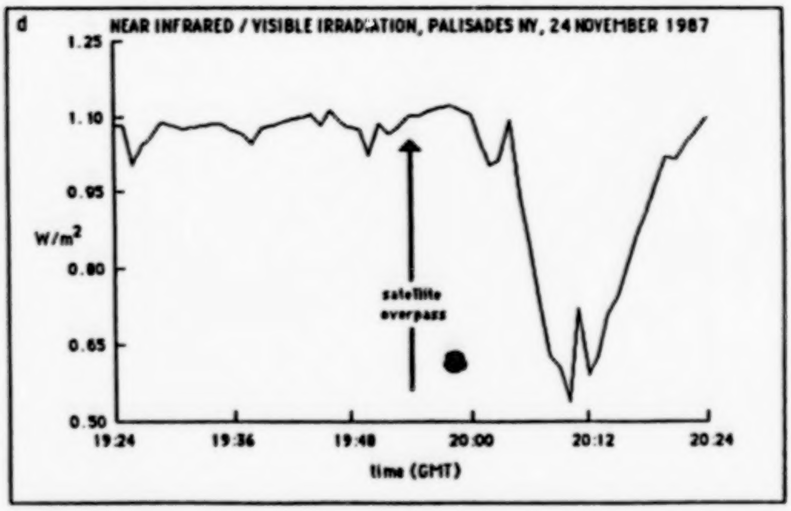

Analysis of the Palisades data has only recently begun. Among the tasks to be performed include:

1) Expansion of the efforts to recognize cirrus from non-cirrus clouds and clear skies using irradiation data. This was begun with data gathered at Wausau, Wisconsin during the FIRE Cirrus Intensive Field Observations project (cf. Robinson and Frei, this volume).

2) A study of cloud space/time statistical structures.

3) Comparison of surface observations of shortwave irradiance taken at satellite overpass times to surface irradiances derived from satellite data.

4) Validation of ISCCP satellite cloud retrieval techniques.

Acknowledgment: This work is supported by NASA grant NAG-1-653.

MEASUREMENTS OF THE LIGHT-ABSORBING MATERIAL INSIDE CLOUD DROPLETS AND ITS EFFECT ON CLOUD ALBEDO

C. H.Twohy[1,3], A. D. Clarke[2], S. G.Warren[1], L. F. Radke[1], and R. J. Charlson[1]

The question of how aerosol pollutants affect the radiative properties of clouds was posed by Twomey [1977], who pointed out that aerosols have two competing effects: they increase the number of particles which might act as cloud condensation nuclei (CCN), but also include materials such as elemental carbon (EC) which are essentially black to solar radiation. Elevated levels of CCN, assumed to result in greater numbers of smaller droplets, would lead to brighter, more reflective clouds, while enhanced absorption due to carbon particles could potentially make clouds darker. Based on the global distribution of cloud cover and absorption measurements which Twomey et al. [1984] used in a later paper, the overall climatic effect of increasing pollution over time was shown by their model to be cooling, of the same order of magnitude as predicted warming from the greenhouse effect of CO_2 alone.

Cloud absorptance values measured directly by aircraft [Reynolds et al., 1975; Stephens et al., 1978] are frequently much higher than those which are theoretically calculated from measured microphysical parameters. One possible explanation of this phenomenon is absorption of radiation by aerosol particles within the cloud. In a comparison of measured and computed reflectance spectra at various wavelengths, Twomey and Cocks [1982] concluded that this process could not be the major explanation since the observed enhanced absorption predominated not at visible wavelengths, but in the near infrared where absorption by particles should be negligible relative to that by liquid water and ice.

Most of the measurements of light-absorbing aerosol particles made previously have been in non-cloudy air and therefore provide no insight into aerosol effects on cloud properties. In this paper, we describe an experiment designed to measure light absorption exclusively due to substances *inside* cloud droplets, compare the results to related light absorption measurements, and evaluate possible effects on the albedo of clouds. The results of this study validate those of Twomey and Cocks and show that the measured levels of light-absorbing material are negligible for the radiative properties of realistic clouds.

Elemental carbon (EC) is the most efficient light-absorbing material present in the atmosphere, and except in unusual cases absorption by aerosols is dominated by elemental carbon [Rosen et al., 1978; Heintzenberg, 1982; Clarke and Charlson, 1985]. It is possible for hydrophobic carbon particles to obtain a hygroscopic coating and be incorporated into clouds by nucleation scavenging. Measurement of EC in cloud droplets, however, is problematic due to the difficulty in collecting cloud droplets separately from interstitial aerosol particles and the tendency of EC to stick to surfaces of collection vessels [Ogren, 1983]. In addition, identification of EC requires relatively long sampling times in many environments. In order to eliminate the first difficulties, cloud droplets were sampled in this experiment with a counterflow virtual impactor (CVI), a probe which by inertial impaction collects only droplets above a certain minimum radius while effectively rejecting interstitial aerosol particles [Ogren et al., 1985; Noone et al., 1988]. The CVI evaporates droplets (leaving the non-volatile aerosol residue) before they touch any surface, minimizing sample contamination and loss of carbon particles to the walls of the sampler. The long sampling time requirement was avoided through the use of a very sensitive technique for measuring the absorption of light by the droplet residue particles. The "Integrating Sandwich Method" [Clarke, 1982], enhances light absorption by particles in the sample by confining them between two highly reflecting surfaces.

---

[1] Department of Atmospheric Sciences, University of Washington, Seattle, Washington 98195.

[2] Hawaii Institute of Geophysics, University of Hawaii, Honolulu, Hawaii 96822.

[3] Currently at National Center for Atmospheric Research, Boulder, Colorado 80307-3000.

Cloud droplets were sampled by the CVI on the University of Washington's C-131 aircraft in the FIRE project off the Southern California coast in June and July, 1987. Droplets above five μm (calculated cut radius) were collected on five different days for light absorption analysis of the droplet residue particles, which were impacted onto Nuclepore polycarbonate filters. The C-131 typically flew at cloud base, above the cloud, or inside the cloud for periods of twenty to thirty minutes at an airspeed of 80-85 meters s^{-1} with occasional shallow descents or ascents through the stratus deck. Sampling times in cloud ranged from 22 to 143 minutes, resulting in collection of droplets from about 3-20 cubic meters of cloudy air.

Absorption coefficients representing the absorption per unit length of droplet-laden air were calculated directly from the amount of light absorption by the filter sample and the sample volume of air. Model trajectories [Kloesel et al., 1988] revealed that air reaching the 925 mb level had been located west, northwest, or north of the project area on the days prior to the flights, and windspeeds were highly variable. Examination of the droplet size spectrum measured by the Forward Scattering Spectrometer Probe (FSSP) on the aircraft indicated that some occasions, the air appeared to be of marine origin but many times the spectra showed continental influence. Four of the measured absorption coefficients for the droplet residue ranged from 6 to 20×10^{-8} m^{-1}, while one (from July 7, 1987) exhibited much less absorption. The absorption coefficients were generally higher than those measured in aerosol at remote locations such as Mauna Loa Observatory [Clarke and Charlson, 1985] and the South Pole [Clarke et al., in preparation], and fell within the range measured at Hurricane Ridge on the western coast of Washington State [Clarke, 1982]. They were, however, much lower than those typical of extremely polluted air at industrially influenced locations like St. Louis, Missouri [Weiss, 1980].

The mass concentration of elemental carbon inside the droplets was estimated from the measured absorption coefficients and the liquid water content, with the assumption that all absorption was due to elemental carbon with a mass absorption coefficient of 10 m^2 g^{-1}. Resulting concentrations of EC in cloud water were 23-79 ng EC g^{-1} for four of the five cases. These values were comparable with those measured in rainwater [Ogren, 1983] at Seattle, Washington and at less polluted sites in Sweden. Samples of interstitial particles were also taken during the project, but were analyzed for light absorption by a less sensitive method, and all were below the detection limit. From these results an absolute upper bound on the concentration of interstitial elemental carbon (IEC) was established for each flight.

The maximum possible effect of the measured EC on cloud albedo was determined by calculating albedo at wavelength 0.475 μm where liquid water has its weakest absorption [Hale and Querry, 1973], by using the largest measured in-cloud EC concentrations, and by assessing the effect upon an optically "semi-infinite" cloud. In another scenario but still at the most sensitive wavelength, the effect of EC on the albedo of a more realistic (thinner) cloud was evaluated. The surface-area-weighted or "effective" mean radius [Hansen and Travis, 1974], r_{eff}, which determines the effect of the droplet size distribution on the single-scattering albedo, ω, was calculated and averaged for each sampling period from the FSSP data, and the Mie program of Wiscombe [1980] was used to obtain values for ω, asymmetry factor, and extinction efficiency.

Figures 1 and 2 show the calculated effect of elemental carbon on the albedo of clouds with different r_{eff} values. Figure 1 applies to a semi-infinite cloud (optical thickness $\tau^* = \infty$) with the shaded area representing the range of EC concentrations under consideration, explained in more detail in the figure caption. Curved lines show the effect of different r_{eff} values on albedo, with a greater albedo reduction resulting when EC is present in larger droplets. If an r_{eff} of 10 μm (slightly larger than the ones calculated) is assumed, the change in the albedo of this semi-infinite cloud due to the carbon concentrations considered ranges from -0.014 to -0.029. EC has less effect on albedo as optical thickness decreases, and Figure 2 shows the results for a more realistic cloud with $\tau^* = 30$. (The calculated optical thicknesses of the FIRE clouds during the five sampling periods were all smaller than 30, so their albedos should be slightly less affected.) Assuming the same r_{eff} and range of EC concentrations as before, the reduction in albedo in this case is only 0.001 even under the most stringent circumstances. Due to the higher absorption of water at wavelengths other than 0.475 µm, reduction in spectrally-averaged albedos will be approximately half as large as those presented here.

We have found, therefore, that for the measured clouds which appear to have been moderately polluted, the amount of EC present was insufficient to affect albedo. Much higher contaminant levels or much larger droplets than those measured would be necessary to significantly alter the radiative properties. The effect of the concentrations of EC actually measured on the albedo of snow, however, would be much more pronounced since in contrast to clouds, snowpacks are usually optically semi-infinite and have large particle sizes.

Acknowledgements: This work was supported in part by NSF grant ATM-86-07377 and the Defense Nuclear Agency, through funds made available under document 57-0343 from Sandia National Laboratory. Radiative transfer calculations were made at NCAR and supported by NSF grant ATM-86-05134. We thank David Covert, Kevin Noone, and Steven Domonkos for their invaluable advice and aid in installing instruments aboard the aircraft. Thanks also are due to John Ogren and Jost Heintzenberg for building the first CVI.

Note: The full version of this paper is in preparation for the *Journal of Geophysical Research*.

Bohren, C. F., and D. R. Hoffman, in *Absorption and scattering of light by small particles*, p.446, Wiley-Interscience, New York, 1983.
Chylek, P., Ramaswamy, V., and V. J. Srivastava, Albedo of soot-contaiminated snow, *J. Geophys. Res.*, *88*, 10837-10843, 1983.
Clarke, A. D., Integrating Sandwich: a new method of measurement of the light absorption coefficient for atmospheric aerosols, *Appl. Opt.*, *21*, 3011-3020, 1982.
Clarke, A. D., and R. J. Charlson, Radiative properties of the background aerosol: absorption component of extinction, *Science*, *229*, 263-265, 1985.
Clarke, A. D., Warren, S. G., and T. C. Grenfell, Soot in the atmosphere and snow surface of Antarctica, *J. Geophys. Res.*, in preparation.
Hale, G. M., and M. R. Querry, Optical constants of water in the 200-nm to 200-µm wavelength range, *Appl. Opt.*, *12*, 555-562, 1973.
Hansen, J. E., and L. D. Travis, Light Scattering in Planetary Atmospheres, *Space Sci. Rev.*, *16*, 527-610, 1974.
Heintzenberg, J., Size-segregated particulate elemental carbon and aerosol light absorption at remote Arctic locations, *Atmos. Env.*, *16*, 2461-2469, 1982.
Kloesel, K. A., Albrecht, B. A., and D. P. Wyle, FIRE marine stratocumulus observations--summary of operations and synoptic conditions, Penn State University, 1988.
Noone, K. J., Charlson, R. J., Covert, D. S., Ogren, J. A. and J. E. Heintzenberg, Design and calibration of a counterflow virtual impactor for sampling of atmospheric fog and cloud droplets. Accepted in *Aer.Sci.and Tech.*, 1988.
Ogren, J. A., Elemental carbon in the atmosphere, Ph.D. dissertation, University of Washington, Seattle, 1983.
Ogren, J. A., Heintzenberg, J., and R. J. Charlson, In-situ sampling of cloud droplets with a droplet to aerosol converter, *Geophys. Res. Lett.*, *12*, 121-124, 1985.
Rosen, H., Hansen, D. A., Gundel, L., and T. Novakov, Identification of the optically absorbing component in urban aerosols, *Appl. Opt.*, *17*, 3859-3861, 1978.
Stephens, G., Paltridge, G., and C. Platt, Radiation profiles in extended water clouds. III: Observations, *J.Atmos. Sci.*, *35*, 2133-2141, 1978.
Twomey, S., The influence of pollution on the short-wave albedo of clouds, *J. Atmos Sci.*, *34*, 1149-1152, 1977.
Twomey, S., and T. Cocks, Spectral reflectance of clouds in the near-infrared: comparison of measurements and calculations, *J. Meteor. Soc. Jap.*, *60, 583-592*, 1982.
Twomey, S. A., Piepgrass, M., and T. L. Wolfe, An assessment of the impact of pollution on global cloud albedo, *Tellus*, *36B*, 356-366, 1984.
Weiss, R. E., The optical absorption properties of suspended particles in the lower troposphere at visible wavelengths, Ph.D. dissertation, University of Washington, Seattle, 1980.
Wiscombe, W. J., Improved Mie scattering algorithms, *Appl. Opt.*, *19*, 1505-1509, 1980.

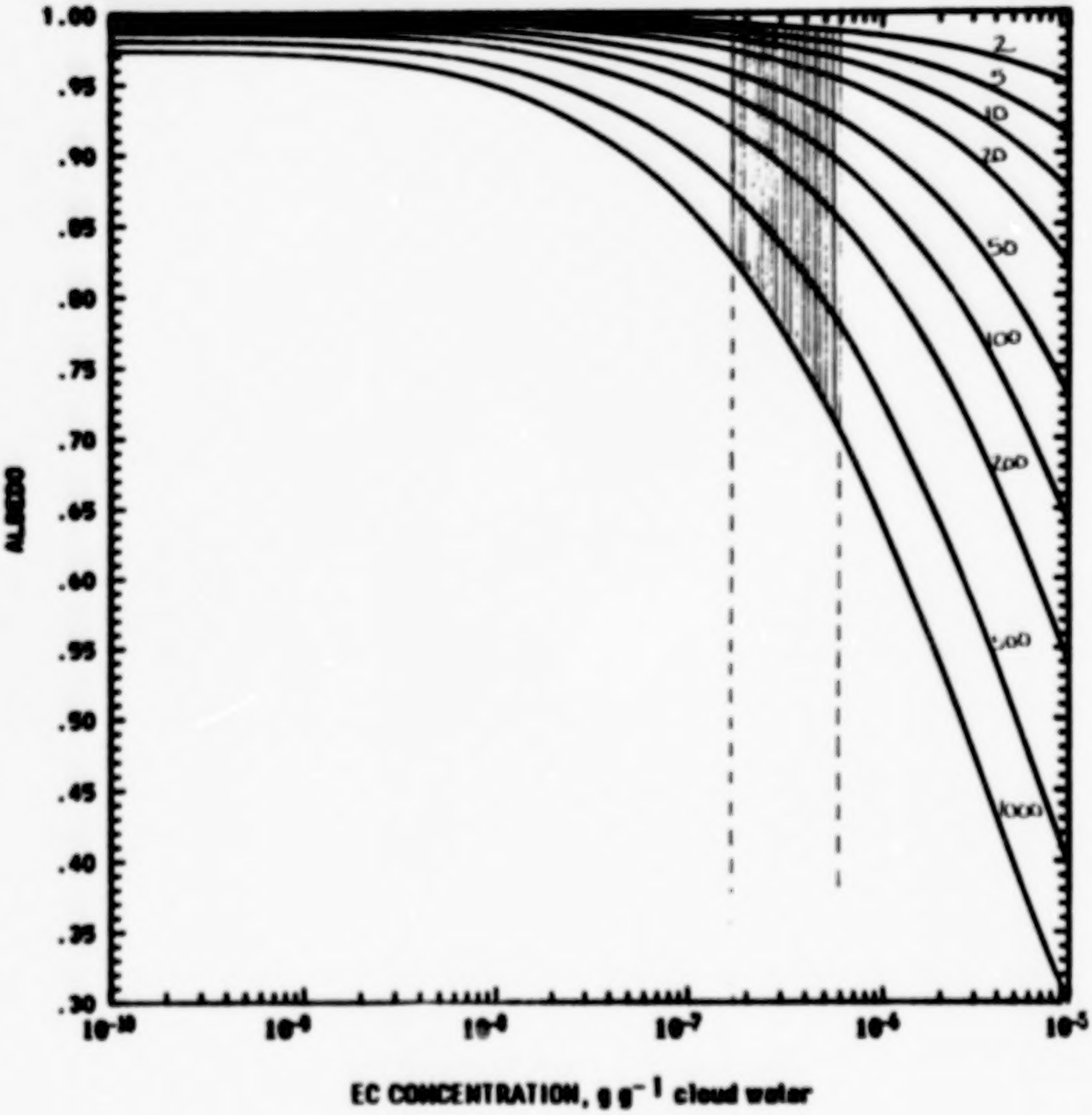

Figure 1. The effect of different concentrations of elemental carbon (EC) on the albedo of a semi-infinite cloud (optical thickness = ∞) at $\lambda = 0.475$ µm, with curved lines representing different values of effective droplet radii in µm. The shaded area represents the range of concentrations under consideration: from 1.6x10^{-7} which assumes the only EC in the cloud is the maximum amount measured *inside* droplets, to 5.9x10^{-7} which includes the maximum possible value for interstitial carbon as well. Since calculations modeled EC as an external mixture, the inside-droplet value was doubled to account for the enhanced absorption of EC inside water droplets [Chylek, 1983; Bohren, 1983].

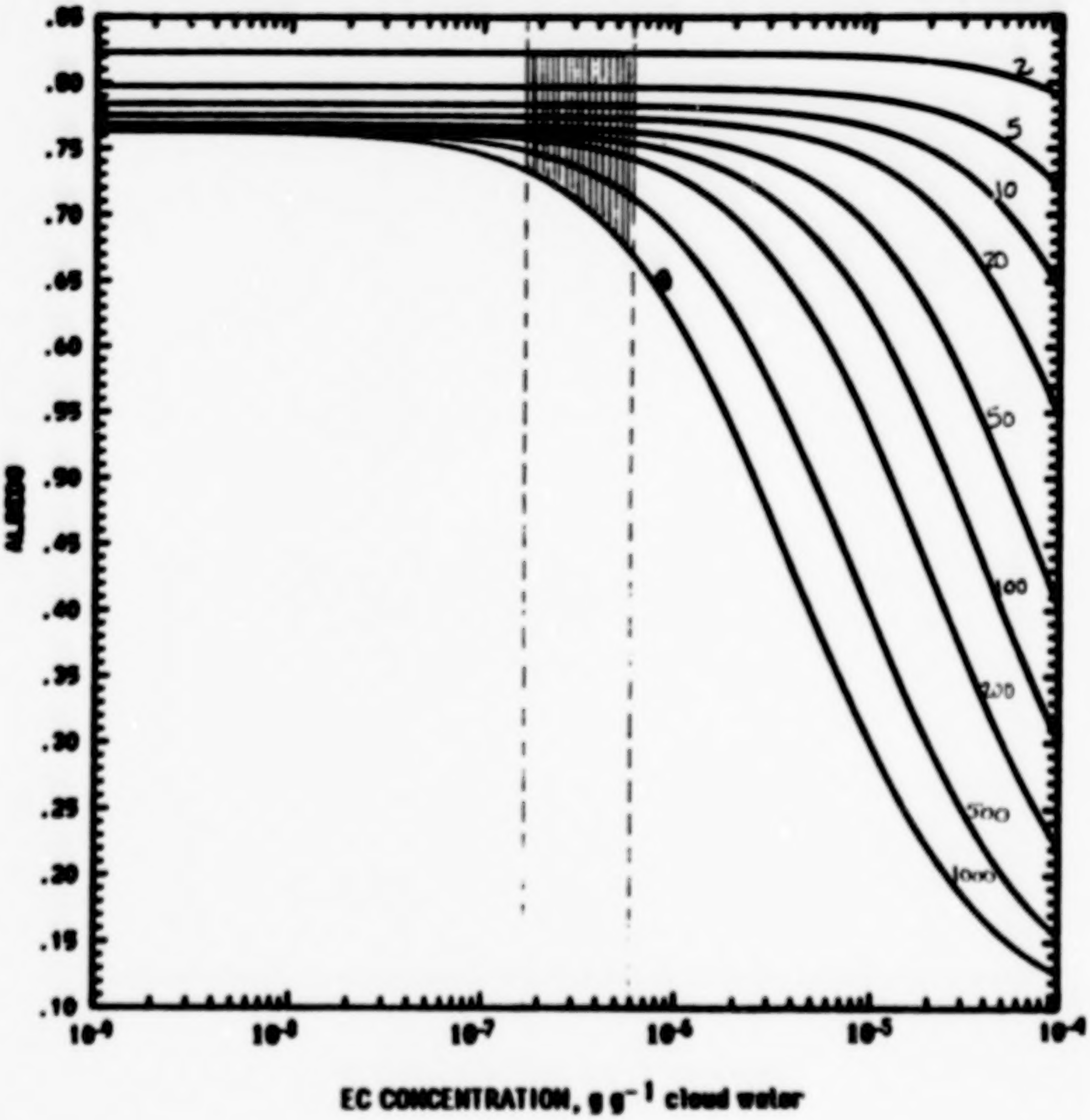

Figure 2. Same as Figure 1 except with a more realistic optical thickness of 30.

Preliminary Results of Radiation Measurements from the Marine Stratus FIRE Experiment

Francisco P. J. Valero, Philip D. Hammer, Thomas P. Ackerman[*],
Warren J. Y. Gore and Melinda L. Weil

NASA Ames Research Center, m/s 245-6, Moffett Field, CA 94035

[*]Dept. of Meteorology, Pennsylvania State University, University
Park, PA 16802

During the marine stratocumulus phase of the First International Satellite Cloud Climatology Regional Experiment (FIRE) in July 1987, we acquired radiative flux data from a variety of instruments which we flew on the NASA ER-2 high altitude aircraft. The spectral coverage ranged from the near UV to beyond 40 microns. In this paper we present a survey and selected preliminary analyses of these measurements.

The specific instruments used in the experiment were chosen primarily for measuring quantities of specific interest for marine stratocumulus fields. However, testing and evaluation of instrumentation and techniques to be used in the future inland cirrus experiment was also an important consideration. Details of the instruments and the significance of what they measure are given below.

A pair of multichannel narrow spectral band detectors spanning the near UV to near IR were mounted on the ER-2 fusilage, one each on top and bottom. Each covered a hemispherical field of view. Specific band center wavelengths were 380, 412, 500, 675, 778, 862, and 1064 nm with a typical bandwidth of 10 nm (FWHM). The measurements of interest are the reflected solar fluxes, from which spectral albedo values may be determined.

A pair of selectable solar spectral band detectors (0.2 to 3.5 or 0.6 to 3.5 micron) covering the upper and lower hemispheres were also mounted on the fusilage. Although the interpretation of these measurements is complicated by the absorption of atmospheric molecules, a rough estimate of the solar IR albedo of the cloud field may be obtained from the upwelling flux measurements. The flux results may be used together with the broad band IR flux measurements described below to determine thermal IR fluxes.

A two channel narrow spectral band and narrow field of view detector was contained in a pod mounted on the fusilage. Both elements detect upwelling radiation within a conical field half-angle of about 15 degrees. A liquid nitrogen cooled zero-radiation reference is an integral part of this detector and serves to eliminate systematic measurement errors in absolute flux determinations. One channel with a 9.90 - 10.87 micron bandwidth was designed to lie within an atmospheric transmission window. The second channel with a 6.14 - 7.14 micron bandwidth covers a strong water vibrational band. Because of the low altitudes at which marine stratus cloud fields reside it is expected that interpretation of the 6 micron channel measurements will be very difficult due to intervening water vapor absorption. However, under the proper circumstances, the 10 micron channel measurements may be used to estimate optical depths in this region of the spectra. The primary use of the 6 micron data will be as an indicator of higher altitude clouds.

A rotating platform on the wing of the ER-2 allows for 2 selectable detectors. The platform periodically rotates 180 degrees in flight so that each detector alternately measures upwelling and downwelling flux. This serves to eliminate systematic measurement errors in absolute net flux determinations. For the majority of the flights, two hemispherical field of view detectors were used, one with a solar spectral bandwidth like that described above (0.6 to 3.5 microns) and the other with a broadband spectral sensitivity ranging from about 0.6 to beyond 40 microns. The system is designed to yield accurate net flux measurements for the solar and terestrial thermal spectral regions. Although analysis with respect to the marine stratus cloud fields is expected to have problems similar to those discussed above, it is of interest to constrast these results with those of the FIRE cirrus measurements of October 1986. The high altidutes at which the cirrus clouds resided substantially reduced the problems of interference from intervening molecular gasses.

The data are presented in the light of the above instrumental considerations. Where appropriate, comparisons are made to FIRE cirrus results.

Third Generation Earth Radiation Budget Measurements; ERBE in the Context of Earlier Systems

Thomas H. Vonder Haar

Cooperative Institute for Research in the Atmosphere
Colorado State University
Fort Collins, Colorado 80523

The Earth Radiation Budget Experiment observations are just becoming available for scientific use. These represent the third generation of measurements with steadily improving accuracy and resolution. Beginning in the 1960s observations by spherical detectors established the mean albedo of the earth near 30% in substantial variance from presatellite estimates. The Nimbus 6 and 7 wide field of view ERB measurements represent a long-term climatology of measurements at 1000 km resolution. The ERBE measurements introduce higher accuracy and higher space and time resolution result.

Comparisons will be presented of several April ERB measurements to illustrate what this improvement in resolution and accuracy can yield. Simultaneous ERBE and Nimbus 7 measurements for April 1985 show nearly identical results on the large scale. Comparison of measurements of direct solar energy from ERBE, Solar Max Mission and Nimbus 7 suggest a "solar constant" value of 1368 w/m^2 for the 1979-1986 period. The long-term record of earth radiation budget (Aprils from 1976-1985) over large regions is shown to have interannual variation of ± 20-30 w/m^2. The new ERBE data will allow this climate record measurement to continue.

For presentation at
FIRE Science Team Meeting
Vail, Colorado
July 11-15, 1988

Figure 1. Zonal means of ERBS, NOAA 9 and Nimbus 7 April, 1985 emitted exitance. The Nimbus 7 data has been deconvolved using the spherical harmonic approach.

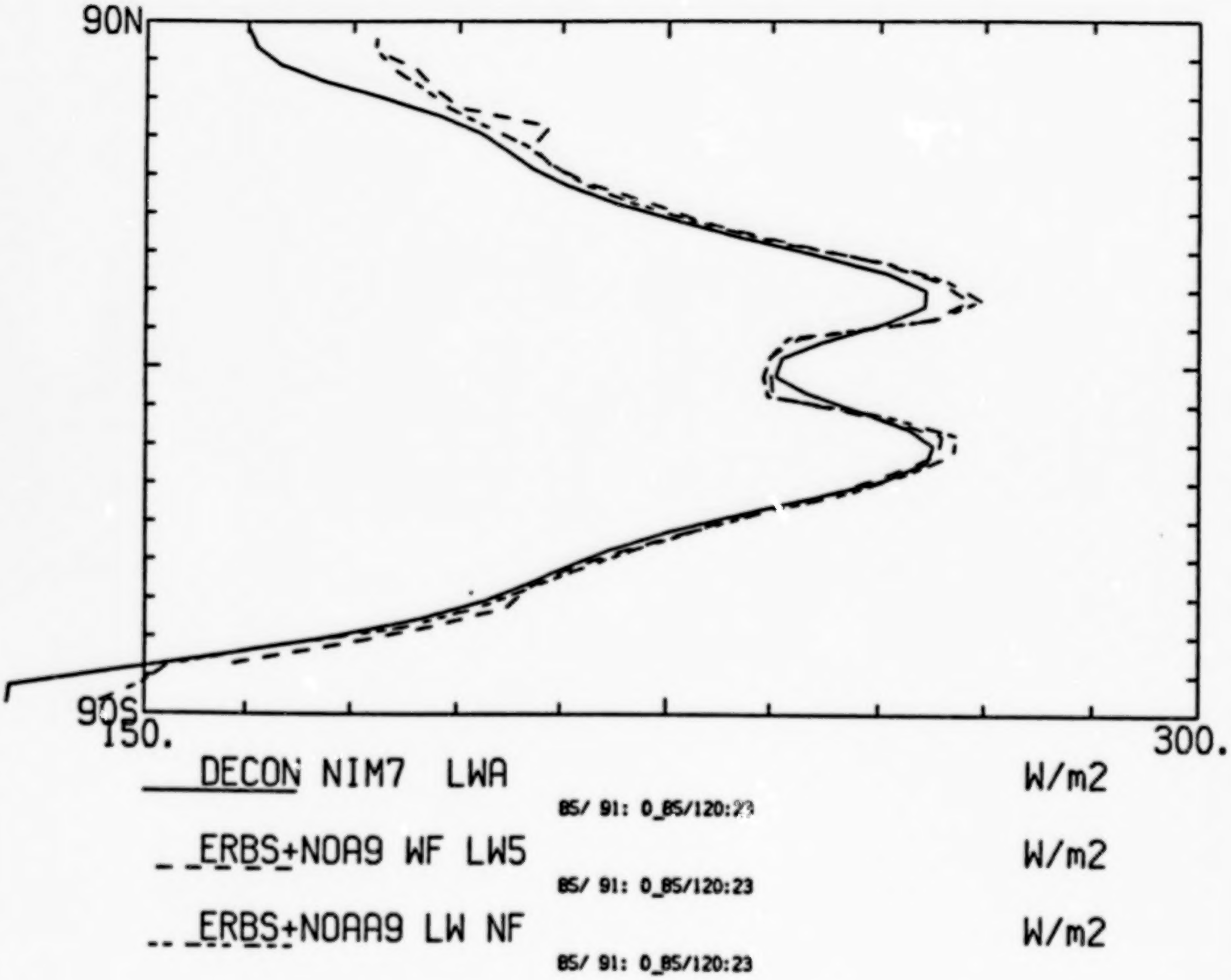

Figure 2. Map of the difference between combined NOAA 9+ ERBS and Nimbus 7 emitted exitance. The ERBE data was filtered to the same spherical harmonic resolution as the Nimbus 7 data, order 15.

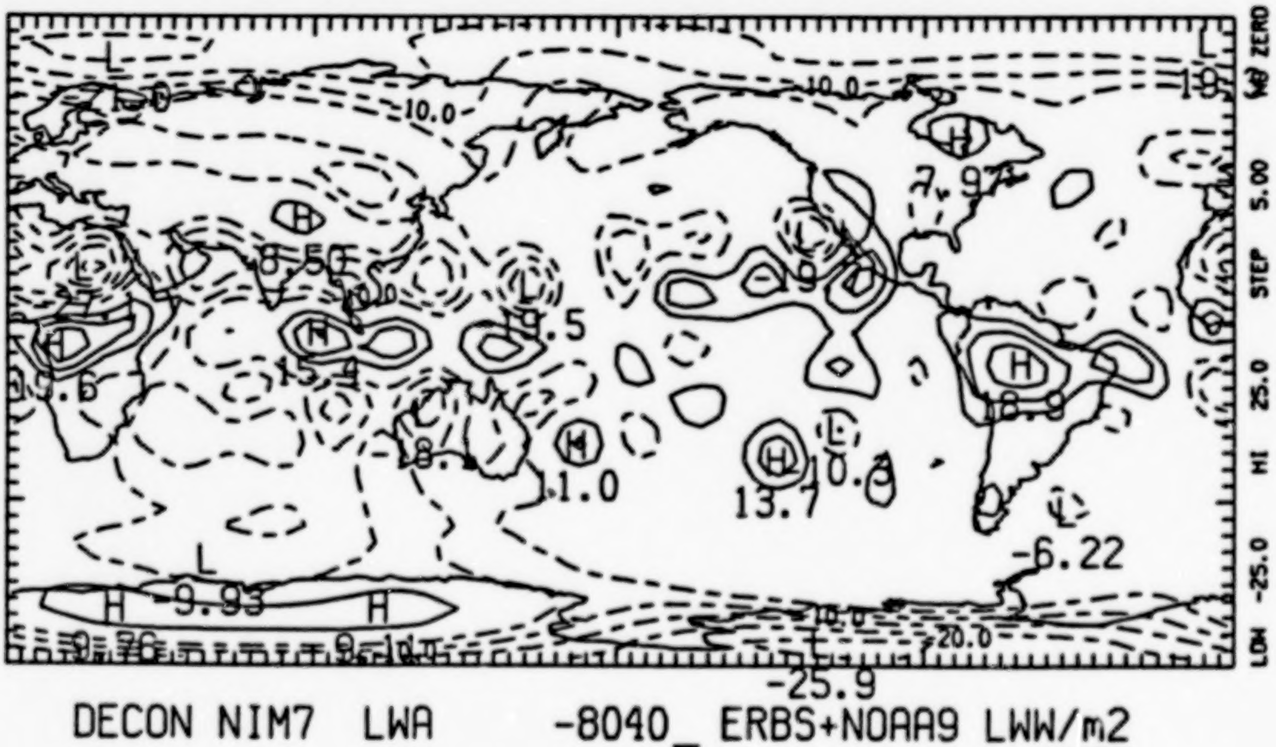
ZERO
5.00
STEP
25.0
HI
-25.0
LOW
10.0
-19.
7.97
8.50
15.4
9.5
18.9
11.0
13.7
10.8
-6.22
-9.93
-25.9
-20.0
H
L
DECON NIM7 LWA -8040_ ERBS+NOAA9 LWW/m2

— April, 1985 —

Figure 3. Time series for different regions of the emitted exitance. Included are 4/76, 4/77, 4/78 from Nimbus 6, 4/79 and 4/80 from the old Nimbus 7 analysis scheme and 4/81, 4/82, 4/83, 4/84, 4/85 from the new Nimbus 7 analysis. The symbols N (NOAA 9) and B (NOAA 9, ERBS) represent the monthly means for ERBE.

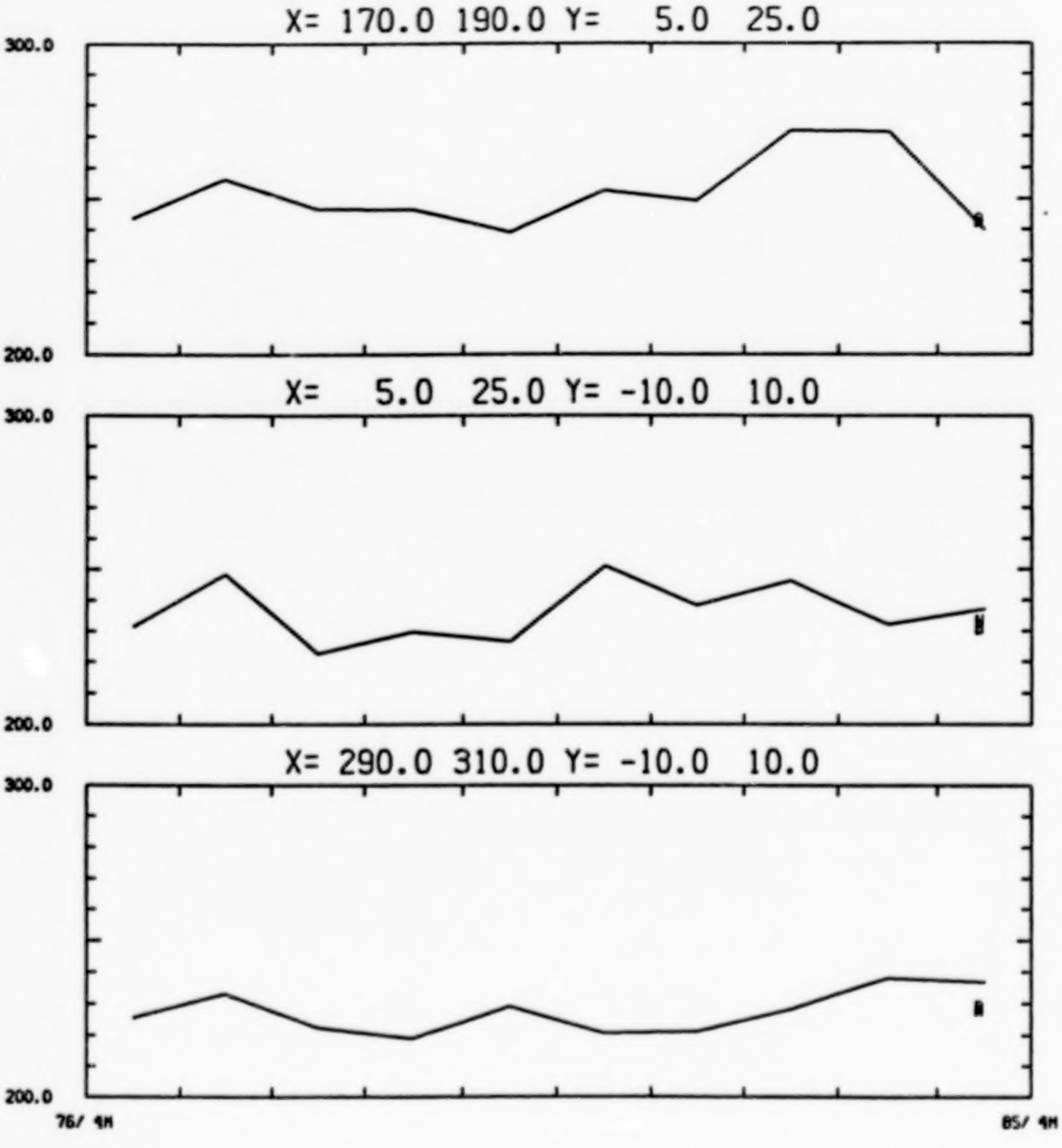

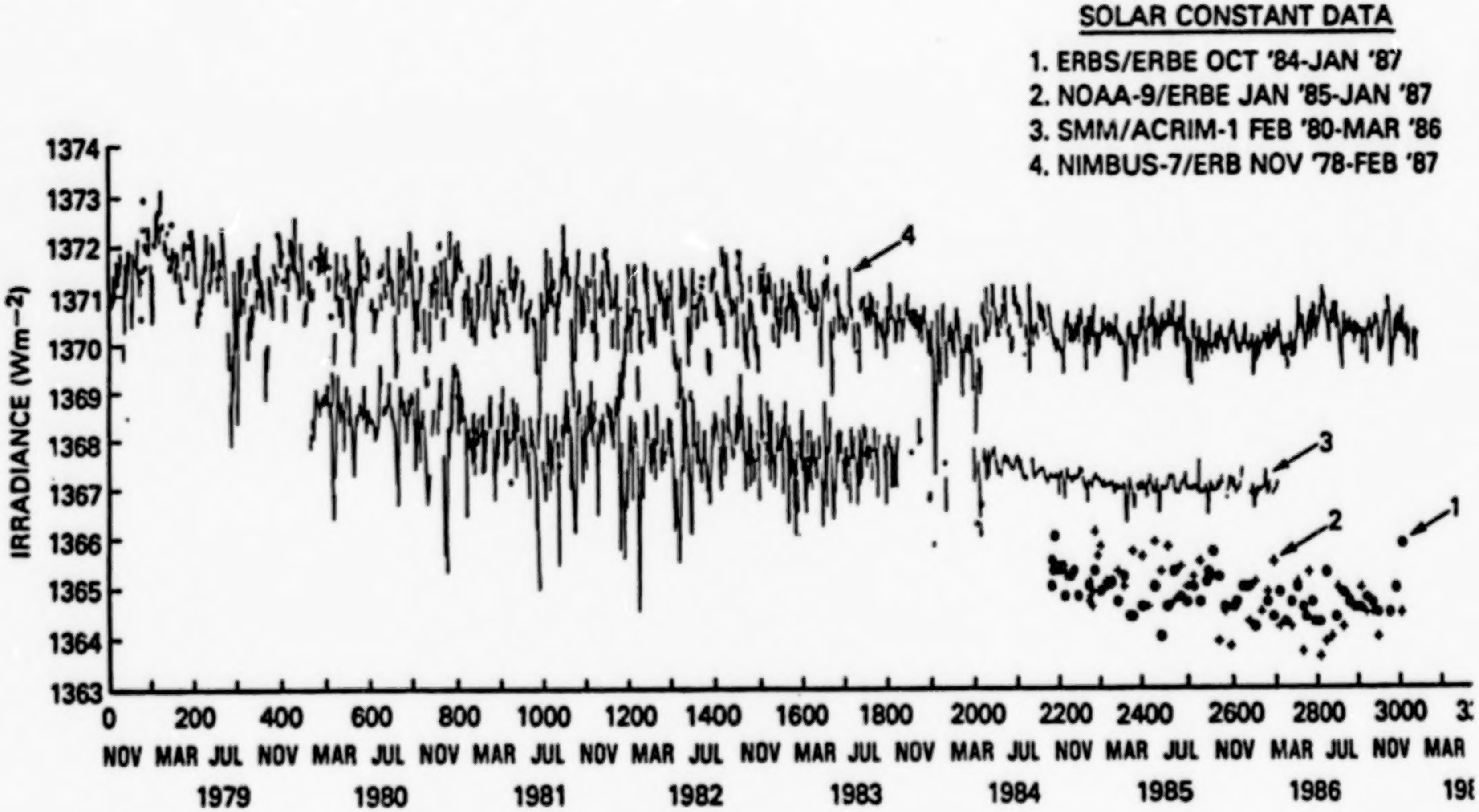

Figure 4. (after Mercherikunnel, Kyle and the Nimbus-7 ERB Experiment Team, 1988)

SAN NICOLAS ISLAND SURFACE RADIATION-METEOROLOGY DATA

by
Christopher M. Johnson-Pasqua
and
Stephen K. Cox
Department of Atmospheric Science
Colorado State University
Fort Collins, CO 80523

The following is a summary of the surface data collected by CSU on San Nicolas Island during the FIRE experiment from 30 June (Julian Day 181) through 19 July (Julian Day 200). The data are available in two formats; hard copy graphs, and processed data on floppy disk.

Table 1. Instrumentation Specifications

Instrument	Serial Number	Dome Type	Measurement Region
Pyranometer	21568F3	WG7	.3 to 2.8 μm
Pyranometer	21570F3	RG8	.7 to 2.8 μm
Pyrgeometer	25690F3	silicon	4 to 50 μm
Dome Thermistor			-10 C to +50 C
Sink Thermistor			-10 C to +50 C
Air Temperature			-33 C to +48 C
Relative Humidity			12% to 100%
Wind Speed			0 to 60 Meters/sec
Wind Direction			0 to 356 Deg

RESEARCH SPONSORED BY:
ONR No. N00014-87-K-0228
and NASA No. NAG 1-554

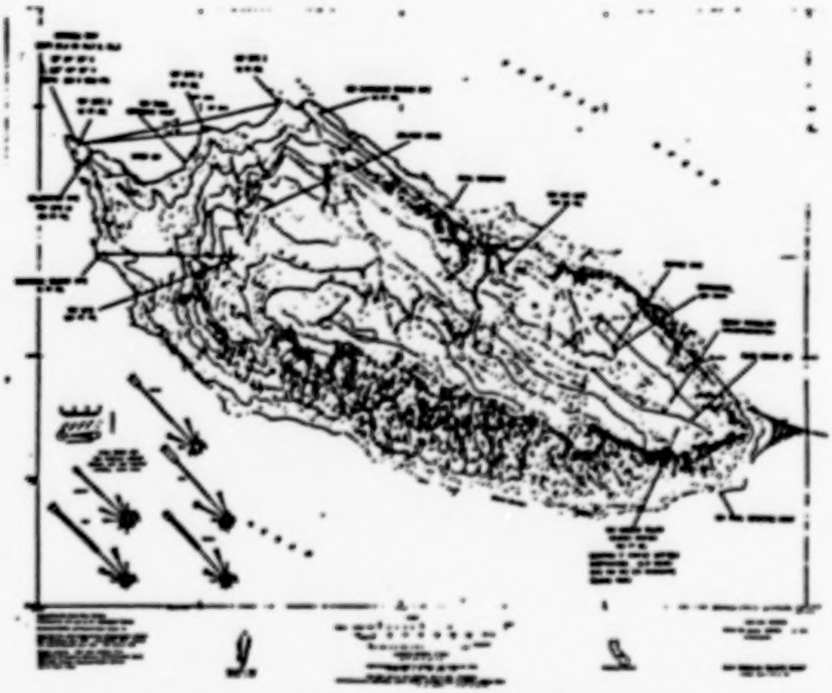

Figure 1: Map of San Nicolas Island, California. The island is approximately 16 km long and 5 km wide. The radiation/meteorological station was deployed at the calibration site (DSP site D) on the west side of Laser Bay. The station was 38 meters above sea level on a ridge approximately 400 meters South East of the Penn State surface instrumentation.

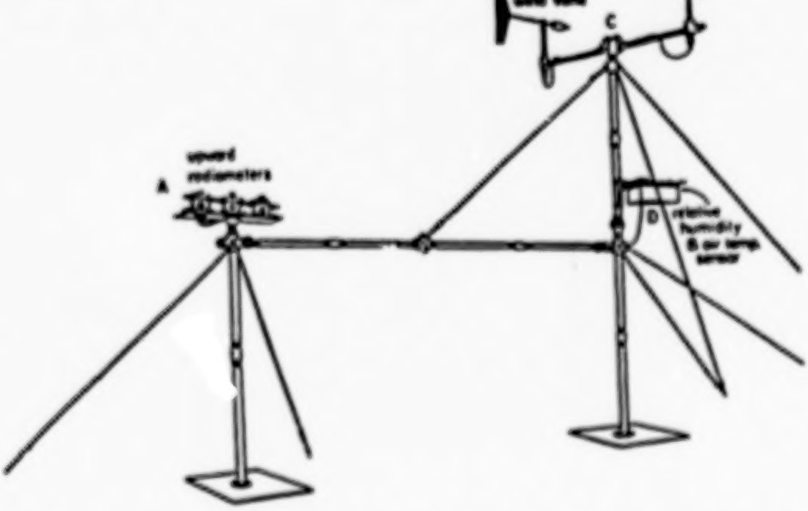
anemometer
wind vane
C
upward radiometers
A
D
relative humidity & air temp. sensor

Figure 2: Schematic Diagram of Radiation/Meteorological station used on San Nicolas Island.

FOUR DAY DATA SAMPLE

FIRE – SNI – SURFACE WIND DATA
JD 186 – JULY 5,1987

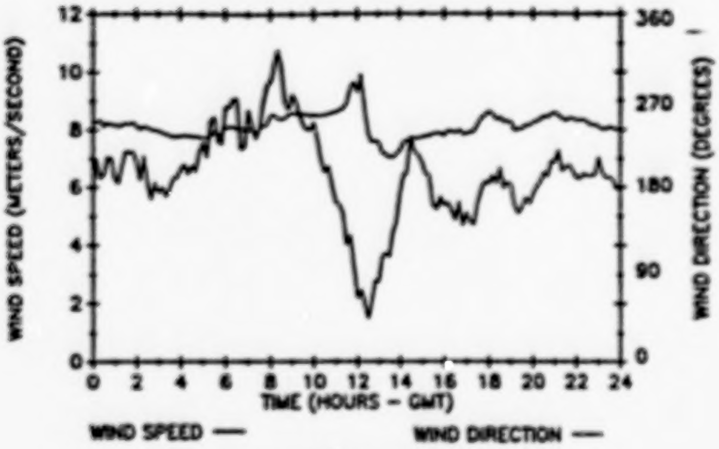

FIRE – SNI – AIR TEMP & RELATIVE HUMIDITY
JD 186 – JULY 5,1987

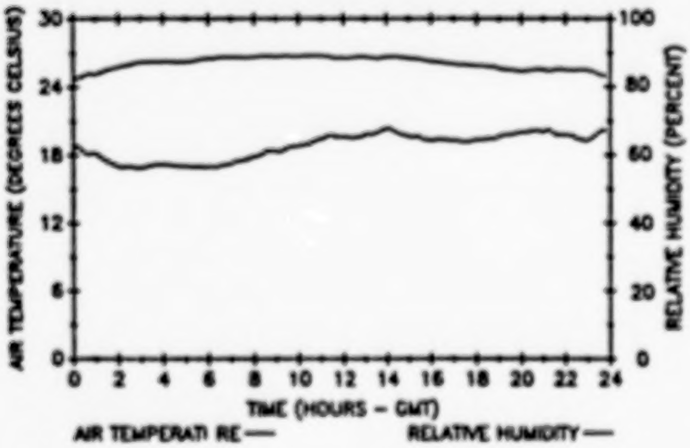

FIRE – SNI – DOWNWELLING SURFACE RADIATION
JD 186 – JULY 5,1987

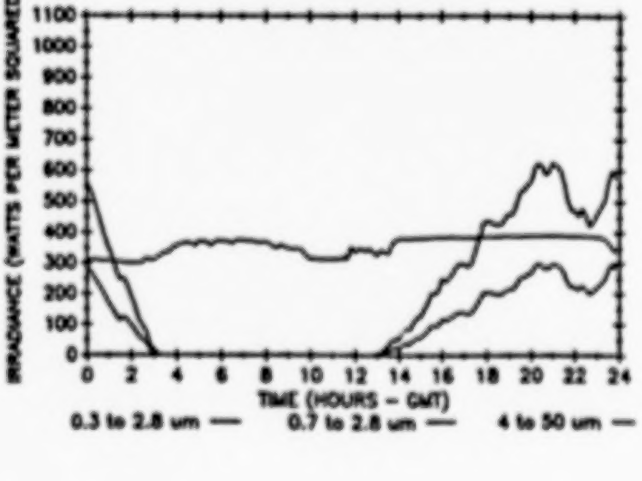

FIRE – SNI – SURFACE WIND DATA
JD 187 – JULY 6,1987

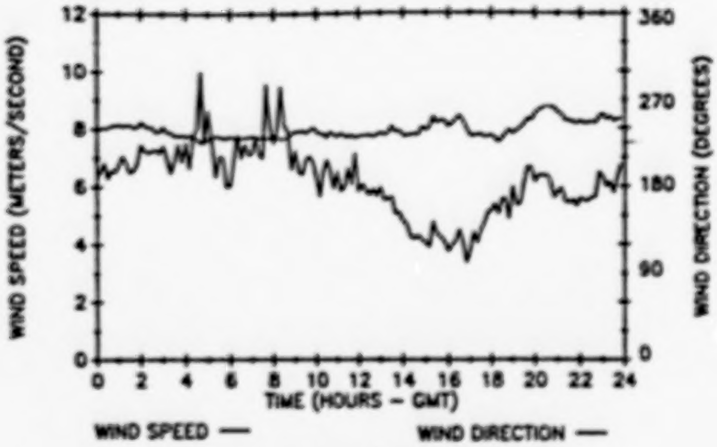

FIRE – SNI – AIR TEMP & RELATIVE HUMIDITY
JD 187 – JULY 6,1987

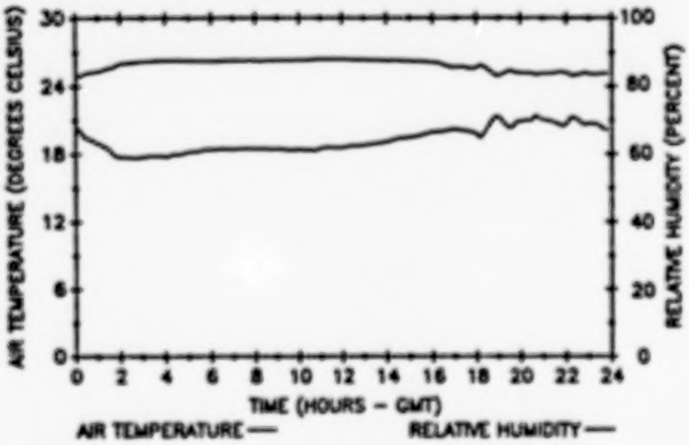

FIRE – SNI – DOWNWELLING SURFACE RADIATION
JD 187 – JULY 6,1987

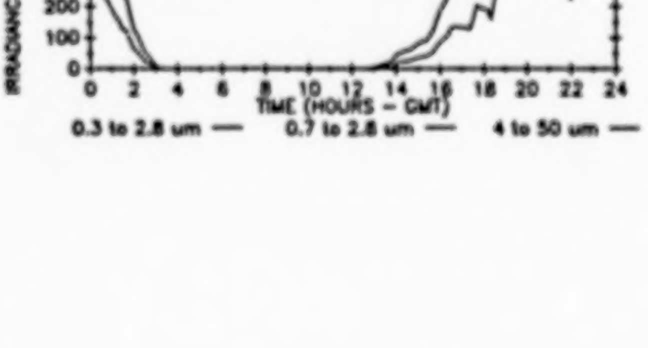

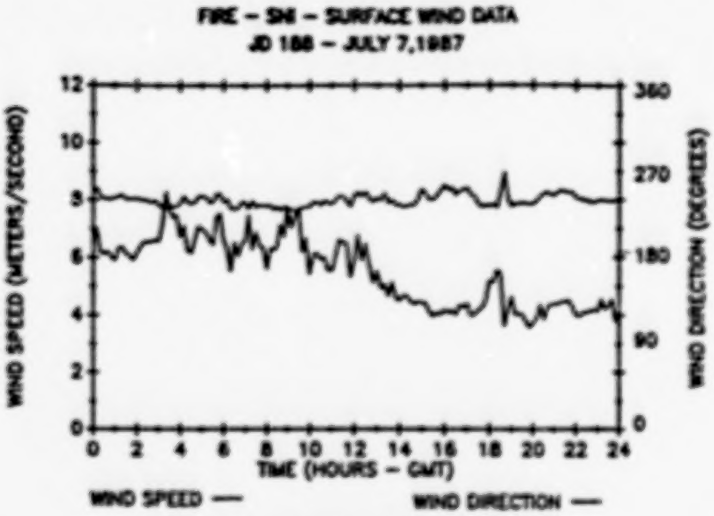

FIRE – SNI – SURFACE WIND DATA
JD 188 – JULY 7,1987

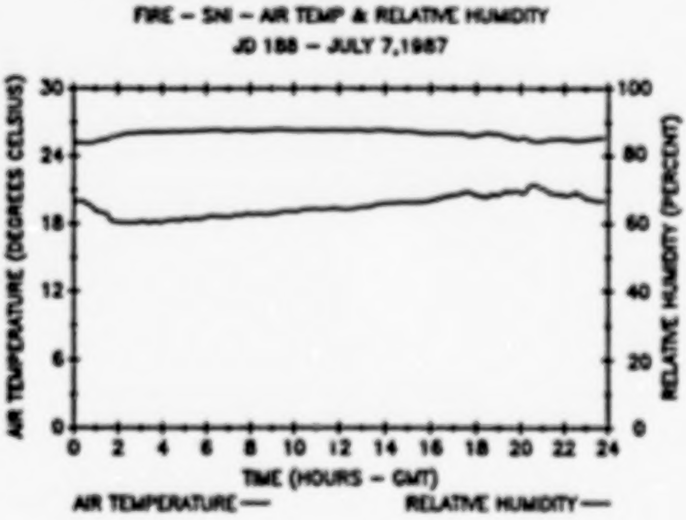

FIRE – SNI – AIR TEMP & RELATIVE HUMIDITY
JD 188 – JULY 7,1987

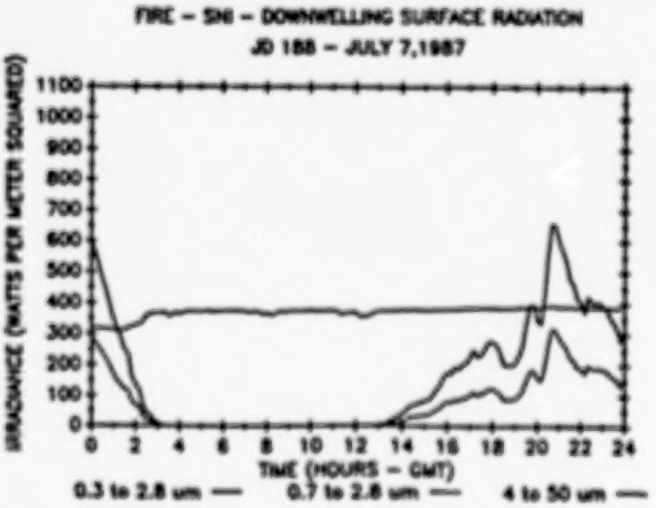

FIRE – SNI – DOWNWELLING SURFACE RADIATION
JD 188 – JULY 7,1987

FIRE – SNI – SURFACE WIND DATA
JD 189 – JULY 8,1987

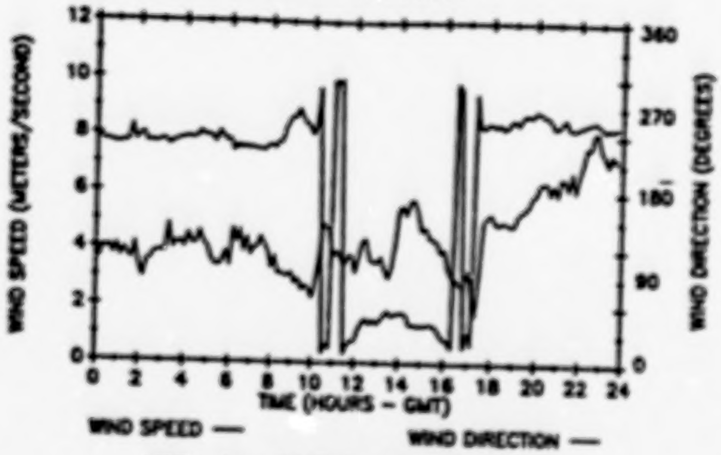

FIRE – SNI – AIR TEMP & RELATIVE HUMIDITY
JD 189 – JULY 8,1987

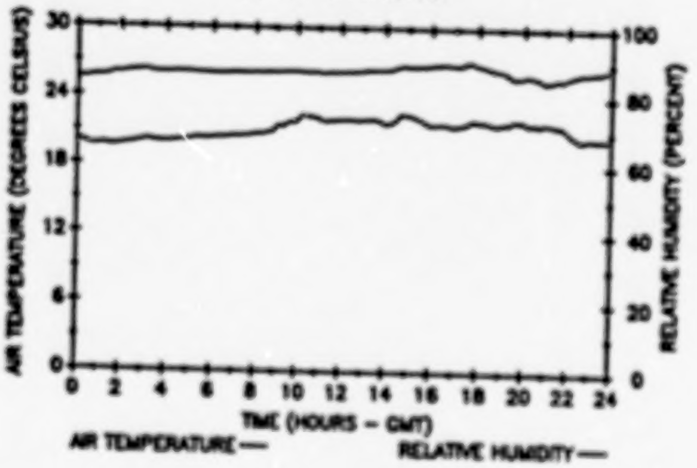

FIRE – SNI – DOWNWELLING SURFACE RADIATION
JD 189 – JULY 8,1987

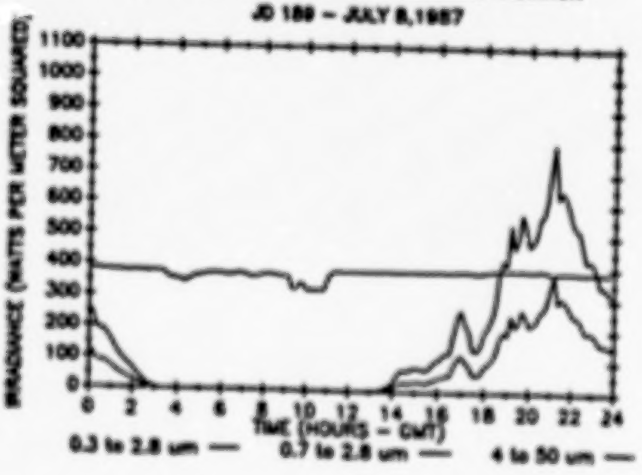

FIRE SCIENCE TEAM MEETING
VAIL, COLORADO
JULY 11-15, 1988

MARINE STRATOCUMULUS

CASE STUDIES - MARINE STRATOCUMULUS IFO - Stephen Nicholls — Friday, July 15, 1988

PAGE

Comparison and Calibration of NCAR Electra Instruments: July 5 and July 7, 1987 — 425
Austin, Philip H.; and Reinout Boers

Thermodynamic Structure of the Stratocumulus-Capped Boundary Layer on 7 July 1987 — 429
Boers, Reinout; Alan K. Betts, and Philip H. Austin

Aircraft/Island/Ship/Satellite Intercomparison: Preliminary Results from July 16, 1987 — 433
Hanson, Howard P.; Ken Davidson, Herman Gerber, Siri Jodha Singh Khalsa,
Kevin A. Kloesel, Ronald Schwiesow, Jack B. Snider, Bruce A. Wielicki,
and Donald P. Wylie

A Preliminary Analysis of LANDSAT and UK C130 Data from Mission 197-A, on 16 July 1987 — 437
Nicholls, S.

Comparison and Calibration of NCAR Electra Instruments: July 5 and July 7, 1987

Philip H. Austin[1] and Reinout Boers[2]

[1]Code 613 and [2]Code 617
Nasa Goddard Space Flight Center
Greenbelt, MD 20771

Measurements of temperature, water vapor, cloud liquid water, and lidar cloud height taken by the NCAR Electra are analyzed for two days of the FIRE stratocumulus field program. Examination of instrument time series, correlations between sensors, soundings through the layer and lidar measurements of cloud base height are used to correct sensor offset problems, check for probe wetting, and choose the most accurate measurements of temperature, humidity, and cloud liquid water.

1) Temperature and Humidity

Three instruments measured water vapor concentration: the top and bottom Cambridge dewpoint thermometers (DPTC and DPBC) and the Lyman-α hygrometer.(RHOLA). Both of the Cambridge mirrored dewpoint instruments displayed the 0.33 Hz oscillations and lagged response typical of these sensors (Boers and Betts, 1988). We applied a simple three point running mean filter to the measurements and introduced a 2 second delay, which brings both dewpoint probes into qualitative agreement with the Lyman-α hygrometer.

A grouped comparison of the two dewpoint thermometers, the Lyman-α hygrometer and the four temperature sensors (fast response (ATKP), reverse flow (ATRF), Rosemount (ATB), and radiometric (PRT6)) can be done when the aircraft is in solid cloud. Cloud penetrations were examined for both July 5 and July 7, and a typical segment is shown in Figure 1. The 10 Hz measurement of droplet number concentration given by the Forward Scattering Spectrometer Probe (FSSP) is > 10 cm^{-3} throughout this section, indicating that the air is close to saturation on 10 meter length scales. The range of readings from the different thermometers, their relative values with respect to one another, and the tendency of the each of the dew point sensors to pair with a different thermometer (DPTC with ATKP and DPBC with ATRF) are typical of cloud penetrations on both July 5 and July 7. The fast response and top dewpoint thermometers are 1 K warmer than the reverse flow and bottom dewpoint thermometers, with the Rosemount probe in between the two extremes. Out of cloud the temperature measured by the reverse flow sensor warms relative to the other instruments, indicating wetting problems. On some cloud penetrations the temperature of the fast response probe also appears to be affected by wetting, as is the output of the Lyman-α hygrometer. The radiometric thermometer (PRT6) gives a 1 K higher temperature reading and is not affected by cloud water, but the air volume measured by the PRT6 depends on the optical thickness of the surrounding cloud.

For purposes of comparison in Figure 1 the Lyman-α absolute humidity measurement is converted into a saturation vapor pressure using the fast response temperature. The vapor pressure is then inverted to find the dewpoint using an approximation from Bolton (1980). As Figure 1 shows, the humidity value given by the Lyman-α instrument is consistently 1 K higher than that given by either dewpoint thermometer. The difference is equivalent to an approximately 1 g m^{-3} offset in the water vapor measurement between the Lyman-α and the dewpoint temperature probes.

An independent check on the absolute accuracy of these divergent temperature measurements can be made using the lidar measurement of cloud base height. The lifting condensation level of sub-cloud air was computed for all pairs of vapor and temperature measurements for the sub-cloud flight legs on the July 5 case, which had a well-mixed boundary layer. Figure 2 shows the cloud base heights above the aircraft determined in this way for three of the instrument pairs as well as the lidar measurement of cloud base height. The best agreement with the lidar-determined cloud base is consistently given by the fast response thermometer (ATKP) and the top dewpoint sensor (DPTC), indicating that the bottom dewpoint sensor, the Rosemount thermometer, the reverse flow thermometer and the Lyman-α hygrometer have offset problems that will have to corrected before use.

2) Liquid water

Vertical profiles of the two analog liquid water probes, the King and the Johnson-Williams (JW), show pressure dependent zero offsets on both July 5 and July 7. At cloud level the zero offsets range from 0.04 - 0.08 g kg^{-1} (JW) and 0.05 - 0.10 g kg^{-1} (King). When these offsets are removed the maximum cloud liquid water content measured by the two sensors agrees within 20% on 10 of the 15 penetrations examined on the two days. On July 7 the liquid water content measured by the FSSP agrees to within 20% with the measurements of both the JW and King probes, but on July 5 it underestimates the cloud liquid water by a factor of 3-5.

3) Work in progress

Further studies are underway to determine the sensitivity of the temperature and water probes to the rapid ascents and descents through the cloud layer ("dolphin" flight legs), to compare conditional sampling of updrafts and downdrafts using cloud droplet concentrations, parcel temperature, and ozone content, and to calculate boundary layer mixing lines using ozone concentration as well as conservative thermodynamic tracers.

References:

Bolton, David, 1980: 'The computation of equivalent potential temperature'. Mon. Wea. Rev., 108, 1046-1053.

Boers, R. and A.K. Betts, 1988: 'Saturation point structure of marine stratocumulus clouds'. J. Atmos. Sci., 45, 1156-1175.

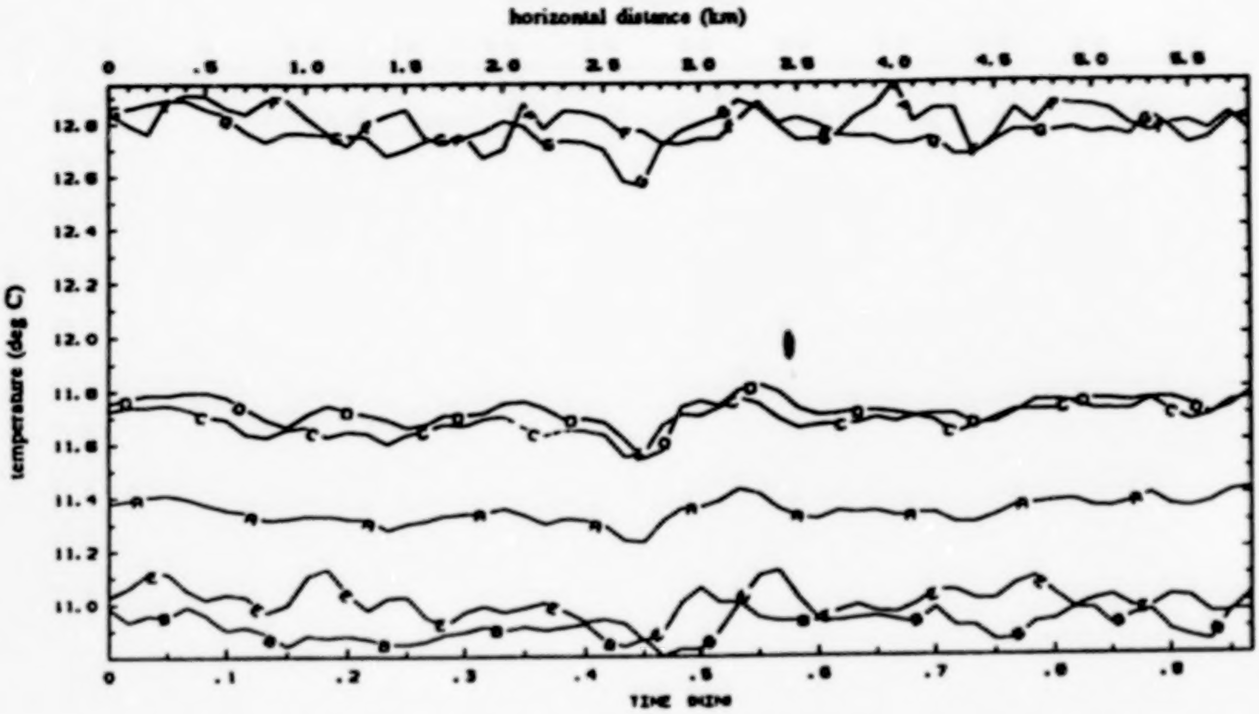

Figure 1: One miniute of in-cloud data (July 7, beginning at 20:16 Z) showing temperature measurements from (a) Rosemount, (b) reverse flow, (c) fast response, (d) top Cambridge dewpoint, (e) bottom Cambridge dewpoint, (f) Barnes PRT-6, (g) Lyman-a hygrometer (see text)

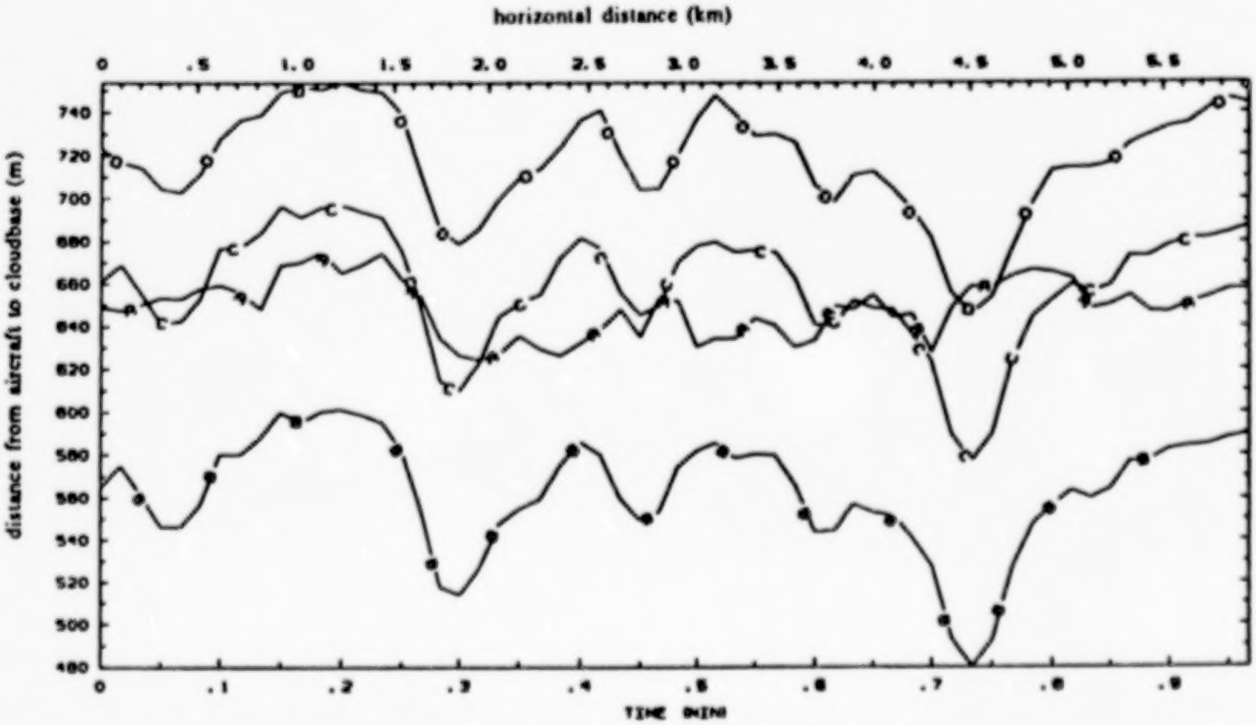

Figure 2: One minute of sub-cloud data (July 5, beginning at 18:11 Z) showing distance from aircraft to cloud base measured by (a) lidar, and computed assuming a well-mixed layer using measurements from (b) Rosemount and top Cambridge dewpoint thermometer, (c) fast response and top Cambridge dewpoint thermometer, (d) fast response and bottom Cambridge dewpoint thermometer.

Thermodynamic structure of the stratocumulus-capped boundary layer on 7 July, 1987

Reinout Boers', Alan K.Betts" and Philip H.Austin•

NASA/Goddard Space Flight Center
'code 617
•code 613
Greenbelt, Maryland 20771

and

"RD2, Box 3300, Middlebury, VT 05753

1. Introduction.

As part of project FIRE a mission was carried out on 7 July 1987 to study the thermodynamic structure of a boundary layer which is in transition from a clear to a cloudy state. The NCAR-Electra flew a pattern in tight coordination with the NASA-ER2 aircraft near 122 West, 31.6 North off the coast of California. The preprocessing of this data is discussed elsewhere in this conference (Austin and Boers), so we will confine ourselves to a description of the thermodynamic structure. Our purpose is to derive the entrainment rate and the fluxes of the thermodynamic variables. To this end we will represent the data in conserved variable diagrams.

2. Mean structure.

Examination of Landsat and Multispectral Cloud Radiometer data revealed that the area was at the edge of a large cloud deck with the boundary stretching out from northeast to southwest near the 122 longitude line. Based on lidar cloud top measurements and observers notes it was determined that the cloud boundary drifted towards the east. It was therefore decided to divide the main east-west flight legs into three regions drifting with the speed of this boundary in order to derive meaningful statistics for this transition. The region towards the west was covered by small cumulus clouds, the middle was covered by broken stratocumulus, while the region towards the east was entirely cloudy. We will call these regions SM, BR, and SC (for SMall cumulus, BRoken stratocumulus, and StratoCumulus). Mean boundary layer wind speeds were out of the northwest at 14 m/s and shifting towards the west in region SC. Above the boundary layer winds shifted towards the north in region SM, while in region SC it remained constant with height. Figure 1 shows the average potential temperature and dewpoint profile for each of the three regions. From west to east the boundary layer dries, cools and rises. The atmosphere aloft in region SM contains almost the same amount of moisture as the the boundary layer, but is separated from it by a very dry layer. This dry layer has a relatively high ozone content and may originate from upper tropospheric levels. In region SC the moist layer above the boundary layer is entirely absent.

3. Conserved variable structure.

In this section we examine the thermodynamic structure in terms of total water content and saturation potential temperature. These thermodynamic variables are conserved under adiabatic translation. Mixing of air parcels and/or layers occurs along straight lines on diagrams which have these variables as their axes. Processing of the raw temperature and dewpoint measurements was similar to that of Boers and Betts (1988). We show the pressure-averaged (5 hPa interval bins) mixing diagrams in Figure 2. It appears from these diagrams that the air above the boundary layer has a different origin in the SM region than in the SC region. This is further supported by the strong shear in mean horizontal wind at the top of the boundary layer in the SM region which is absent in the SC region.
We computed the parameter dp^*/dp, where p is pressure and p^* the saturation pressure. This parameter reflects the degree of mixing of the boundary layer. If $dp^*/dp = 0.0$ then the layer is well-mixed. For $dp^*/dp > 0.0$ the layer is considered partly mixed with gradients in the extensively conserved variables. For this case study we found $dp^*/dp = 0.3$ for the stratocumulus regime. For the subcloud layer in the broken and small cumulus regime dp^*/dp decreased to 0.24. In the cloud layer in the SM and BR region $dp^*/dp = 1.9$, 1.5 respectively.

4. Discussion and outline of further work.

Analysis of the data so far indicates that the thermodynamic structure of the lower troposhere changes dramatically from west to east (from shallow cumulus to broken stratocumulus to stratocumulus). In addition to variability in temperature, moisture and mixing line structure in the lowest 250 hPa of the atmosphere there appears to be a gradient in sea surface temperature with the colder temperatures towards the east. This colder water has the effect of retarding the breakup of the clouds from the west.
We intend to perform an analysis of the thermodynamic budget for the three different sections, so that entrainment and vertical flux structure can be computed for this case study.

Reference: R.Boers and A.K.Betts, 1988: Saturation point structure of marine stratocumulus clouds. J.Atmos.Sci., 45, 1156-1175.

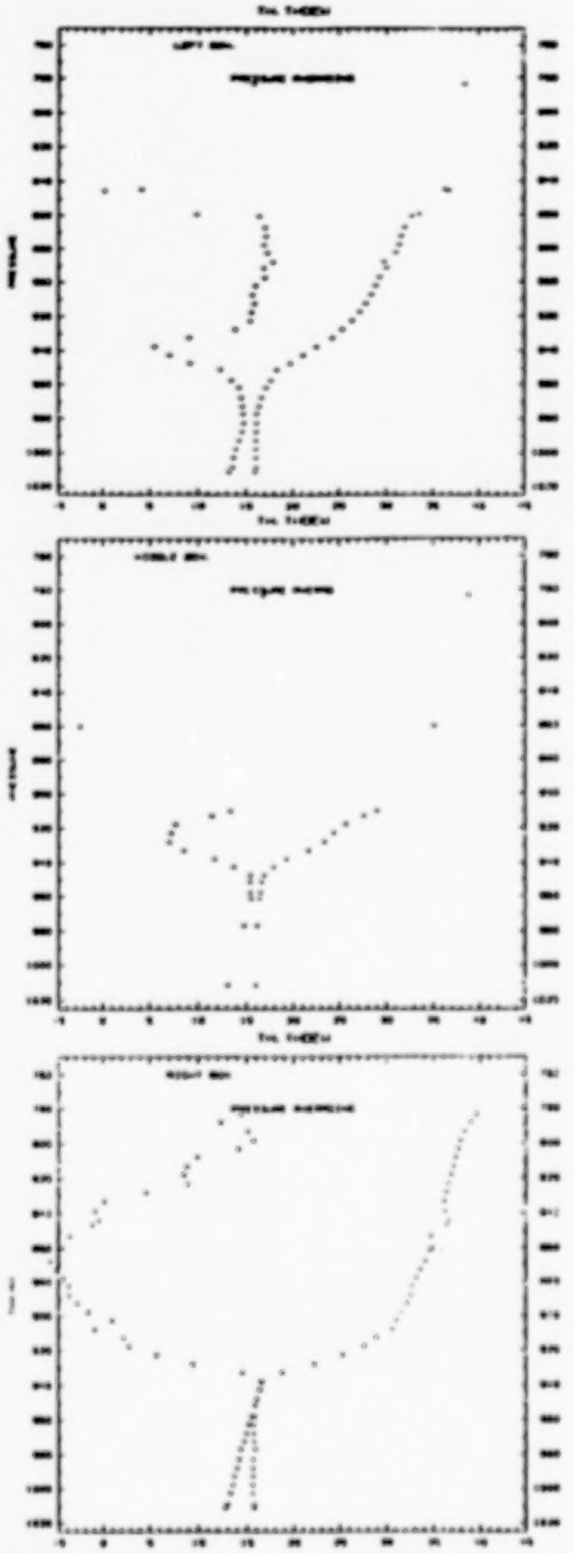

Figure 1. Potential temperature and dewpoint profiles, averaged for the three sections. The top diagram represents region SM, the middle UH and the bottom SC.

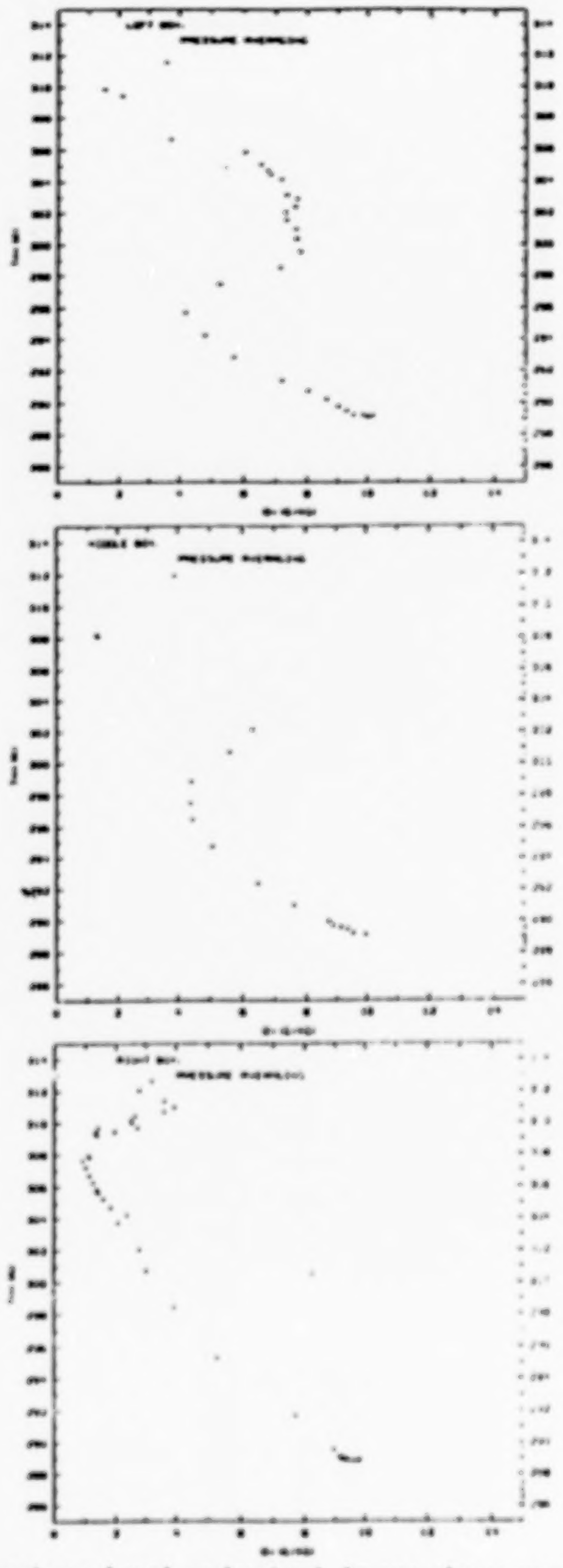

Figure 7. Saturation level potential temperature versus total water content, pressure averaged, for the three sections. The top diagram represents region SM, the middle BR, and the bottom SC.

Aircraft/Island/Ship/Satellite Intercomparison: Preliminary Results from July 16, 1987

Howard P. Hanson(1), Ken Davidson(2), Herman Gerber(3), Siri Jodha Singh Khalsa(1), Kevin A. Kloesel(4), Ronald Schwiesow(5), Jack B. Snider(6), Bruce M. Wielicki(7), Donald P. Wylie(8)

1. Introduction

The FIRE objective of validating and improving satellite algorithms for inferring cloud properties from satellite radiances was one of the central motivating factors in the design of the specific field experimental strategies used in the July, 1987 marine stratocumulus IFO. The *in situ* measuring platforms were deployed to take maximum advantage of redundant measurements (for intercomparison of the *in situ* sensors) and to provide optimal coverage within satellite images. One of the most ambitious of these strategies was the attempt to coordinate measurements from San Nicolas Island (NSI), the R/V *Pt. Sur*, the meteorological aircraft, and the satellites. For the most part, this attempt was frustrated by flight restrictions in the vicinity of NSI. The exception was the mission of July 16, 1987, which achieved remarkable success in the coordination of the platforms. This talk concerns operations conducted by the NCAR Electra and how data from the Electra can be integrated with and compared to data from the *Pt. Sur*, NSI and the satellites. The focus will be on the large-scale, integrated picture of the conditions on July 16 from the perspective of the Electra's flight operations.

2. Electra operations

The NCAR Electra departed NASNI at 1600Z on 16 July for a planned 5-hour mission in the vicinity of NSI. The flight plan involved a ferry to NSI, descent to 50 m and a 50 m turbulence leg toward the *Pt. Sur*, located approximately 50 km to the WNW (Fig. 1). This was to have been followed by other legs between NSI and the *Pt. Sur* and then a series of legs (nearly) perpendicular to this track. Because of dense clouds near NSI, and the possibility of a very low ceiling in the vicinity of NSI's terrain, the first leg toward the *Pt. Sur* was made at 4600 m for lidar mapping purposes. A descent was made at the *Pt. Sur's* location, the ship was located, and subsequent runs were made according to the original plan. Table I (adapted from the *Summary of Operations and Synoptic Conditions* [FIRE Technical Report No. 1] by Kloesel *et al.*) summarizes the various data legs of the mission; the start and end points refer to those on Fig. 1.

---

(1) Cooperative Institute for Research in Environmental Sciences, University of Colorado/NOAA, Boulder, CO 80309-0449

(2) Department of Meteorology, Naval Postgraduate School, Monterey, CA 93943

(3) Naval Research Laboratory, Washington, D.C. 20375

(4) Department of Meteorology, The Pennsylvania State University, University Park, PA 16802

(5) National Center for Atmospheric Research, Boulder, CO 80303

(6) NOAA Wave Propagation Laboratory, Boulder, CO 80303

(7) NASA Langley Research Center, Hampton, VA 23665

(8) Space Science and Engineering Center, University of Wisconsin-Madison, Madison, WI 53706

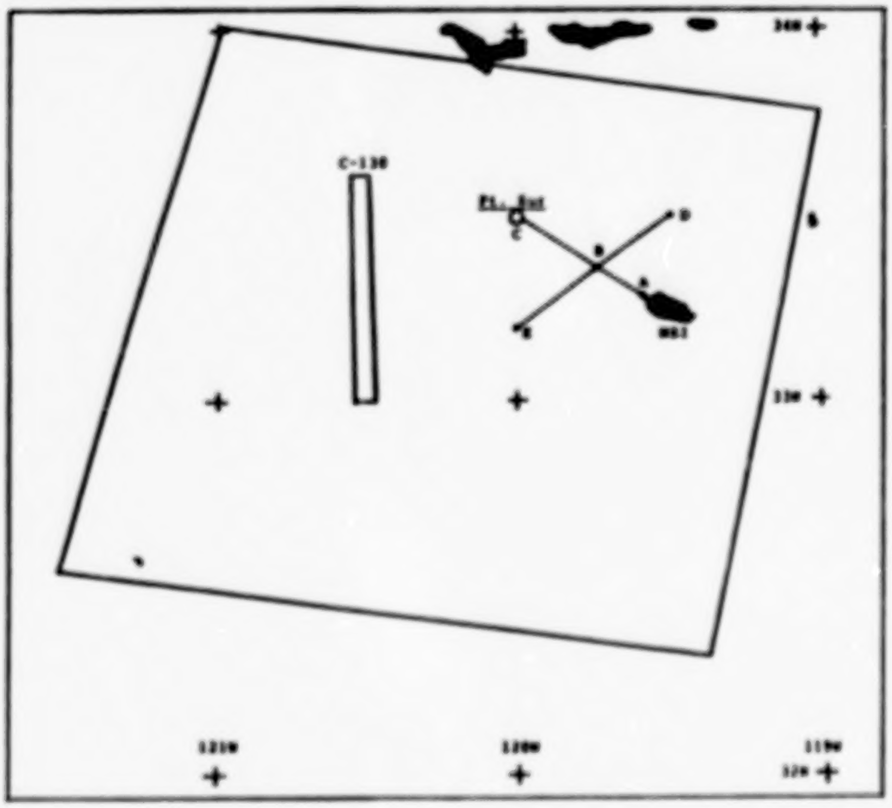

Fig. 1 FIRE-87 IFO, 16 July operations. Shown are the operations areas of the BMO C-130 and the NCAR Electra (among the labeled points). Also shown are the location of the *Pt. Sur* and the area of the LANDSAT scene taken at 1801Z.

The large box in Fig. 1 shows the location of the LANDSAT scene that was taken at 1800Z, when the Electra was in the latter stages of a LIDAR run at 1525 m, near point E. Also shown in Fig. 1 is the location of the operating area of the BMO C-130 during approximately the same time period. In Table 1, the "Porpoise" leg consisted of a sine-wave-like track in the vertical plane with an amplitude of about 150 m, through the cloud top. This was performed for the purpose of obtaining repeated measurements of the inversion strength.

NCAR ELECTRA FLIGHT SUMMARY
16 JULY 1987

Leg Type	Altitude (m)	Start Time (Z)	End Time (Z)	Track (Start-End)
LIDAR	1400	1625	1643	A-C
Sounding	1400-46	1643	1655	C-C
Turbulence	46	1655	1701	C-A
Sounding	Cloud	1704	1717	A-A
Turbulence	640	1717	1724	A-C
Sounding	Cloud	1724	1736	C-C
LIDAR	1370	1736	1741	C-A
LIDAR	1370	1746	1749	A-B
LIDAR	1370	1750	1753	B-D
LIDAR	1525	1756	1804	D-E
Porpoise	Cloud	1804	1817	E-D
Turbulence	610	1819	1829	D-E
Turbulence	490	1831	1840	E-D
Sounding	410-46	1840	1844	D-D
Turbulence	46	1844	1853	D-E
Turbulence	91	1855	1900	E-B
Sounding	91-1615	1900	1911	B-B
LIDAR	1585	1911	1914	B-C
Sounding	1585-46	1914	1922	C-C
Turbulence	91	1930	1940	C-A*
Sounding	91-1525	1943	1951	A-A

* *Pt. Sur* had departed; 8 minutes spent searching, spotting whales and tuna boats.

3. Other data sets

NSI operations

Operations at NSI consisted of two flights of the NRL balloon, five rawinsondes (two of which, at 1600 and 1004Z, are directly relevant to the Electra operations), and the continuous operation of the PSU acoustic and microwave systems, the ERL microwave radiometer, the NPS tower system and the CSU ground station.

Pt. Sur *operations*

The *Pt. Sur* was on station at C until approximately 1900Z. Turbulence measurements were made at the 10-m level, and several radiosondes were released during the time that the Electra was in the vicinity.

Remote sensing

In addition to the LANDSAT image mentioned above (the coverage of which is indicated in Fig. 1), the NASA ER-2 flew over the operations area early in the Electra's mission. GOES data, of course, is available nearly continuously. There was a NOAA-10 overpass at 1648Z.

Synoptic conditions

The ideal scenario for this mission would have been well-established northwesterly flow; in this case, the soundings made from the *Pt. Sur* and NSI would have provided an indication of the advective terms in the thermodynamic and dynamic budgets. However, the winds were relatively light, although generally in the appropriate direction. The cloud structure was quite complex, with multiple layers and breaks during some of the flight legs. Early in the Electra's mision, precipitation was observed.

4. Discussion

The amount of data available for this multiple-platform comparison is daunting, and combining the various data sets into a single coherent picture may not be possible. However, various subsets will lend themselves to valuable intercomparison studies, of relevance both to the FIRE objectives as well as to other scientific issues concerned more with details of stratocumulus convection than satellite validation.

An example of the former includes comparisons of the cloud physics data from the PMS probes obtained during the in-cloud legs with the LIDAR data obtained along the same track (albeit earlier); both of these can be compared to the TMS data from the ER-2 and to the LANDSAT data. The vertical profiles of liquid water obtained by the NRL balloon can be compared to the time series of total integrated liquid water from the ERL microwave radiometer; these, in turn provide the downstream anchor of the Electra's operations area and the Electra data can be used to infer the cloud microphysical properties of the air passingover the Island. Combining the ascents from the *Pt. Sur* and NSI will allow a cross section to be constructed (which the Electra data can fill in) that can be compared to the continuous time series obtained by the acoustic sounder and the profiles on the Island.

Various aspects of these intercomparisons will be discussed in the talk.

Acknowledgments: The research discussed here was supported by the various agencies involved in FIRE; listing them, let alone the individual contracts and grants, would require more space than is reasonably available. Suffice it to say that we are all grateful for our sources of support and that, without them, none of this work would have been possible.

A Preliminary Analysis of LANDSAT and UK C130 Data from Mission 197-A, on 16 July 1987

S Nicholls

Cloud Physics Branch
Meteorological Office, London Road, Bracknell, Berks RG12 2SZ, UK

The co-ordinated LANDSAT-aircraft mission flown on 16 July to the W of San Nicolas Is shows a number of interesting features. There is considerable structure in the Band 4 (0.76-0.90μm) reflectance on km to 10km scales in otherwise complete cloud cover.

In extremely light winds, the C130 performed a series of runs throughout the boundary layer and above for a period of approximately 90 mins on either side of the LANDSAT overpass time. Because of the light winds, the same features can be recognized on the various aircraft penetrations and composited. Futhermore, the accurate renavigation of the aircraft positions enables these to be unambiguously related to the features seen on the LANDSAT image.

Early indications suggest that the reflectance features are related to local thickenings on the cloud layer, associated with slightly deeper convection rising into the overlying stratiform deck. If this is true, then LANDSAT images could possibly be used to remotely infer aspects of the convective regime within the boundary layer.

In addition, the LANDSAT images also display a quasi-linear feature extending for some 50km, although only a km or so wide. This feature was, in fact photographed from the C130 flying just above cloud top and termed a 'cloud-cliff'. It is clearly a rapid and sizeable local change in cloud top height and is therefore presumably a propagating feature. An explanation is still outstanding, but it appears to resemble an undular bore. Further descriptions of this unexpected feature, and its possible origin will be discussed.

FIRE SCIENCE TEAM MEETING
VAIL, COLORADO
JULY 11-15, 1988

MARINE STRATOCUMULUS

==

PANEL DISCUSSION OF MARINE STRAT IFO "NEXT" - David A. Randall Friday, July 15, 1988

==

PAGE

Panel and Audience Discussions ...

AUTHOR INDEX

FIRE SCIENCE TEAM MEETING
VAIL, COLORADO
JULY 11-15, 1988

AUTHOR	EXPERIMENT	SESSION	PAGE
Ackerman, S. A.	Cirrus	Satellite Studies	117
Ackerman, T. P.	Cirrus	Radiative Properties	81
	Cirrus	Radiative Properties	95
	Cirrus	Radiative Properties	99
	Cirrus	Poster Session	***
	Marine Strat	Poster Session	409
Albrecht, B. A.	Marine Strat	Thermodynamic & Dynamic Properties	335
	Marine Strat	Thermodynamic & Dynamic Properties	337
Alvarez, J. M.	Cirrus	Lidar/Radiative Properties/Microphysical	47
	Cirrus	Satellite Studies	147
	Cirrus	Case Study of October 27-28, 1986	157
	Cirrus	Poster Session	175
Arduini, R. F.	Cirrus	Case Study of October 27-28, 1986	163
	Cirrus	Poster Session	***
Arking, A.	Cirrus	Poster Session	193
Austin, P. H.	Marine Strat	Thermodynamic & Dynamic Properties	339
	Marine Strat	Case Studies	425
	Marine Strat	Case Studies	429
Baker, M. B.	Marine Strat	Large Scale Environment & Modeling	231
Barlow, R.	Marine Strat	Large Scale Environment & Modeling	229
	Marine Strat	Thermodynamic & Dynamic Properties	365
Betts, A. K.	Marine Strat	Large Scale Environment & Modeling	213
	Marine Strat	Large Scale Environment & Modeling	225
	Marine Strat	Thermodynamic & Dynamic Properties	339
	Marine Strat	Case Studies	429
Blaskovic, M.	Marine Strat	Large Scale Environment & Modeling	215
Boers, R.	Marine Strat	Thermodynamic & Dynamic Properties	339
	Marine Strat	Poster Session	375
	Marine Strat	Case Studies	425
	Marine Strat	Case Studies	429
Brandeki, S.	Marine Strat	Lidar/Radiative Properties/Microphysical	299
Brest, C.	Cirrus	Satellite Studies	141

AUTHOR INDEX

FIRE SCIENCE TEAM MEETING
VAIL, COLORADO
JULY 11-15, 1988

AUTHOR	EXPERIMENT	SESSION	PAGE
Bretheron, C. S.	Marine Strat	Large Scale Environment & Modeling	231
Cahalan, R. F.	Marine Strat	Satellite Studies	253
Charlson, R. J.	Marine Strat	Poster Session	403
Chen, D. W.	Marine Strat	Satellite Studies	277
Childs, J. D.	Cirrus	Poster Session	193
Chung, H.	Cirrus	Satellite Studies	117
Ciesielski, P. E.	Cirrus	Large Scale Environment & Modeling	29
	Cirrus	Poster Session	***
	Marine Strat	Large Scale Environment & Modeling	221
Clarke, A. D.	Marine Strat	Poster Session	403
Coakley, Jr., J. A.	Marine Strat	Satellite Studies	259
	Marine Strat	Poster Session	377
Consterdine, I.	Marine Strat	Lidar/Radiative Properties/Microphysical	299
Cox, S. K.	Cirrus	Satellite Studies	117
	Cirrus	Case Study of October 27-28, 1986	159
	Cirrus	Poster Session	183
	Cirrus	Poster Session	***
	Marine Strat	Large Scale Environment & Modeling	221
	Marine Strat	Thermodynamic & Dynamic Properties	34[illegible]
	Marine Strat	Poster Session	417
	Marine Strat	Poster Session	***
Davidson, K.	Marine Strat	Case Studies	433
Davies, R.	Marine Strat	Large Scale Environment & Modeling	215
Desbois, M.	Marine Strat	Satellite Studies	271
Dodd, G. C.	Cirrus	Large Scale Environment & Modeling	25
	Cirrus	Radiative Properties	85
Draine, B. T.	Cirrus	Radiative Properties	75
Dubinsky, R.	Cirrus	Poster Session	175

AUTHOR INDEX

FIRE SCIENCE TEAM MEETING
VAIL, COLORADO
JULY 11-15, 1988

AUTHOR	EXPERIMENT	SESSION	PAGE
Duda, D. P.	Marine Strat	Poster Session	***
	Marine Strat	Thermodynamic & Dynamic Properties	341
Durkee, P. A.	Marine Strat	Satellite Studies	265
	Marine Strat	Poster Session	***
Eloranta, E. W.	Cirrus	Lidar/Radiative Properties/Microphysical	49
	Cirrus	Poster Session	177
Fairall, C. W.	Marine Strat	Radiative Properties	307
	Marine Strat	Thermodynamic & Dynamic Properties	337
	Marine Strat	Thermodynamic & Dynamic Properties	371
Flatau, P.	Cirrus	Radiative Properties	75
Foot, J. S.	Marine Strat	Poster Session	383
Frei, A.	Cirrus	Radiative Properties	105
	Cirrus	Poster Session	***
	Marine Strat	Poster Session	397
Frey, R.	Cirrus	Satellite Studies	135
Frouin, R.	Cirrus	Satellite Studies	141
Fuller, W. H.	Cirrus	Poster Session	175
Gathman, S.	Marine Strat	Lidar/Radiative Properties/Microphysical	299
Gautier, C.	Cirrus	Satellite Studies	141
	Marine Strat	Large Scale Environment & Modeling	237
	Marine Strat	Poster Session	***
Gerber, H.	Marine Strat	Lidar/Radiative Properties/Microphysical	299
	Marine Strat	Case Studies	433
Gibson, G. G.	Cirrus	Satellite Studies	123
Glover, V.	Cirrus	Poster Session	183
Gore, W. J. Y.	Cirrus	Radiative Properties	95
	Marine Strat	Poster Session	409
Grams, G.	Cirrus	Poster Session	191

AUTHOR INDEX

FIRE SCIENCE TEAM MEETING
VAIL, COLORADO
JULY 11-15, 1988

AUTHOR	EXPERIMENT	SESSION	PAGE
Griffin, M. K.	Cirrus	Radiative Properties	85
Grimm, P.	Marine Strat	Large Scale Environment & Modeling	207
Grund, C. J.	Cirrus	Lidar/Radiative Properties/Microphysical	49
	Cirrus	Case Study of October 27-28, 1986	157
	Cirrus	Poster Session	177
	Cirrus	Poster Session	***
	Cirrus	Poster Session	***
Guinn, P. A.	Marine Strat	Large Scale Environment & Modeling	221
	Marine Strat	Thermodynamic & Dynamic Properties	341
Gultepe, I.	Cirrus	Lidar/Radiative Properties/Microphysical	67
Gupta, S. K.	Cirrus	Satellite Studies	123
Haack, T.	Marine Strat	Thermodynamic & Dynamic Properties	367
Hahn, C. J.	Cirrus	Large Scale Environment & Modeling	19
Hall, F. F.	Cirrus	Case Study of October 27-28, 1986	157
Hammer, P. D.	Marine Strat	Poster Session	409
Hanson, H. P.	Marine Strat	Poster Session	393
	Marine Strat	Case Studies	433
Harrison, E. F.	Cirrus	Satellite Studies	123
	Cirrus	Satellite Studies	129
	Cirrus	Poster Session	***
	Marine Strat	Large Scale Environment & Modeling	201
	Marine Strat	Satellite Studies	279
	Marine Strat	Poster Session	***
Heck, P. W.	Cirrus	Satellite Studies	123
	Cirrus	Satellite Studies	129
	Cirrus	Satellite Studies	147
	Cirrus	Poster Session	***
Hein, P.	Cirrus	Case Study of October 27-28, 1986	159
	Cirrus	Poster Session	***
Herman, L.	Cirrus	Satellite Studies	117

AUTHOR INDEX

FIRE SCIENCE TEAM MEETING
VAIL, COLORADO
JULY 11-15, 1988

AUTHOR	EXPERIMENT	SESSION	PAGE
Heymsfield, A. J.	Cirrus	Lidar/Radiative Properties/Microphysical	55
	Cirrus	Lidar/Radiative Properties/Microphysical	61
	Cirrus	Lidar/Radiative Properties/Microphysical	67
	Cirrus	Radiative Properties	81
	Cirrus	Radiative Properties	99
	Cirrus	Case Study of October 27-28, 1986	163
	Cirrus	Poster Session	***
	Cirrus	Poster Session	***
Hignett, P.	Marine Strat	Thermodynamic & Dynamic Properties	357
	Marine Strat	Poster Session	***
Hinton, B.	Marine Strat	Large Scale Environment & Modeling	207
Hobbs, P. V.	Marine Strat	Lidar/Radiative Properties/Microphysical	291
	Marine Strat	Radiative Properties	319
	Marine Strat	Poster Session	***
Holben, B. N.	Cirrus	Satellite Studies	141
Howell, H. B.	Cirrus	Radiative Properties	89
Hudson, J. G.	Marine Strat	Lidar/Radiative Properties/Microphysical	287
Hunt, W. H.	Cirrus	Lidar/Radiative Properties/Microphysical	47
	Cirrus	Poster Session	175
Iascone, D.	Cirrus	Large Scale Environment & Modeling	35
James J.	Marine Strat	Lidar/Radiative Properties/Microphysical	299
Jensen, D.	Marine Strat	Thermodynamic & Dynamic Properties	359
Jensen, J. B.	Marine Strat	Radiative Properties	313
Johnson-Pasqua, C.	Marine Strat	Thermodynamic & Dynamic Properties	341
	Marine Strat	Poster Session	417
	Marine Strat	Poster Session	***
Kaufman, Y. J.	Cirrus	Satellite Studies	141
Kent, G.	Cirrus	Poster Session	175

AUTHOR INDEX

FIRE SCIENCE TEAM MEETING
VAIL, COLORADO
JULY 11-15, 1988

AUTHOR	EXPERIMENT	SESSION	PAGE
Khalsa, S. J. S.	Marine Strat	Large Scale Environment & Modeling	237
	Marine Strat	Poster Session	***
	Marine Strat	Case Studies	433
King, M. D.	Marine Strat	Radiative Properties	319
	Marine Strat	Radiative Properties	327
	Marine Strat	Poster Session	***
Kinne, S. A.	Cirrus	Radiative Properties	81
	Cirrus	Radiative Properties	99
	Cirrus	Poster Session	***
Kloesel, K. A.	Marine Strat	Large Scale Environment & Modeling	207
	Marine Strat	Thermodynamic & Dynamic Properties	335
	Marine Strat	Case Studies	433
Knight, N. C.	Cirrus	Lidar/Radiative Properties/Microphysical	55
	Cirrus	Lidar/Radiative Properties/Microphysical	61
Kukla, G.	Cirrus	Poster Session	***
	Marine Strat	Poster Session	397
LeCroy, S. R.	Cirrus	Satellite Studies	141
	Cirrus	Case Study of October 27-28, 1986	169
	Cirrus	Poster Session	***
Leighton, J.	Marine Strat	Thermodynamic & Dynamic Properties	365
Lenschow, D. H.	Marine Strat	Radiative Properties	307
Levin, R.	Cirrus	Satellite Studies	141
Lin, M. -X.	Cirrus	Radiative Properties	89
Liou, K. N.	Cirrus	Radiative Properties	111
London, J.	Cirrus	Large Scale Environment & Modeling	19
Lyons, J. H.	Marine Strat	Lidar/Radiative Properties/Microphysical	291
McCormick, M. P.	Cirrus	Lidar/Radiative Properties/Microphysical	47
	Cirrus	Poster Session	175
McKee, T. B.	Marine Strat	Large Scale Environment & Modeling	221

AUTHOR INDEX

FIRE SCIENCE TEAM MEETING
VAIL, COLORADO
JULY 11-15, 1988

AUTHOR	EXPERIMENT	SESSION	PAGE
Merritt, J.	Cirrus	Poster Session	193
Mineart, G. M.	Marine Strat	Satellite Studies	265
	Marine Strat	Poster Session	***
Minnis, P.	Cirrus	Radiative Properties	111
	Cirrus	Satellite Studies	123
	Cirrus	Satellite Studies	129
	Cirrus	Satellite Studies	147
	Cirrus	Poster Session	***
	Marine Strat	Large Scale Environment & Modeling	201
	Marine Strat	Satellite Studies	279
	Marine Strat	Poster Session	***
Moeng, C. H.	Marine Strat	Large Scale Environment & Modeling	249
Moore, J. D.	Cirrus	Lidar/Radiative Properties/Microphysical	47
Moyer, K. A.	Marine Strat	Thermodynamic & Dynamic Properties	335
Nakajima, T.	Marine Strat	Radiative Properties	319
	Marine Strat	Radiative Properties	327
	Marine Strat	Poster Session	***
Nicholls, S.	Marine Strat	Large Scale Environment & Modeling	229
	Marine Strat	Thermodynamic & Dynamic Properties	365
	Marine Strat	Case Studies	437
Nucciarone, J. J.	Marine Strat	Thermodynamic & Dynamic Properties	335
Olsen, L. M.	Cirrus	Large Scale Environment & Modeling	35
	Cirrus	Poster Session	***
Parker, L.	Cirrus	Case Study of October 27-28, 1986	163
	Cirrus	Poster Session	***
Patterson, E.	Cirrus	Poster Session	191
Poole, B. D.	Cirrus	Lidar/Radiative Properties/Microphysical	47
Poole, L. R.	Cirrus	Lidar/Radiative Properties/Microphysical	47
	Cirrus	Case Study of October 27-28, 1986	169
	Cirrus	Poster Session	***
Rabadi, R.	Marine Strat	Radiative Properties	307

AUTHOR INDEX

FIRE SCIENCE TEAM MEETING
VAIL, COLORADO
JULY 11-15, 1988

AUTHOR	EXPERIMENT	SESSION	PAGE
Radke, L. F.	Marine Strat	Lidar/Radiative Properties/Microphysical	291
	Marine Strat	Radiative Properties	319
	Marine Strat	Poster Session	403
	Marine Strat	Poster Session	***
Randall, D. A.	Cirrus	Large Scale Environment & Modeling	39
	Marine Strat	Large Scale Environment & Modeling	243
Reph, M. G.	Cirrus	Large Scale Environment & Modeling	35
Revercomb, H. E.	Cirrus	Radiative Properties	89
Ridgway, W.	Marine Strat	Large Scale Environment & Modeling	225
Robinson, D. A.	Cirrus	Radiative Properties	105
	Cirrus	Case Study of October 27-28, 1986	169
	Cirrus	Poster Session	***
	Cirrus	Poster Session	***
	Marine Strat	Poster Session	397
Rossow, W. B.	Cirrus	Large Scale Environment & Modeling	17
	Cirrus	Satellite Studies	141
Rouse, B. R.	Cirrus	Lidar/Radiative Properties/Microphysical	47
	Cirrus	Poster Session	175
Sassen, K.	Cirrus	Large Scale Environment & Modeling	25
	Cirrus	Lidar/Radiative Properties/Microphysical	55
	Cirrus	Lidar/Radiative Properties/Microphysical	61
	Cirrus	Radiative Properties	85
	Cirrus	Satellite Studies	147
	Cirrus	Case Study of October 27-28, 1986	157
Schlesinger, M.	Cirrus	Large Scale Environment & Modeling	***
Schubert, W. H.	Marine Strat	Large Scale Environment & Modeling	221
	Marine Strat	Thermodynamic & Dynamic Properties	337
	Marine Strat	Thermodynamic & Dynamic Properties	341
	Marine Strat	Poster Session	***
Schmidt, E.	Cirrus	Poster Session	191
Schwiesow, R.	Marine Strat	Case Studies	433
Sengupta, S. K.	Marine Strat	Satellite Studies	277

AUTHOR INDEX

FIRE SCIENCE TEAM MEETING
VAIL, COLORADO
JULY 11-15, 1988

AUTHOR	EXPERIMENT	SESSION	PAGE
Seze, G.	Marine Strat	Satellite Studies	271
Shirer, H. N.	Marine Strat	Thermodynamic & Dynamic Properties	367
Siems, S. T.	Marine Strat	Large Scale Environment & Modeling	231
Slater, P. N.	Cirrus	Satellite Studies	141
Slingo, A.	Marine Strat	Large Scale Environment & Modeling	227
Smith, G.	Cirrus	Satellite Studies	141
Smith, L.	Marine Strat	Satellite Studies	271
Smith, M.	Marine Strat	Lidar/Radiative Properties/Microphysical	299
Smith, W. L.	Cirrus	Radiative Properties	89
	Cirrus	Satellite Studies	117
	Cirrus	Satellite Studies	135
Smith, Jr., W. L.	Cirrus	Case Study of October 27-28, 1986	159
	Cirrus	Poster Session	183
	Cirrus	Poster Session	***
Snider, J. B.	Marine Strat	Lidar/Radiative Properties/Microphysical	295
	Marine Strat	Radiative Properties	307
	Marine Strat	Thermodynamic & Dynamic Properties	337
	Marine Strat	Thermodynamic & Dynamic Properties	341
	Marine Strat	Poster Session	377
	Marine Strat	Poster Session	***
	Marine Strat	Case Studies	433
Spinhirne, J. D.	Cirrus	Radiative Properties	101
	Cirrus	Case Study of October 27-28, 1986	163
	Cirrus	Poster Session	***
	Cirrus	Poster Session	***
	Marine Strat	Poster Session	375
	Marine Strat	Poster Session	***
Starr, D. O'C	Cirrus	Large Scale Environment & Modeling	3
	Cirrus	Large Scale Environment & Modeling	25
	Cirrus	Case Study of October 27-28, 1986	155
Staylor, W. F.	Cirrus	Satellite Studies	141

AUTHOR INDEX

FIRE SCIENCE TEAM MEETING
VAIL, COLORADO
JULY 11-15, 1988

AUTHOR	EXPERIMENT	SESSION	PAGE
Stephens, G. L.	Cirrus	Radiative Properties	75
Stevens, D. E.	Cirrus	Large Scale Environment & Modeling	29
	Cirrus	Poster Session	***
Suttles, J. T.	Cirrus	Satellite Studies	141
	Cirrus	Case Study of October 27-28, 1986	163
	Cirrus	Poster Session	***
Syrett, W. J.	Marine Strat	Thermodynamic & Dynamic Properties	337
	Marine Strat	Thermodynamic & Dynamic Properties	371
Takano, Y.	Cirrus	Radiative Properties	111
Teillet, P. M.	Cirrus	Satellite Studies	141
Thomson, D. W.	Marine Strat	Thermodynamic & Dynamic Properties	371
Twohy, C. H.	Marine Strat	Poster Session	403
Uthe, E.	Cirrus	Poster Session	***
	Cirrus	Poster Session	***
Valero, F. P. J.	Cirrus	Radiative Properties	95
	Cirrus	Radiative Properties	99
	Marine Strat	Poster Session	409
Vaughn, M. A.	Cirrus	Poster Session	175
Vonder Haar, T. H.	Marine Strat	Poster Session	411
Warren, S. G.	Cirrus	Large Scale Environment & Modeling	19
	Marine Strat	Poster Session	403
Weil, M. L.	Marine Strat	Poster Session	409
Welch, R. M.	Cirrus	Case Study of October 27-28, 1986	163
	Cirrus	Poster Session	***
	Marine Strat	Satellite Studies	277
White, A. B.	Marine Strat	Thermodynamic & Dynamic Properties	371
Whitlock, C. H.	Cirrus	Satellite Studies	141
	Cirrus	Case Study of October 27-28, 1986	169
	Cirrus	Poster Session	***

AUTHOR INDEX

FIRE SCIENCE TEAM MEETING
VAIL, COLORADO
JULY 11-15, 1988

AUTHOR	EXPERIMENT	SESSION	PAGE
Wielicki, B. A.	Cirrus	Satellite Studies	123
	Cirrus	Case Study of October 27-28, 1986	163
	Cirrus	Poster Session	***
	Marine Strat	Case Studies	433
Williams, S. L.	Cirrus	Poster Session	193
Wylie, D. P.	Cirrus	Large Scale Environment & Modeling	3
	Cirrus	Large Scale Environment & Modeling	11
	Cirrus	Satellite Studies	117
	Cirrus	Case Study of October 27-28, 1986	155
	Cirrus	Poster Session	187
	Marine Strat	Large Scale Environment & Modeling	207
	Marine Strat	Case Studies	433
Young, D. F.	Cirrus	Satellite Studies	123
	Cirrus	Satellite Studies	129
	Cirrus	Satellite Studies	147
	Marine Strat	Large Scale Environment & Modeling	201
	Marine Strat	Satellite Studies	279
	Marine Strat	Poster Session	***
Young, G.	Marine Strat	Thermodynamic & Dynamic Properties	335

NASA
National Aeronautics and Space Administration

Report Documentation Page

1. Report No. NASA CP-3083	2. Government Accession No.	3. Recipient's Catalog No.

4. Title and Subtitle FIRE Science Results 1988	5. Report Date July 1990 6. Performing Organization Code
7. Author(s) David S. McDougal and H. Scott Wagner, Editors	8. Performing Organization Report No. L-16814 10. Work Unit No. 672-22-10-70
9. Performing Organization Name and Address NASA Langley Research Center Hampton, VA 23665-5225	11. Contract or Grant No.
12. Sponsoring Agency Name and Address National Aeronautics and Space Administration Washington, DC 20546-0001	13. Type of Report and Period Covered Conference Publication 14. Sponsoring Agency Code

15. Supplementary Notes

Presented at the FIRE Science Team Workshop, Vail, Colorado, July 11-15, 1988. Co-sponsored by National Science Foundation, Office of Naval Research, Department of Energy, Air Force Geophysical Laboratory, and National Oceanic and Atmospheric Administration.

16. Abstract

FIRE (First ISCCP Regional Experiment) is a U.S. cloud-radiation research program that seeks to address the issues of basic understanding and parameterizations of cirrus and marine stratocumulus cloud systems and ISCCP data products. A FIRE Science Team Workshop was held in Vail, Colorado, July 11-15, 1988, to present results of research in progress from the first 4 years of FIRE and to refine the research goals and priorities for the next 3 to 5 years.

This Conference Publication contains the full text of the papers presented at the FIRE Science Team Workshop. The papers describe research analyses of data collected at the 1986 Cirrus Intensive Field Observations (IFO), the 1987 Marine Stratocumulus IFO, and the Extended Time Observations. The papers have been grouped into sessions on Satellite Studies, Lidar/Radiative Properties/Microphysical Studies, Radiative Properties, Thermodynamic and Dynamic Properties, Case Studies, and Large Scale Environment and Modeling Studies.

17. Key Words (Suggested by Author(s)) FIRE ISCCP Cloud-Radiation Cirrus Marine Stratocumulus	18. Distribution Statement Unclassified - Unlimited Subject Category - 47

19. Security Classif. (of this report) Unclassified	20. Security Classif. (of this page) Unclassified	21. No. of pages 466	22. Price A20

NASA FORM 1626 OCT 86

452

For sale by the National Technical Information Service, Springfield, Virginia 22161-2171